Universitat Politècnica de Catalunya
Departament de Física i Enginyeria Nuclear

Accretion onto Neutron Stars: Hydrodynamics and Nucleosynthesis

by

Fermín Moreno

A thesis submitted for the degree of

Doctor in Phylosophy

Advisor: Jordi José

Barcelona, July 2009

A mi familia

Agradecimientos

Muchas han sido las personas que se han cruzado en mi camino durante los años que ha durado esta aventura. Mencionarlas a todas resultaría inviable, pero no cabe duda que la huella de cada una se encuentra, de algún modo, reflejada en esta tesis doctoral.

En primer lugar, quiero agradecerle a mi tutor, Dr. Jordi José, el haberme dado la oportunidad de realizar la tesis junto a él. Desde el principio comprendió, y respetó, la dificultad de compatibilizar mi horario laboral con el de la tesis. Su ayuda, paciencia y supervisión han sido imprescindibles en la realización de este trabajo.

También quiero agradecerle al Prof. Jordi Isern, director de l'Institut d'Estudis Espacials de Catalunya (IEEC), permitirme realizar la tesis en la institución que dirige. Gracias también a la Prof. Margarita Hernanz por su cálido recibimiento en esta institución y su ayuda en los primeros años de doctorado. Darle las gracias al personal administrativo, Anna Bertolín, Mireia Español, Isabel Moltó, Pilar Montes y Eva Notario, por haberme ayudado a compatibilizar mi disponibilidad horaria con los recursos del IEEC. Mención a parte para el administrador de sistemas, Dr. Josep Guerrero, por su inestimable ayuda en el entorno Linux y por haber tenido, siempre, una solución a los problemas informáticos que le he propuesto. Gracias a todos los compañeros que he tenido en el IEEC. A la Dra. Glòria Sala y al Dr. Carles Badenes, ellos fueron los primeros; con ellos compartí los primeros 'Nexus Club' de los viernes. Después vinieron la Dra. Alina Hirschmann, la Dra. Silvia Catalán, el Dr. Miquel Nofrarias, Pep Colomé, y tantos otros, gracias por los ánimos y los buenos momentos.

Agradecer también al Prof. Enrique García-Berro, vice-rector de la Universitat Politècnica de Catalunya (UPC) y director del Grup d'Astrofísica i Astronomia, por haberme permitido formar parte de este magnífico grupo investigador. Gracias también al Prof. Josep Lluís Tamarit, director del Departament de Física i Enginyeria Nuclear de la UPC, y a sus predecesores en estos años, por darme la oportunidad de realizar los últimos años de esta tesis en el magnífico edificio de la Escola Universitària d'Enginyeria Tècnica Industrial de Barcelona (EUETIB). También gracias a Silvia Soriano y Esther Cantos por la ayuda en la parte administrativa.

El traslado a la EUETIB significó un punto de inflexión en la realización de este trabajo, el principio del fin. Aquí he tenido la gran suerte de conocer a Jordi Casanova, mi último compañero de tesis. Su optimismo y energía fueron un revulsivo que llegó cuando más lo necesitaba. Junto a él, he tenido el honor de conocer al Dr. Anuj Parikh, cuya aportación a la parte de nucleosíntesis de esta tesis ha sido determinante. Gracias por tantos momentos felices. Siempre nos quedará el Josep's

bar.

Agradezco al Dr. Alain Coc y a la Dra. Inma Domínguez su disponibilidad para evaluar esta tesis en calidad de referees externos.

Gracias también al Dr. Domingo García. No sólo porque fue la primera persona con la que contacté cuando decidí embarcarme en esta aventura, y quien me puso en contacto con mi tutor, sino también por su explicaciones sobre ecuaciones de estado durante los primeros años de doctorado. También gracias a Rubén Cabezón, por tener siempre una sonrisa y compartir conmigo estas últimas pedaladas de la carrera. También agradecer a Jose Antonio Escartín su ayuda cuando se rozó la tragedia por culpa del disco duro de mi portátil y al Dr. Simon W. Campbell por darme siempre ánimos en los últimos tramos de esta tesis.

También guardo un recuerdo especial para mis ex-compañeros del colegio San José Obrero. Junto a ellos descubrí la belleza de la importante labor docente. Gracias por estos días azules y este sol de la infancia.

Quiero también agradecer a todos mis compañeros del Cos de Mossos d'Esquadra su apoyo, ánimo y comprensión, en la compatibilidad de mi trabajo con esta tesis. Al cabo Sergio Domenech y al cabo Juan Carlos Nievas, gracias por aguantar mis reflexiones sobre lo humano y lo divino. Ahora ya sabéis por qué el cielo es azul.

Para finalizar, quiero darle las gracias a mi familia. A mis padres les debo todo lo que soy, ellos han sido mi referente. Gracias por los valores que me habéis dado. También darle las gracias a mi hermana, por creer siempre en mí. Gracias a Susana, mi mujer, su amor incondicional y comprensión en los momentos más difíciles han sido el óxigeno necesario para llegar hasta el final. Mención especial para mis hijos, Óscar, Elena y Laura, ellos son lo mejor que me ha pasado, las estrellas que iluminan mi camino.

Rompo este huevo y nace la mujer y nace el hombre. Y juntos vivirán y morirán. Pero nacerán nuevamente. Nacerán y volverán a morir y otra vez nacerán. Y nunca dejarán de nacer porque la muerte es mentira.

Eduardo Galeano
Memoria del fuego I (1983)

Contents

Chapter 1

Introduction

1.1 Discovery and pioneering models of X-ray bursts

Type I X-ray bursts (hereafter, XRBs) were serendipitously discovered in 1975, independently by Belian et al. (1976) and Grindlay et al. (1976), as bright sources in the X-ray band of the electromagnetic spectrum, which can only be observed out of the Earth's atmosphere. The two bursting episodes reported by Grindlay et al. were based on observations performed with the *Astronomical Netherlands Satellite* (ANS) onto a previously known X-ray source, 3U 1820-30, located in the globular cluster NGC 6624. Similar events were reported by Belian et al., from X-ray observations of sources of the Norma constellation, performed with two *Vela-5* satellites, covering the 15-month period from May 1969 to August 1970. One year later, three additional bursting sources, one of them, the enigmatic *Rapid Burster* (MXB 1730-335), were identified within a few degrees of the Galactic center (Lewin et al. 1976a,b). Within a year, 20 additional burst sources were discovered, mainly by SAS-3 and OSO-8 satellites. To date, about 90 Galactic X-ray burst sources have been discovered (see Liu et al. 2007, and in 't Zand et al. 2009) among the approximately 187 known *low-mass X-ray binaries*[1] (LMXBs).

Since the 70s, when nuclear instabilities associated with mass-accretion onto neutron stars (NS) were first noted by Hansen & Van Horn (1975), various mechanisms have been proposed to account for the origin of XRBs. In particular, Maraschi & Cavaliere (1977), and independently, Woosley & Taam (1976), were the first to suggest that nuclear shell flashes in the accreted hydrogen- (H) and/or helium-rich (He) envelopes of neutron stars in *low mass X-ray binaries* were at the origin of such cataclysmic events, an idea inspired by the fact that a neutron star envelope may undergo thermal instabilities because of its high electron degeneracy, the thinness of the nuclear burning shell, and the highly temperature-dependent nuclear reaction

[1] Bright X-ray sources ($> 10^{34}\, erg\, s^{-1}$) formed by an accreting neutron star and a low-mass, stellar companion.

rates. However, it was soon realized that the quick succession of flashes exhibited by the Rapid Burster (with recurrence times as short as ∼10 sec), didn't match the general pattern shown by the majority of bursting sources. A major breakthrough for the understanding of the nature of these cataclysmic events was the discovery of two different kinds of bursts associated with the Rapid Burster (Hoffman et al. 1978): a classification of type I and type II bursts was then established, the former associated with thermonuclear flashes, the later linked to accretion instabilities.

In this Thesis, we will focus on type I X-ray bursts, the most frequent type of thermonuclear stellar explosion in the Galaxy (and the third, in terms of total energy output after supernovae and classical novae).

1.2 Type I X-ray bursts

The first evidence of the thermonuclear origin of type I XRBs came from light curve analysis, in particular, the ratio between time-integrated persistent and burst fluxes, α. It was soon realized that the ratio between the gravitational potential energy released by the matter falling onto a neutron star during the accretion stage ($G.M_{NS}/R_{NS} \sim 200$ MeV/nucleon) and the nuclear energy liberated during the burst (~ 5 MeV/nucleon, for a solar mixture transformed into Fe-group nuclei), matches the values inferred for α, in the range ~ 40 - 100.

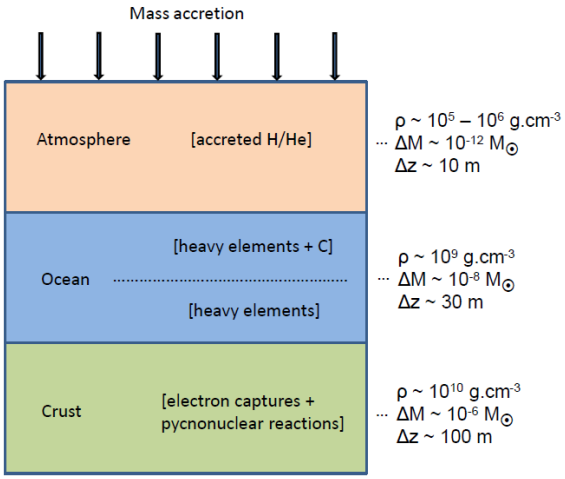

Figure 1.1: Structure of the outer layers of a neutron star.

Hence, the mechanism that powers these bursting episodes is likely driven by the transfer of H/He-rich nuclear fuel from the stellar companion (typically, a faint, low-mass Main Sequence or evolved star with $M < 1$ M$_\odot$, filling its Roche lobe), which, due to angular momentum conservation, ends up forming an accretion disk

that surrounds the neutron star. Ultimately, a fraction of this material spirals in and impacts onto the surface of the neutron star, where it progressively accumulates. This piling up of matter causes a temperature increase, which under the degenerate conditions governing the accreted envelope, drive a violent thermonuclear runaway (TNR). During an XRB, the envelope material is exposed to peak temperatures in the range $(1-2) \times 10^9$ K, and hence, it undergoes severe nuclear processing.

Observationally, this is characterized by a sudden rise in the X-ray luminosity within a few seconds, reaching $L_{peak} \sim 10^{38} - 10^{39}\ erg.s^{-1}$, decaying in a timescale of about 10-100 sec (see Table 1.1, and Fig. 1.2), with a cooling tail shorter at higher energies (Fig. 1.4), and eventually recurring, as accretion resumes, within hours to days. Although the energy released by thermonuclear fusion during an XRB is, as mentioned, only a few MeV per nucleon, the nuclear luminosity can dominate the accretion luminosity for a brief period of time, provided that the nuclear fuel piles up and burns rapidly.

The spatial distribution of type I XRBs matches that of LMXBs, with a clear concentration towards the Galactic center (Galloway et al. 2008). A significant fraction of XRBs is indeed found in globular clusters. This pattern suggests that they consist of old population stars (Lewin et al. 1993). Recently, the first extragalactic XRBs have been discovered in two globular cluster source candidates of the Andromeda galaxy, M31 (see Pietsch & Haberl 2005). Typically, XRB sources have orbital periods ranging from 1 - 15 hours (White et al. 1995).

Table 1.1: Observational classification of X-ray bursts (adapted from Keek et al. 2008, and in 't Zand et al. 2009).

	Normal	Intermediate duration	Superburst
Duration	10 – 100 sec	10^3 sec	10^4 sec
Energy released	10^{39} erg	10^{40} – 10^{41} erg	10^{42} erg
Recurrence time	hours – days	days – months	$\sim$ 1 yr
Fuel	He / H + He	He	C-mixture / pure C
Number observed	1000s	$\sim$ 20	15
Known sources	$\sim$ 90	8	10
Frequency per yr in the Galaxy	10000	100	20

The fact that XRB sources never exhibit X-ray pulsations suggests that the underlying neutron stars have weak magnetic fields ($< 10^{11}$ G). Indeed, pulsations are thought to result from misalignment between the magnetic dipole axis and the rotation axis of the neutron star. Moreover, it is unlikely that XRBs will show up from highly magnetized neutron stars, as a strong magnetic field would funnel the infalling charged plasma towards a small fraction of the neutron star surface, close to the magnetic cups; the effective accretion rate (per unit area) would be so high, that TNRs will likely be inhibited (Joss 1978, Taam & Picklum 1978).

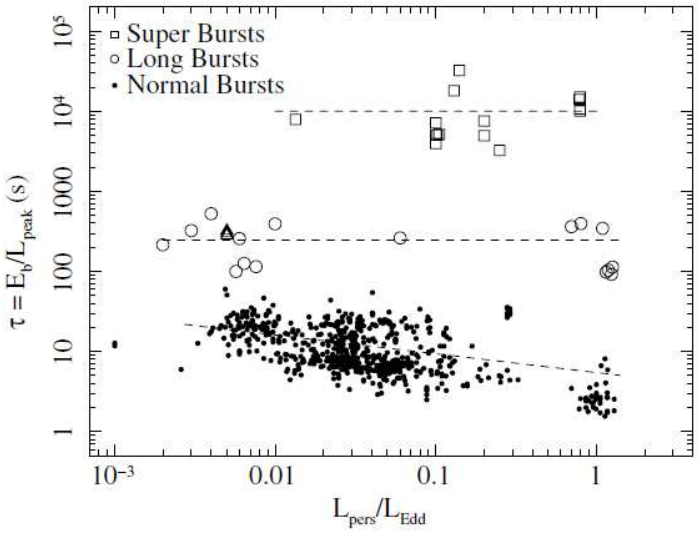

Figure 1.2: Burst durations vs. persistent luminosities for normal type I X-ray bursts (observed with RXTE), intermediate-long bursts, and Superbursts (from Falanga et al. 2008).

The physical properties of XRBs depend mainly on the energy flux outcoming from the neutron star interior, the surface gravity, the metallicity[2] of the accreted matter, as well as the mass-accretion rate (the later determining the ignition regime; see Table 1.2, and Fig. 1.3). For high enough temperatures, stable burning of both hydrogen and helium takes place when matter is piled up on top of the neutron star at high mass-accretion rates ($\geq \dot{M}_{Edd}$, where $\dot{M}_{Edd}$ is the Eddington mass-accretion rate, $\sim 1.7 \times 10^{-8}\, M_{\odot}.yr^{-1}$, for a solar-composition, Thomson scattering-dominated atmosphere). Below this regime, H and He-burning proceeds under high electron degeneracy conditions, making it thermally unstable. In this scenario, three different regimes can be distinguished as a function of the mass-accretion rate (see Taam 1985, and Bildsten 1997, 2000, for details). This is summarized in Table 1.2, where the specific transition $\dot{M}$ correspond to $Z_{CNO} = 0.01$. The values for lower metallicities are smaller, while the window to achieve pure He-ignition becomes narrower.

[2]It has been proposed that during matter infall from the accretion disk onto the neutron star surface, elements heavier than He can be eventually destroyed, via spallation processes, if the stream of matter possesses a significant radial component. In this scenario, the accreted material would be severely depleted in CNO-group nuclei (see Bildsten et al. 1992, for details).

Table 1.2: Nuclear burning regimes at high accretion rates (Bildsten 2000).

Mass-accretion rate ($M_{\odot}.yr^{-1}$)	Burning regime
$\dot{M} < 2 \times 10^{-10}$	Mixed H/He burning triggered by thermally unstable hydrogen ignition
$2 \times 10^{-10} < \dot{M} < (4.4 - 11.1) \times 10^{-10}$	Thermally unstable, pure helium ignition after complete hydrogen burning
$(4.4 - 11.1) \times 10^{-10} < \dot{M} < 2 \times 10^{-8}$	Mixed H/He burning triggered by thermally unstable helium ignition
$\dot{M} > 2 \times 10^{-8}$	Thermally stable, hydrogen and helium burning in a mixed H/He environment

Observationally, most bursting systems undergo mass-accretion episodes at rates in excess of $4.4 \times 10^{-10}\, M_{\odot}.yr^{-1}$. These systems are characterized by mixed H/He burning. Although the early stages of the TNR are driven by H-burning (cold CNO), it is actually unstable He-burning via the triple-α reaction what triggers the explosive burning of hydrogen via the *rp*-process (a series of (p, γ) reactions and β^{+}-decays; see Chapter 4). Moreover, the *rp*-process beyond iron involves a suite of long-lived, unstable isotopes, such as ^{64}Ge, ^{68}Se, ^{72}Kr, or ^{76}Sr, which constitute real *waiting points* that slow down the main nuclear path (from tens to hundreds of seconds), leaving observational imprints in the corresponding light curves. This fact provides, in turn, an excellent indicator that may reveal the presence of hydrogen during the burst, or instead, may point towards a pure helium ignition.

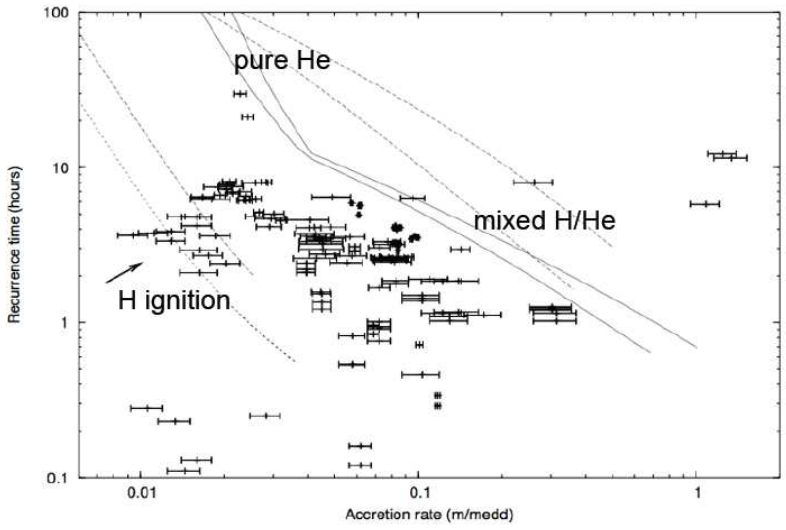

Figure 1.3: Ignition regimes as a function of the mass-accretion rate (from Cumming 2009).

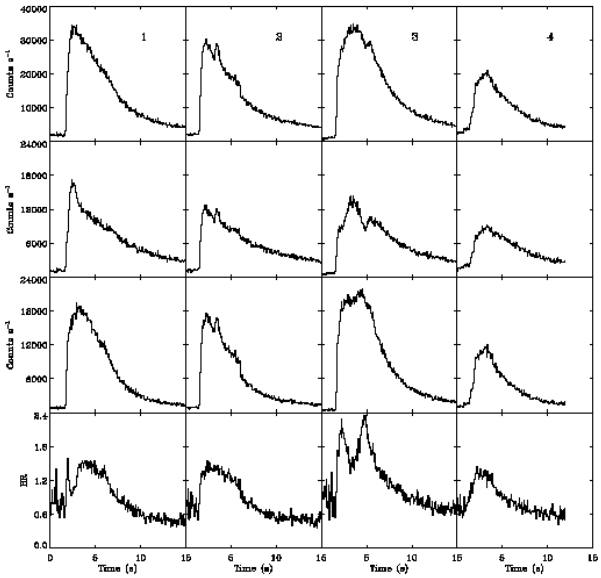

Figure 1.4: A sample of four bursting episodes from the LMXB source 4U 1728-34, as observed with the RXTE satellite. From top to bottom, each sequence shows the total count rate in the energy bands $2-60\,keV$, $2-6\,keV$, and $6-30\,keV$. The bottom panel depicts the hardness ratio $(6-30\,keV)/(2-6\,keV)$. Based on the hardness ratio evolution, bursts 1 and 3 show clear evidence for photospheric radius expansion (PRE). Figure from Strohmayer & Bildsten (2003).

It is also worth noting that because of the factor of ~ 10 larger energy released per nucleon, hydrogen burning constitutes the main energy source for X-ray bursts, and has a dramatic impact in the corresponding light curves. In particularly violent (energetic) XRBs, the luminosity can reach (or exceed) the Eddington limit and the atmosphere of the accreting neutron star can suffer severe expansion driven by radiation pressure. This effect, reported from about 13 XRB sources, has been coined as *photospheric radius expansion* (PRE), and might lead to the ejection of a tiny fraction of the envelope by radiation-driven winds. With this increased radius, the following drop in temperature forces the luminosity to lower below the Eddington value while the photosphere recedes. The photospheric radius expansion is often observed as a 'precursor' of the main burst and has been linked with the appearance of multi-peaked features reported from some XRB light curves (see Figure 1.4).

An interesting feature, observed in the spectra of many XRBs, is a 4.1 keV absorption line (Waki et al. 1984), interpreted as Lyman α lines of helium-like Fe atoms, broadened by Doppler and gravitational effects, likely originated at the inner edge of the accretion disk. Indeed, it has been suggested that time-resolved spectroscopy can in principle allow measurements of the surface gravitational redshift (see Damen

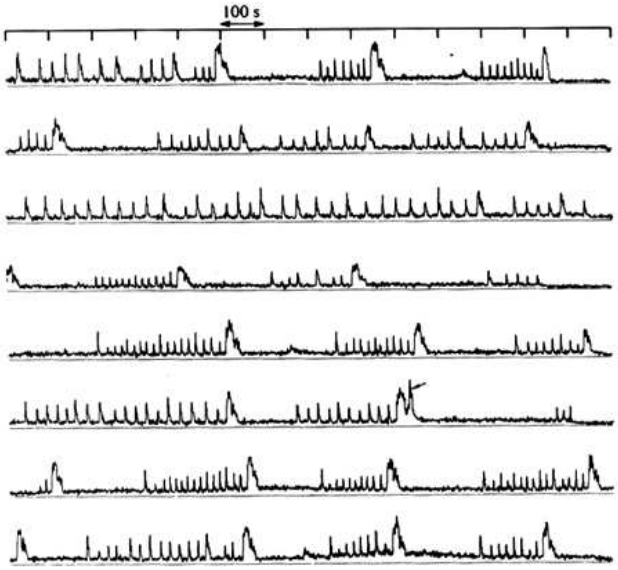

Figure 1.5: Type II XRBs from the *Rapid Burster*, based on SAS-3 observations performed in 1976. The burst pinpointed with an arrow is actually a type I XRB. Figure from Lewin (1977).

et al. 1990, and Smale 2001). Another feature discovered in about ten bursting sources in recent years relies on *millisecond oscillations* of the X-ray flux during bursts, interpreted as anisotropies in the burning across the (rapidly spinning) neutron star surface when the accreted layer ignites at one, or at a few spots. According to this model, slight changes in the observed frequency are accounted by angular momentum conservation of the thermonuclear shells. That is, the frequency changes because of the reduction of rotational velocity during expansion of the atmosphere (and the corresponding reacceleration during contraction). These features certainly require multidimensional hydrodynamic studies to investigate the spreading of the burning front across the neutron star surface.

1.3 Type II X-ray bursts

To date, only two type II X-ray burst sources have been identified: the *Rapid Burster* (see Sec. 1.1), and the *Bursting Pulsar* GRO J1744-28, discovered in 1995. Several bursting episodes observed from the *Rapid Burster* are depicted in Fig. 1.5: note that a big burst is always followed by a long gap, whereas a small burst is quickly followed by another one.

Although not always evident, the basic difference between type I and type II X-ray bursts relies on the shape of their light curves: type II XRB light curves

often rise and fall abruptly, with no gradual decay, and exhibit recurrence times from seconds to minutes. In contrast, type I XRB light curves show a characteristic exponential-like decay and have recurrence times from hours to days.

A neutron star with a strong enough magnetic field to power a magnetosphere has been suggested as the likely scenario for this particular class of bursters. The stream of infalling material stops and progressively accumulates onto the magnetosphere, up to the point when a critical pressure, larger than the magnetic pressure, is achieved. Then, a fraction of this matter effectively penetrates the magnetosphere, falling onto the neutron star surface and powering an X-ray burst from conversion of its gravitational energy. Hence, the larger the stream of infalling material, the more violent the burst, requiring more time to accumulate the critical amount of material to break again the magnetosphere. In this sense, the origin of the X-ray radiation is due to a sudden increase in the local mass-accretion rate.

1.4 Superbursts

In recent years, since the launch of BeppoSAX and RXTE satellites in 1996, 15 extremely powerful X-ray bursts have been discovered from 10 ordinary bursting sources, including GX 17+2, for which 4 superbursts have been identified (in 't Zand et al. 2004). These rare and rather violent events are known as *superbursts* (see Kuulkers 2004, and Cumming 2005, for reviews). The first observation of a superburst was reported by Cornelisse et al. (2000), in the framework of the type I bursting source 4U1735 - 44.

Table 1.3: Main properties of 6 superburst sources observed with RXTE and BeppoSAX satellites (adapted from Strohmayer & Bildsten 2003).

Source	Duration (hr)	L_{pers} (L_{Edd})	k T_{max} (keV)	L_{peak} (10^{38} erg.s^{-1})	E_b (10^{42} erg)	t_{quench}[a] (days)
4U 1820-30[b]	3	~ 0.1	~ 3	3.4	> 1.4	–
4U 1735-44	7	~ 0.25	~ 2.6	1.5	> 0.5	> 7.5
KS 1731-260[b]	12	~ 0.1	~ 2.4	1.4	> 1	> 35
4U 1636-53[b]	$> 2-3$	~ 0.1	–	1.2	$> 0.5-1$	–
Ser X-1	4	~ 0.2	~ 2.6	1.6	> 0.8	~ 34
GX 3+1	> 3.3	~ 0.2	~ 2	0.8	> 0.6	–

Table 1.3 summarizes the main properties of these superbursts. They represent some sort of extreme XRBs: they have long durations, with a typical (exponential) decay time ranging from 1 to 3 hours (including an extreme case, KS 1731 - 260, that lasted for more than 10 hours. See Kuulkers et al. 2002), extremely energetic

[a] Time after a superburst without any type I X-ray bursting activity.
[b] Show a type I XRB as a precursor.

(about $\sim$ 1000 times more energetic than a typical XRB, that is, $\sim 10^{42}$ erg), and with much longer recurrence periods (4.7 yr for the system 4U 1636 - 53, for which two superbursts have been observed to date. See Wijnands 2001). It is worth noting that, although superburst sources also exhibit regular type I XRBs, their occurrence is quenched for about a month after each superburst. A likely explanation suggests that the flux emerging from the deep layers of the neutron star ocean, by the cooling C layer, remains high enough to quench the thermal instability that gives rise to type I bursting activity.

The duration and energetics of superbursts suggest that they result from thermonuclear flashes occurring in fuel layers at much greater depths than for typical X-ray bursts (typically, at densities exceeding 10^9 g.cm^{-3}. See Cumming & Bildsten 2001), more likely, in the C-rich ashes resulting from type I X-ray bursts, as first proposed by Woosley & Taam (1976) (see also Taam & Picklum 1978, Brown & Bildsten 1998, Cumming & Bildsten 2001, Schatz et al. 2003, Weinberg et al. 2006b, and Weinberg & Bildsten 2007). Carbon burning releases $10^{18} erg.g^{-1}$, so that a C mass fraction of $\sim 10\,\%$ is required to achieve the typical energy involved in a superburst. Controversy remains as how much carbon is left after a type I burst: Schatz et al. (1999, 2001) have indeed shown than most of the C is burnt during the previous H/He burning episodes. However, Cumming & Bildsten (2001) concluded that even small amounts of carbon are enough to power a superburst (especially in neutron star oceans enriched from the heavy ashes driven by the rp-process). Cooper et al. (2006) suggested that enough C can survive if H is exhausted before He ignites (pure helium bursts), or if H/He burn stabily during a long period of time before the full thermal instability is triggered (delayed mixed bursts. See Narayan & Heyl 2003). In this case, the energy released during the burst would not be enough to burn most of the thick C layer produced below the ignition region. This is consistent with the observations reported by van Paradijs et al. (1998), and by Cornelisse et al. (2003) who found that, for type I XRB systems accreting mass at a high rate, α increases to values of ≥ 1000. Alternative models have also been proposed to account for the origin of such superbursts, including TNRs on strange quark matter stars (Page & Cumming 2005).

1.5 Mass-radius relation for neutron stars

The mass and the radius of a neutron star depend only on its central density (Shapiro & Teukolsky 1983). Thus, once a suitable equation of state is chosen, a unique mass-radius relation can be established. The radius is often the most difficult quantity to measure. Hence, the usual procedure relies on observational data to infer the neutron star mass while a mass-radius relation is used to derive its size. Figure 1.6 shows several mass-radius relations for a suite of different equations of state computed by Lattimer & Prakash (2007). The area in grey corresponds to the region

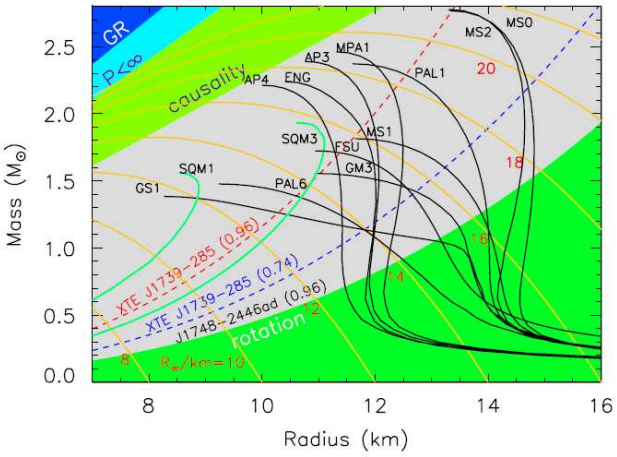

Figure 1.6: Mass-radius trajectories for neutron stars (black curves) and for strange quark matter stars (green curves), for a suite of different equations of state (see Lattimer & Prakash 2007, for details).

of applicability of the models (for instance, the size of a 1.4 $M_\odot$ neutron star, based on this figure, is constrained between ∼10.5 and 14 km. See also Baym & Pethick 1979, for other mass-radius relations using different EOS). Ideally, if observational data for both masses and radii were available, tests on the suitable equation of state could be performed.

Most estimates of neutron star masses rely on the analysis of binary motion. Among them, the most accurate and theory-independent measurement of neutron star masses are those from timing observations of radio pulsars (Manchester & Taylor 1977), including pulsars orbiting around another neutron star, a white dwarf, or a Main Sequence star. This method is based on relativistic corrections to the Keplerian orbital equations (see Thorsett et al. 1993, and Thorsett & Chakrabarty 1999, for details). Masses can also be estimated for neutron stars that are accreting matter from a stellar companion in X-ray binary systems. Some of them are characterized by relatively large masses but their associated errors are also large. Figure 1.7 shows a compilation of measured neutron star masses as of November 2006. All values are given with their corresponding error bars in a 68% confidence limit, assuming that neutron star masses follow a Gaussian distribution. These measurements stress that the most likely value for the mass of a neutron star is $1.35 \pm 0.04\, M_\odot$, very close to the canonical $1.4\, M_\odot$ value. Figure 1.6 shows that, for masses in the range between 1 and $1.5\, M_\odot$, the radius of a neutron star has relatively little dependence on its mass (major exceptions correspond to models SQM1 and SQM3 of strange quark matter stars, and models GS1 and PAL6 of neutron stars with extreme softening densities near the equilibrium density. See Lattimer & Prakash 2007, for details).

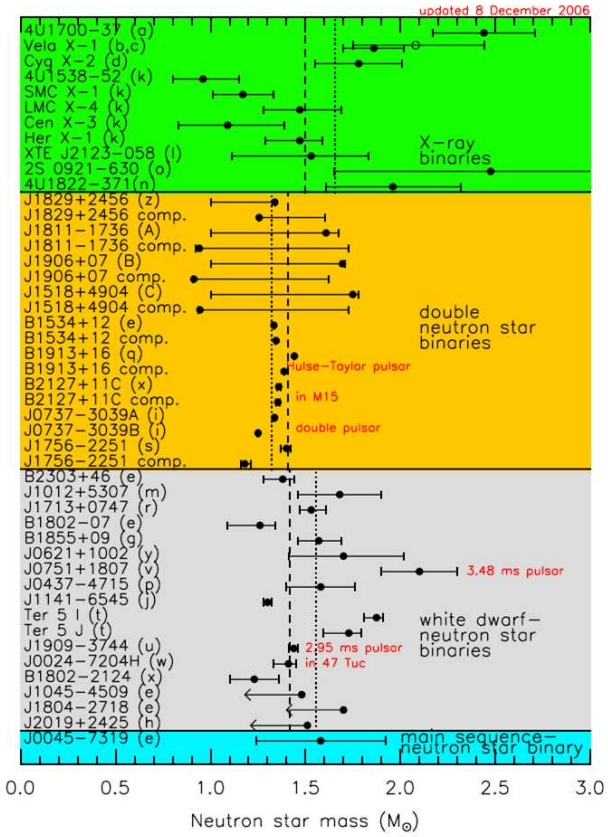

Figure 1.7: Neutron stars masses inferred for radio binary pulsars (gold, silver, and blue regions), and for X-ray accreting binaries (green region). For each region, simple and weighted averages are indicated by a dotted and a dashed line, respectively. From Lattimer & Prakash (2006).

Unlike normal neutron stars, *strange quark matter* stars are self-bound objects (they have finite density, but zero pressure, at their surfaces, and hence, do not require gravity to hold them together). It is however worth noting that there is no observational evidence supporting the existence of strange quark matter stars. The minimum mass for neutron stars has been estimated in $\sim 0.1\,M_{\odot}$. The maximum value is not well constrained since it depends on the knowledge of the appropriate equation of state at high densities (i.e., $\geq 2.8 \times 10^{15}\,g\,cm^{-3}$). Nevertheless, some authors suggest an upper limit of $\leq 3\,M_{\odot}$ (Rhoades & Ruffini 1974).

1.6 This Thesis

Despite of the efforts carried out so far by different groups to provide a reliable description of these bursting sources, several aspects remain yet to be addressed (or revisited).

Because of the relevance of nuclear reaction rates in powering the XRB light curves, as well as in determining the chemical composition of the neutron star crust, it is crucial to test how feasible are the current nucleosynthetic predictions for XRB conditions. To this end, we will perform a detailed study of the influence of nuclear uncertainties affecting the relevant reaction rates on both the energy generation and the nucleosynthetic yields. To achieve this goal, two different approaches will be used: first, an individual reaction-rate analysis, for which each reaction rate will be modified according to its uncertainty limits. Because of the large number of reactions required in a detailed nucleosynthesis study for XRB conditions, a pure hydrodynamical approach would be computationally prohibitive. Hence, a post-processing study relying on a suite of different temperature and density versus time profiles, extracted from the literature or scaled to cover the wide parameter space, will be adopted. A fully updated network, consisting of 606 isotopes, from ^{1}H to ^{113}Xe, and linked through a network of 3551 reactions, will be used for this purpose. The most important results from this study will be reported on Chapter 2.

Next, we will address the feasibility of such individual reaction-rate analyses, questioned by some groups, as compared with a simultaneous variation of all rates (through a Monte Carlo approach), to mimic the complex interplay between multiple nuclear processes in the highly coupled environment of an XRB. Results from this Monte Carlo study, as well as a thorough comparison with the individual reaction-rate analysis, will be presented in Chapter 3.

Once the impact of current nuclear reaction rate uncertainties on the nucleosynthesis accompanying XRBs is quantified, we will tackle hydrodynamic studies of XRBs for different conditions, to specifically address the dependence of XRB properties on the neutron star mass, and on the metallicity of the accreted material. The possible impact of the spatial resolution adopted will be addressed as well. A nuclear reaction network containing 324 isotopes, from ^{1}H to ^{107}Te, linked through a set of 1392 reactions, will be directly coupled to a modified version of the spherically symmetric, Lagrangian, hydrodynamic code SHIVA (José 1996; José & Hernanz 1998). Results will be extensively discussed in Chapter 4.

A brief description of the hydrodynamic code SHIVA, together with details of the input physics (equation of state and nuclear reaction network) adopted in this Thesis, will be presented in Appendixes A, B, and C.

Finally, the most relevant results and conclusions achieved in this work will be summarized in Chapter 5.

Chapter 2

The effect of nuclear uncertainties in type I X-ray burst nucleosynthesis: individual reaction-rate variations

2.1 Introduction

Most of the nuclear reaction rates used in simulations of type I X-ray burst nucleosynthesis (like those reported in Chapter 4), and in particular, rates involving heavy species, rely on theoretical estimates based on statistical models, and therefore may be affected by significant uncertainties. To date, only partial efforts have been made to quantify the impact of such nuclear uncertainties on the overall XRBs properties (Wallace & Woosley 1981; Schatz et al. 1998; Iliadis et al. 1999; Koike et al. 1999, 2004; Thielemann et al. 2001; Fisker et al. 2004, 2006, 2008; Amthor et al. 2006), revealing a complex interplay between nuclear activity and the shape of the light curve (Hanawa et al. 1983; Woosley et al. 2004; Heger et al. 2007).

In order to provide reliable estimates of the composition of neutron star envelopes, it is of paramount importance to fully identify the key reactions whose uncertainties have the largest impact on XRB yields (reactions that probably deserve further improvement through nuclear physics experiments at dedicated facilities). To achieve such a goal, we have performed a comprehensive study of the effects of thermonuclear reaction-rate variations on type I X-ray burst nucleosynthesis, sampling the overall parameter space. The scale of this study makes state-of-the-art hydrodynamic models computationally prohibitive. Hence, we rely on post-processing calculations,

coupling a detailed and fully updated nuclear reaction network with temperature and density profiles extracted from literature.

Two different, somewhat complementary approaches, based on post-processing calculations with temperature and density profiles, can be adopted in a comprehensive sensitivity study. In the first one, all rates are varied individually within uncertainty limits so as to check the impact of each nuclear process on the final yields. At least 2 post-processing calculations are required per nuclear rate to account for the upper and lower limits posed by its associated uncertainty. For a network containing several thousand interactions the overall number of post-processing calculations is indeed extraordinarily large. It is worth mentioning that this technique has been previously applied to a large number of astrophysical sites, including nucleosynthesis in the Sun (Bahcall et al. 1982), type II supernovae (The et al. 1998; Jordan et al. 2003), classical nova explosions (Iliadis et al. 2002), primordial (Big Bang) nucleosynthesis (Coc et al. 2002, 2004), intermediate-mass AGB stars (Izzard et al. 2007), and type I X-ray bursts (Amthor et al. 2006).

A second approach is based on Monte Carlo techniques (see Chapter 3). Here, random enhancement factors (often adopted to follow a log-normal distribution) are applied to each nuclear process of the network simultaneously. The impact on the final yields is then tested through a series of post-processing calculations. This approach requires a large number of trial simulations in order to be statistically sound and has been already applied to Big Bang nucleosynthesis studies (Krauss & Romanelli 1990; Smith et al. 1993), nova nucleosynthesis (Smith et al. 2002; Hix et al. 2002, 2003), and also to type I X-ray bursts (Roberts et al. 2006).

Both approaches have been adopted in this Thesis (Chapters 2 and 3). An interesting issue, recently raised by Roberts et al. (2006), is the feasibility of the first method, as compared with the Monte Carlo approach, to properly address the higher-order correlations between input rates and XRB model predictions because of the large number of reactions simultaneously involved in the production and destruction of each element. It is also the goal of this Thesis to test this conjecture by comparing the results from an individual-variation study with those obtained with a Monte Carlo approach (see Chapter 3).

2.2 Models and input physics

In this work, we have used three temperature-density versus time profiles directly extracted from the literature (see Fig. 2.1 and 2.2).

2.2.1 Model K04

Model K04 (Koike et al. 2004) is based on a spherically symmetric, multizone model of accretion (at a rate $\dot{m}_{acc} = 2.3 \times 10^4\, g.cm^{-2}.s^{-1}$) onto a 1.3 $M_\odot$ neutron star (with $R_{NS} = 8.1\, km$ and $g_{surface} = 3.6 \times 10^{14} cm.s^{-2}$). This model is characterized

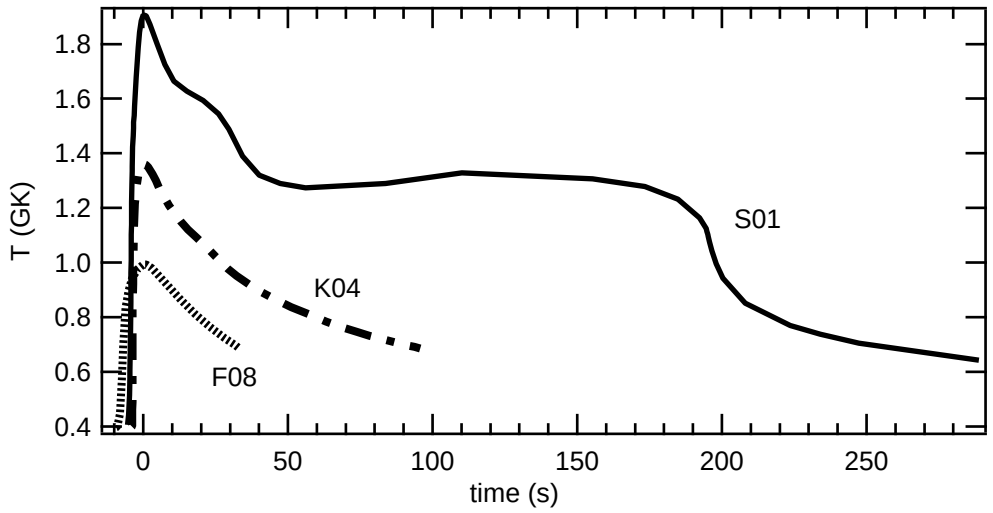

Figure 2.1: Temperature versus time profiles corresponding to Models K04 (Koike et al. 2004), S01 (Schatz et al. 2001), and F08 (Fisker et al. 2008).

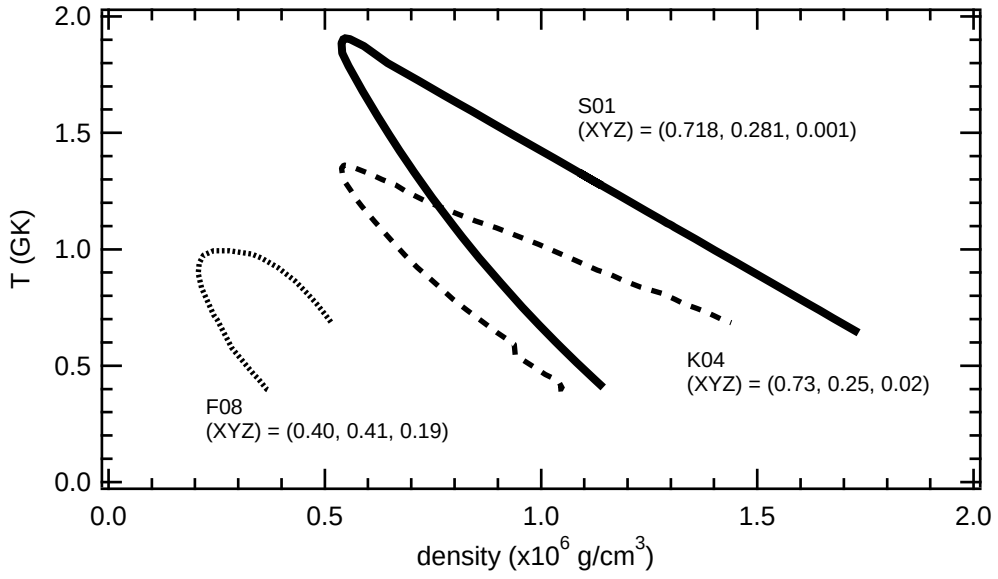

Figure 2.2: Same as Fig. 2.1, for temperature versus density. The initial metallicity adopted for each model is indicated as well.

by a peak temperature of $1.36\,GK$ ($L_{peak} \sim 10^{38} erg.s^{-1}$), densities ranging between $(0.54 - 1.44) \times 10^6\,g.cm^{-3}$ (the column density of the burning region reaches $2.2 \times 10^8\,g.cm^{-2}$), and a burst duration of $\sim 100\,s$. The initial envelope composition adopted in this model is taken directly from Koike et al. (2004), with $X = 0.73$, $Y = 0.25$, and $Z = 0.02$ –roughly solar.

2.2.2 Model F08

Model F08 (Fisker et al. 2008) is based on 1-D general relativistic, hydrodynamic, multizone calculations. In this model, the adopted neutron star has 1.4 $M_\odot$ (with $R_{NS} = 11\,km$, and $g_{surface} = 1.9 \times 10^{14} cm.s^{-2}$), and the mass accretion rate is $0.66 \times 10^4\,g.cm^{-2}.s^{-1}$. It achieves a peak temperature of only $0.993\,GK$ ($L_{peak} \sim 10^{38} erg.s^{-1}$), densities in the range $(2.07 - 5.14) \times 10^5\,g.cm^{-3}$ (the column density of the burning region reaches $0.79 \times 10^8\,g.cm^{-2}$), and a burst duration of $\sim 50\,s$. The initial composition is taken directly from the hottest burning zone (representative of the depth at which most of the relevant nucleosynthetic processes take place) of the hydrodynamic models computed by Fisker et al. (2008), with $X = 0.40$, $Y = 0.41$, and $Z = 0.19$ –a metallicity about ten times solar (see the original manuscript for a detailed account of the distribution of those metals).

2.2.3 Model S01

Finally, Model S01 (based on Schatz et al. 2001) achieves the largest temperature of all models extracted from the literature, with $T_{peak} = 1.907\,GK$. The shape of this temperature profile, based on one-zone model calculations of accretion onto a neutron star (with $g_{surface} = 1.9 \times 10^{14} cm.s^{-2}$, and an adopted mass-accretion rate $\dot{m}_{acc} = 8.8 \times 10^4\,g.cm^{-2}.s^{-1}$), is quite different from those corresponding to Models K04 and F08 (which approximately follow an exponential decay): indeed, it shows a long plateau at about $T \sim 1.4\,GK$ before the final decline. Since no density profile is directly available for this model, and considering the relatively small variation in density during an XRB, we have scaled K04 to match the values reported in Schatz et al. (2001), resulting in densities ranging between $(0.54 - 1.73) \times 10^6\,g.cm^{-3}$. The duration is $\sim 300\,s$. The adopted initial composition is $X = 0.718$, $Y = 0.281$, and $Z = 0.001$ –a metallicity about 20 times lower than solar. Because of the lack of information on the specific metallicity distribution, we assume that all metals correspond to ^{14}N (see also Woosley et al. 2004), following the rapid rearrangement of CNO isotopes that naturally occurs early in the burst (which in this one-dimensional model reaches $L_{peak} \sim 5 \times 10^{38} erg.s^{-1}$). It is worth noting that in realistic hydrodynamic calculations the pressure near the base of the envelope remains almost constant during the entire burst (see Chapter 4) because of the strong gravitational field (degeneracy) of the neutron star. We have checked how the temperature-density versus time profiles from Models K04, F08, and S01 match this

condition along the burst: we found that Models K04 and F08 deviate from constant pressure at most by just 5 % throughout the different epochs of the burst. Model S01, however, shows somewhat larger deviations (about 20 %). We have performed a detailed study of the possible implications of these deviations from constant pressure in the S01 Model and find them to be negligible given our criteria for identifying critical reactions (see Section 2.3).

2.2.4 Models K04-B1 and K04-B2

The three models mentioned above partially cover the parameter space in XRB nucleosynthesis calculations. However, it is difficult, if not impossible, to disentangle the specific role played by the initial metallicity, the peak temperature achieved and the duration of the bursts, since all these models are characterized by different values for these physical quantities. Hence, to appropriately address this issue, we have generated additional models through parameterization of the Koike et al. (2004) temperature-density-time profiles. Parameterized models have been used previously to study, for example, nucleosynthesis in classical novae (Boffin et al. 1993), the alpha-rich freeze-out in type II supernovae (The et al. 1998; Jordan et al. 2003), and XRBs (Wallace & Woosley 1981, 1984).

To evaluate the role played by the duration of the burst (taken as the characteristic timescale of the temperature and density profiles) in the extension of the nuclear path, we have scaled the K04 profiles in duration by a factor 0.1 (short burst, Model K04-B1) and 10 (long burst, Model K04-B2), while preserving T_{peak} and the initial chemical composition.

2.2.5 Models K04-B3, K04-B4, and K04-B5

The role played by the initial metallicity (reflecting that of the stream of infalling material during accretion) has been tested through 3 models: a low-metallicity model ($Z = 10^{-4}$, Model K04-B3), and two high metallicity ones (with $Z = 0.19$, Models K04-B4 & K04-B5). The initial composition of Models K04-B3 and K04-B4 is scaled from the distribution reported in Koike et al. (2004). In contrast, for Model K04-B5, we have adopted the distribution given in Fisker et al. (2008). This will also allow us to test if a different distribution of metals has an impact on the final yields.

2.2.6 Models K04-B6 and K04-B7

Finally, two additional models have been constructed to test the effect of varying the peak temperature achieved during the explosion: we have scaled the temperature and density versus time profiles from Koike et al. (2004) to attain peak values of $0.9 \times 10^9\,K$ (lower peak temperature, Model K04-B6) and $2.5 \times 10^9\,K$ (higher peak temperature, Model K04-B7), while preserving the initial composition and the duration of the burst.

It is worth noting that post-processing calculations are not suited to derive absolute abundances (or to provide any insight into light curve variations and energetics) since they rely only on temperature and density versus time profiles evaluated at a given location of the star (usually, the innermost shells of the envelope). Indeed, it is likely that the evolution at other depths will be characterized by a different set of physical conditions. Furthermore, adjacent shells will eventually mix when convection sets in, altering the chemical abundance pattern in those layers. However, this approach is reliable to identify the key processes governing the main nuclear activity at the specific temperature and density regimes that characterize such bursting episodes. Hence, the goal of this Chapter is to provide a list of key nuclear processes whose uncertainties have the largest influence on the final yields, covering as much as possible the proper range of temperatures, densities, and timescales that characterize XRBs (a feasibility test for nucleosynthetic predictions based on hydrodynamic simulations of type I XRBs, like those presented in Chapter 4). However, any attempt to properly quantify the extent of this impact (for instance, in terms of absolute abundances), must rely on state-of-the-art hydrodynamic codes coupled to detailed nuclear networks.

2.3 Results

Some general procedures must be outlined before a detailed analysis of the main results is presented. For all 10 models considered in this chapter, a first calculation, with *standard* rates (as described in Appendix C) has been performed. This is used to scale the level of changes (indicated in Tables 2.1 & 2.4 - 2.14 as $X_i/X_{i,std}$, that is, the ratio of mass fractions obtained with a modified network -resulting from our exploration of uncertainties- to those obtained with our *standard* network). Following this, a whole series of post-processing calculations have been computed, in which each nuclear rate is varied individually by a factor 10 up and down, for each of the 10 models.

Several important remarks have to be made at this stage: first, we have chosen a factor of 10 for the level of uncertainty affecting theoretical reaction rate estimates, in general. Other authors (see Schatz 2006; Schatz & Rehm 2006; Amthor et al. 2006) claim, instead, that excitation energies of theoretically calculated levels for XRB conditions may suffer uncertainties of $\sim 100\,keV$, which translates into an overall uncertainty in some rates that may reach several orders of magnitude. It is also worth noting that efforts to ascertain systematic uncertainties through a direct comparison between different theoretical models often report variations smaller than a factor of 10. Second, some nuclear rates, such as the triple-α reaction, some (p,γ) reaction rates on low-mass targets, or most of the β-decay rates (note that we used *ground-state* or *laboratory* β-decays), are known with much better precision. This has been addressed when necessary and is discussed in the following sections of this

chapter. Third, it is important to stress that forward and reverse reactions have been varied simultaneously with the same uncertainty factor, to preserve the principle of detailed balance. Fourth, a particular strategy has been adopted to evaluate the impact of beta-decay rate uncertainties: they have initially been varied by a factor of 10, up and down as a way to discriminate the *key* β-decay rates from the rest (see Table 2.2). Then, additional post-processing calculations focused on these key rates have been performed assuming more realistic uncertainties (around 30 %; see Audi et al. 2003b). This approach also helps to test the impact of using stellar versus laboratory decay rates for XRB conditions: we found differences between our (laboratory) decay rates and the available Fuller et al. (1982a,b) stellar decay rates (over $A = 21 - 60$) of as large as a factor 10, but usually more like ∼20 - 60 %; over $A = 50 - 60$, the stellar decay rates of Langanke & Martínez-Pinedo (2000) differ from the Fuller et al. (1982a,b) rates by up to 3 orders of magnitude, but usually more like a factor ∼10. Fifth, some additional tests aimed at identifying the influence of Q-value variations have been performed using the uncertainties estimated by Audi et al. (2003b) (see Tables 2.3, 2.4, & 2.7). This part of our study has been restricted to Models K04 and F08, to proton-capture reactions on $A < 80$ nuclei, and to reactions with $|Q| < 1\,MeV$, for which the estimated uncertainty exceeds $50\,keV$ (see Table 2.3)[1]. Sixth, since the main goal of this Section is to identify the key nuclear processes whose uncertainties have the largest impact on XRB nucleosynthesis, we have restricted the analysis (in the tables and forthcoming discussion) to nuclear species which achieve a mass fraction of at least 10^{-5} at the end of the burst, and deviate from the abundances computed with standard rates by at least a factor of 2. And seventh, for the sake of clarity and conciseness, the isotopes displayed and discussed throughout this study correspond to species that are either stable or have a half-life longer than 1 hour (the rest are assumed to fully decay at the end of the burst and consequently, are added to the corresponding stable or long-lived daughter nuclei).

Next, we report results from a series of $\sim 40,000$ post-processing calculations (requiring 14 CPU-months) performed for this study of X-ray burst nucleosynthesis.

2.3.1 Model K04

Here, we will describe in detail the results obtained from our post-processing calculations using temperature and density versus time profiles extracted from Koike et al. (2004) [Model K04]. A general discussion of the main nuclear path achieved for these profiles can be found in Iliadis (2007). Our main results, from individually varying each reaction rate by a factor 10 (up and down), are summarized in Table 2.1.

[1] A more detailed account of the influence of Q-value variations has been published in *Impact of uncertainties in reaction Q-values on nucleosynthesis in type I x-ray bursts*, Parikh et al. (2009).

Table 2.1: Final abundance ratios, $X_i/X_{i,std}$, for Model K04 (Koike et al. 2004), resulting from reaction-rate variations by a factor of 10 (up and down).

Reaction	Isotope	10	0.1
^{15}O(α, γ)^{19}Ne	^{15}N	...	8.30
^{18}Ne(α, p)^{21}Na	^{15}N	0.43	...
	^{18}F	0.43	...
^{31}Cl(p, γ)^{32}Ar	^{30}Si	0.44	...
^{43}V(p, γ)^{44}Cr	^{44}Ti	...	0.49
^{47}Mn(p, γ)^{48}Fe	^{46}Ti	0.31	...
^{56}Ni(p, γ)^{57}Cu	^{56}Ni	...	7.78
^{56}Cu(p, γ)^{57}Zn	^{55}Co	...	2.64
^{57}Cu(p, γ)^{58}Zn	^{57}Ni	...	2.79
^{58}Cu(p, γ)^{59}Zn	^{58}Ni	...	2.05
^{59}Cu(p, γ)^{60}Zn	^{59}Ni	...	2.02
^{61}Zn(p, γ)^{62}Ga	^{61}Cu	...	2.35
^{61}Ga(p, γ)^{62}Ge	^{60}Ni	0.16	4.10
	^{61}Cu	...	4.25
^{63}Ga(p, γ)^{64}Ge	^{63}Cu	...	3.29
^{65}Ge(p, γ)^{66}As	^{65}Zn	...	8.95
^{65}As(p, γ)^{66}Se	^{64}Zn	0.35	3.50
	^{65}Zn	0.37	2.93
	^{66}Ge	0.44	2.77
	^{67}Ga	0.40	3.22
	^{81}Rb	...	0.50
	^{88}Zr	...	0.49
	^{89}Nb	...	0.49
	^{90}Mo	...	0.48
	^{91}Nb	...	0.47
	^{92}Mo	...	0.47
	^{93}Tc	...	0.46
	^{94}Mo	...	0.45
	^{95}Ru	...	0.44
	^{96}Ru	...	0.43
	^{97}Ru	...	0.40
	^{98}Ru	...	0.39
	^{99}Rh	...	0.38
	^{100}Pd	...	0.38
	^{101}Pd	...	0.38
	^{102}Pd	...	0.37
	^{103}Ag	...	0.38
	^{104}Ag	...	0.40
^{66}Ge(p, γ)^{67}As	^{66}Ge	...	4.86
^{66}As(p, γ)^{67}Se	^{66}Ge	0.18	...
^{67}As(p, γ)^{68}Se	^{67}Ga	0.47	5.71
^{69}Se(p, γ)^{70}Br	^{69}Ge	0.10	8.21
^{70}Se(p, γ)^{71}Br	^{70}Ge	...	5.18
^{70}Br(p, γ)^{71}Kr	^{70}Ge	0.28	...
^{71}Br(p, γ)^{72}Kr	^{71}As	0.20	7.11
^{73}Kr(p, γ)^{74}Rb	^{73}Se	0.10	7.50
^{74}Kr(p, γ)^{75}Rb	^{74}Se	0.30	6.51

Table 2.1: – Continued.

Reaction	Isotope	10	0.1
^{74}Rb(p, γ)^{75}Sr	^{74}Se	0.40	...
^{75}Rb(p, γ)^{76}Sr	^{75}Br	0.15	6.35
^{77}Sr(p, γ)^{78}Y	^{77}Kr	0.11	5.72
^{78}Sr(p, γ)^{79}Y	^{78}Kr	0.17	5.82
^{79}Y(p, γ)^{80}Zr	^{79}Kr	0.12	5.45
^{81}Zr(p, γ)^{82}Nb	^{81}Rb	0.15	3.15
^{82}Zr(p, γ)^{83}Nb	^{82}Sr	0.17	2.92
^{83}Nb(p, γ)^{84}Mo	^{83}Sr	0.27	...
^{84}Nb(p, γ)^{85}Mo	^{84}Sr	0.20	2.44
^{85}Nb(p, γ)^{86}Mo	^{85}Y	0.43	...
^{85}Mo(p, γ)^{86}Tc	^{85}Y	0.48	...
^{86}Mo(p, γ)^{87}Tc	^{86}Zr	0.23	2.43
^{87}Mo(p, γ)^{88}Tc	^{87}Zr	0.32	...
^{88}Tc(p, γ)^{89}Ru	^{88}Zr	0.37	2.04
^{89}Tc(p, γ)^{90}Ru	^{89}Nb	0.24	2.15
^{90}Ru(p, γ)^{91}Rh	^{90}Mo	0.35	...
^{91}Ru(p, γ)^{92}Rh	^{91}Nb	0.37	...
^{92}Ru(p, γ)^{93}Rh	^{92}Mo	0.32	...
^{93}Rh(p, γ)^{94}Pd	^{93}Tc	0.24	2.05
^{94}Rh(p, γ)^{95}Pd	^{94}Mo	0.47	....
^{94}Pd(p, γ)^{95}Ag	^{94}Mo	0.45	....
^{95}Pd(p, γ)^{96}Ag	^{95}Ru	0.31	....
^{96}Ag(p, γ)^{97}Cd	^{96}Ru	0.48	....
	^{97}Ru	...	0.41
	^{98}Ru	...	0.38
	^{99}Rh	...	0.43
	^{100}Pd	...	0.48
^{97}Ag(p, γ)^{98}Cd	^{97}Ru	0.26	2.13
^{98}Ag(p, γ)^{99}Cd	^{98}Ru	0.45	...
^{98}Cd(p, γ)^{99}In	^{98}Ru	0.43	...
^{99}Cd(p, γ)^{100}In	^{99}Rh	0.32	...
^{100}Cd(p, γ)^{101}In	^{100}Pd	0.43	...
^{101}In(p, γ)^{102}Sn	^{101}Pd	0.34	...
^{102}In(p, γ)^{103}Sn	^{102}Pd	0.36	...
	^{103}Ag	...	0.40
	^{104}Ag	...	0.48
^{103}In(p, γ)^{104}Sn	^{104}Ag	2.80	0.24
	^{105}Ag	2.00	...
^{104}In(p, γ)^{105}Sn	^{105}Ag	4.13	...

Because of the moderate peak temperature achieved, the extent of the nuclear activity (defined as the heaviest isotope with $X_i > 10^{-2}$, in the final yields) reaches ^{96}Ru. The most abundant species (stable or with a half-life $> 1\,hr$) at the end of the burst are H (0.20, by mass), ^{4}He (0.021), ^{68}Ge (0.02), ^{72}Se (0.13), ^{64}Zn (0.071), and ^{76}Kr (0.074). Qualitatively, this is in agreement with the results reported by Koike et al. (2004) (Model 2, Table 8), in which the most abundant species, at the

end of the burst, are also ^{68}Ge (0.17), ^{72}Se (0.14), ^{64}Zn (0.27), and ^{76}Kr (0.078). Note that the final mass fraction of ^{4}He reported by Koike et al. (2004), 0.011, is also comparable to the value reported here. However, Koike's Model is fully depleted of H (9.76×10^{-17}, by mass), whereas some H remains at the end of our simulations. This could result from differences in the adopted nuclear reaction networks as well as to the hybrid use of evolutionary and post-processing calculations in Koike et al. (2004). This discrepancy is of some importance as the presence of H in the ashes may induce marginal nuclear activity driving a second burst if the set of necessary conditions for a TNR are satisfied (see Woosley & Weaver 1984, for details).

Our study reveals that the most influential reaction, by far, is the triple-α, which affects a large number of species (^{4}He, ^{18}F, ^{21}Ne, $^{24,25}Mg$, $^{28-30}Si$, $^{33,34}S$, $^{36-38}Ar$, ^{41}Ca, $^{44,46,47}Ti$, ^{49}V, ^{50}Cr, ^{53}Mn, ^{54}Fe, $^{57-59}Ni$, $^{61,63}Cu$, ^{62}Zn, ^{102}Pd, and $^{103,104}Ag$), when its nominal rate is varied by a factor of 10, up and down. A similar result on the importance of the triple-α reaction has been previously reported by Roberts et al. (2006), using a Monte Carlo approach. But, as discussed above, this uncertainty factor is far too large and accordingly, this reaction has been removed from Tables 2.1, 2.5, 2.6, & 2.8 - 2.14. Hereafter, we will drop from the discussion of the different models any additional comment on the importance of the triple-α reaction which, when arbitrarily varied by a factor of 10, systematically becomes the single most influential reaction of the whole network, for all 10 models. Indeed, additional tests performed with a more realistic uncertainty[2] of $\pm\,40\,\%$ (see Angulo et al. 1999) show no effect on any individual isotope, for any of the 10 models (the impact of nuclear uncertainties affecting the triple-α rate on the total energy output will be specifically addressed in Section 2.4).

From the several thousand nuclear processes considered, we find that only 56 reactions –and the corresponding reverse reactions– have an impact on the final yields when their rates are varied by a factor of 10, up and down for this model (see Table 2.1)[3]. Furthermore, our study reveals that the impact of most of these reactions is restricted to the vicinity of the target nuclei. A clear example is $^{15}O(\alpha,\gamma)$: when its nominal rate is multiplied by a factor 0.1, only one isotope, ^{15}N, is modified by more than a factor of 2 (as compared with the mass fraction obtained with the recommended rate –but see also Section 2.4). Indeed, the most influential reaction is by far $^{65}As(p,\gamma)$, due to its bridging effect on the ^{64}Ge-waiting point. To a lesser extent, $^{96}Ag(p,\gamma)$ and $^{102}In(p,\gamma)$ also show an impact on a number of species.

[2]Note that according to Tur et al. (2006), the triple-α rate is known to $\pm\,12\,\%$.

[3]It is worth noting that final yields depend somewhat on the specific choice of time (or equivalently, temperature) at which calculations are stopped. This may be relevant for absolute determinations of yields, but certainly not for the identification of key nuclear reactions. As discussed previously, this chapter focuses chiefly on reaction-rate variations that lead to relative abundance changes of (at least) a factor of 2. As we found differences in the final relative yields caused by different stopping times (corresponding to post-burst temperatures down to $0.1\,GK$) to be typically $5-10\,\%$, this issue has no significant effect on the conclusions of our studies here.

Table 2.2: Important β-decay (and β-delayed proton decay) rates, as found in our ten models.

Reaction
Model K04
^{64}Ge(β^+)^{64}Ga
^{68}Se(β^+)^{68}As
^{72}Kr(β^+)^{72}Br
^{76}Sr(β^+)^{76}Rb
^{80}Zr(β^+)^{80}Y
^{88}Ru(β^+)^{88}Tc
^{92}Pd(β^+)^{92}Rh
^{99}In(β^+)^{99}Cd
Model F08
^{26}Si(β^+)^{26m}Al
^{29}S(β^+)^{29}P
^{29}S(β^+ p)^{28}Si
^{30}S(β^+)^{30}P
^{33}Ar(β^+)^{33}Cl
^{33}Ar(β^+ p)^{32}S
^{34}Ar(β^+)^{34}Cl
^{37}Ca(β^+)^{37}K
^{37}Ca(β^+ p)^{36}Ar
^{38}Ca(β^+)^{38}K
^{60}Zn(β^+)^{60}Cu
^{68}Se(β^+)^{68}As
^{72}Kr(β^+)^{72}Br
^{76}Sr(β^+)^{76}Rb
^{80}Zr(β^+)^{80}Y
Model S01
^{68}Se(β^+)^{68}As
^{72}Kr(β^+)^{72}Br
^{80}Zr(β^+)^{80}Y
^{88}Ru(β^+)^{88}Tc
^{92}Pd(β^+)^{92}Rh
^{101}Sn(β^+)^{101}In
^{102}Sn(β^+)^{102}In
^{103}Sn(β^+)^{103}In
^{104}Sn(β^+)^{104}In
^{105}Sn(β^+)^{105}In
^{106}Sn(β^+)^{106}In
^{106}Sb(β^+)^{106}Sn
Model K04-B1
^{25}Si(β^+)^{25}Al
^{25}Si(β^+ p)^{24}Mg
^{33}Ar(β^+)^{33}Cl
^{33}Ar(β^+ p)^{32}S
^{36}Ca(β^+ p)^{35}Ar
^{36}Ca(β^+)^{36}K

Table 2.2: – Continued.

Reaction
^{37}Ca(β^+)^{37}K
^{37}Ca(β^+ p)^{36}Ar
^{38}Ca(β^+)^{38}K
^{41}Ti(β^+)^{41}Sc
^{41}Ti(β^+ p)^{40}Ca
^{59}Zn(β^+)^{59}Cu
^{62}Ge(β^+)^{62}Ga
^{63}Ge(β^+)^{63}Ga
^{64}Ge(β^+)^{64}Ga
^{68}Se(β^+)^{68}As
Model K04-B2
^{25}Si(β^+)^{25}Al
^{25}Si(β^+ p)^{24}Mg
^{68}Se(β^+)^{68}As
^{72}Kr(β^+)^{72}Br
^{76}Sr(β^+)^{76}Rb
^{80}Zr(β^+)^{80}Y
^{92}Pd(β^+)^{92}Rh
^{94}Pd(β^+)^{94}Rh
^{101}Sn(β^+)^{101}In
^{102}Sn(β^+)^{102}In
^{103}Sn(β^+)^{103}In
^{104}Sn(β^+)^{104}In
Model K04-B3
^{68}Se(β^+)^{68}As
^{72}Kr(β^+)^{72}Br
^{76}Sr(β^+)^{76}Rb
^{80}Zr(β^+)^{80}Y
^{88}Ru(β^+)^{88}Tc
^{92}Pd(β^+)^{92}Rh
^{99}In(β^+)^{99}Cd
Model K04-B4
^{33}Ar(β^+)^{33}Cl
^{33}Ar(β^+ p)^{32}S
^{34}Ar(β^+)^{34}Cl
^{37}Ca(β^+)^{37}K
^{37}Ca(β^+ p)^{36}Ar
^{38}Ca(β^+)^{38}K
^{39}Ca(β^+)^{39}K
^{42}Ti(β^+)^{42}Sc
^{46}Cr(β^+)^{46}V
^{49}Fe(β^+)^{49}Mn
^{49}Fe(β^+ p)^{48}Cr
^{55}Ni(β^+)^{55}Co
^{58}Zn(β^+)^{58}Cu

Table 2.2: – Continued.

Reaction
^{68}Se(β^+)^{68}As
^{72}Kr(β^+)^{72}Br
^{76}Sr(β^+)^{76}Rb
^{80}Zr(β^+)^{80}Y
Model K04-B5
^{21}Mg(β^+)^{21}Na
^{21}Mg(β^+ p)^{20}Ne
^{24}Si(β^+)^{24}Al
^{24}Si(β^+ p)^{23}Mg
^{25}Si(β^+)^{25}Al
^{25}Si(β^+ p)^{24}Mg
^{28}S(β^+)^{28}P
^{28}S(β^+ p)^{27}Si
^{29}S(β^+)^{29}P
^{29}S(β^+ p)^{28}Si
^{30}S(β^+)^{30}P
^{33}Ar(β^+)^{33}Cl
^{33}Ar(β^+ p)^{32}S
^{34}Ar(β^+)^{34}Cl
^{37}Ca(β^+)^{37}K
^{37}Ca(β^+ p)^{36}Ar
^{38}Ca(β^+)^{38}K
^{64}Ge(β^+)^{64}Ga
^{68}Se(β^+)^{68}As
Model K04-B6
^{18}Ne(β^+)^{18}F
^{64}Ge(β^+)^{64}Ga
^{68}Se(β^+)^{68}As
^{72}Kr(β^+)^{72}Br
^{76}Sr(β^+)^{76}Rb
^{80}Zr(β^+)^{80}Y
Model K04-B7
^{68}Se(β^+)^{68}As
^{72}Kr(β^+)^{72}Br
^{76}Sr(β^+)^{76}Rb
^{80}Zr(β^+)^{80}Y
^{88}Ru(β^+)^{88}Tc
^{92}Pd(β^+)^{92}Rh
^{101}Sn(β^+)^{101}In
^{102}Sn(β^+)^{102}In

The most important β-decay rates identified in this model are those of ^{64}Ge, ^{68}Se, ^{72}Kr, ^{76}Sr, ^{80}Zr, ^{88}Ru, ^{92}Pd, and ^{99}In (see Table 2.2). But it is important to stress that additional calculations, in which these (laboratory) β-decay rates were

varied within realistic uncertainties (half-lives varied by $\sim \pm 30\,\%$), have revealed no effect on any single isotope (see Woosley et al. 2004, for a sensitivity study based on variations of groups of weak rates, including all positron emission rates for nuclei heavier than ^{56}Ni, by an order of magnitude).

Table 2.3: List of reactions selected for the Q-value variation study, restricted to proton-capture reactions on $A < 80$ nuclei, with $|Q| < 1\,MeV$, and a Q-value uncertainty $> 50\,keV$ (see Audi et al. 2003b).

Reaction	Q-value[a] (keV)	Uncertainty ΔQ (keV)
^{21}Mg(p, γ)^{22}Al	17	95
^{24}Si(p, γ)^{25}P	-828	197
^{25}Si(p, γ)^{26}P	140	196
^{25}P(p, γ)^{26}S	191	357
^{26}P(p, γ)^{27}S	719	281
^{29}S(p, γ)^{30}Cl	-314	202
^{30}S(p, γ)^{31}Cl[b]	294	50
^{30}Cl(p, γ)^{31}Ar	439	284
^{33}Ar(p, γ)^{34}K	-614	298
^{41}Ti(p, γ)^{42}V	-242	220
^{42}Ti(p, γ)^{43}V	192	233
^{45}Cr(p, γ)^{46}Mn	694	515
^{46}Cr(p, γ)^{47}Mn	78	160
^{49}Fe(p, γ)^{50}Co	-98	224
^{50}Fe(p, γ)^{51}Co	88	161
^{51}Fe(p, γ)^{52}Co	982	67
^{54}Ni(p, γ)^{55}Cu	-298	302
^{55}Ni(p, γ)^{56}Cu	555	140
^{58}Zn(p, γ)^{59}Ga	-888	175
^{59}Zn(p, γ)^{60}Ga	27	118
^{59}Ga(p, γ)^{60}Ge	936	287
^{60}Zn(p, γ)^{61}Ga[b]	192	54
^{63}Ge(p, γ)^{64}As	-100	300
^{64}Ge(p, γ)^{65}As	-80	300
^{67}Se(p, γ)^{68}Br	-560	300
^{68}Se(p, γ)^{69}Br	-450	100
^{72}Kr(p, γ)^{73}Rb	-600	150
^{75}Sr(p, γ)^{76}Y	-629	549
^{76}Sr(p, γ)^{77}Y	-50	50
^{76}Y(p, γ)^{77}Zr[c]	802	400
^{80}Zr(p, γ)^{81}Nb	-750	150

[a] All Q-values and errors are from Audi et al. (2003b), except where indicated. They have been estimated in that work from systematic trends.

[b] Reactions with experimental Q-values and errors in Audi et al. (2003b).

[c] Q-value as used in the Hauser-Feshbach calculation for this rate in our network. No Q-value was estimated in Audi et al. (2003b) for this reaction. The associated uncertainty was assumed to be $400\,keV$.

Table 2.4: Final abundance ratios, $X_i/X_{i,std}$, for Model K04 (Koike et al. 2004), resulting from variations on Q-values (see Table 2.3).

Reaction	Isotope	High-Q $(Q + \Delta Q)$	Low-Q $(Q - \Delta Q)$
^{26}P(p, γ)^{27}S	^{25}Mg	0.35	...
^{46}Cr(p, γ)^{47}Mn	^{46}Ti	0.23	...
^{55}Ni(p, γ)^{56}Cu	^{55}Co	...	3.95
^{60}Zn(p, γ)^{61}Ga	^{60}Ni	0.47	...
^{64}Ge(p, γ)^{65}As	^{64}Zn	0.08	4.13
	^{65}Zn	....	3.04
	^{66}Ge	....	3.05
	^{67}Ga	....	3.65
	^{73}Se	....	0.49
	^{74}Se	....	0.50
	^{77}Kr	....	0.42
	^{78}Kr	....	0.42
	^{79}Kr	....	0.42
	^{80}Sr	....	0.47
	^{81}Rb	....	0.40
	^{82}Sr	....	0.41
	^{83}Sr	....	0.42
	^{84}Sr	....	0.42
	^{85}Y	....	0.42
	^{86}Zr	....	0.40
	^{87}Zr	....	0.39
	^{88}Zr	....	0.38
	^{89}Nb	....	0.38
	^{90}Mo	....	0.37
	^{91}Nb	....	0.36
	^{92}Mo	....	0.36
	^{93}Tc	....	0.36
	^{94}Mo	....	0.35
	^{95}Ru	....	0.34
	^{96}Ru	....	0.33
	^{97}Ru	....	0.31
	^{98}Ru	....	0.30
	^{99}Rh	....	0.29
	^{100}Pd	....	0.30
	^{101}Pd	....	0.29
	^{102}Pd	....	0.29
	^{103}Ag	....	0.30
	^{104}Ag	....	0.32

From the list of nuclear reactions selected for the Q-value variation study (see Table 2.3), only $^{26}P(p,\gamma)^{27}S$, $^{46}Cr(p,\gamma)^{47}Mn$, $^{55}Ni(p,\gamma)^{56}Cu$, $^{60}Zn(p,\gamma)^{61}Ga$, and $^{64}Ge(p,\gamma)^{65}As$ show some impact on the final yields when their Q-values are varied between 1σ uncertainty bounds. However, as summarized in Table 2.4, the effects are restricted to single isotopes, except for the last reaction, $^{64}Ge(p,\gamma)$, whose influence ranges between ^{64}Zn and ^{104}Ag. Indeed, the significance of this reaction on the ^{64}Ge

waiting point is well-known (see e.g., Woosley et al. 2004, Thielemann et al. 2001, Schatz 2006; Schatz & Rehm 2006, Fisker et al. 2008, and references therein). Mass measurements on ^{64}Ge have indeed been performed (Clark et al. 2007; Schury et al. 2007). When combining these measurements with the ^{65}As mass value given by Audi et al. (2003b), the corresponding 1σ uncertainty limits in the $^{64}Ge(p,\gamma)^{65}As$ Q-value ($-74 \pm 303\,keV$, and $-46 \pm 302\,keV$, respectively) are well covered by the range used in our study ($Q = -80 \pm 300\ keV$; Audi et al. 2003b). Clearly, mass measurements on ^{65}As are still required to better determine this Q-value. These are challenging experiments because of the difficulty of producing ^{65}As (Clark, private communication).

2.3.2 Model S01

Here, we summarize the main results obtained from our post-processing calculations with the temperature versus time profile extracted from the one-zone model of Schatz et al. (2001) [Model S01].

Because of the larger peak temperature achieved in this model, the main nuclear activity extends to heavier nuclei (^{107}Cd, for $X > 10^{-2}$) than in Model K04. The most abundant species (stable or with a half-life $> 1\,hr$) at the end of the burst are now H (0.071, by mass), ^{4}He (0.013), and the heavy isotopes ^{104}Ag (0.328), ^{106}Cd (0.244), ^{103}Ag (0.078), and ^{105}Ag (0.085). This chemical pattern bears some resemblance to that reported by Schatz et al. (2001), and also to a similar model (zM) computed by Woosley et al. (2004) with a 1-D hydrodynamic code. For example, a large overproduction of the p-nucleus ^{106}Cd is explicitly mentioned in Schatz et al. (2001), Fig. 4; as well, Woosley et al. (2004) (Fig. 7), find a large mass fraction of ^{106}Sn (which will decay into ^{106}Cd), followed by ^{64}Ge, ^{68}Se, ^{104}In (which will decay into ^{104}Ag), ^{4}He, and H. It is worth noting that the final amount of H is much smaller than in Model K04: here, H and He are almost depleted and hence the next burst will necessarily require the piling-up of fresh H/He-rich fuel on top of this H/He-depleted shell.

Only 64 reactions (and the corresponding reverse processes) from the overall nuclear network turn out to have an impact on the final yields when their rates are varied by a factor of 10, up and down (Table 2.5). As reported for Model K04, the influence of these reactions is often limited to the vicinity of the target nuclei. Remarkable exceptions are $^{56}Ni(\alpha,p)$, $^{59}Cu(p,\gamma)$, and to a lesser extent, $^{103}Sn(\alpha,p)$. Notice also that, among the most important reactions, only three alpha-captures $^{15}O(\alpha,\gamma)$, $^{56}Ni(\alpha,p)$, and $^{103}Sn(\alpha,p)$ are found. The role played by $^{15}O(\alpha,\gamma)$ is as marginal as for Model K04 however (but see discussion in Section 2.4).

Concerning the most influential β-decay rates, we found similar results to those reported for Model K04. Hence, the β-decay rates of ^{68}Se, ^{72}Kr, ^{80}Zr, ^{88}Ru, and ^{92}Pd, are important, but due to the higher peak temperatures reached in this model, the list also extends to heavier species, including $^{101-106}Sn$ and ^{106}Sb (Table 2.2).

Table 2.5: Same as Table 2.1, for Model S01 (Schatz et al. 2001).

Reaction	Isotope	10	0.1
^{15}O(α, γ)^{19}Ne	^{15}N	...	8.84
^{52}Fe(p, γ)^{53}Co	^{52}Fe	...	8.48
^{52}Co(p, γ)^{53}Ni	^{52}Fe	...	2.03
^{56}Ni(p, γ)^{57}Cu	^{56}Ni	...	8.33
^{56}Ni(α, p)^{59}Cu	^{1}H	0.36	...
	^{52}Fe	2.40	...
	^{56}Ni	2.31	...
	^{69}Ge	2.27	...
	^{70}Ge	2.19	...
	^{71}As	2.02	...
	^{73}Se	2.25	...
	^{74}Se	2.19	...
^{57}Ni(p, γ)^{58}Cu	^{57}Ni	...	2.50
^{57}Cu(p, γ)^{58}Zn	^{57}Ni	...	2.09
^{58}Cu(p, γ)^{59}Zn	^{58}Ni	...	4.92
^{59}Cu(p, γ)^{60}Zn	^{1}H	...	0.35
	^{52}Fe	...	2.45
	^{56}Ni	...	2.35
	^{59}Ni	...	6.60
	^{69}Ge	...	2.32
	^{70}Ge	...	2.24
	^{71}As	...	2.07
	^{73}Se	...	2.29
	^{74}Se	...	2.24
^{61}Zn(p, γ)^{62}Ga	^{61}Cu	...	5.59
^{61}Ga(p, γ)^{62}Ge	^{60}Ni	0.29	...
^{62}Zn(p, γ)^{63}Ga	^{62}Zn	...	3.52
^{63}Ga(p, γ)^{64}Ge	^{63}Cu	0.31	6.80
^{65}Ge(p, γ)^{66}As	^{65}Zn	...	7.90
^{66}Ge(p, γ)^{67}As	^{66}Ge	0.22	6.19
^{66}As(p, γ)^{67}Se	^{66}Ge	0.40	...
^{67}As(p, γ)^{68}Se	^{67}Ga	0.13	6.71
^{69}Se(p, γ)^{70}Br	^{69}Ge	0.11	6.14
^{69}Br(p, γ)^{70}Kr	^{72}Se	...	2.06
	^{76}Kr	...	2.06
^{70}Se(p, γ)^{71}Br	^{70}Ge	0.21	7.01
^{71}Br(p, γ)^{72}Kr	^{71}As	0.11	5.53
^{73}Kr(p, γ)^{74}Rb	^{73}Se	0.11	5.53
^{74}Kr(p, γ)^{75}Rb	^{74}Se	0.14	6.84
^{75}Rb(p, γ)^{76}Sr	^{75}Br	0.12	4.54
^{77}Sr(p, γ)^{78}Y	^{77}Kr	0.16	3.17
^{78}Sr(p, γ)^{79}Y	^{78}Kr	0.12	5.42
^{79}Y(p, γ)^{80}Zr	^{79}Kr	0.14	3.43
^{80}Y(p, γ)^{81}Zr	^{80}Sr	0.43	2.84
^{81}Y(p, γ)^{82}Zr	^{81}Rb	...	2.15
^{81}Zr(p, γ)^{82}Nb	^{81}Rb	0.27	...
^{82}Zr(p, γ)^{83}Nb	^{82}Sr	0.20	2.25
^{83}Zr(p, γ)^{84}Nb	^{83}Sr	0.37	...

Table 2.5: – Continued.

Reaction	Isotope	10	0.1
^{84}Zr(p, γ)^{85}Nb	^{84}Sr	0.46	...
^{84}Nb(p, γ)^{85}Mo	^{84}Sr	0.42	...
^{85}Nb(p, γ)^{86}Mo	^{85}Y	0.29	...
^{86}Mo(p, γ)^{87}Tc	^{86}Zr	0.40	...
^{87}Mo(p, γ)^{88}Tc	^{87}Zr	0.36	...
^{88}Mo(p, γ)^{89}Tc	^{88}Zr	0.27	...
^{89}Tc(p, γ)^{90}Ru	^{89}Nb	0.32	...
^{90}Mo(p, γ)^{91}Tc	^{90}Mo	0.45	...
^{91}Tc(p, γ)^{92}Ru	^{91}Nb	0.30	...
^{92}Ru(p, γ)^{93}Rh	^{92}Mo	0.23	...
^{93}Ru(p, γ)^{94}Rh	^{93}Tc	0.47	...
^{93}Rh(p, γ)^{94}Pd	^{93}Tc	0.30	2.29
^{94}Rh(p, γ)^{95}Pd	^{94}Mo	0.28	...
^{94}Pd(p, γ)^{95}Ag	^{94}Mo	0.49	...
^{95}Rh(p, γ)^{96}Pd	^{95}Ru	0.46	...
^{95}Pd(p, γ)^{96}Ag	^{95}Ru	0.32	...
^{96}Ag(p, γ)^{97}Cd	^{96}Ru	0.46	2.29
^{97}Ag(p, γ)^{98}Cd	^{97}Ru	0.22	...
^{97}Cd(p, γ)^{98}In	^{97}Ru	0.43	...
^{98}Ag(p, γ)^{99}Cd	^{98}Ru	0.42	...
^{98}Cd(p, γ)^{99}In	^{98}Ru	0.40	2.30
^{99}Cd(p, γ)^{100}In	^{99}Rh	0.28	...
^{100}Cd(p, γ)^{101}In	^{100}Pd	0.49	...
^{100}In(p, γ)^{101}Sn	^{100}Pd	0.44	...
^{101}In(p, γ)^{102}Sn	^{101}Pd	0.30	...
^{102}In(p, γ)^{103}Sn	^{102}Pd	0.36	...
^{103}In(p, γ)^{104}Sn	^{103}Ag	0.46	...
^{103}Sn(α, p)^{106}Sb	^{106}Cd	0.34	...
	^{107}Cd	0.24	...
	^{108}Cd	0.21	...
	^{109}In	0.21	...
^{105}Sn(p, γ)^{106}Sb	^{105}Ag	0.33	...
^{107}Sn(p, γ)^{108}Sb	^{108}Cd	2.32	...
^{108}Sb(p, γ)^{109}Te	^{109}In	3.33	...
^{109}Sb(p, γ)^{110}Te	^{109}In	0.46	2.32

Additional studies of the specific impact of these decays with realistic uncertainty bounds (Audi et al. 2003a) have also been performed for this case, revealing no effect on any particular isotope.

2.3.3 Model F08

Since this model achieves the lowest peak temperature of the three models extracted from the literature, its main nuclear path is somewhat more limited, reaching only ^{72}Se ($X > 10^{-2}$).

Table 2.6: Same as Table 2.1, for Model F08 (Fisker et al. 2008).

Reaction	Isotope	10	0.1
^{12}C(p, γ)^{13}N	^{12}C	0.41	...
^{12}C(α, γ)^{16}O	^{12}C	0.42	...
	^{16}O	3.27	0.36
	^{20}Ne	3.03	0.42
	^{24}Mg	2.40	...
^{16}O(α, γ)^{20}Ne	^{16}O	0.11	8.36
^{20}Ne(α, γ)^{24}Mg	^{20}Ne	0.10	9.84
^{22}Mg(α, p)^{25}Al	^{25}Mg	...	8.81
	^{27}Al	...	2.23
^{24}Mg(p, γ)^{25}Al	^{25}Mg	3.02	0.43
^{24}Mg(α, γ)^{28}Si	^{24}Mg	0.18	4.16
	^{25}Mg	0.24	4.10
^{25}Al(α, p)^{28}Si	^{25}Mg	0.22	2.36
^{26g}Al(p, γ)^{27}Si	^{27}Al	2.71	0.40
^{26g}Al(α, p)^{29}Si	^{26}Mg	...	2.34
	^{26g}Al	0.08	2.38
	^{27}Al	0.40	...
^{26}Si(α, p)^{29}P	^{26g}Al	0.08	...
	^{27}Al	0.23	...
^{27}Al(α, p)^{30}Si	^{27}Al	0.32	...
^{27}Si(α, p)^{30}P	^{27}Al	0.30	...
^{28}Si(α, γ)^{32}S	^{28}Si	0.43	...
	^{32}S	3.73	0.37
^{29}Si(α, γ)^{33}S	^{33}S	2.15	...
^{30}P(p, γ)^{31}S	^{31}P	2.38	0.29
^{30}P(α, p)^{33}S	^{33}S	2.29	...
^{34}Cl(p, γ)^{35}Ar	^{35}Cl	2.07	...
^{36}Ar(p, γ)^{37}K	^{37}Ar	0.40	2.76
^{39}K(p, γ)^{40}Ca	^{40}Ca	2.15	...
^{44}Ti(p, γ)^{45}V	^{45}Ti	0.18	2.32
^{44}V(p, γ)^{45}Cr	^{45}Ti	...	0.47
^{45}V(p, γ)^{46}Cr	^{45}Ti	...	2.25
^{46}V(p, γ)^{47}Cr	^{47}Ti	2.22	...
^{47}Cr(p, γ)^{48}Mn	^{47}Ti	0.42	2.78
^{49}Mn(p, γ)^{50}Fe	^{49}V	...	2.19
^{52}Fe(p, γ)^{53}Co	^{52}Fe	0.31	3.06
	^{53}Mn	...	0.48
^{53}Co(p, γ)^{54}Ni	^{53}Mn	0.18	4.06
^{54}Co(p, γ)^{55}Ni	^{54}Fe	...	2.01
^{57}Ni(p, γ)^{58}Cu	^{57}Ni	...	7.71
^{57}Cu(p, γ)^{58}Zn	^{56}Ni	...	2.07
	^{57}Ni	0.46	2.31
	^{58}Ni	3.31	0.37
	^{59}Ni	2.20	0.47
^{58}Cu(p, γ)^{59}Zn	^{58}Ni	0.44	5.57
^{59}Cu(p, γ)^{60}Zn	^{59}Ni	...	2.88
^{61}Zn(p, γ)^{62}Ga	^{61}Cu	0.21	3.59
	^{62}Zn	...	0.49

Table 2.6: – Continued.

Reaction	Isotope	10	0.1
^{61}Ga(p, γ)^{62}Ge	^{64}Zn	3.11	...
	^{65}Zn	3.06	...
	^{66}Ge	3.06	...
	^{67}Ga	3.13	...
^{62}Ga(p, γ)^{63}Ge	^{62}Zn	0.23	2.39
^{63}Ga(p, γ)^{64}Ge	^{63}Cu	0.49	2.72
^{65}Ge(p, γ)^{66}As	^{65}Zn	...	3.74
^{66}Ge(p, γ)^{67}As	^{66}Ge	0.49	...
^{67}As(p, γ)^{68}Se	^{67}Ga	0.38	3.20
^{69}Se(p, γ)^{70}Br	^{69}Ge	0.24	3.37
	^{70}Ge	...	0.44
^{70}Se(p, γ)^{71}Br	^{70}Ge	0.41	2.66
^{70}Br(p, γ)^{71}Kr	^{70}Ge	0.33	...
^{71}Br(p, γ)^{72}Kr	^{71}As	0.24	3.89
^{73}Kr(p, γ)^{74}Rb	^{73}Se	0.20	3.64
	^{74}Se	...	0.47
^{74}Kr(p, γ)^{75}Rb	^{74}Se	0.32	2.91
^{74}Rb(p, γ)^{75}Sr	^{74}Se	0.41	...
^{75}Rb(p, γ)^{76}Sr	^{75}Br	0.21	4.13
^{76}Rb(p, γ)^{77}Sr	^{77}Kr	...	0.48
^{77}Sr(p, γ)^{78}Y	^{77}Kr	0.19	3.57
^{78}Sr(p, γ)^{79}Y	^{78}Kr	0.24	3.18
^{78}Y(p, γ)^{79}Zr	^{78}Kr	0.48	...
^{79}Y(p, γ)^{80}Zr	^{79}Kr	...	4.99
^{80}Y(p, γ)^{81}Zr	^{81}Rb	...	0.43
^{81}Zr(p, γ)^{82}Nb	^{81}Rb	0.19	3.35
^{82}Zr(p, γ)^{83}Nb	^{82}Sr	0.21	3.21
	^{83}Sr	...	0.46
^{83}Nb(p, γ)^{84}Mo	^{83}Sr	...	3.62
^{84}Nb(p, γ)^{85}Mo	^{84}Sr	...	4.18
^{85}Mo(p, γ)^{86}Tc	^{85}Y	0.19	2.83
	^{90}Mo	...	0.50
	^{91}Nb	...	0.46
^{86}Mo(p, γ)^{87}Tc	^{86}Zr	0.17	2.97
	^{87}Zr	...	0.44
	^{88}Zr	...	0.40
	^{89}Nb	...	0.44
	^{90}Mo	...	0.42
^{87}Tc(p, γ)^{88}Ru	^{87}Zr	0.21	...
	^{88}Zr	...	0.43
^{88}Tc(p, γ)^{89}Ru	^{89}Nb	...	0.47

The most abundant species (stable or with a half-life $> 1\,hr$) at the end of the burst are now ^{4}He (0.085), ^{56}Ni (0.13), ^{60}Ni (0.38), ^{12}C (0.040), ^{28}Si (0.041), and ^{64}Zn (0.034). Moreover, H has been depleted down to 10^{-11} by mass. Qualitatively, there is good agreement with the relevant chemical pattern reported in Fisker et al.

(2008), Fig. 20. It is worth noting that the large amount of ^{12}C obtained at the end of the burst may have implications for the energy source that powers superbursts (see Section 3.1, and Chapter 4).

Again, only a few reactions –62, and the corresponding reverse reactions– have an impact on the final yields when their rates are varied by a factor of 10, up and down (Table 2.6). The most influential reactions are $^{12}C(\alpha,\gamma)$, $^{26g}Al(\alpha,p)$, $^{57}Cu(p,\gamma)$, $^{61}Ga(p,\gamma)$, and $^{85,86}Mo(p,\gamma)$. Additional discussion and tests on the impact of the $^{12}C(\alpha,\gamma)$ rate are presented in Section 2.4. Thirteen α-capture reactions show some impact on the yields, a larger number than in Models K04 and S01. Indeed, all key reactions affecting $A < 30$ species are mainly (α,γ) or (α,p) reactions. It is worth mentioning, however, that $^{15}O(\alpha,\gamma)$ is absent from this list (see Section 2.4).

The most influential β-decay rates are now shifted towards lighter unstable isotopes, because of the lower T_{peak} value achieved. These include decays of $^{26,29}Si$, $^{29,30}S$, $^{33,34}Ar$, $^{37,38}Ca$, ^{60}Zn, ^{68}Se, ^{72}Kr, ^{76}Sr, and ^{80}Zr (Table 2.2). As in Models K04 and S01 though, no effect is seen on any isotope when realistic uncertainties are adopted for these decay rates.

The only nuclear reaction from Table 2.3 that has a significant impact on the final yields when its Q-value is varied between 1σ uncertainty bounds is $^{45}Cr(p,\gamma)$ (see Table 2.7).

Table 2.7: Same as Table 2.4, for Model F08.

Reaction	Isotope	High-Q ($Q+\Delta Q$)	Low-Q ($Q-\Delta Q$)
^{45}Cr(p, γ)^{46}Mn	^{45}Ti	0.50	...

2.3.4 Effect of the duration of the burst: Model K04-B1 vs. K04-B2

Because of the shorter duration of Model K04-B1, as compared with Model K04, the main nuclear path extends up to ^{68}Ge. In contrast, the longer burst of Model K04-B2 drives the main path up to ^{106}Cd.

The most abundant species at the end of the bursts are: H (0.42, by mass), ^{4}He (0.061), ^{60}Ni (0.10), ^{64}Zn (0.31), and ^{68}Ge (0.023), for the shorter burst of Model K04-B1; and ^{4}He (0.0051), ^{68}Ge (0.159), ^{72}Se (0.121), ^{76}Kr (0.077), ^{80}Sr (0.040), ^{90}Mo (0.042), ^{94}Mo (0.055), ^{98}Ru (0.040), ^{102}Pd (0.034), ^{103}Ag (0.060), ^{104}Ag (0.097), and ^{105}Ag (0.042), for Model K04-B2. The final amount of H in the latter model has decreased down to 10^{-15}. The larger extension of the main nuclear activity reported for Model K04-B2 is a direct consequence of the longer exposure times to higher temperatures. However, the depletion of H results from the complex interplay between exposure time to high temperatures, which decreases the overall H content, and the effect of photodisintegrations, which raise the H abundance.

Table 2.8: Same as Table 2.1, for Model K04-B1.

Reaction	Isotope	10	0.1
^{15}O(α, γ)^{19}Ne	^{15}N	0.11	6.14
^{18}Ne(α, p)^{21}Na	^{15}N	0.28	...
	^{18}F	0.29	...
	^{21}Ne	0.26	2.03
^{22}Mg(p, γ)^{23}Al	^{22}Na	0.49	6.21
^{23}Al(p, γ)^{24}Si	^{22}Na	...	4.45
^{27}P(p, γ)^{28}S	^{27}Al	0.25	6.34
^{31}Cl(p, γ)^{32}Ar	^{30}Si	0.16	2.57
	^{31}P	0.16	2.72
	^{32}S	...	0.29
^{34}Ar(p, γ)^{35}K	^{34}S	0.44	2.25
	^{36}Ar	...	0.30
^{39}Ca(p, γ)^{40}Sc	^{39}K	...	9.70
^{42}Ti(p, γ)^{43}V	^{42}Ca	...	2.11
^{43}V(p, γ)^{44}Cr	^{42}Ca	0.22	7.20
^{47}Mn(p, γ)^{48}Fe	^{46}Ti	0.17	2.38
	^{48}Cr	...	0.26
^{51}Fe(p, γ)^{52}Co	^{51}Cr	...	6.19
^{52}Fe(p, γ)^{53}Co	^{52}Fe	0.35	7.51
^{52}Co(p, γ)^{53}Ni	^{52}Fe	...	2.24
^{55}Ni(p, γ)^{56}Cu	^{55}Co	...	2.83
^{56}Ni(p, γ)^{57}Cu	^{56}Ni	0.33	7.74
^{56}Cu(p, γ)^{57}Zn	^{55}Co	0.34	4.09
	^{56}Ni	...	2.16
^{57}Cu(p, γ)^{58}Zn	^{57}Ni	...	2.33
^{61}Ga(p, γ)^{62}Ge	^{60}Ni	0.17	2.93
	^{61}Cu	0.16	3.01
	^{62}Zn	...	0.35
	^{64}Zn	...	0.39
	^{65}Zn	...	0.37
	^{66}Ge	...	0.37
	^{67}Ga	...	0.38
	^{68}Ge	...	0.33
	^{69}Ge	...	0.31
	^{70}Ge	...	0.31
	^{71}As	...	0.32
	^{72}Se	...	0.30
	^{76}Kr	...	0.29
^{63}Ga(p, γ)^{64}Ge	^{63}Cu	...	2.13
^{65}Ge(p, γ)^{66}As	^{65}Zn	0.25	7.08
^{65}As(p, γ)^{66}Se	^{68}Ge	3.85	...
	^{69}Ge	3.92	...
	^{70}Ge	3.94	...
	^{71}As	4.04	...
	^{72}Se	4.73	0.40
	^{76}Kr	5.05	0.32
^{66}Ge(p, γ)^{67}As	^{66}Ge	...	2.68
^{66}As(p, γ)^{67}Se	^{66}Ge	0.19	2.66

Table 2.8: – Continued.

Reaction	Isotope	10	0.1
^{67}As(p, γ)^{68}Se	^{67}Ga	...	3.15
^{69}Se(p, γ)^{70}Br	^{69}Ge	...	5.91
^{70}Se(p, γ)^{71}Br	^{70}Ge	...	2.96
^{71}Br(p, γ)^{72}Kr	^{71}As	0.42	4.16

Concerning nuclear uncertainties, Model K04-B1 is characterized by 28 critical reactions, the most important ones being $^{61}Ga(p,\gamma)$ and $^{65}As(p,\gamma)$, with a marginal role played by $^{18}Ne(\alpha,p)$ and $^{31}Cl(p,\gamma)$ (Table 2.8). For Model K04-B2, with 51 critical reactions, the most important reactions are $^{65}As(p,\gamma)$ and $^{32}S(\alpha,\gamma)$, followed, to some extent, by $^{12}C(\alpha,\gamma)$, $^{61}Ga(p,\gamma)$, $^{75}Rb(p,\gamma)$, $^{84}Zr(p,\gamma)$, $^{92}Ru(p,\gamma)$, $^{93}Rh(p,\gamma)$, and $^{96}Ag(p,\gamma)$ (Table 2.9). Only 2 α-capture reactions appear to be influential in Model K04-B1 (one being $^{15}O(\alpha,\gamma)$, see Table 2.8), whereas uncertainties affecting 12 α-capture reactions turn out to be critical for Model K04-B2 (see Table 2.9).

Table 2.2 lists the most important β-decay rates for these models, when these rates are varied by a factor of 10, up and down. In summary, β-decay rates of ^{25}Si, ^{33}Ar, $^{36-38}Ca$, ^{41}Ti, ^{59}Zn, $^{62-64}Ge$, and ^{68}Se, become critical in Model K04-B1, whereas those of ^{25}Si, ^{68}Se, ^{72}Kr, ^{76}Sr, ^{80}Zr, $^{92,94}Pd$, and $^{101-104}Sn$ play a major role in Model K04-B2. As before, no noticeable effect remains when realistic uncertainties are adopted for these rates.

2.3.5 Effect of the initial metallicity: Models K04-B3, K04-B4, and K04-B5

In the low metallicity Model K04-B3, the main nuclear path ($X > 10^{-2}$) stops at ^{96}Ru. In contrast, the higher metallicity Models K04-B4 and K04-B5 reach ^{68}Ge and ^{72}Se, respectively. The most abundant species at the end of the bursts are: H (0.194), ^{4}He (0.021), ^{68}Ge (0.205), ^{72}Se (0.132), ^{64}Zn (0.075), ^{76}Kr (0.073), ^{80}Sr (0.041), and ^{82}Sr (0.023), for Model K04-B3; ^{4}He (0.018), ^{60}Ni (0.696), ^{64}Zn (0.161), ^{56}Ni (0.051), ^{32}S (0.014), and ^{68}Ge (0.016), for Model K04-B4; and finally, ^{4}He (0.018), ^{56}Ni (0.273), ^{60}Ni (0.256), ^{39}K (0.057), ^{64}Zn (0.062), and ^{68}Ge (0.041), for Model K04-B5. Note that H has been seriously depleted in both high metallicity models, achieving mass fractions of 4×10^{-14} and 10^{-15}, respectively.

Concerning nuclear uncertainties, Model K04-B3 is characterized by 56 critical reactions, while Models K04-B4 and K04-B5, have 43 and 45 reactions, respectively. The most important ones for Model K04-B3 (Table 2.10) are $^{65}As(p,\gamma)$ and $^{96}Ag(p,\gamma)$, with a marginal role played by $^{102,103}In(p,\gamma)$. For Model K04-B4 (Table 2.11), the most influential reactions are $^{12}C(\alpha,\gamma)$, $^{30}S(\alpha,p)$, and to some extent, $^{30}P(\alpha,p)$, and $^{65}As(p,\gamma)$.

Table 2.9: Same as Table 2.1, for Model K04-B2.

Reaction	Isotope	10	0.1
^{12}C(α, γ)^{16}O	^{12}C	0.19	2.37
	^{24}Mg	...	0.26
	^{28}Si	...	0.29
^{20}Ne(α, γ)^{24}Mg	^{20}Ne	...	8.28
^{24}Mg(α, γ)^{28}Si	^{24}Mg	0.16	3.77
	^{34}S	0.48	4.30
^{24}Mg(α, p)^{27}Al	^{34}S	3.99	0.49
^{28}Si(α, γ)^{32}S	^{28}Si	0.31	2.63
	^{34}S	...	2.56
^{32}S(α, γ)^{36}Ar	^{32}S	0.31	...
	^{33}S	0.48	...
	^{35}Cl	0.24	...
	^{36}Ar	2.43	0.35
	^{39}K	2.20	...
^{32}S(α, p)^{35}Cl	^{35}Cl	2.22	0.30
^{33}S(p, γ)^{34}Cl	^{37}Ar	0.43	...
^{33}S(α, γ)^{37}Ar	^{33}S	0.40	...
	^{37}Ar	4.12	...
^{34}S(p, γ)^{35}Cl	^{34}S	0.35	2.02
^{34}S(α, γ)^{38}Ar	^{34}S	0.41	...
	^{38}Ar	2.18	...
^{35}Cl(p, γ)^{36}Ar	^{35}Cl	0.34	...
^{35}Cl(α, p)^{38}Ar	^{38}Ar	4.47	0.45
^{36}Ar(α, p)^{39}K	^{39}K	5.47	0.23
^{39}K(p, γ)^{40}Ca	^{39}K	0.45	2.07
^{40}Ca(α, p)^{43}Sc	^{44}Ti	...	2.78
^{41}Sc(p, γ)^{42}Ti	^{44}Ti	...	0.50
^{43}Sc(p, γ)^{44}Ti	^{44}Ti	2.78	...
^{51}Mn(p, γ)^{52}Fe	^{51}Cr	...	3.66
^{55}Co(p, γ)^{56}Ni	^{55}Co	...	2.89
^{60}Cu(p, γ)^{61}Zn	^{61}Cu	4.92	0.15
^{61}Ga(p, γ)^{62}Ge	^{60}Ni	...	2.54
	^{61}Cu	...	2.12
	^{63}Cu	...	2.56
^{63}Ga(p, γ)^{64}Ge	^{63}Cu	...	2.73
^{64}Ga(p, γ)^{65}Ge	^{65}Zn	5.48	0.26
^{65}As(p, γ)^{66}Se	^{36}Ar	...	0.49
	^{39}K	...	0.38
	^{61}Cu	...	0.22
	^{64}Zn	0.31	6.16
	^{65}Zn	0.38	2.26
	^{66}Ge	0.34	4.24
	^{67}Ga	...	11.28
	^{71}As	...	0.33
	^{73}As	...	0.42
	^{73}Se	...	0.44
	^{84}Sr	...	0.28
^{67}Ge(p, γ)^{68}As	^{67}Ga	3.47	...

Table 2.9: – Continued.

Reaction	Isotope	10	0.1
^{67}As(p, γ)^{68}Se	^{66}Ge	...	2.09
	^{67}Ga	...	2.49
^{68}As(p, γ)^{69}Se	^{69}Ge	2.46	0.42
^{69}As(p, γ)^{70}Se	^{70}Ge	2.36	...
^{71}Se(p, γ)^{72}Br	^{71}As	8.13	0.13
^{71}Br(p, γ)^{72}Kr	^{70}Ge	0.44	3.95
^{72}Br(p, γ)^{73}Kr	^{73}As	2.75	0.37
	^{73}Se	2.71	0.37
^{74}Kr(p, γ)^{75}Rb	^{75}Br	0.28	...
^{75}Rb(p, γ)^{76}Sr	^{74}Se	...	2.77
	^{75}Se	...	3.79
	^{75}Br	0.24	3.77
^{76}Rb(p, γ)^{77}Sr	^{77}Br	2.52	0.46
	^{77}Kr	2.49	0.46
^{78}Sr(p, γ)^{79}Y	^{78}Kr	...	3.16
^{79}Y(p, γ)^{80}Zr	^{79}Kr	0.12	5.75
^{82}Zr(p, γ)^{83}Nb	^{82}Sr	...	3.49
^{83}Nb(p, γ)^{84}Mo	^{83}Sr	...	2.50
^{84}Zr(p, γ)^{85}Nb	^{84}Sr	2.35	0.17
	^{85}Sr	0.16	...
	^{85}Y	0.15	...
^{84}Nb(p, γ)^{85}Mo	^{83}Sr	...	3.33
^{86}Mo(p, γ)^{87}Tc	^{86}Y	...	2.73
	^{86}Zr	...	2.70
^{87}Mo(p, γ)^{88}Tc	^{87}Y	2.13	...
	^{87}Zr	2.08	...
^{88}Mo(p, γ)^{89}Tc	^{89}Zr	0.19	...
	^{89}Nb	0.19	...
^{92}Ru(p, γ)^{93}Rh	^{92}Mo	2.46	...
	^{93}Mo	0.27	...
	^{93}Tc	0.26	...
^{92}Rh(p, γ)^{93}Pd	^{91}Nb	2.14	...
^{93}Rh(p, γ)^{94}Pd	^{92}Mo	...	2.45
	^{93}Mo	...	2.66
	^{93}Tc	...	2.62
^{96}Ag(p, γ)^{97}Cd	^{95}Tc	...	2.06
	^{95}Ru	...	2.03
	^{96}Ru	0.31	4.80
^{99}Cd(p, γ)^{100}In	^{99}Rh	...	3.19
^{100}In(p, γ)^{101}Sn	^{100}Rh	...	3.12
	^{100}Pd	0.31	3.10
^{101}Cd(p, γ)^{102}In	^{102}Pd	0.45	...

Finally, for Model K04-B5 (Table 2.12), the key reactions are $^{30}S(\alpha,p)$, $^{25}Si(\alpha,p)$, $^{59}Cu(p,\gamma)$, $^{56}Ni(\alpha,p)$, $^{29}S(\alpha,p)$, $^{65}As(p,\gamma)$, and $^{12}C(\alpha,\gamma)$, and to some extent, $^{61}Ga(p,\gamma)$. Note that $^{15}O(\alpha,\gamma)$ is only important for Model K04-B3.

Table 2.10: Same as Table 2.1, for Model K04-B3.

Reaction	Isotope	10	0.1
^{15}O(α, γ)^{19}Ne	^{15}N	...	8.17
^{18}Ne(α, p)^{21}Na	^{15}N	0.43	...
	^{18}F	0.44	...
^{31}Cl(p, γ)^{32}Ar	^{30}Si	0.45	...
^{43}V(p, γ)^{44}Cr	^{42}Ca	...	4.68
	^{44}Ti	...	0.48
^{47}Mn(p, γ)^{48}Fe	^{46}Ti	0.32	...
^{56}Ni(p, γ)^{57}Cu	^{56}Ni	...	7.93
^{56}Cu(p, γ)^{57}Zn	^{55}Co	...	2.63
^{57}Cu(p, γ)^{58}Zn	^{57}Ni	...	2.79
^{58}Cu(p, γ)^{59}Zn	^{58}Ni	...	2.08
^{59}Cu(p, γ)^{60}Zn	^{59}Ni	...	2.05
^{61}Zn(p, γ)^{62}Ga	^{61}Cu	...	2.39
^{61}Ga(p, γ)^{62}Ge	^{60}Ni	0.17	4.17
	^{61}Cu	...	4.33
^{63}Ga(p, γ)^{64}Ge	^{63}Cu	...	3.31
^{65}Ge(p, γ)^{66}As	^{65}Zn	...	8.88
^{65}As(p, γ)^{66}Se	^{64}Zn	0.34	3.41
	^{65}Zn	0.36	2.81
	^{66}Ge	0.43	2.66
	^{67}Ga	0.40	3.12
	^{81}Rb	...	0.48
	^{82}Sr	...	0.49
	^{86}Zr	...	0.50
	^{87}Zr	...	0.49
	^{88}Zr	...	0.48
	^{89}Nb	...	0.48
	^{90}Mo	...	0.47
	^{91}Nb	...	0.46
	^{92}Mo	...	0.46
	^{93}Tc	...	0.45
	^{94}Mo	...	0.44
	^{95}Ru	...	0.44
	^{96}Ru	...	0.43
	^{97}Ru	...	0.41
	^{98}Ru	...	0.39
	^{99}Rh	...	0.39
	^{100}Pd	...	0.39
	^{101}Pd	...	0.38
	^{102}Pd	...	0.38
	^{103}Ag	...	0.39
	^{104}Ag	...	0.42
^{66}Ge(p, γ)^{67}As	^{66}Ge	...	4.81
^{66}As(p, γ)^{67}Se	^{66}Ge	0.18	...
^{67}As(p, γ)^{68}Se	^{67}Ga	0.45	5.73
^{69}Se(p, γ)^{70}Br	^{69}Ge	0.10	8.19
^{70}Se(p, γ)^{71}Br	^{70}Ge	...	5.24
^{70}Br(p, γ)^{71}Kr	^{70}Ge	0.28	...

Table 2.10: – Continued.

Reaction	Isotope	10	0.1
^{71}Br(p, γ)^{72}Kr	^{71}As	0.20	7.01
^{73}Kr(p, γ)^{74}Rb	^{73}Se	0.10	7.53
^{74}Kr(p, γ)^{75}Rb	^{74}Se	0.30	6.30
^{74}Rb(p, γ)^{75}Sr	^{74}Se	0.40	...
^{75}Rb(p, γ)^{76}Sr	^{75}Br	0.15	6.45
^{77}Sr(p, γ)^{78}Y	^{77}Kr	0.11	5.58
^{78}Sr(p, γ)^{79}Y	^{78}Kr	0.17	6.15
^{79}Y(p, γ)^{80}Zr	^{79}Kr	0.12	5.73
^{81}Zr(p, γ)^{82}Nb	^{81}Rb	0.15	3.20
^{82}Zr(p, γ)^{83}Nb	^{82}Sr	0.17	2.94
^{83}Nb(p, γ)^{84}Mo	^{83}Sr	0.29	...
^{84}Nb(p, γ)^{85}Mo	^{84}Sr	0.20	2.51
^{85}Nb(p, γ)^{86}Mo	^{85}Y	0.44	2.01
^{85}Mo(p, γ)^{86}Tc	^{85}Y	0.48	...
^{86}Mo(p, γ)^{87}Tc	^{86}Zr	0.23	2.56
^{87}Mo(p, γ)^{88}Tc	^{87}Zr	0.32	...
^{88}Tc(p, γ)^{89}Ru	^{88}Zr	0.39	...
^{89}Tc(p, γ)^{90}Ru	^{89}Nb	0.25	2.16
^{90}Ru(p, γ)^{91}Rh	^{90}Mo	0.33	...
^{91}Ru(p, γ)^{92}Rh	^{91}Nb	0.36	...
^{92}Ru(p, γ)^{93}Rh	^{92}Mo	0.32	...
^{93}Rh(p, γ)^{94}Pd	^{93}Tc	0.24	...
^{94}Rh(p, γ)^{95}Pd	^{94}Mo	0.45	...
^{94}Pd(p, γ)^{95}Ag	^{94}Mo	0.43	...
^{95}Pd(p, γ)^{96}Ag	^{95}Ru	0.30	...
^{96}Ag(p, γ)^{97}Cd	^{96}Ru	0.45	...
	^{97}Ru	...	0.41
	^{98}Ru	...	0.38
	^{99}Rh	...	0.43
	^{100}Pd	...	0.48
^{97}Ag(p, γ)^{98}Cd	^{97}Ru	0.26	2.04
^{98}Ag(p, γ)^{99}Cd	^{98}Ru	0.45	...
^{98}Cd(p, γ)^{99}In	^{98}Ru	0.44	...
^{99}Cd(p, γ)^{100}In	^{99}Rh	0.33	...
^{100}Cd(p, γ)^{101}In	^{100}Pd	0.44	...
^{101}In(p, γ)^{102}Sn	^{101}Pd	0.34	...
^{102}In(p, γ)^{103}Sn	^{102}Pd	0.38	...
	^{103}Ag	2.05	0.39
	^{104}Ag	...	0.46
^{103}In(p, γ)^{104}Sn	^{103}Ag	0.50	...
	^{104}Ag	2.81	0.25
	^{105}Ag	2.08	...
^{104}In(p, γ)^{105}Sn	^{105}Ag	4.13	...

The number of influential α-induced reactions seems to increase with metallicity: only 2 reactions of this type are important in Models K04 and K04-B3, whereas 22 and 17 are important for Models K04-B4 and K04-B5, respectively.

Table 2.11: Same as Table 2.1, for Model K04-B4.

Reaction	Isotope	10	0.1
^{12}C(α, γ)^{16}O	^{12}C	0.24	2.53
	^{16}O	2.38	...
	^{20}Ne	2.30	0.26
	^{24}Mg	...	0.29
	^{28}Si	...	0.41
^{16}O(α, γ)^{20}Ne	^{16}O	...	7.65
^{20}Ne(α, γ)^{24}Mg	^{20}Ne	...	7.87
^{24}Mg(α, γ)^{28}Si	^{24}Mg	0.20	3.48
	^{30}Si	0.44	5.51
^{24}Mg(α, p)^{27}Al	^{30}Si	5.84	0.44
^{28}Si(α, p)^{31}P	^{31}P	3.39	0.44
^{28}Si(α, γ)^{32}S	^{28}Si	0.30	3.04
	^{31}P	0.42	4.07
^{30}Si(α, γ)^{34}S	^{30}Si	0.39	5.84
^{30}P(p, γ)^{31}S	^{33}S	0.50	...
	^{36}Cl	0.46	...
^{30}P(α, p)^{33}S	^{30}Si	...	23.47
	^{31}P	...	2.12
	^{36}Cl	...	0.37
^{30}S(α, p)^{33}Cl	^{30}Si	...	5.84
	^{31}P	...	2.88
	^{33}S	0.04	6.20
	^{36}Cl	...	4.19
	^{37}Ar	0.42	2.56
^{31}P(α, p)^{34}S	^{31}P	...	4.63
^{32}S(α, γ)^{36}Ar	^{32}S	0.36	...
	^{36}Ar	2.35	0.48
^{33}S(α, p)^{36}Cl	^{36}Cl	5.59	...
^{33}S(α, γ)^{37}Ar	^{33}S	0.05	...
^{34}S(α, γ)^{38}Ar	^{34}S	0.23	...
^{34}Cl(p, γ)^{35}Ar	^{34}S	0.39	...
^{34}Cl(α, p)^{37}Ar	^{34}S	0.26	...
	^{37}Ar	2.72	0.44
^{34}Ar(α, p)^{37}K	^{34}S	0.42	...
^{35}Cl(α, p)^{38}Ar	^{35}Cl	0.36	...
^{37}Ar(α, γ)^{41}Ca	^{41}Ca	3.93	...
^{38}K(α, p)^{41}Ca	^{41}Ca	6.45	0.43
^{39}K(p, γ)^{40}Ca	^{40}Ca	2.28	...
^{40}Ca(α, p)^{43}Sc	^{43}Ca	0.40	...
	^{43}Sc	0.40	...
^{42}Ca(p, γ)^{43}Sc	^{42}Ca	0.29	...
^{43}Sc(p, γ)^{44}Ti	^{44}Ti	2.99	...
^{46}Ti(α, p)^{49}V	^{49}V	2.12	...
^{48}Cr(p, γ)^{49}Mn	^{49}V	...	3.27
^{49}Mn(p, γ)^{50}Fe	^{49}V	...	2.12
^{58}Cu(p, γ)^{59}Zn	^{58}Ni	6.90	0.38
^{60}Cu(p, γ)^{61}Zn	^{61}Cu	3.59	0.39
^{61}Zn(p, γ)^{62}Ga	^{61}Cu	...	2.41

Table 2.11: – Continued.

Reaction	Isotope	10	0.1
^{62}Zn(p, γ)^{63}Ga	^{62}Zn	4.80	0.32
	^{63}Cu	0.33	...
^{64}Ga(p, γ)^{65}Ge	^{65}Zn	2.52	...
^{65}Ge(p, γ)^{66}As	^{65}Zn	...	3.12
^{65}As(p, γ)^{66}Se	^{64}Zn	0.43	...
	^{66}Ge	0.48	...
	^{67}Ga	0.48	...
^{66}Ge(p, γ)^{67}As	^{66}Ge	...	0.24
	^{67}Ga	...	3.62
^{70}Se(p, γ)^{71}Br	^{71}As	...	2.65
^{71}Se(p, γ)^{72}Br	^{71}As	8.95	...
^{73}Kr(p, γ)^{74}Rb	^{73}Se	...	2.16
^{74}Kr(p, γ)^{75}Rb	^{74}Se	...	0.33
	^{75}Br	...	4.28
^{84}Zr(p, γ)^{85}Nb	^{85}Y	0.44	...
^{87}Mo(p, γ)^{88}Tc	^{88}Zr	0.47	...

Finally, the most influential β-decays from Model K04-B3 are ^{68}Se, ^{72}Kr, ^{76}Sr, ^{80}Zr, ^{88}Ru, ^{92}Pd, and ^{99}In. Model K04-B4 is characterized by the importance of the β-decays of $^{33,34}Ar$, $^{37-39}Ca$, ^{42}Ti, ^{46}Cr, ^{49}Fe, ^{55}Ni, ^{58}Zn, ^{68}Se, ^{72}Kr, ^{76}Sr, and ^{80}Zr, whereas for Model K04-B5, the β-decay rates of ^{21}Mg, $^{24,25}Si$, $^{28-30}S$, $^{33,34}Ar$, $^{37,38}Ca$, ^{64}Ge, and ^{68}Se, are the most important (see Table 2.2). Again, no effect shows up when realistic (ground-state) uncertainties are adopted for these rates.

2.3.6 Effect of the peak temperature: Model K04-B6 vs. K04-B7

In Model K04, the main nuclear path ($X > 10^{-2}$) reached ^{96}Ru. Because of the lower peak temperature achieved in Model K04-B6, the main nuclear path reaches ^{82}Sr. In contrast, the higher temperatures achieved in Model K04-B7 drive the main path up to ^{103}Ag.

The most abundant species at the end of the burst are now H (0.151), ^{4}He (0.034), ^{64}Zn (0.375), ^{68}Ge (0.193), ^{60}Ni (0.051), ^{72}Se (0.074), ^{76}Kr (0.031), ^{80}Sr (0.015), and ^{82}Sr (0.011), for the lower peak temperature Model K04-B6 (Table 2.13); and H (0.460), ^{4}He (0.013), ^{68}Ge (0.058), ^{72}Se (0.069), ^{76}Kr (0.048), ^{80}Sr (0.031), and ^{96}Ru (0.026), for Model K04-B7 (Table 2.14). It is worth noting that Model K04-B7 ends with a larger amount of hydrogen than K04-B6 as a result of the major role played by photodisintegration reactions when the temperature exceeds $\sim 2\,GK$. This is illustrated in Fig. 2.3, where the time evolution of the hydrogen mass-fraction is plotted for the two Models K04-B6 (low T) and K04-B7 (high T).

Table 2.12: Same as Table 2.1, for Model K04-B5.

Reaction	Isotope	10	0.1
^{12}C(α, γ)^{16}O	^{12}C	0.26	...
	^{16}O	2.54	...
	^{20}Ne	2.44	0.18
	^{24}Mg	2.13	0.21
	^{28}Si	...	0.46
^{16}O(α, γ)^{20}Ne	^{16}O	...	7.66
^{20}Ne(α, γ)^{24}Mg	^{20}Ne	...	7.87
^{24}Mg(α, γ)^{28}Si	^{24}Mg	0.20	3.38
^{25}Si(α, p)^{28}P	^{30}Si	2.12	0.39
	^{32}S	0.39	...
	^{36}Ar	0.40	...
	^{37}Ar	0.15	2.54
	^{47}Ti	...	2.10
	^{55}Co	...	2.06
	^{56}Ni	0.37	2.10
	^{59}Ni	0.36	2.75
	^{65}Zn	2.21	...
	^{66}Ge	2.28	...
	^{68}Ge	2.03	...
	^{69}Ge	2.30	...
	^{70}Ge	3.48	...
	^{71}As	3.35	0.35
	^{72}Se	2.88	0.48
	^{73}Se	4.12	...
	^{76}Kr	4.02	0.36
	^{80}Sr	5.57	...
^{28}Si(p, γ)^{29}P	^{29}Si	2.88	...
^{28}Si(α, γ)^{32}S	^{28}Si	0.30	2.33
	^{32}S	...	0.34
^{29}Si(p, γ)^{30}P	^{29}Si	0.46	...
^{29}Si(α, γ)^{33}S	^{29}Si	...	3.62
^{29}P(α, p)^{32}S	^{29}Si	...	4.17
^{29}S(α, p)^{32}Cl	^{32}S	0.42	...
	^{36}Ar	0.41	...
	^{37}Ar	0.18	...
	^{56}Ni	0.38	...
	^{59}Ni	0.34	...
	^{66}Ge	2.02	...
	^{69}Ge	2.02	...
	^{70}Ge	2.84	...
	^{71}As	2.81	...
	^{72}Se	2.43	...
	^{73}Se	3.39	...
	^{76}Kr	3.30	...
	^{80}Sr	4.51	...
^{30}P(p, γ)^{31}S	^{30}Si	0.32	...
	^{31}P	2.11	0.35
^{30}P(α, p)^{33}S	^{30}Si	0.03	2.87

Table 2.12: – Continued.

Reaction	Isotope	10	0.1
	^{33}S	...	0.28
^{30}S(α, p)^{33}Cl	^{32}S	0.09	...
	^{33}S	0.20	...
	^{34}S	0.39	...
	^{35}Cl	0.26	...
	^{36}Ar	0.17	2.20
	^{37}Ar	0.05	3.72
	^{38}Ar	0.36	2.05
	^{39}K	0.36	...
	^{40}Ca	0.35	...
	^{42}Ca	0.44	2.18
	^{43}Sc	0.41	...
	^{44}Ti	0.33	...
	^{46}Ti	0.38	2.65
	^{47}Ti	0.37	2.63
	^{48}Ti	0.37	2.65
	^{50}Ti	0.35	2.65
	^{51}Ti	0.36	2.48
	^{54}Fe	0.34	2.67
	^{55}Co	0.33	2.63
	^{56}Ni	0.23	...
	^{59}Ni	0.25	3.66
	^{61}Cu	2.15	...
	^{62}Zn	2.43	...
	^{65}Zn	4.98	...
	^{66}Ge	5.83	...
	^{67}Ga	2.58	...
	^{68}Ge	3.01	...
	^{69}Ge	5.59	...
	^{70}Ge	11.80	...
	^{71}As	8.17	...
	^{72}Se	5.36	...
	^{73}Se	14.32	...
	^{76}Kr	9.40	0.49
	^{80}Sr	15.91	...
^{31}P(α, p)^{34}S	^{31}P	0.17	...
^{32}S(α, γ)^{36}Ar	^{36}Ar	3.60	...
^{33}S(α, γ)^{37}Ar	^{37}Ar	5.33	0.36
^{34}Cl(α, p)^{37}Ar	^{37}Ar	3.19	...
^{38}K(p, γ)^{39}Ca	^{38}Ar	0.44	...
^{40}Ca(α, p)^{43}Sc	^{44}Ti	0.48	...
^{42}Ca(p, γ)^{43}Sc	^{42}Ca	0.35	...
^{43}Sc(p, γ)^{44}Ti	^{44}Ti	4.48	0.29
^{46}Ti(p, γ)^{47}V	^{47}Ti	2.65	...
^{46}V(p, γ)^{47}Cr	^{47}Ti	2.41	...
^{48}Cr(p, γ)^{49}Mn	^{49}V	0.28	...
^{49}Mn(p, γ)^{50}Fe	^{49}V	...	2.30
^{52}Fe(p, γ)^{53}Co	^{52}Fe	...	2.52

Table 2.12: – Continued.

Reaction	Isotope	10	0.1
^{53}Fe(p, γ)^{54}Co	^{53}Mn	...	2.25
^{53}Co(p, γ)^{54}Ni	^{53}Mn	...	3.06
^{56}Ni(α, p)^{59}Cu	^{35}Cl	2.08	...
	^{36}Ar	2.74	...
	^{37}Ar	3.74	...
	^{46}Ti	2.18	...
	^{47}Ti	2.70	...
	^{48}Cr	2.30	...
	^{50}Cr	2.24	...
	^{51}Cr	2.18	...
	^{54}Fe	2.29	...
	^{55}Co	2.31	...
	^{56}Ni	2.48	...
	^{59}Ni	4.43	...
	^{65}Zn	0.49	...
	^{69}Ge	0.45	...
	^{71}As	0.32	...
	^{72}Se	0.42	...
	^{76}Kr	0.31	...
^{57}Cu(p, γ)^{58}Zn	^{56}Ni	...	2.85
	^{59}Ni	2.04	...
^{59}Cu(p, γ)^{60}Zn	^{35}Cl	...	2.10
	^{36}Ar	...	2.79
	^{37}Ar	...	3.83
	^{46}Ti	...	2.20
	^{47}Ti	...	2.77
	^{48}Cr	...	2.35
	^{50}Cr	...	2.29
	^{51}Cr	...	2.21
	^{54}Fe	...	2.32
	^{55}Co	...	2.35
	^{56}Ni	...	2.53
	^{59}Ni	...	8.36
	^{65}Zn	...	0.48
	^{69}Ge	...	0.45
	^{71}As	...	0.30
	^{72}Se	...	0.42
	^{76}Kr	...	0.30
^{61}Zn(p, γ)^{62}Ga	^{61}Cu	0.25	3.37
	^{62}Zn	...	0.44
^{61}Ga(p, γ)^{62}Ge	^{64}Zn	...	0.47
	^{67}Ga	...	0.49
	^{68}Ge	...	0.46
	^{69}Ge	...	0.47
^{62}Ga(p, γ)^{63}Ge	^{62}Zn	0.20	2.75
^{63}Ga(p, γ)^{64}Ge	^{63}Cu	...	2.36
^{64}Ga(p, γ)^{65}Ge	^{65}Zn	...	0.50
^{65}Ge(p, γ)^{66}As	^{65}Zn	0.21	3.68

Table 2.12: – Continued.

Reaction	Isotope	10	0.1
^{65}As(p, γ)^{66}Se	^{68}Ge	2.11	...
	^{69}Ge	2.10	...
	^{70}Ge	2.14	...
	^{71}As	2.15	...
	^{72}Se	2.69	...
	^{73}Se	2.63	...
	^{76}Kr	2.89	0.47
	^{80}Sr	2.97	...
^{66}As(p, γ)^{67}Se	^{66}Ge	0.29	2.13
^{67}As(p, γ)^{68}Se	^{67}Ga	0.48	2.78
^{69}Se(p, γ)^{70}Br	^{69}Ge	...	2.27
^{70}Se(p, γ)^{71}Br	^{70}Ge	2.91	...
	^{71}As	0.38	...
^{71}Br(p, γ)^{72}Kr	^{70}Ge	...	2.36
	^{71}As	0.30	3.81
^{73}Kr(p, γ)^{74}Rb	^{73}Se	...	3.23

Indeed, the *bump* exhibited by Model K04-B7 during the $20\,s$ after T_{peak} (that is, when the temperature ranges between 1.5 and $2.5\,GK$) is caused by the protons released through (γ, p) reactions on a number of nuclear species.

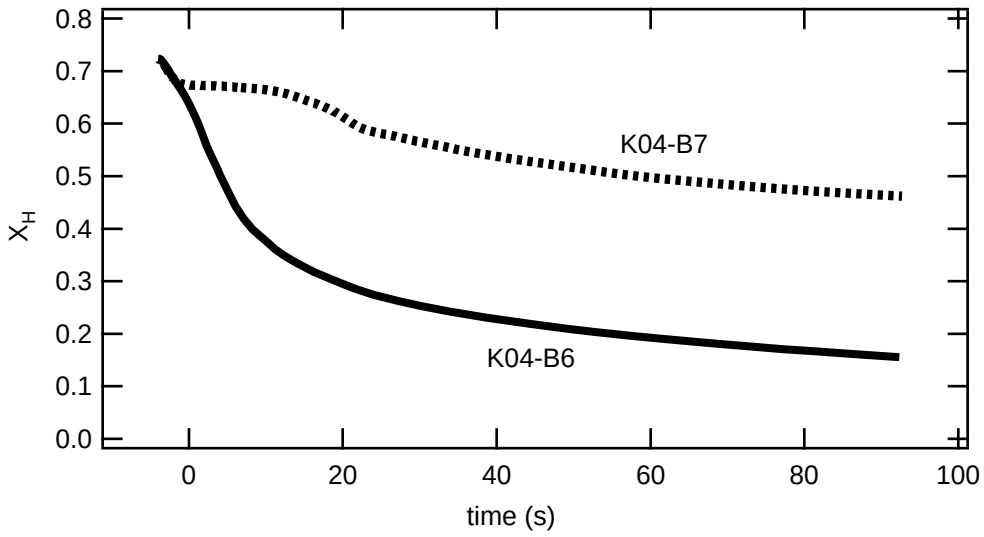

Figure 2.3: Time evolution of the hydrogen mass fraction in Models K04-B6 (low T) and K04-B7 (high T). Models are based on Koike et al. (2004) (see text, for details). The value t = 0 corresponds to the time at which T_{peak} is reached.

Table 2.13: Same as Table 2.1, for Model K04-B6.

Reaction	Isotope	10	0.1
^{15}O(α, γ)^{19}Ne	^{15}N	...	9.47
^{18}Ne(α, p)^{21}Na	^{15}N	0.42	...
	^{18}F	0.41	...
^{22}Mg(p, γ)^{23}Al	^{22}Na	...	3.14
^{23}Al(p, γ)^{24}Si	^{22}Na	...	5.61
^{27}P(p, γ)^{28}S	^{27}Al	...	4.73
	^{28}Si	...	0.48
^{39}Ca(p, γ)^{40}Sc	^{39}K	...	8.52
^{43}V(p, γ)^{44}Cr	^{42}Ca	...	2.65
^{52}Fe(p, γ)^{53}Co	^{52}Fe	...	8.62
^{52}Co(p, γ)^{53}Ni	^{52}Fe	...	2.20
^{53}Co(p, γ)^{54}Ni	^{53}Mn	...	2.07
^{56}Ni(p, γ)^{57}Cu	^{56}Ni	0.25	8.48
^{56}Cu(p, γ)^{57}Zn	^{55}Co	0.30	...
^{57}Cu(p, γ)^{58}Zn	^{57}Ni	0.39	2.86
^{58}Cu(p, γ)^{59}Zn	^{58}Ni	...	2.91
^{59}Cu(p, γ)^{60}Zn	^{59}Ni	...	2.57
^{61}Zn(p, γ)^{62}Ga	^{61}Cu	...	3.74
^{61}Ga(p, γ)^{62}Ge	^{60}Ni	0.16	5.05
	^{61}Cu	0.15	5.71
	^{63}Cu	...	3.22
	^{69}Ge	...	0.49
	^{73}Se	...	0.43
	^{74}Se	...	0.43
	^{75}Br	...	0.43
	^{76}Kr	...	0.47
	^{77}Kr	...	0.40
	^{78}Kr	...	0.40
	^{79}Kr	...	0.40
	^{80}Sr	...	0.44
	^{81}Rb	...	0.39
	^{82}Sr	...	0.40
	^{83}Sr	...	0.40
	^{84}Sr	...	0.41
	^{85}Y	...	0.41
	^{86}Zr	...	0.41
	^{87}Zr	...	0.40
	^{88}Zr	...	0.39
	^{89}Nb	...	0.39
	^{90}Mo	...	0.39
	^{91}Nb	...	0.39
	^{92}Mo	...	0.39
	^{93}Tc	...	0.40
	^{94}Mo	...	0.41
^{63}Ga(p, γ)^{64}Ge	^{63}Cu	...	4.97
^{65}Ge(p, γ)^{66}As	^{65}Zn	0.11	9.19
^{65}As(p, γ)^{66}Se	^{88}Zr	2.01	...
	^{89}Nb	2.06	...

Table 2.13: – Continued.

Reaction	Isotope	10	0.1
	^{90}Mo	2.12	...
	^{91}Nb	2.19	...
	^{92}Mo	2.25	...
	^{93}Tc	2.27	...
	^{94}Mo	2.30	...
^{66}Ge(p, γ)^{67}As	^{66}Ge	0.39	6.27
^{66}As(p, γ)^{67}Se	^{66}Ge	0.23	...
^{67}As(p, γ)^{68}Se	^{67}Ga	0.28	7.20
^{69}Se(p, γ)^{70}Br	^{69}Ge	0.10	7.68
^{70}Se(p, γ)^{71}Br	^{70}Ge	0.39	6.29
^{70}Br(p, γ)^{71}Kr	^{70}Ge	0.39	...
^{71}Br(p, γ)^{72}Kr	^{71}As	0.14	6.88
^{73}Kr(p, γ)^{74}Rb	^{73}Se	0.10	6.83
^{74}Kr(p, γ)^{75}Rb	^{74}Se	0.22	6.80
^{75}Rb(p, γ)^{76}Sr	^{75}Br	0.13	5.73
^{77}Sr(p, γ)^{78}Y	^{77}Kr	0.13	4.46
^{78}Sr(p, γ)^{79}Y	^{78}Kr	0.14	5.35
^{79}Y(p, γ)^{80}Zr	^{79}Kr	0.12	4.53
^{80}Y(p, γ)^{81}Zr	^{81}Rb	...	0.48
^{81}Zr(p, γ)^{82}Nb	^{81}Rb	0.19	2.26
^{82}Zr(p, γ)^{83}Nb	^{82}Sr	0.21	2.12
	^{87}Zr	...	0.49
	^{88}Zr	...	0.48
	^{89}Nb	...	0.48
	^{90}Mo	...	0.47
	^{91}Nb	...	0.47
	^{92}Mo	...	0.46
	^{93}Tc	...	0.46
	^{94}Mo	...	0.45
^{83}Zr(p, γ)^{84}Nb	^{83}Sr	0.49	...
^{83}Nb(p, γ)^{84}Mo	^{83}Sr	0.36	...
^{84}Nb(p, γ)^{85}Mo	^{84}Sr	0.29	...
	^{92}Mo	...	0.48
	^{93}Tc	...	0.44
	^{94}Mo	...	0.41
^{85}Nb(p, γ)^{86}Mo	^{85}Y	0.36	...
^{86}Mo(p, γ)^{87}Tc	^{86}Zr	0.37	...
	^{91}Nb	...	0.47
	^{92}Mo	...	0.43
	^{93}Tc	...	0.40
	^{94}Mo	...	0.37
^{87}Mo(p, γ)^{88}Tc	^{87}Zr	0.34	...
	^{91}Nb	...	0.48
	^{92}Mo	...	0.45
	^{93}Tc	...	0.43
	^{94}Mo	...	0.40
^{88}Mo(p, γ)^{89}Tc	^{88}Zr	0.37	...
	^{89}Nb	...	0.50

Table 2.13: – Continued.

Reaction	Isotope	10	0.1
^{89}Tc(p, γ)^{90}Ru	^{89}Nb	0.31	...
^{91}Tc(p, γ)^{92}Ru	^{91}Nb	0.42	...
	^{92}Mo	...	0.46
^{91}Ru(p, γ)^{92}Rh	^{94}Mo	...	0.49
^{92}Ru(p, γ)^{93}Rh	^{92}Mo	0.30	...
	^{93}Tc	...	0.27
	^{94}Mo	...	0.32
^{93}Rh(p, γ)^{94}Pd	^{93}Tc	0.38	...
^{94}Rh(p, γ)^{95}Pd	^{94}Mo	0.46	...

Hence, the final hydrogen mass fraction may provide a diagnostic of the peak temperature achieved during the explosion (for bursts of similar duration). Concerning nuclear uncertainties, Model K04-B6 is characterized by 49 critical reactions, the most important ones being $^{61}Ga(p,\gamma)$, $^{82}Zr(p,\gamma)$, $^{65}As(p,\gamma)$, $^{86,87}Mo(p,\gamma)$, $^{84}Nb(p,\gamma)$, with a minor role played by $^{92}Ru(p,\gamma)$ (Table 2.13). For Model K04-B7, we find 53 critical reactions, with the largest role played by $^{69}Br(p,\gamma)$, followed by $^{96}Ag(p,\gamma)$, and $^{103}In(p,\gamma)$ (Table 2.14). It is also worth mentioning that in both models only 2 α-induced reactions appear to be influential (one being $^{15}O(\alpha,\gamma)$).

Table 2.14: Same as Table 2.1, for Model K04-B7.

Reaction	Isotope	10	0.1
^{15}O(α, γ)^{19}Ne	^{15}N	...	7.89
^{18}Ne(α, p)^{21}Na	^{18}F	0.48	...
^{31}Cl(p, γ)^{32}Ar	^{30}Si	...	2.17
^{34}Ar(p, γ)^{35}K	^{34}S	0.37	2.14
^{47}Mn(p, γ)^{48}Fe	^{46}Ti	...	3.23
^{57}Cu(p, γ)^{58}Zn	^{57}Ni	...	2.12
^{61}Ga(p, γ)^{62}Ge	^{60}Ni	0.13	5.21
^{65}As(p, γ)^{66}Se	^{64}Zn	0.38	...
^{67}As(p, γ)^{68}Se	^{67}Ga	...	3.13
^{69}Se(p, γ)^{70}Br	^{69}Ge	0.10	9.06
^{69}Br(p, γ)^{70}Kr	^{68}Ge	0.18	...
	^{69}Ge	0.19	...
	^{70}Ge	0.19	...
	^{71}As	0.18	...
^{70}Se(p, γ)^{71}Br	^{70}Ge	...	3.39
^{70}Br(p, γ)^{71}Kr	^{70}Ge	0.17	2.06
^{71}Br(p, γ)^{72}Kr	^{71}As	0.48	5.63
^{73}Kr(p, γ)^{74}Rb	^{73}Se	0.10	8.80
^{74}Kr(p, γ)^{75}Rb	^{74}Se	...	5.35
^{74}Rb(p, γ)^{75}Sr	^{74}Se	0.25	...
^{75}Rb(p, γ)^{76}Sr	^{75}Br	0.31	6.68
^{77}Sr(p, γ)^{78}Y	^{77}Kr	0.11	7.48
^{78}Sr(p, γ)^{79}Y	^{78}Kr	0.27	6.46

Table 2.14: – Continued.

Reaction	Isotope	10	0.1
^{78}Y(p, γ)^{79}Zr	^{78}Kr	0.46	...
^{79}Y(p, γ)^{80}Zr	^{79}Kr	0.13	7.26
^{81}Zr(p, γ)^{82}Nb	^{81}Rb	0.12	4.97
^{82}Zr(p, γ)^{83}Nb	^{82}Sr	0.14	4.15
^{83}Nb(p, γ)^{84}Mo	^{83}Sr	0.17	2.76
^{84}Nb(p, γ)^{85}Mo	^{84}Sr	0.14	3.32
^{85}Mo(p, γ)^{86}Tc	^{85}Y	0.29	...
^{86}Mo(p, γ)^{87}Tc	^{86}Zr	0.17	3.01
^{87}Mo(p, γ)^{88}Tc	^{87}Zr	0.43	...
^{87}Tc(p, γ)^{88}Ru	^{87}Zr	0.42	...
^{88}Tc(p, γ)^{89}Ru	^{88}Zr	0.30	2.44
^{89}Tc(p, γ)^{90}Ru	^{89}Nb	0.28	2.34
^{90}Ru(p, γ)^{91}Rh	^{90}Mo	0.25	2.46
^{91}Ru(p, γ)^{92}Rh	^{91}Nb	0.32	...
^{92}Ru(p, γ)^{93}Rh	^{92}Mo	0.40	...
^{92}Rh(p, γ)^{93}Pd	^{92}Mo	0.45	...
^{93}Rh(p, γ)^{94}Pd	^{93}Tc	0.21	2.41
^{94}Pd(p, γ)^{95}Ag	^{94}Mo	0.35	...
^{95}Pd(p, γ)^{96}Ag	^{95}Ru	0.26	2.11
^{96}Ag(p, γ)^{97}Cd	^{96}Ru	0.39	2.41
	^{97}Ru	...	0.46
	^{98}Ru	...	0.47
^{97}Ag(p, γ)^{98}Cd	^{97}Ru	0.25	2.36
^{97}Cd(p, γ)^{98}In	^{97}Ru	0.47	...
^{98}Ag(p, γ)^{99}Cd	^{98}Ru	0.49	...
^{98}Cd(p, γ)^{99}In	^{98}Ru	0.32	...
^{99}Cd(p, γ)^{100}In	^{99}Rh	0.27	2.10
^{100}Cd(p, γ)^{101}In	^{100}Pd	0.43	...
^{100}In(p, γ)^{101}Sn	^{100}Pd	0.41	...
^{101}In(p, γ)^{102}Sn	^{101}Pd	0.27	...
^{102}In(p, γ)^{103}Sn	^{102}Pd	0.32	...
	^{103}Ag	...	0.45
^{103}In(p, γ)^{104}Sn	^{103}Ag	0.45	...
	^{104}Ag	2.01	0.28
	^{105}Ag	...	0.43
^{104}In(p, γ)^{105}Sn	^{105}Ag	3.03	0.20
	^{106}Cd	...	0.24
^{105}Sn(p, γ)^{106}Sb	^{105}Ag	0.43	...
	^{106}Cd	2.16	0.31

As expected, the most important β-decay rates involve heavier species in Model K04-B7 than in K04-B6, as a result of the former's larger peak temperature (see Table 2.2). Hence, the β-decay rates of ^{18}Ne, ^{64}Ge, ^{68}Se, ^{72}Kr, ^{76}Sr, and ^{80}Zr, are influential in Model K04-B6, whereas those of ^{68}Se, ^{72}Kr, ^{76}Sr, ^{80}Zr, ^{88}Ru, ^{92}Pd, and $^{101,102}Sn$, are important in Model K04-B7 (again only for uncertainty factors of 10, up and down).

Table 2.15: Summary of the most influential nuclear processes, as collected from Tables 2.1, 2.5, 2.6, & 2.8 - 2.14. These reactions affect the yields of, at least, 3 isotopes when their nominal rates are varied by a factor of 10, up and/or down.

Reaction	Models affected
^{12}C(α, γ)^{16}O[a]	F08, K04-B2, K04-B4, K04-B5
^{18}Ne(α, p)^{21}Na[a]	K04-B1[b]
^{25}Si(α, p)^{28}P	K04-B5
^{26g}Al(α, p)^{29}Si	F08
^{29}S(α, p)^{32}Cl	K04-B5
^{30}P(α, p)^{33}S	K04-B4
^{30}S(α, p)^{33}Cl	K04-B4[b], K04-B5[b]
^{31}Cl(p, γ)^{32}Ar	K04-B1
^{32}S(α, γ)^{36}Ar	K04-B2
^{56}Ni(α, p)^{59}Cu	S01[b], K04-B5
^{57}Cu(p, γ)^{58}Zn	F08
^{59}Cu(p, γ)^{60}Zn	S01[b], K04-B5
^{61}Ga(p, γ)^{62}Ge	F08, K04-B1, K04-B2, K04-B5, K04-B6
^{65}As(p, γ)^{66}Se	K04[b], K04-B1, K04-B2[b], K04-B3[b], K04-B4, K04-B5, K04-B6
^{69}Br(p, γ)^{70}Kr	K04-B7
^{75}Rb(p, γ)^{76}Sr	K04-B2
^{82}Zr(p, γ)^{83}Nb	K04-B6
^{84}Zr(p, γ)^{85}Nb	K04-B2
^{84}Nb(p, γ)^{85}Mo	K04-B6
^{85}Mo(p, γ)^{86}Tc	F08
^{86}Mo(p, γ)^{87}Tc	F08, K04-B6
^{87}Mo(p, γ)^{88}Tc	K04-B6
^{92}Ru(p, γ)^{93}Rh	K04-B2, K04-B6
^{93}Rh(p, γ)^{94}Pd	K04-B2
^{96}Ag(p, γ)^{97}Cd	K04, K04-B2, K04-B3, K04-B7
^{102}In(p, γ)^{103}Sn	K04, K04-B3
^{103}In(p, γ)^{104}Sn	K04-B3, K04-B7
^{103}Sn(α, p)^{106}Sb	S01[b]

2.4 Discussion

Table 2.15 summarizes the most important reactions collected from Tables 2.1, 2.5, 2.6, & 2.8 - 2.14. For the sake of brevity, we have restricted Table 2.15 and the discussion here to those reactions that affect the yield of 3 species or more in any of our 10 models. We have also carefully identified reactions that were seen to modify the XRB energy output when their rates were varied by a factor of 10, up or down. This is explicitly indicated in Table 2.16, which lists the subset of reactions with any

[a] Reaction experimentally constrained to better than a factor of ~ 10 at XRB temperatures.

[b] Reaction that affects the total energy generation rate by more than 5 % at some time interval in this model, when its rate is varied by a factor of 10, up and/or down. See Table 2.16.

impact on XRB yields (reactions identified in Tables 2.1, 2.5, 2.6, & 2.8 - 2.14, that affect, at least, one isotope) that simultaneously modify the overall energy output by more than 5 % at some point during the burst, when their nominal rates are varied by a factor of 10, up or down. This table has to be taken as a warning of the limitations of post-processing techniques. Furthermore, we have identified some additional reactions in our studies which affect the energy output, but remarkably did not affect any yields in any of our models (for instance, $^{14}O(\alpha,p)$, $^{27}Si(p,\gamma)$, $^{31}S(p,\gamma)$, or $^{35}S(p,\gamma)$). Several aspects are worth noting here. First, the total number of reactions affecting the energy output, for any model, is small. Second, as indicated in Table 2.16, some of those reactions are known with better precision than a factor of 10. And third, there is no way to overcome this problem in the context of post-processing calculations. Indeed, a self-consistent analysis with a hydrodynamic code capable of self-adjusting both the temperature and the density of the stellar envelope seems mandatory to address this issue, for the few reactions of concern, a challenge that we leave for future work.

It is also worth mentioning that no discussion involving the triple-α reaction or any β-decay rate has been made here, since these reactions, when varied within realistic uncertainty limits, have no effect, neither on yields, nor on the nuclear energy output.

Table 2.16: Nuclear processes affecting the total energy output by more than 5 %, as well as the yield of at least one isotope, when their nominal rates are individually varied by a factor of 10, up and/or down, for the given model.

Reaction	Models affected
^{15}O(α, γ)^{19}Ne[a]	K04, K04-B1, K04-B6
^{18}Ne(α, p)^{21}Na[a]	K04-B1, K04-B6
^{22}Mg(α, p)^{25}Al	F08
^{23}Al(p, γ)^{24}Si	K04-B1
^{24}Mg(α, p)^{27}Al[a]	K04-B2
^{26g}Al(p, γ)^{27}Si[a]	F08
^{28}Si(α, p)^{31}P[a]	K04-B4
^{30}S(α, p)^{33}Cl	K04-B4, K04-B5
^{31}Cl(p, γ)^{32}Ar	K04-B3
^{32}S(α, p)^{35}Cl	K04-B2
^{35}Cl(p, γ)^{36}Ar[a]	K04-B2
^{56}Ni(α, p)^{59}Cu	S01
^{59}Cu(p, γ)^{60}Zn	S01
^{65}As(p, γ)^{66}Se	K04, K04-B2, K04-B3
^{69}Br(p, γ)^{70}Kr	S01
^{71}Br(p, γ)^{72}Kr	K04-B7
^{103}Sn(α, p)^{106}Sb	S01

[a]Reaction experimentally constrained to better than a factor of ~ 10 at XRB temperatures.

We do, however, encourage the development of improved, consistent treatments for calculating stellar weak rates for all isotopes in our network - especially the important rates identified in Table 2.2. Finally, except for the case of $^{64}Ge(p,\gamma)$, the results of our Q-value variations (Tables 2.4 & 2.7) are not accompanied by variations of the energy output.

Table 2.17: Comparison between theoretical rates from Tables 2.15 & 2.16, according to different rate compilations. The table shows, for a particular reaction, the maximum disagreement between our rate and the REACLIBv0 rate over the temperature range covered in all our studies ($\sim 0.4-2.5\,GK$). All Q-values are given in keV.

Reaction	Q-value Audi et al.	Q-value this work[a]	Q-value REACLIBv0[a]	Maximum disagreement
^{22}Mg(α, p)^{25}Al	3655(1)	3655 [NS]	3655 [NS]	20 %
^{25}Si(α, p)^{28}P	6119(11)	6122 [NS]	6119 [NS]	20 %
^{26g}Al(α, p)^{29}Si	4820.68(6)	4823 [NS]	4820 [NS]	40 %
^{29}S(α, p)^{32}Cl	5306(50)	5307 [NS]	5306 [NS]	$\times$2
^{30}S(α, p)^{33}Cl	2077(3)	2076 [NS]	2076 [NS]	$\times$2
^{30}P(α, p)^{33}S	1521.36(34)	1522 [NS]	1521 [NS]	20 %
^{31}Cl(p, γ)^{32}Ar	2422(50)	2404 [Her95]	2404 [Her95]	0
^{32}S(α, γ)^{36}Ar	6640.76(14)	6639 [NS]	6641 [NS]	$\times$2
^{56}Ni(α, p)^{59}Cu	-2411(11)	-2413 [NS]	-2411 [NS]	$\times$3
^{57}Cu(p, γ)^{58}Zn	2277(52)	2277 [For01]	2277 [For01]	0
^{59}Cu(p, γ)^{60}Zn	5120(11)	5121 [NS]	5120 [NS]	10 %
^{61}Ga(p, γ)^{62}Ge	2442(149)[b]	2427 [NS]	2576 [Fis04]	$\times$10
^{65}As(p, γ)^{66}Se	2030(424)[b]	2587 [NS]	2433 [NS]	10 %
^{69}Br(p, γ)^{70}Kr	2489(399)[b]	2434 [NS]	2579 [NS]	10 %
^{71}Br(p, γ)^{72}Kr	4167(568)	4525 [NS]	4167 [NS]	30 %
^{75}Rb(p, γ)^{76}Sr	4311 (38)	4467 [NS]	4311 [NS]	10 %
^{82}Zr(p, γ)^{83}Nb	2055(387)[b]	2060 [NS]	2056 [NS]	20 %
^{84}Nb(p, γ)^{85}Mo	4513(409)[b]	4510 [M]	4513 [NS]	40 %
^{84}Zr(p, γ)^{85}Nb	2946(297)[b]	2109 [NS]	2946 [NS]	40 %
^{85}Mo(p, γ)^{86}Tc	1393(409)[b]	1390 [M]	1393 [NS]	$\times$4
^{86}Mo(p, γ)^{87}Tc	1855(530)[b]	1860 [M]	1855 [NS]	$\times$3
^{87}Mo(p, γ)^{88}Tc	2304(300)[b]	2300 [M]	2304 [NS]	50 %
^{92}Ru(p, γ)^{93}Rh	2054(499)[b]	2002 [NS]	2054 [NS]	20 %
^{93}Rh(p, γ)^{94}Pd	4467(566)[b]	4365 [NS]	4466 [NS]	40 %
^{96}Ag(p, γ)^{97}Cd	3321(566)[b]	3258 [NS]	3321 [NS]	$\times$2
^{102}In(p, γ)^{103}Sn	3554(318)[b]	4095 [NS]	3554 [NS]	$\times$2
^{103}In(p, γ)^{104}Sn	4281(107)	4241 [NS]	4281 [NS]	40 %
^{103}Sn(α, p)^{106}Sb	-5508(432)[b]	-5508 [NS]	-5508 [NS]	10 %

[a]Sources of the theoretical estimates: M=MOST Hauser-Feschbach code; NS=NON-SMOKER Hauser-Feschbach code; For01=Forstner et al. (2001); Fis04=Fisker's shell model calculation –see REACLIBv0 database; Her95=Herndl et al. (1995), shell model calculation.

[b]Q-value estimated from systematics. See Audi et al. (2003b).

Next, from the reactions listed in Tables 2.15 & 2.16, we present the most influential reactions found in this study. First, we will focus on those rates that were drawn from theoretical estimates, due to insufficient or unavailable experimental information. Their main characteristics are summarized in Table 2.17. To help illustrate systematic uncertainties associated with these important reactions, we have compared the theoretical rates adopted in our network with those found in the recent REACLIBv0 compilation[4] over the temperature range covered in our studies. Overall, the agreement is quite good; however, we note that even when using the same basic Hauser-Feshbach code (NON-SMOKER) along with similar Q-values, a difference in the rates as large as a factor of ~ 3 is obtained. Differences as large as a factor of ~ 4 are seen between rates from different statistical model codes, but using similar Q-values[5]. Moreover, the factor of 10 disagreement for the $^{61}Ga(p,\gamma)$ rate arises from the comparison between a NON-SMOKER result and a shell-model calculation. The magnitude of these discrepancies lends support to our choice of varying rates by a factor of 10 rather than by a significantly larger factor.

In Table 2.18, we have collected the principal end-products in all 10 models, as well as those rates that change these particular yields by at least a factor of 2 (when varied by a factor of 10, up and/or down). These rates may have a direct impact on the properties of the neutron star crust (see e.g. Brown & Bildsten 1998) as our studies show that they modify the main post-burst constituents of the crust. The majority of the reactions listed in Table 2.18 are also found in Tables 2.15 & 2.16. We will now focus on the rates listed in Tables 2.15 & 2.16 that have been determined experimentally, and we will assess whether a factor of 10 variation is reasonable for these rates. For those cases where a smaller uncertainty is justified, we have performed additional post-processing calculations to supplement results from Tables 2.1, 2.5, 2.6, 2.8 - 2.14, & 2.16 (namely, to determine the impact of individual rate variations by smaller factors on yields and on the overall nuclear energy output). For reference, we will continue to compare the rate adopted in this work with that used in the REACLIBv0 compilation. Although we do not discuss experimental information (if available) for other reactions listed in Tables 2.1, 2.5, 2.6, & 2.8 - 2.14 (namely, those that affected less than 3 isotopes in any model), this must of course be considered by anyone examining reactions beyond the most influential ones listed in Table 2.15.

- $^{12}C(\alpha,\gamma)^{16}O$: We have used the Kunz et al. (2002) experimental rate which, over the range of temperatures used in our models, agrees to better than 20 % with the recommended NACRE (Angulo et al. 1999) rate, and to better than a factor of ~ 2 with the recommended Buchmann (1996) rate adopted in REACLIBv0. A factor of ~ 3 variation in our rate would cover the limits given

[4] http://www.nscl.msu.edu/~nero/db/

[5] Note, however, that different sets of Q-values have been used in the NON-SMOKER calculations of REACLIBv0 and of the following REACLIBv0.5 (Parikh, private communication).

in both NACRE and Buchmann (1996). Hence, we have varied this rate individually by a factor of 3, up and down, and tested its effect for those models in which a factor of 10 variation, as discussed in Section 2.3, had an impact (Models F08, K04-B2, K04-B4, and K04-B5). Indeed, only Model K04-B2 (where the ^{12}C yield is affected by a factor 0.47 when this rate is multiplied by 3) and K04-B5 (where ^{20}Ne and ^{24}Mg are affected by factors 0.44 and 0.47, respectively, when the rate is reduced by a factor 3) reveal changes in the final yields (note that variation of this reaction by a factor of 10 did not affect the overall nuclear energy output in any of our models).

- $^{18}Ne(\alpha,p)^{21}Na$: We use the Chen et al. (2001) experimental rate, which agrees to a factor ~ 3 with the Görres et al. (1995) Hauser-Feshbach (SMOKER) calculation adopted in REACLIBv0. There is, however, additional data from Groombridge et al. (2002). Indeed, using the information from Chen et al. (2001), for $E_r < 1.7\,MeV$, and that from Groombridge et al. (2002), for $E_r > 1.98\,MeV$, we find a rate which deviates from the Chen et al. (2001) rate by 30 %, a factor of ~ 3, and a factor of ~ 7, at 1.0, 1.4, and $2\,GK$, respectively[6]. Since we found this reaction to affect yields and/or the total nuclear energy in Models K04-B1 and K04-B6, neither of which reach temperatures above $1.36\,GK$, we have restricted our analysis to a variation of the Chen et al. (2001) rate by a factor of 3, up and down. No impact on the yields is found when varying the rate as such; however, Model K04-B1 shows some variation of the total energy output when the rate is multiplied by 3.

- $^{15}O(\alpha,\gamma)^{19}Ne$: We use the Davids et al. (2003) rate, which agrees to a factor of ~ 3 with the Hahn et al. (1996) rate used in REACLIBv0, over the temperatures spanned by our models. If we combine the new information reported by Tan et al. (2007), for $E_x < 4.55\,MeV$, with the information in Davids et al. (2003), for the states at $E_x = 4.600$, 4.712, and $5.092\,MeV$, we calculate a new rate that agrees to a factor ~ 2 with the original Davids et al. (2003) rate, over the relevant temperatures. Varying our rate within a factor ~ 3 would cover the uncertainty limits in the Tan-Davids rate calculation. We have tested the impact of varying our $^{15}O(\alpha,\gamma)$ rate by a factor 3 up and down, for Models K04, K04-B1, and K04-B6. We find that the total nuclear energy is affected only in the early stages of Model K04, when the rate is multiplied by 3. Concerning the yields, only ^{15}N is affected (consistent with Tables 2.1, 2.8, & 2.13): when the rate is reduced by a factor 3, the ^{15}N normalized yields in Models K04, K04-B1, and K04-B6 are 3.13, 2.75, and 3.17, respectively; when the rate is increased by a factor 3, no effect is seen except in Model K04-B1, where the

[6]Some changes in the $^{18}Ne(\alpha,p)^{21}Na$ reaction rate have been recently reported by He et al. (2008, 2009), for temperatures below 0.4 GK, too low for typical XRB conditions, and hence, with no effect on the results presented in this Thesis.

normalized yield of ^{15}N decreases to 0.35.

- $^{23}Al(p,\gamma)^{24}Si$: We use the Schatz et al. (1997) rate, as does REACLIBv0. This rate is based on both theoretical estimates and measurements of excited states in ^{24}Si.

Table 2.18: Reaction rates that affect the principal XRB end-products in our 10 models.

Model	Principal end-products	Most influential reactions
K04	H	...
	^{4}He	...
	^{64}Zn	^{65}As(p, γ)
	^{68}Ge	...
	^{72}Se	...
	^{76}Kr	...
S01	H	^{56}Ni(α, p), ^{59}Cu(p, γ)
	^{4}He	...
	^{103}Ag	^{103}In(p, γ)
	^{104}Ag	...
	^{105}Ag	^{105}Sn(p, γ)
	^{106}Cd	^{103}Sn(α, p)
F08	^{4}He	...
	^{12}C	^{12}C(α, g)^{a}, ^{12}C(p, γ)^{a}
	^{28}Si	^{28}Si(α, g)^{a}
	^{56}Ni	^{57}Cu(p, γ)
	^{60}Ni	...
	^{64}Zn	^{61}Ga(p, γ)
K04-B1	^{4}He	...
	^{60}Ni	^{61}Ga(p, γ)
	^{64}Zn	^{61}Ga(p, γ)
	^{68}Ge	^{61}Ga(p, γ), ^{65}As(p, γ)
K04-B2	^{68}Ge	...
	^{72}Se	...
	^{76}Kr	...
	^{94}Mo	...
	^{103}Ag	...
	^{104}Ag	...
K04-B3	H	...
	^{64}Zn	^{65}As(p, γ)
	^{68}Ge	...
	^{72}Se	...
	^{76}Kr	...
	^{80}Sr	...
K04-B4	^{56}Ni	...
	^{60}Ni	...
	^{64}Zn	^{65}As(p, γ)
K04-B5	^{39}K	^{30}S(α, p)

Table 2.18: – Continued.

Model	Principal end-products	Most influential reactions
	^{56}Ni	^{25}Si(α, p), ^{29}S(α, p), ^{30}S(α, p), ^{56}Ni(α, p), ^{59}Cu(p, γ)
	^{60}Ni	...
	^{64}Zn	^{61}Ga(p, γ)
	^{68}Ge	^{25}Si(α, p), ^{30}S(α, p), ^{61}Ga(p, γ), ^{65}As(p, γ)
K04-B6	H	...
	^{60}Ni	^{61}Ga(p, γ)
	^{64}Zn	...
	^{68}Ge	...
	^{72}Se	...
	^{76}Kr	^{61}Ga(p, γ)
K04-B7	H	...
	^{68}Ge	^{69}Br(p, γ)
	^{72}Se	...
	^{76}Kr	...
	^{80}Sr	...
	^{96}Ru	^{96}Ag(p, γ)

Its uncertainty spans up to 3 orders of magnitude, for typical XRB temperatures. For this reason, we deem our results from varying this rate by a factor 10 to be adequate.

- $^{24}Mg(\alpha,p)^{27}Al$: Both REACLIBv0 and our network rely on the experimental rate reported in Iliadis et al. (2001). Above $0.3\,GK$, this rate is reported to be uncertain by only $\pm 20\,\%$. No effect on the yields is found when the rate is varied by 20 % in our post-processing calculations (Model K04-B2; see Table 2.16). The total nuclear energy is, however, affected when this rate is increased by 20 %, in that particular model.

- $^{26g}Al(p,\gamma)^{27}Si$: We use the (unpublished) rate from the PhD thesis of Vogelaar (1989), as does REACLIBv0[7]. According to NACRE, the experimental information is only sufficient to determine the rate for $T < 0.9\,GK$ (they use Hauser-Feshbach calculations to extend this rate to higher temperatures). Our rate agrees with the NACRE recommended rate to 30 % over the temperature range covered by our models; varying our rate by a factor of 2 up and down would cover the uncertainties reported in NACRE. Assuming such a degree of uncertainty in our rate for Model F08 (see Table 2.16) leads to no effect on any yield, nor on the total nuclear energy.

[a] Rate is experimentally constrained to better than a factor of 10.

[7] The new measurements of the $184\,keV$ resonance (see Ruiz et al. 2006, and Lotay et al. 2009) have no effect on the $^{26g}Al(p,\gamma)^{27}Si$ rate at typical XRB temperatures.

- $^{28}Si(\alpha,p)^{31}P$: The rate used in our network and that of REACLIBv0 is from the compilation of Iliadis et al. (2001). An uncertainty of $\pm 20\,\%$ is assigned to this rate above $0.2\,GK$. Actually, varying this rate by $\pm 20\,\%$ in Model K04-B4 (see Table 2.16) has no effect on any yields, nor on the total nuclear energy.

- $^{32}S(\alpha,p)^{35}Cl$: We use the Iliadis et al. (2001) experimental rate, as does REACLIBv0. The uncertainty of this rate, over XRB typical temperatures, spans up to 3 orders of magnitude (Iliadis et al. 2001). Consequently, we feel that our results, based on a variation of this rate by a factor of 10 (see Table 2.16), are reliable.

- $^{35}Cl(p,\gamma)^{36}Ar$: Again, we adopt the Iliadis et al. (2001) experimental rate, as does REACLIBv0. The uncertainty in this rate is $\sim 20\,\%$ above $0.2\,GK$ (Iliadis et al. 2001). We find no effect on any yield when varying this rate by $\pm 20\,\%$ in our post-processing calculations for Model K04-B2 (see Table 2.16). However, we remarkably find that increasing this rate by $20\,\%$ does indeed affect the total nuclear energy at the early stages of the TNR in this model.

Finally, because of past interest in the literature, we discuss some specific reactions that we found to affect the total nuclear energy when their rates were varied individually by a factor of 10, but affected no yields whatsoever: $^{31}S(p,\gamma)$, $^{35}Ar(p,\gamma)$, $^{27}Si(p,\gamma)$, and $^{14}O(\alpha,p)$.

- $^{31}S(p,\gamma)^{32}Cl$, $^{35}Ar(p,\gamma)^{36}K$, and $^{27}Si(p,\gamma)^{28}P$: For these 3 reactions, we have used the rates reported in Iliadis et al. (1999), determined through the use of experimental information when available (e.g., excitation energies), along with calculations and information from the respective mirror nuclei. Judging from the uncertainties presented in that work, we conclude that uncertainty factors of 2, 3, and 2 (up and down) are more reasonable for the $^{31}S(p,\gamma)$, $^{35}Ar(p,\gamma)$, and $^{27}Si(p,\gamma)$ rates over XRB temperatures, respectively. Accordingly, we individually varied each of these reactions within those limits for the models affected (i.e., Models K04-B1, and K04-B7 for $^{31}S(p,\gamma)$; Models K04-B2, and K04-B7 for $^{35}Ar(p,\gamma)$; and Models K04-B4, and K04-B7 for $^{27}Si(p,\gamma)$) to determine the resulting impact on the total nuclear energy, as no yields were affected by varying any of these by a factor of 10. Increasing the $^{31}S(p,\gamma)$ rate by a factor of 2 changed the total nuclear energy (by at least $5\,\%$ at some point of the burst) in Model K04-B1; increasing the $^{35}Ar(p,\gamma)$ rate by a factor of 3 changed the nuclear energy in Model K04-B2; and increasing the $^{27}Si(p,\gamma)$ rate by a factor of 2 changed the nuclear energy in Model K04-B7. The impact of these reactions on XRB light curves has been examined in Iliadis et al. (1999) and in Thielemann et al. (2001).

- $^{14}O(\alpha,p)^{17}F$: This reaction is of critical importance for breakout from the hot CNO-cycle. We use the rate from Blackmon et al. (2003), which is larger

than the Hahn et al. (1996) rate, adopted by REACLIBv0, by a factor of ~ 10, at typical XRB temperatures. This increased rate is due to the inclusion of some of the contributions from the $^{17}F^{*}$ exit channel by Blackmon et al. (2003); branches for states of $E_x > 7\,MeV$ in ^{18}Ne were not measured though. Actually, Notani et al. (2004a,b) observed what could be the population of $^{17}F^{*}$ through a state at $E_x(^{18}Ne) \sim 7.1\,MeV$, but the interpretation of their results has been questioned by Fu et al. (2007). As the studies of Blackmon et al. (2003) and Notani et al. (2004a,b) are both published in only preliminary forms, and taking into account the argument of Fu et al. (2007), we find it difficult to evaluate the uncertainty in this rate. Variations by a factor of 10 affected nuclear energy in 5 of our 10 models: K04, F08, K04-B1, K04-B3, and K04-B4. Further efforts to constrain this rate, based on analyses of previous measurements and/or new measurements, would certainly be desirable.

In summary, we have identified a very limited number of reactions (see Tables 2.15, & 2.17, and this Section) that play a significant role in XRB nucleosynthesis studies. This limited number of critical (uncertain) rates makes XRB nucleosynthesis studies basically reliable. Our results can help to guide and motivate future measurements by experimental nuclear physicists. Stellar modelers, as well, may tackle the challenge to properly address the role played by the few reactions flagged as affecting the overall energy output, an aspect that lies beyond the possibilities offered by post-processing calculations.

Chapter 3

The effect of nuclear uncertainties in type I X-ray burst nucleosynthesis: Monte Carlo simulations

3.1 Introduction

State-of-the-art simulations of type I X-ray bursts suggest that their main nuclear reaction flow is driven by the *rp-process* (a combination of rapid p-captures and β^+-decays), the 3α-reaction, and the so-called *αp-process* (a sequence of (α,p) and (p,γ) reactions), proceeding far away from the valley of stability, and eventually merging with the proton drip-line beyond A = 38 (Schatz et al. 1999). Detailed nucleosynthesis studies require hundreds of isotopes, up to $SnSbTe$-mass region (Schatz et al. 2001) or beyond (the flow in Koike et al. 2004 reaches ^{126}Xe), and thousands of nuclear interactions.

Recently, it has been claimed that, because of the coupling of so many different reaction channels for XRB conditions, *traditional* sensitivity studies (like those presented in Chapter 2), in which only one reaction is varied while the others are held constant, cannot properly address all the important correlations between rate uncertainties and nucleosynthetic predictions, leading to wrong (or at least, biased) conclusions (Roberts et al. 2006).

In this Chapter, we will examine the impact of simultaneously varying all reaction rates in the highly-coupled environment characteristic of an XRB through a series of Monte Carlo simulations, and will discuss the feasibility of traditional sensitivity studies through a direct comparison. Indeed, Monte Carlo methods have been used with great success in the analysis of Big Bang nucleosynthesis (Krauss & Romanelli 1990; Smith et al. 1993), nova nucleosynthesis (Hix et al. 2000, 2003), and more

recently, type I X-ray bursts (Roberts et al. 2006).

3.2 Monte Carlo techniques

The basic procedure adopted relies on the simultaneous variation of all nuclear reaction rates, with a factor representing their uncertainty limits. To this end, different pseudo-random numbers (hereafter, *enhancement factors*) are assigned to each individual reaction. Since nuclear reaction rates are positive quantities, the distribution of enhancement factors is assumed to follow a log-normal probability function (note that other distributions, such as a Gaussian, may lead to negative, unphysical values).

By means of post-processing techniques, the time evolution of the chemical abundances is computed for a particular temperature-density versus time profile, and the set of modified reaction rates. The final nucleosynthesis is stored, and the whole process is thus iterated for a pre-selected number of trials to achieve statistically sound results, using each time a different set of enhancement factors. In this Thesis, we have used between 1000 - 10,000 trials. Although some previous Monte Carlo studies have sometimes relied on a larger number of trials (10,000, in Smith et al. 2002, and Hix et al. 2003; 50,000, in Roberts et al. 2006), we will show that our choice is sufficient for the goals of this work (see Section 3.4)[1].

The log-normal probability function (hereafter, *pdf*) that describes the set of pseudo-random factors, $X = \{x_1, x_2, ..., x_Q\}$, has the form:

$$LN(x|\mu,\sigma) = \frac{1}{x\,\sigma\,\sqrt{2\pi}}\, e^{-\frac{(ln\,x-\mu)^2}{2\,\sigma^2}},\ x > 0 \tag{3.1}$$

This equation can be transformed into a normal *pdf* through

$$ln\,x \equiv y\ \rightarrow\ \frac{1}{x}\,dx = dy$$

leading to:

$$N(y|\mu,\sigma) = LN(x|\mu,\sigma)\,\frac{dx}{dy} = \frac{1}{\sigma\,\sqrt{2\pi}}\, e^{-\frac{(y-\mu)^2}{2\,\sigma^2}} \tag{3.2}$$

Using the linear transformation

$$\frac{x-\mu}{\sigma} \equiv z\ \rightarrow\ \frac{1}{\sigma}\,dx = dz$$

we obtain a standard normal *pdf:*

[1]Note also that the same enhancement factor has been applied to a forward-reverse reaction pair. A rigorous Monte Carlo procedure would require a random sampling of the reaction Q-value for the calculation of the reverse reaction rate. We did not address this extra complication, which we leave for future investigations.

$$N(z|0,1) = N(y|\mu,\sigma)\,\frac{dy}{dz} = \frac{1}{\sqrt{2\pi}}\,e^{-\frac{z^2}{2}} \tag{3.3}$$

In practice, it is easier to sample two independent normal random variables together (2-D):

$$N(z_1,z_2|0,1) = N(z_1|0,1)\cdot N(z_2|0,1) = \frac{1}{2\pi}\,e^{-\frac{(z_1^2+z_2^2)}{2}} \tag{3.4}$$

Now, the equation can be rewritten in terms of the independent polar coordinates, r and φ, by the transformation

$$z_1 = r\cdot cos\,\varphi$$

$$z_2 = r\cdot sin\,\varphi$$

which leads to

$$N(r,\varphi|0,1) = N(z_1,z_2|0,1)\cdot \left|\begin{array}{cc} \frac{\partial z_1}{\partial r} & \frac{\partial z_1}{\partial \varphi} \\ \frac{\partial z_2}{\partial r} & \frac{\partial z_2}{\partial \varphi} \end{array}\right| = \frac{1}{2\pi}\,e^{-\frac{r^2}{2}}\cdot r \tag{3.5}$$

Finally, applying

$$\varphi = 2\pi\,\xi_1$$

$$r = \sqrt{-2\cdot ln\,\xi_2}$$

we obtain

$$U(\xi_1,\xi_2|0,1) = N(r,\varphi|0,1)\cdot \left|\begin{array}{cc} \frac{\partial r}{\partial \xi_1} & \frac{\partial r}{\partial \xi_2} \\ \frac{\partial \varphi}{\partial \xi_1} & \frac{\partial \varphi}{\partial \xi_2} \end{array}\right| = 1 \tag{3.6}$$

which corresponds to a uniform *pdf*, with ξ_1, $\xi_2\,\epsilon\,(0,1)$.

Now, going backwards and undoing the set of transformations, we can express the initial random variable, x, as a function of ξ:

$$x_1 = e^{\sigma\cdot\left(\sqrt{-2\cdot ln\,\xi_1}\cdot cos\,(2\pi\,\xi_2)\right)+\mu}$$

$$x_2 = e^{\sigma\cdot\left(\sqrt{-2\cdot ln\,\xi_2}\cdot sin\,(2\pi\,\xi_1)\right)+\mu}$$

At this point, for each pair (ξ_1,ξ_2), we obtain two values of x. In the literature, there are many algorithms that generate *pseudo-random* numbers, ξ. In this Thesis, we have used those from Guardiola et al. (1995). Note that μ and σ correspond to the *mean* and the *standard deviation* of $ln\,x$, which follows a normal *pdf*. Since we

will basically deal with x, instead of $ln\,x$, it is more useful to rely on the *geometric mean* (or *median*), μ^*, and on the *geometric standard deviation*, σ^*:

$$\mu^* = e^{\mu} \tag{3.7}$$

$$\sigma^* = e^{\sigma} \tag{3.8}$$

These two parameters are often used to estimate confidence intervals for log-normal *pdfs*. Since the *median* we expect is 1, we fix $\mu^* = 1$ (that is, $\mu = 0$). Thus, the probability that x will be larger (or smaller) than 1 is 50 %, and the probability that all the values will be in the interval:

$$\left[\mu^* / \left(\sigma^*\right)^2, \mu^* \cdot \left(\sigma^*\right)^2\right] = \left[1/\left(\sigma^*\right)^2, 1 \cdot \left(\sigma^*\right)^2\right] \tag{3.9}$$

is 95.5 %.

As discussed in Chapter 2, we assume that reaction rates can be affected by a factor of 10 uncertainty, so the random enhancement factors must lay inside the interval $[0.1, 10]$. Now, taking into account Eq. 3.9, we have $\sigma^* = \sqrt{10}$, and from Eq. 3.8, we obtain $\sigma = \ln \sqrt{10}$. The corresponding *pdf* is shown in Fig. 3.1.

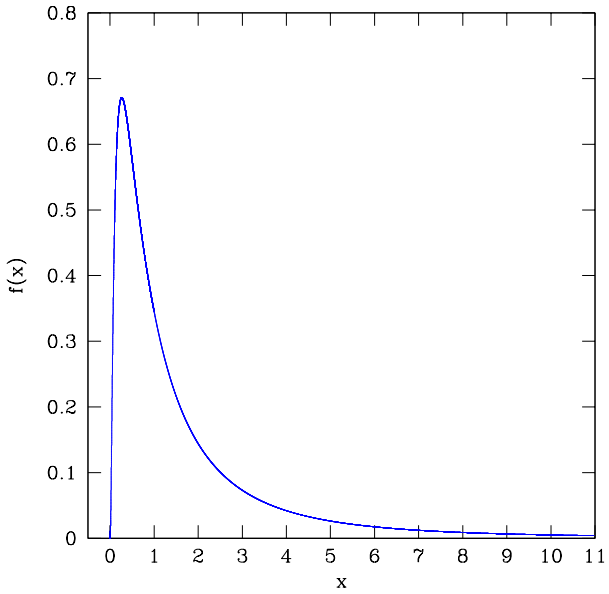

Figure 3.1: Log-normal *pdf* used in this Thesis, with $\mu = 0$, and $\sigma = \ln \sqrt{10}$. The probability to generate a random number within the interval $[0.1, 10]$ is 95.5 %.

3.3 Nucleosynthesis calculations

Once a suite of random factors, $X = \{x_1, x_{2,}, ..., x_Q\}$ (with Q being the overall number of reaction rates), is generated, it is applied to the set of nuclear reaction rates of our network, $R = \{r_1, r_2, ..., r_Q\}$, obtaining a new set of *randomize* reaction rates, $R^* = \{r_1^*, r_2^*, ..., r_Q^*\}$, with:

$$r_i^* = r_i * x_i$$

The new chemical abundances, $Y = \{y_1, y_2, ..., y_P\}$ (with P being the number of isotopes in the network), is then computed with the set of randomize reaction rates, for a given T-ρ versus time profile, through post-processing. The procedure is then iterated N times, with different sets of random factors (see Figure 3.2). The final abundances and the corresponding deviation bars are then obtained by calculating the *geometric mean value*, Y^*, and the *geometric standard deviation*, S^* (see Carobbi et al. 2003, and Limpert et al. 2001):

$$y_j^* = \left(\prod_{i=1}^{N} y_{i,j} \right)^{\frac{1}{N}} , \; j = 1, 2, ..., P$$

$$s_j^* = exp \left(\left[\frac{1}{N} \sum_{i=1}^{N} \left[\ln \left(\frac{y_{i,j}}{y_j^*} \right) \right]^2 \right]^{\frac{1}{2}} \right) , \; j = 1, 2, ..., P$$

Because the goal of this Chapter is to identify key reactions whose uncertainties deeply affect nucleosynthetic predictions, it seems meaningless to rely on absolute yields. Instead, we will consider *relative abundances*, that is, the geometric mean abundances obtained from the set of Monte Carlo trials *normalized* to the abundances obtained with *standard* rates

$$y_j^{'} = y_j^* / y_j^{st} \; , \; j = 1, 2, ..., P \tag{3.10}$$

In turn, the *normalized* geometric standard deviations become:

$$[y_j^{'}/(s_j^*)^2, y_j^{'} \cdot (s_j^*)^2] \tag{3.11}$$

3.4 Results

We have applied the Monte Carlo technique to our set of models discussed in Chapter 2. However, since results are in all cases qualitatively similar to those obtained with individual-rate variations, we will restrict the discussion here to Models K04 (Koike et al. 2004) and F08 (Fisker et al. 2008).

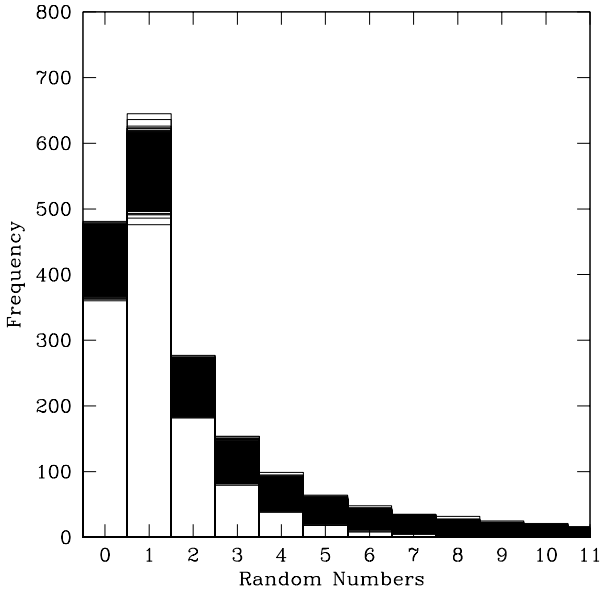

Figure 3.2: Histogram of the random factors used for 10,000 trials. Notice that its shape follows a log-normal-like distribution. Black areas correspond to the overlap of many similar frequencies for a given interval.

Before a thorough analysis of the results is made, several aspects must be emphasized. First, the simultaneous variation of all nuclear processes in bulk, between 0.1 and 10, according to our log-normal distribution, results in large uncertainty bars for many isotopes. Notice, however, that these final abundance uncertainties are overestimated since all β^+-decays, as well as some important, relatively well-known reactions, such as the triple-α, were allowed to vary in this way. As discussed in Chapter 2, more realistic uncertainties must be used instead, since these rates are known with better precision (usually better than $\sim 30\,\%$, for β-decay rates). Indeed, when all nuclear processes, except the triple-α and all the β-decay rates, are allowed to vary between roughly 0.1 and 10 in the Monte Carlo study, the overall uncertainties in the final yields decrease dramatically (see Subsection 3.4.5).

A second warning associated with Monte Carlo simulations involves the reduced subset of reactions whose variation affects the overall energy production (see Section 2.4, in Chapter 2). In individual reaction-rate variation studies, these reactions can be appropriately flagged for separate, detailed analysis with better numerical tools (semi-analytical or hydrodynamic codes that can properly address changes in the temperature and density profiles driven by variations in the total energy output). In Monte Carlo studies, however, one cannot simply remove those trials in which the overall energy production is modified as this would affect the input distribution of

enhancement factors (which are assumed to be random). Therefore, while results from individual reaction-rate variations are not corrupted by these effects, Monte Carlo simulations cannot disentangle this from the overall analysis and hence the interpretation of the results has to be taken with caution.

And third, as discussed in Chapter 2, we have restricted the analysis (in the tables, figures, and forthcoming discussion) to nuclear species which achieve a mass fraction of at least 10^{-5} at the end of the burst.

3.4.1 Model K04

Figure 3.3 shows the impact of the simultaneous variation of all rates (except for the triple-α and all the β-decay rates) on the final yields, for the temperature and density versus time profiles of Model K04 (Koike et al. 2004). It illustrates the interplay of multiple nuclear processes in the highly coupled environment of an XRB. The identification of key reactions, whose uncertainties have the largest impact on the final yields, is more complicated than in *traditional* sensitivity studies. Figure 3.3 shows indeed which isotopes are mostly affected by uncertainties associated with the rates. However, the identification of those specific reactions that are perhaps most responsible for those changes is, by no means, straightforward. Following Smith et al. (2002), Hix et al. (2003), and Roberts et al. (2006), we have searched for possible correlations between variations in the final abundance of a specific nucleus and each nuclear reaction rate that was varied in the Monte Carlo routine.

As shown in Fig. 3.2, the random factors used in this work follow a log-normal distribution, but what does the distribution of final abundances look like? Figure 3.4 shows histograms of the final abundances of ^{15}N, ^{41}Ca, ^{46}Ti, and ^{60}Ni, selected as representative isotopes, ordered by increasing error bar. Notice that for small variations (i.e., ^{41}Ca and ^{46}Ti), shapes are closer to a normal distribution, whereas for larger error bars (i.e., ^{15}N and ^{60}Ni) shapes follow a log-normal distribution. The size of the error bars can be used as a diagnostic in determining which isotopes, for a given network, are less affected by reaction rate uncertainties.

To identify those reactions whose uncertainties deeply affect the final abundances it is necessary to calculate the correlations between isotopes present in the nuclear network and each modified reaction. In this way, we can check not only the correlation but also the *slope* of the linear fit, which indicates the change in abundance when the reaction rate is varied. For instance, ^{69}Ge is strongly correlated with $^{69}Se(p,\gamma)^{70}Br$ (and its reverse reaction), and the linear fit shows a large slope (see Fig. 3.5a), which means that the corresponding reaction rate would play an important role in the final nucleosynthesis. On the other hand, ^{72}Se shows a high correlation with $^{65}As(p,\gamma)^{66}Se$ (and its reverse reaction) but the slope of the linear fit is almost zero, meaning that the uncertainty associated with this reaction rate has no impact on the final abundance for this isotope (Fig. 3.5b). Another example is ^{69}Ge, which is weakly correlated with $^{56}Ni(\alpha,p)^{59}Cu$ (and its reverse rate). In this

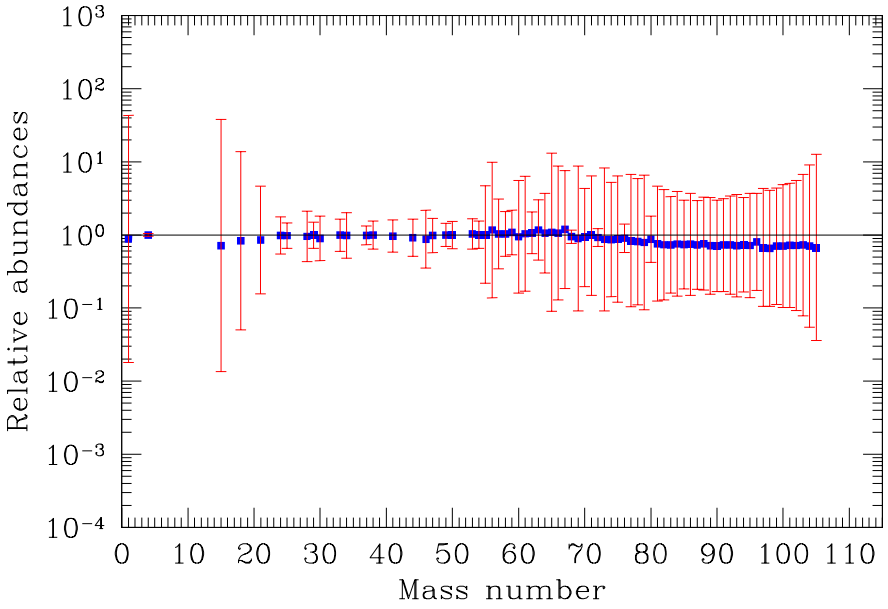

Figure 3.3: Uncertainties in the final distribution of abundances (for $X > 10^{-5}$) resulting from the simultaneous variation of all nuclear processes (except the triple-α and all the β-decay rates) in bulk, by factors ranging roughly between 0.1 and 10, for Model K04.

case, although its abundance exhibits a significant variability, it cannot be attributed to the uncertainty affecting the $^{56}Ni(\alpha,p)^{59}Cu$ rate (Fig. 3.5c). Finally, ^{66}Ge shows an intermediate correlation with $^{66}As(p,\gamma)^{67}Se$ (Fig. 3.5d), which indicates that its abundance is affected by this reaction but not critically. Hence, a key reaction in the Monte Carlo approach must have a significant correlation with the yield of an isotope (as indicated by the correlation coefficient) as well as a pronounced impact on the final abundance of an isotope when its rate is varied (as indicated by the slope of the fit). Isotopes with a correlation coefficient between reaction rates and (relative) final yields larger than 0.5, for any reaction, are displayed in Table 3.1. Reactions that have an impact of less than a factor of 2 in the final yields are indicated with brackets in the slope column.

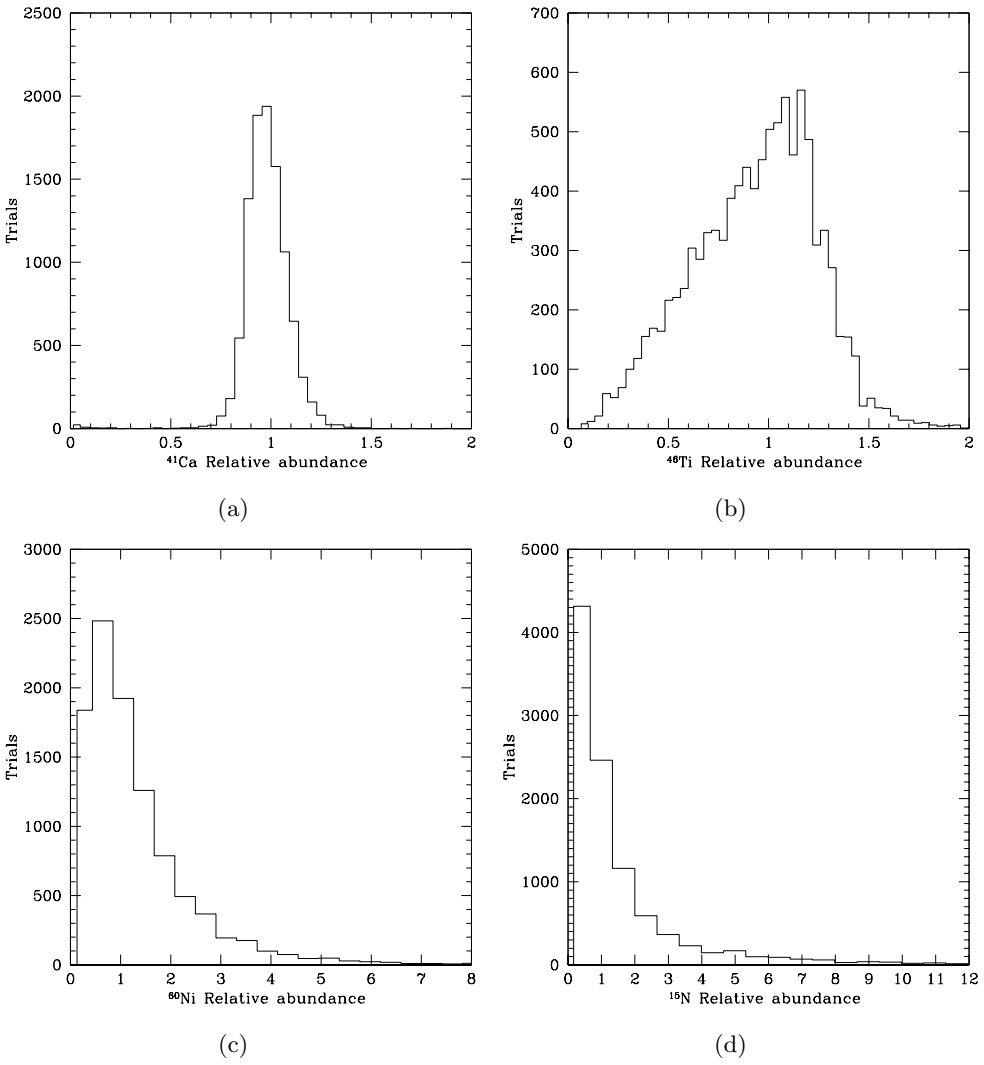

Figure 3.4: Histograms of final relative abundances after 10,000 iterations ordered by increasing error bar. The value of the error bars (see Figure 3.3) are: *a)* ^{41}Ca $[0.58, 1.61]$, *b)* ^{46}Ti $[0.35, 2.18]$, *c)* ^{60}Ni $[0.09, 8.76]$, and *d)* ^{15}N $[0.01, 37.90]$.

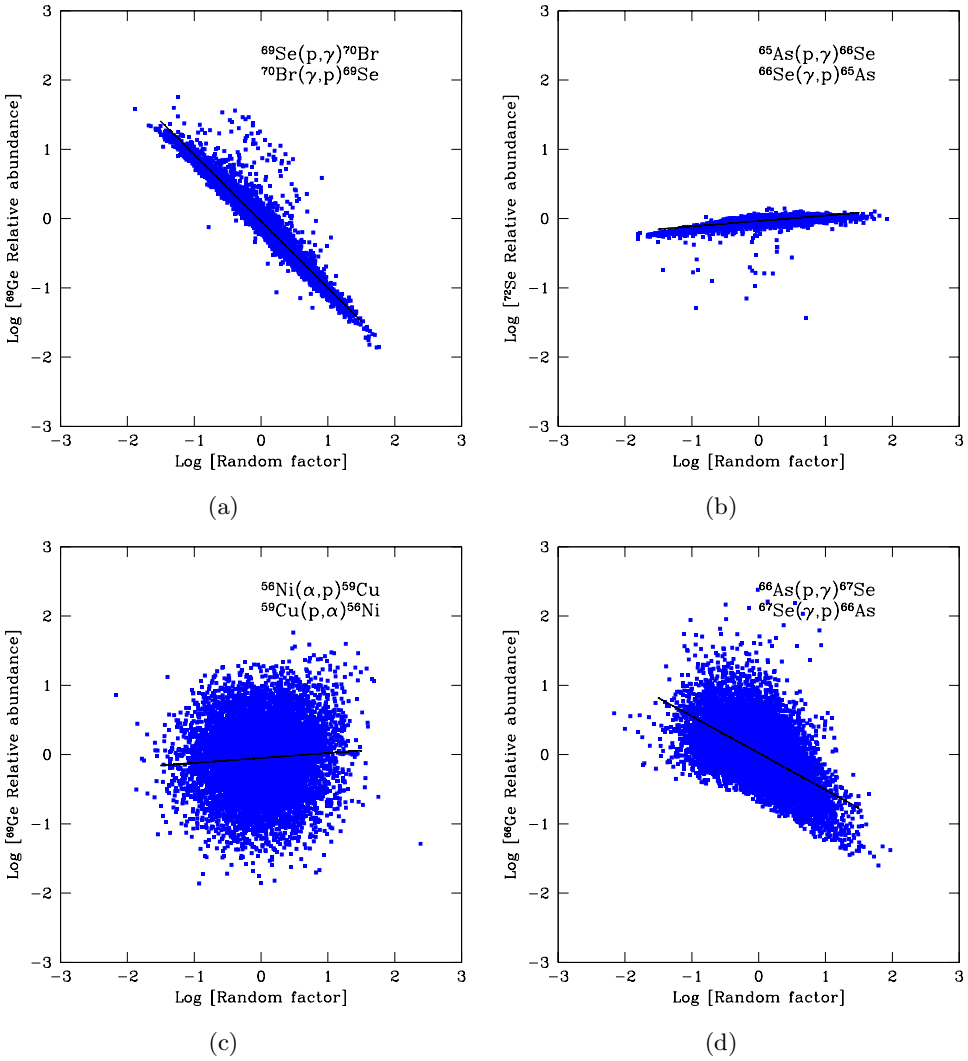

Figure 3.5: Examples of correlations: *a)* A strong correlation ($r = 0.969$) and a big slope ($r = 0.961$) indicate that $^{69}Se(p,\gamma)^{70}Br$ is one of the key reactions in ^{69}Ge synthesis. *b)* Example of a strong correlation ($r = 0.635$) but a small slope ($m = 0.079$), meaning that uncertainties in $^{65}As(p,\gamma)^{66}Se$ (and its reverse reaction) do not have a deep effect in the final ^{72}Se abundance. *c)* A weak correlation between the abundance of ^{69}Ge and the random factor applied to $^{56}Ni(\alpha,p)^{59}Cu$ ($r = 0.072$), suggesting that the slope of the fit is not meaningful. *d)* An intermediate correlation ($r = 0.580$) plus a medium slope ($m = 0.531$) indicate that $^{66}As(p,\gamma)^{67}Se$ affects the final abundance of ^{66}Ge, but not critically.

Table 3.1: Correlations between final yields and enhancement factors applied to reaction rates in the Monte Carlo approach, for Model K04. All correlations with $r > 0.5$ are included. Reactions that have an impact of less than a factor of 2 on the final yields of correlated isotopes (for enhancement factors ranging between roughly 0.1 and 10) are indicated by brackets in the last column, in which slopes of the different linear fits (final isotopic yield vs. rate enhancement factor, see e.g. Fig. 3.8(d)) are given. The error associated with the slopes is typically $\sim 1\,\%$.

Isotope	Reaction	Correlation coefficient, r	Slope
^{15}N	^{15}O(α, γ)^{19}Ne	-0.568	-0.960
^{30}Si	^{31}Cl(p, γ)^{32}Ar	-0.643	[-0.194]
^{34}S	^{34}Ar(p, γ)^{35}K	-0.508	[-0.154]
^{44}Ti	^{43}V(p, γ)^{44}Cr	0.570	[0.144]
^{46}Ti	^{47}Mn(p, γ)^{48}Fe	-0.756	-0.301
^{53}Mn	^{53}Co(p, γ)^{54}Ni	-0.562	[-0.116]
^{55}Co	^{56}Cu(p, γ)^{57}Zn	-0.715	-0.476
^{56}Ni	^{56}Ni(p, γ)^{57}Cu	-0.780	-0.721
^{57}Ni	^{57}Cu(p, γ)^{58}Zn	-0.800	-0.380
^{58}Ni	^{58}Cu(p, γ)^{59}Zn	-0.572	[-0.173]
^{59}Ni	^{59}Cu(p, γ)^{60}Zn	-0.604	[-0.185]
^{60}Ni	^{61}Ga(p, γ)^{62}Ge	-0.902	-0.698
^{61}Cu	^{61}Ga(p, γ)^{62}Ge	-0.901	-0.711
^{62}Zn	^{61}Ga(p, γ)^{62}Ge	0.629	[0.179]
	^{62}Ga(p, γ)^{63}Ge	-0.582	[-0.166]
^{63}Cu	^{63}Ga(p, γ)^{64}Ge	-0.769	-0.322
^{64}Zn	^{65}As(p, γ)^{66}Se	-0.956	-0.520
^{65}Zn	^{65}Ge(p, γ)^{66}As	-0.844	-0.907
^{66}Ge	^{66}As(p, γ)^{67}Se	-0.580	-0.531
	^{66}Ge(p, γ)^{67}As	-0.533	-0.489
^{67}Ga	^{67}As(p, γ)^{68}Se	-0.698	-0.565
	^{65}As(p, γ)^{66}Se	-0.570	-0.458
^{68}Ge	^{69}Br(p, γ)^{70}Kr	-0.673	[-0.060]
^{69}Ge	^{69}Se(p, γ)^{70}Br	-0.969	-0.961
^{70}Ge	^{70}Se(p, γ)^{71}Br	-0.745	-0.501
^{71}As	^{71}Br(p, γ)^{72}Kr	-0.957	-0.784
^{72}Se	^{65}As(p, γ)^{66}Se	0.635	[0.079]
^{73}Se	^{73}Kr(p, γ)^{74}Rb	-0.961	-0.938
^{74}Se	^{74}Kr(p, γ)^{75}Rb	-0.871	-0.681
^{75}Br	^{75}Rb(p, γ)^{76}Sr	-0.955	-0.826
^{76}Kr	^{65}As(p, γ)^{66}Se	0.577	[0.113]
^{77}Kr	^{77}Sr(p, γ)^{78}Y	-0.938	-0.849
^{78}Kr	^{78}Sr(p, γ)^{79}Y	-0.915	-0.790
^{79}Kr	^{79}Y(p, γ)^{80}Zr	-0.933	-0.851
^{80}Sr	^{80}Y(p, γ)^{81}Zr	-0.556	[-0.176]
^{81}Rb	^{81}Zr(p, γ)^{82}Nb	-0.861	-0.670
^{82}Sr	^{82}Zr(p, γ)^{83}Nb	-0.855	-0.642
^{83}Sr	^{83}Nb(p, γ)^{84}Mo	-0.649	-0.431
^{84}Sr	^{84}Nb(p, γ)^{85}Mo	-0.767	-0.552
^{85}Y	^{85}Nb(p, γ)^{86}Mo	-0.606	-0.372
^{86}Zr	^{86}Mo(p, γ)^{87}Tc	-0.758	-0.527
^{87}Zr	^{87}Mo(p, γ)^{88}Tc	-0.656	-0.395
^{88}Zr	^{88}Tc(p, γ)^{89}Ru	-0.578	-0.368

Table 3.1: – Continued.

Isotope	Reaction	Correlation coefficient, r	Slope
^{89}Nb	^{89}Tc(p, γ)^{90}Ru	-0.722	-0.478
^{90}Mo	^{90}Ru(p, γ)^{91}Rh	-0.637	-0.396
^{91}Nb	^{91}Ru(p, γ)^{92}Rh	-0.549	-0.345
^{92}Mo	^{92}Ru(p, γ)^{93}Rh	-0.600	-0.401
^{93}Tc	^{93}Rh(p, γ)^{94}Pd	-0.650	-0.459
^{95}Ru	^{95}Pd(p, γ)^{96}Ag	-0.536	-0.386
^{97}Ru	^{97}Ag(p, γ)^{98}Cd	-0.517	-0.416
^{105}Ag	^{104}In(p, γ)^{105}Sn	0.512	0.654

Notice that these reactions correspond to the smallest slopes independently of the value of the correlation coefficient, meaning that the final abundances do not critically depend on these reactions. Furthermore, the impact of these reactions is restricted to the vicinity of the target nuclei. Certainly, the larger the correlation coefficient is, the more critical the nuclear reaction becomes. Notice also that among all reactions, only a couple of them affect more than one isotope, and hence can be considered as the most influential (see Table 3.2).

Table 3.2: Reactions that affect more than one isotope for Model K04.

Reaction	Isotopes
$^{61}Ga(p,\gamma)^{62}Ge$	^{60}Ni, ^{61}Cu, ^{62}Zn
$^{65}As(p,\gamma)^{66}Se$	^{64}Zn, ^{67}Ga, ^{72}Se, ^{76}Kr

3.4.2 Model F08

The results obtained for this case are very similar to those reported for Model K04. Figure 3.6 shows the impact of the simultaneous variation of all reaction rates (except for the triple-α reaction, and all β-decays) on the final yields, for the temperature and density versus time profiles of Model F08 (Fisker et al. 2008).

The list of isotopes with a correlation coefficient larger than 0.5, for any reaction, is now shown in Table 3.3 (see also Fig. 3.6). As pointed out for Model K04, reactions that have an impact of less than a factor of 2 (slope values between brackets) correspond to the smallest variation bars. Reactions affecting more than one isotope are shown in Table 3.4.

Table 3.3: Same as Table 3.1, for Model F08.

Isotope	Reaction	Correlation coefficient, r	Slope
^{4}He	^{12}C(α, γ)^{16}O	-0.658	[-0.029]
	^{12}C(p, γ)^{13}N	-0.521	[-0.023]
^{12}C	^{12}C(p, γ)^{13}N	-0.604	[-0.212]

Table 3.3: – Continued.

Isotope	Reaction	Correlation coefficient, r	Slope
	^{12}C(α, γ)^{16}O	-0.543	[-0.188]
^{16}O	^{16}O(α, γ)^{20}Ne	-0.874	-0.943
^{20}Ne	^{20}Ne(α, γ)^{24}Mg	-0.891	-0.982
^{24}Mg	^{24}Mg(α, γ)^{28}Si	-0.832	-0.665
^{25}Mg	^{22}Mg(α, p)^{25}Al	-0.506	-0.624
^{26}Mg	^{26g}Al(α, p)^{29}Si	-0.657	-0.582
	^{26}Si(α, p)^{29}P	-0.517	-0.457
^{26g}Al	^{26g}Al(α, p)^{29}Si	-0.692	-0.724
	^{26}Si(α, p)^{29}P	-0.503	-0.525
^{29}Si	^{26g}Al(α, p)^{29}Si	0.552	[0.211]
^{30}Si	^{30}P(p, γ)^{31}S	-0.711	[-0.147]
^{31}P	^{30}P(p, γ)^{31}S	0.853	0.465
^{32}S	^{28}Si(α, γ)^{32}S	0.832	0.476
^{33}S	^{30}P(α, p)^{33}S	0.559	[0.195]
	^{29}Si(α, γ)^{33}S	0.507	[0.175]
^{34}S	^{34}Cl(p, γ)^{35}Ar	-0.632	[-0.117]
^{35}Cl	^{34}Cl(p, γ)^{35}Ar	0.702	0.308
^{37}Ar	^{36}Ar(p, γ)^{37}K	-0.911	-0.475
^{38}Ar	^{38}K(p, γ)^{39}Ca	-0.634	[-0.091]
^{39}K	^{40}Sc(p, γ)^{41}Ti	-0.721	[-0.142]
^{40}Ca	^{39}K(p, γ)^{40}Ca	0.615	[0.206]
^{43}Sc	^{44}V(p, γ)^{45}Cr	-0.816	[-0.242]
^{44}Ti	^{44}V(p, γ)^{45}Cr	0.504	[0.178]
^{45}Ti	^{44}Ti(p, γ)^{45}V	-0.768	-0.568
^{47}Ti	^{47}Cr(p, γ)^{48}Mn	-0.723	-0.399
^{48}Cr	^{48}Cr(p, γ)^{49}Mn	-0.641	[-0.168]
^{49}V	^{49}Mn(p, γ)^{50}Fe	-0.856	[-0.293]
^{50}Cr	^{50}Mn(p, γ)^{51}Fe	-0.554	[-0.092]
^{51}Cr	^{52}Co(p, γ)^{53}Ni	-0.795	[-0.165]
^{52}Fe	^{52}Fe(p, γ)^{53}Co	-0.931	-0.511
^{53}Mn	^{53}Co(p, γ)^{54}Ni	-0.915	-0.678
^{54}Fe	^{54}Co(p, γ)^{55}Ni	-0.730	[-0.248]
^{55}Co	^{55}Co(p, γ)^{56}Ni	-0.761	[-0.182]
^{56}Ni	^{57}Cu(p, γ)^{58}Zn	-0.826	[-0.276[
^{57}Ni	^{57}Ni(p, γ)^{58}Cu	-0.899	-0.870
^{58}Ni	^{58}Cu(p, γ)^{59}Zn	-0.740	-0.567
	^{57}Cu(p, γ)^{58}Zn	0.624	0.475
^{59}Ni	^{57}Cu(p, γ)^{58}Zn	0.679	0.335
	^{59}Cu(p, γ)^{60}Zn	-0.663	-0.329
^{60}Ni	^{57}Cu(p, γ)^{58}Zn	0.609	[0.096]
^{61}Cu	^{61}Zn(p, γ)^{62}Ga	-0.905	-0.623
^{62}Zn	^{62}Ga(p, γ)^{63}Ge	-0.795	-0.507
^{63}Cu	^{63}Ga(p, γ)^{64}Ge	-0.862	-0.402
^{64}Zn	^{61}Ga(p, γ)^{62}Ge	0.938	0.343
^{65}Zn	^{65}Ge(p, γ)^{66}As	-0.825	-0.646
^{66}Ge	^{66}As(p, γ)^{67}Se	-0.619	-0.457
^{67}Ga	^{67}As(p, γ)^{68}Se	-0.747	-0.501
	^{61}Ga(p, γ)^{62}Ge	0.519	0.344

Table 3.3: – Continued.

Isotope	Reaction	Correlation coefficient, r	Slope
^{68}Ge	^{61}Ga(p, γ)^{62}Ge	0.837	[0.031]
^{69}Ge	^{69}Se(p, γ)^{70}Br	-0.945	-0.586
^{70}Ge	^{70}Se(p, γ)^{71}Br	-0.678	-0.424
	^{70}Br(p, γ)^{71}Kr	-0.507	-0.318
^{71}As	^{71}Br(p, γ)^{72}Kr	-0.930	-0.630
^{72}Se	^{72}Br(p, γ)^{73}Kr	-0.512	[-0.005]
^{73}Se	^{73}Kr(p, γ)^{74}Rb	-0.935	-0.636
^{74}Se	^{74}Kr(p, γ)^{75}Rb	-0.790	-0.501
^{75}Br	^{75}Rb(p, γ)^{76}Sr	-0.934	-0.666
^{76}Kr	^{75}Rb(p, γ)^{76}Sr	0.567	[0.020]
^{77}Kr	^{77}Sr(p, γ)^{78}Y	-0.924	-0.641
^{78}Kr	^{78}Sr(p, γ)^{79}Y	-0.853	-0.565
^{79}Kr	^{79}Y(p, γ)^{80}Zr	-0.934	-0.785
^{81}Rb	^{81}Zr(p, γ)^{82}Nb	-0.900	-0.625
^{82}Sr	^{82}Zr(p, γ)^{83}Nb	-0.915	-0.594
^{83}Sr	^{83}Nb(p, γ)^{84}Mo	-0.904	-0.674
^{84}Sr	^{84}Nb(p, γ)^{85}Mo	-0.932	-0.736
^{85}Y	^{85}Mo(p, γ)^{86}Tc	-0.896	-0.584
^{86}Zr	^{86}Mo(p, γ)^{87}Tc	-0.915	-0.616
^{87}Zr	^{87}Tc(p, γ)^{88}Ru	-0.764	-0.460
^{88}Zr	^{87}Tc(p, γ)^{88}Ru	0.504	[0.279]

Table 3.4: Reactions that affect more than one isotope for Model F08.

Reaction	Isotopes
$^{12}C(p,\gamma)^{13}N$	^{4}He, ^{12}C
$^{12}C(\alpha,\gamma)^{16}O$	^{4}He, ^{12}C
$^{26g}Al(\alpha,p)^{29}S$	^{26}Mg, ^{26g}Al, ^{29}Si
$^{26}Si(\alpha,p)^{29}P$	^{26}Mg, ^{26g}Al
$^{30}P(p,\gamma)^{31}S$	^{30}Si, ^{31}P, ^{33}S
$^{34}Cl(p,\gamma)^{35}Ar$	^{34}S, ^{35}Cl
$^{44}V(p,\gamma)^{45}Cr$	^{43}Sc, ^{44}Ti
$^{57}Cu(p,\gamma)^{58}Zn$	^{56}Ni, ^{58}Ni, ^{59}Ni, ^{60}Ni
$^{61}Ga(p,\gamma)^{62}Ge$	^{64}Zn, ^{67}Ga, ^{68}Ge
$^{75}Rb(p,\gamma)^{76}Sr$	^{75}Br, ^{76}Kr
$^{65}As(p,\gamma)^{66}Se$	^{64}Zn, ^{67}Ga, ^{72}Se, ^{76}Kr

3.4.3 Monte Carlo vs. Individual-rate variations

In order to determine whether Monte Carlo methods and Individual-rate variations are reliable methods for sensitivity studies, we have compared the results obtained in previous Chapter with those reported above. For conciseness, we restrict the discussion here to Models K04 and F08, since results turn out to be qualitatively

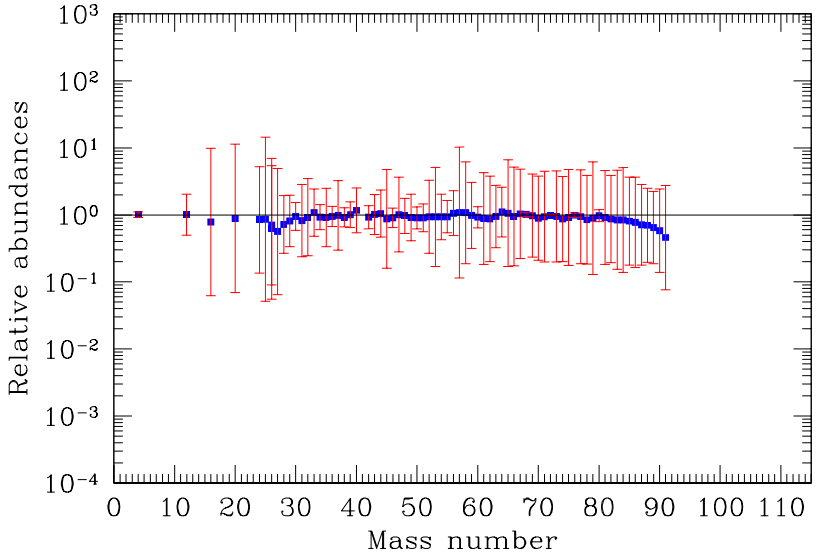

Figure 3.6: Same as Fig. 3.3, but for Model F08.

similar for all cases.

Reactions that have the largest effect on the final yields for Model K04, according to the individual reaction-rate variation study (Table 2.1, in Chapter 2) and Monte Carlo simulations (Table 3.1, without brackets in the slope column, in this Chapter), are displayed in Table 3.5. In the Table, reactions were restricted to those that, either in the individual reaction-rate variation study or in the Monte Carlo simulations, affected the final abundances by at least a factor of 2, while in the Monte Carlo case, the correlation coefficient is also requested to be > 0.5. Results are in excellent agreement: first, all the reactions flagged in the Monte Carlo study were previously identified in the individual reaction-rate variation study; and second, when both the restriction imposed on the correlation coefficient and on the impact on final yields (> 2) are slightly relaxed, a total agreement between results based on the two approaches is reached.

For Model F08 (see Table 3.6), the comparison between both methods yields also a similar agreement. In this case, only one reaction, ^{66}As(p, γ)^{67}Se, was found in the Monte Carlo study but not in the individual reaction-rate variation analysis.

Table 3.5: Isotopes mostly affected by nuclear uncertainties, according to our sensitivity studies. Results from the individual reaction-rate variations approach (Table 2.1) are compared with those obtained from Monte Carlo simulations (Table 3.2), for Model K04.

Isotope	Reaction (Individual-rate variations)	Reaction (Monte Carlo)
^{15}N	^{15}O(α, γ)^{19}Ne	^{15}O(α, γ)^{19}Ne
	^{18}Ne(α, p)^{21}Na	–
^{18}F	^{18}Ne(α, p)^{21}Na	–
^{30}Si	^{31}Cl(p, γ)^{32}Ar	–
^{44}Ti	^{43}V(p, γ)^{44}Cr	–
^{46}Ti	^{47}Mn(p, γ)^{48}Fe	^{47}Mn(p, γ)^{48}Fe
^{55}Co	^{56}Cu(p, γ)^{57}Zn	^{56}Cu(p, γ)^{57}Zn
^{56}Ni	^{56}Ni(p, γ)^{57}Cu	^{56}Ni(p, γ)^{57}Cu
^{57}Ni	^{57}Cu(p, γ)^{58}Zn	^{57}Cu(p, γ)^{58}Zn
^{58}Ni	^{58}Cu(p, γ)^{59}Zn	–
^{59}Ni	^{59}Cu(p, γ)^{60}Zn	–
^{60}Ni	^{61}Ga(p, γ)^{62}Ge	^{61}Ga(p, γ)^{62}Ge
^{61}Cu	^{61}Ga(p, γ)^{62}Ge	^{61}Ga(p, γ)^{62}Ge
	^{61}Zn(p, γ)^{62}Ga	–
^{63}Cu	^{63}Ga(p, γ)^{64}Ge	^{63}Ga(p, γ)^{64}Ge
^{64}Zn	^{65}As(p, γ)^{66}Se	^{65}As(p, γ)^{66}Se
^{65}Zn	^{65}Ge(p, γ)^{66}As	^{65}Ge(p, γ)^{66}As
	^{65}As(p, γ)^{66}Se	–
^{66}Ge	^{66}Ge(p, γ)^{67}As	^{66}Ge(p, γ)^{67}As
	^{65}As(p, γ)^{66}Se	–
	^{66}As(p, γ)^{67}Se	^{66}As(p, γ)^{67}Se
^{67}Ga	^{67}As(p, γ)^{68}Se	^{67}As(p, γ)^{68}Se
	^{65}As(p, γ)^{66}Se	^{65}As(p, γ)^{66}Se
^{69}Ge	^{69}Se(p, γ)^{70}Br	^{69}Se(p, γ)^{70}Br
^{70}Ge	^{70}Se(p, γ)^{71}Br	^{70}Se(p, γ)^{71}Br
	^{70}Br(p, γ)^{71}Kr	–
^{71}As	^{71}Br(p, γ)^{72}Kr	^{71}Br(p, γ)^{72}Kr
^{73}Se	^{73}Kr(p, γ)^{74}Rb	^{73}Kr(p, γ)^{74}Rb
^{74}Se	^{74}Kr(p, γ)^{75}Rb	^{74}Kr(p, γ)^{75}Rb
	^{74}Rb(p, γ)^{75}Sr	–
^{75}Br	^{75}Rb(p, γ)^{76}Sr	^{75}Rb(p, γ)^{76}Sr
^{77}Kr	^{77}Sr(p, γ)^{78}Y	^{77}Sr(p, γ)^{78}Y
^{78}Kr	^{78}Sr(p, γ)^{79}Y	^{78}Sr(p, γ)^{79}Y
^{79}Kr	^{79}Y(p, γ)^{80}Zr	^{79}Y(p, γ)^{80}Zr
^{81}Rb	^{81}Zr(p, γ)^{82}Nb	^{81}Zr(p, γ)^{82}Nb
	^{65}As(p, γ)^{66}Se	–
^{82}Sr	^{82}Zr(p, γ)^{83}Nb	^{82}Zr(p, γ)^{83}Nb
^{83}Sr	^{83}Nb(p, γ)^{84}Mo	^{83}Nb(p, γ)^{84}Mo
^{84}Sr	^{84}Nb(p, γ)^{85}Mo	^{84}Nb(p, γ)^{85}Mo
^{85}Y	^{85}Mo(p, γ)^{86}Tc	–
	^{85}Nb(p, γ)^{86}Mo	^{85}Nb(p, γ)^{86}Mo
^{86}Zr	^{86}Mo(p, γ)^{87}Tc	^{86}Mo(p, γ)^{87}Tc
^{87}Zr	^{87}Mo(p, γ)^{88}Tc	^{87}Mo(p, γ)^{88}Tc
^{88}Zr	^{88}Tc(p, γ)^{89}Ru	^{88}Tc(p, γ)^{89}Ru
	^{65}As(p, γ)^{66}Se	–
^{89}Nb	^{89}Tc(p, γ)^{90}Ru	^{89}Tc(p, γ)^{90}Ru

Table 3.5: – Continued.

Isotope	Reaction (Individual-rate variations)	Reaction (Monte Carlo)
	^{65}As(p, γ)^{66}Se	–
^{90}Mo	^{90}Ru(p, γ)^{91}Rh	^{90}Ru(p, γ)^{91}Rh
	^{65}As(p, γ)^{66}Se	–
^{91}Nb	^{91}Ru(p, γ)^{92}Rh	^{91}Ru(p, γ)^{92}Rh
	^{65}As(p, γ)^{66}Se	–
^{92}Mo	^{92}Ru(p, γ)^{93}Rh	^{92}Ru(p, γ)^{93}Rh
	^{65}As(p, γ)^{66}Se	–
^{93}Tc	^{93}Rh(p, γ)^{94}Pd	^{93}Rh(p, γ)^{94}Pd
	^{65}As(p, γ)^{66}Se	–
^{94}Mo	^{65}As(p, γ)^{66}Se	–
	^{94}Pd(p, γ)^{95}Ag	–
	^{94}Rh(p, γ)^{95}Pd	–
^{95}Ru	^{95}Pd(p, γ)^{96}Ag	^{95}Pd(p, γ)^{96}Ag
	^{65}As(p, γ)^{66}Se	–
^{96}Ru	^{65}As(p, γ)^{66}Se	–
	^{96}Ag(p, γ)^{97}Cd	–
^{97}Ru	^{97}Ag(p, γ)^{98}Cd	^{97}Ag(p, γ)^{98}Cd
	^{65}As(p, γ)^{66}Se	–
	^{96}Ag(p, γ)^{97}Cd	–
^{98}Ru	^{96}Ag(p, γ)^{97}Cd	–
	^{65}As(p, γ)^{66}Se	–
	^{98}Cd(p, γ)^{99}In	–
	^{98}Ag(p, γ)^{99}Cd	–
^{99}Rh	^{99}Cd(p, γ)^{100}In	–
	^{65}As(p, γ)^{66}Se	–
	^{96}Ag(p, γ)^{97}Cd	–
^{100}Pd	^{65}As(p, γ)^{66}Se	–
	^{100}Cd(p, γ)^{101}In	–
	^{96}Ag(p, γ)^{97}Cd	–
^{101}Pd	^{101}In(p, γ)^{102}Sn	–
	^{65}As(p, γ)^{66}Se	–
^{102}Pd	^{102}In(p, γ)^{103}Sn	–
	^{65}As(p, γ)^{66}Se	–
^{103}Ag	^{65}As(p, γ)^{66}Se	–
	^{102}In(p, γ)^{103}Sn	–
^{104}Ag	^{103}In(p, γ)^{104}Sn	–
	^{65}As(p, γ)^{66}Se	–
	^{102}In(p, γ)^{103}Sn	–
^{105}Ag	^{103}In(p, γ)^{104}Sn	–
	^{104}In(p, γ)^{105}Sn	^{104}In(p, γ)^{105}Sn

Table 3.6: Same as Table 3.5, for Model F08.

Isotope	Reaction (Individual-rate variations)	Reaction (Monte Carlo)
^{12}C	^{12}C(p, γ)^{13}N	–
	^{12}C(α, γ)^{16}O	–
^{16}O	^{16}O(α, γ)^{20}Ne	^{16}O(α, γ)^{20}Ne
	^{12}C(α, γ)^{16}O	–
^{20}Ne	^{20}Ne(α, γ)^{24}Mg	^{20}Ne(α, γ)^{24}Mg
	^{12}C(α, γ)^{16}O	–
^{24}Mg	^{24}Mg(α, γ)^{28}Si	^{24}Mg(α, γ)^{28}Si
	^{12}C(α, γ)^{16}O	–
^{25}Mg	^{22}Mg(α, p)^{25}Al	^{22}Mg(α, p)^{25}Al
	^{24}Mg(α, γ)^{28}Si	–
	^{24}Mg(p, γ)^{25}Al	–
	^{25}Al(α, p)^{28}Si	–
^{26}Mg	^{26g}Al(α, p)^{29}Si	^{26g}Al(α, p)^{29}Si
	–	^{26}Si(α, p)^{29}P
^{26g}Al	^{26g}Al(α, p)^{29}Si	^{26g}Al(α, p)^{29}Si
	^{26}Si(α, p)^{29}P	^{26}Si(α, p)^{29}P
^{27}Al	^{26}Si(α, p)^{29}P	–
	^{27}Si(α, p)^{30}P	–
	^{27}Al(α, p)^{30}Si	–
	^{26g}Al(p, γ)^{27}Si	–
	^{26g}Al(α, p)^{29}Si	–
	^{22}Mg(α, p)^{25}Al	–
^{28}Si	^{28}Si(α, γ)^{32}S	–
^{31}P	^{30}P(p, γ)^{31}S	^{30}P(p, γ)^{31}S
^{32}S	^{28}Si(α, γ)^{32}S	^{28}Si(α, γ)^{32}S
^{33}S	^{29}Si(α, γ)^{33}S	–
	^{30}P(α, p)^{33}S	–
^{35}Cl	^{34}Cl(p, γ)^{35}Ar	^{34}Cl(p, γ)^{35}Ar
^{37}Ar	^{36}Ar(p, γ)^{37}K	^{36}Ar(p, γ)^{37}K
^{40}Ca	^{39}K(p, γ)^{40}Ca	–
^{45}Ti	^{44}Ti(p, γ)^{45}V	^{44}Ti(p, γ)^{45}V
	^{44}V(p, γ)^{45}Cr	–
	^{45}V(p, γ)^{46}Cr	–
^{47}Ti	^{47}Cr(p, γ)^{48}Mn	^{47}Cr(p, γ)^{48}Mn
	^{46}V(p, γ)^{47}Cr	–
^{49}V	^{49}Mn(p, γ)^{50}Fe	–
^{52}Fe	^{52}Fe(p, γ)^{53}Co	^{52}Fe(p, γ)^{53}Co
^{53}Mn	^{53}Co(p, γ)^{54}Ni	^{53}Co(p, γ)^{54}Ni
	^{52}Fe(p, γ)^{53}Co	–
^{54}Fe	^{54}Co(p, γ)^{55}Ni	–
^{56}Ni	^{57}Cu(p, γ)^{58}Zn	–
^{57}Ni	^{57}Ni(p, γ)^{58}Cu	^{57}Ni(p, γ)^{58}Cu
	^{57}Cu(p, γ)^{58}Zn	–
^{58}Ni	^{58}Cu(p, γ)^{59}Zn	^{58}Cu(p, γ)^{59}Zn
	^{57}Cu(p, γ)^{58}Zn	^{57}Cu(p, γ)^{58}Zn
^{59}Ni	^{59}Cu(p, γ)^{60}Zn	^{59}Cu(p, γ)^{60}Zn
	^{57}Cu(p, γ)^{58}Zn	^{57}Cu(p, γ)^{58}Zn
^{61}Cu	^{61}Zn(p, γ)^{62}Ga	^{61}Zn(p, γ)^{62}Ga

Table 3.6: – Continued.

Isotope	Reaction (Individual-rate variations)	Reaction (Monte Carlo)
^{62}Zn	^{62}Ga(p, γ)^{63}Ge	^{62}Ga(p, γ)^{63}Ge
	^{61}Zn(p, γ)^{62}Ga	–
^{63}Cu	^{63}Ga(p, γ)^{64}Ge	^{63}Ga(p, γ)^{64}Ge
^{64}Zn	^{61}Ga(p, γ)^{62}Ge	^{61}Ga(p, γ)^{62}Ge
^{65}Zn	^{65}Ge(p, γ)^{66}As	^{65}Ge(p, γ)^{66}As
	^{61}Ga(p, γ)^{62}Ge	–
^{66}Ge	^{61}Ga(p, γ)^{62}Ge	–
	^{66}Ge(p, γ)^{67}As	–
	–	^{66}As(p, γ)^{67}Se
^{67}Ga	^{67}As(p, γ)^{68}Se	^{67}As(p, γ)^{68}Se
	^{61}Ga(p, γ)^{62}Ge	^{61}Ga(p, γ)^{62}Ge
^{69}Ge	^{69}Se(p, γ)^{70}Br	^{69}Se(p, γ)^{70}Br
^{70}Ge	^{70}Br(p, γ)^{71}Kr	^{70}Br(p, γ)^{71}Kr
	^{70}Se(p, γ)^{71}Br	^{70}Se(p, γ)^{71}Br
	^{69}Se(p, γ)^{70}Br	–
^{71}As	^{71}Br(p, γ)^{72}Kr	^{71}Br(p, γ)^{72}Kr
^{73}Se	^{73}Kr(p, γ)^{74}Rb	^{73}Kr(p, γ)^{74}Rb
^{74}Se	^{74}Kr(p, γ)^{75}Rb	^{74}Kr(p, γ)^{75}Rb
	^{74}Rb(p, γ)^{75}Sr	–
	^{73}Kr(p, γ)^{74}Rb	–
^{75}Br	^{75}Rb(p, γ)^{76}Sr	^{75}Rb(p, γ)^{76}Sr
^{77}Kr	^{77}Sr(p, γ)^{78}Y	^{77}Sr(p, γ)^{78}Y
	^{76}Rb(p, γ)^{77}Sr	–
^{78}Kr	^{78}Sr(p, γ)^{79}Y	^{78}Sr(p, γ)^{79}Y
	^{78}Y(p, γ)^{79}Zr	–
^{79}Kr	^{79}Y(p, γ)^{80}Zr	^{79}Y(p, γ)^{80}Zr
^{81}Rb	^{81}Zr(p, γ)^{82}Nb	^{81}Zr(p, γ)^{82}Nb
	^{80}Y(p, γ)^{81}Zr	–
^{82}Sr	^{82}Zr(p, γ)^{83}Nb	^{82}Zr(p, γ)^{83}Nb
^{83}Sr	^{83}Nb(p, γ)^{84}Mo	^{83}Nb(p, γ)^{84}Mo
	^{82}Zr(p, γ)^{83}Nb	–
^{84}Sr	^{84}Nb(p, γ)^{85}Mo	^{84}Nb(p, γ)^{85}Mo
^{85}Y	^{85}Mo(p, γ)^{86}Tc	^{85}Mo(p, γ)^{86}Tc
^{86}Zr	^{86}Mo(p, γ)^{87}Tc	^{86}Mo(p, γ)^{87}Tc
^{87}Zr	^{87}Tc(p, γ)^{88}Ru	^{87}Tc(p, γ)^{88}Ru
	^{86}Mo(p, γ)^{87}Tc	–
^{88}Zr	^{86}Mo(p, γ)^{87}Tc	–
	^{87}Tc(p, γ)^{88}Ru	–
^{89}Nb	^{86}Mo(p, γ)^{87}Tc	–
	^{88}Tc(p, γ)^{89}Ru	–
^{90}Mo	^{86}Mo(p, γ)^{87}Tc	–
	^{85}Mo(p, γ)^{86}Tc	–
^{91}Nb	^{85}Mo(p, γ)^{86}Tc	–

3.4.4 Effect of the number of trials

How critical is the number of trials adopted in the Monte Carlo method? To address this issue, we have compared the final (relative) abundances obtained for 10, 100, 1000, and 10,000 trials. Results are shown in Fig. 3.7, both for Models K04 and F08. The plots show quite similar patterns for all species with final abundances above 10^{-5}, except Model K04 for 10 iterations, where ^{47}Ti is absent, and Model F08 for 100 iterations, where ^{91}Nb is absent too. It is worth noting that the 10 iteration case shows the largest variation of abundances (in both models) likely attributed to the reduced number of trials adopted.

Concerning the correlation between yields and variation of nuclear reaction rates, our tests suggest that the number of trials adopted is not critical. For illustrative purposes, let's focus, for instance, on the case of ^{69}Ge: as shown in Fig. 3.8, the final abundance of this isotope is always well correlated with $^{69}Se(p,\gamma)^{70}Br$ (and its reverse reaction), regardless of the number of trials adopted. Indeed, correlation coefficients and slopes of the linear fits are also very similar, and almost independent of the number of trials. Similar results have been obtained for Model F08 (Fig. 3.9).

All in all, we conclude that reasonable results can already be obtained with a limited number of trials (around ~ 100), which makes our Monte Carlo studies with 10,000 trials fully reliable and statistically sound.

3.4.5 Effect of variations of the triple-α and β-decay rates

All the post-processing calculations reported in this Thesis so far, have been computed assuming no variation for the triple-α and β-decay reaction rates, the reason being that despite their importance for the nucleosynthesis accompanying type I X-ray bursts, these rates are known with much better precision than the adopted factor of 10, up and down. Nevertheless, it is worth analyzing what would be the impact of varying such rates. This is illustrated in Fig. 3.10, where final (relative) abundances obtained when variations of the triple-α and β-decay reactions are allowed (top panels) or suppressed (bottom panels), are compared for Models K04 and F08, for a series of 1000 trials.

In both models, and as expected, the corresponding deviation bars are much shorter when these reactions are not varied, which results from the fact that XRBs are powered by a series of p- and α-captures followed by β-disintegration reactions, and hence, have a dramatic impact in the overall nuclear activity.

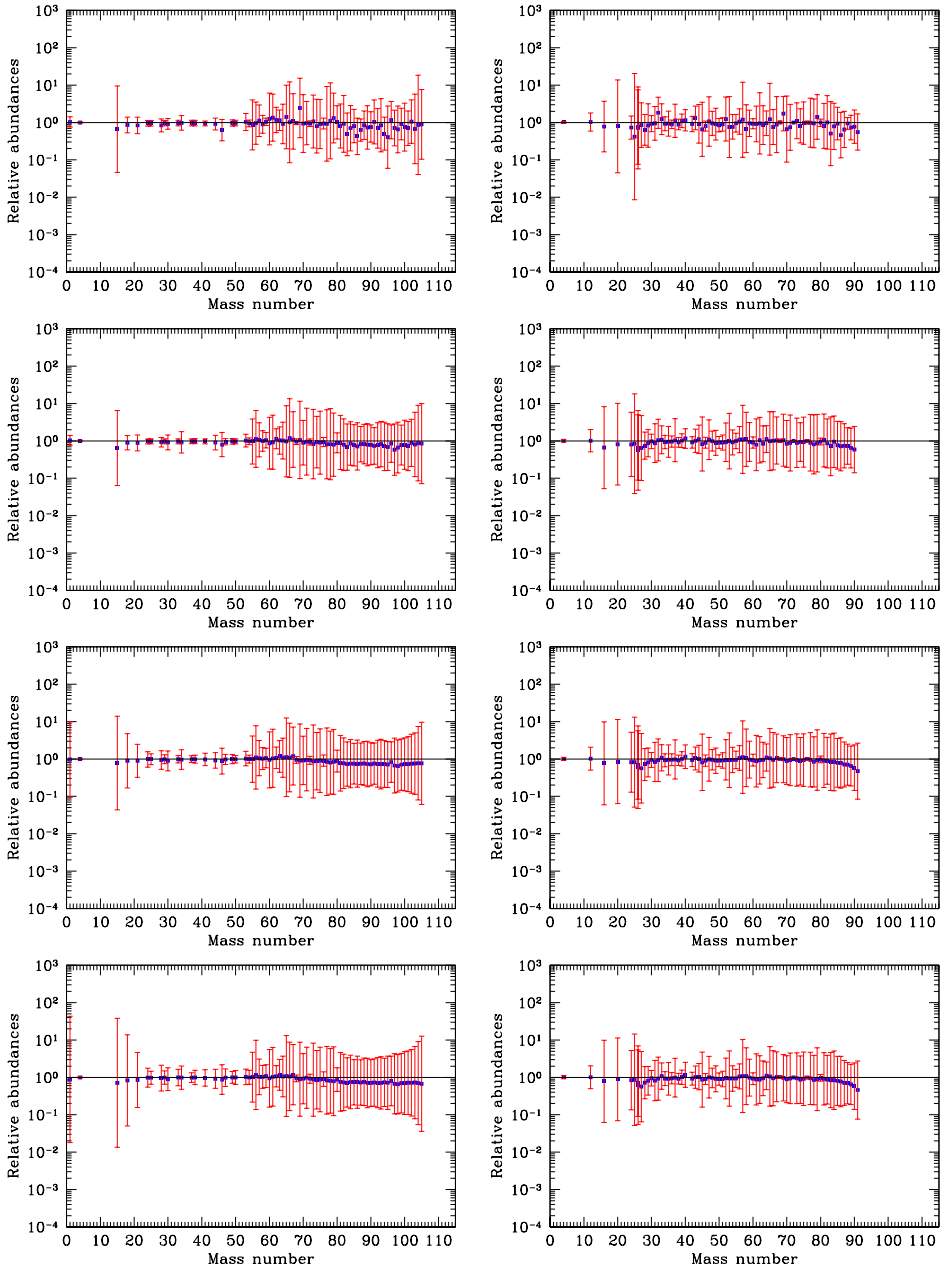

Figure 3.7: Final (relative) abundances ($X > 10^{-5}$) for Models K04 (left panels) and F08 (right panels), as a function of the adopted number of trials (from top to bottom: 10, 100, 1000, and 10,000 trials).

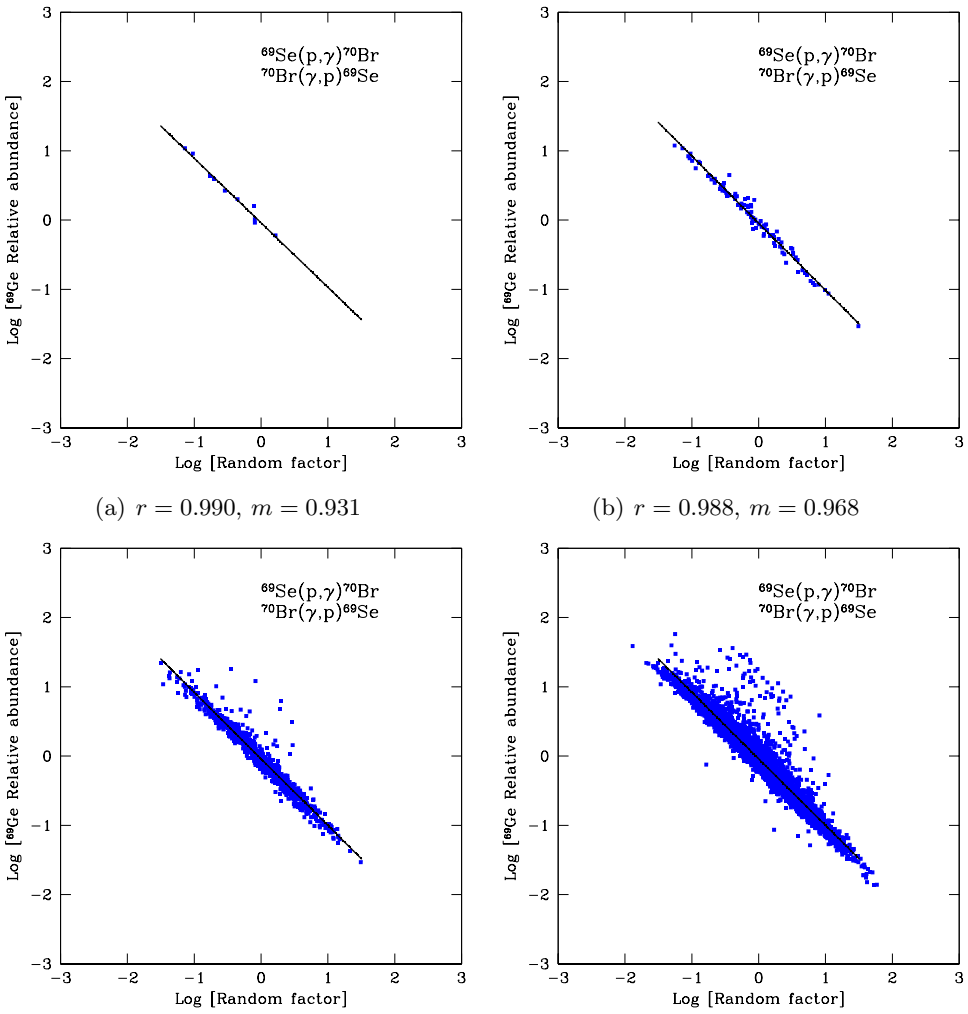

(a) $r = 0.990$, $m = 0.931$

(b) $r = 0.988$, $m = 0.968$

(c) $r = 0.972$, $m = 0.961$

(d) $r = 0.969$, $m = 0.961$

Figure 3.8: Correlation between the abundance of ^{69}Ge and reaction-rate variations of $^{69}Se(p,\gamma)^{70}Br$ (and its reverse reaction), for 10, 100, 1000, and 10,000 trials.

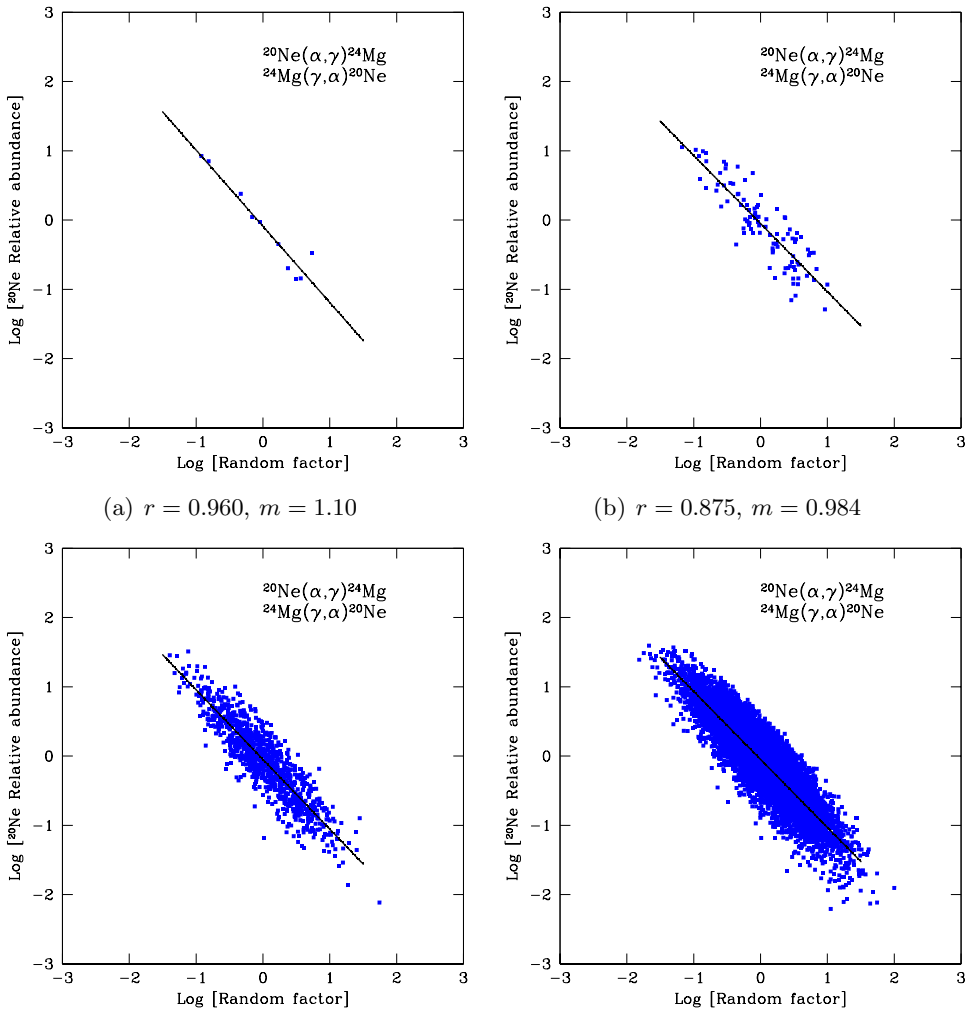

(a) $r = 0.960$, $m = 1.10$ (b) $r = 0.875$, $m = 0.984$

(c) $r = 0.894$, $m = 0.1, 01$ (d) $r = 0.891$, $m = 0.982$

Figure 3.9: Same as Fig. 3.8, but for the abundance of ^{20}Ne and reaction-rate variations of $^{20}Ne(\alpha,\gamma)^{24}Mg$ (and its reverse reaction), for Model F08.

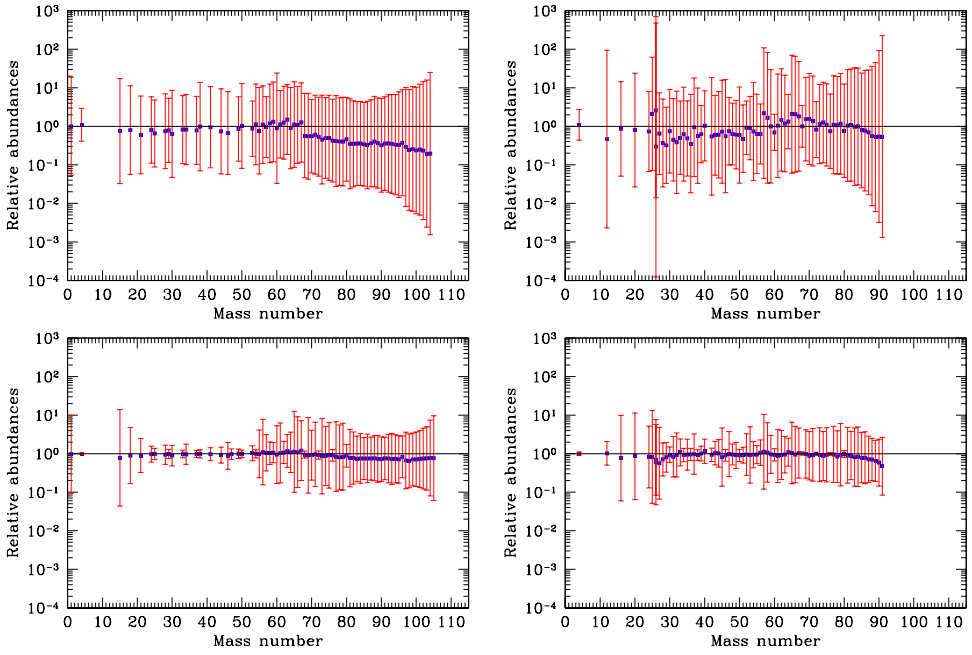

Figure 3.10: Comparison between final (relative) abundances ($X > 10^{-5}$) for Models K04 (left panels) and F08 (right panels), when variations of the triple-α, and β-decay reactions are allowed (top panels) or suppressed (bottom panels).

Chapter 4

Hydrodynamic simulations of type I X-ray bursts

Modeling of type I X-ray bursts and their associated nucleosynthesis (see pioneering models by Woosley & Taam 1976, Maraschi & Cavaliere 1977, and Joss 1977) has been extensively addressed by different groups, reflecting the astrophysical interest in determining the nuclear processes that power the explosion as well as in providing reliable estimates for the post-burst composition of the neutron star surface. Indeed, several thermal (Miralda-Escudé et al. 1990; Schatz et al. 1999), radiative (Paczyński 1983), electrical (Brown & Bildsten 1998; Schatz et al. 1999), and mechanical properties (Bildsten & Cutler 1995; Bildsten & Cumming 998b) of the neutron star depend critically on the specific chemical abundance pattern of its outer layers. The diversity of shapes in XRB light curves ($L_{peak} \sim 10^{38} - 10^{39}$ erg s^{-1}; see e.g., Galloway et al. 2008, Lewin et al. 1993, and Kuulkers et al. 2003) is also likely due to different nuclear histories (see Heger et al. 2007, for an account of the interplay between long bursts and the extension of the rp-process in XRBs), suggesting that the final composition is not unique. It is worth noting that, as discussed by Taam (1980) and Woosley et al. (2004), the properties of the bursts recurring in a given stellar source are affected by *compositional inertia*; that is, they are sensitive to the fact that accretion proceeds onto the ashes of previous bursts. Indeed, this compositional inertia seems to reduce the expected recurrence times between bursts (particularly for scenarios involving accretion of low-metallicity matter). Moreover, these ashes may provide characteristic signatures such as gravitationally redshifted atomic absorption lines from the surface of the neutron star, which could be identified through high-resolution X-ray spectra (Cottam et al. 2002; Bildsten et al. 2003; Chang et al. 2005, 2006; Weinberg et al. 2006b), providing a valuable tool[1] to constrain XRB models.

[1] Although Cottam et al. (2002) reported features in the burst spectra of 28 XRBs detected from EXO 0748-676, obtained during a 335 ks observation made in the calibration phase of XMM-Newton, which they interpreted as gravitationally redshifted absorption lines of Fe XXVI (during the early

Furthermore, the mechanism responsible for superbursts, highly energetic ($\sim 10^{42}$ erg), long duration ($\tau \sim 10^4$ s) bursts (see Cornelisse et al. 2000, Wijnands 2001, and references therein), first reported from the source 4U 1735-44 (Cornelisse et al. 2000), also depends upon XRB nucleosynthesis. These phenomena are attributed to ignition in a C-layer accumulated from successive type I XRBs (first proposed by Woosley & Taam 1976; see also Taam & Picklum 1978, Brown & Bildsten 1998, Cumming & Bildsten 2001, Schatz et al. 2003, Weinberg et al. 2006b, and Weinberg & Bildsten 2007).

The potential impact of XRB nucleosynthesis on Galactic abundances is still a matter of debate: although ejection from a neutron star is unlikely because of its large gravitational potential (matter accreted onto a neutron star of mass M and radius R releases $\mathrm{GMm}_p/\mathrm{R} \sim 200$ MeV/nucleon, whereas only a few MeV/nucleon are released from thermonuclear fusion), radiation-driven winds during photospheric radius expansion may lead to ejection of a tiny fraction of the envelope (containing nuclear processed material –see Weinberg et al. 2006a, and MacAlpine et al. 2007). Indeed, XRBs may help to explain the Galactic abundances of the problematic light *p-nuclei* (Schatz et al. 1998).

With a neutron star as the underlying compact object, temperatures and densities in the accreted envelope reach quite high values: $\mathrm{T}_{peak} > 10^9$ K, and $\rho \sim 10^6$ g.cm^{-3} (note that during superbursts, however, densities may exceed 10^9 g.cm^{-3} – see Cumming & Bildsten 2001). As a result, detailed nucleosynthesis studies require the use of hundreds of isotopes, up to the SnSbTe mass region [2] (Schatz et al. 2001) or beyond (the nuclear activity in the XRB nucleosynthesis studies of Koike et al. 2004 reaches ^{126}Xe), and thousands of nuclear interactions. The main nuclear reaction flow is driven by the *rp-process* (rapid proton-captures and β^+-decays), the 3α-reaction and the *αp-process* (a sequence of (α,p) and (p,γ) reactions), and is expected to proceed far away from the valley of stability, merging with the proton drip-line beyond A $\sim$ 38 (Schatz et al. 1999).

Until recently, because of computational limitations, studies of XRB nucleosynthesis have been performed using limited nuclear reaction networks, truncated around Ni (Woosley & Weaver 1984; Taam et al. 1993; Taam et al. 1996 –all using a 19-isotope network), Kr (Hanawa et al. 1983 –274-isotope network; Koike et al. 1999 –463 nuclides), Cd (Wallace & Woosley 1984 –16-isotope network), or Y (Wallace & Woosley 1981 –250-isotope network). On the other hand, Schatz et al. (1999, 2001) have carried out very detailed nucleosynthesis calculations with a network containing more than 600 isotopes (up to Xe, in Schatz et al. 2001), but using a one-zone

phase of the bursts), Fe XXV, and perhaps O VIII (during the late stages), no evidence for such spectral features was found neither after a 200 ks observation with XMM-Newton of GS 1826-24, from which 16 type I X-ray bursts were detected (Kong et al. 2007), nor after a $\sim$ 600 ks observation of the original source EXO 0748-676 (Cottam et al. 2008; see also Rauch et al. 2008, for discussion).

[2] The existence of a closed SnSbTe cycle, which might define the likely nucleosynthetic endpoint for XRBs (Schatz et al. 2001), has been questioned, among others, by Elomaa et al. (2009).

approach. Koike et al. (2004) have also performed detailed one-zone nucleosynthesis calculations, with temperature and density profiles obtained from a spherically symmetric evolutionary code, linked to a 1270-isotope network extending up to ^{198}Bi.

It is worth noting however that different numerical approaches and approximations (hydrodynamic simulations with limited networks or one-zone calculations with detailed networks) have been adopted in all those works, and hence, the predicted nucleosynthesis in each case has to be taken with caution. Indeed, recent attempts to couple hydrodynamic stellar calculations (in 1-D) and detailed networks include Fisker et al. (2004, 2006, 2007, 2008) and Tan et al. (2007) (using networks of $\sim$ 300 isotopes, up to ^{107}Te), José & Moreno (2006) (using a network of 2640 nuclear reactions and 478 isotopes, up to Te), and Woosley et al. (2004) (using up to 1300 isotopes with an adaptive network).

Despite the wide range of values covered by these series of computations, there is a lack of reanalysis of some crucial aspects and their dependence on the physics, on the method of computation and on the initial models adopted. In view of these considerations, we have computed a new set of numerical models of type I X-ray bursts with SHIVA, a 1-D, spherically symmetric, hydrodynamic, implicit, Lagrangian code (see José & Hernanz 1998), linked to a fully updated nuclear reaction network containing 324 species and 1392 reaction rates, for a wide range of conditions, including different neutron star masses, initial metallicities, as well as two different resolutions (see Table 4.1). A summary of the main characteristics of the SHIVA code is given in Appendix A.

Table 4.1: Summary of the models computed in this work.

Model	M_{NS} ($M_\odot$)	Metallicity	Number of shells	Number of bursts computed	CPU time (months)
1	1.4	0.02	60	4	4.6
2	1.4	0.02	200	2	9.1
3	1.4	1×10^{-3}	60	5	7.4
4	1.8	0.02	200	3	5.8

4.1 Model 1

In this Section, we summarize the gross properties of a series of thermonuclear bursts driven by mass accretion onto a 1.4 $M_\odot$ neutron star ($L_{ini} = 1.6 \times 10^{34}$ erg.s^{-1} = 4.14 $L_\odot$), at a rate $\dot{M}_{acc} = 1.75 \times 10^{-9}$ $M_\odot$.yr^{-1} (or, in terms of the Eddington critical mass-accretion rate, 0.08 $\dot{M}_{Edd}$). The composition of the accreted material is assumed to be solar-like (X=0.7048, Y=0.2752, Z=0.02). All metals are initially

added up in the form of ^{14}N, following the rapid rearrangement of CNO isotopes that naturally occurs early in the burst (see Woosley et al. 2004). This model is indeed qualitatively similar to Model ZM, computed by Woosley et al. (2004) in the framework of the 1-D, hydrodynamic, implicit KEPLER code. Notice, however, that whereas Woosley et al. assume a value of 10 km for the neutron star radius, our model yields a radius of 13.1 km, following the integration of the neutron star structure from the core to its surface, in hydrostatic equilibrium. Differences in the neutron star size (and in turn, in surface gravity) may affect the strength of the explosion (mass accreted, peak temperature, nucleosynthesis...).

Accretion is computed by redistributing material through a constant number of envelope shells (see Kutter & Sparks 1980, for details). To handle this procedure, a very small envelope, containing 1.1×10^{18} g of material (less than 1 permil of the total envelope mass accreted before the first bursting episode), distributed along 60 shells, is put initially in place (the influence of the number of envelope shells on burst properties will be discussed in Model 2). The model is initially relaxed using a few, very large timesteps, to guarantee a perfect hydrostatic equilibrium. After that phase, accretion and nuclear reactions are initiated. At that stage, the temperature at the bottom of the envelope barely reaches 2.7×10^7 K, whereas the density is just 1.4×10^3 g.cm^{-3} (corresponding to a pressure of 5.7×10^{18} dyn.cm^{-2}).

4.1.1 First burst

The piling up of solar-like material on top of the neutron star during the accretion stage progressively compresses and heats the envelope. Indeed, just 145 seconds since the beginning of accretion, the temperature at the base of the envelope has reached $T_{base} = 5 \times 10^7$ K (with ρ_{base} exceeding 10^4 g.cm^{-3}).

At t=2327 s, the envelope achieves $T_{base} \sim 10^8$ K ($\rho_{base} \sim 6.5 \times 10^4$ g.cm^{-3}). The nuclear activity (with $\epsilon_{nuc} \sim 1.2 \times 10^{14}$ erg.g^{-1}.s^{-1}) is fully dominated by the CNO-cycle, resulting from proton-captures on the initial ^{14}N nuclei. At this stage, H has been scarcely burned (X(H) is now 0.689). The main reaction path (see Fig. 4.1, upper and lower panels) is led by ^{15}N(p, α)^{12}C, which powers ^{12}C(p, γ)^{13}N(p, γ)^{14}O(β^+)^{14}N (also noticeable is the chain ^{14}N(p, γ)^{15}O(β^+)^{15}N). This suite of nuclear processes is followed by ^{13}N(β^+)^{13}C(p, γ)^{14}N, and to a lesser extent, by ^{15}N(p, γ)^{16}O(p, γ)^{17}F(β^+)^{17}O(p, α)^{14}N. Besides H and He, by far the most abundant species in the envelope, several nuclei have already achieved an abundance $> 10^{-9}$, by mass: ^{12}C (5.4×10^{-5}), ^{13}C (1.4×10^{-7}), ^{13}N (4.2×10^{-4}), ^{14}N (2.4×10^{-3}), ^{14}O (6.1×10^{-3}), ^{15}N (4.5×10^{-8}), ^{15}O (1.2×10^{-2}, the most abundant CNO-group nucleus at the base of the envelope, powered by ^{14}N(p,γ)^{15}O), ^{16}O (1.1×10^{-5}), ^{17}O (1.1×10^{-7}), ^{17}F (5.9×10^{-6}), and ^{18}Ne (1.6×10^{-9}).

4.49 hours (16,163 s) after the beginning of accretion, T_{base} reaches 2.1×10^8 K (ρ_{base} achieves 2.7×10^5 g.cm^{-3}, and $P_{base} = 9.12 \times 10^{21}$ dyn.cm^{-2}). The total luminosity of the star has increased to a value of 2.5×10^{35} erg.s^{-1}. The main nuclear

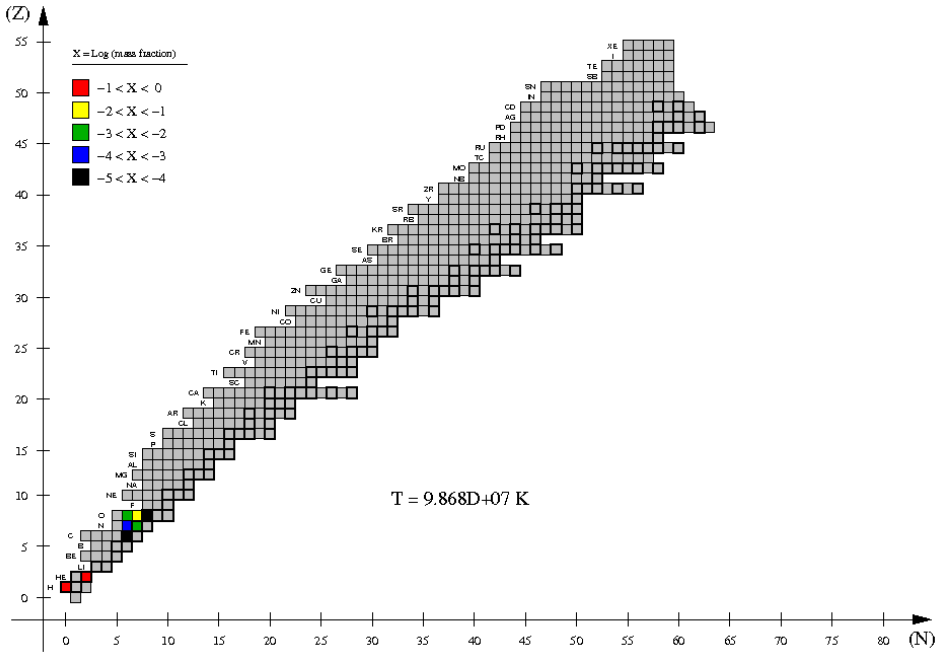

(a)

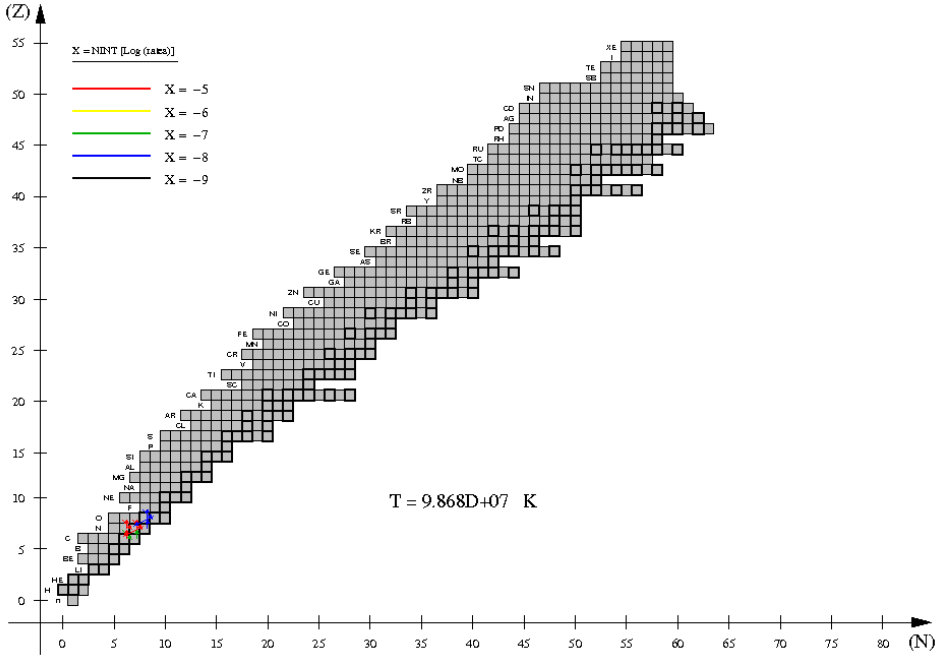

(b)

Figure 4.1: Main nuclear activity at the innermost envelope shell for Model 1 (M_{NS} = 1.4 $M_\odot$, $\dot{M}_{acc} = 1.75 \times 10^{-9}$ $M_\odot.yr^{-1}$, Z = 0.02), at the early stages of accretion ($T_{base} = 9.9 \times 10^7$ K). Upper panel: mass fractions of the most abundant species ($X > 10^{-5}$); Lower panel: main reaction fluxes ($F > 10^{-10}$ reactions.s^{-1}.cm^{-3}).

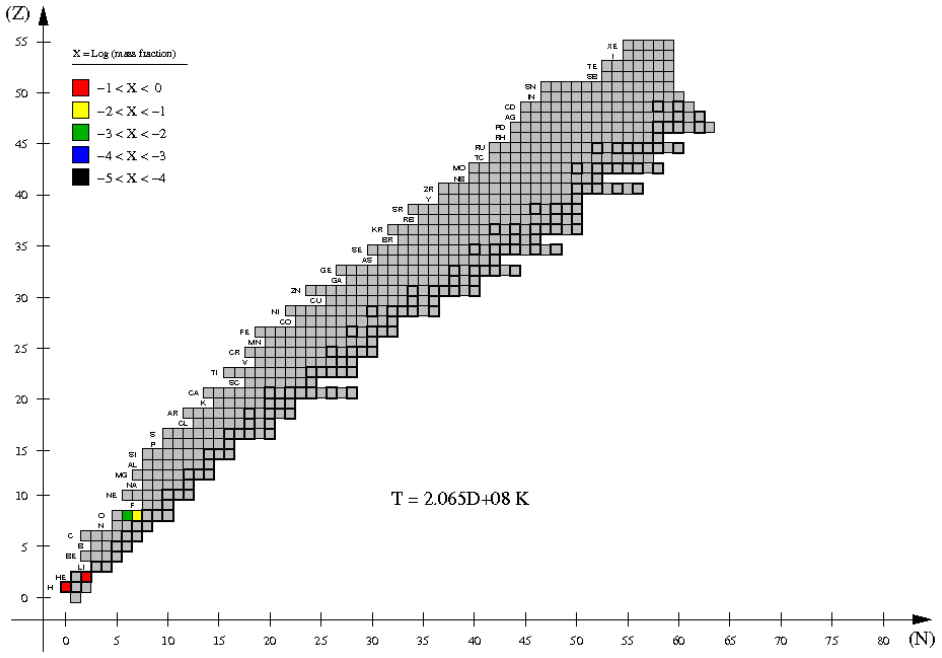

(a)

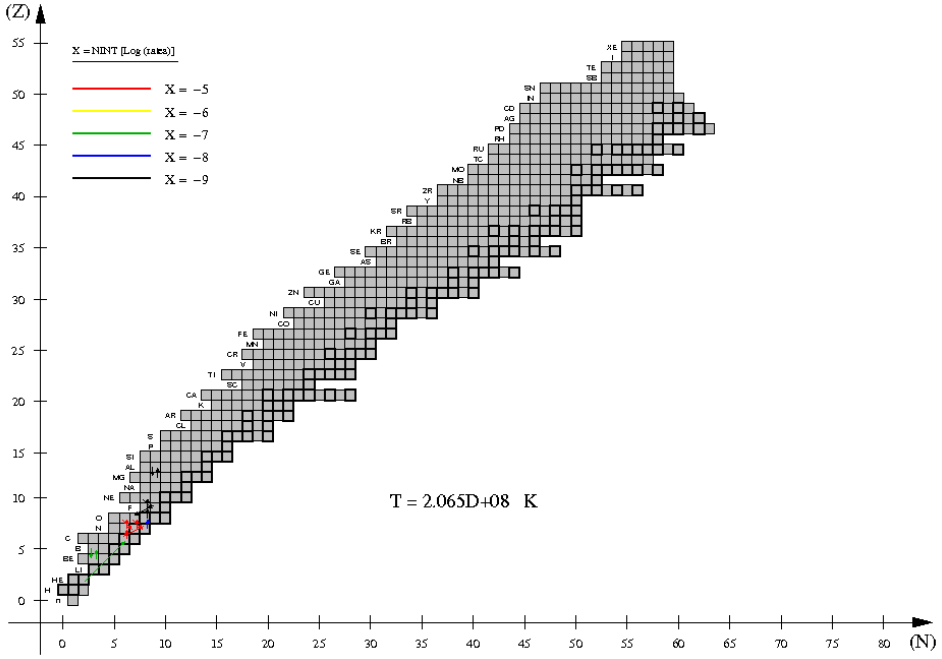

(b)

Figure 4.2: Same as Fig. 4.1, but for $T_{base} = 2.1 \times 10^8$ K.

activity (Fig. 4.2) is still governed by ^{15}N(p, α)^{12}C, followed by ^{12}C(p, γ)^{13}N(p, γ)^{14}O(β^+)^{14}N, and ^{14}N(p, γ)^{15}O(β^+)^{15}N. Contribution from other reactions, such as ^{15}N(p, γ)^{16}O(p, γ)^{17}F, now followed by ^{17}F(p, γ)^{18}Ne(β^+)^{18}F(p, α)^{15}O, or from the 3α, is also noticed. Secondary activity is also powered by ^{7}Be(p, γ)^{8}B and its reverse photodisintegration reaction ^{8}B(γ, p)^{7}Be, almost at equilibrium (and hence, not contributing to the energy output; the same applies to the direct and reverse processes ^{21}Mg(p, γ)^{22}Al and ^{22}Al(γ, p)^{21}Mg). In terms of chemical abundances, the numerous p-captures have reduced significantly the hydrogen content down to a value of 0.408. ^{4}He has increased to 0.570, becoming now the most abundant species at the base of the envelope (the next most abundant isotopes are the short-lived species ^{14}O [7.7×10^{-3}] and ^{15}O [1.4×10^{-2}]). Most of the CNO nuclei have been reduced to $10^{-8} - 10^{-9}$, by mass (except ^{13}N, that achieves 2.8×10^{-7}). The extension of the main nuclear activity (arbitrarily defined as the point in the network above which all heavier isotopes have abundances $< 10^{-9}$) reaches ^{40}Ca. Actually, ^{32}S (1.3×10^{-6}) and ^{40}Ca (1.4×10^{-6}) are the only species in the whole range Ne-Ca with abundances above 10^{-9}, by mass.

Convection sets in erratically when T_{base} reaches 3.92×10^8 K, well above the core-envelope interface (at $\sim$ 1 m; the overall envelope size, Δz, is $\sim$ 14 m, at this stage), and progressively extends throughout the whole envelope. Time evolution of density, temperature, pressure, and rate of nuclear energy generation, at the innermost envelope shell, as well as of the overall neutron star luminosity and envelope size, are shown in Figs. 4.7 and 4.8.

Shortly after, at t=5.88 hours (21,181 s) from the onset of accretion, T_{base} reaches 4×10^8 K (with $\rho_{base} = 2.9 \times 10^5$ g.cm^{-3} and $P_{base} = 1.2 \times 10^{22}$ dyn.cm^{-2}). The hydrogen content has dropped to 0.209, whereas ^{4}He achieves 0.625. In turn, the rate of nuclear energy generation has increased to a value of 2.8×10^{16} erg.g^{-1}.s^{-1}. It is worth noting that the metallicity of this innermost envelope shell has increased from an initial value of 0.02 to 0.17, due to leakage from CNO cycle (mainly through ^{15}O(α, γ)). As before, the next most abundant species are ^{14}O (6.9×10^{-2}), and ^{15}O (6.5×10^{-2}), but the number of isotopes with moderately large abundances has now increased. Indeed, ^{40}Ca, ^{22}Mg, ^{18}Ne, ^{34}Ar, ^{48}Cr, and ^{42,44}Ti, have achieved mass fractions of the order of 10^{-3}, whereas ^{45,46,47,49,50}Cr, ^{21}Mg, ^{44,45,46,47}V, ^{27}P, ^{29,30,31}S, ^{37,38,39}Ca, ^{24,25}Si, ^{43,45,46}Ti, ^{48,49}Mn, ^{33}Ar, ^{31,32}Cl, or ^{41}Sc, have reached $\sim 10^{-4}$. The nuclear activity has extended as far as ^{53}Co, and is mainly dominated by three different processes operating almost at equilibrium with their inverse photodisintegration reactions: ^{21}Mg(p, γ)^{22}Al(γ, p)^{21}Mg, ^{30}S(p, γ)^{31}Cl(γ, p)^{30}S, and ^{25}Si(p, γ)^{26}P(γ, p)^{25}Si. Additional activity is powered by 3α $\rightarrow$^{12}C(p, γ)^{13}N(p, γ)^{14}O, followed by ^{14}O(α, p)^{17}F(p, γ)^{18}Ne. The suite of secondary nuclear paths is rich and complex (see Fig. 4.3), and is mainly dominated by p-capture reactions and β^+-decays. Let us also mention the contribution from the CNO-breakout α-capture reaction ^{15}O(α, γ)^{19}Ne. It is worth noting that the main nuclear path above Ca begins to move away from the valley of stability, towards the proton-drip line (see

Fig. 4.3, lower panel).

Just 2.3 seconds later (t = 21,183 s), T_{base} achieves 5×10^8 K. ρ_{base} has slightly decreased to 2.3×10^5 g.cm^{-3} because of a mild envelope expansion ($\Delta z \sim 15.5$ m). Notice, however, that $P_{base} = 1.2 \times 10^{22}$ dyn.cm^{-2}. Hence, the TNR is taking place nearly at constant pressure. Time-dependent, convective mixing with adjacent shells, with a characteristic timescale of $\tau_{conv} \sim 10^{-4}$ s ($v_{conv} \sim 10^3 - 10^5$ cm.s^{-1}), causes a slight increase in the H abundance at the base of the envelope. Indeed, the H abundance is now 0.288, by mass, whereas the ^{4}He content has slightly decreased to 0.563 (because of the high temperatures). The next most abundant species is now ^{18}Ne (4.4×10^{-2}), together with ^{14,15}O (4.2×10^{-2} and 1.8×10^{-2}, respectively). Several isotopes, such as ^{21,22}Mg, ^{29,30}S, ^{50,52}Fe, ^{27}P, ^{24,25}Si, ^{49,50,51}Mn, and ^{34}Ar, have achieved abundances an order of magnitude lower ($\sim 10^{-3}$), whereas ^{49,51}Fe, ^{46,48,49,50}Cr, ^{37,38,39}Ca, ^{33}Ar, ^{52}Co, ^{42}Ti, ^{48}Mn, ^{38}S, and ^{31}Cl reach $\sim 10^{-4}$. The nuclear activity extends up to ^{57}Cu now, and powers an energy generation rate of 1.2×10^{17} erg.g^{-1}.s^{-1}. The overall stellar luminosity is now 1.3×10^{36} erg.s^{-1}. The main nuclear flow is, as before, dominated by the direct and reverse reactions ^{30}S(p, γ)^{31}Cl(γ, p)^{30}S, ^{21}Mg(p, γ)^{22}Al(γ, p)^{21}Mg, and ^{25}Si(p, γ)^{26}P(γ, p)^{25}Si, together with ^{14}O(α, p)^{17}F(p, γ)^{18}Ne. Notice that ^{14}O+α becomes the most important α-capture reaction, with a flux slightly larger than that of ^{15}O(α, γ), or the 3α reaction. Additional activity is driven by ^{18}Ne(β^+)^{18}F(p, α)^{15}O, ^{19}Ne(p, γ)^{20}Na(p, γ)^{21}Mg, ^{21}Na(p, γ)^{22}Mg(p, γ)^{23}Al, ^{12}C(p, γ)^{13}N(p, γ)^{14}O, and ^{26}Si(p, γ)^{27}P. Indeed, the next 100 most important reactions, in terms of reaction fluxes, are all p-captures (rp-process), β^+-decays, or reverse photodisintegration reactions (almost at equilibrium with the direct processes), involving intermediate-mass or moderately heavy species (up to ^{52}Co).

A qualitatively similar picture is found when T_{base} achieves 7×10^8 K (t = 21,185 s), with the most abundant species at the envelope base being H (0.308), ^{4}He (0.507), ^{18}Ne (4.8×10^{-2}), ^{22}Mg (2.5×10^{-2}), ^{29,30}S (1.1×10^{-2} and 2.2×10^{-2}, respectively), and ^{24,25}Si (1.1×10^{-2} and 1.7×10^{-2}, respectively). The number of species with abundances of the order of 10^{-3} includes now ^{54,55,56}Ni, ^{15}O, ^{28}S, ^{52}Fe, ^{27}P, ^{38}Ca, and ^{33,34}Ar (many other species, such as ^{46}Cr, ^{37,39}Ca, ^{26}Si, ^{58,59,60}Zn, ^{53,54,55}Co, ^{56,57,58,59}Cu, ^{41,42}Ti, ^{53,57}Ni, or ^{49,50}Fe, achieve mass fractions of $\sim 10^{-4}$), with the main nuclear activity (see Fig. 4.4) extending all the way up to ^{60}Zn. Again, the most relevant nuclear reactions are the quasiequilibrium processes ^{30}S(p, γ)^{31}Cl(γ, p)^{30}S, ^{21}Mg(p, γ)^{22}Al(γ, p)^{21}Mg, and ^{25}Si(p, γ)^{26}P(γ, p)^{25}Si, supplemented now by ^{26}Si(p, γ)^{27}P(γ, p)^{26}Si, ^{22}Mg(p, γ)^{23}Al(γ, p)^{22}Mg, ^{29}S(p, γ)^{30}Cl(γ, p)^{29}S, and ^{16}O(p, γ)^{17}F(γ, p)^{16}O. Additional activity is powered mainly by p-capture reactions and β^+-decays, such as the chain ^{19}Ne(p, γ)^{20}Na(p, γ)^{21}Mg(β^+)^{21}Na(p, γ)^{22}Mg, or ^{17}F(p, γ)^{18}Ne(β^+)^{18}F(p, α)^{15}O. This is followed by the three most important α-capture reactions ^{15}O(α, γ)^{19}Ne, ^{14}O(α, p)^{17}F, and the 3α. Secondary activity is driven by ^{23,24,25}Al(p, γ)^{24,25,26}Si (together with ^{24,25}Si β^+-decays), ^{27,28,29}P(p, γ)^{28,29,30}S (together with ^{28}S β^+-decay), ^{12}C(p, γ)^{13}N(p, γ)^{14}O, ^{23}Mg(p, γ)^{24}Al,

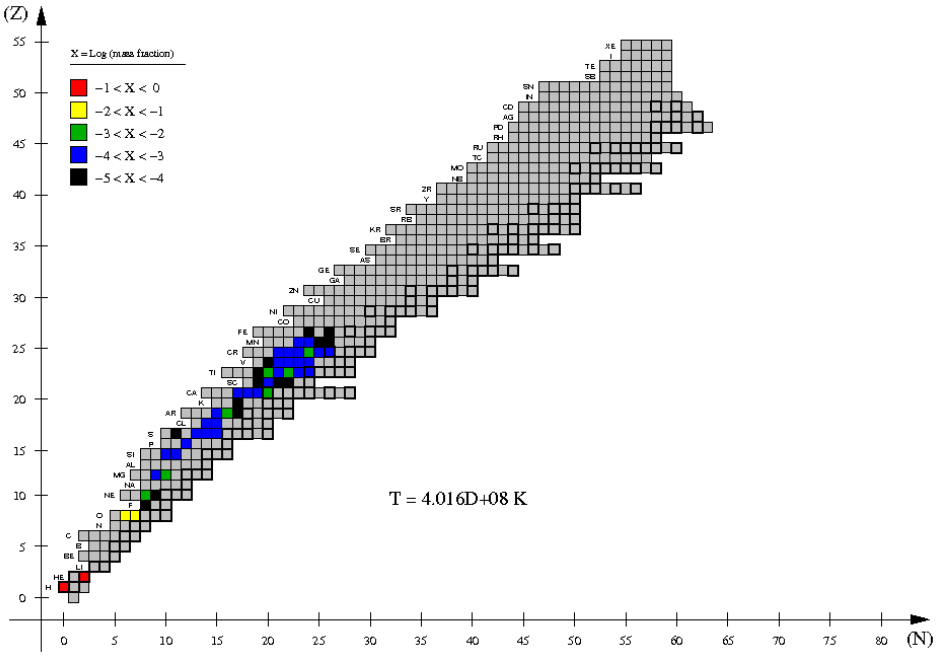

(a)

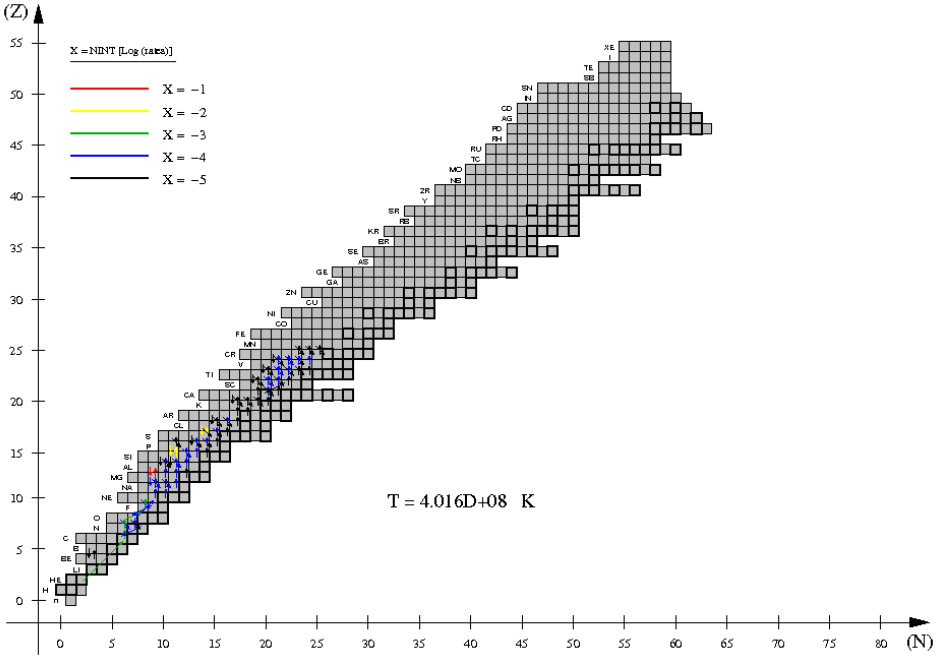

(b)

Figure 4.3: Same as Fig. 4.1, but for $T_{base} = 4 \times 10^8$ K.

and the quasiequilibrium pairs ^{55}Ni(p, γ)^{56}Cu(γ, p)^{55}Ni, ^{42}Ti(p, γ)^{43}V(γ, p)^{42}Ti, and ^{26}P(p, γ)^{27}S(γ, p)^{26}P.

One second later (t = 21,186 s), T_{base} achieves 9×10^8 K. The hectic nuclear activity, which at this stage releases $\epsilon_{nuc} \sim 3.7 \times 10^{17}$ erg.g^{-1}.s^{-1}, has reduced the H and ^{4}He abundances down to 0.262 and 0.457, respectively. The next most abundant species are now ^{22}Mg (3.3×10^{-2}), ^{25}Si (1.8×10^{-2}), ^{28,29,30}S (2.2×10^{-2}, 3.3×10^{-2}, and 8.7×10^{-2}, respectively), ^{33,34}Ar (1.2×10^{-2} and 2.5×10^{-2}, respectively), and ^{60}Zn (1.0×10^{-2}). The main nuclear path has reached already ^{68}Se. As shown in Fig. 4.5 (lower panel), all dominant nuclear reactions are the quasiequilibrium processes ^{25,26}Si(p, γ)^{26,27}P(γ, p)^{25,26}Si, ^{30}S(p, γ)^{31}Cl(γ, p)^{30}S, ^{21,22}Mg(p, γ)^{22,23}Al(γ, p)^{21,22}Mg, ^{29}S(p, γ)^{30}Cl(γ, p)^{29}S, ^{16}O(p, γ)^{17}F(γ, p)^{16}O, ^{42}Ti(p, γ)^{43}V(γ, p)^{42}Ti, ^{45,46}Cr(p, γ)^{46,47}Mn(γ, p)^{45,46}Cr, ^{60}Zn(p, γ)^{61}Ga(γ, p)^{60}Zn, and ^{55}Ni(p, γ)^{56}Cu(γ, p)^{55}Ni, except for a handful of p-captures and β^+-decays (mainly ^{25}Al(p, γ)^{26}Si, ^{27,28,29}P(p, γ)^{28,29,30}S, and ^{28}S(β^+)^{28}P). Moreover, the most important α-capture reactions, ^{22}Mg(α, p)^{25}Al, the 3α, ^{18}Ne(α, p)^{21}Na, and ^{14}O(α, p)^{17}F, have fluxes of the order of F $\sim 10^{-3}$ (notice the moderate extension of α-captures towards heavier species as a result of the increase in temperature). The envelope has reached a size $\Delta z \sim 33$ m.

At t = 21,188 s, when T_{base} achieves 1×10^9 K, the energy generation rate by nuclear reactions reaches its maximum value: $\epsilon_{nuc,max} \sim 4.1 \times 10^{17}$ erg.g^{-1}.s^{-1}. Two seconds later, the envelope will attain maximum expansion, with a size $\Delta z_{max} \sim$ 44 m. Proton and α-captures continue to reduce the overall H and He abundances at the envelope base (0.191 and 0.400, respectively). The next most abundant species is now ^{30}S (0.103) -a waiting point for the main nuclear path-, followed by ^{33,34}Ar (1.8×10^{-2} and 8.2×10^{-2}, respectively), ^{37,38}Ca (2.0×10^{-2} and 4.1×10^{-2}, respectively), ^{42}Ti (1.3×10^{-2}), ^{46}Cr (1.9×10^{-2}), ^{50}Fe (1.1×10^{-2}), ^{56}Ni (1.0×10^{-2}), and ^{60}Zn (2.8×10^{-2}). The nuclear activity has extended already up to ^{76}Sr, and is still governed by a suite of quasiequilibrium processes: ^{30}S(p, γ)^{31}Cl(γ, p)^{30}S, ^{25,26}Si(p, γ)^{26,27}P(γ, p)^{25,26}Si, ^{45,46}Cr(p, γ)^{46,47}Mn(γ, p)^{45,46}Cr, ^{41,42,43}Ti(p, γ)^{42,43,44}V(γ, p)^{41,42,43}Ti, ^{16}O(p, γ)^{17}F(γ, p)^{16}O, ^{54,55}Ni(p, γ)^{55,56}Cu(γ, p)^{54,55}Ni, ^{59,60}Zn(p, γ)^{60,61}Ga(γ, p)^{59,60}Zn, ^{38}Ca(p, γ)^{39}Sc(γ, p)^{38}Ca, ^{49,50,51}Fe(p, γ)^{50,51,52}Co(γ, p)^{49,50,51}Fe, ^{29}S(p, γ)^{30}Cl(γ, p)^{29}S, ^{22}Mg(p, γ)^{23}Al(γ, p)^{22}Mg, and ^{34}Ar(p, γ)^{35}K(γ, p)^{34}Ar (plus ^{39}Ca(p, γ)^{40}Sc; see Fig. 4.6).

Four seconds later, the envelope base achieves a maximum temperature of $T_{peak} \sim 1.06 \times 10^9$ K. Besides H (0.220) and ^{4}He (0.370), the next most abundant isotope is now ^{60}Zn (0.159) -another waiting point for the nuclear flow-, followed by ^{30}S (3.3×10^{-2}), ^{34}Ar (3.2×10^{-2}), ^{38}Ca (2.4×10^{-2}), ^{46}Cr (1.8×10^{-2}), ^{50}Fe (1.3×10^{-2}), ^{55,56}Ni (1.8×10^{-2} and 2.3×10^{-2}, respectively), and ^{59}Zn (1.8×10^{-2}). As shown in Fig. 4.9, the extension of the main nuclear path reaches ^{80}Zr, and is still governed by quasiequilibrium processes ((p, γ) reactions on ^{25,26}Si, ^{30}S, ^{45,46}Cr, ^{59,60}Zn, ^{41,42}Ti, ^{54,55}Ni, ^{16}O, ^{49,50,51}Fe, ^{38}Ca, ^{29}S, and ^{22}Mg, as well as the corresponding reverse photodisintegrations). The most important α-capture reactions, the triple-α, ^{14}O(α,

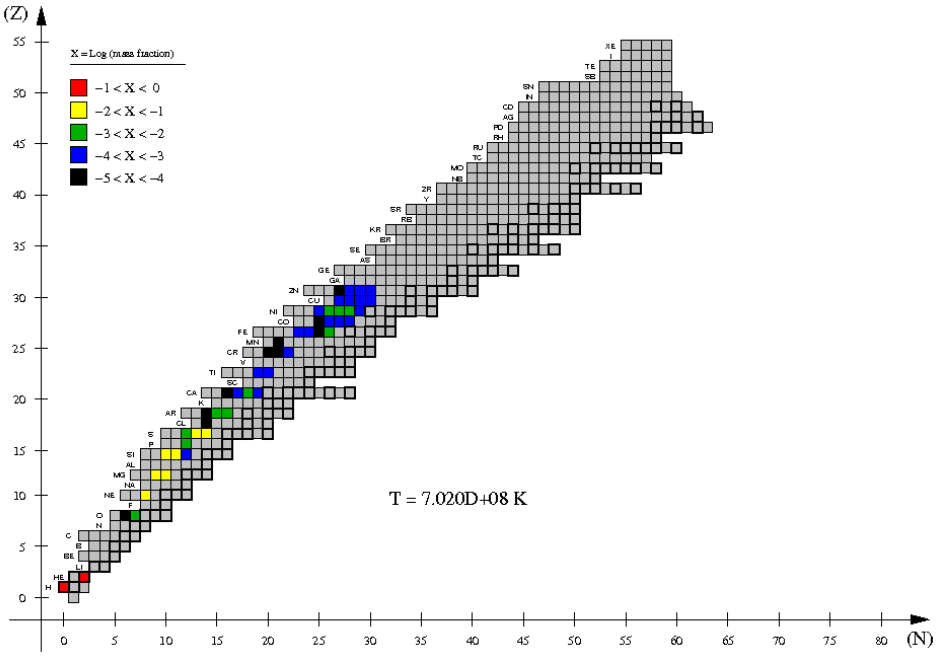

(a)

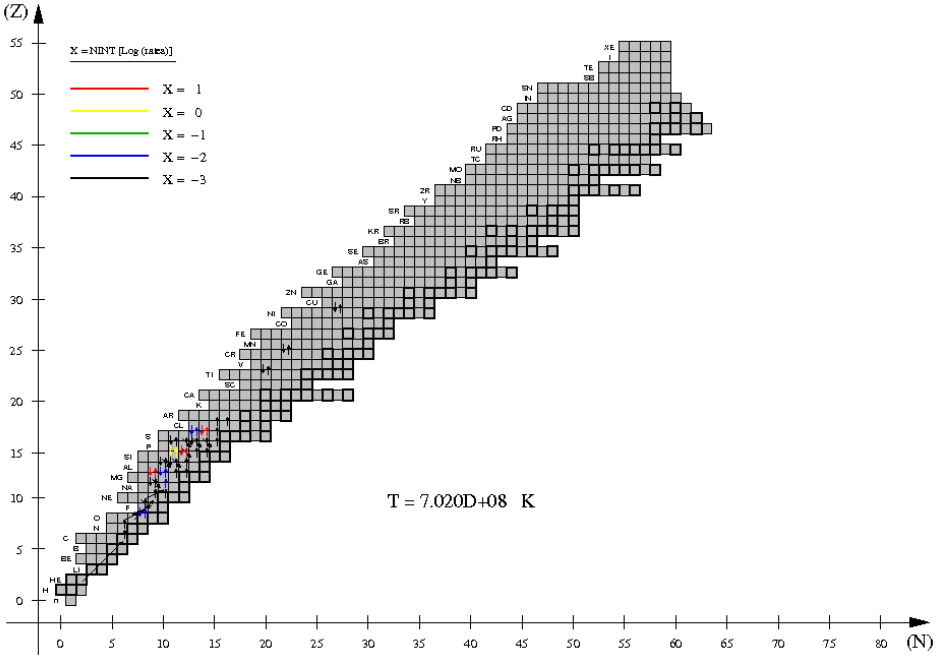

(b)

Figure 4.4: Same as Fig. 4.1, but for $T_{base} = 7 \times 10^8$ K.

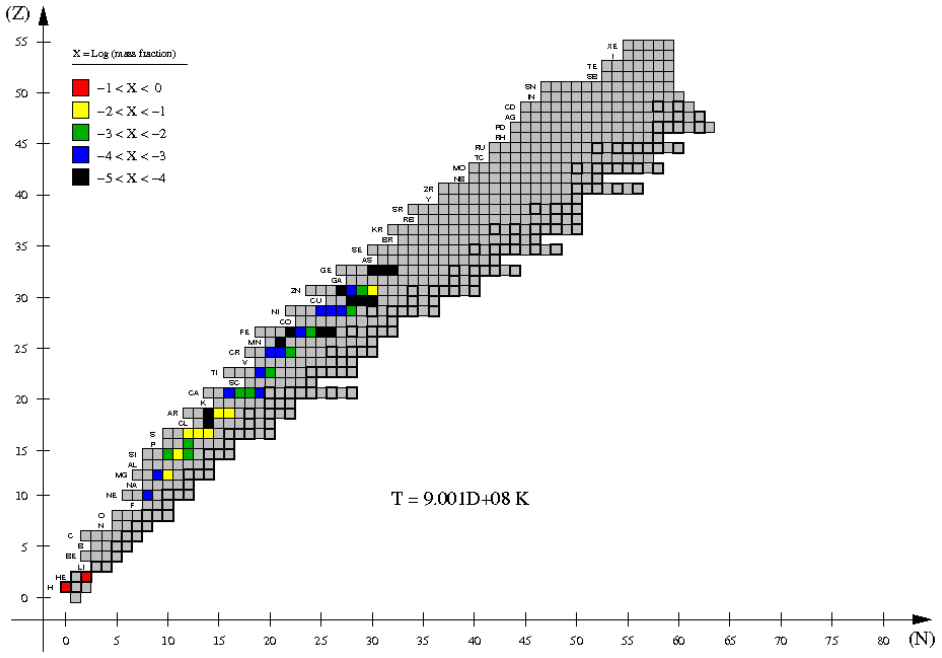

(a)

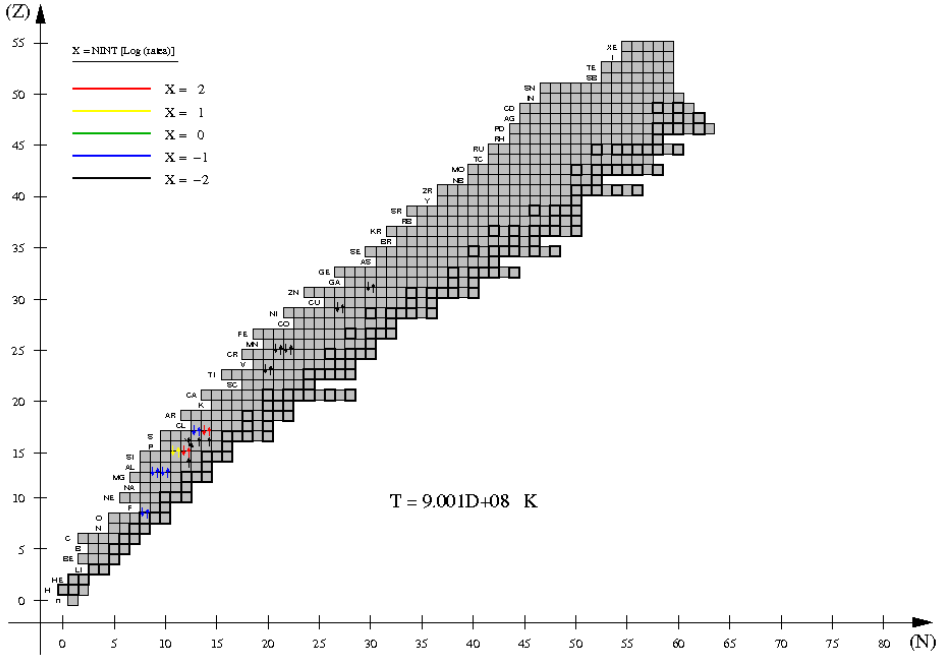

(b)

Figure 4.5: Same as Fig. 4.1, but for $T_{base} = 9 \times 10^8$ K.

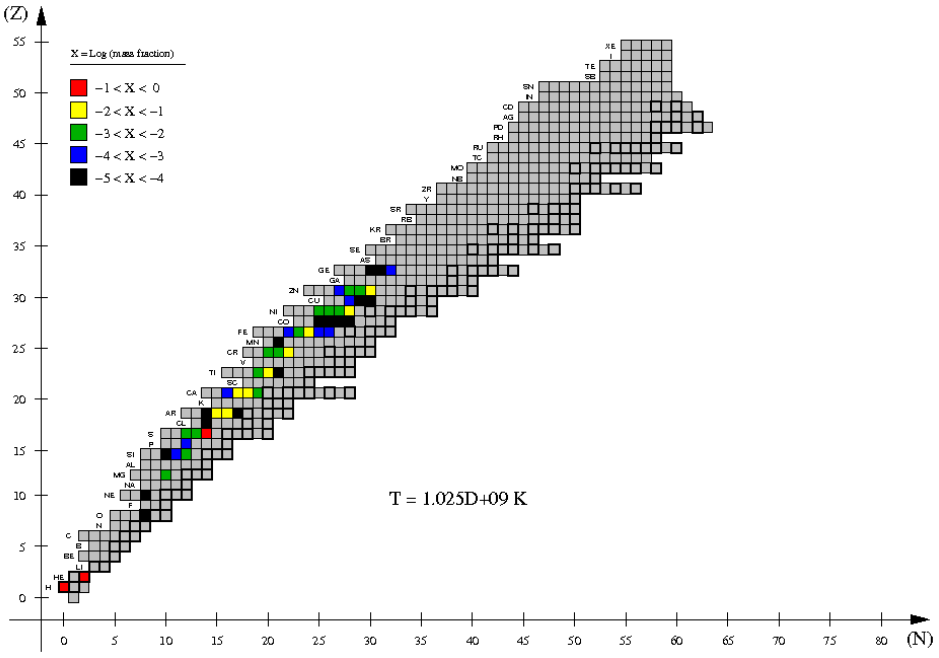

(a)

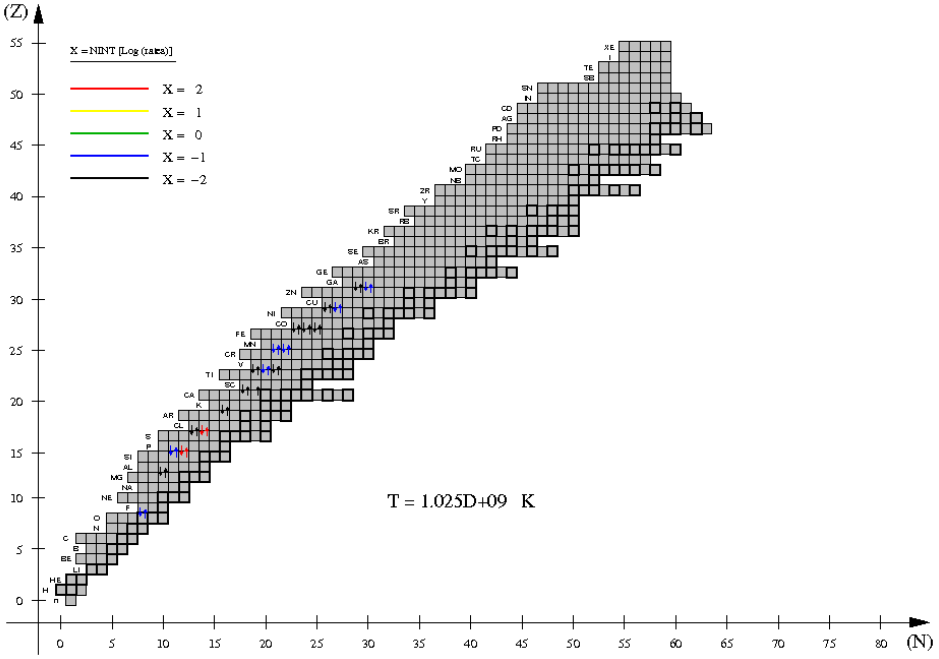

(b)

Figure 4.6: Same as Fig. 4.1, but for $T_{base} = 10^9$ K.

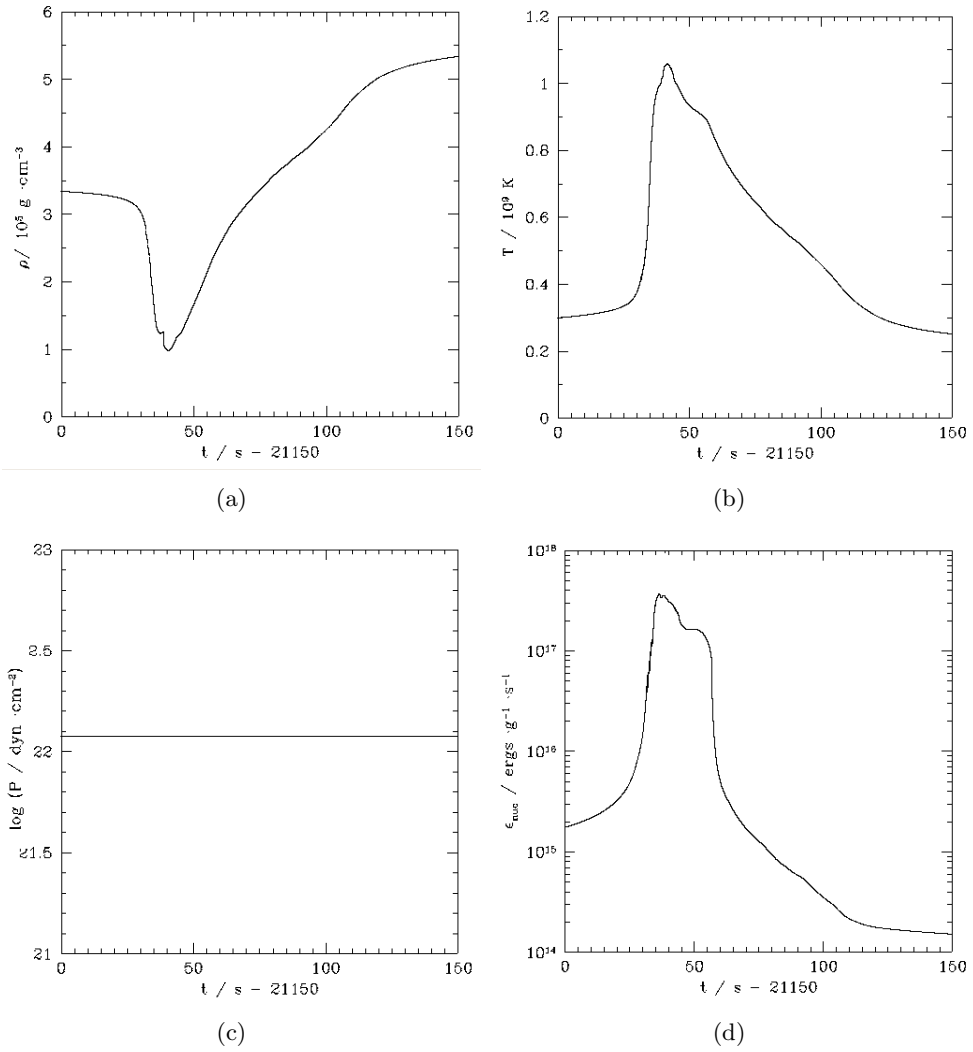

Figure 4.7: Time evolution of density (panel a), temperature (panel b), pressure (panel c), and nuclear energy generation rate (panel d), at the innermost envelope shell for Model 1 ($M_{NS} = 1.4\ M_\odot$, $\dot{M}_{acc} = 1.75 \times 10^{-9}\ M_\odot.yr^{-1}$, Z = 0.02), along the first bursting episode. The origin of the time coordinate is arbitrarily chosen as 21,150 s, for which $T_{base} \sim 3 \times 10^8$ K.

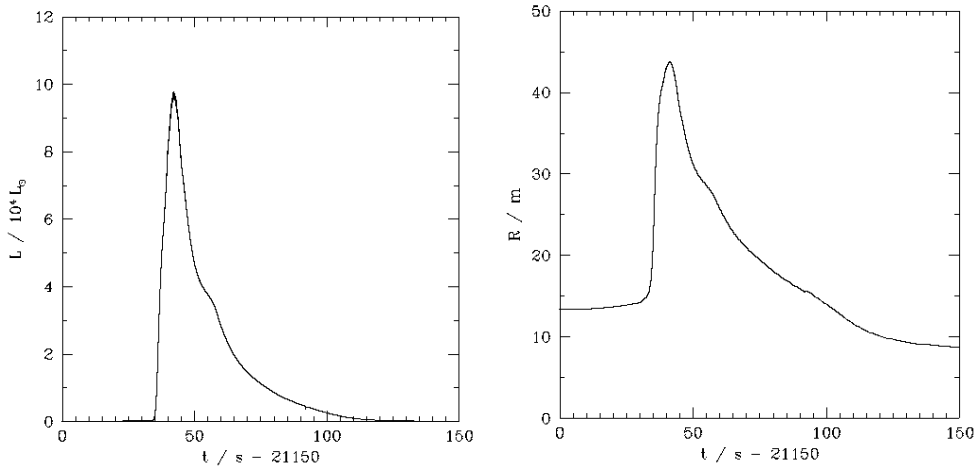

(a) (b)

Figure 4.8: Same as Fig. 4.7, but for the overall neutron star luminosity (panel a), and envelope size (panel b), as measured from the core-envelope interface.

p)^{17}F, ^{22}Mg(α, p)^{25}Al, and ^{18}Ne(α, p)^{21}Na, have fluxes of the order of $F \sim 10^{-3}$ reactions.s^{-1}.cm^{-3}, and hence lay outside the plot.

Less than a second later (t = 21,192.3 s), the neutron star reaches maximum luminosity, $L_{max} = 3.8 \times 10^{38}$ erg.s^{-1} (9.8×10^4 L$_\odot$).

The numerous proton-captures on many species during the decline from T_{peak} reduce dramatically the H content in the innermost shell. Indeed, when T_{base} achieves 9.3×10^8 K (t = 21,200 s), the H abundance drops below 0.1, while X(^{4}He) = 0.283. Actually, the most abundant species in this shell is now ^{60}Zn (0.43, by mass), followed by ^{30}S (2.7×10^{-2}), ^{34}Ar (2.1×10^{-2}), ^{38}Ca (1.3×10^{-2}), ^{56}Ni (1.8×10^{-2}), and ^{64}Ge (3.3×10^{-2}). The nuclear activity reaches ^{90}Ru, and is still dominated by the quasiequilibrium processes described above.

Five seconds later (t = 21,205 s), when T_{base} drops to 9.0×10^8 K, ^{60}Zn achieves a maximum abundance of 0.519, by mass. H has been reduced to 1.3×10^{-2}, and ^{4}He to 0.226. The next most abundant species are now ^{26}Si (1.2×10^{-2}), ^{30}S (1.9×10^{-2}), ^{34}Ar (1.8×10^{-2}), ^{38}Ca (1.1×10^{-2}), ^{56}Ni (6.7×10^{-2}), and ^{64}Ge (4.7×10^{-2}). The extent of the nuclear activity is stuck at ^{90}Ru, while still governed by proton-captures and reverse photodisintegration reactions at quasiequilibrium, including ^{25,26}Si(p, γ)^{26,27}P(γ, p)^{25,26}Si, ^{30}S(p, γ)^{31}Cl(γ, p)^{30}S, ^{16}O(p, γ)^{17}F(γ, p)^{16}O, ^{60}Zn(p, γ)^{61}Ga(γ, p)^{60}Zn, ^{51}Fe(p, γ)^{52}Co(γ, p)^{51}Fe, ^{42,43}Ti(p, γ)^{43}V(γ, p)^{42,43}Ti, ^{45,46}Cr(p, γ)^{46,47}Mn(γ, p)^{45,46}Cr, ^{55}Ni(p, γ)^{56}Cu(γ, p)^{55}Ni, and ^{22}Mg(p, γ)^{23}Al(γ, p)^{22}Mg. Many secondary quasiequilibrium pairs (as well as α-capture reactions like the triple-α, ^{14}O(α, p)^{17}F, or ^{22}Mg(α, p)) contribute, in a lesser extent, to the overall nuclear activity (see Fig. 4.10).

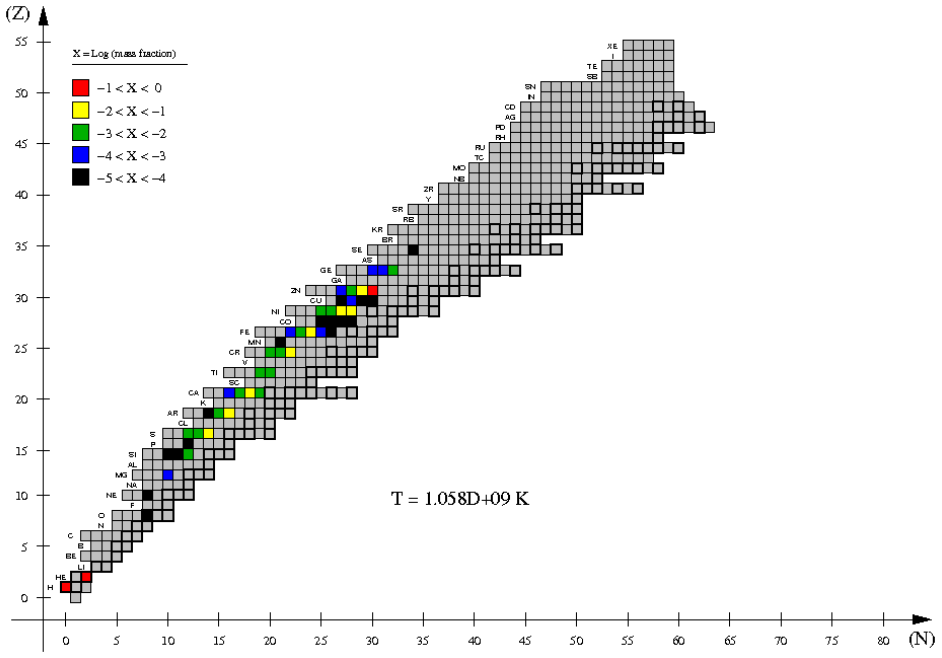

(a)

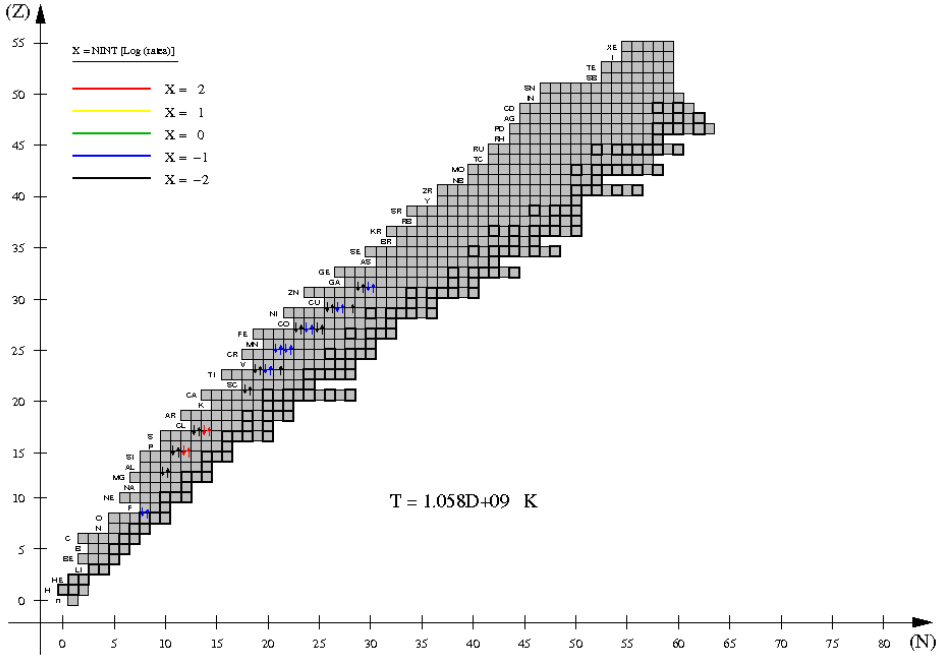

(b)

Figure 4.9: Same as Fig. 4.1, but for the time when temperature at the envelope base reaches a peak value of $T_{peak} = 1.06 \times 10^9$ K.

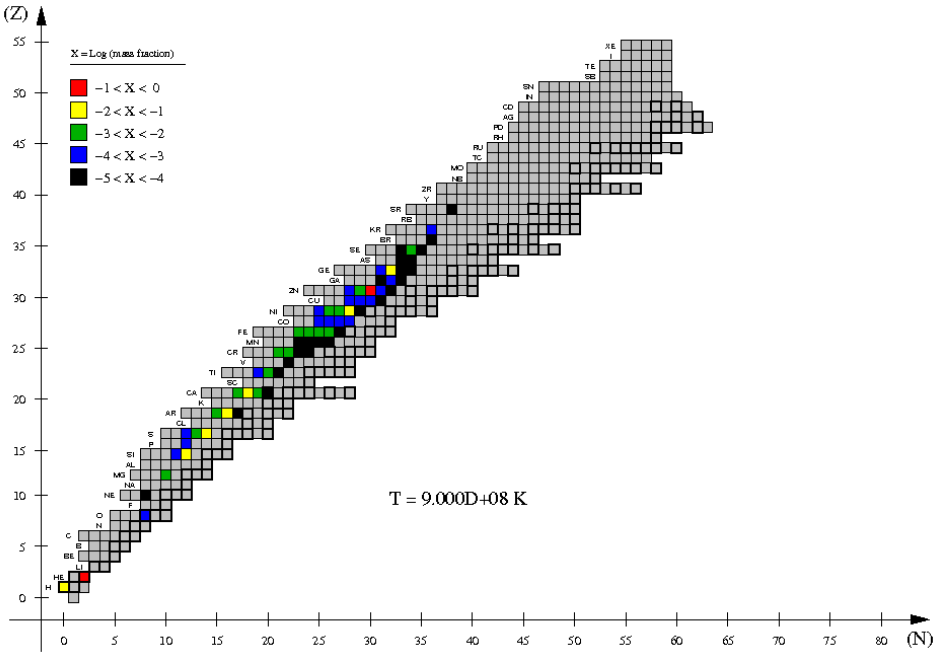

(a)

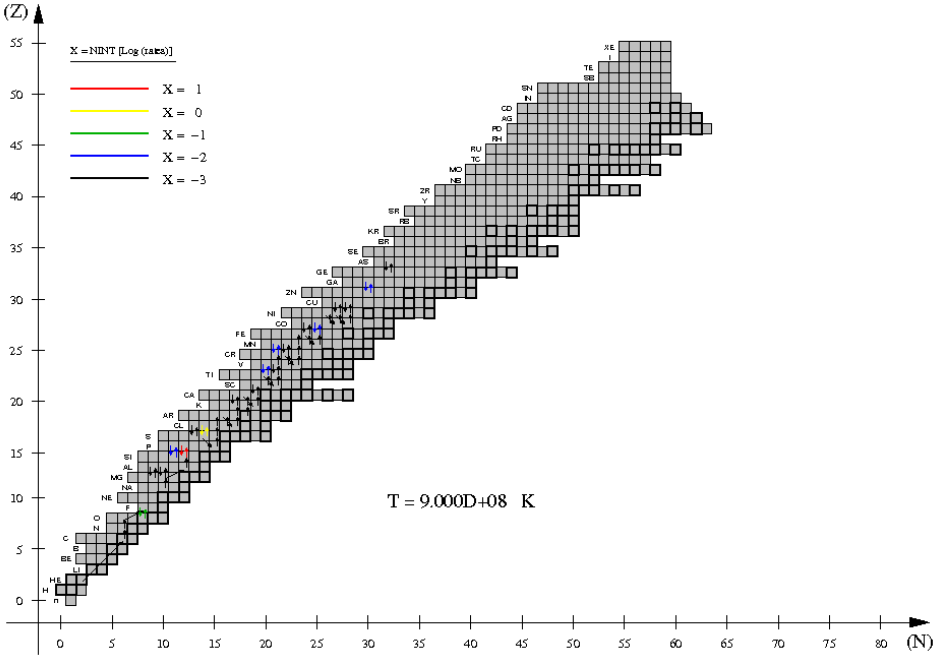

(b)

Figure 4.10: Same as Fig. 4.1, but for $T_{base} = 9 \times 10^8$ K.

Following the fast decline in temperature, when $T_{base} = 8.0 \times 10^8$ K (t = 21,212 s), the ^{60}Zn abundance has dropped to 0.509, due to β^+-decays. H is heavily depleted (5×10^{-11}), whereas ^{4}He is slightly reduced to an abundance of 0.190. The next most abundant species are ^{12}C (1.6×10^{-2}), ^{30}P (1.3×10^{-2}), ^{39}K (1.5×10^{-2}), ^{56}Ni (8.4×10^{-2}), ^{60}Cu (1.3×10^{-2}), and ^{64}Ge (4.5×10^{-2}). The number of isotopes that reach mass fractions of the order of $\sim 10^{-3}$ increases dramatically. This includes intermediate-mass elements, such as ^{24,25,26}Mg, ^{25,26,27}Al, ^{26,27,28}Si, as well as ^{31}P, ^{33,34}S, ^{34,35}Cl, ^{36}Ar, ^{38}K, ^{40,42}Ca, ^{43}Sc, ^{46}Ti, ^{48,49,50}Cr, ^{51}Mn, ^{52,54}Fe, ^{55}Co, ^{64}Ga, and ^{68}Se. The extent of the nuclear activity (Fig. 4.11) keeps limited to ^{90}Ru, and will not move beyond this endpoint, first because of the heavy H depletion, and second, the temperature is already too low to drive proton and/or α-captures on heavier species because of their large Coulomb barriers. At this stage, the single, most important reaction, in terms of reaction fluxes, is the triple-α, followed by a suite of β^+-decay reactions, such as ^{26}Si(β^+)^{26m}Al(β^+)^{26}Mg, ^{34}Cl(β^+)^{34}S, ^{60}Zn(β^+)^{60}Cu, or ^{27}Si(β^+)^{27}Al. Several α-captures follow the triple-α reaction as a chain: ^{12}C(α, γ)^{16}O(α, γ)^{20}Ne(α, γ)^{24}Mg(α, γ)^{28}Si(α, γ)^{32}S, or through alternative paths, proceeding close to the valley of stability, up to $\sim$ Ar, such as ^{13}N(α, p)^{16}O, ^{25,27}Al(α, p)^{28,30}Si, ^{22}Mg(α, p)^{25}Al, ^{22}Na(α, p)^{25}Mg, or ^{26,27}Si(α, p)^{29,30}P, to quote some representative cases (see Fig. 4.11, for a detailed analysis). ϵ_{nuc} has already declined to a value of $\sim 3.8 \times 10^{15}$ erg.g^{-1}.s^{-1}.

When T_{base} drops to 4.3×10^8 K (t = 21,254 s), the nuclear energy generation rate (which is powered by β^+-decays; see below) has also declined to a value of $\epsilon_{nuc} \sim 3 \times 10^{14}$ erg.g^{-1}.s^{-1}. The ^{60}Zn abundance has been slightly reduced down to 0.416, whereas X(^{4}He) = 0.137 (see the nuclear activity in Fig. 4.12). The next most abundant species is ^{60}Cu (0.104), followed by ^{12}C (6.5×10^{-2}), ^{26}Mg (1.0×10^{-2}), ^{30}P (1.2×10^{-2}), ^{34}S (1.4×10^{-2}), ^{39}K (1.5×10^{-2}), ^{56}Ni (8.4×10^{-2}), ^{64}Ga (1.7×10^{-2}), and ^{64}Ge (2.9×10^{-2}). At this stage, the nuclear activity is already dominated by ^{60}Zn(β^+)^{60}Cu, because of its very large abundance, and it's followed by the triple-α reaction, and by a suite of additional β^+-decays, such as ^{64}Ge(β^+)^{64}Ga, ^{30}P(β^+)^{30}Si, ^{64}Ga(β^+)^{64}Zn ^{60}Cu(β^+)^{60}Ni, ^{38}K(β^+)^{38}Ar, ^{26m}Al(β^+)^{26}Mg, ^{68}Se(β^+)^{68}As, ^{25}Al(β^+) ^{25}Mg, ^{68}As(β^+)^{68}Ge, ^{63}Ga(β^+) ^{63}Zn, ^{59}Cu(β^+)^{59}Ni, or ^{61}Zn(β^+)^{61}Cu. It is worth noting the marginal activity driven by a few additional α-capture reactions, such as ^{12}C(α, γ)^{16}O(α, γ)^{20}Ne(α, γ)^{24}Mg. At this stage, the size of the envelope has shrunk to $\Delta z \sim$ 13m, whereas the overall luminosity of the star has decreased to $L_{NS} = 7.7 \times 10^{36}$ erg.s^{-1}.

When T_{base} reaches 2×10^8 K (t = 21,618 s), ^{60}Zn has remarkably decayed into ^{60}Cu, which now constitutes the most abundant species (with 0.393) at the base of the envelope. ^{4}He is kept constant, at about 0.136, because of the low temperature. The next most abundant species are ^{12}C (6.7×10^{-2}), ^{26}Mg (1.0×10^{-2}), ^{30}Si (1.3×10^{-2}), ^{34}S (1.4×10^{-2}), ^{39}K (1.5×10^{-2}), ^{56}Ni (8.4×10^{-2}), ^{60}Ni (5.6×10^{-2}), ^{60}Zn (7.2×10^{-2}), ^{64}Ga (1.2×10^{-2}), and ^{64}Zn (3.5×10^{-2}). At this stage, and except for the (limited) contribution of the triple-α reaction, the main nuclear path (Fig. 4.13) is

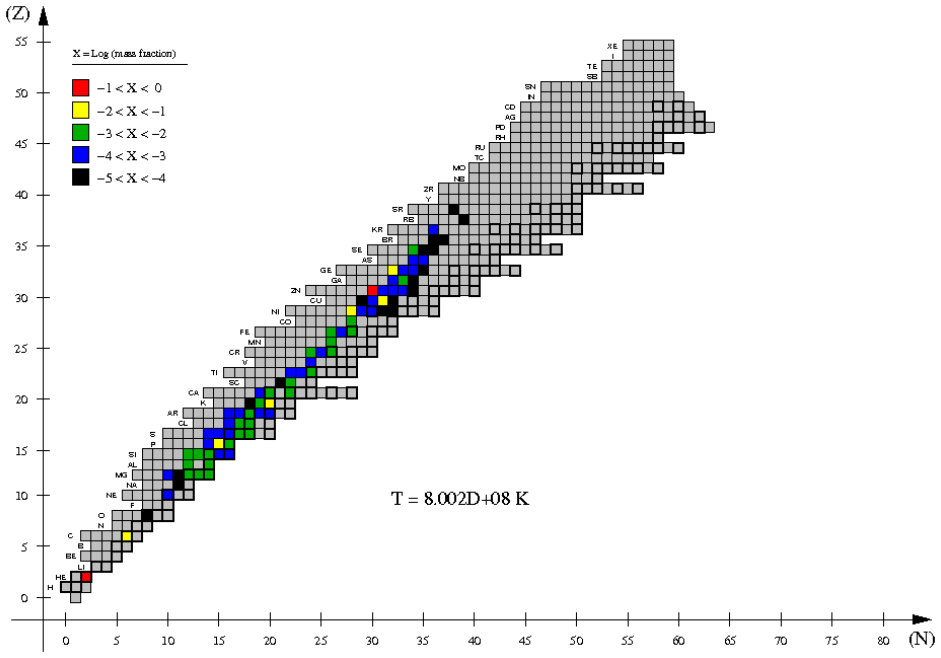

(a)

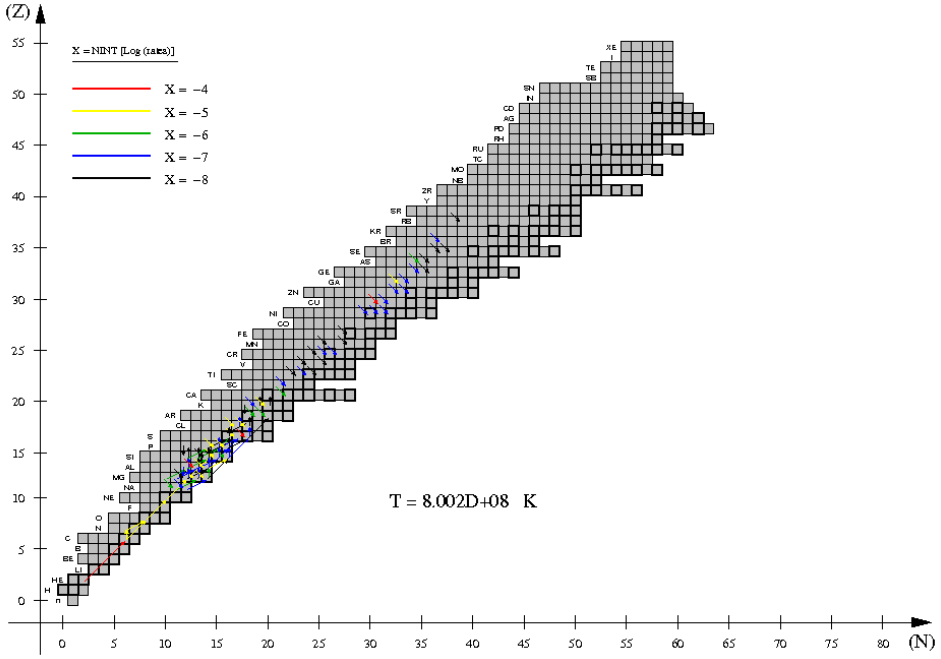

(b)

Figure 4.11: Same as Fig. 4.1, but for $T_{base} = 8 \times 10^8$ K.

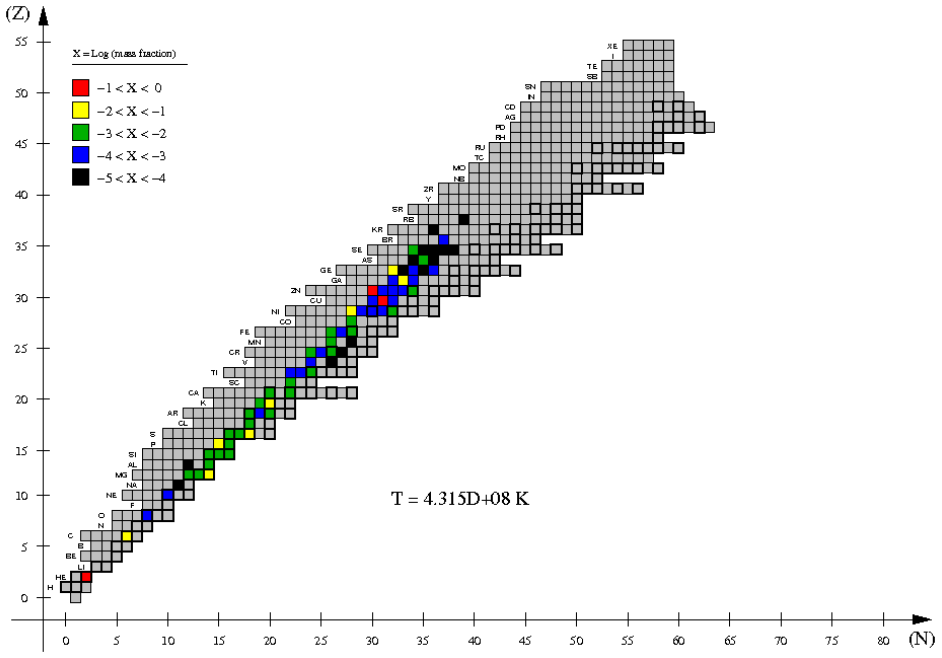

(a)

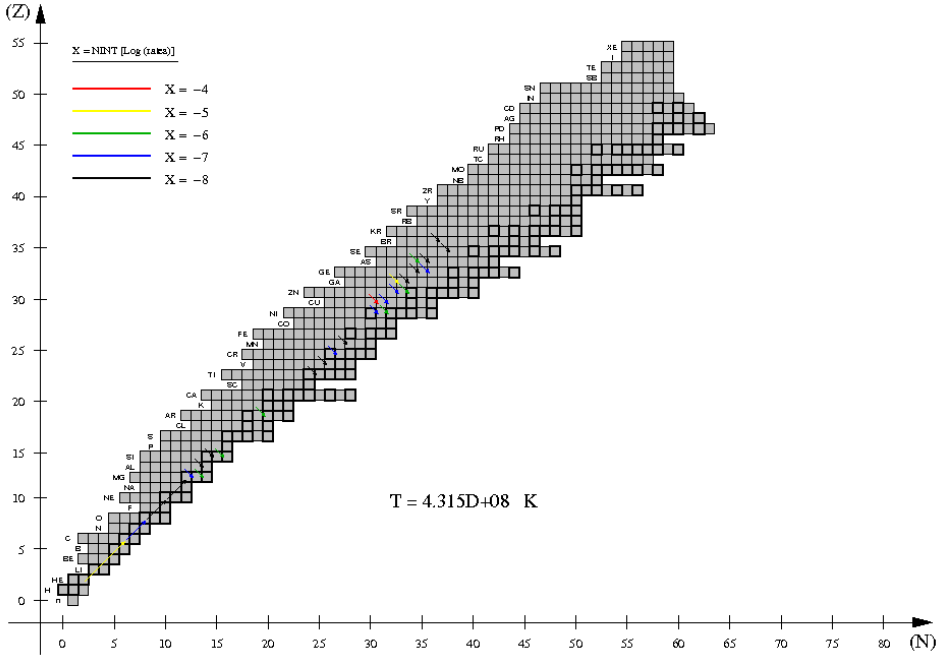

(b)

Figure 4.12: Same as Fig. 4.1, but for $T_{base} = 4.3 \times 10^8$ K.

fully dominated by β^+-decays, such as ^{60}Zn(β^+)^{60}Cu, ^{60}Cu(β^+)^{60}Ni,^{64}Ga(β^+)^{64}Zn, ^{30}P(β^+)^{30}Si, ^{38}K(β^+)^{38}Ar, ^{64}Ge(β^+)^{64}Ga, ^{68}As(β^+)^{68}Ge, ^{51}Mn(β^+)^{51}Cr, ^{53}Fe(β^+) ^{53}Mn, or ^{49}Cr(β^+)^{49}V, all the way up to ^{72}Br.

When t = 28,250 s, T_{base} reaches a minimum value of 1.67×10^8 K, which somewhat marks the end of the first burst in the simulations. ^{60}Cu has decayed already into ^{60}Ni, now the most abundant species at the envelope's base with 0.504, by mass, followed by ^{4}He (0.136, and hence not fully consumed during the TNR), and by ^{12}C (6.7×10^{-2}), ^{26}Mg (1.0×10^{-2}), ^{30}Si (1.5×10^{-2}), ^{34}S (1.4×10^{-2}), ^{39}K (1.5×10^{-2}), ^{56}Ni (8.3×10^{-2}), ^{60}Cu (1.7×10^{-2}), and ^{64}Zn (4.8×10^{-2}; see Fig. 4.14). The rate of nuclear energy generation, powered by β-decays, is now $\epsilon_{nuc} \sim 8.8 \times 10^{11}$ erg.g^{-1}.s^{-1}. Finally, the size of the envelope has shrunk to $\Delta z \sim 8$m, whereas the overall luminosity of the star has decreased to $L_{NS} = 8.3 \times 10^{34}$ erg.s^{-1}.

Profiles of density, temperature, rate of energy generation, pressure, and size along the accreted envelope are shown in Figs. 4.15 and 4.16.

At the end of the first burst, the mean, mass-averaged chemical composition of the envelope is mainly dominated by ^{60}Ni (0.32), ^{4}He (0.31), ^{1}H (0.17), ^{64}Zn (0.03), ^{12}C (0.02), ^{52}Fe (0.02), and ^{56}Fe (0.02) (see Table 4.2, for the mean composition of species -stable or with a half-life $>$ 1 hr- which achieve $X_i > 10^{-9}$), with a nucleosynthetic endpoint (defined as the heaviest isotope with $X_i > 10^{-9}$) around ^{89}Nb.

It is worth noting that the presence of unburned H and ^{4}He in the envelope, at the end of the first burst, will have consequences for the subsequent eruptions (see Section 4.1.2). Notice, however (Fig. 4.17), that the innermost envelope is devoid of H and hence, the next burst will likely initiate well above the core-envelope interface. Another interesting issue is posed by the presence on unburned ^{12}C, particularly in the inner envelope layers, which has implications for studies of the physical mechanisms that power superbursts: these simulations suggest that not enough ^{12}C is left at the end of the burst to power a superburst (which requires $X(^{12}C)_{min} \geq 0.1$, at the envelope base; see Cumming & Bildsten 2001, Strohmayer & Brown 2002, Brown 2004, Cooper & Narayan 2004, 2005, Cumming 2005, or Cooper et al. 2006).

In terms of overproduction factors, f (ratio of the mass-averaged composition of a given isotope over its solar abundance; see also Fig. 4.17), it is worth mentioning that ^{43}Ca, ^{45}Sc, ^{49}Ti, ^{51}V, ^{60,61}Ni, ^{63,65}Cu, ^{64,67,68}Zn, ^{69}Ga, ^{74}Se, and ^{78}Kr achieve $f \sim 10^4$.

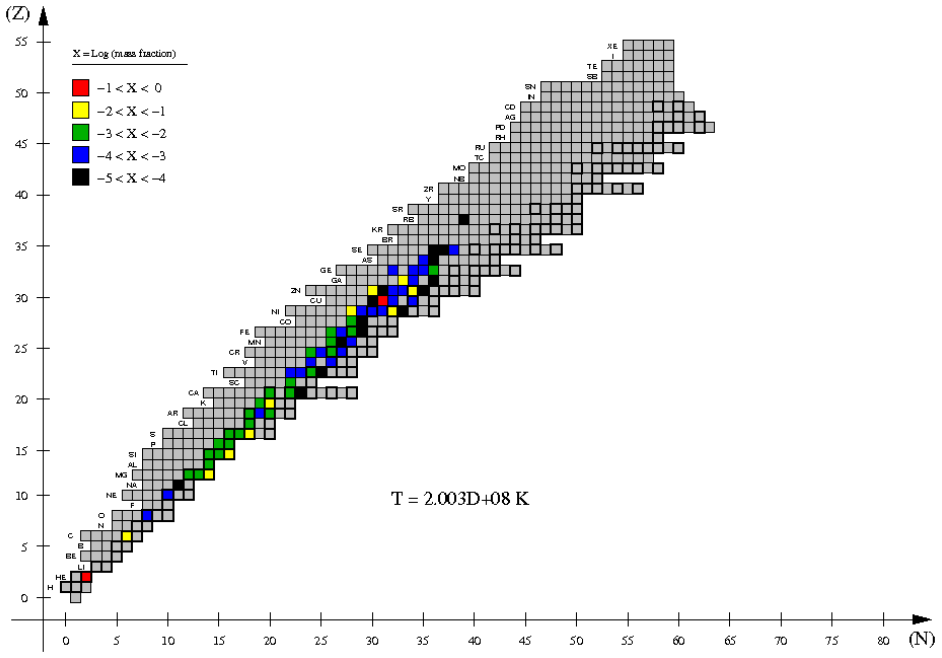

(a)

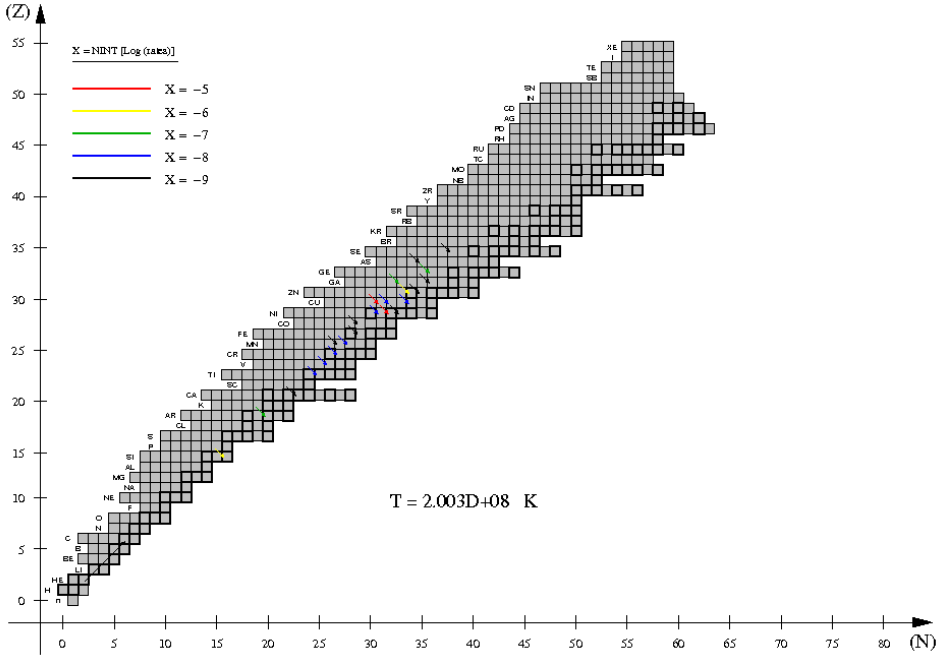

(b)

Figure 4.13: Same as fig. 4.1, but for $T_{base} = 2 \times 10^8$ K.

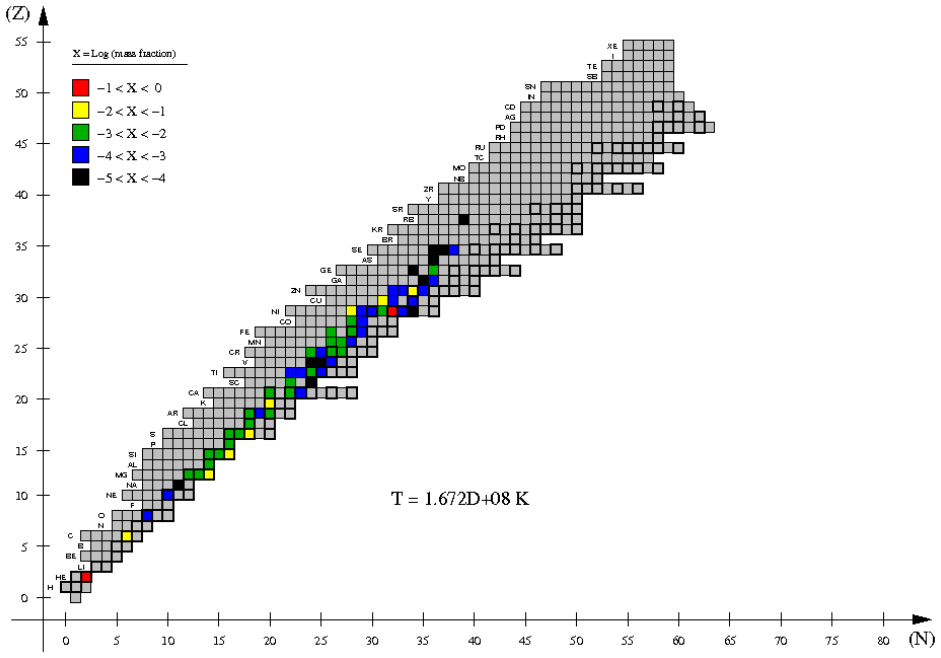

(a)

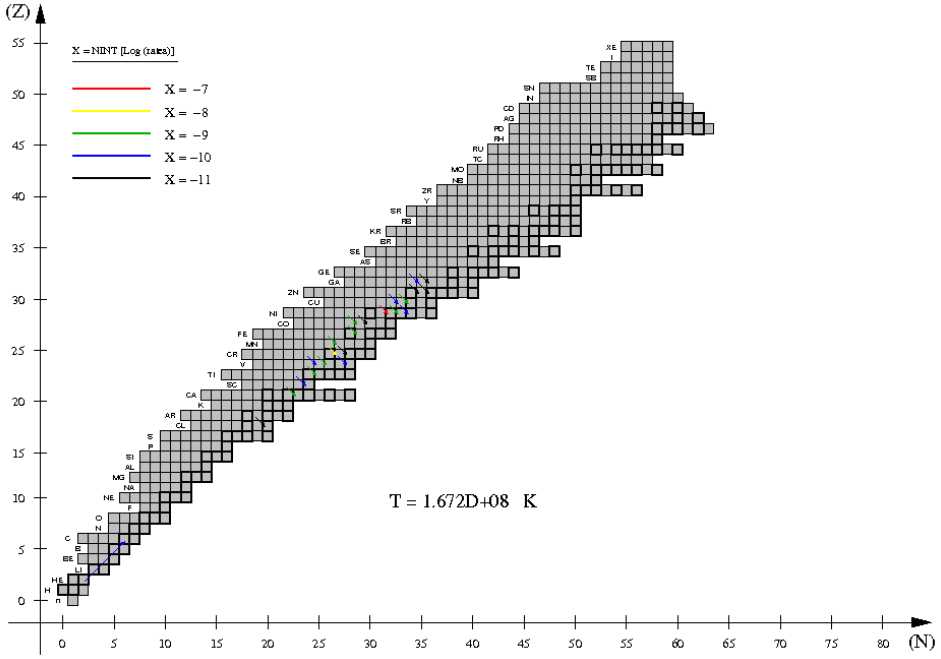

(b)

Figure 4.14: Same as Fig. 4.1, but for the time when the temperature at the envelope base achieves a minimum value of $T_{min} = 1.67 \times 10^8$ K.

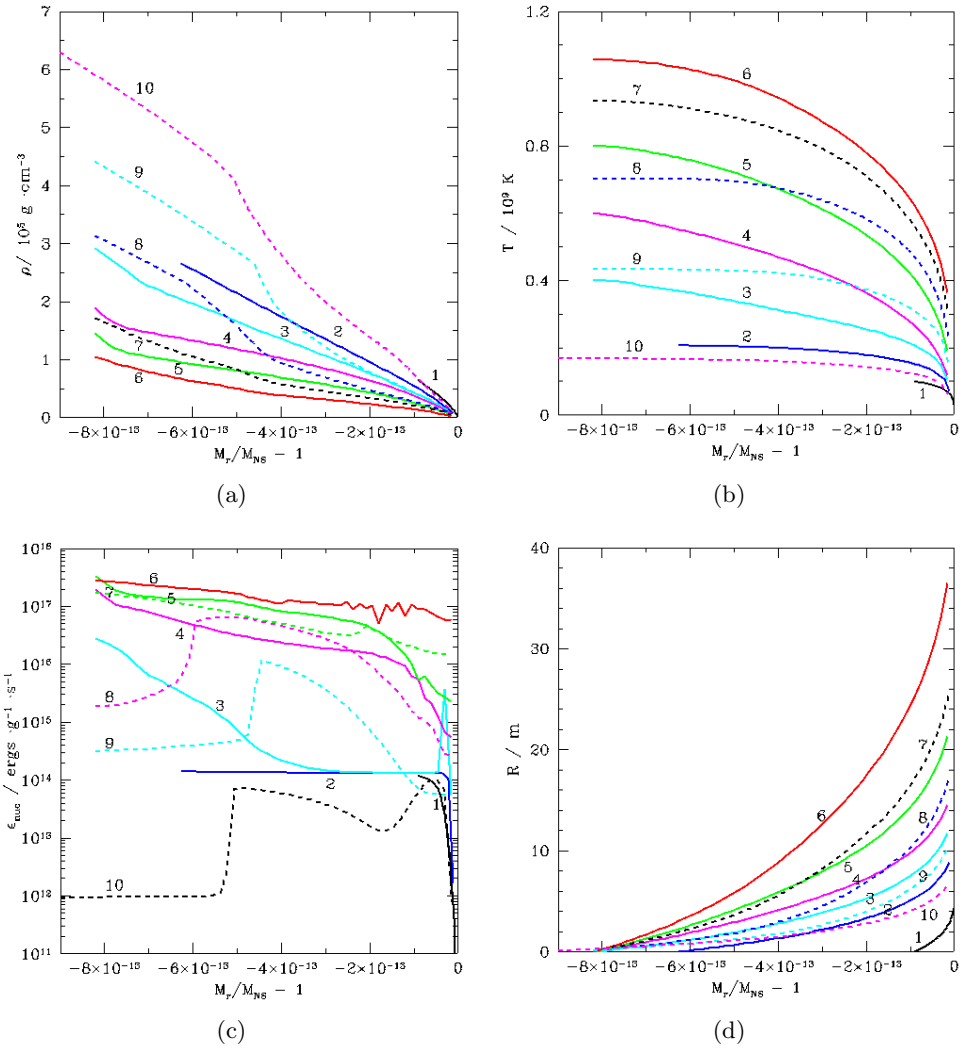

Figure 4.15: Profiles of density (panel a), temperature (panel b), nuclear energy generation rate (panel c), and envelope size (measured from the core-envelope interface; panel d), for Model 1 (M_{NS} = 1.4 $M_{\odot}$, $\dot{M}_{acc}$ = 1.75 × 10^{-9} $M_{\odot}.yr^{-1}$, Z = 0.02), along the first bursting episode. Labels indicate different moments during the TNR, for which T_{base} reaches a value of: (1) 9.9 × 10^7 K, (2) 2.1 × 10^8 K, (3) 4 × 10^8 K, (4) 6 × 10^8 K, (5) 8 × 10^8 K, (6) 1.06 × 10^9 K (T_{peak}), (7) 9.3 × 10^8 K, (8) 7 × 10^8 K, (9) 4.3 × 10^8 K, and (10) 1.7 × 10^8 K (T_{min}).

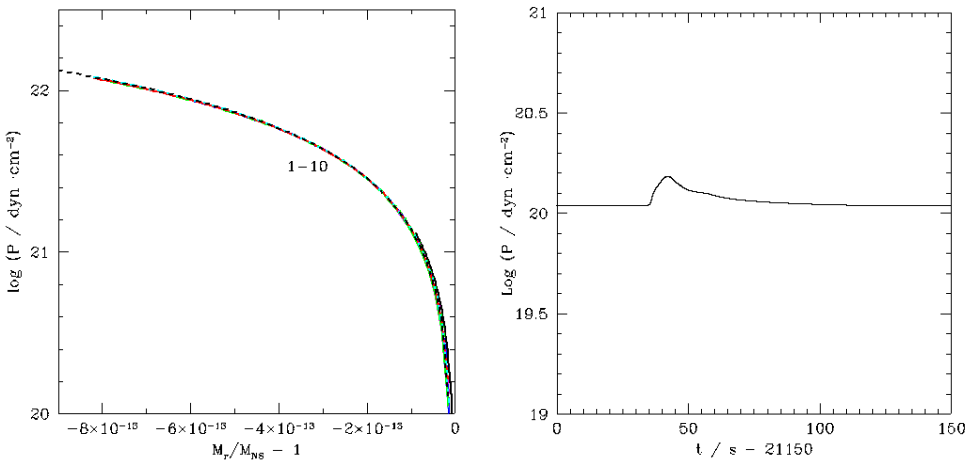

(a) (b)

Figure 4.16: Left panel: same as Fig. 4.15, but for pressure. Right panel: Time evolution of the total pressure at the outermost envelope shell.

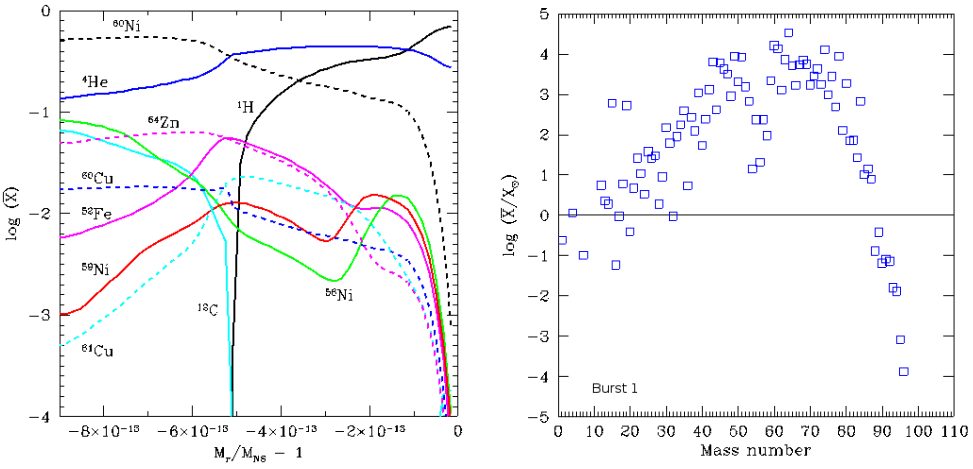

(a) (b)

Figure 4.17: Left panel: mass fractions of the ten most abundant, stable (or $\tau > 1$ hr) isotopes, at the end of the first burst, for Model 1. Right panel: same as left panel, but for overproduction factors relative to solar (for $f > 10^{-5}$).

Table 4.2: Mean composition of the envelope ($X_i > 10^{-9}$) at the end of each burst, for Model 1.

Nucleus	Burst 1	Burst 2	Burst 3	Burst 4
^{1}H	1.7×10^{-1}	8.8×10^{-2}	6.3×10^{-2}	3.9×10^{-2}
^{4}He	3.1×10^{-1}	2.0×10^{-1}	1.4×10^{-1}	1.0×10^{-1}
^{12}C	1.7×10^{-2}	2.5×10^{-2}	2.0×10^{-2}	1.9×10^{-2}
^{13}C	8.4×10^{-5}	1.4×10^{-4}	1.3×10^{-4}	1.1×10^{-4}
^{14}N	2.1×10^{-3}	1.5×10^{-3}	1.1×10^{-3}	7.6×10^{-4}
^{15}N	2.6×10^{-3}	2.0×10^{-3}	1.4×10^{-3}	9.6×10^{-4}
^{16}O	5.7×10^{-4}	5.2×10^{-4}	3.3×10^{-4}	2.9×10^{-4}
^{17}O	3.7×10^{-6}	6.3×10^{-6}	6.8×10^{-6}	1.2×10^{-5}
^{18}O	6.7×10^{-5}	2.3×10^{-5}	1.7×10^{-5}	6.1×10^{-6}
^{18}F	6.2×10^{-5}	5.4×10^{-5}	3.1×10^{-5}	2.5×10^{-5}
^{19}F	2.1×10^{-4}	1.8×10^{-4}	1.1×10^{-4}	7.3×10^{-5}
^{20}Ne	6.3×10^{-4}	5.4×10^{-4}	3.5×10^{-4}	4.0×10^{-4}
^{21}Ne	2.0×10^{-5}	9.5×10^{-6}	6.7×10^{-6}	6.2×10^{-6}
^{22}Ne	9.9×10^{-5}	4.2×10^{-5}	3.2×10^{-5}	2.9×10^{-5}
^{22}Na	3.3×10^{-3}	1.9×10^{-3}	1.2×10^{-3}	9.2×10^{-4}
^{23}Na	3.7×10^{-4}	2.1×10^{-4}	1.2×10^{-4}	1.3×10^{-4}
^{24}Mg	1.7×10^{-3}	1.4×10^{-3}	9.1×10^{-4}	1.3×10^{-3}
^{25}Mg	2.6×10^{-3}	1.7×10^{-3}	1.2×10^{-3}	1.5×10^{-3}
^{26}Mg	1.8×10^{-3}	2.5×10^{-3}	1.7×10^{-3}	1.1×10^{-3}
^{26}Al^{g}	2.6×10^{-4}	9.8×10^{-5}	5.7×10^{-5}	1.1×10^{-4}
^{27}Al	1.8×10^{-3}	1.5×10^{-3}	8.8×10^{-4}	6.7×10^{-4}
^{28}Si	1.2×10^{-3}	5.3×10^{-3}	7.0×10^{-3}	1.3×10^{-2}
^{29}Si	3.1×10^{-4}	8.6×10^{-4}	4.6×10^{-4}	6.9×10^{-4}
^{30}Si	3.5×10^{-3}	5.6×10^{-3}	3.8×10^{-3}	3.0×10^{-3}
^{31}P	5.1×10^{-4}	1.4×10^{-3}	1.7×10^{-3}	1.8×10^{-3}
^{32}S	3.8×10^{-4}	2.9×10^{-2}	5.8×10^{-2}	9.0×10^{-2}
^{33}S	2.9×10^{-4}	3.1×10^{-3}	4.3×10^{-3}	5.1×10^{-3}
^{34}S	3.2×10^{-3}	1.1×10^{-2}	1.6×10^{-2}	1.8×10^{-2}
^{35}Cl	1.0×10^{-3}	4.8×10^{-3}	1.0×10^{-2}	1.0×10^{-2}
^{36}Ar	4.2×10^{-4}	4.0×10^{-3}	9.2×10^{-3}	1.0×10^{-2}
^{37}Cl	3.6×10^{-7}	6.4×10^{-7}	1.8×10^{-6}	4.1×10^{-6}
^{37}Ar	2.3×10^{-4}	5.7×10^{-4}	1.0×10^{-3}	1.1×10^{-3}
^{38}Ar	1.9×10^{-3}	4.9×10^{-3}	8.5×10^{-3}	8.9×10^{-3}
^{39}K	3.8×10^{-3}	7.8×10^{-3}	1.2×10^{-2}	1.3×10^{-2}
^{40}Ca	3.2×10^{-3}	4.3×10^{-3}	5.6×10^{-3}	5.3×10^{-3}
^{41}K	-	9.3×10^{-9}	4.8×10^{-8}	7.6×10^{-8}
^{41}Ca	6.5×10^{-5}	6.9×10^{-5}	6.0×10^{-5}	7.2×10^{-5}

Table 4.2: – Continued.

Nucleus	Burst 1	Burst 2	Burst 3	Burst 4
^{42}Ca	5.5×10^{-4}	1.2×10^{-3}	1.7×10^{-3}	1.9×10^{-3}
^{43}Ca	1.8×10^{-4}	3.6×10^{-4}	7.7×10^{-4}	1.2×10^{-3}
^{43}Sc	4.3×10^{-4}	9.5×10^{-4}	1.2×10^{-3}	9.7×10^{-4}
^{44}Ca	4.3×10^{-8}	3.7×10^{-6}	1.8×10^{-5}	3.2×10^{-5}
^{44}Sc	2.5×10^{-7}	1.9×10^{-5}	3.6×10^{-5}	2.9×10^{-5}
^{44}Ti	5.8×10^{-4}	7.2×10^{-4}	7.3×10^{-4}	7.5×10^{-4}
^{45}Sc	8.2×10^{-5}	7.9×10^{-5}	9.3×10^{-5}	1.2×10^{-4}
^{45}Ti	1.5×10^{-4}	1.7×10^{-4}	1.1×10^{-4}	1.0×10^{-4}
^{46}Ti	9.5×10^{-4}	1.9×10^{-3}	2.4×10^{-3}	2.7×10^{-3}
^{47}Ti	6.6×10^{-4}	8.7×10^{-4}	9.2×10^{-4}	9.5×10^{-4}
^{48}Ti	2.1×10^{-7}	5.6×10^{-7}	1.6×10^{-6}	3.4×10^{-6}
^{48}V	1.2×10^{-4}	1.4×10^{-4}	2.4×10^{-4}	3.7×10^{-4}
^{48}Cr	1.8×10^{-3}	2.1×10^{-3}	2.0×10^{-3}	2.0×10^{-3}
^{49}Ti	1.4×10^{-7}	4.4×10^{-7}	6.9×10^{-7}	8.9×10^{-7}
^{49}V	1.5×10^{-3}	1.5×10^{-3}	1.2×10^{-3}	1.4×10^{-3}
^{50}Cr	1.5×10^{-3}	2.3×10^{-3}	2.7×10^{-3}	3.0×10^{-3}
^{51}V	3.4×10^{-6}	6.4×10^{-6}	1.6×10^{-5}	3.0×10^{-5}
^{51}Cr	3.2×10^{-3}	4.5×10^{-3}	5.1×10^{-3}	5.8×10^{-3}
^{52}Cr	1.5×10^{-5}	2.2×10^{-5}	4.9×10^{-5}	9.4×10^{-5}
^{52}Mn	3.4×10^{-3}	2.3×10^{-3}	2.7×10^{-3}	4.0×10^{-3}
^{52}Fe	2.0×10^{-2}	1.5×10^{-2}	9.9×10^{-3}	1.2×10^{-2}
^{53}Mn	1.2×10^{-3}	1.1×10^{-3}	8.6×10^{-4}	1.1×10^{-3}
^{54}Fe	1.0×10^{-3}	1.4×10^{-3}	1.6×10^{-3}	1.8×10^{-3}
^{55}Mn	6.6×10^{-9}	2.3×10^{-8}	7.1×10^{-8}	1.6×10^{-7}
^{55}Fe	2.3×10^{-4}	3.1×10^{-4}	6.4×10^{-4}	1.0×10^{-3}
^{55}Co	2.9×10^{-3}	3.8×10^{-3}	4.0×10^{-3}	4.3×10^{-3}
^{56}Fe	8.0×10^{-8}	5.4×10^{-7}	1.7×10^{-6}	3.5×10^{-6}
^{56}Co	2.2×10^{-4}	5.3×10^{-4}	1.1×10^{-3}	1.8×10^{-3}
^{56}Ni	2.4×10^{-2}	4.5×10^{-2}	5.2×10^{-2}	5.9×10^{-2}
^{57}Fe	2.6×10^{-8}	1.6×10^{-7}	2.0×10^{-7}	2.5×10^{-7}
^{57}Co	2.5×10^{-4}	1.2×10^{-4}	1.4×10^{-4}	2.0×10^{-4}
^{57}Ni	6.5×10^{-3}	3.9×10^{-3}	2.7×10^{-3}	2.9×10^{-3}
^{58}Ni	4.7×10^{-3}	2.7×10^{-3}	1.9×10^{-3}	2.2×10^{-3}
^{59}Ni	7.3×10^{-3}	4.3×10^{-3}	3.3×10^{-3}	3.8×10^{-3}
^{60}Ni	3.2×10^{-1}	3.3×10^{-1}	3.1×10^{-1}	3.1×10^{-1}
^{61}Ni	3.9×10^{-3}	1.7×10^{-3}	1.9×10^{-3}	2.4×10^{-3}
^{61}Cu	8.2×10^{-3}	6.0×10^{-3}	3.5×10^{-3}	3.8×10^{-3}
^{62}Ni	5.0×10^{-4}	3.1×10^{-4}	4.4×10^{-4}	5.8×10^{-4}

Table 4.2: – Continued.

Nucleus	Burst 1	Burst 2	Burst 3	Burst 4
^{62}Zn	3.2×10^{-3}	2.5×10^{-3}	1.4×10^{-3}	1.5×10^{-3}
^{63}Cu	4.1×10^{-3}	4.4×10^{-3}	3.1×10^{-3}	3.3×10^{-3}
^{64}Zn	3.4×10^{-2}	1.0×10^{-1}	1.3×10^{-1}	1.3×10^{-1}
^{65}Cu	2.5×10^{-7}	2.9×10^{-7}	5.1×10^{-7}	9.2×10^{-7}
^{65}Zn	1.4×10^{-3}	2.5×10^{-3}	1.9×10^{-3}	2.2×10^{-3}
^{66}Zn	3.2×10^{-5}	5.0×10^{-5}	1.3×10^{-4}	2.4×10^{-4}
^{66}Ga	4.0×10^{-4}	5.1×10^{-4}	5.5×10^{-4}	6.3×10^{-4}
^{66}Ge	5.4×10^{-4}	1.3×10^{-3}	7.5×10^{-4}	8.7×10^{-4}
^{67}Ga	4.7×10^{-4}	1.0×10^{-3}	9.7×10^{-4}	1.1×10^{-3}
^{68}Ge	2.9×10^{-3}	2.6×10^{-2}	4.4×10^{-2}	4.5×10^{-2}
^{69}Ge	2.2×10^{-4}	1.3×10^{-3}	1.5×10^{-3}	1.8×10^{-3}
^{70}Ge	7.3×10^{-5}	4.1×10^{-4}	4.6×10^{-4}	6.0×10^{-4}
^{71}As	7.7×10^{-5}	4.7×10^{-4}	6.0×10^{-4}	7.7×10^{-4}
^{72}Se	2.5×10^{-4}	5.7×10^{-3}	1.4×10^{-2}	1.6×10^{-2}
^{73}Se	3.0×10^{-5}	4.2×10^{-4}	7.6×10^{-4}	1.0×10^{-3}
^{74}Se	1.3×10^{-5}	1.8×10^{-4}	3.3×10^{-4}	4.8×10^{-4}
^{75}Br	1.2×10^{-5}	1.8×10^{-4}	3.7×10^{-4}	5.3×10^{-4}
^{76}Kr	3.0×10^{-5}	1.4×10^{-3}	4.5×10^{-3}	5.6×10^{-3}
^{77}Kr	4.5×10^{-6}	1.5×10^{-4}	4.1×10^{-4}	6.1×10^{-4}
^{78}Kr	2.7×10^{-6}	9.2×10^{-5}	2.5×10^{-4}	4.1×10^{-4}
^{79}Kr	1.6×10^{-6}	5.9×10^{-5}	1.7×10^{-4}	2.7×10^{-4}
^{80}Sr	3.9×10^{-6}	4.0×10^{-4}	1.6×10^{-3}	2.2×10^{-3}
^{81}Rb	8.4×10^{-7}	6.8×10^{-5}	2.7×10^{-4}	4.3×10^{-4}
^{82}Sr	7.9×10^{-7}	8.2×10^{-5}	3.2×10^{-4}	5.6×10^{-4}
^{83}Sr	3.0×10^{-7}	4.3×10^{-5}	1.9×10^{-4}	3.2×10^{-4}
^{84}Sr	1.9×10^{-7}	3.8×10^{-5}	1.4×10^{-4}	2.6×10^{-4}
^{85}Y	1.1×10^{-7}	4.0×10^{-5}	2.1×10^{-4}	3.5×10^{-4}
^{86}Zr	7.1×10^{-8}	4.4×10^{-5}	2.3×10^{-4}	4.6×10^{-4}
^{87}Zr	2.7×10^{-8}	3.6×10^{-5}	1.8×10^{-4}	3.9×10^{-4}
^{88}Zr	5.6×10^{-9}	1.8×10^{-5}	1.4×10^{-4}	2.6×10^{-4}
^{89}Nb	4.0×10^{-9}	3.1×10^{-5}	2.9×10^{-4}	5.8×10^{-4}
^{90}Mo	-	1.1×10^{-5}	1.1×10^{-4}	2.2×10^{-4}
^{91}Nb	-	5.4×10^{-6}	5.3×10^{-5}	1.1×10^{-4}
^{92}Mo	-	2.1×10^{-6}	1.9×10^{-5}	4.5×10^{-5}
^{93}Tc	-	1.3×10^{-6}	1.3×10^{-5}	4.5×10^{-5}
^{94}Tc	-	6.9×10^{-7}	7.6×10^{-6}	3.8×10^{-5}
^{95}Ru	-	1.1×10^{-7}	1.1×10^{-6}	4.7×10^{-6}
^{96}Ru	-	9.4×10^{-9}	1.1×10^{-7}	7.6×10^{-7}

Table 4.2: – Continued.

Nucleus	Burst 1	Burst 2	Burst 3	Burst 4
^{97}Ru	-	3.9×10^{-9}	5.1×10^{-8}	3.9×10^{-7}
^{98}Ru	-	-	1.3×10^{-8}	9.2×10^{-8}
^{99}Rh	-	-	2.4×10^{-9}	1.5×10^{-8}
^{100}Pd	-	-	-	2.2×10^{-9}

4.1.2 Second, third, and fourth bursts

No mass ejection is obtained at the end of the first burst. Hence, it is computationally feasible to follow successive bursting episodes in this Lagrangian framework, since the numerical difficulties to remove ejected shells from the computational domain are avoided.

For conciseness, in this Section we will focus on the main differences found between the first and successive bursts computed for Model 1. A first, remarkable difference is due to the so-called *compositional inertia* (Taam 1980; Woosley et al. 2004), which accounts for differences in the gross properties of the bursts driven by changes in the chemical content of the envelope. Indeed, mass-accretion will proceed on top of a metal-enriched envelope (the initial metallicity, $Z_{ini} \sim 0.02$, has risen to a mass-averaged value of $Z \sim 0.52$, at the end of the first burst), and devoid of H at its innermost layers. This will cause a shift in the ignition region that will progressively move away from the core-envelope interface in successive flashes (see Fig. 4.18b).

Table 4.3: Summary of burst properties for Model 1.

Burst	T_{peak} (K)	$t(T_{peak})$ (s)	τ_{rec} (hr)	L_{peak} ($L_\odot$)	$\tau_{0.01}$ (s)	α
1	1.06×10^9	21192	5.9	9.7×10^4	75.8	60
2	1.15×10^9	44342	6.4	1.7×10^5	62.3	40
3	1.26×10^9	62137	4.9	2.1×10^5	55.4	34
4	1.12×10^9	80568	5.1	1.2×10^5	75.7	36

This is shown as well in Fig. 4.18(a), that depicts the distribution of convective shells along the envelope during the four bursting episodes computed for this model.

From the nucleosynthetic viewpoint, and as shown in Table 4.2 and Fig. 4.19, the nuclear activity extends progressively towards heavier species, reaching endpoints ($X_i > 10^{-9}$) around ^{89}Nb (1^{st} burst), ^{97}Ru (2^{nd} burst), ^{99}Rh (3^{rd} burst), and ^{100}Pd (4^{th} burst). The main nuclear activity and the dominant reaction fluxes at peak temperature, during the 4^{th} burst computed for Model 1, are indeed shown in Fig.

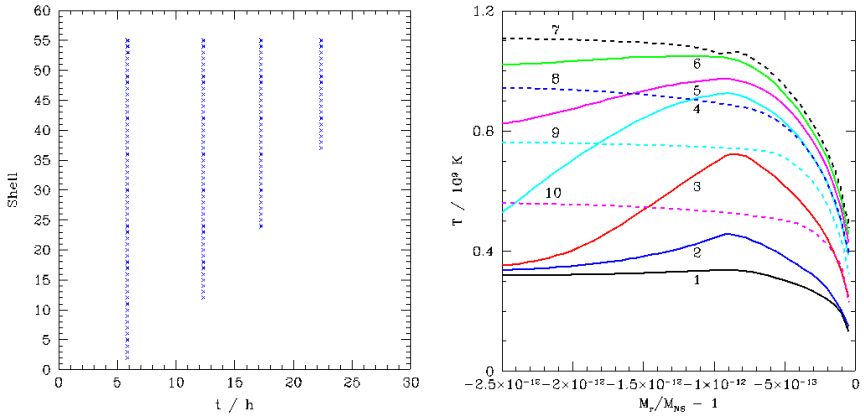

(a) (b)

Figure 4.18: Left panel: Convective regions in the accreted envelope for the four bursts computed in Model 1. Right panel: Temperature profiles, showing the location of the ignition point (shell #37, ~ 5.6 m above the core-envelope interface), along the fourth bursting episode, for Model 1 ($M_{NS} = 1.4$ $M_\odot$, $\dot{M}_{acc} = 1.75 \times 10^{-9}$ $M_\odot.yr^{-1}$, Z = 0.02). Labels indicate different moments during the TNR, for which the temperature at the ignition shell reaches a value of: (1) 3.4×10^8 K, (2) 4.5×10^8 K, (3) 7×10^8 K, (4) 9.2×10^8 K, (5) 9.7×10^8 K, (6) 1.04×10^9 K, (7) 1.06×10^9 K, (8) 8.9×10^8 K, (9) 7.4×10^8 K, and (10) 5.3×10^8 K.

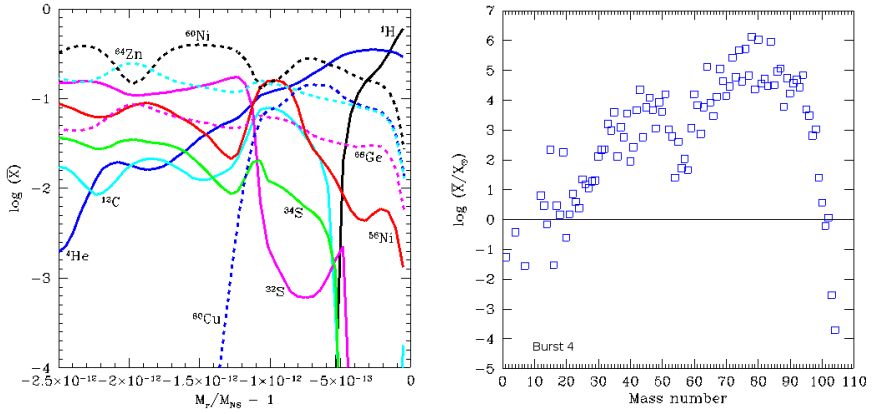

(a) (b)

Figure 4.19: Left panel: mass fractions of the ten most abundant, stable (or $\tau > 1$ hr) isotopes, at the end of the fourth burst, for Model 1. Right panel: same as left panel, but for overproduction factors relative to solar (for $f > 10^{-5}$).

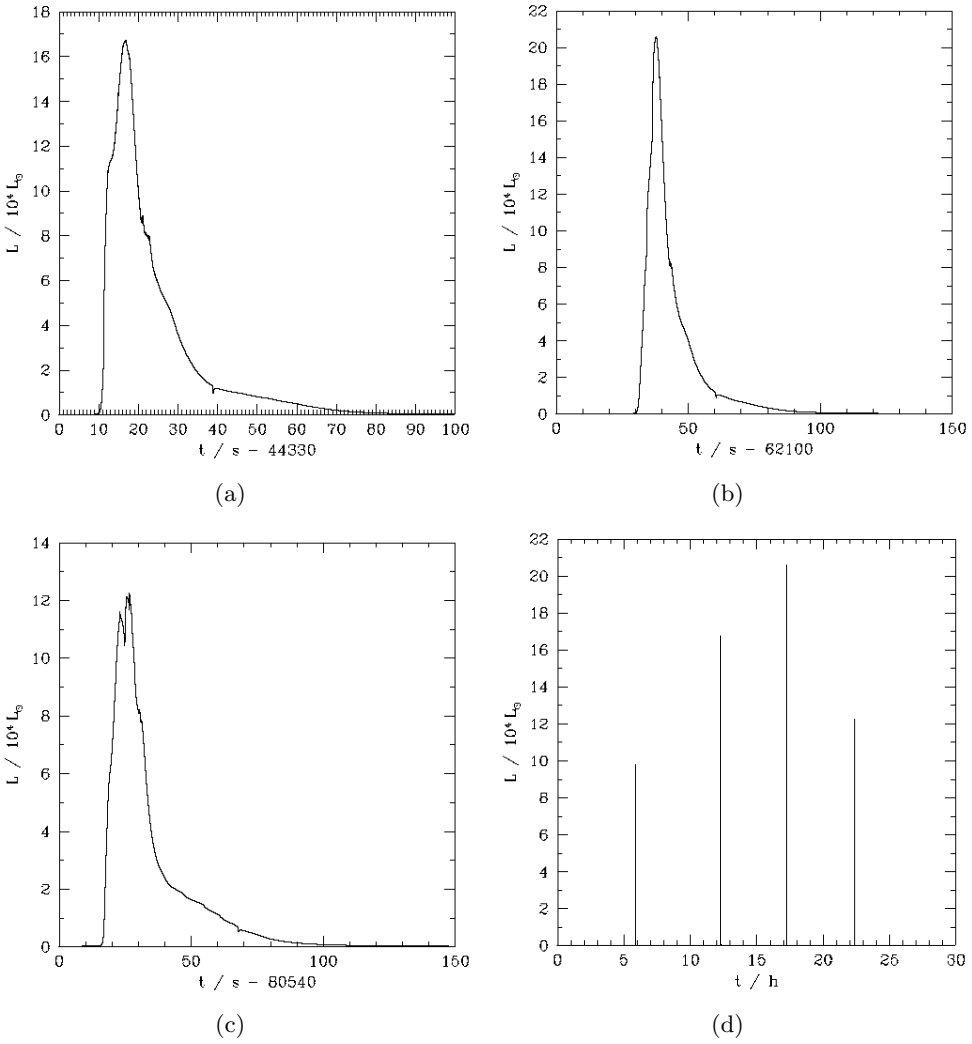

Figure 4.20: Light curves corresponding to the second (panel a), third (panel b), and fourth bursts (panel c), and for the overall computed time (panel d), for Model 1.

4.21. Notice also the increase in the overall mean metallicity (Z) of the envelope (0.52 [1^{st} burst], 0.71 [2^{nd} burst], 0.80 [3^{rd} burst], and 0.86 [4^{th} burst]), while the H and ^{4}He contents drop progressively. A similar ^{12}C yield of ~ 0.02 is systematically obtained at the end of each of the 4 bursts computed. With respect to overproduction factors, the increase in nuclear activity that accompany successive bursts translates also into larger values (as high as $f \sim 10^6$, for ^{76}Se, ^{78,80}Kr, and ^{84}Sr, or $f \sim 10^5$, for species such as ^{64,68}Zn, ^{72,73}Ge, ^{74,77}Se, ^{82}Kr, ^{86,87}Sr, ^{89}Y, and ^{94}Mo, for the 4^{th} burst computed in Model 1; see Fig. 4.19).

A summary of the gross properties that characterize the four bursting episodes computed for this model is given in Table 4.3. Recurrence times between bursts around $\tau_{rec} \sim 5^{hr} - 6.5^{hr}$, and ratios between persistent[3] and burst luminosities (integrated over the time the burst has 1% of its peak luminosity, $\tau_{0.01}$) around $\alpha \sim 35 - 40$ (except for the first burst) have been obtained, in agreement with the values inferred from well-observed XRBs (see Galloway et al. 2008), such as the *textbook burster* GS 1826-24 [$\tau_{rec} = 5.74 \pm 0.13$ hr, $\alpha = 41.7 \pm 1.6$], 4U 1323-62 [$\tau_{rec} = 5.3$ hr, $\alpha = 38 \pm 4$], or 4U 1608-52 [$\tau_{rec} = 4.14 - 7.5$ hr, $\alpha = 41 - 54$]. As reported by Woosley et al. (2004), there is also some trend towards stabilization of these values with the burst number. Moreover, peak temperatures around $T_{peak} \sim (1.1 - 1.3) \times 10^9$ K, and peak luminosities around $L_{peak} \sim (1 - 2) \times 10^5 L_{\odot}$, are also reported.

Fig. 4.20 depicts the corresponding light curves from the second to the fourth burst. As described for the first burst, the shapes of the light curves are exponential-like in the decline phase. A quite interesting feature, observed in some XRBs such as 4U 1608-52 (Penninx et al. 1989), 4U 17+2 (Kuulkers et al. 2002), or 4U 1709-267 (Jonker et al. 2004), is the appearance of a double-peaked burst[4] (see Fig. 4.20c). Double (or triple) peaked bursts can be classified in two categories (Watts & Maurer 2007): the first one corresponds to the so-called *photospheric radius expansion* bursts, which exhibit multi-peaked bursts in the X-ray band but not in the bolometric luminosity. The second type of multi-peaked bursts are also visible in the bolometric light curves, and have been attributed to different causes, ranging from a stepped release of thermonuclear energy caused either by mixing induced by hydrodynamical instabilities (Fujimoto et al. 1988), or driven by a nuclear waiting-point impedance in the thermonuclear reaction flow (Fisker et al. 2004). A preliminary analysis of the 4^{th} burst reported for Model 1 suggests a likely nuclear physics origin (waiting-point impedance) for this feature.

[3]Notice that during the interburst period, the accretion luminosity, $L_{acc} = GM\dot{M}/R \sim 1.5 \times 10^{37} erg.s^{-1}$, will hide the thermal emission from the cooling ashes, as shown in Figs. 4.8(a) and 4.20.

[4]See also Fig. 1.6, for several double-peaked bursts from 4U 1728-34, as observed with the RXTE satellite (Strohmayer & Bildsten 2003).

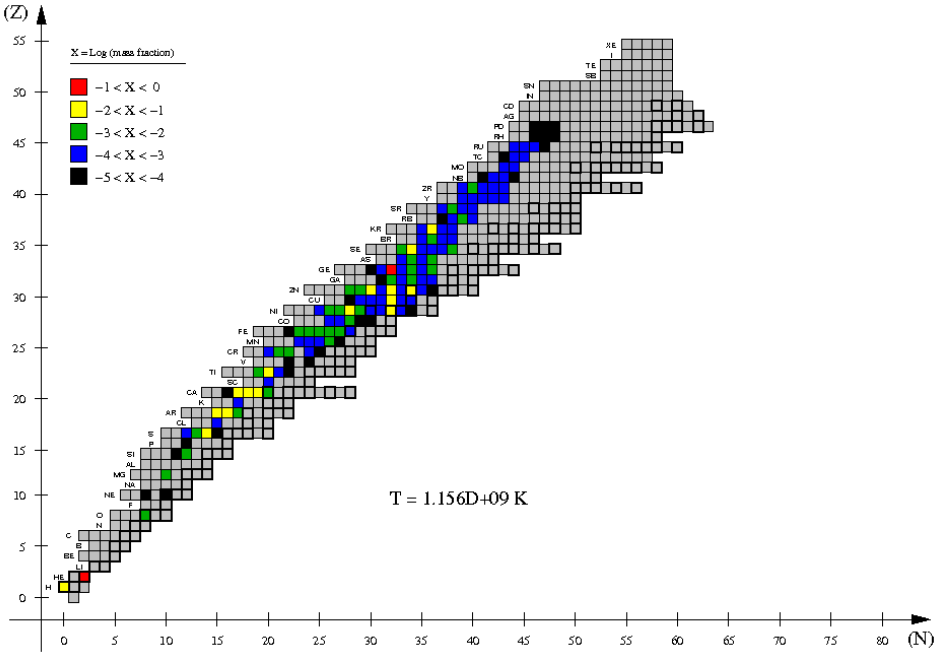

(a)

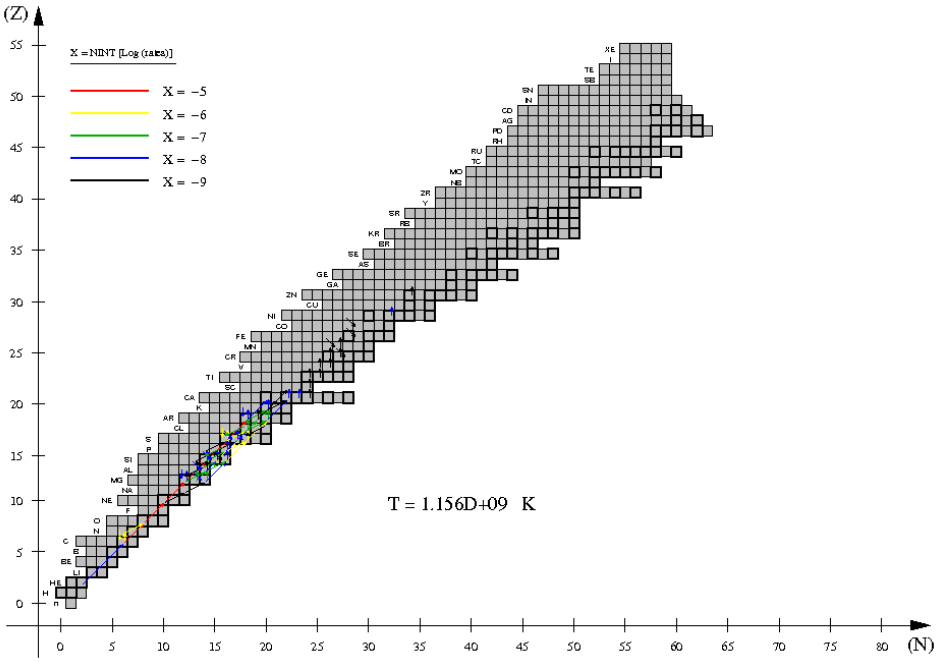

(b)

Figure 4.21: Upper panel: main nuclear activity at the ignition shell (shell #37, ∼5.6 m above the core-envelope interface), when temperature reaches a peak value of $T_{peak} = 1.16 \times 10^9$ K, during the 4^{th} burst computed for Model 1. Lower panel: main reaction fluxes (F $> 10^{-10}$ reactions.s^{-1}.cm^{-3}).

4.2 Model 2

In the previous Section, we have reported results from a sequence of type I X-ray bursts computed with a coarse resolution, in which the accreted envelope was discretized in 60 shells. We have checked the influence of the adopted number of envelope shells on the gross properties of the bursts by performing another simulation, identical to Model 1, but computed with a finer resolution: 200 shells (hereafter, Model 2).

Table 4.4: Summary of burst properties for Model 2.

Burst	T_{peak} (K)	$t(T_{peak})$ (s)	τ_{rec} (hr)	L_{peak} ($L_\odot$)	$\tau_{0.01}$ (s)	α
1	1.05×10^9	21189	5.9	9.0×10^4	59.2	62
2	1.20×10^9	37783	4.6	1.5×10^5	73.9	31

A summary of the main properties of the two bursts computed for Model 2 is given in Table 4.4: the recurrence times obtained lay in the same range of those reported for Model 1 (4 - 6 hr). The same applies to the ratios between persistent and burst luminosities, as well as to peak temperatures and luminosities. Similar light curves (without any double-peaked feature) have also been obtained.

There is also good agreement from the nucleosynthetic viewpoint, with only minor differences in the final, mass-averaged abundances, as shown in Table 4.5 (particularly, for the heavier species of the network, since their low abundances are very sensitive to the specific thermal history of the explosion). It is worth noting that both Models 1 & 2 reach almost identical nucleosynthetic endpoints ($X_i > 10^{-9}$): ^{89}Nb, for the first burst computed in both models, and ^{97}Ru (Model 1) and ^{99}Rh (Model 2), for the second burst. Furthermore, the amounts of unburned H, ^{4}He, and ^{12}C (see previous Section, for the connection between the amount of ^{12}C left over after the bursting episode and the mechanism that drives superbursts) are very similar in both models. As expected from the abovementioned similarities in the final nucleosynthetic yields, there is also good agreement in terms of overproduction factors, dominated by ^{64}Zn and ^{60}Ni (with $f \sim 10^4$) in the first burst computed for Model 1, and by ^{64}Zn, ^{72}Ge, ^{74,76}Se, ^{78,80}Kr, and ^{84}Sr ($f \sim 10^5$), in the second.

All in all, we conclude that the resolution adopted in Model 1 is appropriate for XRB simulations. This is in agreement with the studies performed by Fisker et al. (2004), who concluded that the minimum discretization of the envelope, in 1-D hydrodynamic simulations of X-ray bursts, is about 25 shells.

Table 4.5: Mean composition of the envelope ($X_i > 10^{-9}$) at the end of each burst, for Model 2.

Nucleus	Burst 1	Burst 2
^{1}H	2.3×10^{-1}	1.0×10^{-1}
^{4}He	3.0×10^{-1}	1.9×10^{-1}
^{12}C	1.8×10^{-2}	2.2×10^{-2}
^{13}C	6.8×10^{-5}	6.2×10^{-5}
^{14}N	2.0×10^{-3}	1.4×10^{-3}
^{15}N	2.6×10^{-3}	2.0×10^{-3}
^{16}O	5.3×10^{-4}	3.9×10^{-4}
^{17}O	4.8×10^{-6}	3.0×10^{-6}
^{18}O	6.3×10^{-5}	2.8×10^{-5}
^{18}F	2.1×10^{-4}	5.7×10^{-5}
^{19}F	3.6×10^{-4}	1.7×10^{-4}
^{20}Ne	5.4×10^{-4}	4.1×10^{-4}
^{21}Ne	2.2×10^{-5}	7.3×10^{-6}
^{22}Ne	7.7×10^{-5}	4.4×10^{-5}
^{22}Na	3.6×10^{-3}	1.6×10^{-3}
^{23}Na	2.3×10^{-4}	1.7×10^{-4}
^{24}Mg	1.2×10^{-3}	1.3×10^{-3}
^{25}Mg	1.8×10^{-3}	1.4×10^{-3}
^{26}Mg	3.1×10^{-3}	1.6×10^{-3}
^{26}Al^{g}	1.0×10^{-4}	1.1×10^{-4}
^{27}Al	1.6×10^{-3}	1.1×10^{-3}
^{28}Si	1.2×10^{-3}	7.5×10^{-3}
^{29}Si	4.6×10^{-4}	6.7×10^{-4}
^{30}Si	4.7×10^{-3}	4.6×10^{-3}
^{31}P	6.1×10^{-4}	1.4×10^{-3}
^{32}S	4.7×10^{-4}	2.7×10^{-2}
^{33}S	4.0×10^{-4}	2.4×10^{-3}
^{34}S	4.3×10^{-3}	9.6×10^{-3}
^{35}Cl	1.1×10^{-3}	3.8×10^{-3}
^{36}Ar	5.8×10^{-4}	2.9×10^{-3}
^{37}Cl	1.6×10^{-7}	5.3×10^{-7}
^{37}Ar	2.9×10^{-4}	4.0×10^{-4}
^{38}Ar	2.6×10^{-3}	5.2×10^{-3}
^{39}K	4.9×10^{-3}	8.7×10^{-3}
^{40}Ca	3.1×10^{-3}	3.4×10^{-3}
^{41}K	-	8.7×10^{-9}
^{41}Ca	6.8×10^{-5}	4.5×10^{-5}

Table 4.5: – Continued.

Nucleus	Burst 1	Burst 2
^{42}Ca	7.3×10^{-4}	1.2×10^{-3}
^{43}Ca	9.6×10^{-5}	4.3×10^{-4}
^{43}Sc	7.2×10^{-4}	1.2×10^{-3}
^{44}Ca	5.8×10^{-9}	2.3×10^{-6}
^{44}Sc	9.6×10^{-8}	1.1×10^{-5}
^{44}Ti	5.6×10^{-4}	4.8×10^{-4}
^{45}Sc	3.5×10^{-5}	4.9×10^{-5}
^{45}Ti	2.1×10^{-4}	1.2×10^{-4}
^{46}Ti	1.2×10^{-3}	1.9×10^{-3}
^{47}Ti	6.8×10^{-4}	6.3×10^{-4}
^{48}Ti	2.8×10^{-8}	2.5×10^{-7}
^{48}V	4.4×10^{-5}	9.4×10^{-5}
^{48}Cr	1.9×10^{-3}	1.7×10^{-3}
^{49}Ti	2.4×10^{-8}	2.9×10^{-7}
^{49}V	1.4×10^{-3}	1.2×10^{-3}
^{50}Cr	1.6×10^{-3}	2.2×10^{-3}
^{51}V	6.4×10^{-7}	5.5×10^{-6}
^{51}Cr	3.4×10^{-3}	4.9×10^{-3}
^{52}Cr	1.6×10^{-6}	8.1×10^{-6}
^{52}Mn	1.0×10^{-3}	1.5×10^{-3}
^{52}Fe	1.7×10^{-2}	1.3×10^{-2}
^{53}Mn	9.9×10^{-4}	8.4×10^{-4}
^{54}Fe	9.2×10^{-4}	1.2×10^{-3}
^{55}Mn	-	1.3×10^{-8}
^{55}Fe	7.9×10^{-5}	2.6×10^{-4}
^{55}Co	2.8×10^{-3}	3.7×10^{-3}
^{56}Fe	1.4×10^{-8}	3.6×10^{-7}
^{56}Co	1.1×10^{-4}	5.0×10^{-4}
^{56}Ni	3.2×10^{-2}	5.0×10^{-2}
^{57}Fe	2.6×10^{-9}	6.6×10^{-8}
^{57}Co	6.9×10^{-5}	7.4×10^{-5}
^{57}Ni	5.1×10^{-3}	3.4×10^{-3}
^{58}Ni	3.4×10^{-3}	2.3×10^{-3}
^{59}Ni	4.8×10^{-3}	3.7×10^{-3}
^{60}Ni	2.9×10^{-1}	3.2×10^{-1}
^{61}Ni	9.1×10^{-4}	1.4×10^{-3}
^{61}Cu	6.3×10^{-3}	5.8×10^{-3}
^{62}Ni	9.9×10^{-5}	1.9×10^{-4}

Table 4.5: – Continued.

Nucleus	Burst 1	Burst 2
^{62}Zn	1.8×10^{-3}	2.1×10^{-3}
^{63}Cu	2.2×10^{-3}	3.2×10^{-3}
^{64}Zn	2.3×10^{-2}	1.2×10^{-1}
^{65}Cu	2.4×10^{-8}	2.7×10^{-7}
^{65}Zn	5.4×10^{-4}	3.1×10^{-3}
^{66}Zn	1.7×10^{-6}	2.9×10^{-5}
^{66}Ga	6.4×10^{-5}	6.2×10^{-4}
^{66}Ge	2.8×10^{-4}	1.7×10^{-3}
^{67}Ga	1.8×10^{-4}	1.2×10^{-3}
^{68}Ge	1.6×10^{-3}	2.8×10^{-2}
^{69}Ge	7.3×10^{-5}	1.8×10^{-3}
^{70}Ge	2.0×10^{-5}	5.9×10^{-4}
^{71}As	2.4×10^{-5}	6.2×10^{-4}
^{72}Se	1.2×10^{-4}	5.8×10^{-3}
^{73}Se	8.0×10^{-6}	6.1×10^{-4}
^{74}Se	3.2×10^{-6}	2.7×10^{-4}
^{75}Br	3.3×10^{-6}	2.7×10^{-4}
^{76}Kr	1.2×10^{-5}	1.6×10^{-3}
^{77}Kr	1.2×10^{-6}	2.3×10^{-4}
^{78}Kr	6.7×10^{-7}	1.5×10^{-4}
^{79}Kr	4.0×10^{-7}	9.2×10^{-5}
^{80}Sr	1.5×10^{-6}	4.9×10^{-4}
^{81}Rb	2.3×10^{-7}	1.1×10^{-4}
^{82}Sr	2.2×10^{-7}	1.4×10^{-4}
^{83}Sr	9.4×10^{-8}	7.0×10^{-5}
^{84}Sr	6.4×10^{-8}	6.3×10^{-5}
^{85}Y	4.5×10^{-8}	6.4×10^{-5}
^{86}Zr	3.1×10^{-8}	7.8×10^{-5}
^{87}Zr	1.4×10^{-8}	6.9×10^{-5}
^{88}Zr	3.5×10^{-9}	3.3×10^{-5}
^{89}Nb	2.5×10^{-9}	5.7×10^{-5}
^{90}Mo	-	2.4×10^{-5}
^{91}Nb	-	1.3×10^{-5}
^{92}Mo	-	7.3×10^{-6}
^{93}Tc	-	6.9×10^{-6}
^{94}Tc	-	5.0×10^{-6}
^{95}Ru	-	9.2×10^{-7}
^{96}Ru	-	9.1×10^{-8}

Table 4.5: – Continued.

Nucleus	Burst 1	Burst 2
^{97}Ru	-	3.7×10^{-8}
^{98}Ru	-	9.1×10^{-9}
^{99}Rh	-	1.8×10^{-9}

4.3 Model 3

In this Section, we will analyze the role played by the metallicity of the accreted material (that reflects the surface composition of the companion star) on the overall properties of the bursts. To this end, we have computed another series of thermonuclear bursts (hereafter, Model 3), driven by accretion of metal-deficient material (Z $\sim Z_{\odot}/20$) onto a 1.4 $M_{\odot}$ neutron star ($L_{ini} = 1.6 \times 10^{34}$ erg.s^{-1} = 4.14 $L_{\odot}$), at a rate $\dot{M}_{acc} = 1.75 \times 10^{-9}$ $M_{\odot}$.yr^{-1}. The composition of the accreted material is assumed to be X=0.759, Y=0.240, and Z=10^{-3}, and as for Model 1, all metals are initially added up in the form of ^{14}N. This model is indeed qualitatively similar to Model zM, from Woosley et al. (2004). Both the envelope zoning and the initial relaxation phase are identical to those described for Model 1.

4.3.1 First burst

The piling up of matter on top of the neutron star during the accretion stage progressively compresses and heats the envelope.

At t=4337 s, the envelope achieves $T_{base} \sim 10^8$ K ($\rho_{base} \sim 9.8 \times 10^4$ g.cm^{-3}). The nuclear activity ($\epsilon_{nuc} \sim 6.2 \times 10^{12}$ erg.g^{-1}.s^{-1}) is fully dominated by the CNO-cycle, resulting from proton-captures on the initial ^{14}N nuclei. In contrast to Model 1, the smaller metallicity of this model limits substantially the role of proton captures. Indeed, at this stage, H has only been reduced to 0.757 at the envelope base. The main reaction fluxes are actually an order of magnitude lower than those reported from Model 1, for the same temperature. It is worth noting that also because of the lower metallicity of this model, the time required to achieve $T_{base} \sim 10^8$ K is about twice the value reported for Model 1. This results in a thicker, more massive accreted envelope (see comparison in Table 4.6) which will somewhat affect the forthcoming explosion. The main reaction path is led by ^{15}N(p, α)^{12}C, which powers ^{12}C(p, γ)^{13}N(p, γ)^{14}O(β^+)^{14}N(p, γ)^{15}O(β^+)^{15}N. This suite of nuclear processes is followed, to a lesser extent, by ^{13}N(β^+)^{13}C(p, γ)^{14}N, and by ^{15}N(p, γ)^{16}O(p, γ)^{17}F(β^+)^{17}O(p, α)^{14}N. Besides H and He (0.242), by far the most abundant nuclei in the envelope, the nuclear activity in the CNO region increases the chemical abundances of many species in this mass range, such as ^{12}C (1.4×10^{-6}), ^{13}C (1.8×10^{-9}), ^{13}N (10^{-5}), ^{14}N

(5.5×10^{-5}), ^{14}O (3.4×10^{-4}), ^{15}N (1.1×10^{-9}), ^{15}O (6.3×10^{-4}, the most abundant CNO-group nucleus at the envelope base, fed by ^{14}N(p,γ)^{15}O), ^{16}O (1.9×10^{-7}), ^{17}O (2.3×10^{-9}), and ^{17}F (2.5×10^{-7}).

16.8 hours (60,347 s) after the beginning of accretion, T_{base} has reached 2×10^8 K (with $\rho_{base} = 5.7 \times 10^5$ g.cm^{-3} and $P_{base} = 3.4 \times 10^{22}$ dyn.cm^{-2}). The total luminosity of the star is only 6.9×10^{34} erg.s^{-1}. The main nuclear activity is still governed by ^{15}N(p, α)^{12}C, now followed by ^{7}Be(p, γ)^{8}B, at equilibrium with its reverse photodisintegration reaction ^{8}B(γ, p)^{7}Be, and by ^{12}C(p, γ)^{13}N(p, γ)^{14}O(β^+)^{14}N(p, γ)^{15}O(β^+)^{15}N. Contribution from other reactions includes the 3α, ^{15}N(p, γ)^{16}O(p, γ)^{17}F(p, γ)^{18}Ne(β^+)^{18}F(p, α)^{15}O, or the direct and reverse processes ^{21}Mg(p, γ)^{22}Al(γ, p)^{21}Mg. Because of the limited number of CNO-catalysts in this low-metallicity model, some proton-proton chain reactions, such as the *pep*, ^{3}He(α, γ)^{7}Be, or ^{8}Be $\rightarrow 2^{4}$He, are relatively frequent. In terms of chemical abundances, the now frequent p-captures have reduced the hydrogen content down to a value of 0.695 (while X(^{4}He) = 0.303). The next most abundant isotopes in the network are the short-lived species ^{15}O (1.4×10^{-3}) and ^{14}O (8×10^{-4}). The nuclear activity ($X_i > 10^{-9}$) reaches ^{40}Ca at this stage (X(^{40}Ca) = 4.6×10^{-7}).

Table 4.6: Properties of the first burst computed in Models 1 & 3.

	Model 1	Model 3
ρ_{max} (g.cm^{-3})	3.4×10^5	5.9×10^5
P_{max} (dyn.cm^{-2})	1.2×10^{22}	3.7×10^{22}
τ_{acc} (hr)	5.9	18
Δm_{acc} (M$_\odot$)	1.2×10^{-12}	3.6×10^{-12}
T_{peak} (K)	1.1×10^9	1.4×10^9
L_{peak} (L$_\odot$)	9.7×10^4	1.0×10^5
Δz_{max} (m)	44	74

18.1 hours (65,081 s) from the onset of accretion, T_{base} reaches 4×10^8 K ($\rho_{base} = 4.8 \times 10^5$ g.cm^{-3}, whereas $P_{base} = 3.7 \times 10^{22}$ dyn.cm^{-2}). Hydrogen continues to decrease smoothly (X(H) = 0.689), whereas the ^{4}He abundance reaches 0.280. The rate of nuclear energy generation is now 7.1×10^{15} erg.g^{-1}.s^{-1}. As before, the next most abundant nuclei are ^{14}O (1.4×10^{-2}) and ^{15}O, now followed by ^{52}Fe and ^{18}Ne, with mass fractions of the order of 10^{-3}; other isotopes, such as ^{33,34}Ar, ^{21,22}Mg, ^{49,50,51}Mn, ^{27}P, ^{29}S, ^{37,38}Ca, ^{24}Si, ^{31}Cl, or ^{46,48}Cr, reach abundances of the order of 10^{-4}. The nuclear activity extends up to ^{58}Cu, and is mainly dominated by different processes that operate almost at equilibrium with their inverse photodisintegration reactions, such as ^{21}Mg(p, γ)^{22}Al(γ, p)^{21}Mg, ^{30}S(p, γ)^{31}Cl(γ, p)^{30}S, ^{25}Si(p, γ)^{26}P(γ, p)^{25}Si, and ^{7}Be(p, γ)^{8}B(γ, p)^{7}Be. Additional activity is powered mainly by 3$\alpha \rightarrow ^{12}$C(p, γ)^{13}N(p, γ)^{14}O, followed by ^{14}O(α, p)^{17}F(p, γ)^{18}Ne(β^+)^{18}F(p, α)^{15}O(α,

$\gamma)^{19}$Ne(p, $\gamma)^{20}$Na(p, $\gamma)^{21}$Mg.

Six seconds later (t = 65,087 s), T_{base} achieves 5×10^8 K. ρ_{base} has slightly decreased to 4.3×10^5 g.cm^{-3} because of a mild envelope expansion ($\Delta z \sim 19.7$ m). Time-dependent, convective mixing with the adjacent shells, with a characteristic timescale of $\tau_{conv} \sim 10^{-4}$ s, causes a slight increase in the H abundance at the envelope's base. Indeed, the H abundance is now 0.700, by mass, whereas ^{4}He has slightly decreased to 0.267, as a result of α-captures driven by the high temperatures achieved. The next most abundant species are now ^{18}Ne (10^{-2}), together with ^{14,15}O (3.5×10^{-3} and 7.5×10^{-3}, respectively), ^{52}Fe (2.8×10^{-3}), and ^{34}Ar (1.1×10^{-3}). The nuclear activity reaches now ^{61}Ga, and powers an energy generation rate of 2.8×10^{16} erg.g^{-1}.s^{-1}. The overall stellar luminosity is now 2.5×10^{35} erg.s^{-1}. It is worth noting that the main nuclear path above Ca begins to move away from the valley of stability towards the proton-drip line. The dominant nuclear reactions are, as before, the direct and reverse processes ^{30}S(p, $\gamma)^{31}$Cl(γ, p)^{30}S, ^{21}Mg(p, $\gamma)^{22}$Al(γ, p)^{21}Mg, ^{25}Si(p, $\gamma)^{26}$P(γ, p)^{25}Si, and ^{7}Be(p, $\gamma)^8$B(γ, p)^{7}Be. Additional activity is powered mainly by ^{14}O(α, p)^{17}F(p, $\gamma)^{18}$Ne. Indeed, ^{14}O+α becomes the most important α-capture reaction, with a flux slightly larger than that of ^{15}O(α, γ), or the 3α reaction. Additional activity is driven by ^{18}Ne(β^+)^{18}F(p, $\alpha)^{15}$O, ^{19}Ne(p, $\gamma)^{20}$Na(p, $\gamma)^{21}$Mg, ^{21}Na(p, $\gamma)^{22}$Mg(p, $\gamma)^{23}$Al, ^{12}C(p, $\gamma)^{13}$N(p, $\gamma)^{14}$O, ^{26}Si(p, $\gamma)^{27}$P(γ, p)^{26}Si, and ^{26}P(p, $\gamma)^{27}$S.

A qualitatively similar picture is found when T_{base} achieves 7×10^8 K (at t = 65,090 s), with the most abundant species at the envelope's base being H (0.705), ^{4}He (0.250), ^{18}Ne (1.4×10^{-2}), ^{28,29,30}S (2.2×10^{-3}, 2.8×10^{-3}, and 5.1×10^{-3}, respectively), ^{24,25}Si (3.3×10^{-3} and 4.4×10^{-3}, respectively), ^{60}Zn (2.6×10^{-3}), ^{21}Mg (1.9×10^{-3}), and ^{34}Ar (1.8×10^{-3}). The nuclear activity extends all the way up to ^{68}Se.

One second later (t = 65,091 s), T_{base} achieves 10^9 K. The nuclear activity (with $\epsilon_{nuc} \sim 1.5 \times 10^{17}$ erg.g^{-1}.s^{-1}; see Fig. 4.22) continues to reduce the H and ^{4}He abundances down to 0.680 and 0.224, respectively. The next most abundant species are now ^{28,29,30}S (6.3×10^{-3}, 1.1×10^{-2}, and 3.3×10^{-2}, respectively), ^{33,34}Ar (5.7×10^{-3} and 6.1×10^{-3}, respectively), ^{24,25}Si (2.1×10^{-3} and 6.1×10^{-3}, respectively), ^{60}Zn (5×10^{-3}), ^{36,37,38}Ca (1.9×10^{-3}, 3.7×10^{-3}, and 5×10^{-3}, respectively), and ^{64}Ge (10^{-3}), with the main nuclear path reaching ^{72}Kr. All dominant nuclear reactions are the quasiequilibrium processes ^{29,30}S(p, $\gamma)^{30,31}$Cl(γ, p)^{29,30}S, ^{25,26}Si(p, $\gamma)^{26,27}$P(γ, p)^{25,26}Si, ^{59,60}Zn(p, $\gamma)^{60,61}$Ga(γ, p)^{59,60}Zn, ^{45,46}Cr(p, $\gamma)^{46,47}$Mn(γ, p)^{45,46}Cr, ^{21,22}Mg(p, $\gamma)^{22,23}$Al(γ, p)^{21,22}Mg, ^{38}Ca(p, $\gamma)^{39}$Sc(γ, p)^{38}Ca, ^{55}Ni(p, $\gamma)^{56}$Cu(γ, p)^{55}Ni, ^{41,42}Ti(p, $\gamma)^{42,43}$V(γ, p)^{41,42}Ti, ^{49,50}Fe(p, $\gamma)^{50,51}$Co(γ, p)^{49,50}Fe, ^{16}O(p, $\gamma)^{17}$F(γ, p)^{16}O, ^{26}P(p, $\gamma)^{27}$S(γ, p)^{26}P, ^{7}Be(p, $\gamma)^8$B(γ, p)^{7}Be, and ^{33}Ar(p, $\gamma)^{34}$K(γ, p)^{33}Ar.

In contrast to Model 1, which achieved a peak temperature of 1.06×10^9 K, Model 3 reaches relatively higher values. Hence, at t = 65,093 s, T_{base} achieves 1.2×10^9 K. The H and ^{4}He abundances have been reduced to 0.648 and 0.205, respectively. The

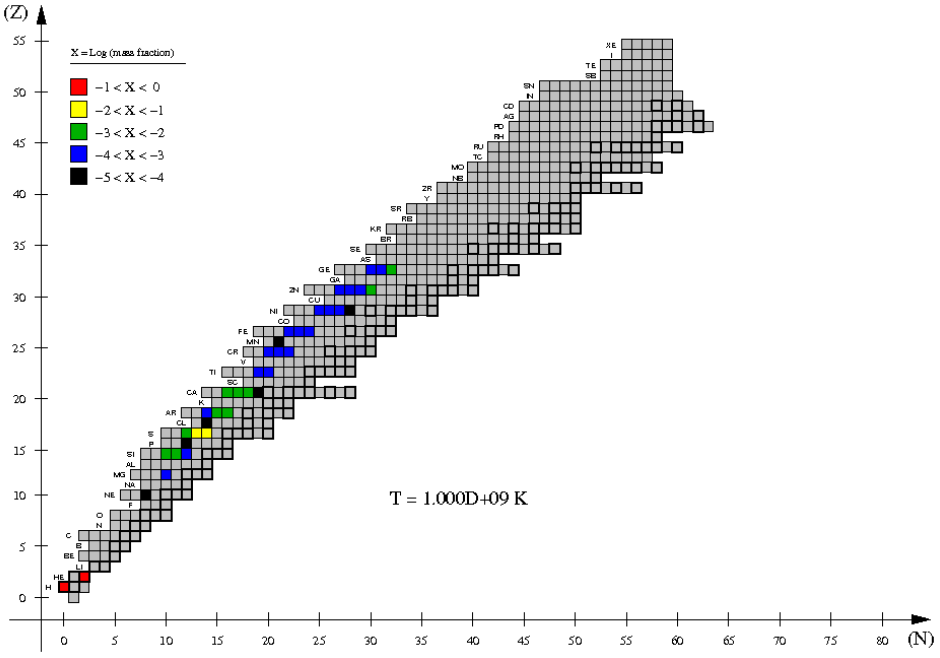

(a)

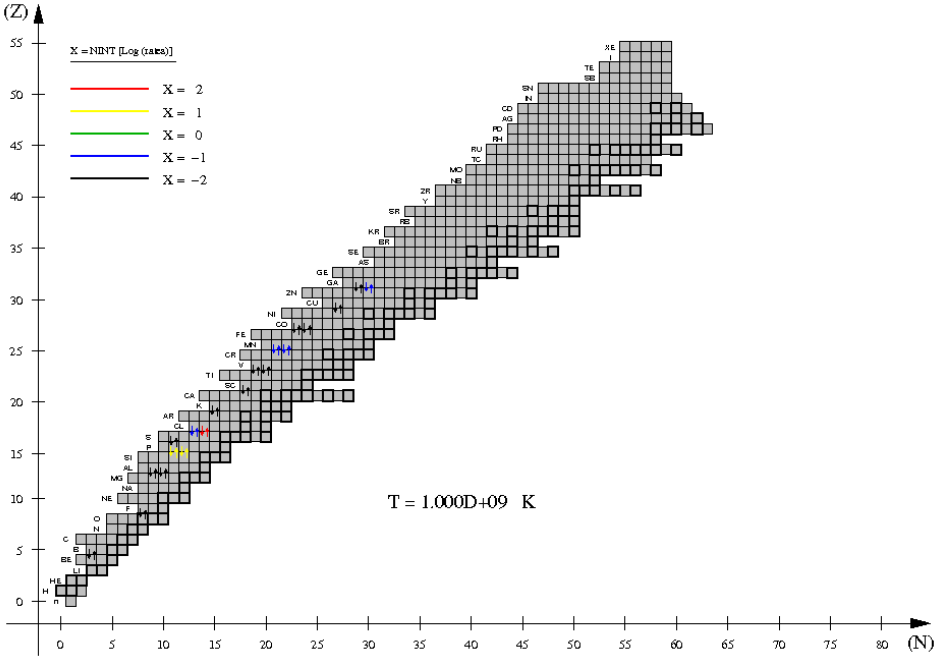

(b)

Figure 4.22: Main nuclear activity at the innermost envelope shell for Model 3 (M_{NS} = 1.4 $M_\odot$, $\dot{M}_{acc} = 1.75\times10^{-9}$ $M_\odot.yr^{-1}$, $Z = 10^{-3}$), at the time when the temperature at the envelope base reaches $T_{base} = 10^9$ K. Upper panel: mass fractions of the most abundant species ($X > 10^{-5}$); Lower panel: main reaction fluxes ($F > 10^{-3}$ reactions.s^{-1}.cm^{-3}).

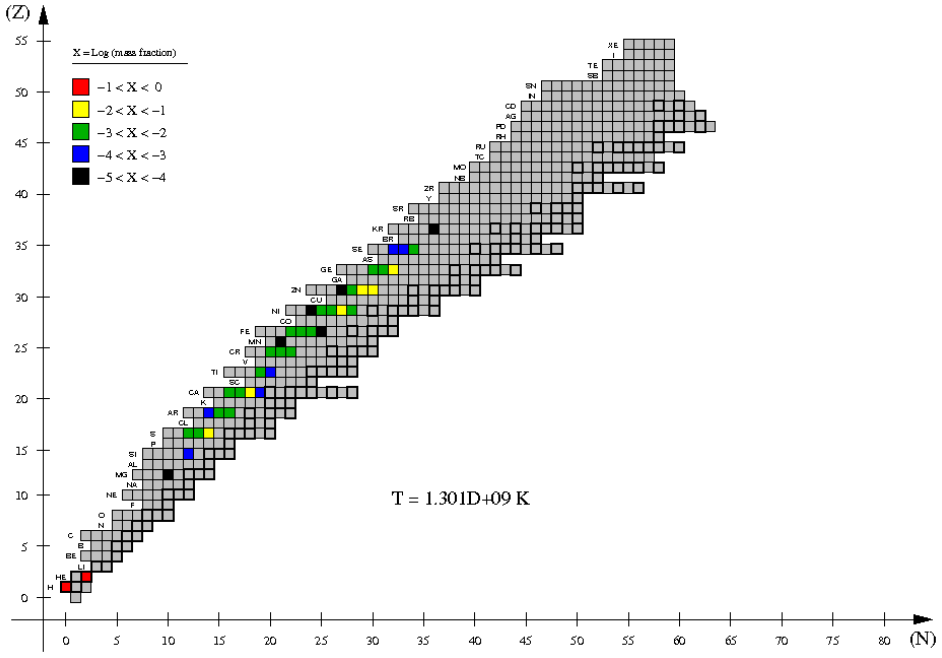

(a)

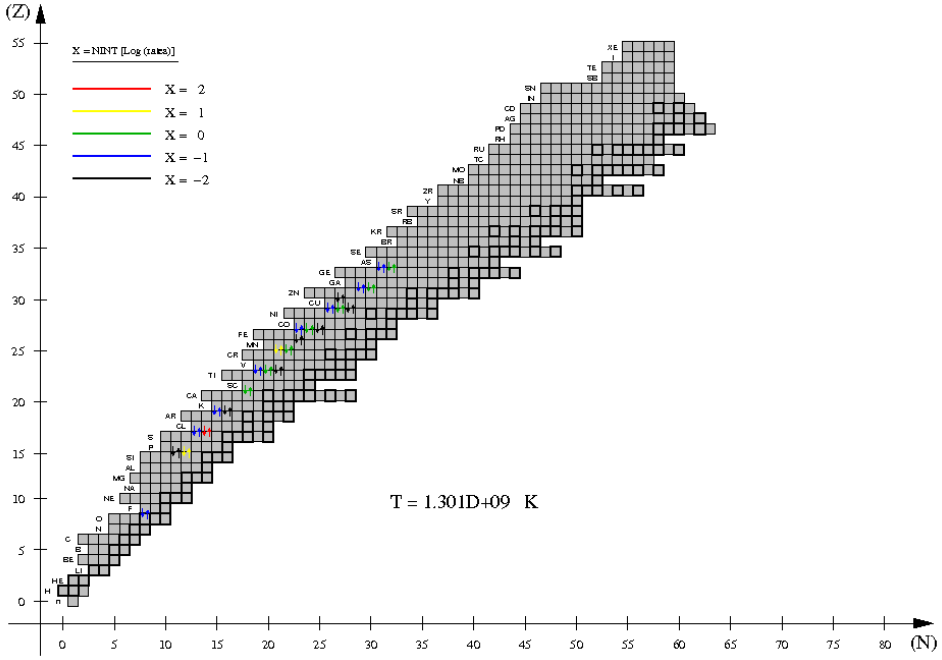

(b)

Figure 4.23: Same as Fig. 4.22, but for $T_{base} = 1.3 \times 10^9$ K.

next most abundant nucleus is still ^{30}S (3.1×10^{-2}), followed by ^{38}Ca (2×10^{-2}), and by a large number of species with abundances of the order of 10^{-3}, such as ^{36,37}Ca, ^{28,29}S, ^{32,33,34}Ar, ^{58,59,60}Zn, ^{62,63,64}Ge, ^{48,49,50}Fe, ^{53,54,55}Ni, ^{41}Ti, and ^{44,45,46}Cr. At this stage, the main nuclear path reaches ^{76}Sr, being dominated by most of the quasiequilibrium processes discussed above.

One second later, at t = 65,094 s, the rate of nuclear energy generation achieves a maximum value of $\epsilon_{nuc,max} \sim 2.1 \times 10^{17}$ erg.g^{-1}.s^{-1}.

At t = 65,095 s, while $T_{base} = 1.3 \times 10^9$ K, the main nuclear path reaches ^{80}Zr (see Fig. 4.23). Because of the large temperature achieved, the number of proton- and α-captures increases, which in turn efficiently reduces the H (0.621) and ^{4}He (0.197) abundances. The next most abundant nucleus is now ^{60}Zn (2.8×10^{-2}), followed by ^{64}Ge (2.3×10^{-2}), ^{38}Ca (1.8×10^{-2}), ^{30}S (1.6×10^{-2}), ^{55}Ni (1.2×10^{-2}), and ^{59}Zn (1.1×10^{-2}), plus a handful of species with mass fractions $\sim 10^{-3}$, such as ^{33,34}Ar, ^{28,29}S, ^{36,37}Ca, ^{48,49,50}Fe, ^{53,54,56}Ni, ^{44,45,46}Cr, ^{62,63}Ge, ^{58}Zn, ^{41}Ti, and ^{68}Se. As before, the largest reaction fluxes correspond to a suite of quasiequilibrium processes, such as ^{29,30}S(p, γ)^{30,31}Cl(γ, p)^{29,30}S, ^{26}Si(p, γ)^{27}P(γ, p)^{26}Si, ^{59,60}Zn(p, γ)^{60,61}Ga(γ, p)^{59,60}Zn, ^{45,46}Cr(p, γ)^{46,47}Mn(γ, p)^{45,46}Cr, ^{38}Ca(p, γ)^{39}Sc(γ, p)^{38}Ca, ^{41,42}Ti(p, γ)^{42,43}V(γ, p)^{41,42}Ti, ^{49,50}Fe(p, γ)^{50,51}Co(γ, p)^{49,50}Fe, ^{54,55}Ni(p, γ)^{55,56}Cu(γ, p)^{54,55}Ni, ^{16}O(p, γ)^{17}F(γ, p)^{16}O, ^{33}Ar(p, γ)^{34}K(γ, p)^{33}Ar, or ^{63,64}Ge(p, γ)^{64,65}As(γ, p)^{63,64}Ge.

Shortly after, at t = 65,098 s, a peak temperature of $T_{peak} = 1.4 \times 10^9$ K is achieved at the envelope base. This was followed, less than a second later, by a maximum expansion of the envelope, $\Delta z_{max} \sim 73.9$ m, and by a maximum luminosity, $L_{max} = 4.0 \times 10^{38}$ erg.s^{-1} (10^5 L$_\odot$). The main nuclear path reaches ^{93}Pd (already beyond the nucleosynthetic endpoint achieved in Model 1; see Fig. 4.24). With respect to the chemical abundances, the envelope base is still dominated by H (0.560) and ^{4}He (0.175), with ^{60}Zn reaching a mass fraction of 0.111. The next most abundant species are ^{64}Ge (6.3×10^{-2}), and ^{68}Se (2×10^{-2}). As before, a suite of nuclei reach $\sim 10^{-3}$ (^{34}Ar, ^{58,59}Zn, ^{37,38}Ca, ^{53,54,55,56}Ni, ^{49,50}Fe, ^{30}S, ^{62,63}Ge, ^{45,46}Cr, and ^{67}Se). The most relevant quasiequilibrium processes that achieve the largest reaction fluxes are depicted in Fig. 4.24.

At t=65,110 s, following the decline from peak temperature, the envelope base achieves $T_{base} = 1.3 \times 10^9$ K (Fig. 4.25). At this stage, the main nuclear activity has already reached the SnSbTe-mass region (^{104}Sn, in particular). The chemical abundances at the envelope base are still dominated by H (0.471), now followed by ^{64}Ge (0.162), and ^{68}Se (0.161), while ^{4}He has dropped to 0.131. The next most abundant species shift to ^{60}Zn (2.1×10^{-2}), and ^{72}Kr (1.9×10^{-2}), with a suite of nuclei reaching $\sim 10^{-3}$ (^{30}S, ^{67}Se, ^{37,38}Ca, ^{76}Sr, ^{62,63}Ge, ^{59}Zn, ^{55}Ni, ^{34}Ar, or ^{50}Fe). At this stage, the main quasiequilibrium processes correspond to ^{29,30}S(p, γ)^{30,31}Cl(γ, p)^{29,30}S, ^{26}Si(p, γ)^{27}P(γ, p)^{26}Si, ^{59,60}Zn(p, γ)^{60,61}Ga(γ, p)^{59,60}Zn, ^{45,46}Cr(p, γ)^{46,47}Mn(γ, p)^{45,46}Cr, ^{38}Ca(p, γ)^{39}Sc(γ, p)^{38}Ca, ^{41,42}Ti(p, γ)^{42,43}V(γ, p)^{41,42}Ti, ^{49,50}Fe(p, γ)^{50,51}Co(γ, p)^{49,50}Fe, ^{54,55}Ni(p, γ)^{55,56}Cu(γ, p)^{54,55}Ni, ^{16}O(p, γ)^{17}F(γ, p)^{16}O, ^{68}Se(p, γ)^{69}Br(γ,

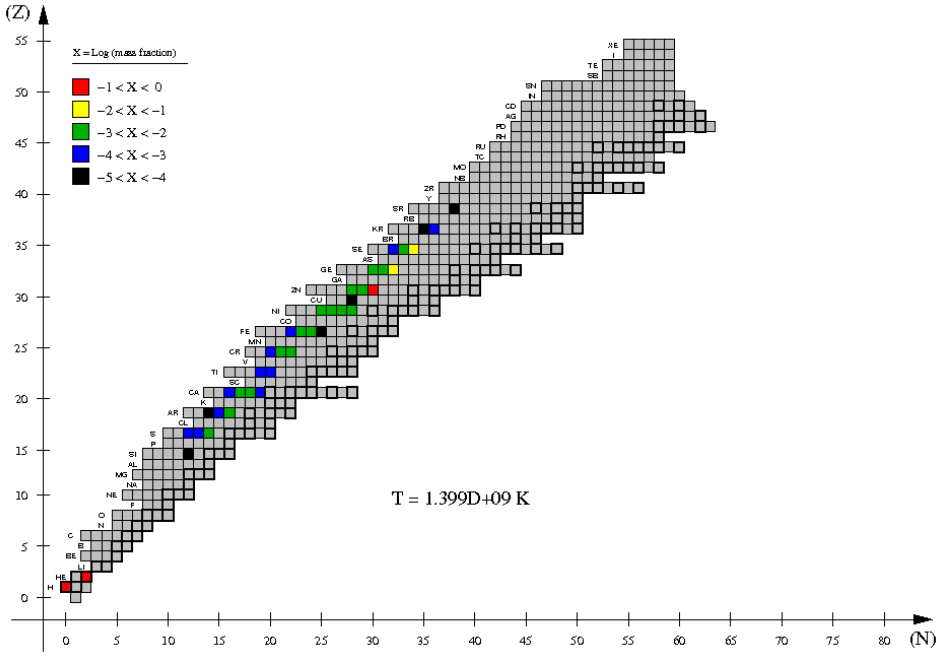

(a)

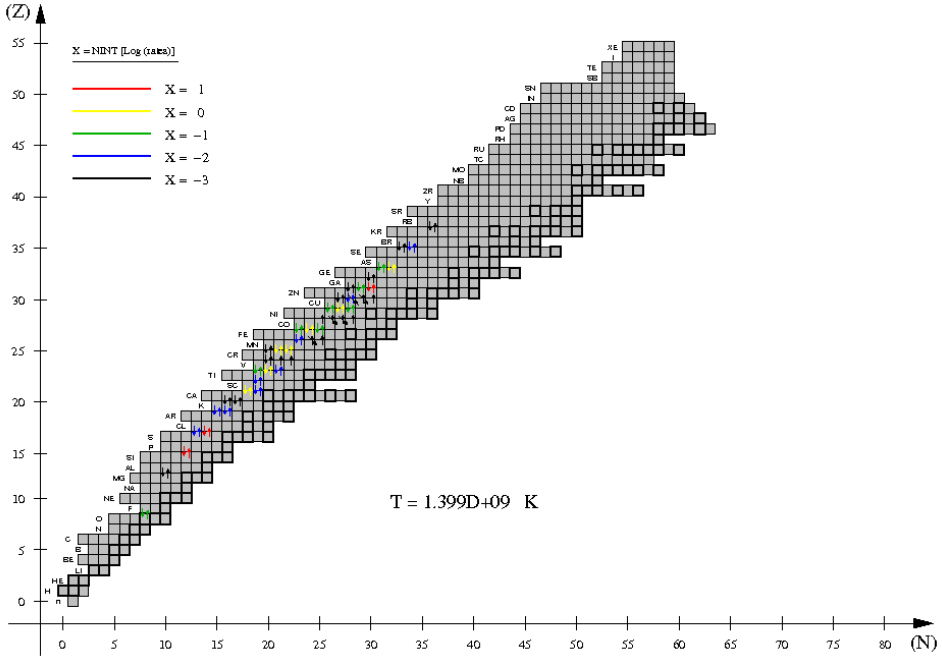

(b)

Figure 4.24: Same as Fig. 4.22, but for the time when temperature at the envelope base reaches a peak value of $T_{peak} = 1.4 \times 10^9$ K.

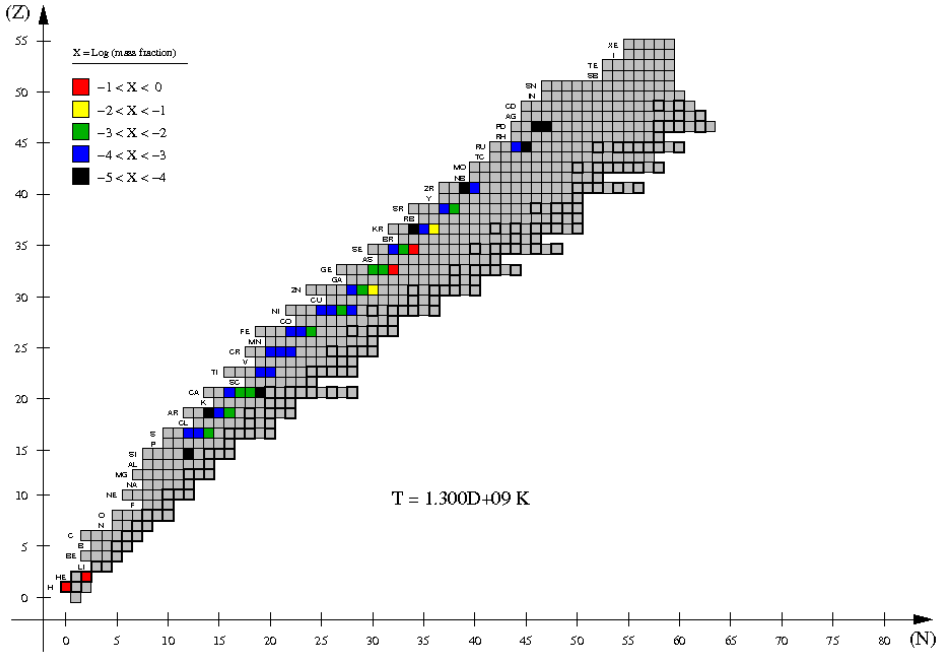

(a)

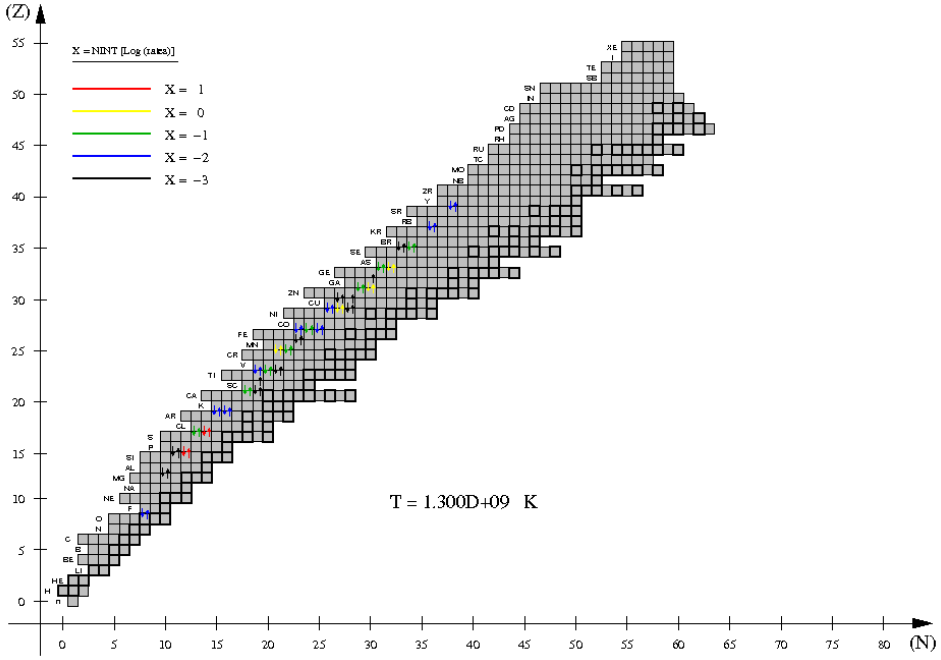

(b)

Figure 4.25: Same as Fig. 4.22, but for $T_{base} = 1.3 \times 10^9$ K.

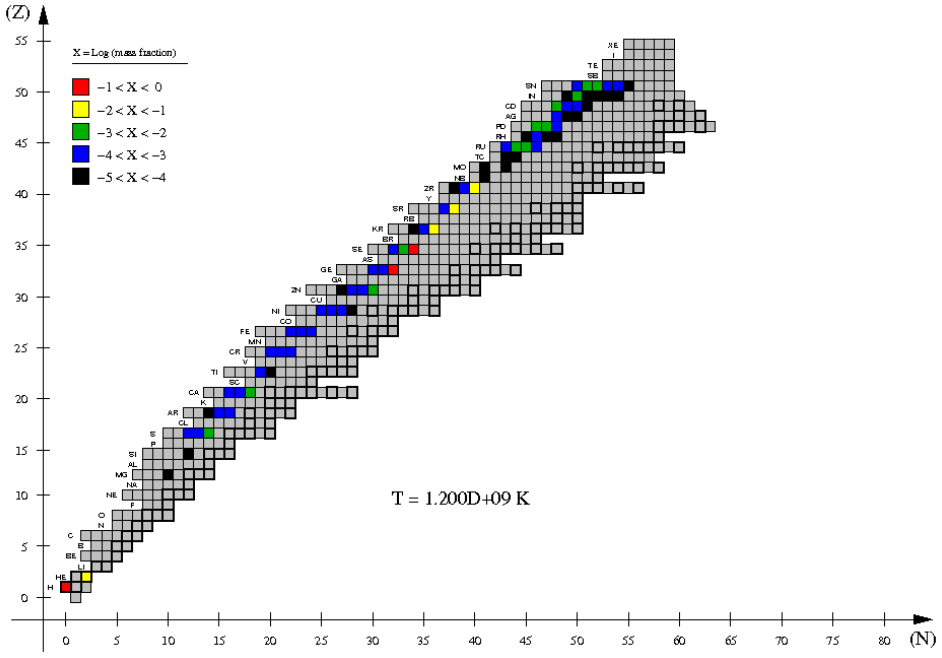

(a)

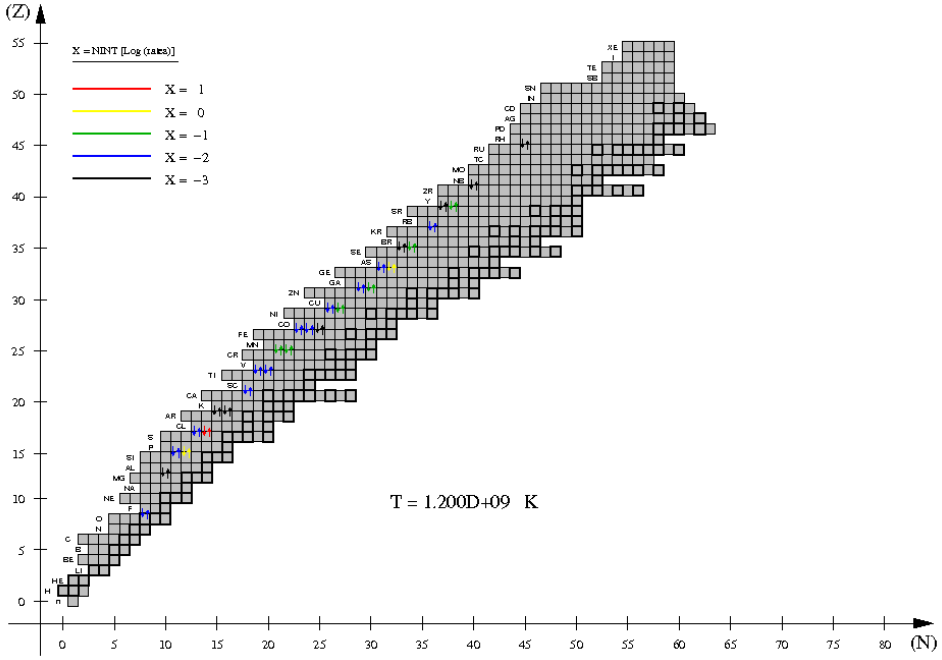

(b)

Figure 4.26: Same as Fig. 4.22, but for $T_{base} = 1.2 \times 10^9$ K.

p)^{68}Se, or ^{63,64}Ge(p, γ)^{64,65}As(γ, p)^{63,64}Ge. It is worth noting that the most important α-capture reaction, the triple-α, has a flux $\sim 10^{-4}$, an order of magnitude smaller than the minimum value shown in Fig. 4.24(b).

Twenty-two seconds later (t=65,132 s), the temperature at the envelope base has decreased to $T_{base} = 1.2\times10^9$ K (Fig. 4.26). The H content has been slightly reduced to 0.370, whereas ^{4}He reaches 8.74×10^{-2}. Indeed, after H, the most abundant species at the envelope base are now ^{68}Se (0.270), and ^{64}Ge (0.104), followed by ^{72}Kr (8.7×10^{-2}), ^{76}Sr (2.8×10^{-2}), and ^{80}Zr (1.2×10^{-2}). At this stage, some of the heaviest species of the network have already achieved an abundance of $\sim 10^{-3}$ (such as ^{88,89}Ru, ^{92,93}Pd, ^{96}Cd, ^{99}In, or ^{101,102}Sn, together with the lighter nuclei ^{30}S, ^{38}Ca, ^{59,60}Zn, and ^{67}Se), with the nuclear activity extending all the way up to ^{107}Te.

At t=65,264 s, following the temperature decline, the envelope base achieves $T_{base} = 10^9$ K (Fig. 4.27). Now, the most abundant element at the envelope base is ^{105}Sn (0.228), followed by a large number of species with abundances $\sim 10^{-2}$, such as ^{104}Sn (9.9×10^{-2}), ^{68}Se (7.2×10^{-2}), ^{72}Kr (5.1×10^{-2}), ^{104}In (5×10^{-2}), ^{94}Pd (4.6×10^{-2}), ^{64}Ge (4.5×10^{-2}), ^{103}In (3.7×10^{-2}), ^{76}Sr (3.3×10^{-2}) –all more abundant than H (1.8×10^{-2}) and ^{4}He (2.6×10^{-2}), at this stage–, ^{103}Sn (2.3×10^{-2}), ^{95}Ag (2.3×10^{-2}), ^{107}Te (2.2×10^{-2}), ^{102}In (2.1×10^{-2}), ^{101}In (2×10^{-2}), ^{80}Zr (1.9×10^{-2}), ^{100}In (1.7×10^{-2}), ^{60}Zn (1.6×10^{-2}), ^{98}Cd (1.3×10^{-2}), ^{99}Cd (1.2×10^{-2}), and ^{102}Sn (1.1×10^{-2}). Notice that, since the heaviest element included in our network, ^{107}Te, achieved already an abundance of 2.2×10^{-2}, leakage from the SnSbTe-mass region cannot be discarded. As before, the largest reaction fluxes correspond to a suite of quasiequilibrium processes, such as ^{29,30}S(p, γ)^{30,31}Cl(γ, p)^{29,30}S, ^{25,26}Si(p, γ)^{26,27}P(γ, p)^{25,26}Si, ^{59,60}Zn(p, γ)^{60,61}Ga(γ, p)^{59,60}Zn, ^{45,46}Cr(p, γ)^{46,47}Mn(γ, p)^{45,46}Cr, ^{38}Ca(p, γ)^{39}Sc(γ, p)^{38}Ca, ^{42}Ti(p, γ)^{43}V(γ, p)^{42}Ti, ^{49,50,51}Fe(p, γ)^{50,51,52}Co(γ, p)^{49,50,51}Fe, ^{55}Ni(p, γ)^{56}Cu(γ, p)^{55}Ni, ^{16}O(p, γ)^{17}F(γ, p)^{16}O, ^{76}Sr(p, γ)^{77}Y(γ, p)^{76}Sr, ^{68}Se(p, γ)^{69}Br(γ, p)^{68}Se, ^{72}Kr(p, γ)^{73}Rb(γ, p)^{72}Kr, ^{21,22}Mg(p, γ)^{22,23}Al(γ, p)^{21,22}Mg, or ^{64}Ge(p, γ)^{65}As(γ, p)^{64}Ge. These reactions are accompanied by a handful of β^+-decays (such as ^{80}Zr(β^+)^{80}Y, ^{76}Sr(β^+)^{76}Rb, ^{84}Mo(β^+)^{84}Nb, and ^{82}Nb(β^+)^{82}Zr), since H depletion and the decrease in temperature limit the extent of charged-particle reactions. Indeed, these weak interactions will become progressively relevant during the last stages of the burst.

At t=65,362 s, the temperature at the envelope base has already declined to $T_{base} = 7.6 \times 10^8$ K (Fig. 4.28). H is fully depleted (7.6×10^{-12}), while ^{4}He barely reaches 1.8×10^{-2}. As before, the most abundant element at the envelope base is ^{105}Sn (0.251), followed by ^{104}In (0.142), and by a large number of species with abundances $\sim 10^{-2}$ (including the daughter nuclei of some of the short-lived, β^+-unstable nuclei listed above), such as ^{94}Pd (7.5×10^{-2}), ^{103}In (5.9×10^{-2}), ^{68}As (3.4×10^{-2}), ^{102}In (3×10^{-2}), ^{101}In(2.6×10^{-2}), ^{76}Rb (2.3×10^{-2}) ^{72}Br (2.2×10^{-2}), ^{107}Te (2.2×10^{-2}), ^{100}In (2×10^{-2}), ^{64}Ga (1.7×10^{-2}), ^{64}Ge (1.7×10^{-2}), ^{99}Cd (1.6×10^{-2}), ^{98}Ag (1.6×10^{-2}), ^{89}Ru (1.5×10^{-2}), ^{80}Y (1.4×10^{-2}), ^{72}Se (1.3×10^{-2}), ^{60}Zn (1.3×10^{-2}),

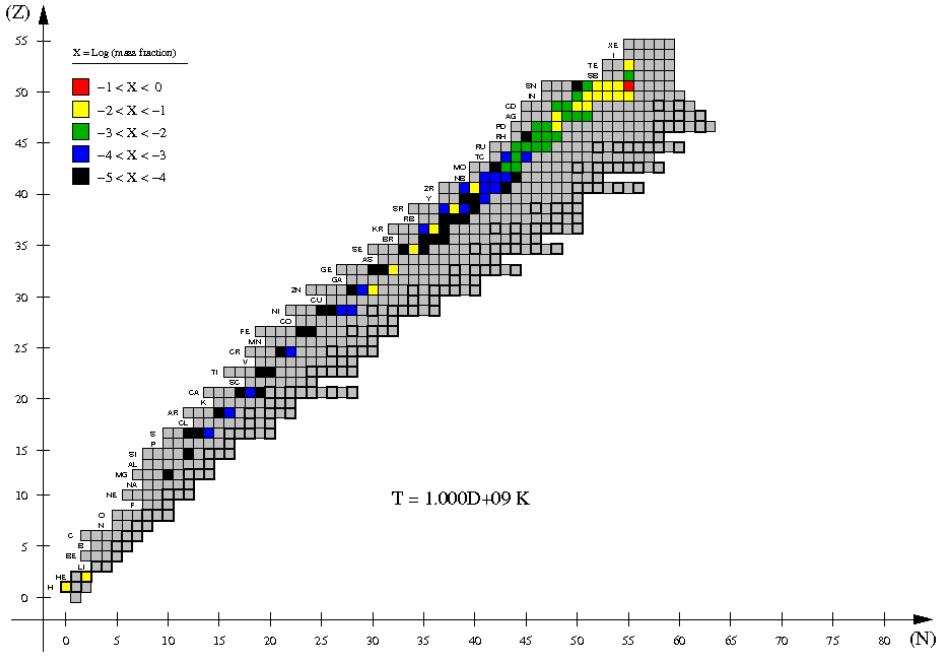

(a)

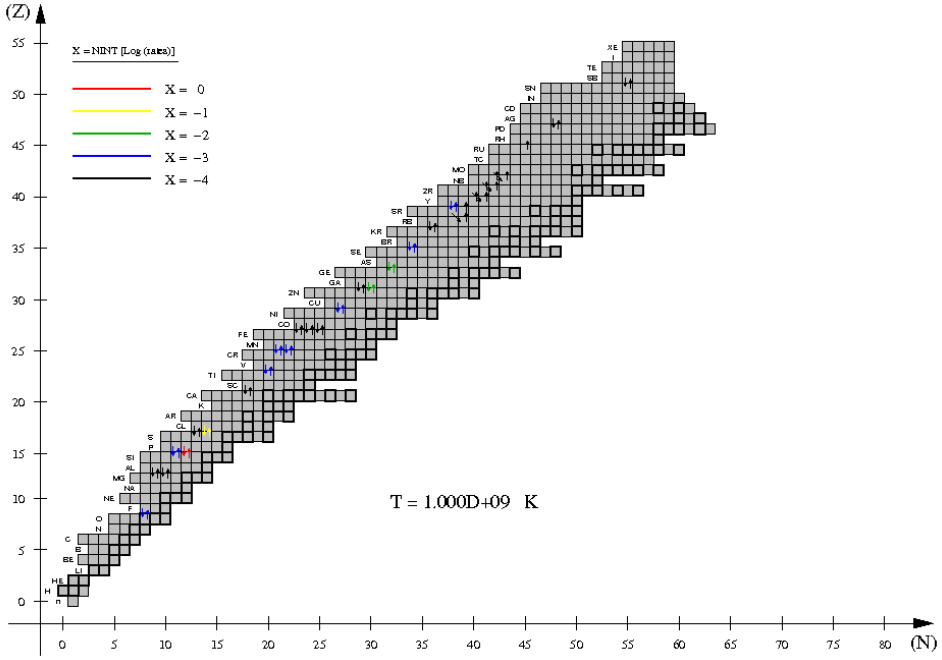

(b)

Figure 4.27: Same as Fig. 4.22, but for $T_{base} = 10^9$ K.

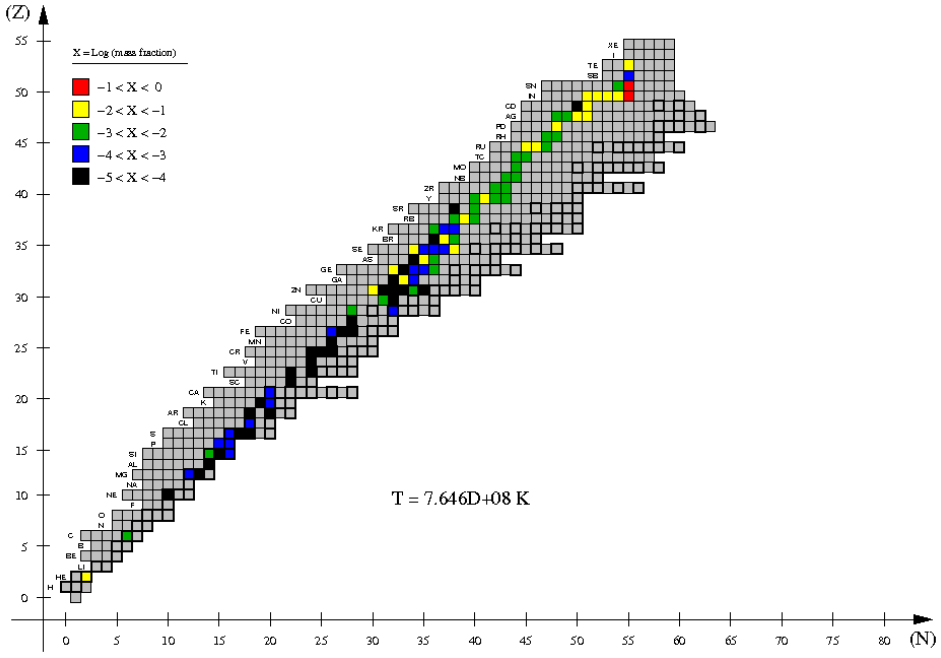

(a)

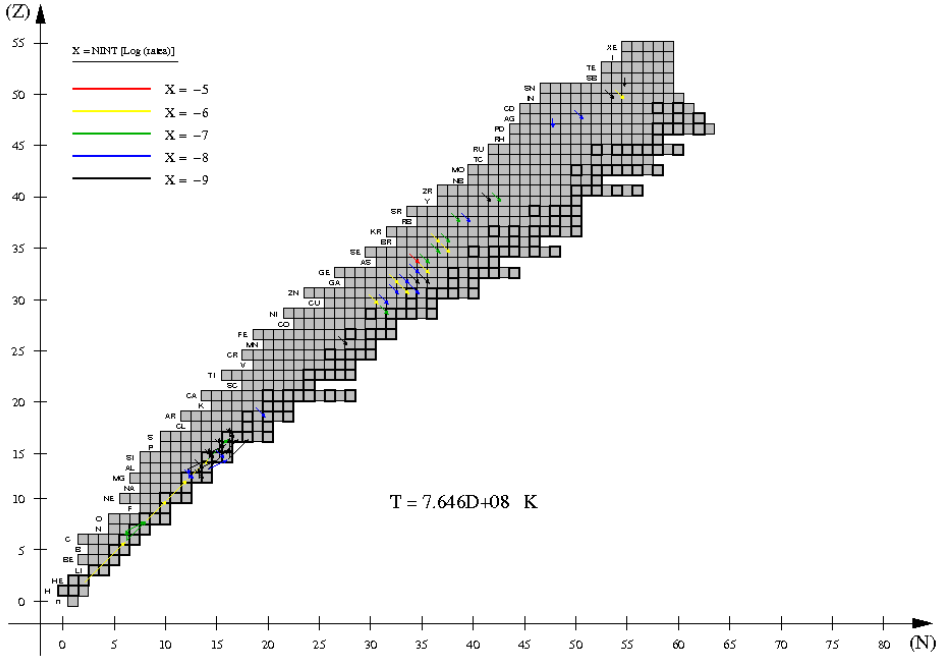

(b)

Figure 4.28: Same as Fig. 4.22, but for $T_{base} = 7.6 \times 10^8$ K.

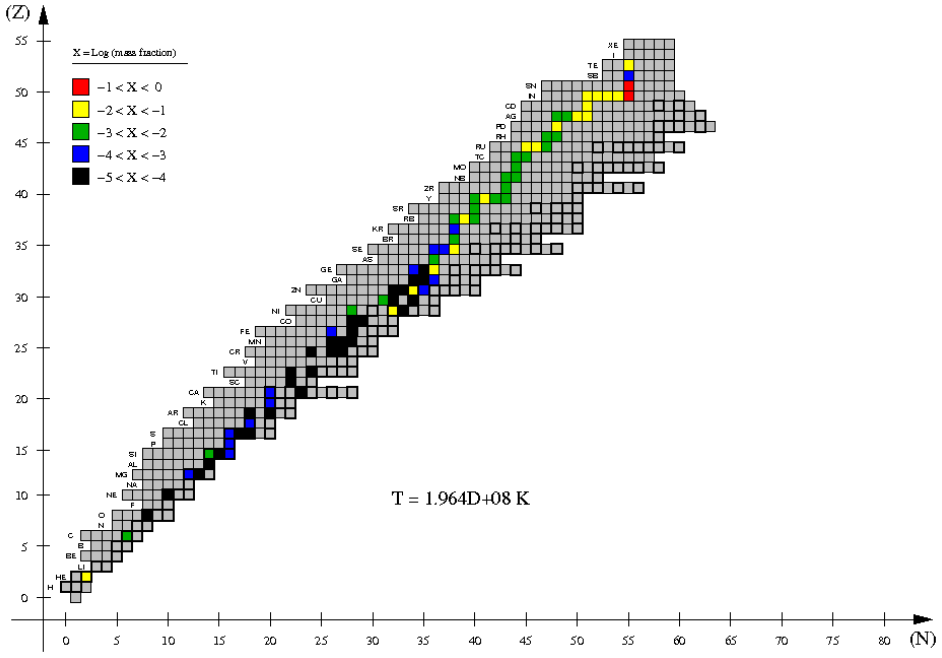

(a)

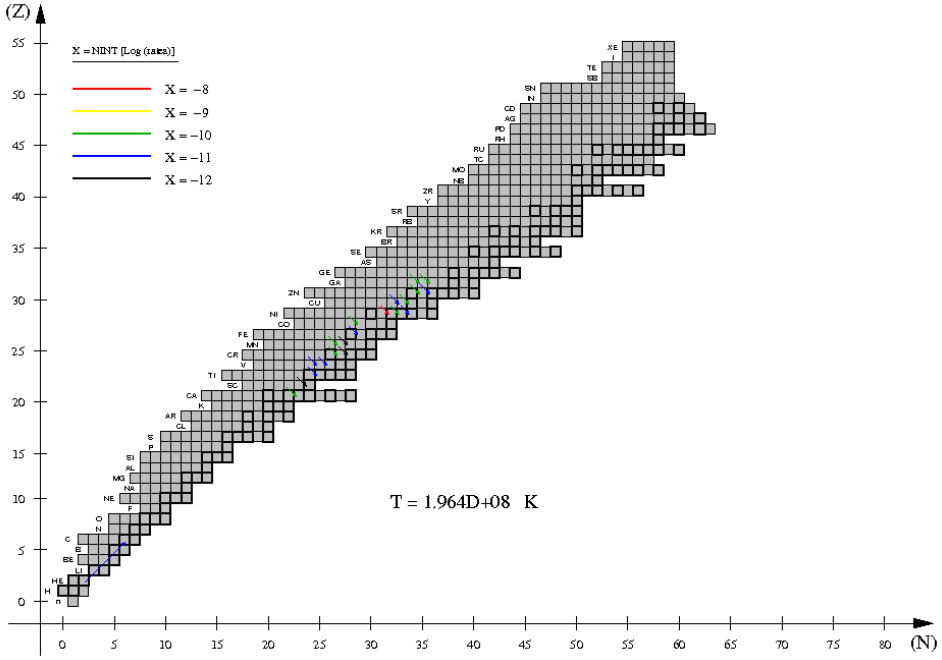

(b)

Figure 4.29: Same as Fig. 4.22, but for the time when the temperature at the envelope base achieves a minimum value of $T_{min} = 2 \times 10^8$ K.

^{68}Se (1.3×10^{-2}), ^{90}Ru (10^{-2}), and ^{97}Ag (10^{-2}). The depletion of H dramatically reduces the fluxes of most of the (p, γ) reactions, now overcome by many β^+-decays (such as ^{68,69}Se(β^+)^{68,69}As, ^{68}As(β^+)^{68}Ge, ^{64}Ge(β^+)^{64}Ga, ^{71,72}Br(β^+)^{71,72}Se, ^{60}Zn(β^+)^{60}Cu(β^+)^{60}Ni, ^{72,73}Kr(β^+)^{72,73}Br, ^{104}Sn(β^+)^{104}In, ^{64}Ga(β^+)^{64}Zn, ^{82}Zr(β^+) ^{82}Y, or ^{76}Sr(β^+)^{76}Rb), and the chain of α-captures $3\alpha \rightarrow ^{12}$C($\alpha$, γ)^{16}O(α, γ)^{20}Ne(α, γ)^{24}Mg(α, γ)^{28}Si(α, γ)^{32}S, or ^{13}N(α, p)^{16}O.

At t=69,715 s, after a long decline, a minimum temperature is achieved at the envelope base, $T_{base} = 2 \times 10^8$ K (Fig. 4.29), which somewhat marks the end of the first bursting episode for this model. At this stage, H is fully depleted (3.2×10^{-23}) at the envelope base, while ^{4}He is only 1.5×10^{-2}. The distribution of most abundant elements almost follows the one described for $T_{base} = 7.6 \times 10^8$ K (Fig. 4.28), and is dominated by ^{105}Sn (0.251), followed by ^{104}In (0.147), and by a large number of species with abundances $\sim 10^{-2}$, such as ^{94}Pd (7.5×10^{-2}), ^{103}In (5.9×10^{-2}), ^{68}Ge (5.4×10^{-2}), ^{64}Zn (3.7×10^{-2}), ^{72}Se (3.7×10^{-2}), ^{102}In (3×10^{-2}), ^{101}In(2.6×10^{-2}), ^{76}Rb (2.3×10^{-2}) ^{107}Te (2.2×10^{-2}), ^{100}In (2×10^{-2}), ^{60}Ni (1.7×10^{-2}), ^{99}Cd (1.6×10^{-2}), ^{98}Ag (1.6×10^{-2}), ^{89}Ru (1.5×10^{-2}), ^{80}Y (1.4×10^{-2}), ^{90}Ru (10^{-2}), and ^{97}Ag (10^{-2}). The list of isotopes that achieve a mass fraction of 10^{-3} at the envelope base, at the end of this first burst, includes ^{87,88}Tc, ^{92,93}Rh, ^{86}Mo, ^{95,96}Ag, ^{91}Ru, ^{79,81,82}Y, ^{84,85}Nb, ^{83}Zr, ^{69}As, ^{12}C, ^{56}Ni, ^{28}Si, ^{75,77}Rb, ^{60}Cu, ^{73}Br, and ^{78}Sr. At this stage, the dominant reactions are all β^+-decays (^{60,61}Cu(β^+)^{60,61}Ni, ^{66,67}Ge(β^+)^{66,67}Ga, ^{65}Ga(β^+)^{65}Zn, ^{51}Mn(β^+)^{51}Cr, ^{52}Fe(β^+)^{52}Mn, ^{63}Zn(β^+)^{63}Cu, ^{56}Ni(β^+)^{56}Co, or ^{43}Sc(β^+)^{43}Ca), except for the triple-α reaction.

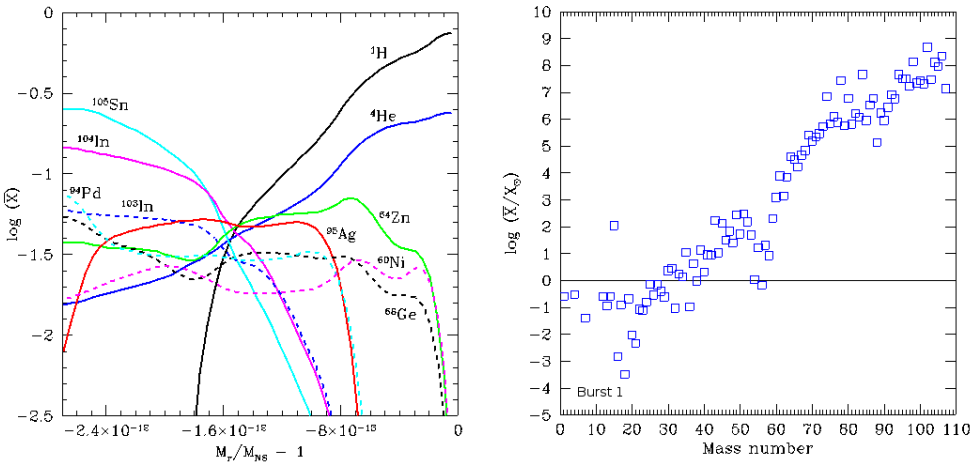

(a) (b)

Figure 4.30: Left panel: mass fractions of the ten most abundant stable (or $\tau > 1$ hr) isotopes, at the end of the first burst, for Model 3. Right panel: same as left panel, but for overproduction factors relative to solar (for $f > 10^{-5}$).

The mean, mass-averaged chemical composition of the whole envelope, at the end of the first bursting episode, is dominated by the presence of unburned H (0.18) and ^{4}He (0.084), followed by ^{105}Ag (0.075), ^{104}Pd (0.053), ^{64}Zn (0.042), ^{95}Ru (0.031), ^{68}Ge (0.028), ^{94}Tc (0.026), and ^{103}Ag (0.026) (see Table 4.8, for the mean composition of species -stable or with a half-life $>$ 1 hr- which achieve $X_i > 10^{-9}$), with a nucleosynthetic endpoint (defined as the heaviest isotope with $X_i > 10^{-9}$) around ^{107}Cd. In contrast, the first burst computed in Model 1 yielded, in general, lighter nuclei (^{60}Ni, ^{4}He, ^{1}H, ^{64}Zn, ^{12}C, and ^{52,56}Fe), with a more modest nucleosynthetic endpoint around ^{89}Nb (see Table 4.2). As reported as well for Model 1, the amount of unburned ^{12}C, left over at the end of the first burst ($\sim 7.7 \times 10^{-4}$, by mass), turns out to be too small to power a superburst.

In terms of overproduction factors (see Fig. 4.30), while Model 1 showed moderate values ($f \sim 10^4$) for a handful of intermediate-mass elements, such as ^{43}Ca, ^{45}Sc, ^{49}Ti, ^{51}V, ^{60,61}Ni, ^{63,65}Cu, ^{64,67,68}Zn, ^{69}Ga, ^{74}Se, or ^{78}Kr, Model 3 achieves moderate overproduction factors ($\geq 10^4$), for all stable species $>^{64}$Zn, and as high as $\sim 10^8$ for ^{98}Ru, ^{102,104}Pd, and ^{106}Cd.

4.3.2 Second, third, fourth, and fifth bursts

In this Section, we will report on the main properties of the following bursting episodes computed for Model 3, stressing the differences between Model 1 (evolved with a solar metallicity envelope) and Model 3 (for which a metal-deficient -$Z_{\odot}$/20- envelope was assumed).

Table 4.7: Summary of burst properties for Model 3.

Burst	T_{peak} (K)	t(T_{peak}) (s)	τ_{rec} (hr)	L_{peak} ($L_{\odot}$)	$\tau_{0.01}$ (s)	α
1	1.40×10^9	65110	18.1	1.0×10^5	423	34
2	1.39×10^9	98879	9.4	1.1×10^5	296	24
3	1.32×10^9	130816	8.9	9.8×10^4	281	24
4	1.30×10^9	162777	8.9	1.0×10^5	252	27
5	1.26×10^9	194266	8.8	1.0×10^5	250	30

Table 4.7 summarizes the most relevant properties that characterize the five bursting episodes computed for Model 3. Recurrence times between bursts around $\tau_{rec} \sim 9^{hr}$ (except for the first one, for which $\tau_{rec} \sim 18^{hr}$), persistent over burst luminosity ratios around $\alpha \sim 20 - 30$, and peak luminosities around $L_{peak} \sim 10^5 L_{\odot}$, represent the basic observables associated with this model. Indeed, the recurrence times obtained are in agreement with the values reported for the XRB sources (see Galloway et al. 2008) 1A 1905+00 [$\tau_{rec} = 8.9$ hr], 4U 1254-69 [$\tau_{rec} = 9.2$ hr], or XTE

J1710-281 [$\tau_{rec} = 8.9$ hr, $\alpha = 22 - 100$], A striking result is the quick stabilization of the recurrence times, that show a regular periodicity after the second burst.

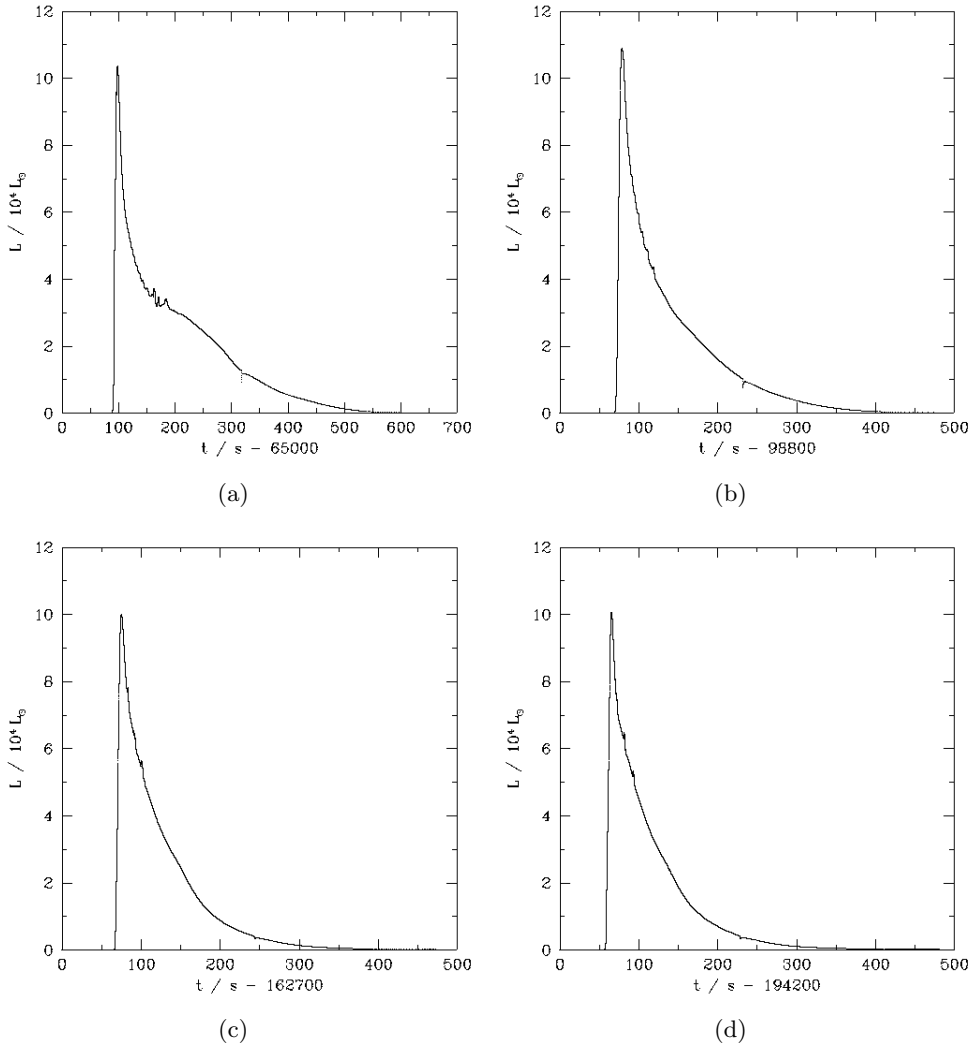

Figure 4.31: Light curves corresponding to the first (panel a), second (panel b), fourth (panel c), and fifth bursts (panel d), obtained for Model 3.

It is worth noting that the recurrence periods are larger and the persistent over burst luminosity ratios are lower than those reported for Model 1, showing a clear dependence with the metallicity of the accreted material: the smaller the metal content, the larger the recurrence time (and the smaller the α).

The corresponding light curves (4.31) exhibit, in turn, a clear pattern. As shown in Fig. 4.32(a), where light curves of the third bursting episodes computed in Mod-

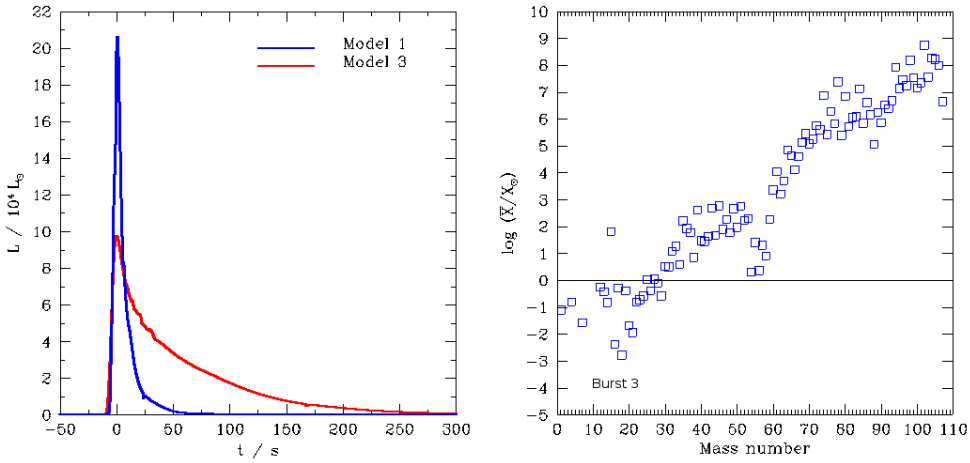

(a) (b)

Figure 4.32: Left panel: light curve comparison for the third burst computed in Models 1 & 3. Right panel: overproduction factors relative to solar (for $f > 10^{-5}$), at the end of the third burst, for Model 3.

els 1 & 3 are compared, explosions in metal-deficient envelopes (i.e., Model 3) are characterized by lower peak luminosities and longer decline times. A similar pattern has been reported by Heger et al. (2007), in the framework of 1-D, hydrodynamic models of XRBs performed with the KEPLER code. It is worth noting that no double-peaked bursts have been obtained in Model 3.

Larger peak temperatures, around $T_{peak} \sim (1.3 - 1.4) \times 10^9$ K, are also obtained in Model 3. This, together with the longer exposure times to high temperatures (driven by a slower decline phase) cause a dramatic extension of the main nuclear path towards the SnSbTe-mass region (or beyond)[5].

From the nucleosynthetic viewpoint, and as shown in Table 4.8 and Fig. 4.32(b), the nuclear activity already reaches the end of the network (^{107}Te) at the last stages of the first bursting episode. As for Model 1, the overall mean metallicity of the envelope increases with the burst number (0.74 [1^{st} burst], 0.85 [2^{nd} burst], 0.90 [3^{rd} burst], 0.92 [4^{th} burst], and 0.93 [5^{th} burst]), while the H and ^{4}He contents are progressively reduced. Notice that, although the accreted material is more metal-deficient in Model 3 than in Model 1, the post-burst mean metallicity of the envelope

[5]We are currently computing another series of type I XRBs driven by accretion of extremely metal-poor material (with $Z \sim 10^{-5}$) onto a 1.4 M$_\odot$ neutron star. This model, which somehow mimics accretion conditions in very primitive stellar binaries, is characterized by larger peak temperatures ($T_{peak} \sim 2 \times 10^9$ K) and recurrence times (57^{hr}, for the first burst), in agreement with the metallicity dependence discussed above for Models 1 and 3. Results from this model will be reported in a forthcoming publication.

is larger in Model 3, since the combination of higher temperatures and longer burst durations (driven by much slower decline phases) favors CNO-breakout. A final ^{12}C yield of $\sim 2 \times 10^{-3}$ is obtained at the end of each bursting episode (except the first one, for which the final ^{12}C content is a factor of ~ 3 smaller). Finally, huge overproduction factors (see Fig. 4.32b), involving heavy species such as ^{102,104,105}Pd, ^{98}Ru, or ^{94}Mo (with $f \sim 10^8$, at the end of the fifth burst), have been obtained in Model 3, in contrast with the somewhat more modest values achieved in Model 1, with maximum overproduction factors about $f \sim 10^6$ (at the end of the fourth burst), and involving lighter species, such as ^{76}Se, ^{78,80}Kr, and ^{84}Sr.

Table 4.8: Mean composition of the envelope ($X_i > 10^{-9}$) at the end of each burst, for Model 1.

Nucleus	Burst 1	Burst 2	Burst 3	Burst 4	Burst 5
^{1}H	1.8×10^{-1}	8.6×10^{-2}	5.5×10^{-2}	4.5×10^{-2}	3.7×10^{-2}
^{4}He	8.4×10^{-2}	5.8×10^{-2}	4.4×10^{-2}	3.8×10^{-2}	3.3×10^{-2}
^{12}C	7.7×10^{-4}	1.7×10^{-3}	1.8×10^{-3}	1.7×10^{-3}	1.5×10^{-3}
^{13}C	4.2×10^{-6}	8.9×10^{-6}	1.4×10^{-5}	2.3×10^{-5}	2.7×10^{-5}
^{14}N	2.8×10^{-4}	2.1×10^{-4}	1.7×10^{-4}	1.5×10^{-4}	1.4×10^{-4}
^{15}N	4.9×10^{-4}	3.6×10^{-4}	2.9×10^{-4}	2.4×10^{-4}	2.2×10^{-4}
^{16}O	1.4×10^{-5}	2.9×10^{-5}	4.1×10^{-5}	3.7×10^{-5}	3.8×10^{-5}
^{17}O	4.8×10^{-7}	6.8×10^{-7}	2.1×10^{-6}	1.3×10^{-6}	2.0×10^{-6}
^{18}O	-	3.7×10^{-9}	9.4×10^{-9}	9.5×10^{-9}	8.1×10^{-9}
^{18}F	6.4×10^{-9}	1.3×10^{-8}	2.8×10^{-8}	2.4×10^{-8}	2.3×10^{-8}
^{19}F	8.7×10^{-8}	1.6×10^{-7}	1.7×10^{-7}	2.0×10^{-7}	8.0×10^{-8}
^{20}Ne	1.5×10^{-5}	2.9×10^{-5}	3.5×10^{-5}	3.0×10^{-5}	3.1×10^{-5}
^{21}Ne	1.9×10^{-8}	4.4×10^{-8}	4.9×10^{-8}	5.2×10^{-8}	4.4×10^{-8}
^{22}Ne	2.9×10^{-7}	6.6×10^{-7}	4.3×10^{-7}	1.1×10^{-6}	7.5×10^{-7}
^{22}Na	1.1×10^{-5}	2.4×10^{-5}	2.0×10^{-5}	2.3×10^{-5}	1.9×10^{-5}
^{23}Na	2.6×10^{-6}	6.5×10^{-6}	6.5×10^{-6}	6.5×10^{-6}	5.7×10^{-6}
^{24}Mg	8.2×10^{-5}	1.4×10^{-4}	1.4×10^{-4}	1.2×10^{-4}	1.1×10^{-4}
^{25}Mg	4.9×10^{-5}	7.3×10^{-5}	7.4×10^{-5}	7.2×10^{-5}	6.6×10^{-5}
^{26}Mg	1.1×10^{-5}	1.9×10^{-5}	1.8×10^{-5}	2.2×10^{-5}	2.0×10^{-5}
^{26}Al^{g}	1.2×10^{-5}	1.4×10^{-5}	1.3×10^{-5}	1.2×10^{-5}	1.1×10^{-5}
^{27}Al	4.1×10^{-5}	6.3×10^{-5}	6.5×10^{-5}	6.8×10^{-5}	6.2×10^{-5}
^{28}Si	2.6×10^{-4}	6.2×10^{-4}	5.2×10^{-4}	3.9×10^{-4}	3.6×10^{-4}
^{29}Si	8.6×10^{-6}	1.1×10^{-5}	9.2×10^{-6}	1.3×10^{-5}	1.1×10^{-5}
^{30}Si	5.5×10^{-5}	8.8×10^{-5}	8.0×10^{-5}	1.1×10^{-4}	9.9×10^{-5}
^{31}P	2.3×10^{-5}	3.6×10^{-5}	2.6×10^{-5}	3.2×10^{-5}	2.6×10^{-5}
^{32}S	3.7×10^{-5}	2.1×10^{-3}	4.9×10^{-3}	5.8×10^{-3}	7.7×10^{-3}
^{33}S	5.7×10^{-6}	4.2×10^{-5}	6.1×10^{-5}	5.6×10^{-5}	9.2×10^{-5}

Table 4.8: – Continued.

Nucleus	Burst 1	Burst 2	Burst 3	Burst 4	Burst 5
^{34}S	2.6×10^{-5}	6.7×10^{-5}	7.2×10^{-5}	7.3×10^{-5}	7.5×10^{-5}
^{35}Cl	2.9×10^{-5}	1.5×10^{-4}	4.2×10^{-4}	5.0×10^{-4}	5.9×10^{-4}
^{36}Ar	8.2×10^{-6}	2.9×10^{-3}	6.8×10^{-3}	9.9×10^{-3}	1.2×10^{-2}
^{37}Cl	3.5×10^{-9}	2.8×10^{-8}	5.4×10^{-8}	1.5×10^{-7}	2.2×10^{-7}
^{37}Ar	3.7×10^{-6}	2.6×10^{-5}	5.1×10^{-5}	1.1×10^{-4}	1.6×10^{-4}
^{38}Ar	1.5×10^{-5}	6.4×10^{-5}	1.1×10^{-4}	1.7×10^{-4}	2.0×10^{-4}
^{39}K	4.7×10^{-5}	9.4×10^{-4}	1.4×10^{-3}	2.1×10^{-3}	2.5×10^{-3}
^{40}Ca	1.3×10^{-4}	1.3×10^{-3}	1.8×10^{-3}	2.3×10^{-3}	2.6×10^{-3}
^{41}K	-	-	-	-	1.1×10^{-9}
^{41}Ca	2.5×10^{-6}	6.4×10^{-6}	7.7×10^{-6}	1.4×10^{-5}	1.7×10^{-5}
^{42}Ca	3.7×10^{-6}	1.6×10^{-5}	1.8×10^{-5}	3.3×10^{-5}	3.5×10^{-5}
^{43}Ca	3.3×10^{-6}	1.1×10^{-5}	1.0×10^{-5}	2.0×10^{-5}	2.6×10^{-5}
^{43}Sc	1.4×10^{-5}	4.0×10^{-5}	3.7×10^{-5}	5.3×10^{-5}	5.2×10^{-5}
^{44}Ca	-	4.2×10^{-9}	5.7×10^{-7}	1.6×10^{-6}	5.1×10^{-6}
^{44}Sc	6.0×10^{-9}	2.8×10^{-8}	2.2×10^{-6}	3.3×10^{-6}	9.2×10^{-6}
^{44}Ti	1.5×10^{-5}	4.9×10^{-5}	6.3×10^{-5}	8.0×10^{-5}	9.0×10^{-5}
^{45}Sc	1.2×10^{-6}	1.9×10^{-6}	6.0×10^{-6}	1.3×10^{-5}	2.3×10^{-5}
^{45}Ti	4.0×10^{-6}	6.0×10^{-6}	1.8×10^{-5}	1.9×10^{-5}	2.3×10^{-5}
^{46}Ti	7.0×10^{-6}	1.4×10^{-5}	1.8×10^{-5}	3.9×10^{-5}	5.4×10^{-5}
^{47}Ti	1.4×10^{-5}	3.0×10^{-5}	3.9×10^{-5}	5.7×10^{-5}	6.7×10^{-5}
^{48}Ti	2.6×10^{-9}	5.8×10^{-9}	4.9×10^{-8}	2.0×10^{-7}	5.4×10^{-7}
^{48}V	2.4×10^{-6}	4.8×10^{-6}	1.3×10^{-5}	2.7×10^{-5}	4.7×10^{-5}
^{48}Cr	5.2×10^{-5}	1.0×10^{-4}	1.2×10^{-4}	1.3×10^{-4}	1.3×10^{-4}
^{49}Ti	1.9×10^{-9}	2.2×10^{-8}	4.8×10^{-8}	8.3×10^{-8}	1.2×10^{-7}
^{49}V	4.7×10^{-5}	6.3×10^{-5}	7.9×10^{-5}	8.8×10^{-5}	9.5×10^{-5}
^{50}Cr	3.9×10^{-5}	5.7×10^{-5}	6.9×10^{-5}	1.0×10^{-4}	1.3×10^{-4}
^{51}V	5.3×10^{-8}	1.1×10^{-7}	3.2×10^{-7}	7.9×10^{-7}	1.7×10^{-6}
^{51}Cr	1.2×10^{-4}	1.9×10^{-4}	2.2×10^{-4}	2.7×10^{-4}	3.1×10^{-4}
^{52}Cr	5.6×10^{-7}	7.4×10^{-7}	4.0×10^{-6}	1.3×10^{-5}	2.8×10^{-5}
^{52}Mn	2.1×10^{-4}	2.5×10^{-4}	4.0×10^{-4}	6.0×10^{-4}	7.7×10^{-4}
^{52}Fe	2.1×10^{-3}	2.2×10^{-3}	2.1×10^{-3}	1.8×10^{-3}	1.6×10^{-3}
^{53}Mn	8.8×10^{-5}	2.1×10^{-4}	3.6×10^{-4}	4.0×10^{-4}	4.2×10^{-4}
^{54}Fe	7.7×10^{-5}	1.2×10^{-4}	1.5×10^{-4}	1.8×10^{-4}	1.9×10^{-4}
^{55}Mn	-	-	5.1×10^{-9}	1.6×10^{-8}	3.4×10^{-8}
^{55}Fe	1.0×10^{-5}	1.7×10^{-5}	4.5×10^{-5}	7.7×10^{-5}	1.1×10^{-4}
^{55}Co	2.2×10^{-4}	3.1×10^{-4}	3.0×10^{-4}	3.0×10^{-4}	2.9×10^{-4}
^{56}Fe	1.0×10^{-9}	1.3×10^{-8}	1.4×10^{-7}	4.7×10^{-7}	9.9×10^{-7}
^{56}Co	4.6×10^{-6}	2.2×10^{-5}	8.4×10^{-5}	1.6×10^{-4}	2.5×10^{-4}

Table 4.8: – Continued.

Nucleus	Burst 1	Burst 2	Burst 3	Burst 4	Burst 5
^{56}Ni	7.8×10^{-4}	2.1×10^{-3}	2.7×10^{-3}	3.3×10^{-3}	3.6×10^{-3}
^{57}Fe	-	3.3×10^{-8}	6.2×10^{-8}	1.0×10^{-7}	1.5×10^{-7}
^{57}Co	1.3×10^{-5}	1.5×10^{-5}	2.9×10^{-5}	4.8×10^{-5}	6.6×10^{-5}
^{57}Ni	5.6×10^{-4}	5.8×10^{-4}	5.7×10^{-4}	5.1×10^{-4}	4.8×10^{-4}
^{58}Ni	4.1×10^{-4}	4.0×10^{-4}	4.0×10^{-4}	3.7×10^{-4}	3.6×10^{-4}
^{59}Ni	6.9×10^{-4}	6.4×10^{-4}	6.3×10^{-4}	5.8×10^{-4}	5.7×10^{-4}
^{60}Ni	2.4×10^{-2}	3.7×10^{-2}	4.6×10^{-2}	5.2×10^{-2}	5.8×10^{-2}
^{61}Ni	1.5×10^{-3}	2.1×10^{-3}	3.8×10^{-3}	5.5×10^{-3}	6.3×10^{-3}
^{61}Cu	5.7×10^{-3}	6.9×10^{-3}	6.5×10^{-3}	4.7×10^{-3}	3.7×10^{-3}
^{62}Ni	3.3×10^{-4}	5.8×10^{-4}	1.4×10^{-3}	1.8×10^{-3}	2.0×10^{-3}
^{62}Zn	3.6×10^{-3}	4.4×10^{-3}	3.3×10^{-3}	2.3×10^{-3}	1.9×10^{-3}
^{63}Cu	4.1×10^{-3}	3.3×10^{-3}	2.9×10^{-3}	2.5×10^{-3}	2.5×10^{-3}
^{64}Zn	4.2×10^{-2}	5.6×10^{-2}	7.0×10^{-2}	8.1×10^{-2}	9.1×10^{-2}
^{65}Cu	8.1×10^{-7}	1.2×10^{-6}	4.9×10^{-6}	1.1×10^{-5}	1.7×10^{-5}
^{65}Zn	8.3×10^{-3}	9.7×10^{-3}	1.2×10^{-2}	1.2×10^{-2}	1.2×10^{-2}
^{66}Zn	1.3×10^{-4}	2.3×10^{-4}	9.9×10^{-4}	1.8×10^{-3}	2.3×10^{-3}
^{66}Ga	2.8×10^{-3}	2.7×10^{-3}	3.1×10^{-3}	2.7×10^{-3}	2.2×10^{-3}
^{66}Ge	6.8×10^{-3}	4.9×10^{-3}	3.8×10^{-3}	2.3×10^{-3}	1.9×10^{-3}
^{67}Ga	4.1×10^{-3}	3.4×10^{-3}	3.6×10^{-3}	3.2×10^{-3}	3.0×10^{-3}
^{68}Ge	2.8×10^{-2}	4.5×10^{-2}	5.6×10^{-2}	6.5×10^{-2}	7.1×10^{-2}
^{69}Ge	1.0×10^{-2}	1.0×10^{-3}	1.2×10^{-2}	1.1×10^{-2}	1.1×10^{-2}
^{70}Ge	6.5×10^{-3}	5.2×10^{-3}	5.3×10^{-3}	4.6×10^{-3}	4.2×10^{-3}
^{71}As	6.1×10^{-3}	4.8×10^{-3}	5.0×10^{-3}	4.4×10^{-3}	4.2×10^{-3}
^{72}Se	1.7×10^{-2}	2.8×10^{-2}	3.4×10^{-2}	3.8×10^{-2}	4.1×10^{-2}
^{73}Se	9.1×10^{-3}	6.5×10^{-3}	7.0×10^{-3}	6.4×10^{-3}	6.3×10^{-3}
^{74}Se	7.2×10^{-3}	6.5×10^{-3}	7.7×10^{-3}	7.4×10^{-3}	7.2×10^{-3}
^{75}Br	8.4×10^{-3}	4.5×10^{-3}	3.3×10^{-3}	2.2×10^{-3}	2.0×10^{-3}
^{76}Kr	1.3×10^{-2}	1.8×10^{-2}	2.0×10^{-2}	2.2×10^{-2}	2.3×10^{-2}
^{77}Kr	7.2×10^{-3}	6.0×10^{-3}	6.2×10^{-3}	5.9×10^{-3}	5.7×10^{-3}
^{78}Kr	8.7×10^{-3}	7.3×10^{-3}	7.5×10^{-3}	6.9×10^{-3}	6.5×10^{-3}
^{79}Kr	7.0×10^{-3}	3.5×10^{-3}	3.0×10^{-3}	2.5×10^{-3}	2.4×10^{-3}
^{80}Sr	1.3×10^{-2}	1.3×10^{-2}	1.4×10^{-2}	1.5×10^{-2}	1.5×10^{-2}
^{81}Rb	8.0×10^{-3}	6.4×10^{-3}	6.4×10^{-3}	6.0×10^{-3}	5.8×10^{-3}
^{82}Sr	1.7×10^{-2}	1.3×10^{-2}	1.2×10^{-2}	1.2×10^{-2}	1.1×10^{-2}
^{83}Sr	1.3×10^{-2}	1.2×10^{-2}	1.4×10^{-2}	1.3×10^{-2}	1.3×10^{-2}
^{84}Sr	1.3×10^{-2}	6.1×10^{-3}	3.8×10^{-3}	2.6×10^{-3}	2.2×10^{-3}
^{85}Y	9.8×10^{-3}	7.9×10^{-3}	7.7×10^{-3}	7.2×10^{-3}	6.9×10^{-3}
^{86}Zr	1.7×10^{-2}	1.9×10^{-2}	2.1×10^{-2}	2.1×10^{-2}	2.0×10^{-2}

Table 4.8: – Continued.

Nucleus	Burst 1	Burst 2	Burst 3	Burst 4	Burst 5
^{87}Zr	2.1×10^{-2}	9.1×10^{-3}	5.1×10^{-3}	3.8×10^{-3}	3.0×10^{-3}
^{88}Zr	5.9×10^{-3}	5.5×10^{-3}	5.0×10^{-3}	5.1×10^{-3}	5.3×10^{-3}
^{89}Nb	1.8×10^{-2}	2.0×10^{-2}	1.9×10^{-2}	1.8×10^{-2}	1.8×10^{-2}
^{90}Mo	1.2×10^{-2}	1.1×10^{-2}	9.9×10^{-3}	9.6×10^{-3}	9.2×10^{-3}
^{91}Nb	8.2×10^{-3}	9.4×10^{-3}	1.0×10^{-2}	1.0×10^{-2}	9.9×10^{-3}
^{92}Mo	7.6×10^{-3}	4.1×10^{-3}	2.3×10^{-3}	1.8×10^{-3}	1.4×10^{-3}
^{93}Tc	9.5×10^{-3}	8.8×10^{-3}	8.1×10^{-3}	7.6×10^{-3}	7.4×10^{-3}
^{94}Tc	2.6×10^{-2}	4.6×10^{-2}	4.6×10^{-2}	4.6×10^{-2}	4.6×10^{-2}
^{95}Ru	3.1×10^{-2}	2.4×10^{-2}	1.4×10^{-2}	9.3×10^{-3}	7.6×10^{-3}
^{96}Ru	8.1×10^{-3}	8.7×10^{-3}	7.4×10^{-3}	6.6×10^{-3}	6.2×10^{-3}
^{97}Ru	1.0×10^{-2}	1.2×10^{-2}	1.0×10^{-2}	9.5×10^{-3}	9.1×10^{-3}
^{98}Ru	1.2×10^{-2}	1.4×10^{-2}	1.3×10^{-2}	1.3×10^{-2}	1.2×10^{-2}
^{99}Rh	1.3×10^{-2}	2.1×10^{-2}	2.1×10^{-2}	2.0×10^{-2}	1.9×10^{-2}
^{100}Pd	1.6×10^{-2}	9.2×10^{-3}	8.7×10^{-3}	8.0×10^{-3}	8.2×10^{-3}
^{101}Pd	1.7×10^{-2}	1.8×10^{-2}	1.8×10^{-2}	1.8×10^{-2}	1.7×10^{-2}
^{102}Pd	1.6×10^{-2}	1.8×10^{-2}	1.9×10^{-2}	1.9×10^{-2}	1.8×10^{-2}
^{103}Ag	2.6×10^{-2}	3.2×10^{-2}	3.2×10^{-2}	3.3×10^{-2}	3.2×10^{-2}
^{104}Pd	5.3×10^{-2}	7.2×10^{-2}	7.4×10^{-2}	7.5×10^{-2}	7.5×10^{-2}
^{105}Ag	7.5×10^{-2}	1.3×10^{-1}	1.4×10^{-1}	1.4×10^{-1}	1.4×10^{-1}
^{106}Cd	1.2×10^{-2}	9.8×10^{-3}	5.3×10^{-3}	3.2×10^{-3}	2.5×10^{-3}
^{107}Cd	9.5×10^{-3}	6.4×10^{-3}	3.1×10^{-3}	1.9×10^{-3}	1.5×10^{-3}

4.4 Model 4

Observations of type I XRBs have posed constraints on the masses of the underlying neutron stars hosting such explosions. As shown in Fig. 1.2, most of the neutron star masses inferred from binary pulsars lay around ~ 1.4 M$_\odot$. The situation, however, is far more complex for neutron stars in X-ray bursting systems. Indeed, a wealth of evidence around the existence of more massive neutron stars has been piling up in recent years. Examples include the bursting source EXO 0748-676 (Villarreal & Strohmayer 2004), with an estimated neutron star mass in the range $1.5 \leq M(M_\odot) \leq 2.4$, and a best fit for 1.8 M$_\odot$ (see Lattimer & Prakash 2004, 2006, for a list of > 1.4 M$_\odot$ neutron stars in binary systems).

As discussed in Chapter 1, a major problem in the modeling of the structure of a neutron star is the equation of state (EOS) that governs the high-density regime of its interior. In this Thesis, we have adopted a simple Harrison-Wheeler EOS (see Shapiro & Teukolsky 1983) to build up the initial neutron star configuration

in hydrostatic equilibrium conditions, which yielded a reasonable value of 13 km for the radius of a 1.4 $M_\odot$ neutron star. The size of a 1.8 $M_\odot$ neutron star is still a matter of debate: it can be larger or smaller than a 1.4 $M_\odot$ neutron star, depending on the specific EOS adopted (Lattimer 2009). In particular, the Harrison-Wheeler EOS adopted in this Thesis yields a size of 17 km. Independently of how realistic is this value, important conclusions can be outlined from the study of bursting episodes on top of a 1.8 $M_\odot$ neutron star: our models of 1.4 $M_\odot$ (13 km) neutron stars are characterized by a (Newtonian) surface gravity of $GM/R^2 \sim 1.1 \times 10^{14} cm.s^{-2}$, while values obtained for our 1.8 $M_\odot$ neutron star yield a smaller value, $\sim 8.3 \times 10^{13} cm.s^{-2}$, which will allow us to directly test the influence of the surface gravity on the gross properties of XRBs.

To this end, we have performed extensive calculations of thermonuclear bursts driven by mass accretion onto a 1.8 $M_\odot$ neutron star ($L_{ini} = 1.6 \times 10^{34}$ erg.s^{-1} = 4.14 $L_\odot$), at a rate $\dot{M}_{acc} = 1.75 \times 10^{-9}$ $M_\odot$.yr^{-1} (0.06 $\dot{M}_{Edd}$; hereafter, Model 4). The composition of the accreted material is assumed to be solar-like (X=0.7048, Y=0.2752, Z=0.02).

Table 4.9: Summary of burst properties for Model 4.

Burst	T_{peak} (K)	$t(T_{peak})$ (s)	τ_{rec} (hr)	L_{peak} ($L_\odot$)	$\tau_{0.01}$ (s)	α
1	1.03×10^9	33590	9.3	1.7×10^5	62.3	77
2	1.08×10^9	44342	8.5	2.6×10^5	46.3	46
3	1.10×10^9	80568	8.9	2.1×10^5	59.5	45

Table 4.9 summarizes the main results obtained along the three bursting episodes computed in this model, including recurrence times between bursts around $\tau_{rec} \sim 8.5 - 9.5^{hr}$, persistent over burst luminosity ratios about $\alpha \sim 45 - 75$, and peak temperatures and luminosities around $T_{peak} \sim (1 - 1.1) \times 10^9$ K and $\sim 2 \times 10^5$ $L_\odot$, respectively. These values are not dramatically different from those reported for Model 1, which points towards a weak dependence of XRB properties on the mass of the neutron star hosting the explosion (or on its surface gravity). Indeed, only slightly lower -higher- peak temperatures -luminosities and α- have been obtained in the lower surface gravity environment of Model 4, whereas a somewhat larger influence seems to affect the burst recurrence times (almost a factor of ∼2 larger in Model 4). The corresponding light curves bear a clear resemblance with those reported in Model 1, without any double-peaked event.

With respect to the associated nucleosynthesis, the different bursting episodes computed (Table 4.10) are dominated by the presence of ^{4}He (0.40, by mass), H (0.16), ^{60,56}Ni (0.093 and 0.083, respectively), and ^{12}C (0.05), at the end of the first burst, switching into ^{4}He (0.19, by mass), ^{60,56}Ni (0.17 and 0.12, respectively), ^{32}S

(0.11), and H (0.046), after the third burst. Notice that the most abundant elements reported in Model 1 were ^{60}Ni (0.32, by mass), ^{4}He (0.31), H (0.17), ^{64}Zn (0.034), and ^{56}Ni (0.024), at the end of the first burst, whereas the fourth burst computed in that model was dominated by ^{60}Ni (0.31, by mass), ^{64}Zn (0.13), ^{4}He (0.10), ^{32}S (0.09), and ^{56}Ni (0.059). In agreement with the results reported for Model 1, the nuclear activity extends towards heavier species with the burst number, reaching endpoints ($X_i > 10^{-9}$) around ^{76}Kr (1^{st} burst), ^{91}Nb (2^{nd} burst), and ^{91}Nb (3^{rd} burst). It is however worth noting that the nuclear activity in Model 1 reached heavier species (^{89}Nb, after the 1^{st} burst, ^{97}Ru in the 2^{nd}, and ^{99}Rh in the 3^{rd}). As for previous models, the successive bursting episodes computed in Model 4 are characterized by an increase in the overall mean metallicity (Z) of the envelope (0.44 [1^{st} burst], 0.67 [2^{nd} burst], and 0.77 [3^{rd} burst]; again, more modest values than those reported for Model 1), with the H and ^{4}He contents dropping progressively, and final ^{12}C yields in the range $\sim 0.04 - 0.05$. Modest overproduction factors, with $f \sim 10^4$, have been obtained in Model 4. This includes species such as ^{43}Ca, ^{51}V, and ^{46,49}, at the end of the first burst, supplemented by ^{64,68}Zn, ^{78,80}Kr, ^{72}Ge, ^{74,76}Se, or ^{84}Sr, after the third bursting episode. In contrast, the largest overproduction factors achieved in Model 1 correspond to ^{60,61}Ni, ^{64}Zn, and ^{74}Se (with $f \sim 10^4$), at the end of the first burst, and to ^{78,80}Kr and ^{84}Sr (with $f \sim 10^6$), at the end of the fourth burst.

Table 4.10: Mean composition of the envelope ($X_i > 10^{-9}$) at the end of each burst, for Model 4.

Nucleus	Burst 1	Burst 2	Burst 3
^{1}H	1.6×10^{-1}	6.5×10^{-2}	4.6×10^{-2}
^{4}He	4.0×10^{-1}	2.7×10^{-1}	1.9×10^{-1}
^{12}C	5.0×10^{-2}	4.9×10^{-2}	4.4×10^{-2}
^{13}C	2.4×10^{-4}	1.7×10^{-4}	9.3×10^{-5}
^{14}N	2.8×10^{-3}	1.5×10^{-3}	1.0×10^{-3}
^{15}N	3.5×10^{-3}	1.6×10^{-3}	1.1×10^{-3}
^{16}O	4.8×10^{-4}	6.2×10^{-4}	4.8×10^{-4}
^{17}O	3.2×10^{-6}	7.5×10^{-6}	4.3×10^{-6}
^{18}O	3.6×10^{-5}	1.0×10^{-4}	6.3×10^{-5}
^{18}F	5.7×10^{-5}	1.4×10^{-4}	9.0×10^{-5}
^{19}F	2.3×10^{-4}	4.1×10^{-4}	2.7×10^{-4}
^{20}Ne	3.4×10^{-4}	5.0×10^{-4}	4.3×10^{-4}
^{21}Ne	6.5×10^{-6}	8.9×10^{-6}	8.1×10^{-6}
^{22}Ne	6.8×10^{-5}	4.4×10^{-5}	4.3×10^{-5}
^{22}Na	1.1×10^{-3}	2.2×10^{-3}	1.4×10^{-3}
^{23}Na	7.6×10^{-5}	1.5×10^{-4}	9.9×10^{-5}
^{24}Mg	9.9×10^{-4}	1.8×10^{-3}	1.7×10^{-3}

Table 4.10: – Continued.

Nucleus	Burst 1	Burst 2	Burst 3
^{25}Mg	5.9×10^{-4}	1.2×10^{-3}	1.5×10^{-3}
^{26}Mg	4.9×10^{-3}	4.2×10^{-3}	2.8×10^{-3}
^{26}Al^{g}	2.3×10^{-5}	4.9×10^{-5}	5.0×10^{-5}
^{27}Al	1.7×10^{-3}	1.8×10^{-3}	1.0×10^{-3}
^{28}Si	2.8×10^{-3}	2.6×10^{-2}	4.5×10^{-2}
^{29}Si	1.1×10^{-4}	2.0×10^{-3}	2.0×10^{-3}
^{30}Si	7.8×10^{-3}	1.0×10^{-2}	8.1×10^{-3}
^{31}P	1.0×10^{-3}	3.7×10^{-3}	4.2×10^{-3}
^{32}S	9.8×10^{-4}	5.3×10^{-2}	1.1×10^{-1}
^{33}S	7.0×10^{-4}	3.4×10^{-3}	5.5×10^{-3}
^{34}S	8.8×10^{-3}	2.0×10^{-2}	2.8×10^{-2}
^{35}Cl	1.6×10^{-3}	5.7×10^{-3}	7.2×10^{-3}
^{36}Ar	1.7×10^{-3}	4.7×10^{-3}	6.5×10^{-3}
^{37}Cl	3.9×10^{-7}	1.4×10^{-6}	3.3×10^{-6}
^{37}Ar	3.7×10^{-4}	5.3×10^{-4}	6.3×10^{-4}
^{38}Ar	6.6×10^{-3}	1.0×10^{-2}	1.1×10^{-2}
^{39}K	1.4×10^{-2}	1.9×10^{-2}	1.9×10^{-2}
^{40}Ca	9.5×10^{-3}	9.6×10^{-3}	9.8×10^{-3}
^{41}K	-	1.2×10^{-8}	2.9×10^{-8}
^{41}Ca	5.2×10^{-5}	8.8×10^{-5}	1.0×10^{-4}
^{42}Ca	2.1×10^{-3}	3.2×10^{-3}	3.2×10^{-3}
^{43}Ca	7.0×10^{-4}	2.1×10^{-3}	3.0×10^{-3}
^{43}Sc	2.7×10^{-3}	2.4×10^{-3}	1.4×10^{-3}
^{44}Ca	2.9×10^{-8}	1.0×10^{-5}	3.4×10^{-5}
^{44}Sc	2.3×10^{-7}	3.4×10^{-5}	3.4×10^{-5}
^{44}Ti	1.5×10^{-3}	1.4×10^{-3}	1.5×10^{-3}
^{45}Sc	8.6×10^{-5}	1.3×10^{-4}	2.2×10^{-4}
^{45}Ti	2.6×10^{-4}	1.9×10^{-4}	1.3×10^{-4}
^{46}Ti	3.2×10^{-3}	4.3×10^{-3}	4.3×10^{-3}
^{47}Ti	1.5×10^{-3}	1.4×10^{-3}	1.5×10^{-3}
^{48}Ti	2.3×10^{-7}	2.7×10^{-6}	1.0×10^{-5}
^{48}V	1.9×10^{-4}	4.0×10^{-4}	8.1×10^{-4}
^{48}Cr	4.5×10^{-3}	3.2×10^{-3}	3.0×10^{-3}
^{49}Ti	1.7×10^{-7}	1.4×10^{-6}	2.3×10^{-6}
^{49}V	3.4×10^{-3}	2.5×10^{-3}	2.6×10^{-3}
^{50}Cr	4.7×10^{-3}	4.6×10^{-3}	4.7×10^{-3}
^{51}V	6.3×10^{-6}	4.3×10^{-5}	9.0×10^{-5}
^{51}Cr	1.1×10^{-2}	1.0×10^{-2}	1.0×10^{-2}

Table 4.10: – Continued.

Nucleus	Burst 1	Burst 2	Burst 3
^{52}Cr	1.4×10^{-5}	1.1×10^{-4}	3.2×10^{-4}
^{52}Mn	4.8×10^{-3}	5.7×10^{-3}	9.4×10^{-3}
^{52}Fe	4.2×10^{-2}	1.6×10^{-2}	1.4×10^{-2}
^{53}Mn	2.5×10^{-3}	1.7×10^{-3}	1.8×10^{-3}
^{54}Fe	2.8×10^{-3}	2.5×10^{-3}	2.6×10^{-3}
^{55}Mn	8.9×10^{-9}	1.6×10^{-7}	5.0×10^{-7}
^{55}Fe	4.6×10^{-4}	1.3×10^{-3}	2.2×10^{-3}
^{55}Co	8.7×10^{-3}	6.5×10^{-3}	5.6×10^{-3}
^{56}Fe	1.3×10^{-7}	3.5×10^{-6}	1.3×10^{-5}
^{56}Co	5.2×10^{-4}	2.4×10^{-3}	5.2×10^{-3}
^{56}Ni	8.3×10^{-2}	1.3×10^{-1}	1.2×10^{-1}
^{57}Fe	2.4×10^{-8}	5.7×10^{-7}	1.2×10^{-6}
^{57}Co	3.4×10^{-4}	4.4×10^{-4}	9.7×10^{-4}
^{57}Ni	1.3×10^{-3}	1.1×10^{-2}	8.9×10^{-3}
^{58}Ni	7.7×10^{-3}	6.2×10^{-3}	6.0×10^{-3}
^{59}Ni	1.1×10^{-2}	8.7×10^{-3}	9.2×10^{-3}
^{60}Ni	9.3×10^{-2}	1.5×10^{-1}	1.7×10^{-1}
^{61}Ni	1.6×10^{-3}	1.4×10^{-3}	2.5×10^{-3}
^{61}Cu	5.4×10^{-3}	2.0×10^{-3}	2.2×10^{-3}
^{62}Ni	1.8×10^{-4}	2.4×10^{-4}	5.1×10^{-4}
^{62}Zn	1.7×10^{-3}	7.7×10^{-4}	1.2×10^{-3}
^{63}Cu	1.3×10^{-3}	1.1×10^{-3}	2.1×10^{-3}
^{64}Zn	2.0×10^{-3}	3.8×10^{-2}	3.9×10^{-2}
^{65}Cu	1.5×10^{-8}	9.3×10^{-8}	4.0×10^{-7}
^{65}Zn	1.4×10^{-4}	4.9×10^{-4}	6.7×10^{-4}
^{66}Zn	7.6×10^{-7}	1.0×10^{-5}	7.6×10^{-5}
^{66}Ga	1.5×10^{-5}	1.0×10^{-4}	2.0×10^{-4}
^{66}Ge	3.2×10^{-5}	1.8×10^{-4}	2.2×10^{-4}
^{67}Ga	1.2×10^{-5}	2.3×10^{-4}	3.5×10^{-4}
^{68}Ge	2.0×10^{-5}	6.6×10^{-3}	7.5×10^{-3}
^{69}Ge	1.7×10^{-6}	1.8×10^{-4}	2.6×10^{-4}
^{70}Ge	3.5×10^{-7}	4.6×10^{-5}	7.9×10^{-5}
^{71}As	2.2×10^{-7}	7.6×10^{-5}	1.2×10^{-4}
^{72}Se	3.0×10^{-7}	7.2×10^{-4}	1.2×10^{-3}
^{73}Se	2.6×10^{-8}	3.2×10^{-5}	6.4×10^{-5}
^{74}Se	7.4×10^{-9}	1.3×10^{-5}	2.7×10^{-5}
^{75}Br	5.3×10^{-9}	1.7×10^{-5}	3.3×10^{-5}
^{76}Kr	7.8×10^{-9}	9.1×10^{-5}	2.2×10^{-4}

Table 4.10: – Continued.

Nucleus	Burst 1	Burst 2	Burst 3
^{77}Kr	-	6.4×10^{-6}	1.9×10^{-5}
^{78}Kr	-	3.8×10^{-6}	1.2×10^{-5}
^{79}Kr	-	2.4×10^{-6}	7.4×10^{-6}
^{80}Sr	-	1.2×10^{-5}	4.5×10^{-5}
^{81}Rb	-	1.4×10^{-6}	6.6×10^{-6}
^{82}Sr	-	1.4×10^{-6}	7.6×10^{-6}
^{83}Sr	-	6.6×10^{-7}	3.9×10^{-6}
^{84}Sr	-	4.6×10^{-7}	2.9×10^{-6}
^{85}Y	-	3.9×10^{-7}	2.5×10^{-6}
^{86}Zr	-	2.9×10^{-7}	1.9×10^{-6}
^{87}Zr	-	1.7×10^{-7}	1.1×10^{-6}
^{88}Zr	-	6.6×10^{-8}	3.5×10^{-7}
^{89}Nb	-	6.0×10^{-8}	2.8×10^{-7}
^{90}Mo	-	7.6×10^{-9}	3.9×10^{-8}
^{91}Nb	-	1.2×10^{-9}	6.7×10^{-9}

4.5 Discussion

4.5.1 Comparison with previous work

For consistency, the results presented in this Thesis have been compared with those computed with similar spherically symmetric, hydrodynamic models. Indeed, Model 1 (this Thesis) is qualitatively similar to Model ZM of Woosley et al. (2004), as well as to the model reported by Fisker et al. (2008).

The twelve bursts computed by Woosley et al. (2004) in their (Newtonian) Model ZM, were characterized by recurrence times of about $\sim$ 2.7 hr, peak luminosities of $L_{peak} \sim (1.5 - 2) \times 10^{38} erg.s^{-1}$, and burst over persistent luminosity ratios of $\alpha \sim 60 - 65$. Fisker et al. (2008), in turn, reported on five bursting sequences, with $\tau_{rec} \sim 3.5 - 4$ hr, $L_{peak} \sim (7 - 8) \times 10^{37} erg.s^{-1}$, and $\alpha \sim 65 - 70$, as measured at infinity. Our calculations (Model 1, Newtonian frame) yielded $\tau_{rec} \sim 5 - 6.5$ hr, $L_{peak} \sim (3 - 7) \times 10^{38} erg.s^{-1}$, and $\alpha \sim 35 - 40$. Notice, however, that the local surface gravity of our model is somewhat smaller than those used in Woosley et al. (2004) and Fisker et al. (2008): whereas a 10 km radius is assigned to the 1.4 $M_\odot$ neutron star in Woosley et al. (2004), the integration of the neutron star structure from the core to its surface, in hydrostatic equilibrium, yielded 13.1 km for our 1.4 $M_\odot$ neutron star (corresponding to a 14.3 km, after general relativity corrections are introduced; see Subsection 4.5.2); the calculations reported by Fisker et al. (2008), in a general relativity framework, relied in turn on 11 km as the radius

of a 1.4 $M_\odot$ neutron star. Although, as discussed for Model 4 (see Section 4.4), XRB properties weakly depend upon the neutron star mass (or surface gravity), part of the differences outlined between the three calculations can be clearly attributed to the combined effect of the adopted neutron star size and to differences in the input physics adopted (opacities, nuclear reaction network...). One double-peaked burst has been obtained in our Model 1, a characteristic feature observed in some light curves of XRB sources, such as 4U 1608-52, 4U 17+2, or 4U 1709-267. In contrast, no double peak is reported neither in Woosley et al. (2004), nor in Fisker et al. (2008).

It is also worth noting that, because of the moderate peak temperatures achieved in our calculations (< 1.3 GK), most of the nuclear activity stops around mass $A \sim 60$, and hence, no large concentrations in the SnSbTe-mass region are achieved. This is in agreement with the computations reported by Fisker et al. (2008) and Woosley et al. (2004), which contradict previous results from Schatz et al. (2001), which relied on higher peak temperatures through a one-zone approach. Also in agreement with Fisker et al. (2008) and Woosley et al. (2004), Model 1 yields a very small post-burst abundance of ^{12}C, below the threshold amount required to power superbursts.

The role played by the metallicity of the accreted material (Model 3, with $Z = Z_\odot/20 = 0.001$) agrees fairly well with the results reported for Model zM in Woosley et al. (2004) (see also, Heger et al. 2007). Longer recurrence times of ~ 9 hours, peak temperatures about $(1.3 - 1.4) \times 10^9$ K, and burst over persistent luminosity ratios around $\alpha \sim 20 - 30$ (with $L_{peak} \sim 10^{38}$ erg.s^{-1}) have been obtained in the 5 bursts computed in Model 3. The fifteen bursts computed by Woosley et al. (2004) for Model zM, were characterized by recurrence times of about $3 - 3.5$ hr, peak luminosities of $L_{peak} \sim 10^{38} erg.s^{-1}$, and burst over persistent luminosity ratios of $\alpha \sim 50-60$. Results reveal a clear dependence of burst properties with the metallicity of the accreted material: the smaller the metal content, the larger the recurrence time (and the smaller the α). In turn, explosions in metal-deficient envelopes (i.e., Model 3) are characterized by lower peak luminosities and longer decline times, in perfect agreement with the pattern described in Woosley et al. (2004) and Heger et al. (2007). This, together with the longer exposure times to high temperatures (driven by a slower decline phase), cause a dramatic extension of the main nuclear path towards the SnSbTe-mass region, in agreement with the previously mentioned papers.

No calculation for neutron star masses other than 1.4 $M_\odot$ is available neither in Woosley et al. (2004), nor in Fisker et al. (2008), although the weak dependence of the XRB properties on the neutron star mass (or surface gravity) obtained for Model 4 is in agreement with the qualitative arguments outlined by Woosley et al. (2004), in their Section 4.4.

4.5.2 General relativity corrections

The calculations reported in this Thesis have been performed assuming Newtonian gravity. Since the envelope layers considered here are very thin, it is easy to introduce general relativity corrections to this Newtonian framework (see Ayasli & Joss 1982, Lewin et al. 1993, Taam et al. 1993, Cumming et al. 2002, and Woosley et al. 2004). To this end, the surface gravity is rewritten as $g = G.M_*/R_*^2.(1+z)$, where M_* is the gravitational mass, R_* is the stellar radius (defined in such a way that the surface area is $4\pi R_*^2$), and z is the gravitational redshift given by $1+z = (1-2G.M_*/R_*c^2)^{-1/2}$.

Our results, obtained for a specific choice of M_{NS} and R_{NS} (for instance, 1.4 $M_\odot$ and 13.1 km), can be applied to any stellar configuration, (M_*, R_*), that yields the same surface gravity that in our Newtonian framework ($G.M_{NS}/R_{NS}^2 = 1.08 \times 10^{14} cm.s^{-2}$, for our 1.4 $M_\odot$ model). Hence, a value of $M_* = 1.4$ $M_\odot$ requires $R_* =$ 14.3 km, and a gravitational redshift of $z = 0.19$.

Once the redshift and radius are determined, for a given stellar mass, it is straightforward to derive the set of correcting factors to the physical magnitudes described in the previous sections for a suitable observer at infinity. Hence, the recurrence times and burst durations should be increased by a factor $1+z$. The mass-accretion rate as well as the burst luminosity have to take into account both the difference in surface area (compared to the Newtonian framework) and the gravitational redshift term. The energy and rest mass-accretion rate scale as $R_*^2/(1+z)$, while the luminosity $\propto R_*^2/(1+z)^2$.

As discussed in Woosley et al. (2004), when M_* is taken exactly as M_{NS} (Newtonian framework; for instance, 1.4 $M_\odot$ and 13.1 km), the surface area and redshift corrections for energy and accretion rate cancel out, since $g \propto (1+z)/R_*^2 = constant$, and hence, no correction to the observed burst energy or mass-accretion rate is necessary, while the luminosity correction is simply given by $1/(1+z) = 0.84$. In addition, the accretion luminosity for an observer at infinity changes only by a factor 1.012, that is, the ratio between gravitational energy release per unit mass in general relativity, $c^2.z/(1+z)$, and the Newtonian value, GM_{NS}/R_{NS}. Finally, the luminosity measured at infinity will be smaller by a factor of $(1+z) = 1.19$.

Chapter 5

Summary and conclusions

One of the goals of this Thesis has been the identification of the key nuclear processes whose uncertainties deeply influence the final yields in type I X-ray burst simulations. To this end, a twofold approach has been adopted: first, the effect of individual reaction-rate variations has been quantified in the framework of post-processing calculations with a set of 10 different models (Chapter 2), which differ in the corresponding temperature and density versus time profiles (to specifically test the role of the thermal history of the explosion –peak temperature and duration of the burst–, as well as of the initial metallicity, in the accompanying nucleosynthesis). For that purpose, an extensive nuclear network containing 606 isotopes (ranging from H to ^{113}Xe), and linked through a suite of 3551 nuclear processes, has been implemented. Each reaction of the network has been varied within uncertainty limits (typically, a factor of 10, up and down), and about ∼40,000 post-processing calculations (requiring 14 CPU-months) have been performed. The most influential reaction of the network turned out to be, as expected, the triple-α. However, when more realistic uncertainty limits are adopted for this reaction (±12%; Tur et al. 2006), no effect neither on the final yields nor on the overall energy output has been found. Similar results have been obtained for the set of β-decay rates included in the network. As summarized in Table 2.15, only a handful of reactions (28, plus the corresponding reverse reactions, out of the 3551 nuclear processes considered) have an impact on the final yields larger than a factor of 2 (on, at least, 3 isotopes of the network, in any of the 10 models computed) when their nominal rates are varied by a factor of 10, up and down. This includes mostly p-capture reactions, such as ^{65}As(p, γ)^{66}Se, ^{61}Ga(p, γ)^{62}Ge, ^{96}Ag(p, γ)^{97}Cd, ^{59}Cu(p, γ)^{60}Zn, ^{86}Mo(p, γ)^{87}Tc, ^{92}Ru(p, γ)^{93}Rh, or ^{102,103}In(p, γ)^{103,104}Sn, as well as some α-capture reactions like ^{12}C(α, γ)^{16}O (although this rate is constrained to better than a factor of $\sim$ 10 for XRB conditions), ^{30}S(α, p)^{33}Cl, or ^{56}Ni(α, p)^{59}Cu. The effect of these reactions is mainly restricted to isotopes with masses and atomic numbers similar to those of the interacting particles. It is also worth noting that only 17 reactions have

been flagged as affecting the total energy output by more than 5% (as well as the yield of at least one isotope; Table 2.16), when their nominal rates are individually varied within a factor of 10, up and down. This has to be taken as a warning of the limitations of post-processing techniques, since a self-consistent analysis would require a hydrodynamic code capable of self-adjusting both the temperature and the density of the stellar envelope. The impact of uncertainties in reaction Q-values (Table 2.3) on the final yields have also been tested for 2 of the 10 models reported in Chapter 2: only ^{26}P(p,γ)^{27}S, ^{45,46}Cr(p,γ)^{46,47}Mn, ^{55}Ni(p,γ)^{56}Cu, ^{60}Zn(p,γ)^{61}Ga, and ^{64}Ge(p,γ)^{65}As show an effect on the final yields when their Q-values are varied between 1σ uncertainty bounds (Table 2.4). Indeed, the largest effect corresponds to ^{64}Ge(p,γ)^{65}As, whose influence ranges between ^{64}Zn and ^{104}Ag. Our study clearly stresses the need to perform mass measurements on ^{65}As to better determine this Q-value[1]. In summary, the study presented in Chapter 2 has led to the identification of a limited number of reactions whose nuclear uncertainties play a key role in XRB nucleosynthesis studies.

A second, somewhat complementary approach to the individual-reaction rate variation study relies on the simultaneous variation of all reaction rates through a Monte Carlo approach, to mimic the complex interplay between multiple nuclear processes in the highly coupled environment of an XRB (Chapter 3). In this procedure, all reaction rates are arbitrarily multiplied by a random factor that follows a Log-Normal distribution, with an expected value of 1, and a probability of 95.5% to range between 0.1 and 10 (the same uncertainty limits adopted in the previous approach). Results are in all cases qualitatively similar to the ones reported in the individual-reaction rate variation study. Hence, for conciseness, our discussion has mainly focused on Models K04 and F08 (for which 20,000 Monte Carlo trials – requiring 7 CPU-months– have been performed). Since all reaction rates are changed simultaneously, the identification of the most influential reactions for a given isotope is not straightforward. Moreover, it is worth noting that Monte Carlo trials, where a subset of reactions affects the overall energy production (by more than a 5%), cannot be easily removed since this would affect the input distribution of enhancement factors (which are assumed to be random). Therefore, while results from individual reaction-rate variations are not corrupted by these effects, Monte Carlo simulations cannot disentangle this from the overall analysis and hence the interpretation of the results has to be taken with caution. In this procedure, the identification of the most influential reactions relies on the determination of correlation coefficients between each isotope and all reaction rates: the larger the correlation coefficient, the more influential the reaction. Moreover, the impact of a given reaction on a specific isotope is quantified through a linear fit between the final yield and the corresponding (random) variation factor, whose slope indicates the strength of this dependence. The

[1] A more detailed account of the influence of Q-value variations, not included in this Thesis, has been recently published in *Impact of uncertainties in reaction Q-values on nucleosynthesis in type I X-ray bursts*, by Parikh et al. (2009).

most influential reactions on the network of isotopes (for which a correlation coefficient > 0.5 is imposed), obtained for Models K04 and F08, are summarized in Tables 3.1 & 3.4. Like in the individual reaction-rate variation study, only a small subset of the thousands of reactions considered has an impact on the final yields. Indeed, all reactions flagged as important in the Monte Carlo simulations were previously identified in the individual reaction-rate variation study (Tables 3.5 & 3.6). When not too restrictive conditions are applied to the Monte Carlo studies, a total agreement on the results obtained with both techniques is achieved. We have also tested the impact of the number of Monte Carlo trials on the final results, obtaining that reasonable values can already be achieved with only ~ 100 trials, which makes our study with $10,000$ trials fully reliable and statistically sound. All in all, we conclude that both techniques yield similar results. However, the individual reaction-rate variation study turns out to be better suited for flagging reactions that affect the overall energy output or for handling specific reactions whose rates are known with better precision. The results reported in Chapters 2 & 3 will actually help to guide and motivate future experiments performed by nuclear physicists at dedicated facilities. Stellar modelers, as well, may tackle the challenge to properly address the role played by the few reactions flagged as affecting the overall energy output, an aspect that lies beyond the possibilities offered by post-processing calculations.

In the second part of this Thesis (Chapter 4), we have reported on a new set of numerical models of type I X-ray bursts computed with a modified version of SHIVA, a 1-D, spherically symmetric, hydrodynamic, implicit, Lagrangian code (José 1996; José & Hernanz 1998), linked to a fully updated nuclear reaction network containing 324 species and 1392 reaction rates, for a wide range of conditions, including different neutron star masses(1.4 and $1.8 M_{\odot}$), initial metallicities (0.02 and 0.001), as well as two different resolutions (60 and 200 shells; see Table 4.1). A total number of 14 bursting episodes have been computed for the 4 models reported in this Thesis (requiring $\sim$2.2 CPU-years), which allowed to influence of the *thermal* and *compositional inertia* on the properties of successive bursts.

The 4 bursting episodes computed in Model 1 ($M_{NS} = 1.4 M_{\odot}$, $\dot{M} = 1.75 \times 10^{-9}\, M_{\odot}.yr^{-1}$ [0.08 $\dot{M}_{Edd}$], $Z = 0.02$, and 60 shells) are characterized by recurrence times about $\sim 5 - 6.5$ hours, maximum temperatures of $(1.1 - 1.3) \times 10^9$ K, peak luminosities about $(5 - 8) \times 10^{38} erg.s^{-1}$, and burst over persistent luminosity ratios in the range $\alpha \sim 35 - 40$, quite in agreement with the burst properties of well-observed XRB sources such as GS 1826-24, 4U 1323-62, or 4U 1608-52. The nuclear activity extends progressively towards heavier species with the burst number, reaching nucleosynthetic endpoints ($X_i > 10^{-9}$) around ^{89}Nb (1^{st} burst), ^{97}Ru (2^{nd} burst), ^{99}Rh (3^{rd} burst), and ^{100}Pd (4^{th} burst). This is also accompanied by an increase of the overall envelope metallicity (0.52 for the 1^{st} burst, 0.71 for the 2^{nd}, 0.80 for the 3^{rd}, and 0.86 for the 4^{th}). The mean, mass-averaged chemical composition of the envelope at the end of fourth burst is mainly dominated by the presence of ^{60}Ni (0.31, by mass), ^{64}Zn (0.13), ^{4}He (0.10), ^{32}S (0.09), ^{56}Ni (0.06), ^{68}Ge (0.05), ^{1}H (0.04), ^{34}S

(0.02), and ^{12}C (0.02) (see Table 4.2). A similar ^{12}C yield is systematically obtained at the end of each of the 4 bursts computed. However, its amount turns out to be too small to potentially power a superburst (which requires $X(^{12}C_{min}) \sim 0.1$). With respect to overproduction factors, the increase in nuclear activity that accompanies successive bursts translates also into larger values, as high as $f \sim 10^6$, for ^{76}Se, ^{78,80}Kr, and ^{84}Sr, or $f \sim 10^5$, for species such as ^{64,68}Zn, ^{72,73}Ge, ^{74,77}Se, ^{82}Kr, ^{86,87}Sr, ^{89}Y, and ^{94}Mo, for the 4^{th} burst computed in this model. A quite interesting feature, observed in some XRBs such as 4U 1608-52, 4U 17+2, or 4U 1709-267, is the appearance of a double-peaked burst. This has been obtained in burst #4, of the series computed in Model 1, and its origin is likely caused by a waiting-point impedance, as described by Fisker et al. (2004).

The influence of the adopted number of envelope shells on the gross properties of the bursts has been checked through another simulation, identical to Model 1, but computed with a finer resolution (200 shells; hereafter, Model 2). To this end, 2 bursting episodes have been computed, yielding recurrence times, peak temperatures and luminosities, burst over persistent luminosity ratios, and final nucleosynthesis, very similar to those reported for Model 1. This is in agreement with Fisker et al. (2004), who concluded that the effects of a coarse resolution, in hydrodynamic XRB simulations, are avoided with a minimum discretization of the envelope of about 25 shells.

The role played by the metallicity of the accreted material (that reflects the surface composition of the companion star) on the overall properties of the bursts has been analyzed by means of another series of thermonuclear bursts (hereafter, Model 3), driven by accretion of metal-deficient material ($Z = Z_\odot/20 = 0.001$) onto a 1.4 $M_\odot$ neutron star ($L_{ini} = 1.6 \times 10^{34}$ erg.s^{-1} = 4.14 $L_\odot$), at a rate $\dot{M}_{acc} = 1.75 \times 10^{-9}$ $M_\odot$.yr^{-1}. Longer (but more regular) recurrence times of $\sim$ 9 hours, peak temperatures about $(1.3 - 1.4) \times 10^9$ K, and burst over persistent luminosity ratios around $\alpha \sim 20 - 30$ (with $L_{peak} \sim 10^{38}$ erg.s^{-1}) have been obtained in the 5 bursts computed in Model 3, in agreement with the values reported for several XRB sources, such as 1A 1905+00, 4U 1254-69, or XTE J1710-281. Results reveal a clear dependence of burst properties with the metallicity of the accreted material: the smaller the metal content, the larger the recurrence time (and the smaller the α). In turn, explosions in metal-deficient envelopes (i.e., Model 3) are characterized by lower peak luminosities and longer decline times. It is worth noting that no double-peaked bursts have been obtained in Model 3. Larger peak temperatures, around $T_{peak} \sim (1.3 - 1.4) \times 10^9$ K, have also been obtained in Model 3. This, together with the longer exposure times to high temperatures (driven by a slower decline phase) cause a dramatic extension of the main nuclear path towards the SnSbTe-mass region. Indeed, although the accreted material is more metal-deficient than in Model 1, the post-burst metallicity of the envelope is larger in Model 3 (0.74, for the 1^{st} burst; 0.85, for the 2^{nd}; 0.90, for the 3^{rd}; 0.92, for the 4^{th}; and 0.93, for the 5^{th}), being ^{105}Ag (0.14, by mass), ^{64}Zn (0.09), ^{104}Pd (0.08), and ^{68}Ge (0.07),

the most abundant species at the end of the last burst computed. The amount of unburned ^{12}C that survives the successive bursts is smaller than in Model 1 (a mean, mass-averaged value of only 0.001, by mass, at the end of the fifth burst). Huge overproduction factors, involving quite heavy species such as ^{102,104,105}Pd, ^{98}Ru, or ^{94}Mo (with $f \sim 10^8$, at the end of the fifth burst), have been obtained as well in this model, in sharp contrast with the more modest values achieved in Model 1, with maximum overproduction factors about $f \sim 10^6$ (at the end of the fourth burst), involving lighter species, such as ^{76}Se, ^{78,80}Kr, and ^{84}Sr.

Finally, motivated by the wealth of evidence on the existence of more massive neutron stars (including the bursting source EXO 0748-676, with an estimated neutron star mass in the range $1.5 \leq M(M_\odot) \leq 2.4$, and a best fit for 1.8 $M_\odot$), we have checked the influence of the surface gravity on the gross properties of XRBs. To this end, we have performed extensive calculations of thermonuclear bursts (Model 4) driven by mass accretion onto a 1.8 $M_\odot$ neutron star ($L_{ini} = 1.6 \times 10^{34}$ erg.s^{-1} = 4.14 $L_\odot$), at a rate $\dot{M}_{acc} = 1.75 \times 10^{-9}$ $M_\odot$.yr^{-1} (0.06 $\dot{M}_{Edd}$), and assuming a solar-like composition for the accreted material. Three bursts have been computed for this model, which yielded recurrence times of $\sim$ 9 hours, peak temperatures about $(1.0 - 1.1) \times 10^9$ K, peak luminosities around $\sim 8 \times 10^{38} erg.s^{-1}$, and $\alpha \sim 45$. With the exception of the recurrence times, these values are similar to those reported for Model 1 which points towards a weak dependence of the XRB properties with the mass of the neutron star hosting the explosion. From the nucleosynthetic viewpoint, the chemical abundance at the end of the third burst is dominated by the presence ^{4}He (0.19, by mass), ^{60,56}Ni (0.17 and 0.12, respectively), ^{32}S (0.11), and H (0.046), somewhat different from the pattern reported in Model 1. As for the other models reported in this Thesis, the nuclear activity extends towards heavier species with the burst number, reaching endpoints around ^{76}Kr (1^{st} burst), ^{91}Nb (2^{nd} burst), and ^{91}Nb (3^{rd} burst). It is however worth noting that the nuclear activity in Model 1 reached already heavier species. The successive bursting episodes computed in Model 4 are also characterized by an increase in the overall mean metallicity (Z) of the envelope (0.44 [1^{st} burst], 0.67 [2^{nd} burst], and 0.77 [3^{rd} burst]; again, more modest values than those reported for Model 1), with the H and ^{4}He contents dropping progressively, and final ^{12}C yields in the range $\sim 0.04 - 0.05$. Modest overproduction factors, with $f \sim 10^4$, have been obtained in Model 4, including species such as ^{43}Ca, ^{51}V, ^{46,49}, ^{64,68}Zn, ^{78,80}Kr, ^{72}Ge, ^{74,76}Se, or ^{84}Sr, after the third bursting episode.

Tiny effects driven by general relativity corrections to our Newtonian framework have also been discussed. A gravitational redshift of $z = 0.19$ has been obtained for our 1.4 $M_\odot$ models, which translates into recurrence times and burst durations increased by a factor $1 + z = 1.19$. No correction to the observed burst energy or mass-accretion rate is necessary, while the luminosity correction is simply given by $1/(1 + z) = 0.84$. Finally, the accretion luminosity for an observer at infinity will change by a factor 1.012, while the overall luminosity will be smaller by a factor of $(1 + z) = 1.19$.

A thorough analysis of the results reported in this Thesis shows good agreement with similar XRB models computed by other groups (Woosley et al. 2004; Fisker et al. 2008).

We plan to extend the scope of the work presented in this Thesis in the forthcoming future, with special emphasis in the following aspects:

- Study of the dependence of XRB properties on the M–R relation obtained with different EOS for the neutron star interior
- Implementation of OPAL opacities for the chemically challenging environment that characterizes XRBs
- Parallelization of the SHIVA code
- Inclusion of general relativity corrections to the equations of stellar structure (Ayasli & Joss 1982), or transformation of the SHIVA code into a fully relativistic hydrocode (May & White 1967)
- Characterization of XRB properties in primordial stellar binaries
- Implementation of an adaptive nucleosynthesis network
- Hydrodynamic studies of the impact of nuclear uncertainties in specific reaction rates, in connection with future experiments in dedicated nuclear physics facilities
- Multidimensional studies of point-like ignition and flame propagation in the envelopes of accreting neutron stars

Appendix A

Method of computation

The hydrodynamic simulations reported in this Thesis have been computed with a modified version of SHIVA, a one-dimensional (spherically symmetric), hydrodynamic code, in Lagrangian formulation, built originally to model classical nova outbursts (José 1996; José & Hernanz 1998). A flow chart describing the basic structure of the SHIVA code is outlined in Fig. A.2. The code uses a co-moving coordinate system, where time derivatives of any variable are calculated with respect to a grid attached to the fluid, as described in Kutter & Sparks (1972). This formulation avoids the spurious generation of numerical diffusion, which causes many problems in the attempt to model burning fronts.

Despite convective mixing has certainly a multi-dimensional nature, most of the main observational features that characterize type I X-ray bursts (XRBs) can be reproduced by spherically symmetric models. From a hydrodynamical viewpoint, nova outbursts and XRBs are similar objects: both are powered by thermonuclear explosions driven by mass accretion on the surface of a compact star (a white dwarf, in the case of a nova; a neutron star, for an XRB). Although the basic stellar structure equations governing nova explosions and XRBs are identical, the different surface gravity (much stronger in a neutron star) induces dramatic differences in the physical conditions that define such cataclysmic events.

A.1 Shell structure

In our simulations, the outermost layers of the neutron star are divided into N concentric mass shells (with intershells labeled with a subscript i, ranging from 1, at the very center -or innermost shell- of the star, to $N+1$ at the surface; see Fig. A.1). This structure defines a Lagrangian grid, where the mass interior to the i^{th}-intershell, m_i, and the star's age, t, are taken as the independent variables. The code computes the time evolution of several physical variables, such as the luminosity, L, the radius, r, the velocity, v, the temperature, T, and the density, ρ,

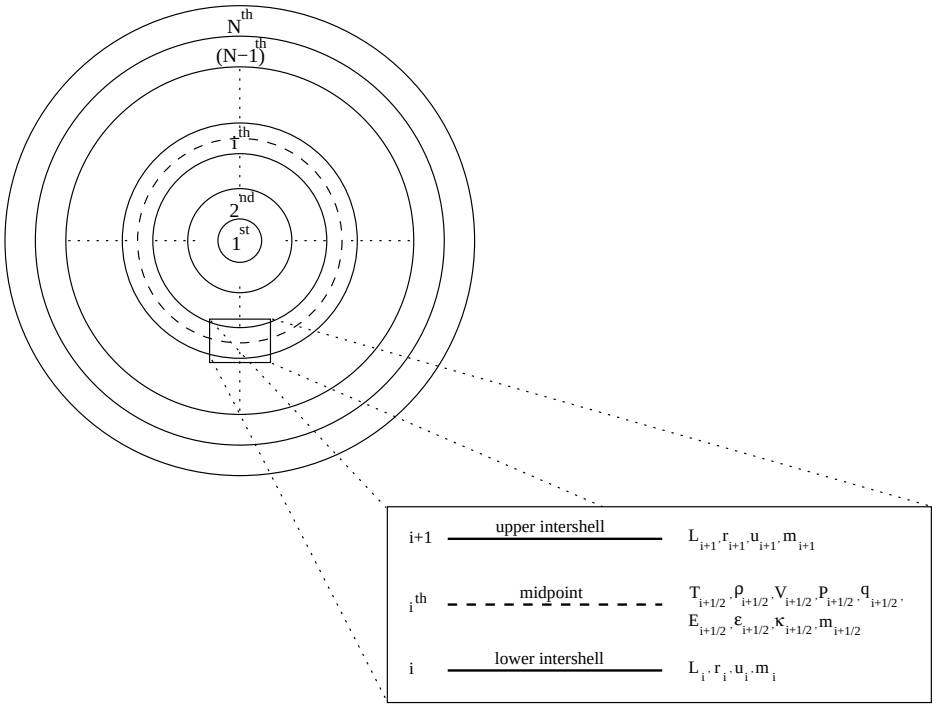

Figure A.1: Shell structure and assignment of variables at grid points.

for each shell. Following Kutter & Sparks (1972), L, r, and v are evaluated at the intershells (and are denoted by subscripts i), whereas other variables, such as T, or ρ, are shell-centered (i.e. evaluated at mass points defined by geometric averages, as $m_{i+1/2} = \sqrt{m_{i+1}.m_i}$, and denoted by subscripts $i + 1/2$). The time step is defined as $\Delta t^{n+1/2} = t^{n+1} - t^n$, where t^n represents the time elapsed since the beginning of the simulation[1].

A.2 Stellar structure

A.2.1 Stellar structure equations in Lagrangian formulation

The structure and time evolution of a star is determined by the following set of five coupled mechanical and thermal equations, written in Lagrangian formulation:

- Conservation of mass:

$$V = \frac{4\pi}{3}\frac{\partial r^3}{\partial m} \tag{A.1}$$

[1]In the following, a superscript n will denote a variable evaluated at time t^n, whereas no superscript will be used for variables evaluated at the present time, t^{n+1}.

- Conservation of momentum:

$$\frac{\partial u}{\partial t} + 4\pi r^2 \frac{\partial (P+q)}{\partial m} = -\frac{Gm}{r^2} \tag{A.2}$$

- Conservation of energy:

$$\frac{\partial E}{\partial t} = \epsilon - \frac{\partial L}{\partial m} - (P+q)\frac{\partial V}{\partial t} \tag{A.3}$$

where ϵ is the total nuclear energy released (a balance between nuclear reactions and neutrino losses), $\epsilon = \epsilon_{nuc} - \epsilon_{\nu}$.

- Energy transport[2] (by radiation and convection):

$$L = -\frac{256\sigma\pi^2 r^4 T^3}{3\kappa}\frac{\partial T}{\partial m} + L_{conv} \tag{A.4}$$

where $\sigma = 5.67 \times 10^{-5}\, erg.cm^{-2}.s^{-1}.K^{-4}$ is the Stefan-Boltzmann constant, and L_{conv} is the convective luminosity.

- Lagrangian velocity:

$$u = \frac{\partial r}{\partial t} \tag{A.5}$$

Table A.1: Definition of variables, notation, and units of measure.

Physical magnitude	Notation	Units of measure (c.g.s.)
Lagrangian mass	m_i	g
Star's age	t^n	s
Luminosity	L_i	$erg.s^{-1}$
Radius	r_i	cm
Velocity	u_i	$cm.s^{-1}$
Temperature	$T_{i+1/2}$	K
Density	$\rho_{i+1/2}$	$g.cm^{-3}$
Specific volume	$V_{i+1/2}$	$cm^3.g^{-1}$
Pressure	$P_{i+1/2}$	$dyne.cm^{-2}$
Artificial viscosity	$q_{i+1/2}$	$dyne.cm^{-2}$
Specific internal energy	$E_{i+1/2}$	$erg.g^{-1}$
Energy generation rate	$\varepsilon_{i+1/2}$	$erg.g^{-1}.s^{-1}$
Opacity	$\kappa_{i+1/2}$	$cm^2.g^{-1}$

[2]Following Paczyński (1983), the electron thermal conductivity can be ignored whenever the mass accretion rate is above $10^{-4}\ \dot{M}_{Edd}$, where $\dot{M}_{Edd}$ is the Eddington limit. In this Thesis, a value of $0.08\ \dot{M}_{Edd}$ has been adopted for Models 1 – 3, whereas $0.06\ \dot{M}_{Edd}$ has been used for Model 4.

A.2.2 Boundary conditions

In order to solve the system of 5 coupled differential equations, we have adopted the following set of boundary conditions:

- Innermost shell:

$$m = m_1 \longrightarrow u = 0,\, L = L_1,\, r = r_1 \tag{A.6}$$

In the special case of the stellar center:

$$m = 0 \longrightarrow u = L = r = 0 \tag{A.7}$$

- Surface:

$$m = M_{NS} \longrightarrow T^4 = \frac{3}{4} T_{eff}^4 \,(\frac{2}{3} + \tau),\, P = P_{rad} \tag{A.8}$$

where τ is the optical depth, and P_{rad} is the radiative pressure.

A.2.3 Constitutive equations

The set of partial differential equations mentioned above is linked to the constitutive equations, which express P, q, E, κ, and ϵ as functions of T, ρ, and the chemical composition, X. Details can be found in José (1996), unless otherwise stated:

- Pressure (see Appendix B):

$$P = P(T,\, \rho,\, X) \tag{A.9}$$

- Artificial viscosity:

$$q = q(T,\, \rho,\, X) \tag{A.10}$$

The inclusion of an artificial viscosity term, q, to the momentum conservation equation (A.2) is required to handle shock waves. To provide the appropriate dissipation, the artificial viscosity is usually expressed as the divergence of the velocity (von Newmann & Richtmyer 1950), thus ensuring that this term remains small except close to shocks. A procedure to add the artificial viscosity to pressure is to check whenever a mass-shell is compressed (i.e., $\rho_{i+1/2}^{n+1} > \rho_{i+1/2}^{n}$):

$$q_{i+1/2}^{n+1/2} = \begin{cases} 0 & if \quad \rho_{i+1/2}^{n+1} \leq \rho_{i+1/2}^{n} \\ q_0 \frac{(r_{i+1}^{n+1} - r_i^{n+1})^2 (W_{i+1/2}^{n+1} - W_{i+1/2}^{n})^2}{V_{i+1/2}^{n+1} (\Delta t^{n+1/2})^2} & if \quad \rho_{i+1/2}^{n+1} > \rho_{i+1/2}^{n} \end{cases} \tag{A.11}$$

with q_0 a constant of the order of unity, and $W = ln\, V = -ln\, \rho$.

- Internal energy (see Appendix B):

$$E = E(T,\, \rho,\, X) \tag{A.12}$$

- Opacity (see details in José 1996):

$$\kappa = \kappa(T,\, \rho,\, X) \tag{A.13}$$

- Energy generation rate (see Appendix C):

$$\epsilon = \epsilon(T,\, \rho,\, X) \tag{A.14}$$

A.3 Numerical procedure

The system of partial differential equations, together with the boundary conditions, the constitutive equations, and a suitable initial model, represent a well-defined mathematical problem. The procedure for solving numerically this system is described in Kippenhahn et al. (1967), and relies on a Henyey-type method (a generalized Newton-Raphson method for solving problems with boundary conditions on both edges of the interval).

In order to avoid numerical overflows, physical magnitudes are transformed into suitable variables. Natural logarithms and scaling factors are used to restrict their range of variability:

- Mass: $Q_i = 1 - \frac{m_i}{M_0}$
- Radius: $R_i = ln\, r_i$
- Specific volume: $W_{i+1/2} = ln\, V_{i+1/2}$
- Temperature: $Z_{i+1/2} = ln\, T_{i+1/2}$
- Luminosity: $B_i = \frac{L_i}{L_\odot}$

where $M_0 = (1+\delta)M_{NS}$ is related to the total mass of the star, and $\delta \simeq 10^{-18}$ is introduced to avoid singularities near the surface. $L_\odot = 3.86 \times 10^{33} erg.s^{-1}$ is the solar luminosity.

A.3.1 Discretization of the system of partial differential equations

Following Potter (1973), partial differential equations involving time-derivatives in the form

$$\frac{\partial y}{\partial t} = Ly \tag{A.15}$$

where L represents a general differential operator, can be discretized in a general way

$$y^{n+1} = y^n + Ly^n(1-\beta)\Delta t + Ly^{n+1}\beta\Delta t \tag{A.16}$$

with y^n and y^{n+1} being the values of function y at time points t^n and $t^{n+1} = t^n + \Delta t$. β is an interpolation parameter ($0 \leq \beta \leq 1$) that distinguishes different computation schemes. The choice $\beta = 0$ leads to an explicit determination of y^{n+1} from the previous, known value y^n. This condition leads to *explicit* methods. Otherwise, $\beta \neq 0$ defines *implicit* methods. In general, implicit schemes allow larger time steps despite requiring iterative procedures to solve the system at each step. On the other hand, explicit schemes are only stable if the time step is limited by the *Courant-Friedrichs-Levy condition* (i.e., the time step should avoid that a disturbance traveling at the speed of sound will traverse more than one zone; see Richtmyer & Morton 1994). $\beta = 0.5$ is the only value that ensures second-order accuracy and neither artificial damping nor unphysical amplification takes place (Kutter & Sparks 1972). We have adopted the choice $\beta = 1$ during the hydrostatic accretion phase (in order to get large time steps), and $\beta = 0.5$ to properly follow the hydrodynamic stages.

Making use of these auxiliar variables, the set of partial differential equations is transformed into a system of finite difference equations which take the following form:

- Conservation of mass:

$$-V_{i-1/2} = \frac{4\pi}{3M_0}\frac{r_i^3 - r_{i-1}^3}{Q_i - Q_{i-1}} \tag{A.17}$$

- Conservation of momentum:

$$\frac{u_i - u_i^n}{\Delta t^{n+1/2}} = (1-\beta)F_i^n + \beta F_i + \frac{4\pi}{M_0}\frac{1}{Q_{i+1/2} - Q_{i-1/2}}\left[(1-\beta)(r_i^n)^2 \cdot \right.$$
$$\left. \cdot \left(q_{i+1/2}^{n+1/2}\frac{V_{i+1/2}}{V_{i+1/2}^n} - q_{i-1/2}^{n+1/2}\frac{V_{i-1/2}}{V_{i-1/2}^n}\right) + \beta\,(r_i)^2\left(q_{i+1/2}^{n+1/2} - q_{i-1/2}^{n+1/2}\right)\right] \tag{A.18}$$

where

$$F_i = \frac{4\pi r_i^2}{M_0}\frac{P_{i+1/2} - P_{i-1/2}}{Q_{i+1/2} - Q_{i-1/2}} - G\frac{m_i}{r_i^2}$$

- Conservation of energy:

$$\frac{E_{i-1/2}-E^n_{i-1/2}}{\Delta t^{n+1/2}}=\epsilon^n_{i-1/2}+(1-\beta)G^n_{i-1/2}+\beta G_{i-1/2}-$$
$$-q^{n+1/2}_{i-1/2}V_{i-1/2}\frac{W_{i-1/2}-W^n_{i-1/2}}{\Delta t^{n+1/2}} \tag{A.19}$$

where

$$G_{i-1/2}=\frac{L_\odot}{M_0}\frac{B_i-B_{i-1}}{Q_i-Q_{i-1}}-P_{i-1/2}V_{i-1/2}\frac{W_{i-1/2}-W^n_{i-1/2}}{\Delta t^{n+1/2}}$$

- Energy transport:

$$B_i=\frac{256\sigma\pi^2r_i^4T_i^4}{3L_\odot M_0\kappa_i}\frac{Z_{i+1/2}-Z_{i-1/2}}{Q_{i+1/2}-Q_{i-1/2}}-H^n_i\frac{r_iT_i}{V_i}$$

where

$$H^n_i=\left\{\begin{array}{ll} 0 & if\ \bigtriangledown^n_i\le\bigtriangledown^n_{ad,i} \\ \frac{\pi}{L_\odot}\sqrt{\frac{G}{2}}H^{-3/2}_{p,i}l^2_{m,i}m^{1/2}_i c_{p,i}\cdot & \\ \cdot\sqrt{\frac{\partial W}{\partial Z}}\left(\bigtriangledown_i-\bigtriangledown_{ad,i}\right)^{3/2} & if\ \bigtriangledown^n_i>\bigtriangledown^n_{ad,i}\ \ ;\bigtriangledown\neq\bigtriangledown(t) \\ \frac{2\pi}{L_\odot}v_i r_i c_{p,i}\frac{l_{m,i}}{H_{p,i}}\left(\bigtriangledown_i-\bigtriangledown^{'}_i\right)_{eff} & if\ \bigtriangledown^n_i>\bigtriangledown^n_{ad,i}\ \ ;\bigtriangledown=\bigtriangledown(t) \end{array}\right\}$$

At the surface, we make use of the boundary conditions and neglect convection between grid points $N+1/2$ and $N+1$, so the equation is transformed as follows:

$$B_{N+1}=\frac{16\sigma\pi r^2_{N+1}T^4_{N+1/2}}{3L_\odot\left(-\frac{M_0}{4\pi}\left(Q_{N+1}-Q_{N-1/2}\right)\frac{\kappa_{N+1/2}}{2\sqrt{r^3_{N+1}r_N}}+\frac{2}{3}\right)} \tag{A.20}$$

It is worth noting that convection and the energy source term ϵ are linked explicitly to the set of difference equations. This has the advantage to save computing time.

- Lagrangian velocity:

$$\frac{R_i-R^n_i}{\Delta t^{n+1/2}}=(1-\beta)\frac{u^n_i}{r^n_i}+\beta\frac{u_i}{r_i} \tag{A.21}$$

A.3.2 Henyey's method

The integration of systems of differential equations subject to given boundary conditions is a quite common problem in theoretical astrophysics. Several numerical techniques for solving these large sets of equations, usually written in matrix form, have been developed. One of such techniques was originally proposed by Henyey et al. (1964) and has become very popular among astrophysicists since it was explicitly created for the integration of stellar structure equations. The main advantage of this method lies in exploiting the specific structure of the matrix, with non-zero values distributed only in a band, near the main diagonal.

This method determines the values of the $5N$ unknown variables (with N the number of grid points) by means of a sequence of iterations, starting with a trial solution, progressively improved through a Newton-Raphson technique until corrections become smaller than an arbitrarily fixed value.

A.4 The accretion algorithm

The accretion algorithm adopted in the SHIVA code was devised by Kutter & Sparks (1980), and consists of mass rezoning within a tiny initial envelope preserving the total number of mass shells:

1. The procedure begins with a converged and updated model (initial or previous model) at time t_0. We choose a time step Δt and compute a new converged model at time t_1, with $t_1 = t_o + \Delta t$, as explained in the previous Section.

2. The mass accreted during the time interval Δt is determined through $\Delta M = \dot{M}\Delta t$.

3. The accreted mass, ΔM, is then added to the overall envelope mass, $M_{\dot{e}nv} = M_{env}+\Delta M$, by shifting the boundaries of the N shells that define the envelope's computational grid. In the process, the initial mass ratio of neighboring zones is conserved.

4. Radii, luminosities and velocities are then interpolated accordingly for the new mass grid. Assuming conservation of mass, and from the interpolated radii, new specific volumes (or densities) are estimated.

5. Midpoint temperatures along the envelope are then interpolated with the new (shell-centered) specific volumes.

6. Finally, changes in chemical composition due to rezoning are evaluated.

Steps 2 to 6 have updated our converged model at time t_1. Stability criteria for convection, nuclear reaction rates, and the corresponding changes in chemical

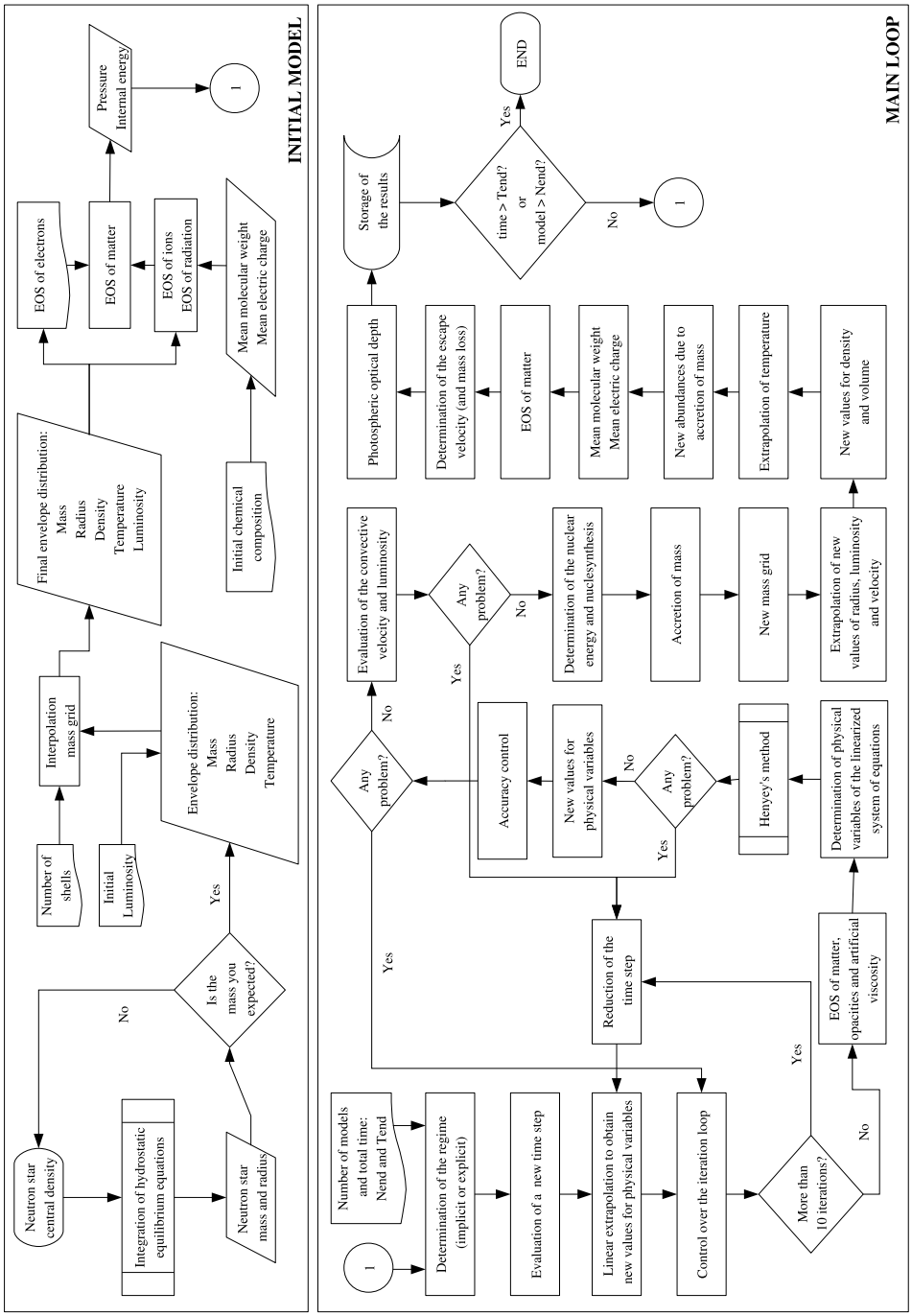

Figure A.2: Flow chart of the SHIVA code.

composition are then computed before the model is evolved. In the models described in this Thesis, accretion is never switched off.

Generally, the algorithms devised for spherically symmetric accretion onto neutron stars assume that the accreted matter is thermally adjusted to the underlying mass (see Woosley et al. 2004 and Fisker et al. 2008), and hence the impact of the accreted matter can be fully neglected. In order to check the feasibility of this approximation, and following Kutter & Sparks (1980), we performed a quantitative evaluation of the effect of the accretion shock front on the neutron star envelope. The effect on pressure, estimated from the ram pressure generated in the shock front, $\dot{M}u_{esc}/4\pi R_{NS}^2$, turns out to be negligible. Indeed, the ram pressure (about $\sim 10^{14} dyn.cm^{-2}$, for typical values of the neutron star size, escape velocity, and mass accretion rate adopted in this Thesis), is several orders of magnitude lower than the midpoint pressure of the outermost envelope shell (about $\sim 3 \times 10^{18} dyn.cm^{-2}$, at the onset of the calculations). It is worth noting, however, that during the interpulse period characteristic of type I X-ray bursts, the accretion luminosity would obscure the thermal emission from the cooling ashes (see Woosley et al. 2004 and Fisker et al. 2008), and hence a persistent luminosity fully driven by accretion ($\sim 1.5 \times 10^{37} erg.s^{-1}$) has to be taken into account to properly compare the numerical results with the observed light curves (see Chapter 4).

A.5 Time steps and accuracy criteria

The choice of an optimal time step, Δt, is crucial for the accuracy of the results and for the convergence of the iteration process, with reasonable computing time requirements. Hence, a compromise between a certain degree of accuracy and computing time seems mandatory. In the version of the SHIVA code used for the simulations reported in this Thesis, several conditions to control the effective time step have been implemented:

- First, we limit the fractional change of temperature, specific volume, and radius in the form:

$$\frac{\frac{dX}{dt}}{X}\Delta t \leq \delta \tag{A.22}$$

which can be expressed in finite differences as:

$$\Delta t_i^{n+1/2} \leq \delta \frac{X_i^n}{X_i^n - X_i^{n-1}} \Delta t_i^{n-1/2} \qquad i = 1,\, N \tag{A.23}$$

where the minimum of all $\Delta t_i^{n+1/2}$ is chosen as the new time step. The maximum fractional change assumed for these variables is of 1%.

- Second, when temperature exceeds $T \sim 4 \times 10^8 K$ (for an envelope of solar composition), convection sets in, progressively extending all the way through the accreted envelope. The transport of energy by convection induces changes in several physical magnitudes, in particular, a sharp rise in luminosity. Hence, whenever convection appears in a given shell, we limit the time step in order to reduce the fractional change in any magnitude, thus contributing to convergence.

- Finally, we limit the time step by changes in the chemical composition, assuming that the relative abundance variation of the most abundant nuclei (i.e., $Y > 10^{-14}$, with $Y = X/A$ being the mole number) do not exceed 15%.

Also, as a general accuracy criterion, the iteration method stops whenever all the independent physical variables satisfy:

$$\frac{\delta X}{X} \leq \epsilon \tag{A.24}$$

where we have adopted a value of 10^{-4} for the accuracy parameter, ϵ.

With respect to the spatial grid, we have made different tests to establish the optimal number of mass shells that can accomplish a sequence of evolutionary models with the expected accuracy and a reasonable computational time. We have used different resolutions in our calculations (in the range between 60 and 200 numerical shells), obtaining similar results (see Chapter 4).

Due to the inclusion of an artificial viscosity term in the equations of conservation of momentum and energy, we have carefully checked the overall conservation of energy (Christy 1964):

$$\frac{\partial}{\partial t}\left[\frac{u^2}{2} - \frac{Gm}{r} + E\right] + \frac{\partial L}{\partial m} + \frac{\partial}{\partial m}\left[4\pi r^2 u\,(P+q)\right] = \epsilon_{nuc} - \epsilon_{\nu} \tag{A.25}$$

which is satisfied to about 1 - 5%.

Finally, it is worth mentioning that since the SHIVA code is implicit, we do not need to deal with other restrictive conditions on the time step, such as the Courant-Friedrichs-Levy condition.

Appendix B

The equation of state

A typical neutron star ($M_{NS} = 1.4\,M_{\odot}$ and $R_{NS} \sim 10\,km$) has a surface gravity $\sim 10^{11}$ times larger than the terrestrial value. In these conditions, the matter accreted by a neutron star is fully ionized (either due to pressure or to temperature). Consequently, the equation of state and the overall properties of the accreted matter (consisting of photons, electrons, and ions) can be described under fully ionized conditions.

For a mixture of nuclei, the abundance of species k can be expressed in terms of its mass fraction:

$$X_k = \frac{N_k m_k}{\sum_k N_k m_k} = \frac{n_k m_k}{\rho} \tag{B.1}$$

where N_k, m_k, and n_k are the number, the mass, and the density of particles of type k, while ρ is the density of the stellar matter.

This can be expressed as well in terms of the atomic mass of species k, A_k, and the Avogadro's number, N_A:

$$X_k = \frac{n_k A_k}{\rho N_A}$$

with $m_k = A_k/N_A$.

For fully ionized matter, other useful definitions include the *mean molecular weight per ion*, μ_i, and the *mean molecular weight per electron*, μ_e, that represent the mean weight of an ion and of an electron of the mixture, respectively:

$$\mu_i = \left(\sum_k \frac{X_k}{A_k} \right)^{-1} \tag{B.2}$$

$$\mu_e = \left(\sum_k \frac{X_k Z_k}{A_k} \right)^{-1} \tag{B.3}$$

which are related to the *mean molecular weight per particle*, μ, as:

$$\mu = \left(\mu_i^{-1} + \mu_e^{-1}\right)^{-1} \tag{B.4}$$

Another useful definition in this regime is the *mean electric charge* of a multi-component plasma, $< Z >$, which takes into account the contribution of each species of the mixture to the total electric charge:

$$< Z >= \sum_k x_k Z_k$$

where x_k represents the chemical abundance by number of species k:

$$x_k = \frac{X_k/A_k}{\sum_k X_k/A_k} = \mu_i \frac{X_k}{A_k}$$

Typically, conditions for complete ionization are given by:

- Temperature ionization: $kT > Z^2 Ry$
- Pressure ionization: $E_F > Z^2 Ry \rightarrow \rho \gg 0.66 \frac{Z^3}{\mu_e}\, g \cdot cm^{-3}$

where E_F is the Fermi energy and μ_e the mean molecular weight per electron.

B.1 The equation of state for radiation

The contribution to the overall pressure due to photons can be modeled assuming that the surface of the neutron star behaves like a *black body*. Under this approximation, and from Planck's law, the specific internal energy of radiation is given by:

$$u_{rad} = \frac{a}{\rho} T^4$$

where $a = \frac{4\sigma}{c} = \frac{8\pi^5 \kappa^4}{15(hc)^3} = 7.5657 \times 10^{-15}\, erg\, cm^{-3}\, K^{-4}$ is the radiation constant. Thus, the radiation pressure is given by:

$$P_{rad} = \frac{1}{3}\rho u_{rad} = \frac{a}{3} T^4$$

The partial derivatives of these thermodynamical variables are calculated as follows:

$$\left(\frac{\partial P_{rad}}{\partial T}\right)_\rho = \frac{4a}{3} T^3$$
$$\left(\frac{\partial P_{rad}}{\partial \rho}\right)_T = 0$$
$$\left(\frac{\partial u_{rad}}{\partial T}\right)_\rho = \frac{4a}{\rho} T^3$$
$$\left(\frac{\partial u_{rad}}{\partial \rho}\right)_T = -\frac{a}{\rho^2} T^4$$

B.2 The equation of state for the ion plasma

As mentioned above, the ions present in the accreted matter are fully ionized and its state will depend only on the plasma temperature. Following Brush et al. (1996), in the zeroth-order approximation, ions can be considered as classical particles in a uniform background of electrons without any kind of interaction among them, such that the whole system is electrically neutral. In this context, at high temperatures, thermal effects dominate over Coulomb interactions and the state of ions can be approximated by means of a simple ideal gas law. Nevertheless, at low temperatures, Coulomb interactions become the dominant contribution and the ions are forced into a crystal lattice forming a *body centered cubic* solid structure (hereafter, *bcc*), that minimizes the electrostatic energy of the system formed by ions and electrons.

This state of ions can be characterized by means of the dimensionless Coulomb coupling parameter, Γ, which represents the ratio between the Coulomb potential energy and the thermal energy:

$$\Gamma = \frac{Z^2 e^2}{a_{ion} \kappa T}$$

where a_{ion} is the radius of the Wigner-Seitz ion-sphere, $a_{ion} = \left(\frac{3}{4\pi n_{ion}}\right)^{1/3}$, Z is the atomic number of the ions, e is the charge of the electron, κ is the Boltzmann's constant, and n_{ion} is the number of ions per cubic centimeter.

B.2.1 One component plasma (OCP)

Let's assume an idealized system of ions of the same type immersed in a uniform sea of electrons. In order to study the thermodynamics of the ion states, it is useful to rely on the corresponding Helmholtz free energy, F. Following the discussion in previous section, the total Helmholtz free energy for the ion plasma can be described by means of an ideal gas term, $F_{ideal-gas}$, and, in a first-order approximation, a Coulombian interaction term, $F_{Coulomb}$:

$$F_{ion} = F_{ideal-gas} + F_{Coulomb}$$

with

$$F_{ideal-gas} = N_{ion} \kappa T \left(ln \left[n_{ion} \left(\frac{2\pi\hbar^2}{m_{ion} \kappa T} \right)^{3/2} \right] - 1 \right)$$

Several cases of interest can be distinguished in terms of the dimensionless Coulomb coupling parameter, Γ:

- $\Gamma = 0$: the ion plasma behaves like an *ideal gas*. Therefore,

$$F_{Coulomb} = 0$$

- $\Gamma \ll 1$: the ion plasma behaves like a *real gas* (Debye-Hückel limit) because Coulomb interactions appear. Thus,

$$F_{Coulomb} = -N_{ion}\kappa T \frac{1}{\sqrt{3}}\Gamma^{3/2}$$

- $\Gamma > 1$: in this phase, ions form a *Coulomb liquid* and the excess of free energy due to Coulomb interactions can be evaluated from detailed Monte Carlo calculations (see Slattery et al. 1980, 1982). Results can be fitted with high accuracy by means of the analytic expression (DeWitt 1976):

$$F_{Coulomb} = -N_{ion}\kappa T \left[a\Gamma + 4\left(b\Gamma^{1/4} - c\Gamma^{-1/4}\right) + d\, ln\, \Gamma + e\right]$$

with $a = -0.089774$, $b = 0.95043$, $c = 0.18956$, $d = -0.81487$, and $e = -2.5820$. Calculations by Ogata & Ichimaru (1987) provided new values for the constants: $a = -0.0898004$, $b = 0.96786$, $c = 0.220703$, $d = -0.86097$, and $e = -2.5269$.

- The region $0 < \Gamma < 1$ is fitted with an interpolation formula given by Yakovlev & Shalybkov (1989):

$$F_{Coulomb} = N_{ion}\kappa T \left[-\frac{1}{\sqrt{3}}\Gamma^{3/2} + \frac{\beta}{\gamma}\Gamma^{\gamma}\right]$$

where $\beta = 0.29561$ and $\gamma = 1.9885$ have been calculated imposing continuity at $\Gamma = 1$, for $u(\Gamma)$ and $\frac{du(\Gamma)}{d\Gamma}$. Note that for $\Gamma \ll 1$, the classical Debye-Hückel theory is recovered.

- $\Gamma > \Gamma_m \simeq 180$: the ion plasma *crystallizes* into a *bcc* solid. Following Pollock & Hansen (1973), we have:

$$F_{Coulomb} = N_{ion}\kappa T \left[-0.895929\Gamma + \frac{3}{2}\, ln\, \Gamma - \frac{3225}{2\Gamma^2} - 1.1703\right]$$

The pressure and the specific internal energy of ions, as well as other physical variables, can be recovered from the Helmholtz free energy, F:

$$P = -F + \rho\left(\frac{\partial F}{\partial \rho}\right)_T$$

$$u = \frac{F}{\rho} - \frac{T}{\rho}\left(\frac{\partial F}{\partial T}\right)_\rho$$

Thus, we have:

$$P_{ion} = P_{ideal-gas} + P_{Coulomb}$$

$$u_{ion} = u_{ideal-gas} + u_{Coulomb}$$

with

$$P_{ideal-gas} = \frac{\rho RT}{\mu_{ion}}$$

$$u_{ideal-gas} = \frac{3RT}{2\mu_{ion}}$$

and $P_{Coulomb}$ and $u_{Coulomb}$ are expressed as a function of the coupling parameter, Γ, in the different regimes described before.

B.2.2 Multi component plasma (MCP)

Let's now assume a mixture of different species of ions in a rigid and uniform background of electrons, being the overall system electrically neutral. To obtain the equation of state for the ions, different procedures have been proposed in the last decades. One is the so-called *linear mixing*, in which the thermodynamical variables are recovered from the total free energy of the mixture, which is obtained through the addition of the independent terms corresponding to each ion. Another procedure, suggested by Hansen et al. (1977) and used in the this work, relies on the approximation of any MCP as a OCP with an effective plasma charge, Z_{eff}, given by:

$$Z_{eff} =< Z >^{1/3} < Z^{5/3} > \tag{B.5}$$

According to this procedure, the expressions for a OCP are extended to the case of a MCP adopting an effective Coulomb coupling parameter, Γ_{eff}, given by:

$$\Gamma_{eff} = \frac{Z_{eff}^2 e^2}{a_{ion} \kappa T} \tag{B.6}$$

From Eq. B.5, we have:

$$\Gamma_{eff} = \frac{< Z^{5/3} > e^2}{a_{ion} / < Z >^{1/3} \kappa T}$$

Now, we define an electron-sphere radius, a_e, to properly account for a uniform background, as $a_e = a_{ion} / < Z >^{1/3}$. Thus, we have:

$$\Gamma_{eff} =< Z^{5/3} > \Gamma_e$$

with

$$\Gamma_e = \frac{e^2}{a_e \kappa T}$$

In this work, the expressions adopted for the contribution of the MCP, according to the procedure of Hansen et al. (1977), are:

$$P_{ion} = P_{ideal-gas} + P_{Coulomb}$$

$$u_{ion} = u_{ideal-gas} + u_{Coulomb}$$

with

$$P_{ideal-gas} = \frac{\rho RT}{\mu_{ion}}$$

$$u_{ideal-gas} = \frac{3RT}{2\mu_{ion}}$$

and $P_{Coulomb}$ and $u_{Coulomb}$ can be expressed as a function of the Coulomb coupling parameter, Γ:

- $\Gamma \geq 1$:

$$P_{Coulomb} = \left(\frac{a}{3} < Z^{5/3} > \Gamma_e + \frac{b}{3} < Z^{5/12} > \Gamma_e^{1/4} + \frac{c}{3} \right) \frac{\rho RT}{\mu_{ion}}$$

$$u_{Coulomb} = \frac{3}{\rho} P_{Coulomb} = \left(\frac{a}{3} < Z^{5/3} > \Gamma_e + \frac{b}{3} < Z^{5/12} > \Gamma_e^{1/4} + \frac{c}{3} \right) \frac{3RT}{\mu_{ion}}$$

with a, b, and c, constants given by Ogata & Ichimaru (1987), and specified for $\Gamma > 1$ in the case of a OCP.

- $\Gamma < 1$:

$$P_{Coulomb} = -\left(0.288675 < Z^{5/2} > \Gamma_e^{3/2} - \frac{\beta}{3} < Z^{5\gamma/2} > \Gamma_e^{\gamma} \right) \frac{\rho RT}{\mu_{ion}}$$

$$u_{Coulomb} = \frac{3}{\rho} P_{Coulomb} = -\left(0.288675 < Z^{5/2} > \Gamma_e^{3/2} - \frac{\beta}{3} < Z^{5\gamma/2} > \Gamma_e^{\gamma} \right) \frac{3RT}{\mu_{ion}}$$

with β and γ constants given by Yakovlev & Shalybkov (1989), and specified for $0 < \Gamma < 1$ in the case of a OCP.

No additional corrections have been taken into account for the ideal ion plasma term (like quantum or electron-screening corrections).

B.3 The equation of state for an electron-positron gas

A Fermi gas is a collection of non-interacting particles with a spin 1/2 (fermions and antifermions) described by means of the Fermi-Dirac statistics. In our case, we will assume a system formed by electrons and positrons (with an interaction energy much smaller than their kinetic energy) which contribute to the total pressure, energy, and density of the matter. Following Blinnikov et al. (1996), we present a set of thermodynamical functions, covering the entire temperature-density plane for different relativistic regimes and/or degrees of degeneracy.

The most general expression for the pressure of an ideal Fermi gas is given by:

$$P_- = \frac{mc^2}{3\pi^2\alpha^4}\left(\frac{mc}{\hbar}\right)^3 f(\varphi,\alpha) \tag{B.7}$$

with

$$f(\varphi,\alpha) = \int_0^\infty \frac{x^4\left(x^2+\alpha^2\right)^{-1/2}dx}{1+exp\left[\left(x^2+\alpha^2\right)^{1/2}-\varphi\right]} \tag{B.8}$$

where α and φ are two dimensionless parameters defined by:

$$\alpha \equiv \frac{mc^2}{\kappa T}$$

$$\varphi \equiv \frac{\mu}{\kappa T}$$

and m is the mass of the electron, c is the speed of light, $\hbar$ is the reduced Planck's constant $(h/2\pi)$, and μ is the chemical potential.

Now, let's introduce two additional parameters, combinations of α and φ, defined as:

$$\psi \equiv \frac{\mu}{mc^2} = \frac{\varphi}{\alpha}$$

$$\chi \equiv \frac{(\mu - mc^2)}{\kappa T} = \varphi - \alpha$$

where ψ represents the *chemical potential* in units of the electron energy at rest, while χ is the *degeneracy parameter*. Sometimes it is more convenient to rely on $x = \alpha\xi$, and express all the thermodynamic functions that characterize the gas as:

$$P_- = \frac{mc^2}{3\lambda^3} I_P(\psi,\alpha) \tag{B.9}$$

$$u_- = \frac{mc^2}{\lambda^3} I_u(\psi,\alpha) \tag{B.10}$$

$$S_- = \frac{mc^2}{3\lambda^3\rho T} I_S(\psi,\alpha) \tag{B.11}$$

$$n_- = \frac{1}{\lambda^3} I_n(\psi,\alpha) \tag{B.12}$$

with

$$I_P(\psi,\alpha) = \int_0^\infty \frac{\xi^4\left(\xi^2+1\right)^{-1/2}d\xi}{1+exp\left\{\alpha\left[\left(\xi^2+1\right)^{1/2}-\psi\right]\right\}} \tag{B.13}$$

$$I_u(\psi,\alpha)=\int_0^\infty \frac{\xi^2\left(\xi^2+1\right)^{-1/2}d\xi}{1+exp\left\{\alpha\left[\left(\xi^2+1\right)^{1/2}-\psi\right]\right\}} \tag{B.14}$$

$$I_S(\psi,\alpha)=\int_0^\infty \frac{\xi^2\left[3+4\xi^2-3\mu\left(\xi^2+1\right)^{1/2}\right]\left(\xi^2+1\right)^{-1/2}d\xi}{1+exp\left\{\alpha\left[\left(\xi^2+1\right)^{1/2}-\psi\right]\right\}} \tag{B.15}$$

$$I_n(\psi,\alpha)=\int_0^\infty \frac{\xi^2 d\xi}{1+exp\left\{\alpha\left[\left(\xi^2+1\right)^{1/2}-\psi\right]\right\}} \tag{B.16}$$

where we have introduced λ as a natural unit of distance (of the order of the Compton length):

$$\lambda^3=\pi^2\left(\frac{\hbar}{mc}\right)^3$$

For positrons, the expressions for P_+, u_+, S_+, and n_+, are quite analogous (just replacing ψ by $-\psi$). The overall pressure, energy, and density of the gas result from the sum of the corresponding contribution of electrons and positrons. The electron excess per unit volume can be obtained from

$$n_- - n_+ = \rho N_A Y \tag{B.17}$$

where N_A is the Avogadro's number and Y is the electron excess per baryon. Since the left-hand side of equation B.17 depends on T and φ, we can derive an expression for φ (or ψ) as a function of ρ and T. Notice also that the first derivatives of P, u, and S, with respect to ρ and T, must satisfy the following thermodynamic identities:

$$\left(\frac{\partial S}{\partial T}\right)_\rho=\frac{1}{T}\left(\frac{\partial E}{\partial T}\right)_\rho \tag{B.18}$$

$$\left(\frac{\partial S}{\partial \rho}\right)_T=\frac{1}{T}\left[\left(\frac{\partial E}{\partial \rho}\right)_T-\frac{P}{\rho^2}\right] \tag{B.19}$$

$$\left[\left(\frac{\partial E}{\partial \rho}\right)_T-\frac{P}{\rho^2}\right]=-\frac{1}{\rho^2}\left(\frac{\partial P}{\partial T}\right)_\rho \tag{B.20}$$

Next, we will present a set of equations of state covering the entire $T-\rho Y$ plane (see Figure B.1) for different relativistic regimes, γ_r, and/or degrees of degeneracy, χ:

$$\gamma_r=\frac{\varepsilon}{(n_- - n_+)\,mc^2}$$

$$\chi=\frac{(\mu-mc^2)}{\kappa T}$$

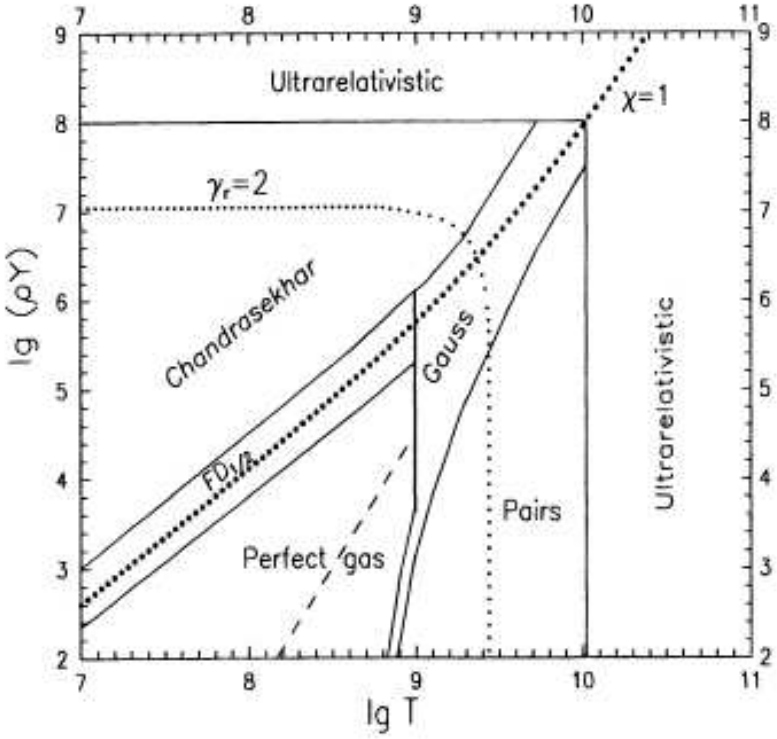

Figure B.1: Boundaries of highest efficiency for different equations of state. The gas is strongly relativistic above and to the right of the dotted line (for which $\gamma_r = 2$), and is strongly degenerate above the line drawn by asterisks (for which $\chi = 1$). Above the dashed line, in the region for a nearly classical perfect gas, the contribution of pairs becomes negligible. From Blinnikov et al. (1996).

where $\varepsilon = u\rho$ is the internal energy per unit volume, and m, c, κ, and μ have their usual meaning (see Eq. B.8).

The domains of applicability of the different expansions shown in Figure B.1 overlap (e.g., the half-integer Fermi-Dirac expansion covers all the region of the perfect gas; Chandrasekhar does work in the cold ultrarelativistic zone, etc.). So, the criterion for drawing boundaries was not only accuracy but also the search for optimum efficiency in the calculations.

B.3.1 Moderate degeneracy (half-integer Fermi-Dirac integrals)

In this Subsection, we will describe the thermodynamical functions valid in the region of low or moderate degeneracy

$$\psi \leq 2$$

and weakly relativistic regime

$$\alpha > 1$$

Making some changes of variables in Equations B.13 and B.14, and after a series expansion, we find the corresponding equation of state for *moderate degeneracy*:

$$P = \frac{mc^2}{3\lambda^3}\frac{2\sqrt{2}}{\alpha^{5/2}}\left[\Phi^+_{3/2}(\chi,\alpha) + \frac{3}{4\alpha}\Phi^+_{5/2}(\chi,\alpha) + \frac{3}{32\alpha^2}\Phi^+_{7/2}(\chi,\alpha) + \ldots\right] \tag{B.21}$$

$$u = \frac{mc^2}{\lambda^3}\frac{\sqrt{2}}{\rho\alpha^{3/2}}\left[\Phi^+_{1/2}(\chi,\alpha) + \frac{9}{4\alpha}\Phi^+_{3/2}(\chi,\alpha) + \frac{47}{32\alpha^2}\Phi^+_{5/2}(\chi,\alpha) + \right.$$
$$\left. + \frac{25}{128\alpha^3}\Phi^+_{7/2}(\chi,\alpha) + \ldots\right] - mc^2 N_A Y \tag{B.22}$$

$$S = \frac{5\kappa\alpha P}{2mc^2\rho} - \frac{2\kappa}{3\lambda^3\rho}\sqrt{\frac{2}{\alpha}}\left\{\frac{3}{2}\frac{\chi}{\alpha}\Phi^-_{1/2}(\chi,\alpha) - 3F_{1/2}(-\chi-2\alpha) + \right.$$
$$+\frac{3}{4\alpha}\left[\frac{5}{2}\frac{\chi}{\alpha}\Phi^-_{3/2}(\chi,\alpha) - 5F_{3/2}(-\chi-2\alpha)\right] + \frac{3}{32\alpha^2}\left[\frac{7}{2}\frac{\chi}{\alpha}\Phi^-_{5/2}(\chi,\alpha) - 7F_{3/2}(-\chi-2\alpha)\right] -$$
$$\left. - \frac{3}{4\alpha^2}\left[\Phi^+_{5/2}(\chi,\alpha) + \frac{1}{4\alpha}\Phi^+_{7/2}(\chi,\alpha)\right] + \ldots\right\} \tag{B.23}$$

$$n = \frac{\sqrt{2}}{\lambda^3}\frac{1}{\alpha^{3/2}}\left[\Phi^-_{1/2}(\chi,\alpha) + \frac{5}{4\alpha}\Phi^-_{3/2}(\chi,\alpha) + \frac{7}{32\alpha^2}\Phi^-_{5/2}(\chi,\alpha) - \right.$$
$$\left. - \frac{3}{128\alpha^3}\Phi^-_{7/2}(\chi) + \ldots\right] \tag{B.24}$$

with

$$\Phi^-_\nu(\chi,\alpha) = F_\nu - F_\nu(-\chi-2\alpha)$$
$$\Phi^+_\nu(\chi,\alpha) = F_\nu + F_\nu(-\chi-2\alpha)$$

where $F_\nu(x)$ are Fermi-Dirac integrals.

B.3.2 Ultrarelativistic case (integer Fermi-Dirac integrals)

In this case, the region of interest is delimited by $\alpha < \chi$ (for $\chi > 1$), and $\alpha < 1$ (for $\chi \leq 1$). Like in previous Subsection, rewriting Equations B.13 and B.14, and after a series expansion, one obtains the thermodynamical functions for an *ultrarelativistic gas* formed by electrons and positrons:

$$P = \frac{mc^2}{12\lambda^3}\left[\psi^4 + \left(\frac{2\pi^2}{\alpha^2} - 3\right)\psi^2 + \frac{7\pi^4}{15\alpha^4} - \frac{\pi^2}{\alpha^2}\right] \tag{B.25}$$

$$u = \frac{3P}{\rho} + \frac{mc^2}{2\lambda^3\rho}\left(\psi^2 + \frac{\pi^2}{3\alpha^2}\right) - mc^2 N_A Y \tag{B.26}$$

$$S = \frac{\pi^2\kappa}{3\lambda^3\alpha\rho}\left(\psi^2 + \frac{7\pi^2}{15\alpha^2} - \frac{1}{2}\right) \tag{B.27}$$

$$n = \frac{1}{\lambda^3}\left[\frac{\psi^3}{3} + \left(\frac{\pi^2}{3\alpha^2} - \frac{1}{2}\right)\psi\right] \tag{B.28}$$

B.3.3 Perfect gas

A gas formed by electrons and positrons can be considered a *perfect gas*, with corrections for pairs and degeneracy, whenever temperature and density lay in the region:

$$T \leq 10^9\, K$$

$$1.5 \cdot 10^6 T_9^{3/2} exp\left(-\frac{5.93 \cdot 10^9}{T}\right) g \cdot cm^{-3} \leq \frac{\rho}{Y} \leq 2.1 \cdot 10^5 T_9^{3/2} g \cdot cm^{-3}$$

Valid thermodynamical expressions for these conditions can be approximated by:

$$P = \kappa T \rho N_A Y \left[1 + Q\rho Y \left(\frac{mc^2}{\kappa T}\right)^{3/2}\left(1 - \frac{45}{16\alpha} + \frac{2865}{512\alpha^2}\right) + \frac{B}{(\rho Y)^2}\left(\frac{\kappa T}{mc^2}\right)^3 \cdot \right.$$
$$\left. \cdot\, exp\left(-\frac{2mc^2}{\kappa T}\right)\left(1 + \frac{15}{4\alpha} + \frac{165}{32\alpha^2}\right)\right] \tag{B.29}$$

$$u = \frac{3}{2}\kappa T \rho N_A Y \left[1 + \frac{5}{4\alpha} - \frac{5}{4\alpha^2} + \frac{45}{64\alpha^3} Q\rho Y \left(\frac{mc^2}{\kappa T}\right)^{3/2}\left(1 - \frac{45}{16\alpha} + \frac{955}{512\alpha^2}\right) + \right.$$
$$\left. + \frac{2B}{3(\rho Y)^2}\left(\frac{\kappa T}{mc^2}\right)^2 exp\left(-\frac{2mc^2}{\kappa T}\right)\left(1 + \frac{21}{4\alpha} + \frac{405}{32\alpha^2}\right)\right] \tag{B.30}$$

$$S = \kappa N_A Y \left[\frac{5}{2} - \ln\left(\frac{2^{1/2}\rho\lambda^3 N_A Y \alpha^{3/2}}{\pi^{1/2}}\right) + \frac{15}{4\alpha}\left(1 - \frac{3}{4\alpha} + \frac{3}{8\alpha^2}\right) + \right.$$
$$+ \frac{1}{2} Q\rho Y \left(\frac{mc^2}{\kappa T}\right)^{3/2}\left(1 - \frac{45}{16\alpha} - \frac{8595}{512\alpha^2}\right) + \frac{B}{(\rho Y)^2}\left(\frac{\kappa T}{mc^2}\right)^2 \cdot$$
$$\left. \cdot \exp\left(-\frac{2mc^2}{\kappa T}\right)\left(1 + \frac{23}{4\alpha} + \frac{465}{32\alpha^2}\right)\right] \tag{B.31}$$

where

$$Q = \frac{N_A \lambda^3}{4\sqrt{\pi}} = 4.82744 \cdot 10^8 \, cm^3 g^{-1}$$

$$B = \frac{\pi}{N_A^2 \lambda^6} = 2.68192 \cdot 10^{13} \, cm^{-6} g^2$$

B.3.4 Chandrasekhar expansion

In this case, if the inequality $\alpha(\psi - 1) > 1$ is fulfilled, the positron contribution to the equation of state can be neglected. If one denotes the dimensionless Fermi momentum as

$$x = \sqrt{\psi^2 - 1} = \frac{p_F}{mc}$$

then, using the Chandrasekhar expansion, the thermodynamic functions for a *highly degenerate electron gas* can be approximated as follows:

$$P_- = \frac{mc^2}{24\lambda^3} \left[f_0(x) + \frac{C_2}{\alpha^2} f_2(x) + \frac{C_4}{\alpha^4} f_4(x) + \cdots \right] \tag{B.32}$$

$$u_- = \frac{mc^2}{8\lambda^3 \rho} \left[g_0(x) + \frac{C_2}{\alpha^2} g_2(x) + \frac{C_4}{\alpha^4} g_4(x) + \cdots \right] \tag{B.33}$$

$$S_- = \frac{\kappa^2 T}{12\lambda^3 \rho mc^2} \left[C_2 f_2(x) + \frac{2C_4}{\alpha^2} f_4(x) + \cdots \right] \tag{B.34}$$

$$n_- = \frac{1}{3\lambda^3} \left[h_0(x) + \frac{C_2}{\alpha^2} h_2(x) + \frac{C_4}{\alpha^4} h_4(x) + \cdots \right] \tag{B.35}$$

where C_n are defined by the Riemann ζ-function, $C_n = 2\zeta(n)\left(1 - 2^{1-n}\right)$, and the suite of additional functions are defined as follows:

$$f_0(x) = x\left(2x^2 - 3\right)\sqrt{x^2+1} + 3\ln\left(x + \sqrt{x^2+1}\right)$$

$$f_2(x) = 24x\sqrt{x^2+1}$$

$$f_4(x) = \frac{24}{x}\left(2x^2 - 1\right)\sqrt{x^2+1}$$

$$g_0(x) = x\left(2x^2 + 1\right)\sqrt{x^2+1} - \ln\left(x + \sqrt{x^2+1}\right) - \frac{8}{3}x^3$$

$$g_2(x) = \frac{8}{x}\left[\left(3x^2+1\right)\sqrt{x^2+1} - \left(2x^2+1\right)\right]$$

$$g_4(x) = \frac{24}{x^5}\{\left[4 + \left(x^2+1\right)\left(2x^2-3\right)\right]\sqrt{x^2+1} - 1\}$$

$$h_0(x) = x^3$$

$$h_2(x) = \frac{3}{x}\left(2x^2+1\right)$$

$$h_4(x) = \frac{9}{x^5}$$

B.3.5 Gauss quadrature

A generalized Gauss numerical quadrature method has to be used when the accuracy of asymptotic expansions is not sufficient. With this method, it is possible to obtain approximate expressions for the integrals that describe the thermodynamic properties of an electron-positron gas for any degree of degeneracy. After a set of transformations, similar to those described in previous subsections, the equation of state for an electron-positron gas may be expressed as:

$$P = \frac{mc^2}{3\lambda^3\alpha^4}\left[G_2\left(\alpha,\psi\right) + G_2\left(\alpha,-\psi-2\alpha\right)\right] \tag{B.36}$$

$$u = \frac{mc^2}{\lambda^3\rho\alpha^4}\left[G_4\left(\alpha,\psi\right) + G_4\left(\alpha,-\psi-2\alpha\right) + 2\alpha G_1\left(\alpha,-\psi-2\alpha\right)\right] \tag{B.37}$$

$$\begin{aligned} S = \frac{\kappa}{\lambda^3\rho\alpha^3}\{3\left[G_4\left(\alpha,\psi\right) + G_4\left(\alpha,-\psi-2\alpha\right)\right] + 3\psi\left[G_1\left(\alpha,\psi\right) - G_1\left(\alpha,-\psi-2\alpha\right)\right] + \\ +6\alpha G_1\left(\alpha,-\psi-2\alpha\right) + \left[G_2\left(\alpha,\psi\right) + G_2\left(\alpha,-\psi-2\alpha\right)\right]\} \end{aligned} \tag{B.38}$$

$$n = \frac{1}{\lambda^3\alpha^3}\left[G_1\left(\alpha,\psi\right) + G_1\left(\alpha,-\psi-2\alpha\right)\right] \tag{B.39}$$

where

$$G_1\left(\alpha,\psi\right) = \int_0^\infty \frac{\left(u+\alpha\right)\sqrt{u\left(u+2\alpha\right)}}{1+exp\left(u-\psi\right)}du$$

$$G_2\left(\alpha,\psi\right) = \int_0^\infty \frac{u\left(u+2\alpha\right)\sqrt{u\left(u+2\alpha\right)}}{1+exp\left(u-\psi\right)}du$$

$$G_4\left(\alpha,\psi\right) = \int_0^\infty \frac{u\left(u+\alpha\right)\sqrt{u\left(u+2\alpha\right)}}{1+exp\left(u-\psi\right)}du$$

G_1, G_2, and G_4 functions for a positron gas can be obtained replacing ψ by $-\left(\psi+2\alpha\right)$. Values for these functions can be found in Tables $11-13$ of Blinnikov et al. (1996), whereas values for the density n (Eq. B.39) are listed in Table 14.

Appendix C

Nucleosynthesis and energy generation

Thermonuclear reactions provide the energy source (and the changes in composition) of stars, playing a key role in any stage of their evolution.

In the framework of X-ray burst simulations, the concert of many different nuclear interactions is required to handle detailed nucleosynthesis studies. In this Thesis, we have used two different nuclear reaction networks: a large one (see Fig. C.1), containing 605 isotopes, linked through 3551 nuclear processes, which has been used for the post-processing calculations reported in Chapters 2 & 3, and a subset containing 323 isotopes and 1392 reactions, directly coupled to the hydrodynamic code (Chapter 4), as a compromise between computing time requirements and accuracy.

C.1 Time evolution of the nuclear abundances

A typical nuclear reaction may be described by two particles, P_i and P_j, which mutually interact, producing a pair of particles, P_k and P_l, in the form:

$$ {}^{Z_i}_{A_i}P_i + {}^{Z_j}_{A_j}P_j \rightarrow {}^{Z_k}_{A_k}P_k + {}^{Z_l}_{A_l}P_l $$

where Z_i and A_i are the atomic and mass numbers of particle i, respectively.

Nuclear reactions are governed by the standard laws of conservation of energy, linear and angular momentum, mass number, and charge. The time evolution of species i is then computed from a detailed balance between reactions that create and destroy such isotope. The equations governing this evolution can be written as:

$$ \frac{dY_i}{dt} = \sum_{k \neq i} \lambda_{k \rightarrow i} Y_k + \sum_{k \neq i,\, l \geq k} [kl \rightarrow i] Y_k Y_l - \lambda_i Y_i - \sum_j [ij] Y_i Y_j \qquad \text{(C.1)} $$

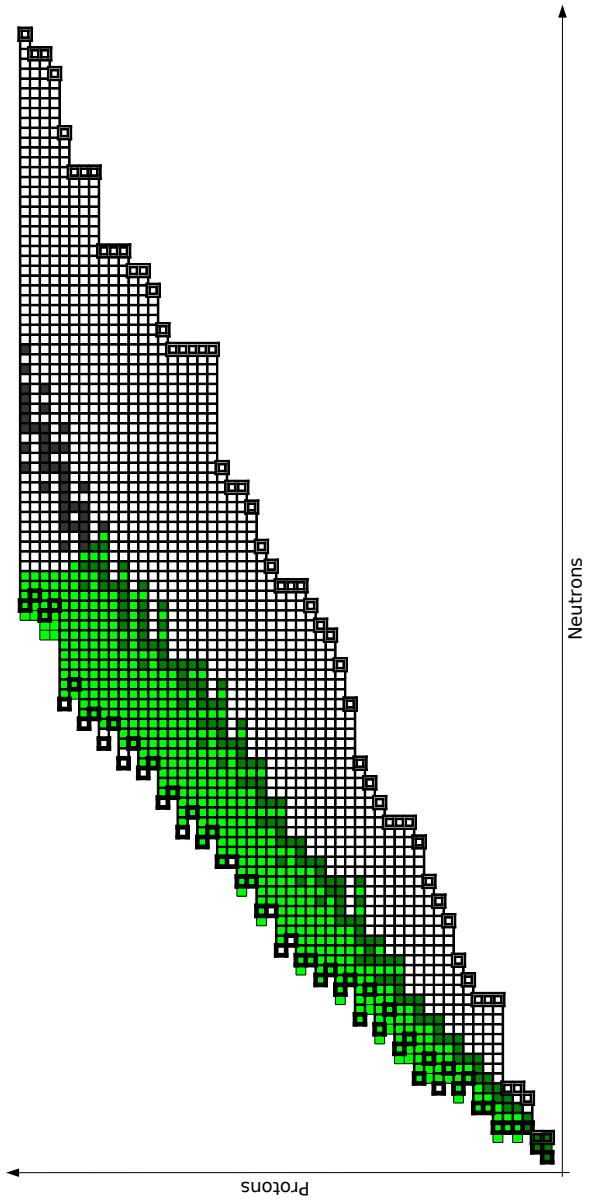

Figure C.1: Scheme of the network of isotopes used in this Thesis for post-processing calculations, containing 605 elements, ranging from ^{1}H to ^{113}Xe (green squares). The location of the proton-drip line (left-hand side of the diagram), the neutron-drip line (right-hand side), and the set of stable isotopes (dark grey squares) are based on Audi et al. (2003b). The hydrodynamic calculations performed in this Thesis have relied on a subset of this network, containing 323 isotopes, ranging from ^{1}H to ^{107}Te (see Table C.1).

where $Y_i = \frac{X_i}{A_i}$ is the mole fraction (with X_i being the mass fraction of particle i), $\lambda_{k\rightarrow i}$ is the photodisintegration or $\beta - decay$ rate of nucleus k leading to the formation of nucleus i, $[kl \rightarrow i]$ is the reaction rate between species k and l leading to the formation of nucleus i, $[kl \rightarrow i] = N_A\rho < \sigma v >_{k,l\rightarrow i}$ (with N_A being the Avogadro number, ρ the density, and $< \sigma v >_{k,l\rightarrow i}$ the Maxwellian-averaged product of the cross section and the velocity of the two nuclides k and l), λ_i is the total rate for all photodisintegration or $\beta - decay$ channels of nucleus i, and $[ij]$ is the total rate for all exit channels involving destruction of nucleus i.

C.2 The nuclear reaction network

As mentioned above, we have adopted two different networks for the calculations reported in this Thesis: the most extensive one contains 605 isotopes, ranging from hydrogen (^1H) to xenon (^{113}Xe), and linked through an updated network that includes up to 3551 reactions; the second one, used in the hydrodynamic simulations, contains a subset of 323 isotopes and 1392 reactions (see Tables C.1 and C.2).

Temperatures and densities achieved in XRB nucleosynthesis are sufficiently high so that many nuclear reactions, especially those with relatively small Q-values, achieve an equilibrium between the forward and reverse process. For instance, if the reaction $A(p,\gamma)B$ has a small Q-value, then the strong $B(\gamma,p)A$ photodisintegration will give rise to a small equilibrium abundance of nuclei B that may then capture another proton. Such cases, which are called (sequential) two-proton captures, must be considered carefully since they represent waiting points (and may even be candidates for *termination points*) for a continuous abundance flow toward heavier mass nuclei. Among the most important of these waiting points are ^{64}Ge, ^{68}Se, and ^{72}Kr (Schatz et al. 1998). When a reaction rate equilibrium has been established, the most important nuclear physics information needed are the reaction Q-value (which enters exponentially in the effective decay constant of A) of the link $A(p,\gamma)B$ and the reaction rate of the second-step reaction $B(p,\gamma)C$, but the *rate* of the reaction $A(p,\gamma)B$ becomes irrelevant. Note that for the three nuclei mentioned above, the (p,γ) Q-values have not been measured directly yet. According to Audi et al. (2003b), their predicted values amount to $Q = -80 \pm 300$, -450 ± 100 and $-600 \pm 150\,keV$, respectively. Some encouraging progress has been made through mass measurements of ^{64}Ge (Clark et al. 2007; Schury et al. 2007), ^{68}Se (Clark et al. 2004; Wöhr et al. 2004; Chartier et al. 2005), and ^{72}Kr (Rodríguez et al. 2004). In order to set up the reaction library for this Thesis, we started by adopting the proton drip line from Audi et al. (2003a,b). For reactions $A(p,\gamma)B$ with Q-values below $1\,MeV$, the rates (below the element Pd) are calculated using the Hauser-Feshbach code MOST (Goriely 1998; Arnould & Goriely 2006), and the corresponding reverse photodisintegrations are computed with the *extrapolated* proton separation energies from Audi et al. (2003b).

Table C.1: List of isotopes adopted in this Thesis for post-processing calculations.

Number	Isotope[b]	Number	Isotope[b]	Number	Isotope[b]
1	$^{1}H^{a}$	49	$^{22}Na^{a}$	97	$^{33}Ar^{a}$
2	$^{2}H^{a}$	50	$^{22}Mg^{a}$	98	$^{34}S^{a}$
3	$^{3}H^{a}$	51	$^{22}Al^{a}$	99	$^{34}Cl^{a}$
4	$^{3}He^{a}$	52	^{22}Si	100	$^{34}Ar^{a}$
5	$^{4}He^{a}$	53	$^{23}Na^{a}$	101	$^{34}K^{a}$
6	^{6}Li	54	$^{23}Mg^{a}$	102	^{34}Ca
7	^{6}Be	55	$^{23}Al^{a}$	103	^{35}S
8	$^{7}Li^{a}$	56	^{23}Si	104	$^{35}Cl^{a}$
9	$^{7}Be^{a}$	57	$^{24}Mg^{a}$	105	$^{35}Ar^{a}$
10	^{8}Be	58	$^{24}Al^{a}$	106	$^{35}K^{a}$
11	$^{8}B^{a}$	59	$^{24}Si^{a}$	107	^{35}Ca
12	^{8}C	60	$^{25}Mg^{a}$	108	^{36}S
13	^{9}Be	61	$^{25}Al^{a}$	109	^{36}Cl
14	^{9}B	62	$^{25}Si^{a}$	110	$^{36}Ar^{a}$
15	^{9}C	63	$^{25}P^{a}$	111	$^{36}K^{a}$
16	^{10}B	64	$^{26}Mg^{a}$	112	$^{36}Ca^{a}$
17	^{10}C	65	$^{26m}Al^{a}$	113	$^{37}Cl^{a}$
18	^{11}B	66	^{26x}Al	114	$^{37}Ar^{a}$
19	^{11}C	67	^{26y}Al	115	$^{37}K^{a}$
20	$^{12}C^{a}$	68	^{26z}Al	116	$^{37}Ca^{a}$
21	^{12}N	69	$^{26g}Al^{a}$	117	$^{38}Ar^{a}$
22	$^{13}C^{a}$	70	$^{26}Si^{a}$	118	$^{38}K^{a}$
23	$^{13}N^{a}$	71	$^{26}P^{a}$	119	$^{38}Ca^{a}$
24	^{13}O	72	^{26}S	120	^{38}Ti
25	$^{14}N^{a}$	73	$^{27}Al^{a}$	121	^{39}Ar
26	$^{14}O^{a}$	74	$^{27}Si^{a}$	122	$^{39}K^{a}$
27	$^{15}N^{a}$	75	$^{27}P^{a}$	123	$^{39}Ca^{a}$
28	$^{15}O^{a}$	76	$^{27}S^{a}$	124	$^{39}Sc^{a}$
29	$^{16}O^{a}$	77	$^{28}Si^{a}$	125	^{39}Ti
30	^{16}Ne	78	$^{28}P^{a}$	126	^{40}Ar
31	$^{17}O^{a}$	79	$^{28}S^{a}$	127	^{40}K
32	$^{17}F^{a}$	80	$^{29}Si^{a}$	128	$^{40}Ca^{a}$
33	^{17}Ne	81	$^{29}P^{a}$	129	$^{40}Sc^{a}$
34	$^{18}O^{a}$	82	$^{29}S^{a}$	130	$^{40}Ti^{a}$
35	$^{18}F^{a}$	83	$^{30}Si^{a}$	131	$^{41}K^{a}$
36	$^{18}Ne^{a}$	84	$^{30}P^{a}$	132	$^{41}Ca^{a}$
37	$^{19}F^{a}$	85	$^{30}S^{a}$	133	$^{41}Sc^{a}$
38	$^{19}Ne^{a}$	86	$^{30}Cl^{a}$	134	$^{41}Ti^{a}$
39	$^{19}Na^{a}$	87	^{30}Ar	135	$^{42}Ca^{a}$
40	^{19}Mg	88	$^{31}P^{a}$	136	$^{42}Sc^{a}$
41	$^{20}Ne^{a}$	89	$^{31}S^{a}$	137	$^{42}Ti^{a}$
42	$^{20}Na^{a}$	90	$^{31}Cl^{a}$	138	$^{42}V^{a}$
43	^{20}Mg	91	$^{31}Ar^{a}$	139	^{42}Cr
44	$^{21}Ne^{a}$	92	$^{32}S^{a}$	140	$^{43}Ca^{a}$
45	$^{21}Na^{a}$	93	$^{32}Cl^{a}$	141	$^{43}Sc^{a}$
46	$^{21}Mg^{a}$	94	$^{32}Ar^{a}$	142	$^{43}Ti^{a}$
47	^{21}Al	95	$^{33}S^{a}$	143	$^{43}V^{a}$
48	$^{22}Ne^{a}$	96	$^{33}Cl^{a}$	144	^{43}Cr

Table C.1: – Continued.

Number	Isotope[b]	Number	Isotope[b]	Number	Isotope[b]
145	$^{44}Ca^{a}$	193	$^{52}Cr^{a}$	241	$^{61}Ni^{a}$
146	$^{44}Sc^{a}$	194	$^{52}Mn^{a}$	242	$^{61}Cu^{a}$
147	$^{44}Ti^{a}$	195	$^{52}Fe^{a}$	243	$^{61}Zn^{a}$
148	$^{44}V^{a}$	196	$^{52}Co^{a}$	244	$^{61}Ga^{a}$
149	$^{44}Cr^{a}$	197	$^{52}Ni^{a}$	245	$^{61}Ge^{a}$
150	^{45}Ca	198	$^{53}Cr^{a}$	246	$^{62}Ni^{a}$
151	$^{45}Sc^{a}$	199	$^{53}Mn^{a}$	247	$^{62}Cu^{a}$
152	$^{45}Ti^{a}$	200	$^{53}Fe^{a}$	248	$^{62}Zn^{a}$
153	$^{45}V^{a}$	201	$^{53}Co^{a}$	249	$^{62}Ga^{a}$
154	$^{45}Cr^{a}$	202	$^{53}Ni^{a}$	250	$^{62}Ge^{a}$
155	$^{45}Mn^{a}$	203	^{54}Cr	251	^{63}Ni
156	^{45}Fe	204	^{54}Mn	252	$^{63}Cu^{a}$
157	^{46}Ca	205	$^{54}Fe^{a}$	253	$^{63}Zn^{a}$
158	$^{46}Ti^{a}$	206	$^{54}Co^{a}$	254	$^{63}Ga^{a}$
159	$^{46}V^{a}$	207	$^{54}Ni^{a}$	255	$^{63}Ge^{a}$
160	$^{46}Cr^{a}$	208	^{54}Zn	256	^{64}Ni
161	$^{46}Mn^{a}$	209	$^{55}Mn^{a}$	257	^{64}Cu
162	^{46}Fe	210	$^{55}Fe^{a}$	258	$^{64}Zn^{a}$
163	^{47}Ca	211	$^{55}Co^{a}$	259	$^{64}Ga^{a}$
164	$^{47}Ti^{a}$	212	$^{55}Ni^{a}$	260	$^{64}Ge^{a}$
165	$^{47}V^{a}$	213	$^{55}Cu^{a}$	261	$^{64}As^{a}$
166	$^{47}Cr^{a}$	214	^{55}Zn	262	^{64}Se
167	$^{47}Mn^{a}$	215	$^{56}Fe^{a}$	263	$^{65}Cu^{a}$
168	^{47}Fe	216	$^{56}Co^{a}$	264	$^{65}Zn^{a}$
169	^{48}Ca	217	$^{56}Ni^{a}$	265	$^{65}Ga^{a}$
170	$^{48}Ti^{a}$	218	$^{56}Cu^{a}$	266	$^{65}Ge^{a}$
171	$^{48}V^{a}$	219	$^{56}Zn^{a}$	267	$^{65}As^{a}$
172	$^{48}Cr^{a}$	220	$^{57}Fe^{a}$	268	$^{65}Se^{a}$
173	$^{48}Mn^{a}$	221	$^{57}Co^{a}$	269	$^{66}Zn^{a}$
174	$^{48}Fe^{a}$	222	$^{57}Ni^{a}$	270	$^{66}Ga^{a}$
175	$^{49}Ti^{a}$	223	$^{57}Cu^{a}$	271	$^{66}Ge^{a}$
176	$^{49}V^{a}$	224	$^{57}Zn^{a}$	272	$^{66}As^{a}$
177	$^{49}Cr^{a}$	225	^{58}Fe	273	$^{66}Se^{a}$
178	$^{49}Mn^{a}$	226	^{58}Co	274	^{67}Zn
179	$^{49}Fe^{a}$	227	$^{58}Ni^{a}$	275	$^{67}Ga^{a}$
180	^{50}Ti	228	$^{58}Cu^{a}$	276	$^{67}Ge^{a}$
181	^{50}V	229	$^{58}Zn^{a}$	277	$^{67}As^{a}$
182	$^{50}Cr^{a}$	230	$^{59}Co^{a}$	278	$^{67}Se^{a}$
183	$^{50}Mn^{a}$	231	$^{59}Ni^{a}$	279	^{68}Zn
184	$^{50}Fe^{a}$	232	$^{59}Cu^{a}$	280	^{68}Ga
185	$^{50}Co^{a}$	233	$^{59}Zn^{a}$	281	$^{68}Ge^{a}$
186	^{50}Ni	234	$^{59}Ga^{a}$	282	$^{68}As^{a}$
187	$^{51}V^{a}$	235	^{59}Ge	283	$^{68}Se^{a}$
188	$^{51}Cr^{a}$	236	$^{60}Ni^{a}$	284	$^{68}Br^{a}$
189	$^{51}Mn^{a}$	237	$^{60}Cu^{a}$	285	^{68}Kr
190	$^{51}Fe^{a}$	238	$^{60}Zn^{a}$	286	^{69}Zn
191	$^{51}Co^{a}$	239	$^{60}Ga^{a}$	287	^{69}Ga
192	^{51}Ni	240	$^{60}Ge^{a}$	288	^{69}Ge

Table C.1: – Continued.

Number	Isotope[b]	Number	Isotope[b]	Number	Isotope[b]
289	$^{69}As^{a}$	337	^{76}Kr	385	^{83}Kr
290	$^{69}Se^{a}$	338	$^{76}Rb^{a}$	386	^{83}Rb
291	$^{69}Br^{a}$	339	$^{76}Sr^{a}$	387	^{83}Sr
292	$^{69}Kr^{a}$	340	$^{76}Y^{a}$	388	^{83}Y
293	^{70}Zn	341	^{77}Se	389	$^{83}Zr^{a}$
294	^{70}Ga	342	^{77}Br	390	$^{83}Nb^{a}$
295	^{70}Ge	343	^{77}Kr	391	$^{83}Mo^{a}$
296	^{70}As	344	$^{77}Rb^{a}$	392	^{84}Kr
297	$^{70}Se^{a}$	345	$^{77}Sr^{a}$	393	^{84}Rb
298	$^{70}Br^{a}$	346	$^{77}Y^{a}$	394	^{84}Sr
299	$^{70}Kr^{a}$	347	^{77}Zr	395	^{84}Y
300	^{71}Ga	348	^{78}Se	396	^{84}Zr
301	^{71}Ge	349	^{78}Br	397	$^{84}Nb^{a}$
302	^{71}As	350	^{78}Kr	398	$^{84}Mo^{a}$
303	$^{71}Se^{a}$	351	^{78}Rb	399	^{85}Kr
304	$^{71}Br^{a}$	352	$^{78}Sr^{a}$	400	^{85}Rb
305	$^{71}Kr^{a}$	353	$^{78}Y^{a}$	401	^{85}Sr
306	^{72}Ge	354	$^{78}Zr^{a}$	402	^{85}Y
307	^{72}As	355	^{79}Se	403	^{85}Zr
308	$^{72}Se^{a}$	356	^{79}Br	404	$^{85}Nb^{a}$
309	$^{72}Br^{a}$	357	^{79}Kr	405	$^{85}Mo^{a}$
310	$^{72}Kr^{a}$	358	^{79}Rb	406	$^{85}Tc^{a}$
311	$^{72}Rb^{a}$	359	^{79}Sr	407	^{86}Kr
312	^{72}Sr	360	$^{79}Y^{a}$	408	^{86}Rb
313	^{73}Ge	361	$^{79}Zr^{a}$	409	^{86}Sr
314	^{73}As	362	^{80}Se	410	^{86}Y
315	^{73}Se	363	^{80}Br	411	^{86}Zr
316	$^{73}Br^{a}$	364	^{80}Kr	412	^{86}Nb
317	$^{73}Kr^{a}$	365	^{80}Rb	413	$^{86}Mo^{a}$
318	$^{73}Rb^{a}$	366	^{80}Sr	414	$^{86}Tc^{a}$
319	^{73}Sr	367	$^{80}Y^{a}$	415	$^{86}Ru^{a}$
320	^{74}Ge	368	$^{80}Zr^{a}$	416	^{87}Rb
321	^{74}As	369	^{81}Se	417	^{87}Sr
322	^{74}Se	370	^{81}Br	418	^{87}Y
323	^{74}Br	371	^{81}Kr	419	^{87}Zr
324	$^{74}Kr^{a}$	372	^{81}Rb	420	^{87}Nb
325	$^{74}Rb^{a}$	373	^{81}Sr	421	^{87}Mo
326	$^{74}Sr^{a}$	374	$^{81}Y^{a}$	422	$^{87}Tc^{a}$
327	^{75}Ge	375	$^{81}Zr^{a}$	423	$^{87}Ru^{a}$
328	^{75}As	376	$^{81}Nb^{a}$	424	^{88}Sr
329	^{75}Se	377	^{82}Se	425	^{88}Y
330	^{75}Br	378	^{82}Kr	426	^{88}Zr
331	^{75}Kr	379	^{82}Rb	427	^{88}Nb
332	$^{75}Rb^{a}$	380	^{82}Sr	428	^{88}Mo
333	$^{75}Sr^{a}$	381	$^{82}Y^{a}$	429	$^{88}Tc^{a}$
334	^{76}Ge	382	$^{82}Zr^{a}$	430	$^{88}Ru^{a}$
335	^{76}Se	383	$^{82}Nb^{a}$	431	^{89}Y
336	^{76}Br	384	$^{82}Mo^{a}$	432	^{89}Zr

Table C.1: – Continued.

Number	Isotope[b]	Number	Isotope[b]	Number	Isotope[b]
433	^{89}Nb	481	^{95}Rh	529	$^{100}Sn^{a}$
434	^{89}Mo	482	^{95}Pd	530	^{101}Ru
435	^{89}Tc	483	$^{95}Ag^{a}$	531	^{101}Rh
436	$^{89}Ru^{a}$	484	$^{95}Cd^{a}$	532	^{101}Pd
437	$^{89}Rh^{a}$	485	^{96}Zr	533	^{101}Ag
438	^{90}Zr	486	^{96}Mo	534	^{101}Cd
439	^{90}Nb	487	^{96}Tc	535	$^{101}In^{a}$
440	^{90}Mo	488	^{96}Ru	536	$^{101}Sn^{a}$
441	^{90}Tc	489	^{96}Rh	537	^{102}Ru
442	$^{90}Ru^{a}$	490	^{96}Pd	538	^{102}Rh
443	$^{90}Rh^{a}$	491	$^{96}Ag^{a}$	539	^{102}Pd
444	$^{90}Pd^{a}$	492	$^{96}Cd^{a}$	540	^{102}Ag
445	^{91}Zr	493	$^{96}In^{a}$	541	^{102}Cd
446	^{91}Nb	494	^{97}Mo	542	$^{102}In^{a}$
447	^{91}Mo	495	^{97}Tc	543	$^{102}Sn^{a}$
448	^{91}Tc	496	^{97}Ru	544	^{103}Ru
449	$^{91}Ru^{a}$	497	^{97}Rh	545	^{103}Rh
450	$^{91}Rh^{a}$	498	^{97}Pd	546	^{103}Pd
451	$^{91}Pd^{a}$	499	$^{97}Ag^{a}$	547	^{103}Ag
452	^{92}Zr	500	$^{97}Cd^{a}$	548	^{103}Cd
453	^{92}Nb	501	$^{97}In^{a}$	549	$^{103}In^{a}$
454	^{92}Mo	502	^{97}Sn	550	$^{103}Sn^{a}$
455	^{92}Tc	503	^{98}Mo	551	^{104}Ru
456	^{92}Ru	504	^{98}Tc	552	^{104}Pd
457	$^{92}Rh^{a}$	505	^{98}Ru	553	^{104}Ag
458	$^{92}Pd^{a}$	506	^{98}Rh	554	^{104}Cd
459	^{92}Ag	507	^{98}Pd	555	$^{104}In^{a}$
460	^{93}Zr	508	$^{98}Ag^{a}$	556	$^{104}Sn^{a}$
461	^{93}Nb	509	$^{98}Cd^{a}$	557	$^{104}Sb^{a}$
462	^{93}Mo	510	$^{98}In^{a}$	558	^{105}Pd
463	^{93}Tc	511	^{98}Sn	559	^{105}Ag
464	^{93}Ru	512	^{99}Mo	560	^{105}Cd
465	$^{93}Rh^{a}$	513	^{99}Tc	561	^{105}In
466	$^{93}Pd^{a}$	514	^{99}Ru	562	$^{105}Sn^{a}$
467	$^{93}Ag^{a}$	515	^{99}Rh	563	$^{105}Sb^{a}$
468	^{93}Cd	516	^{99}Pd	564	^{105}Te
469	^{94}Zr	517	^{99}Ag	565	^{106}Pd
470	^{94}Mo	518	$^{99}Cd^{a}$	566	^{106}Ag
471	^{94}Tc	519	$^{99}In^{a}$	567	^{106}Cd
472	^{94}Ru	520	^{99}Sn	568	^{106}In
473	^{94}Rh	521	^{100}Mo	569	^{106}Sn
474	$^{94}Pd^{a}$	522	^{100}Tc	570	$^{106}Sb^{a}$
475	$^{94}Ag^{a}$	523	^{100}Ru	571	$^{106}Te^{a}$
476	^{94}Cd	524	^{100}Rh	572	^{107}Pd
477	^{95}Zr	525	^{100}Pd	573	^{107}Ag
478	^{95}Mo	526	^{100}Ag	574	^{107}Cd
479	^{95}Tc	527	^{100}Cd	575	^{107}In
480	^{95}Ru	528	$^{100}In^{a}$	576	^{107}Sn

Table C.1: – Continued.

Number	Isotope[b]	Number	Isotope[b]	Number	Isotope[b]
577	^{107}Sb	587	^{109}Pd	597	^{110}Te
578	$^{107}Te^{a}$	588	^{109}Ag	598	^{110}I
579	^{108}Pd	589	^{109}Cd	599	^{110}Xe
580	^{108}Ag	590	^{109}In	600	^{111}Te
581	^{108}Cd	591	^{109}Sn	601	^{111}I
582	^{108}In	592	^{109}Sb	602	^{111}Xe
583	^{108}Sn	593	^{109}Te	603	^{112}I
584	^{108}Sb	594	^{109}I	604	^{112}Xe
585	^{108}Te	595	^{109}Xe	605	^{113}Xe
586	^{108}I	596	^{110}Sb		

[b]Isotopes highlighted with a superscript ^{a} form the subset of nuclear species used in the hydrodynamic simulations reported in Chapter 4. ^{26g}Al and ^{26m}Al stand for ^{26}Al ground and isomeric states, respectively. ^{26x}Al, ^{26y}Al, and ^{26z}Al correspond to other excited states (Iliadis, private communication; see also Coc, Porquet, & Nowacki 2000).

Notice that nuclear masses enter twice: first, in the calculation of the forward Hauser-Feshbach rate, and second, in the calculation of the reverse photodisintegration rate. The second-step reactions, $B(p,\gamma)C$, are also computed with the code MOST. We had to include many nuclides beyond the proton drip line in order to properly account for sequential two-proton captures. For all other reactions for which experimental rates are not available, we used the results from the Hauser-Feshbach code NON-SMOKER (Rauscher & Thielemann 2000). For the weak interactions, we use laboratory decay rates (Audi et al. 2003a); the impact of β-delayed nucleon emission has also been considered. For a discussion on employing *stellar* versus *laboratory* decay rates, see Woosley et al. (2004). Also, note that many computed stellar decay rates (Fuller et al. 1982a,b) do not converge to their laboratory values at lower temperatures and densities, calling into question the model used for such calculations. In order to avoid this problem, we decided against using available stellar decay rates[1].

C.3 Numerical treatment

The time evolution of the nuclear abundances for the whole set of isotopes included in our network is quite complex due to the large number of reactions that link a given isotope with the rest. To derive the new chemical composition of the whole envelope at a given time, we have to solve the system of differential equations given by C.1. This can be written as a matrix equation, after linearization of the abovementioned system of equations (see Wagoner 1969):

$$A \cdot X = X_0 \tag{C.2}$$

where A is a matrix containing information on the different nuclear reaction rates, X is the matrix with the (unknown) new abundances, and X_0 is the matrix containing the set of abundances of the previous step.

This equation is solved by means of an iterative technique, based on Wagoner's two-step linearization procedure (1969), as described in Prantzos et al. (1987). The procedure assumes X_0 as an initial guess to the new value of X, and a first-order correction $\delta^1 X$ to the initial X_0 value is obtained applying a pseudo-Gaussian elimination technique to the equation

$$A \cdot \delta^1 X = X_0 - A \cdot X_0$$

From this, a first-order approximation to the value of X is found:

$$X \approx X_1 = X_0 + \delta^1 X$$

[1]Stellar decay rates for $A = 21 - 60$ and $45 - 65$ can be found in Fuller et al. (1982a,b) and Langanke & Martínez-Pinedo (2000), respectively.

To achieve better accuracy, a second order correction $\delta^2 X$ is obtained through a similar procedure:

$$A \cdot \delta^2 X = X_0 - A \cdot X_1$$

leading to the final solution:

$$X \approx X_2 = X_0 + \delta^1 X + \delta^2 X$$

which ensures conservation of the baryonic number up to 11 digits.

This procedure is particularly suited for the special properties of matrix A: essentially, a *sparse* matrix consisting of an upper left square matrix, an upper horizontal band, a left vertical band, and a diagonal band. This special geometry is due to the fact that the isotopes, ordered in terms of increasing atomic number, are only linked -through nuclear processes- either with close neighbors or with light particle (p, α, ...).

C.4 Numerical treatment of the composition in convective regions

When convection initiates in a given region of the accreted envelope, it may involve partial or complete mixing between adjacent shells. This basically depends on the comparison between the characteristic convective turnover time, τ_{conv}:

$$\tau_{conv} \sim \frac{l_m}{v_{conv}}$$

where l_m is the mixing length, and v_{conv} is the average velocity of a convective element, and the corresponding time step of the simulation, Δt.

C.4.1 Time-independent convection and complete mixing

This is assumed whenever $\tau_{conv} < \Delta t$. As of this moment, complete, time-independent mixing over the entire convective region is assumed, with a fully homogeneous composition given by:

$$X_{i,k} = \frac{\sum_{k=I,J} X_{i,k} \Delta m_k}{\Delta m_{conv}}, \ with \ \begin{cases} i = 1,\ N_{isot} \\ k = I,\ J \end{cases}$$

where $X_{i,k}$ represents the abundance of the i^{th} isotope in the k^{th} envelope layer (of mass Δm_k), Δm_{conv} is the mass of the overall convective region, and N_{isot}, I, and J, are the total number of isotopes of the network, and the shell interfaces that enclose the convective zone.

C.4.2 Time-dependent convection and partial mixing

This is adopted whenever $\tau_{conv} \geq \Delta t$, using the prescription devised by Prialnik et al. (1979), which assumes that adjacent convective layers should mix gradually. Here, convective transfer is taken as a diffusion process. The procedure assumes fixed mass boundaries of the convective region, no chemical changes driven by nuclear reactions, and no convective overshooting. In this framework, the diffusion equation, at time t and position r, for this (time-dependent) convective process, becomes:

$$\frac{\partial X_{i,k}(r,t)}{\partial t} = K \frac{\partial^2 X_{i,k}(r,t)}{\partial r^2}, \text{ with } \begin{cases} i = 1,\, N_{isot} \\ k = I,\, J \end{cases} \tag{C.3}$$

where K is the diffusion coefficient, $K = l_m \cdot v_{conv}$.

Eq. C.3 is transformed into a finite difference equation, which is solved for each nuclear species of the network over the $J - I$ convective shells, in the form:

$$X_{i,k}^{t+1} = X_{i,k}^{t} + \frac{F_{i,k}^{t+1} - F_{i,k-1}^{t+1}}{\Delta m_k} \Delta t \; with \; \begin{cases} i = 1,\, N_{isot} \\ k = I,\, J \end{cases}$$

where:

$$F_{i,k}^{t+1} = K_k \frac{X_{i,k+1}^{t+1} - X_{i,k}^{t+1}}{\overline{\Delta m_k}} (4\pi r_k^2 \overline{\rho_k})^2$$

and $\overline{\Delta m_k}$ and $\overline{\rho_k}$ are geometric averages of the values computed at adjacent shells (i.e., $\sqrt{m_k \cdot m_{k-1}}$ and $\sqrt{\rho_k \cdot \rho_{k-1}}$). The boundary conditions imposed are $F_{i,I}^{t+1} = F_{i,J}^{t+1} = 0$, for all i.

C.5 Electron shielding and screening factors

The free electrons that surround every nucleus of the multicomponent plasma play an important role on the possible thermonuclear reactions that these species can undergo. Indeed, the presence of these electrons modify the structure of the electric potential of the nucleus, *shielding* them in such a way that the incoming particle will *feel* the effect of a net reduction of the electric charge of the target, as compared with the corresponding value for a fully isolated nucleus.

According to the prescriptions devised by Graboske et al. (1973), and DeWitt et al. (1973), the screening factor obeys a simple power-law dependence on the screening parameters (basically, the electric charge of the two interacting particles, their abundances, the mean electric charge of the ions, and the plasma temperature and density). Depending on the screening parameters, three different regimes can be considered: weak, intermediate, and strong. Screening effects for nuclear reactions involving two charged particles rely on the determination of the Coulomb interaction

energy between the reacting particles and the surrounding plasma. The resulting reaction rate follows from multiplying the unscreened value by a factor, f, of the form (Salperter 1954):

$$f = exp[H_{12}(0)] \tag{C.4}$$

where $H_{12}(0)$ is the screening factor at zero separation.

For weak screening, the Coulomb interaction energy is much smaller than the kinetic energy. In this case, the screening function is given by:

$$H_{12}^{w}(0) = 1.88 \cdot 10^{8} Z_1 Z_2 z' \sqrt{\frac{\rho}{\mu_i T^3}} \tag{C.5}$$

where Z_1, Z_2 represent the electric charges of the two interacting particles, and z' is the mean average charge given by:

$$z' = \sqrt{\sum_i \frac{Z_i^2 X_i}{A_i} + \sum_i \frac{Z_i X_i}{A_i \theta_e}} \tag{C.6}$$

The parameter θ_e is the electron degeneracy factor (i.e., a measure of the electron freeze-out), given by the ratio of two Fermi-Dirac integrals:

$$\theta_e = \left[\frac{1}{\sqrt{\pi}} \int_0^{\infty} \frac{x^{-1/2} dx}{exp(-\alpha_e + x^2) + 1}\right] / \left[\frac{h^3 n_e}{2(2\pi m_e \kappa T)^{3/2}}\right] = \frac{I_{-1/2}(\alpha_e)}{I_{1/2}(\alpha_e)} \tag{C.7}$$

When $H_{12}^{w}(0)$ exceeds 0.1, intermediate or strong screening regimes are considered. The different regimes can be summarized as follows:

- Weak screening: $H_{12}^{w}(0) < 0.1$

$$H_{12}(0) = H_{12}^{w}(0)$$

- Intermediate screening: $0.1 \leq H_{12}^{w}(0) < 2$

$$H_{12}(0) = H_{12}^{i}(0)$$

- Strong screening: $H_{12}^{w}(0) \geq 2$

$$H_{12}(0) = min(H_{12}^{i}(0), H_{12}^{s}(0) \;\; for \;\; 2 \leq H_{12}^{w}(0) \leq 5$$

$$H_{12}(0) = H_{12}^{s}(0) \;\; for \;\; H_{12}^{w}(0) > 5$$

where

$$H_{12}^{i} = 0.71 \cdot 10^{8} \left(\sqrt{\frac{\rho}{\mu_i T^3}}\right)^{0.86} \frac{\sum_i Z_i^{1.58} X_i / A_i}{(z')^{0.58} \left(\sum_i Z_i X_i / A_i\right)^{0.28}} \left[(Z_1 + Z_2)^{1.86} - Z_1^{1.86} - Z_2^{1.86}\right]$$

and

$$H_{12}^{s} = 1.17 \cdot 10^{8} \left(\sqrt{\frac{\rho}{\mu_i T^3}}\right)^{2/3} \left(\sum_i Z_i X_i / A_i\right)^{1/3} \left\{ \left[(Z_1 + Z_2)^{5/3} - Z_1^{5/3} - Z_2^{5/3} \right] + \right.$$

$$+0.316 \left[(Z_1 + Z_2)^{4/3} - Z_1^{4/3} - Z_2^{4/3} \right] \left(\frac{\sum_i Z_i X_i / A_i}{\sum_i X_i / A_i} \right)^{1/3} +$$

$$\left. + \frac{0.737 \left[(Z_1 + Z_2)^{2/3} - Z_1^{2/3} - Z_2^{2/3} \right]}{\left(\sum_i Z_i X_i / A_i\right) \left[1.88 \cdot 10^{8} \sqrt{\rho / \left(\mu_i T^3\right)} / \left(\sum_i X_i / A_i\right) \right]^{2/3}} \right\}$$

Table C.2: Same as Table C.1, but for the nuclear reaction network.

Number	Reaction	Energy (MeV)	Number	Reaction	Energy (Mev)
1	$2\,^1H(\beta^+)^2H^a$	1.442	49	$^9Be(p,\gamma)^{10}B$	6.586
2	$^2H(p,\gamma)^3He^a$	5.494	50	$^9Be(p,D)2\,^4He$	0.651
3	$2\,^2H(\gamma,p)^3H^a$	4.033	51	$^9Be(p,\alpha)^6Li$	2.126
4	$2\,^2H(\beta^+)^4He^a$	23.847	52	$^9C(\alpha,p)^{12}N$	6.711
5	$^3H(p,\gamma)^4He^a$	19.814	53	$^9C(\gamma,p)2\,^4He$	16.774
6	$^3H(p,\gamma)2\,^2H^a$	-4.033	54	$^9C(\gamma,p)^8B$	-1.300
7	$^3H(\beta^+)^3He^a$	0.019	55	$^{10}B(p,\gamma)^{11}C$	8.690
8	$^3He(p,\gamma)^4He^a$	19.796	56	$^{10}B(p,\alpha)^7Be$	1.146
9	$^3He(D,p)^4He^a$	18.353	57	$^{10}B(\alpha,p)^{13}C$	4.062
10	$^3He(T,D)^4He^a$	14.320	58	$^{10}B(\gamma,p)^9Be$	-6.586
11	$^3He(\gamma,p)^2H^a$	-5.494	59	$^{10}B(\gamma,\alpha)^6Li$	-4.460
12	$^3He(\beta^+)^3H^a$	-0.019	60	$^{10}C(\beta^+)^{10}B$	3.651
13	$2\,^3He(\gamma,2p)^4He^a$	12.860	61	$^{11}B(p,\gamma)3\,^4He$	8.682
14	$^4He(2p,\gamma)2\,^3He^a$	-12.860	62	$^{11}B(p,\gamma)^{12}C$	15.957
15	$^4He(p,D)^3He^a$	-18.353	63	$^{11}B(\gamma,\alpha)^7Li$	-8.664
16	$2\,^4He(p,D)^7Be^a$	-16.766	64	$^{11}C(p,\alpha)^8B$	-7.406
17	$^4He(D,\gamma)^6Li$	1.475	65	$^{11}C(p,\gamma)^{12}N$	0.601
18	$2\,^4He(D,p)^9Be$	-0.651	66	$^{11}C(\alpha,p)^{14}N$	2.923
19	$^4He(D,T)^3He^a$	-14.320	67	$^{11}C(\gamma,\alpha)^7Be$	-7.545
20	$^4He(T,\gamma)^7Li^a$	2.468	68	$^{11}C(\gamma,p)^{10}B$	-8.690
21	$^4He(^3He,p)^6Li$	-4.018	69	$^{11}C(\beta^+)^{11}B$	1.982
22	$^4He(^3He,\gamma)^7Be^a$	1.588	70	$^{12}C(p,\gamma)^{13}N^a$	1.944
23	$3\,^4He(\gamma,p)^{11}B$	-8.682	71	$^{12}C(\alpha,p)^{15}N^a$	-4.966
24	$^4He(\beta^+)2\,^2H^a$	-23.847	72	$^{12}C(\alpha,\gamma)^{16}O^a$	7.162
25	$2\,^4He(\gamma,p)^7Li^a$	-17.346	73	$^{12}C(\beta^+)3\,^4He^a$	-7.275
26	$^4He(\gamma,p)^3H^a$	-19.814	74	$^{12}C(\gamma,p)^{11}B$	-15.957
27	$3\,^4He(\beta^+)^{12}C^a$	7.275	75	$^{12}N(p,\alpha)^9C$	-6.711
28	$^6Li(p,^3He)^4He$	4.018	76	$^{12}N(p,\gamma)^{13}O$	1.516
29	$^6Li(p,\gamma)^7Be$	5.606	77	$^{12}N(\alpha,p)^{15}O$	9.618
30	$^6Li(D,p)^7LI$	5.026	78	$^{12}N(\beta^+)^{12}C$	17.338
31	$^6Li(\alpha,p)^9Be$	-2.126	79	$^{12}N(\gamma,p)^{11}C$	-0.601
32	$^6Li(\alpha,\gamma)^{10}B$	4.460	80	$^{12}N(\beta^+)3\,^4He$	10.063
33	$^6Li(\gamma,D)^4He$	-1.475	81	$^{13}C(p,\gamma)^{14}N^a$	7.551
34	$^7Li(p,\gamma)2\,^4He^a$	17.346	82	$^{13}C(p,\alpha)^{10}B$	-4.062
35	$^7Li(p,D)^6LI$	-5.026	83	$^{13}N(p,\gamma)^{14}O^a$	4.627
36	$^7Li(\alpha,\gamma)^{11}B$	8.664	84	$^{13}N(\alpha,p)^{16}O^a$	5.218
37	$^7Li(\gamma,T)^4He^a$	-2.468	85	$^{13}N(\gamma,p)^{12}C^a$	-1.944
38	$^7Be(p,\gamma)^8B^a$	0.137	86	$^{13}N(\beta^+)^{13}C^a$	2.221
39	$^7Be(D,p)2\,^4He^a$	16.766	87	$^{13}O(\alpha,2p)^{15}O$	8.102
40	$^7Be(\alpha,p)^{10}B$	-1.146	88	$^{13}O(\gamma,p)^{12}N$	-1.516
41	$^7Be(\alpha,\gamma)^{11}C$	7.544	89	$^{13}O(\beta^+)^{13}N$	17.765
42	$^7Be(\gamma,p)^6Li$	-5.606	90	$^{13}O(\gamma,p)^{12}C$	15.821
43	$^7Be(\beta^+)^7Li^a$	0.862	91	$^{14}N(p,\alpha)^{11}C$	-2.923
44	$^7Be(\gamma,^3He)^4He^a$	-1.588	92	$^{14}N(p,\gamma)^{15}O^a$	7.297
45	$^8B(p,\gamma)^9C$	1.300	93	$^{14}N(\alpha,\gamma)^{18}F^a$	4.415
46	$^8B(\alpha,p)^{11}C$	7.406	94	$^{14}N(\alpha,p)^{17}O^a$	-1.191
47	$^8B(\beta^+)2\,^4He^a$	18.070	95	$^{14}N(\gamma,p)^{13}C^a$	-7.551
48	$^8B(\gamma,p)^7Be^a$	-0.137	96	$^{14}O(\alpha,p)^{17}F^a$	1.191

Table C.2: – Continued.

Number	Reaction	Energy (Mev)	Number	Reaction	Energy (Mev)
97	$^{14}O(\alpha,\gamma)^{18}Ne^a$	5.112	145	$^{19}F(\alpha,p)^{22}Ne^a$	1.675
98	$^{14}O(\beta^+)^{14}N^a$	5.144	146	$^{19}F(\gamma,\alpha)^{15}N^a$	-4.014
99	$^{14}O(\gamma,p)^{13}N^a$	-4.627	147	$^{19}F(\gamma,p)^{18}O^a$	-7.994
100	$^{15}N(p,\gamma)^{16}O^a$	12.127	148	$^{19}Ne(p,\gamma)^{20}Na^a$	2.193
101	$^{15}N(p,\alpha)^{12}C^a$	4.966	149	$^{19}Ne(\alpha,\gamma)^{23}Mg^a$	9.648
102	$^{15}N(\alpha,p)^{18}O^a$	-3.981	150	$^{19}Ne(\alpha,p)^{22}Na^a$	2.068
103	$^{15}N(\alpha,\gamma)^{19}F^a$	4.014	151	$^{19}Ne(\beta^+)^{19}F^a$	3.238
104	$^{15}O(2p,\alpha)^{13}O$	-8.102	152	$^{19}Ne(\gamma,\alpha)^{15}O^a$	-3.529
105	$^{15}O(p,\alpha)^{12}N$	-9.618	153	$^{19}Ne(\gamma,p)^{18}F^a$	-6.411
106	$^{15}O(\alpha,\gamma)^{19}Ne^a$	3.529	154	$^{19}Na(p,\gamma)^{20}Mg$	2.647
107	$^{15}O(\alpha,p)^{18}F^a$	-2.882	155	$^{19}Na(\alpha,\gamma)^{23}Al^a$	8.586
108	$^{15}O(\gamma,p)^{14}N^a$	-7.297	156	$^{19}Na(\alpha,p)^{22}Mg^a$	8.461
109	$^{15}O(\beta^+)^{15}N^a$	2.754	157	$^{19}Na(\gamma,p)^{18}Ne^a$	0.320
110	$^{16}O(p,\alpha)^{13}N^a$	-5.218	158	$^{19}Mg(\alpha,p)^{22}Al$	9.012
111	$^{16}O(p,\gamma)^{17}F^a$	0.600	159	$^{19}Mg(\alpha,\gamma)^{23}Si$	11.648
112	$^{16}O(\alpha,\gamma)^{20}Ne^a$	4.730	160	$^{20}Ne(p,\alpha)^{17}F^a$	-4.134
113	$^{16}O(\alpha,p)^{19}F^a$	-8.114	161	$^{20}Ne(p,\gamma)^{21}Na^a$	2.431
114	$^{16}O(\gamma,\alpha)^{12}C^a$	-7.162	162	$^{20}Ne(\alpha,\gamma)^{24}Mg^a$	9.316
115	$^{16}O(\gamma,p)^{15}N^a$	-12.127	163	$^{20}Ne(\alpha,p)^{23}Na^a$	-2.376
116	$^{17}O(p,\alpha)^{14}N^a$	1.191	164	$^{20}Ne(\gamma,p)^{19}F^a$	-12.844
117	$^{17}O(p,\gamma)^{18}F^a$	5.607	165	$^{20}Ne(\gamma,\alpha)^{16}O^a$	-4.730
118	$^{17}O(\alpha,\gamma)^{21}Ne^a$	7.351	166	$^{20}Na(p,\gamma)^{21}Mg^a$	3.222
119	$^{17}F(p,\alpha)^{14}O^a$	-1.191	167	$^{20}Na(p,\alpha)^{17}Ne$	-4.776
120	$^{17}F(p,\gamma)^{18}Ne^a$	3.924	168	$^{20}Na(\alpha,p)^{23}Mg^a$	7.454
121	$^{17}F(\alpha,p)^{20}Ne^a$	4.134	169	$^{20}Na(\alpha,\gamma)^{24}Al^a$	9.325
122	$^{17}F(\beta^+)^{17}O^a$	2.761	170	$^{20}Na(\gamma,p)^{19}Ne^a$	-2.193
123	$^{17}F(\gamma,p)^{16}O^a$	-0.600	171	$^{20}Na(\beta^+)^{20}Ne^a$	13.887
124	$^{17}Ne(\alpha,\gamma)^{21}Mg$	7.998	172	$^{20}Na(\gamma,\alpha)^{16}O^a$	9.156
125	$^{17}Ne(\alpha,p)^{20}Na$	4.776	173	$^{20}Mg(p,\gamma)^{21}Al$	-1.260
126	$^{17}Ne(\beta^+)^{17}F$	14.528	174	$^{20}Mg(\alpha,\gamma)^{24}Si$	9.241
127	$^{17}Ne(\gamma,\alpha)^{13}N$	8.717	175	$^{20}Mg(\alpha,p)^{23}Al$	5.939
128	$^{17}Ne(\gamma,p)^{16}O$	13.935	176	$^{20}Mg(\gamma,p)^{19}Ne$	8.531
129	$^{18}O(p,\alpha)^{15}N^a$	3.981	177	$^{20}Mg(\gamma,p)^{19}Na$	-2.647
130	$^{18}O(p,\gamma)^{19}F^a$	7.994	178	$^{20}Mg(\beta^+)^{20}Na$	10.731
131	$^{18}O(\alpha,\gamma)^{22}Ne^a$	9.668	179	$^{21}Ne(p,\gamma)^{22}Na^a$	6.738
132	$^{18}F(p,\gamma)^{19}Ne^a$	6.411	180	$^{21}Ne(\alpha,\gamma)^{25}Mg^a$	9.882
133	$^{18}F(p,\alpha)^{15}O^a$	2.882	181	$^{21}Ne(\gamma,\alpha)^{17}O^a$	-7.351
134	$^{18}F(\beta^+)^{18}O^a$	1.655	182	$^{21}Na(p,\alpha)^{18}Ne^a$	-2.639
135	$^{18}F(\gamma,\alpha)^{14}N^a$	-4.415	183	$^{21}Na(p,\gamma)^{22}Mg^a$	5.508
136	$^{18}F(\gamma,p)^{17}O^a$	-5.607	184	$^{21}Na(\alpha,\gamma)^{25}Al^a$	9.156
137	$^{18}Ne(p,\gamma)^{19}Na^a$	-0.320	185	$^{21}Na(\alpha,p)^{24}Mg^a$	6.880
138	$^{18}Ne(\alpha,p)^{21}Na^a$	2.639	186	$^{21}Na(\beta^+)^{21}Ne^a$	3.548
139	$^{18}Ne(\alpha,\gamma)^{22}Mg^a$	8.141	187	$^{21}Na(\gamma,p)^{20}Ne^a$	-2.431
140	$^{18}Ne(\gamma,\alpha)^{14}O^a$	-5.112	188	$^{21}Mg(p,\gamma)^{22}Al^a$	0.020
141	$^{18}Ne(\gamma,p)^{17}F^a$	-3.924	189	$^{21}Mg(\alpha,p)^{24}Al^a$	6.102
142	$^{18}Ne(\beta^+)^{18}F^a$	4.446	190	$^{21}Mg(\alpha,\gamma)^{25}Si^a$	9.511
143	$^{19}F(p,\gamma)^{20}Ne^a$	12.844	191	$^{21}Mg(\gamma,\alpha)^{17}Ne$	-7.998
144	$^{19}F(p,\alpha)^{16}O^a$	8.114	192	$^{21}Mg(\gamma,p)^{20}Na^a$	-3.222

Table C.2: – Continued.

Number	Reaction	Energy (Mev)	Number	Reaction	Energy (Mev)
193	$^{21}Mg(\beta^+)^{21}Na^a$	13.101	241	$^{23}Al(p,\alpha)^{20}Mg$	-5.939
194	$^{21}Mg(\gamma,p)^{20}Ne^a$	10.664	242	$^{23}Al(\alpha,p)^{26}Si^a$	9.048
195	$^{21}Al(p,\gamma)^{22}Si$	1.240	243	$^{23}Al(\alpha,\gamma)^{27}P^a$	9.945
196	$^{21}Al(\alpha,\gamma)^{25}P$	8.383	244	$^{23}Al(\gamma,\alpha)^{19}Na^a$	-8.586
197	$^{21}Al(\alpha,p)^{24}Si$	11.801	245	$^{23}Al(\gamma,p)^{22}Mg^a$	-0.123
198	$^{21}Al(\gamma,p)^{20}Mg$	1.260	246	$^{23}Al(\beta^+)^{23}Mg^a$	12.240
199	$^{22}Ne(p,\gamma)^{23}Na^a$	8.794	247	$^{23}Al(\gamma,p)^{22}Na^a$	4.660
200	$^{22}Ne(p,\alpha)^{19}F^a$	-1.675	248	$^{23}Si(\alpha,\gamma)^{27}S$	8.807
201	$^{22}Ne(\alpha,\gamma)^{26}Mg^a$	10.612	249	$^{23}Si(\alpha,p)^{26}P$	7.355
202	$^{22}Ne(\gamma,\alpha)^{18}O^a$	-9.668	250	$^{23}Si(\beta^+)^{23}Al$	17.010
203	$^{22}Na(p,\alpha)^{19}Ne^a$	-2.068	251	$^{23}Si(\gamma,p)^{22}Mg$	16.879
204	$^{22}Na(p,\gamma)^{23}Mg^a$	7.579	252	$^{23}Si(\gamma,\alpha)^{19}Mg$	-11.648
205	$^{22}Na(\alpha,\gamma)^{26g}Al^a$	9.450	253	$^{23}Si(\gamma,p)^{22}Al$	-1.724
206	$^{22}Na(\alpha,p)^{25}Mg^a$	3.146	254	$^{24}Mg(p,\alpha)^{21}Na^a$	-6.880
207	$^{22}Na(\beta^+)^{22}Ne^a$	2.842	255	$^{24}Mg(p,\gamma)^{25}Al^a$	2.271
208	$^{22}Na(\gamma,p)^{21}Ne^a$	-6.738	256	$^{24}Mg(\alpha,\gamma)^{28}Si^a$	9.984
209	$^{22}Mg(p,\alpha)^{19}Na^a$	-8.461	257	$^{24}Mg(\alpha,p)^{27}Al^a$	-1.601
210	$^{22}Mg(p,\gamma)^{23}Al^a$	0.123	258	$^{24}Mg(\gamma,\alpha)^{20}Ne^a$	-9.317
211	$^{22}Mg(\alpha,\gamma)^{26}Si^a$	9.173	259	$^{24}Mg(\gamma,p)^{23}Na^a$	-11.693
212	$^{22}Mg(\alpha,p)^{25}Al^a$	3.655	260	$^{24}Al(p,\alpha)^{21}Mg^a$	-6.102
213	$^{22}Mg(\beta^+)^{22}Na^a$	4.788	261	$^{24}Al(p,\gamma)^{25}Si^a$	3.409
214	$^{22}Mg(\gamma,\alpha)^{18}Ne^a$	-8.141	262	$^{24}Al(\alpha,\gamma)^{28}P^a$	9.531
215	$^{22}Mg(\gamma,p)^{21}Na^a$	-5.508	263	$^{24}Al(\alpha,p)^{27}Si^a$	7.466
216	$^{22}Al(p,\alpha)^{19}Mg$	-9.012	264	$^{24}Al(\gamma,\alpha)^{20}Na^a$	-9.325
217	$^{22}Al(p,\gamma)^{23}Si$	1.724	265	$^{24}Al(\gamma,p)^{23}Mg^a$	-1.871
218	$^{22}Al(\alpha,\gamma)^{26}P^a$	9.079	266	$^{24}Al(\beta^+)^{24}Mg^a$	13.878
219	$^{22}Al(\alpha,p)^{25}Si^a$	9.978	267	$^{24}Si(p,\alpha)^{21}Al$	-11.801
220	$^{22}Al(\beta^+)^{22}Mg^a$	18.577	268	$^{24}Si(p,\gamma)^{25}P^a$	-0.830
221	$^{22}Al(\gamma,p)^{21}Na^a$	13.075	269	$^{24}Si(\alpha,\gamma)^{28}S^a$	9.106
222	$^{22}Al(\gamma,p)^{21}Mg^a$	-0.020	270	$^{24}Si(\alpha,p)^{27}P^a$	6.643
223	$^{22}Si(\alpha,p)^{25}P$	7.785	271	$^{24}Si(\gamma,p)^{23}Al^a$	-3.301
224	$^{22}Si(\alpha,\gamma)^{26}S$	7.855	272	$^{24}Si(\beta^+)^{24}Al^a$	10.810
225	$^{22}Si(\gamma,p)^{21}Mg$	13.964	273	$^{24}Si(\gamma,p)^{23}Mg^a$	8.938
226	$^{22}Si(\gamma,p)^{21}Al$	-1.240	274	$^{24}Si(\gamma,\alpha)^{20}Mg$	-9.241
227	$^{22}Si(\beta^+)^{22}Al$	13.980	275	$^{25}Mg(p,\alpha)^{22}Na^a$	-3.146
228	$^{23}Na(p,\gamma)^{24}Mg^a$	11.693	276	$^{25}Mg(p,\gamma)^{26g}Al^a$	6.307
229	$^{23}Na(p,\alpha)^{20}Ne^a$	2.376	277	$^{25}Mg(p,\gamma)^{26m}Al^a$	6.078
230	$^{23}Na(\alpha,p)^{26}Mg^a$	1.821	278	$^{25}Mg(\alpha,\gamma)^{29}Si^a$	11.127
231	$^{23}Na(\alpha,\gamma)^{27}Al^a$	10.092	279	$^{25}Mg(\gamma,\alpha)^{21}Ne^a$	-9.882
232	$^{23}Na(\gamma,p)^{22}Ne^a$	-8.794	280	$^{25}Al(p,\alpha)^{22}Mg^a$	-3.655
233	$^{23}Mg(p,\gamma)^{24}Al^a$	1.871	281	$^{25}Al(p,\gamma)^{26}Si^a$	5.518
234	$^{23}Mg(p,\alpha)^{20}Na^a$	-7.454	282	$^{25}Al(\alpha,\gamma)^{29}P^a$	10.461
235	$^{23}Mg(\alpha,p)^{26g}Al^a$	1.871	283	$^{25}Al(\alpha,p)^{28}Si^a$	7.713
236	$^{23}Mg(\alpha,\gamma)^{27}Si^a$	9.337	284	$^{25}Al(\beta^+)^{25}Mg^a$	4.277
237	$^{23}Mg(\gamma,p)^{22}Na^a$	-7.579	285	$^{25}Al(\gamma,\alpha)^{21}Na^a$	-9.156
238	$^{23}Mg(\beta^+)^{23}Na^a$	4.058	286	$^{25}Al(\gamma,p)^{24}Mg^a$	-2.271
239	$^{23}Mg(\gamma,\alpha)^{19}Ne^a$	-9.648	287	$^{25}Si(p,\alpha)^{22}Al^a$	-9.978
240	$^{23}Al(p,\gamma)^{24}Si^a$	3.301	288	$^{25}Si(p,\gamma)^{26}P^a$	0.140

Table C.2: – Continued.

Number	Reaction	Energy (Mev)	Number	Reaction	Energy (Mev)
289	$^{25}Si(\alpha,\gamma)^{29}S^a$	9.409	337	$^{26}P(p,\gamma)^{27}S^a$	0.720
290	$^{25}Si(\alpha,p)^{28}P^a$	6.122	338	$^{26}P(\alpha,\gamma)^{30}Cl^a$	8.904
291	$^{25}Si(\gamma,\alpha)^{21}Mg^a$	-9.511	339	$^{26}P(\alpha,p)^{29}S^a$	9.223
292	$^{25}Si(\gamma,p)^{24}Al^a$	-3.409	340	$^{26}P(\gamma,p)^{25}Si^a$	-0.140
293	$^{25}Si(\beta^+)^{25}Al^a$	12.742	341	$^{26}P(\beta^+)^{26}Si^a$	18.118
294	$^{25}Si(\gamma,p)^{24}Mg^a$	10.470	342	$^{26}P(\gamma,\alpha)^{22}Al^a$	-9.079
295	$^{25}P(p,\alpha)^{22}Si$	-7.785	343	$^{26}S(\alpha,\gamma)^{30}Ar$	10.216
296	$^{25}P(p,\gamma)^{26}S$	0.190	344	$^{26}S(\beta^+)^{26}P$	15.000
297	$^{25}P(\alpha,p)^{28}S^a$	11.784	345	$^{26}S(\gamma,\alpha)^{22}Si$	-7.855
298	$^{25}P(\gamma,p)^{24}Si^a$	0.830	346	$^{26}S(\gamma,p)^{25}P$	-0.190
299	$^{25}P(\gamma,\alpha)^{21}Al$	-8.383	347	$^{27}Al(p,\alpha)^{24}Mg^a$	1.601
300	$^{26}Mg(p,\gamma)^{27}Al^a$	8.272	348	$^{27}Al(p,\gamma)^{28}Si^a$	11.586
301	$^{26}Mg(p,\alpha)^{23}Na^a$	-1.821	349	$^{27}Al(\alpha,\gamma)^{31}P^a$	9.669
302	$^{26}Mg(\alpha,\gamma)^{30}Si^a$	10.644	350	$^{27}Al(\alpha,p)^{30}Si^a$	2.372
303	$^{26}Mg(\gamma,\alpha)^{22}Ne^a$	-10.612	351	$^{27}Al(\gamma,p)^{26}Mg^a$	-8.272
304	$^{26m}Al(p,\gamma)^{27}Si^a$	7.693	352	$^{27}Al(\gamma,\alpha)^{23}Na^a$	-10.092
305	$^{26m}Al(\beta^+)^{26y}Al$	-0.830	353	$^{27}Si(p,\alpha)^{24}Al^a$	-7.466
306	$^{26m}Al(\beta^+)^{26}Mg^a$	4.006	354	$^{27}Si(p,\gamma)^{28}P^a$	2.065
307	$^{26m}Al(\gamma,p)^{25}Mg^a$	-6.078	355	$^{27}Si(\alpha,\gamma)^{31}S^a$	9.085
308	$^{26m}Al(\beta^+)^{26z}Al$	-1.841	356	$^{27}Si(\alpha,p)^{30}P^a$	2.952
309	$^{26m}Al(\beta^+)^{26x}Al$	-0.189	357	$^{27}Si(\gamma,\alpha)^{23}Mg^a$	-9.337
310	$^{26z}Al(\beta^+)^{26x}Al$	1.652	358	$^{27}Si(\gamma,p)^{26m}Al^a$	-7.693
311	$^{26z}Al(\beta^+)^{26y}Al$	1.011	359	$^{27}Si(\gamma,p)^{26g}Al^a$	-7.464
312	$^{26z}Al(\beta^+)^{26m}Al$	1.841	360	$^{27}Si(\beta^+)^{27}Al^a$	4.810
313	$^{26y}Al(\beta^+)^{26}Mg$	5.064	361	$^{27}P(p,\alpha)^{24}Si^a$	-6.643
314	$^{26y}Al(\beta^+)^{26z}Al$	-1.011	362	$^{27}P(p,\gamma)^{28}S^a$	2.463
315	$^{26y}Al(\beta^+)^{26m}Al$	0.830	363	$^{27}P(\alpha,\gamma)^{31}Cl^a$	8.736
316	$^{26y}Al(\beta^+)^{26x}Al$	0.641	364	$^{27}P(\alpha,p)^{30}S^a$	8.445
317	$^{26x}Al(\beta^+)^{26g}Al$	0.417	365	$^{27}P(\gamma,p)^{26}Si^a$	-0.859
318	$^{26x}Al(\beta^+)^{26z}Al$	-1.652	366	$^{27}P(\gamma,\alpha)^{23}Al^a$	-9.945
319	$^{26x}Al(\beta^+)^{26y}Al$	-0.641	367	$^{27}P(\beta^+)^{27}Si^a$	11.635
320	$^{26x}Al(\beta^+)^{26m}Al$	0.189	368	$^{27}S(\alpha,p)^{30}Cl^a$	7.452
321	$^{26g}Al(p,\alpha)^{23}Mg^a$	-1.871	369	$^{27}S(\alpha,\gamma)^{31}Ar^a$	8.855
322	$^{26g}Al(p,\gamma)^{27}Si^a$	7.464	370	$^{27}S(\gamma,\alpha)^{23}Si$	-8.807
323	$^{26g}Al(\alpha,\gamma)^{30}P^a$	10.424	371	$^{27}S(\gamma,p)^{26}P^a$	-0.720
324	$^{26g}Al(\alpha,p)^{29}Si^a$	4.823	372	$^{27}S(\beta^+)^{27}P^a$	18.260
325	$^{26g}Al(\gamma,\alpha)^{22}Na^a$	-9.450	373	$^{28}Si(p,\gamma)^{29}P^a$	2.747
326	$^{26g}Al(\gamma,p)^{25}Mg^a$	-6.307	374	$^{28}Si(p,\alpha)^{25}Al^a$	-7.713
327	$^{26g}Al(\beta^+)^{26}Mg^a$	4.006	375	$^{28}Si(\alpha,p)^{31}P^a$	-1.917
328	$^{26g}Al(\beta^+)^{26x}Al$	-0.417	376	$^{28}Si(\alpha,\gamma)^{32}S^a$	6.948
329	$^{26}Si(p,\alpha)^{23}Al^a$	-9.048	377	$^{28}Si(\gamma,\alpha)^{24}Mg^a$	-9.984
330	$^{26}Si(p,\gamma)^{27}P^a$	0.859	378	$^{28}Si(\gamma,p)^{27}Al^a$	-11.586
331	$^{26}Si(\alpha,\gamma)^{30}S^a$	9.343	379	$^{28}P(p,\gamma)^{29}S^a$	3.290
332	$^{26}Si(\alpha,p)^{29}P^a$	4.943	380	$^{28}P(p,\alpha)^{25}Si^a$	-6.122
333	$^{26}Si(\gamma,\alpha)^{22}Mg^a$	-9.173	381	$^{28}P(\alpha,p)^{31}S^a$	7.019
334	$^{26}Si(\gamma,p)^{25}Al^a$	-5.518	382	$^{28}P(\alpha,\gamma)^{32}Cl^a$	8.594
335	$^{26}Si(\beta^+)^{26m}Al^a$	5.064	383	$^{28}P(\beta^+)^{28}Si^a$	14.331
336	$^{26}P(p,\alpha)^{23}Si$	-7.355	384	$^{28}P(\gamma,\alpha)^{24}Al^a$	-9.531

Table C.2: – Continued.

Number	Reaction	Energy (Mev)	Number	Reaction	Energy (Mev)
385	$^{28}P(\gamma,p)^{27}Si^a$	-2.065	433	$^{30}Cl(\alpha,\gamma)^{34}K^a$	8.322
386	$^{28}S(p,\alpha)^{25}P^a$	-11.784	434	$^{30}Cl(\gamma,p)^{29}S^a$	0.319
387	$^{28}S(\alpha,p)^{31}Cl^a$	6.273	435	$^{30}Cl(\gamma,\alpha)^{26}P^a$	-8.904
388	$^{28}S(\alpha,\gamma)^{32}Ar^a$	8.677	436	$^{30}Ar(\alpha,\gamma)^{34}Ca$	8.718
389	$^{28}S(\gamma,p)^{27}Si^a$	9.168	437	$^{30}Ar(\gamma,\alpha)^{26}S$	-10.216
390	$^{28}S(\gamma,\alpha)^{24}Si^a$	-9.106	438	$^{31}P(p,\gamma)^{32}S^a$	8.864
391	$^{28}S(\gamma,p)^{27}P^a$	-2.463	439	$^{31}P(p,\alpha)^{28}Si^a$	1.917
392	$^{28}S(\beta^+)^{28}P^a$	11.291	440	$^{31}P(\alpha,p)^{34}S^a$	0.626
393	$^{29}Si(p,\gamma)^{30}P^a$	5.595	441	$^{31}P(\alpha,\gamma)^{35}Cl^a$	6.997
394	$^{29}Si(p,\alpha)^{26g}Al^a$	-4.823	442	$^{31}P(\gamma,p)^{30}Si^a$	-7.297
395	$^{29}Si(\alpha,\gamma)^{33}S^a$	7.116	443	$^{31}P(\gamma,\alpha)^{27}Al^a$	-9.669
396	$^{29}Si(\gamma,\alpha)^{25}Mg^a$	-11.127	444	$^{31}S(p,\gamma)^{32}Cl^a$	1.574
397	$^{29}P(p,\gamma)^{30}S^a$	4.400	445	$^{31}S(p,\alpha)^{28}P^a$	-7.019
398	$^{29}P(p,\alpha)^{26}Si^a$	-4.943	446	$^{31}S(\alpha,p)^{34}Cl^a$	0.530
399	$^{29}P(\alpha,p)^{32}S^a$	4.199	447	$^{31}S(\alpha,\gamma)^{35}Ar^a$	6.428
400	$^{29}P(\alpha,\gamma)^{33}Cl^a$	6.476	448	$^{31}S(\beta^+)^{31}P^a$	5.394
401	$^{29}P(\beta^+)^{29}Si^a$	4.945	449	$^{31}S(\gamma,\alpha)^{27}Si^a$	-9.085
402	$^{29}P(\gamma,\alpha)^{25}Al^a$	-10.461	450	$^{31}S(\gamma,p)^{30}P^a$	-6.133
403	$^{29}P(\gamma,p)^{28}Si^a$	-2.747	451	$^{31}Cl(p,\gamma)^{32}Ar^a$	2.404
404	$^{29}S(p,\gamma)^{30}Cl^a$	-0.319	452	$^{31}Cl(p,\alpha)^{28}S^a$	-6.273
405	$^{29}S(p,\alpha)^{26}P^a$	-9.223	453	$^{31}Cl(\alpha,p)^{34}Ar^a$	6.449
406	$^{29}S(\alpha,p)^{32}Cl^a$	5.307	454	$^{31}Cl(\alpha,\gamma)^{35}K^a$	6.527
407	$^{29}S(\alpha,\gamma)^{33}Ar^a$	8.647	455	$^{31}Cl(\gamma,p)^{30}S^a$	-0.291
408	$^{29}S(\gamma,p)^{28}P^a$	-3.290	456	$^{31}Cl(\gamma,\alpha)^{27}P^a$	-8.736
409	$^{29}S(\beta^+)^{29}P^a$	13.790	457	$^{31}Cl(\beta^+)^{31}S^a$	11.975
410	$^{29}S(\gamma,p)^{28}Si^a$	11.044	458	$^{31}Ar(\alpha,\gamma)^{35}Ca$	8.318
411	$^{29}S(\gamma,\alpha)^{25}Si^a$	-9.409	459	$^{31}Ar(\alpha,p)^{34}K^a$	6.919
412	$^{30}Si(p,\alpha)^{27}Al^a$	-2.372	460	$^{31}Ar(\gamma,p)^{30}Cl^a$	-0.440
413	$^{30}Si(p,\gamma)^{31}P^a$	7.297	461	$^{31}Ar(\beta^+)^{31}Cl^a$	18.360
414	$^{30}Si(\alpha,\gamma)^{34}S^a$	7.924	462	$^{31}Ar(\gamma,\alpha)^{27}S^a$	-8.855
415	$^{30}Si(\gamma,\alpha)^{26}Mg^a$	-10.644	463	$^{31}Ar(\gamma,p)^{30}S^a$	18.069
416	$^{30}P(p,\gamma)^{31}S^a$	6.133	464	$^{32}S(p,\alpha)^{29}P^a$	-4.199
417	$^{30}P(p,\alpha)^{27}Si^a$	-2.952	465	$^{32}S(p,\gamma)^{33}Cl^a$	2.275
418	$^{30}P(\alpha,p)^{33}S^a$	1.522	466	$^{32}S(\alpha,\gamma)^{36}Ar^a$	6.639
419	$^{30}P(\alpha,\gamma)^{34}Cl^a$	6.664	467	$^{32}S(\alpha,p)^{35}Cl^a$	-1.867
420	$^{30}P(\gamma,\alpha)^{26g}Al^a$	-10.424	468	$^{32}S(\gamma,\alpha)^{28}Si^a$	-6.948
421	$^{30}P(\gamma,p)^{29}Si^a$	-5.595	469	$^{32}S(\gamma,p)^{31}P^a$	-8.864
422	$^{30}P(\beta^+)^{30}Si^a$	4.226	470	$^{32}Cl(p,\alpha)^{29}S^a$	-5.307
423	$^{30}S(p,\gamma)^{31}Cl^a$	0.291	471	$^{32}Cl(p,\gamma)^{33}Ar^a$	3.339
424	$^{30}S(p,\alpha)^{27}P^a$	-8.445	472	$^{32}Cl(\alpha,\gamma)^{36}K^a$	6.519
425	$^{30}S(\alpha,p)^{33}Cl^a$	2.076	473	$^{32}Cl(\alpha,p)^{35}Ar^a$	4.853
426	$^{30}S(\alpha,\gamma)^{34}Ar^a$	6.740	474	$^{32}Cl(\gamma,\alpha)^{28}P^a$	-8.594
427	$^{30}S(\beta^+)^{30}P^a$	6.144	475	$^{32}Cl(\gamma,p)^{31}S^a$	-1.574
428	$^{30}S(\gamma,\alpha)^{26}Si^a$	-9.343	476	$^{32}Cl(\beta^+)^{32}S^a$	12.686
429	$^{30}S(\gamma,p)^{29}P^a$	-4.400	477	$^{32}Ar(\alpha,p)^{35}K^a$	4.124
430	$^{30}Cl(p,\gamma)^{31}Ar^a$	0.440	478	$^{32}Ar(\alpha,\gamma)^{36}Ca^a$	6.685
431	$^{30}Cl(p,\alpha)^{27}S^a$	-7.452	479	$^{32}Ar(\beta^+)^{32}Cl^a$	11.150
432	$^{30}Cl(\alpha,p)^{33}Ar^a$	7.802	480	$^{32}Ar(\gamma,p)^{31}S^a$	9.576

Table C.2: – Continued.

Number	Reaction	Energy (Mev)	Number	Reaction	Energy (Mev)
481	$^{32}Ar(\gamma,\alpha)^{28}S^a$	-8.677	529	$^{35}S(p,\gamma)^{36}Cl$	7.965
482	$^{32}Ar(\gamma,p)^{31}Cl^a$	-2.404	530	$^{35}S(\alpha,\gamma)^{39}Ar$	6.820
483	$^{33}S(p,\gamma)^{34}Cl^a$	5.142	531	$^{35}S(\beta^+)^{35}Cl$	0.167
484	$^{33}S(p,\alpha)^{30}P^a$	-1.522	532	$^{35}Cl(p,\gamma)^{36}Ar^a$	8.506
485	$^{33}S(\alpha,p)^{36}Cl$	-1.928	533	$^{35}Cl(p,\alpha)^{32}S^a$	1.867
486	$^{33}S(\alpha,\gamma)^{37}Ar^a$	6.787	534	$^{35}Cl(\alpha,p)^{38}Ar^a$	0.837
487	$^{33}S(\gamma,\alpha)^{29}Si^a$	-7.116	535	$^{35}Cl(\alpha,\gamma)^{39}K^a$	7.218
488	$^{33}Cl(p,\gamma)^{34}Ar^a$	4.664	536	$^{35}Cl(\gamma,p)^{34}S^a$	-6.371
489	$^{33}Cl(p,\alpha)^{30}S^a$	-2.076	537	$^{35}Cl(\gamma,\alpha)^{31}P^a$	-6.997
490	$^{33}Cl(\alpha,p)^{36}Ar^a$	4.363	538	$^{35}Ar(p,\gamma)^{36}K^a$	1.668
491	$^{33}Cl(\alpha,\gamma)^{37}K^a$	6.221	539	$^{35}Ar(p,\alpha)^{32}Cl^a$	-4.853
492	$^{33}Cl(\gamma,\alpha)^{29}P^a$	-6.476	540	$^{35}Ar(\alpha,p)^{38}K^a$	0.889
493	$^{33}Cl(\gamma,p)^{32}S^a$	-2.275	541	$^{35}Ar(\alpha,\gamma)^{39}Ca^a$	6.653
494	$^{33}Cl(\beta^+)^{33}S^a$	5.583	542	$^{35}Ar(\gamma,p)^{34}Cl^a$	-5.898
495	$^{33}Ar(p,\gamma)^{34}K^a$	-0.610	543	$^{35}Ar(\beta^+)^{35}Cl^a$	5.965
496	$^{33}Ar(p,\alpha)^{30}Cl^a$	-7.802	544	$^{35}Ar(\gamma,\alpha)^{31}S^a$	-6.428
497	$^{33}Ar(\alpha,p)^{36}K^a$	3.179	545	$^{35}K(p,\gamma)^{36}Ca^a$	2.561
498	$^{33}Ar(\alpha,\gamma)^{37}Ca^a$	6.204	546	$^{35}K(p,\alpha)^{32}Ar^a$	-4.124
499	$^{33}Ar(\gamma,p)^{32}Cl^a$	-3.339	547	$^{35}K(\alpha,p)^{38}Ca^a$	6.028
500	$^{33}Ar(\beta^+)^{33}Cl^a$	11.622	548	$^{35}K(\alpha,\gamma)^{39}Sc^a$	5.426
501	$^{33}Ar(\gamma,p)^{32}S^a$	9.345	549	$^{35}K(\gamma,\alpha)^{31}Cl^a$	-6.527
502	$^{33}Ar(\gamma,\alpha)^{29}S^a$	-8.647	550	$^{35}K(\gamma,p)^{34}Ar^a$	-0.078
503	$^{34}S(p,\gamma)^{35}Cl^a$	6.371	551	$^{35}K(\beta^+)^{35}Ar^a$	11.879
504	$^{34}S(p,\alpha)^{31}P^a$	-0.626	552	$^{35}Ca(\alpha,\gamma)^{39}Ti$	6.744
505	$^{34}S(\alpha,p)^{37}Cl^a$	-3.034	553	$^{35}Ca(\gamma,p)^{34}Ar$	15.688
506	$^{34}S(\alpha,\gamma)^{38}Ar^a$	7.208	554	$^{35}Ca(\gamma,p)^{34}K$	-1.399
507	$^{34}S(\gamma,\alpha)^{30}Si^a$	-7.924	555	$^{35}Ca(\beta^+)^{35}K$	15.769
508	$^{34}Cl(p,\gamma)^{35}Ar^a$	5.898	556	$^{35}Ca(\gamma,\alpha)^{31}Ar$	-8.318
509	$^{34}Cl(p,\alpha)^{31}S^a$	-0.530	557	$^{36}S(p,\gamma)^{37}Cl$	8.387
510	$^{34}Cl(\alpha,p)^{37}Ar^a$	1.644	558	$^{36}S(\alpha,\gamma)^{40}Ar$	6.801
511	$^{34}Cl(\alpha,\gamma)^{38}K^a$	6.787	559	$^{36}Cl(p,\gamma)^{37}Ar$	8.715
512	$^{34}Cl(\beta^+)^{34}S^a$	5.494	560	$^{36}Cl(p,\alpha)^{33}S$	1.928
513	$^{34}Cl(\gamma,\alpha)^{30}P^a$	-6.664	561	$^{36}Cl(\alpha,p)^{39}Ar$	-1.144
514	$^{34}Cl(\gamma,p)^{33}S^a$	-5.142	562	$^{36}Cl(\alpha,\gamma)^{40}K$	6.438
515	$^{34}Ar(p,\gamma)^{35}K^a$	0.078	563	$^{36}Cl(\gamma,p)^{35}S$	-7.965
516	$^{34}Ar(p,\alpha)^{31}Cl^a$	-6.449	564	$^{36}Cl(\beta^+)^{36}Ar$	0.709
517	$^{34}Ar(\alpha,p)^{37}K^a$	1.556	565	$^{36}Ar(p,\gamma)^{37}K^a$	1.857
518	$^{34}Ar(\alpha,\gamma)^{38}Ca^a$	6.105	566	$^{36}Ar(p,\alpha)^{33}Cl^a$	-4.363
519	$^{34}Ar(\gamma,\alpha)^{30}S^a$	-6.740	567	$^{36}Ar(\alpha,p)^{39}K^a$	-1.288
520	$^{34}Ar(\gamma,p)^{33}Cl^a$	-4.664	568	$^{36}Ar(\alpha,\gamma)^{40}Ca^a$	7.040
521	$^{34}Ar(\beta^+)^{34}Cl^a$	6.059	569	$^{36}Ar(\gamma,p)^{35}Cl^a$	-8.506
522	$^{34}K(p,\gamma)^{35}Ca$	1.399	570	$^{36}Ar(\gamma,\alpha)^{32}S^a$	-6.639
523	$^{34}K(p,\alpha)^{31}Ar^a$	-6.919	571	$^{36}K(p,\gamma)^{37}Ca^a$	3.025
524	$^{34}K(\alpha,p)^{37}Ca^a$	7.280	572	$^{36}K(p,\alpha)^{33}Ar^a$	-3.179
525	$^{34}K(\gamma,p)^{33}Ar^a$	0.610	573	$^{36}K(\alpha,p)^{39}Ca^a$	4.987
526	$^{34}K(\gamma,\alpha)^{30}Cl^a$	-8.322	574	$^{36}K(\alpha,\gamma)^{40}Sc^a$	5.526
527	$^{34}Ca(\alpha,\gamma)^{38}Ti$	6.874	575	$^{36}K(\beta^+)^{36}Ar^a$	12.805
528	$^{34}Ca(\gamma,\alpha)^{30}Ar$	-8.718	576	$^{36}K(\gamma,\alpha)^{32}Cl^a$	-6.519

Table C.2: – Continued.

Number	Reaction	Energy (Mev)	Number	Reaction	Energy (Mev)
577	$^{36}K(\gamma,p)^{35}Ar^a$	-1.668	625	$^{38}Ca(\alpha,\gamma)^{42}Ti^a$	5.487
578	$^{36}Ca(\alpha,\gamma)^{40}Ti^a$	4.836	626	$^{38}Ca(\alpha,p)^{41}Sc^a$	1.719
579	$^{36}Ca(\alpha,p)^{39}Sc^a$	2.865	627	$^{38}Ca(\gamma,p)^{37}K^a$	-4.549
580	$^{36}Ca(\gamma,p)^{35}Ar^a$	9.320	628	$^{38}Ca(\beta^+)^{38}K^a$	6.740
581	$^{36}Ca(\gamma,\alpha)^{32}Ar^a$	-6.685	629	$^{38}Ca(\gamma,\alpha)^{34}Ar^a$	-6.105
582	$^{36}Ca(\gamma,p)^{35}K^a$	-2.561	630	$^{38}Ti(\alpha,\gamma)^{42}Cr$	6.199
583	$^{36}Ca(\beta^+)^{36}K^a$	10.986	631	$^{38}Ti(\gamma,\alpha)^{34}Ca$	-6.874
584	$^{37}Cl(p,\alpha)^{34}S^a$	3.034	632	$^{39}Ar(p,\alpha)^{36}Cl$	1.144
585	$^{37}Cl(p,\gamma)^{38}Ar^a$	10.242	633	$^{39}Ar(p,\gamma)^{40}K$	7.582
586	$^{37}Cl(\alpha,\gamma)^{41}K^a$	6.222	634	$^{39}Ar(\alpha,\gamma)^{43}Ca$	7.591
587	$^{37}Cl(\alpha,p)^{40}Ar$	-1.586	635	$^{39}Ar(\gamma,\alpha)^{35}S$	-6.820
588	$^{37}Cl(\gamma,p)^{36}S$	-8.387	636	$^{39}Ar(\beta^+)^{39}K$	0.563
589	$^{37}Ar(p,\alpha)^{34}Cl^a$	-1.644	637	$^{39}K(p,\alpha)^{36}Ar^a$	1.288
590	$^{37}Ar(p,\gamma)^{38}K^a$	5.143	638	$^{39}K(p,\gamma)^{40}Ca^a$	8.328
591	$^{37}Ar(\alpha,\gamma)^{41}Ca^a$	6.614	639	$^{39}K(\alpha,\gamma)^{43}Sc^a$	4.806
592	$^{37}Ar(\alpha,p)^{40}K$	-2.278	640	$^{39}K(\alpha,p)^{42}Ca^a$	-0.124
593	$^{37}Ar(\beta^+)^{37}Cl^a$	0.814	641	$^{39}K(\gamma,p)^{38}Ar^a$	-6.381
594	$^{37}Ar(\gamma,\alpha)^{33}S^a$	-6.787	642	$^{39}K(\gamma,\alpha)^{35}Cl^a$	-7.218
595	$^{37}Ar(\gamma,p)^{36}Cl$	-8.715	643	$^{39}Ca(p,\alpha)^{36}K^a$	-4.987
596	$^{37}K(p,\alpha)^{34}Ar^a$	-1.556	644	$^{39}Ca(p,\gamma)^{40}Sc^a$	0.539
597	$^{37}K(p,\gamma)^{38}Ca^a$	4.549	645	$^{39}Ca(\alpha,\gamma)^{43}Ti^a$	4.469
598	$^{37}K(\alpha,\gamma)^{41}Sc^a$	6.268	646	$^{39}Ca(\alpha,p)^{42}Sc^a$	-0.019
599	$^{37}K(\alpha,p)^{40}Ca^a$	5.183	647	$^{39}Ca(\gamma,p)^{38}K^a$	-5.764
600	$^{37}K(\gamma,\alpha)^{33}Cl^a$	-6.221	648	$^{39}Ca(\beta^+)^{39}K^a$	6.529
601	$^{37}K(\gamma,p)^{36}Ar^a$	-1.857	649	$^{39}Ca(\gamma,\alpha)^{35}Ar^a$	-6.653
602	$^{37}K(\beta^+)^{37}Ar^a$	6.147	650	$^{39}Sc(p,\alpha)^{36}Ca^a$	-2.865
603	$^{37}Ca(p,\alpha)^{34}K^a$	-7.280	651	$^{39}Sc(p,\gamma)^{40}Ti^a$	1.971
604	$^{37}Ca(\alpha,\gamma)^{41}Ti^a$	6.771	652	$^{39}Sc(\alpha,\gamma)^{43}V^a$	6.178
605	$^{37}Ca(\alpha,p)^{40}Sc^a$	4.208	653	$^{39}Sc(\alpha,p)^{42}Ti^a$	6.589
606	$^{37}Ca(\gamma,p)^{36}K^a$	-3.025	654	$^{39}Sc(\gamma,\alpha)^{35}K^a$	-5.426
607	$^{37}Ca(\beta^+)^{37}K^a$	11.639	655	$^{39}Sc(\gamma,p)^{38}Ca^a$	0.602
608	$^{37}Ca(\gamma,p)^{36}Ar^a$	9.780	656	$^{39}Sc(\beta^+)^{39}Ca^a$	13.096
609	$^{37}Ca(\gamma,\alpha)^{33}Ar^a$	-6.204	657	$^{39}Ti(\alpha,p)^{42}V$	5.148
610	$^{38}Ar(p,\alpha)^{35}Cl^a$	-0.837	658	$^{39}Ti(\alpha,\gamma)^{43}Cr$	6.494
611	$^{38}Ar(p,\gamma)^{39}K^a$	6.381	659	$^{39}Ti(\gamma,\alpha)^{35}Ca$	-6.744
612	$^{38}Ar(\alpha,\gamma)^{42}Ca^a$	6.257	660	$^{39}Ti(\beta^+)^{39}Sc$	15.400
613	$^{38}Ar(\alpha,p)^{41}K^a$	-4.020	661	$^{39}Ti(\gamma,p)^{38}Ca$	16.002
614	$^{38}Ar(\gamma,\alpha)^{34}S^a$	-7.208	662	$^{40}Ar(p,\alpha)^{37}Cl$	1.586
615	$^{38}Ar(\gamma,p)^{37}Cl^a$	-10.242	663	$^{40}Ar(p,\gamma)^{41}K$	7.808
616	$^{38}K(p,\alpha)^{35}Ar^a$	-0.889	664	$^{40}Ar(\alpha,\gamma)^{44}Ca$	8.854
617	$^{38}K(p,\gamma)^{39}Ca^a$	5.764	665	$^{40}Ar(\gamma,\alpha)^{36}S$	-6.801
618	$^{38}K(\alpha,\gamma)^{42}Sc^a$	5.744	666	$^{40}K(p,\gamma)^{41}Ca$	8.892
619	$^{38}K(\alpha,p)^{41}Ca^a$	1.472	667	$^{40}K(p,\alpha)^{37}Ar$	2.278
620	$^{38}K(\gamma,p)^{37}Ar^a$	-5.143	668	$^{40}K(\alpha,p)^{43}Ca$	0.010
621	$^{38}K(\beta^+)^{38}Ar^a$	5.913	669	$^{40}K(\alpha,\gamma)^{44}Sc$	6.706
622	$^{38}K(\gamma,\alpha)^{34}Cl^a$	-6.787	670	$^{40}K(\beta^+)^{40}Ca$	1.312
623	$^{38}Ca(p,\alpha)^{35}K^a$	-6.028	671	$^{40}K(\beta^+)^{40}Ar$	1.505
624	$^{38}Ca(p,\gamma)^{39}Sc^a$	-0.602	672	$^{40}K(\gamma,\alpha)^{36}Cl$	-6.438

Table C.2: – Continued.

Number	Reaction	Energy (Mev)	Number	Reaction	Energy (Mev)
673	$^{40}K(\gamma,p)^{39}Ar$	-7.582	721	$^{42}Ca(p,\alpha)^{39}K^a$	0.124
674	$^{40}Ca(p,\gamma)^{41}Sc^a$	1.085	722	$^{42}Ca(\alpha,p)^{45}Sc^a$	-2.342
675	$^{40}Ca(p,\alpha)^{37}K^a$	-5.183	723	$^{42}Ca(\alpha,\gamma)^{46}Ti^a$	8.003
676	$^{40}Ca(\alpha,p)^{43}Sc^a$	-3.523	724	$^{42}Ca(\gamma,p)^{41}K^a$	-10.277
677	$^{40}Ca(\alpha,\gamma)^{44}Ti^a$	5.127	725	$^{42}Ca(\gamma,\alpha)^{38}Ar^a$	-6.257
678	$^{40}Ca(\gamma,\alpha)^{36}Ar^a$	-7.040	726	$^{42}Sc(p,\gamma)^{43}Ti^a$	4.488
679	$^{40}Ca(\gamma,p)^{39}K^a$	-8.328	727	$^{42}Sc(p,\alpha)^{39}Ca^a$	0.019
680	$^{40}Sc(p,\gamma)^{41}Ti^a$	2.563	728	$^{42}Sc(\alpha,p)^{45}Ti^a$	2.022
681	$^{40}Sc(p,\alpha)^{37}Ca^a$	-4.208	729	$^{42}Sc(\alpha,\gamma)^{46}V^a$	7.378
682	$^{40}Sc(\alpha,p)^{43}Ti^a$	4.446	730	$^{42}Sc(\beta^+)^{42}Ca^a$	6.422
683	$^{40}Sc(\alpha,\gamma)^{44}V^a$	5.491	731	$^{42}Sc(\gamma,\alpha)^{38}K^a$	-5.744
684	$^{40}Sc(\gamma,\alpha)^{36}K^a$	-5.526	732	$^{42}Sc(\gamma,p)^{41}Ca^a$	-4.272
685	$^{40}Sc(\gamma,p)^{39}Ca^a$	-0.539	733	$^{42}Ti(p,\gamma)^{43}V^a$	0.190
686	$^{40}Sc(\beta^+)^{40}Ca^a$	14.318	734	$^{42}Ti(p,\alpha)^{39}Sc^a$	-6.589
687	$^{40}Ti(\alpha,\gamma)^{44}Cr^a$	6.683	735	$^{42}Ti(\alpha,p)^{45}V^a$	1.889
688	$^{40}Ti(\alpha,p)^{43}V^a$	3.932	736	$^{42}Ti(\alpha,\gamma)^{46}Cr^a$	6.775
689	$^{40}Ti(\gamma,\alpha)^{36}Ca^a$	-4.836	737	$^{42}Ti(\beta^+)^{42}Sc^a$	7.002
690	$^{40}Ti(\gamma,p)^{39}Sc^a$	-1.971	738	$^{42}Ti(\gamma,\alpha)^{38}Ca^a$	-5.487
691	$^{40}Ti(\beta^+)^{40}Sc^a$	11.463	739	$^{42}Ti(\gamma,p)^{41}Sc^a$	-3.768
692	$^{40}Ti(\gamma,p)^{39}Ca^a$	11.137	740	$^{42}V(p,\gamma)^{43}Cr$	1.346
693	$^{41}K(p,\alpha)^{38}Ar^a$	4.020	741	$^{42}V(p,\alpha)^{39}Ti$	-5.148
694	$^{41}K(p,\gamma)^{42}Ca^a$	10.277	742	$^{42}V(\alpha,p)^{45}Cr^a$	6.788
695	$^{41}K(\alpha,\gamma)^{45}Sc^a$	7.935	743	$^{42}V(\alpha,\gamma)^{46}Mn^a$	6.795
696	$^{41}K(\alpha,p)^{44}Ca^a$	1.046	744	$^{42}V(\gamma,p)^{41}Ti^a$	0.240
697	$^{41}K(\gamma,p)^{40}Ar$	-7.808	745	$^{42}V(\beta^+)^{42}Ti^a$	16.902
698	$^{41}K(\gamma,\alpha)^{37}Cl^a$	-6.222	746	$^{42}Cr(\alpha,\gamma)^{46}Fe$	7.883
699	$^{41}Ca(p,\alpha)^{38}K^a$	-1.472	747	$^{42}Cr(\alpha,p)^{45}Mn$	6.491
700	$^{41}Ca(p,\gamma)^{42}Sc^a$	4.272	748	$^{42}Cr(\beta^+)^{42}V$	9.042
701	$^{41}Ca(\alpha,\gamma)^{45}Ti^a$	6.294	749	$^{42}Cr(\gamma,\alpha)^{38}Ti$	-6.199
702	$^{41}Ca(\alpha,p)^{44}Sc^a$	-2.186	750	$^{43}Ca(p,\alpha)^{40}K$	-0.010
703	$^{41}Ca(\gamma,\alpha)^{37}Ar^a$	-6.614	751	$^{43}Ca(p,\gamma)^{44}Sc^a$	6.696
704	$^{41}Ca(\gamma,p)^{40}K$	-8.892	752	$^{43}Ca(\alpha,\gamma)^{47}Ti^a$	8.948
705	$^{41}Ca(\beta^+)^{41}K^a$	0.420	753	$^{43}Ca(\gamma,\alpha)^{39}Ar$	-7.591
706	$^{41}Sc(p,\alpha)^{38}Ca^a$	-1.719	754	$^{43}Sc(p,\alpha)^{40}Ca^a$	3.523
707	$^{41}Sc(p,\gamma)^{42}Ti^a$	3.768	755	$^{43}Sc(p,\gamma)^{44}Ti^a$	8.650
708	$^{41}Sc(\alpha,\gamma)^{45}V^a$	5.656	756	$^{43}Sc(\alpha,\gamma)^{47}V^a$	8.241
709	$^{41}Sc(\alpha,p)^{44}Ti^a$	4.042	757	$^{43}Sc(\alpha,p)^{46}Ti^a$	3.073
710	$^{41}Sc(\gamma,p)^{40}Ca^a$	-1.085	758	$^{43}Sc(\gamma,p)^{42}Ca^a$	-4.930
711	$^{41}Sc(\beta^+)^{41}Ca^a$	6.495	759	$^{43}Sc(\beta^+)^{43}Ca^a$	2.222
712	$^{41}Sc(\gamma,\alpha)^{37}K^a$	-6.268	760	$^{43}Sc(\gamma,\alpha)^{39}K^a$	-4.806
713	$^{41}Ti(p,\gamma)^{42}V^a$	-0.240	761	$^{43}Ti(p,\alpha)^{40}Sc^a$	-4.446
714	$^{41}Ti(\alpha,p)^{44}V^a$	2.928	762	$^{43}Ti(p,\gamma)^{44}V^a$	1.045
715	$^{41}Ti(\alpha,\gamma)^{45}Cr^a$	6.028	763	$^{43}Ti(\alpha,\gamma)^{47}Cr^a$	7.657
716	$^{41}Ti(\beta^+)^{41}Sc^a$	12.943	764	$^{43}Ti(\alpha,p)^{46}V^a$	2.889
717	$^{41}Ti(\gamma,p)^{40}Ca^a$	11.844	765	$^{43}Ti(\beta^+)^{43}Sc^a$	6.866
718	$^{41}Ti(\gamma,\alpha)^{37}Ca^a$	-6.771	766	$^{43}Ti(\gamma,\alpha)^{39}Ca^a$	-4.469
719	$^{41}Ti(\gamma,p)^{40}Sc^a$	-2.563	767	$^{43}Ti(\gamma,p)^{42}Sc^a$	-4.488
720	$^{42}Ca(p,\gamma)^{43}Sc^a$	4.930	768	$^{43}V(p,\alpha)^{40}Ti^a$	-3.932

Table C.2: – Continued.

Number	Reaction	Energy (Mev)	Number	Reaction	Energy (Mev)
769	$^{43}V(p,\gamma)^{44}Cr^a$	2.751	817	$^{45}Sc(\alpha,\gamma)^{49}V^a$	9.312
770	$^{43}V(\alpha,\gamma)^{47}Mn^a$	6.382	818	$^{45}Sc(\alpha,p)^{48}Ti^a$	2.554
771	$^{43}V(\alpha,p)^{46}Cr^a$	6.058	819	$^{45}Sc(\gamma,p)^{44}Ca^a$	-6.889
772	$^{43}V(\gamma,\alpha)^{39}Sc^a$	-6.165	820	$^{45}Sc(\gamma,\alpha)^{41}K^a$	-7.935
773	$^{43}V(\gamma,p)^{42}Ti^a$	-0.190	821	$^{45}Ti(p,\alpha)^{42}Sc^a$	-2.022
774	$^{43}V(\beta^+)^{43}Ti^a$	11.401	822	$^{45}Ti(p,\gamma)^{46}V^a$	5.356
775	$^{43}Cr(\alpha,p)^{46}Mn$	5.449	823	$^{45}Ti(\alpha,\gamma)^{49}Cr^a$	8.743
776	$^{43}Cr(\alpha,\gamma)^{47}Fe$	7.057	824	$^{45}Ti(\alpha,p)^{48}V^a$	0.603
777	$^{43}Cr(\gamma,\alpha)^{39}Ti$	-6.494	825	$^{45}Ti(\gamma,p)^{44}Sc^a$	-8.480
778	$^{43}Cr(\gamma,p)^{42}V$	-1.346	826	$^{45}Ti(\beta^+)^{45}Sc^a$	2.061
779	$^{43}Cr(\beta^+)^{43}V$	15.890	827	$^{45}Ti(\gamma,\alpha)^{41}Ca^a$	-6.294
780	$^{43}Cr(\gamma,p)^{42}Ti$	15.695	828	$^{45}V(p,\alpha)^{42}Ti^a$	-1.889
781	$^{44}Ca(p,\alpha)^{41}K^a$	-1.046	829	$^{45}V(p,\gamma)^{46}Cr^a$	4.886
782	$^{44}Ca(p,\gamma)^{45}Sc^a$	6.889	830	$^{45}V(\alpha,\gamma)^{49}Mn^a$	8.162
783	$^{44}Ca(\alpha,\gamma)^{48}Ti^a$	9.443	831	$^{45}V(\alpha,p)^{48}Cr^a$	6.078
784	$^{44}Ca(\gamma,\alpha)^{40}Ar$	-8.854	832	$^{45}V(\gamma,p)^{44}Ti^a$	-1.615
785	$^{44}Sc(p,\gamma)^{45}Ti^a$	8.480	833	$^{45}V(\beta^+)^{45}Ti^a$	7.132
786	$^{44}Sc(p,\alpha)^{41}Ca^a$	2.186	834	$^{45}V(\gamma,\alpha)^{41}Sc^a$	-5.656
787	$^{44}Sc(\alpha,p)^{47}Ti^a$	2.252	835	$^{45}Cr(p,\alpha)^{42}V^a$	-6.788
788	$^{44}Sc(\alpha,\gamma)^{48}V^a$	9.084	836	$^{45}Cr(p,\gamma)^{46}Mn^a$	0.690
789	$^{44}Sc(\gamma,\alpha)^{40}K$	-6.706	837	$^{45}Cr(\alpha,\gamma)^{49}Fe^a$	6.420
790	$^{44}Sc(\gamma,p)^{43}Ca^a$	-6.696	838	$^{45}Cr(\alpha,p)^{48}Mn^a$	4.081
791	$^{44}Sc(\beta^+)^{44}Ca^a$	3.653	839	$^{45}Cr(\gamma,p)^{44}V^a$	-3.100
792	$^{44}Ti(p,\gamma)^{45}V^a$	1.615	840	$^{45}Cr(\beta^+)^{45}V^a$	12.460
793	$^{44}Ti(p,\alpha)^{41}Sc^a$	-4.042	841	$^{45}Cr(\gamma,p)^{44}Ti^a$	10.847
794	$^{44}Ti(\alpha,p)^{47}V^a$	-0.408	842	$^{45}Cr(\gamma,\alpha)^{41}Ti^a$	-6.028
795	$^{44}Ti(\alpha,\gamma)^{48}Cr^a$	7.692	843	$^{45}Mn(p,\alpha)^{42}Cr$	-6.491
796	$^{44}Ti(\beta^+)^{44}Sc^a$	0.266	844	$^{45}Mn(p,\gamma)^{46}Fe$	1.392
797	$^{44}Ti(\gamma,\alpha)^{40}Ca^a$	-5.127	845	$^{45}Mn(\alpha,p)^{48}Fe^a$	8.150
798	$^{44}Ti(\gamma,p)^{43}Sc^a$	-8.650	846	$^{45}Mn(\gamma,p)^{44}Cr^a$	1.060
799	$^{44}V(p,\gamma)^{45}Cr^a$	3.100	847	$^{46}Ca(\alpha,\gamma)^{50}Ti$	10.716
800	$^{44}V(p,\alpha)^{41}Ti^a$	-2.928	848	$^{46}Ti(p,\alpha)^{43}Sc^a$	-3.073
801	$^{44}V(\alpha,p)^{47}Cr^a$	4.503	849	$^{46}Ti(p,\gamma)^{47}V^a$	5.168
802	$^{44}V(\alpha,\gamma)^{48}Mn^a$	7.181	850	$^{46}Ti(\alpha,\gamma)^{50}Cr^a$	8.554
803	$^{44}V(\gamma,p)^{43}Ti^a$	-1.045	851	$^{46}Ti(\alpha,p)^{49}V^a$	-1.033
804	$^{44}V(\beta^+)^{44}Ti^a$	13.749	852	$^{46}Ti(\gamma,p)^{45}Sc^a$	-10.345
805	$^{44}V(\gamma,\alpha)^{40}Sc^a$	-5.491	853	$^{46}Ti(\gamma,\alpha)^{42}Ca^a$	-8.003
806	$^{44}Cr(p,\gamma)^{45}Mn^a$	-1.060	854	$^{46}V(p,\alpha)^{43}Ti^a$	-2.889
807	$^{44}Cr(\alpha,\gamma)^{48}Fe^a$	6.695	855	$^{46}V(p,\gamma)^{47}Cr^a$	4.768
808	$^{44}Cr(\alpha,p)^{47}Mn^a$	3.631	856	$^{46}V(\alpha,\gamma)^{50}Mn^a$	7.972
809	$^{44}Cr(\gamma,p)^{43}V^a$	-2.751	857	$^{46}V(\alpha,p)^{49}Cr^a$	3.387
810	$^{44}Cr(\beta^+)^{44}V^a$	10.310	858	$^{46}V(\beta^+)^{46}Ti^a$	7.049
811	$^{44}Cr(\gamma,p)^{43}Ti^a$	8.496	859	$^{46}V(\gamma,\alpha)^{42}Sc^a$	-7.378
812	$^{44}Cr(\gamma,\alpha)^{40}Ti^a$	-6.683	860	$^{46}V(\gamma,p)^{45}Ti^a$	-5.356
813	$^{45}Ca(\alpha,\gamma)^{49}Ti$	10.170	861	$^{46}Cr(p,\alpha)^{43}V^a$	-6.058
814	$^{45}Ca(\beta^+)^{45}Sc$	0.255	862	$^{46}Cr(p,\gamma)^{47}Mn^a$	0.080
815	$^{45}Sc(p,\alpha)^{42}Ca^a$	2.342	863	$^{46}Cr(\alpha,\gamma)^{50}Fe^a$	7.425
816	$^{45}Sc(p,\gamma)^{46}Ti^a$	10.345	864	$^{46}Cr(\alpha,p)^{49}Mn^a$	3.275

Table C.2: – Continued.

Number	Reaction	Energy (Mev)	Number	Reaction	Energy (Mev)
865	$^{46}Cr(\gamma,p)^{45}V^a$	-4.886	913	$^{47}Fe(\gamma,\alpha)^{43}Cr$	-7.057
866	$^{46}Cr(\beta^+)^{46}V^a$	7.603	914	$^{48}Ti(p,\gamma)^{49}V^a$	6.758
867	$^{46}Cr(\gamma,\alpha)^{42}Ti^a$	-6.775	915	$^{48}Ti(p,\alpha)^{45}Sc^a$	-2.554
868	$^{46}Mn(p,\alpha)^{43}Cr$	-5.449	916	$^{48}Ti(\alpha,p)^{51}V^a$	-1.154
869	$^{46}Mn(p,\gamma)^{47}Fe$	1.608	917	$^{48}Ti(\alpha,\gamma)^{52}Cr^a$	9.351
870	$^{46}Mn(\alpha,\gamma)^{50}Co^a$	7.338	918	$^{48}Ti(\gamma,\alpha)^{44}Ca^a$	-9.443
871	$^{46}Mn(\alpha,p)^{49}Fe^a$	6.413	919	$^{48}V(p,\gamma)^{49}Cr^a$	8.140
872	$^{46}Mn(\gamma,p)^{45}Cr^a$	-0.690	920	$^{48}V(p,\alpha)^{45}Ti^a$	-0.603
873	$^{46}Mn(\beta^+)^{46}Cr^a$	17.100	921	$^{48}V(\alpha,p)^{51}Cr^a$	2.106
874	$^{46}Mn(\gamma,p)^{45}V^a$	12.214	922	$^{48}V(\alpha,\gamma)^{52}Mn^a$	8.651
875	$^{46}Mn(\gamma,\alpha)^{42}V^a$	-6.795	923	$^{48}V(\gamma,\alpha)^{44}Sc^a$	-9.084
876	$^{46}Fe(\alpha,\gamma)^{50}Ni$	7.060	924	$^{48}V(\gamma,p)^{47}Ti^a$	-6.832
877	$^{46}Fe(\gamma,p)^{45}Cr$	12.441	925	$^{48}V(\beta^+)^{48}Ti^a$	4.015
878	$^{46}Fe(\gamma,p)^{45}Mn$	-1.392	926	$^{48}Cr(p,\gamma)^{49}Mn^a$	2.084
879	$^{46}Fe(\beta^+)^{46}Mn$	13.130	927	$^{48}Cr(p,\alpha)^{45}V^a$	-6.078
880	$^{46}Fe(\gamma,\alpha)^{42}Cr$	-7.883	928	$^{48}Cr(\alpha,p)^{51}Mn^a$	0.558
881	$^{47}Ti(p,\alpha)^{44}Sc^a$	-2.252	929	$^{48}Cr(\alpha,\gamma)^{52}Fe^a$	7.939
882	$^{47}Ti(p,\gamma)^{48}V^a$	6.832	930	$^{48}Cr(\gamma,p)^{47}V^a$	-8.100
883	$^{47}Ti(\alpha,\gamma)^{51}Cr^a$	8.938	931	$^{48}Cr(\beta^+)^{48}V^a$	1.654
884	$^{47}Ti(\alpha,p)^{50}V$	-0.578	932	$^{48}Cr(\gamma,\alpha)^{44}Ti^a$	-7.692
885	$^{47}Ti(\gamma,\alpha)^{43}Ca^a$	-8.948	933	$^{48}Mn(p,\gamma)^{49}Fe^a$	2.339
886	$^{47}V(p,\alpha)^{44}Ti^a$	0.408	934	$^{48}Mn(p,\alpha)^{45}Cr^a$	-4.081
887	$^{47}V(p,\gamma)^{48}Cr^a$	8.100	935	$^{48}Mn(\alpha,p)^{51}Fe^a$	5.926
888	$^{47}V(\alpha,\gamma)^{51}Mn^a$	8.658	936	$^{48}Mn(\alpha,\gamma)^{52}Co^a$	7.476
889	$^{47}V(\alpha,p)^{50}Cr^a$	3.386	937	$^{48}Mn(\beta^+)^{48}Cr^a$	13.598
890	$^{47}V(\beta^+)^{47}Ti^a$	2.927	938	$^{48}Mn(\gamma,\alpha)^{44}V^a$	-7.181
891	$^{47}V(\gamma,\alpha)^{43}Sc^a$	-8.241	939	$^{48}Mn(\gamma,p)^{47}Cr^a$	-2.678
892	$^{47}V(\gamma,p)^{46}Ti^a$	-5.168	940	$^{48}Fe(p,\alpha)^{45}Mn^a$	-8.150
893	$^{47}Cr(p,\alpha)^{44}V^a$	-4.503	941	$^{48}Fe(\alpha,p)^{51}Co^a$	4.888
894	$^{47}Cr(p,\gamma)^{48}Mn^a$	2.678	942	$^{48}Fe(\alpha,\gamma)^{52}Ni^a$	7.060
895	$^{47}Cr(\alpha,\gamma)^{51}Fe^a$	8.090	943	$^{48}Fe(\gamma,p)^{47}Cr^a$	9.155
896	$^{47}Cr(\alpha,p)^{50}Mn^a$	3.205	944	$^{48}Fe(\gamma,\alpha)^{44}Cr^a$	-6.695
897	$^{47}Cr(\beta^+)^{47}V^a$	7.449	945	$^{48}Fe(\gamma,p)^{47}Mn^a$	-3.064
898	$^{47}Cr(\gamma,\alpha)^{43}Ti^a$	-7.657	946	$^{48}Fe(\beta^+)^{48}Mn^a$	11.180
899	$^{47}Cr(\gamma,p)^{46}V^a$	-4.768	947	$^{49}Ti(p,\gamma)^{50}V$	7.949
900	$^{47}Mn(p,\alpha)^{44}Cr^a$	-3.631	948	$^{49}Ti(\alpha,\gamma)^{53}Cr^a$	9.148
901	$^{47}Mn(p,\gamma)^{48}Fe^a$	3.064	949	$^{49}Ti(\gamma,\alpha)^{45}Ca$	-10.170
902	$^{47}Mn(\alpha,\gamma)^{51}Co^a$	7.952	950	$^{49}V(p,\gamma)^{50}Cr^a$	9.587
903	$^{47}Mn(\alpha,p)^{50}Fe^a$	6.583	951	$^{49}V(p,\alpha)^{46}Ti^a$	1.033
904	$^{47}Mn(\gamma,\alpha)^{43}V^a$	-6.382	952	$^{49}V(\alpha,p)^{52}Cr^a$	2.593
905	$^{47}Mn(\gamma,p)^{46}Cr^a$	-0.080	953	$^{49}V(\alpha,\gamma)^{53}Mn^a$	9.153
906	$^{47}Mn(\beta^+)^{47}Cr^a$	12.290	954	$^{49}V(\beta^+)^{49}Ti^a$	0.602
907	$^{47}Mn(\gamma,p)^{46}V^a$	7.522	955	$^{49}V(\gamma,\alpha)^{45}Sc^a$	-9.312
908	$^{47}Fe(\alpha,p)^{50}Co$	5.730	956	$^{49}V(\gamma,p)^{48}Ti^a$	-6.758
909	$^{47}Fe(\alpha,\gamma)^{51}Ni$	6.685	957	$^{49}Cr(p,\gamma)^{50}Mn^a$	4.585
910	$^{47}Fe(\gamma,p)^{46}Mn$	-1.608	958	$^{49}Cr(p,\alpha)^{46}V^a$	-3.387
911	$^{47}Fe(\beta^+)^{47}Mn$	15.640	959	$^{49}Cr(\alpha,p)^{52}Mn^a$	0.512
912	$^{47}Fe(\gamma,p)^{46}Cr$	15.565	960	$^{49}Cr(\alpha,\gamma)^{53}Fe^a$	8.041

Table C.2: – Continued.

Number	Reaction	Energy (Mev)	Number	Reaction	Energy (Mev)
961	$^{49}Cr(\gamma,p)^{48}V^a$	-8.140	1009	$^{50}Co(\alpha,p)^{53}Ni^a$	6.823
962	$^{49}Cr(\beta^+)^{49}V^a$	2.629	1010	$^{50}Co(\gamma,\alpha)^{46}Mn^a$	-7.338
963	$^{49}Cr(\gamma,\alpha)^{45}Ti^a$	-8.743	1011	$^{50}Co(\gamma,p)^{49}Fe^a$	0.100
964	$^{49}Mn(p,\gamma)^{50}Fe^a$	4.150	1012	$^{50}Co(\beta^+)^{50}Fe^a$	16.970
965	$^{49}Mn(p,\alpha)^{46}Cr^a$	-3.275	1013	$^{50}Co(\gamma,p)^{49}Mn^a$	13.126
966	$^{49}Mn(\alpha,p)^{52}Fe^a$	5.855	1014	$^{50}Ni(\alpha,\gamma)^{54}Zn$	4.474
967	$^{49}Mn(\alpha,\gamma)^{53}Co^a$	7.454	1015	$^{50}Ni(\beta^+)^{50}Co$	11.607
968	$^{49}Mn(\gamma,\alpha)^{45}V^a$	-8.162	1016	$^{50}Ni(\gamma,\alpha)^{46}Fe$	-7.060
969	$^{49}Mn(\gamma,p)^{48}Cr^a$	-2.084	1017	$^{51}V(p,\gamma)^{52}Cr^a$	10.505
970	$^{49}Mn(\beta^+)^{49}Cr^a$	7.716	1018	$^{51}V(p,\alpha)^{48}Ti^a$	1.154
971	$^{49}Fe(p,\gamma)^{50}Co^a$	-0.100	1019	$^{51}V(\alpha,p)^{54}Cr$	-0.133
972	$^{49}Fe(p,\alpha)^{46}Mn^a$	-6.413	1020	$^{51}V(\alpha,\gamma)^{55}Mn^a$	7.934
973	$^{49}Fe(\alpha,p)^{52}Co^a$	5.137	1021	$^{51}V(\gamma,p)^{50}Ti$	-8.061
974	$^{49}Fe(\alpha,\gamma)^{53}Ni^a$	7.748	1022	$^{51}Cr(p,\gamma)^{52}Mn^a$	6.545
975	$^{49}Fe(\gamma,\alpha)^{45}Cr^a$	-6.420	1023	$^{51}Cr(p,\alpha)^{48}V^a$	-2.106
976	$^{49}Fe(\gamma,p)^{48}Mn^a$	-2.339	1024	$^{51}Cr(\alpha,p)^{54}Mn$	-0.758
977	$^{49}Fe(\beta^+)^{49}Mn^a$	13.030	1025	$^{51}Cr(\alpha,\gamma)^{55}Fe^a$	8.455
978	$^{49}Fe(\gamma,p)^{48}Cr^a$	10.944	1026	$^{51}Cr(\beta^+)^{51}V^a$	0.750
979	$^{50}Ti(p,\gamma)^{51}V$	8.061	1027	$^{51}Cr(\gamma,\alpha)^{47}Ti^a$	-8.938
980	$^{50}Ti(\alpha,\gamma)^{54}Cr$	7.928	1028	$^{51}Cr(\gamma,p)^{50}V$	-9.516
981	$^{50}Ti(\gamma,\alpha)^{46}Ca$	-10.716	1029	$^{51}Mn(p,\gamma)^{52}Fe^a$	7.381
982	$^{50}V(p,\gamma)^{51}Cr$	9.516	1030	$^{51}Mn(p,\alpha)^{48}Cr^a$	-0.558
983	$^{50}V(p,\alpha)^{47}Ti$	0.578	1031	$^{51}Mn(\alpha,p)^{54}Fe^a$	3.148
984	$^{50}V(\alpha,p)^{53}Cr$	1.199	1032	$^{51}Mn(\alpha,\gamma)^{55}Co^a$	8.212
985	$^{50}V(\alpha,\gamma)^{54}Mn$	8.759	1033	$^{51}Mn(\gamma,\alpha)^{47}V^a$	-8.658
986	$^{50}V(\gamma,p)^{49}Ti$	-7.949	1034	$^{51}Mn(\gamma,p)^{50}Cr^a$	-5.272
987	$^{50}Cr(p,\gamma)^{51}Mn^a$	5.272	1035	$^{51}Mn(\beta^+)^{51}Cr^a$	3.210
988	$^{50}Cr(p,\alpha)^{47}V^a$	-3.386	1036	$^{51}Fe(p,\gamma)^{52}Co^a$	0.980
989	$^{50}Cr(\alpha,p)^{53}Mn^a$	-0.435	1037	$^{51}Fe(p,\alpha)^{48}Mn^a$	-5.926
990	$^{50}Cr(\alpha,\gamma)^{54}Fe^a$	8.419	1038	$^{51}Fe(\alpha,p)^{54}Co^a$	2.924
991	$^{50}Cr(\gamma,p)^{49}V^a$	-9.587	1039	$^{51}Fe(\alpha,\gamma)^{55}Ni^a$	7.538
992	$^{50}Cr(\gamma,\alpha)^{46}Ti^a$	-8.554	1040	$^{51}Fe(\beta^+)^{51}Mn^a$	8.020
993	$^{50}Mn(p,\gamma)^{51}Fe^a$	4.885	1041	$^{51}Fe(\gamma,\alpha)^{47}Cr^a$	-8.090
994	$^{50}Mn(p,\alpha)^{47}Cr^a$	-3.205	1042	$^{51}Fe(\gamma,p)^{50}Mn^a$	-4.885
995	$^{50}Mn(\alpha,p)^{53}Fe^a$	3.456	1043	$^{51}Co(p,\gamma)^{52}Ni^a$	2.172
996	$^{50}Mn(\alpha,\gamma)^{54}Co^a$	7.809	1044	$^{51}Co(p,\alpha)^{48}Fe^a$	-4.888
997	$^{50}Mn(\beta^+)^{50}Cr^a$	7.630	1045	$^{51}Co(\alpha,p)^{54}Ni^a$	6.853
998	$^{50}Mn(\gamma,\alpha)^{46}V^a$	-7.972	1046	$^{51}Co(\alpha,\gamma)^{55}Cu^a$	5.942
999	$^{50}Mn(\gamma,p)^{49}Cr^a$	-4.585	1047	$^{51}Co(\beta^+)^{51}Fe^a$	12.798
1000	$^{50}Fe(p,\gamma)^{51}Co^a$	0.090	1048	$^{51}Co(\gamma,\alpha)^{47}Mn^a$	-7.952
1001	$^{50}Fe(p,\alpha)^{47}Mn^a$	-6.583	1049	$^{51}Co(\gamma,p)^{50}Fe^a$	-0.090
1002	$^{50}Fe(\alpha,p)^{53}Co^a$	3.304	1050	$^{51}Ni(\alpha,\gamma)^{55}Zn$	4.663
1003	$^{50}Fe(\alpha,\gamma)^{54}Ni^a$	7.160	1051	$^{51}Ni(\gamma,\alpha)^{47}Fe$	-6.685
1004	$^{50}Fe(\gamma,\alpha)^{46}Cr^a$	-7.425	1052	$^{51}Ni(\gamma,p)^{50}Co$	-0.955
1005	$^{50}Fe(\gamma,p)^{49}Mn^a$	-4.150	1053	$^{51}Ni(\beta^+)^{51}Co$	11.882
1006	$^{50}Fe(\beta^+)^{50}Mn^a$	8.156	1054	$^{52}Cr(p,\gamma)^{53}Mn^a$	6.560
1007	$^{50}Co(p,\gamma)^{51}Ni$	0.955	1055	$^{52}Cr(p,\alpha)^{49}V^a$	-2.593
1008	$^{50}Co(p,\alpha)^{47}Fe$	-5.730	1056	$^{52}Cr(\alpha,p)^{55}Mn^a$	-2.571

Table C.2: – Continued.

Number	Reaction	Energy (Mev)	Number	Reaction	Energy (Mev)
1057	$^{52}Cr(\alpha,\gamma)^{56}Fe^a$	7.613	1105	$^{53}Co(p,\alpha)^{50}Fe^a$	-3.304
1058	$^{52}Cr(\gamma,\alpha)^{48}Ti^a$	-9.351	1106	$^{53}Co(p,\gamma)^{54}Ni^a$	3.856
1059	$^{52}Cr(\gamma,p)^{51}V^a$	-10.505	1107	$^{53}Co(\alpha,\gamma)^{57}Cu^a$	7.091
1060	$^{52}Mn(p,\gamma)^{53}Fe^a$	7.529	1108	$^{53}Co(\alpha,p)^{56}Ni^a$	6.396
1061	$^{52}Mn(p,\alpha)^{49}Cr^a$	-0.512	1109	$^{53}Co(\gamma,\alpha)^{49}Mn^a$	-7.454
1062	$^{52}Mn(\alpha,p)^{55}Fe^a$	1.910	1110	$^{53}Co(\gamma,p)^{52}Fe^a$	-1.599
1063	$^{52}Mn(\alpha,\gamma)^{56}Co^a$	7.759	1111	$^{53}Co(\beta^+)^{53}Fe^a$	8.302
1064	$^{52}Mn(\gamma,p)^{51}Cr^a$	-6.545	1112	$^{53}Ni(p,\alpha)^{50}Co^a$	-6.823
1065	$^{52}Mn(\beta^+)^{52}Cr^a$	4.712	1113	$^{53}Ni(\alpha,\gamma)^{57}Zn^a$	4.910
1066	$^{52}Mn(\gamma,\alpha)^{48}V^a$	-8.651	1114	$^{53}Ni(\alpha,p)^{56}Cu^a$	3.390
1067	$^{52}Fe(p,\gamma)^{53}Co^a$	1.599	1115	$^{53}Ni(\gamma,p)^{52}Co^a$	-2.611
1068	$^{52}Fe(p,\alpha)^{49}Mn^a$	-5.855	1116	$^{53}Ni(\beta^+)^{53}Co^a$	13.230
1069	$^{52}Fe(\alpha,p)^{55}Co^a$	0.830	1117	$^{53}Ni(\gamma,p)^{52}Fe^a$	11.661
1070	$^{52}Fe(\alpha,\gamma)^{56}Ni^a$	7.995	1118	$^{53}Ni(\gamma,\alpha)^{49}Fe^a$	-7.748
1071	$^{52}Fe(\gamma,p)^{51}Mn^a$	-7.381	1119	$^{54}Cr(p,\gamma)^{55}Mn$	8.067
1072	$^{52}Fe(\beta^+)^{52}Mn^a$	2.372	1120	$^{54}Cr(p,\alpha)^{51}V$	0.133
1073	$^{52}Fe(\gamma,\alpha)^{48}Cr^a$	-7.939	1121	$^{54}Cr(\alpha,\gamma)^{58}Fe$	7.645
1074	$^{52}Co(p,\gamma)^{53}Ni^a$	2.611	1122	$^{54}Cr(\gamma,\alpha)^{50}Ti$	-7.928
1075	$^{52}Co(p,\alpha)^{49}Fe^a$	-5.137	1123	$^{54}Mn(p,\alpha)^{51}Cr$	0.758
1076	$^{52}Co(\alpha,p)^{55}Ni^a$	6.449	1124	$^{54}Mn(p,\gamma)^{55}Fe$	9.213
1077	$^{52}Co(\alpha,\gamma)^{56}Cu^a$	6.001	1125	$^{54}Mn(\alpha,\gamma)^{58}Co$	6.715
1078	$^{52}Co(\beta^+)^{52}Fe^a$	14.031	1126	$^{54}Mn(\alpha,p)^{57}Fe$	-0.240
1079	$^{52}Co(\gamma,\alpha)^{48}Mn^a$	-7.476	1127	$^{54}Mn(\gamma,\alpha)^{50}V$	-8.759
1080	$^{52}Co(\gamma,p)^{51}Fe^a$	-0.980	1128	$^{54}Mn(\gamma,p)^{53}Cr$	-7.560
1081	$^{52}Ni(\alpha,\gamma)^{56}Zn^a$	4.808	1129	$^{54}Mn(\beta^+)^{54}Cr$	1.377
1082	$^{52}Ni(\alpha,p)^{55}Cu^a$	3.770	1130	$^{54}Fe(p,\alpha)^{51}Mn^a$	-3.148
1083	$^{52}Ni(\gamma,\alpha)^{48}Fe^a$	-7.060	1131	$^{54}Fe(p,\gamma)^{55}Co^a$	5.064
1084	$^{52}Ni(\gamma,p)^{51}Co^a$	-2.172	1132	$^{54}Fe(\alpha,\gamma)^{58}Ni^a$	6.400
1085	$^{52}Ni(\beta^+)^{52}Co^a$	11.660	1133	$^{54}Fe(\alpha,p)^{57}Co^a$	-1.772
1086	$^{52}Ni(\gamma,p)^{51}Fe^a$	10.274	1134	$^{54}Fe(\gamma,p)^{53}Mn^a$	-8.854
1087	$^{53}Cr(p,\alpha)^{50}V$	-1.199	1135	$^{54}Fe(\gamma,\alpha)^{50}Cr^a$	-8.419
1088	$^{53}Cr(p,\gamma)^{54}Mn$	7.560	1136	$^{54}Co(p,\alpha)^{51}Fe^a$	-2.924
1089	$^{53}Cr(\alpha,\gamma)^{57}Fe^a$	7.320	1137	$^{54}Co(p,\gamma)^{55}Ni^a$	4.614
1090	$^{53}Cr(\gamma,\alpha)^{49}Ti^a$	-9.148	1138	$^{54}Co(\alpha,\gamma)^{58}Cu^a$	6.079
1091	$^{53}Mn(p,\alpha)^{50}Cr^a$	0.435	1139	$^{54}Co(\alpha,p)^{57}Ni^a$	3.205
1092	$^{53}Mn(p,\gamma)^{54}Fe^a$	8.854	1140	$^{54}Co(\beta^+)^{54}Fe^a$	8.240
1093	$^{53}Mn(\alpha,\gamma)^{57}Co^a$	7.081	1141	$^{54}Co(\gamma,\alpha)^{50}Mn^a$	-7.809
1094	$^{53}Mn(\alpha,p)^{56}Fe^a$	1.053	1142	$^{54}Co(\gamma,p)^{53}Fe^a$	-4.353
1095	$^{53}Mn(\gamma,\alpha)^{49}V^a$	-9.153	1143	$^{54}Ni(p,\alpha)^{51}Co^a$	-6.853
1096	$^{53}Mn(\gamma,p)^{52}Cr^a$	-6.560	1144	$^{54}Ni(p,\gamma)^{55}Cu^a$	-0.300
1097	$^{53}Mn(\beta^+)^{53}Cr^a$	0.596	1145	$^{54}Ni(\alpha,\gamma)^{58}Zn^a$	5.512
1098	$^{53}Fe(p,\alpha)^{50}Mn^a$	-3.456	1146	$^{54}Ni(\alpha,p)^{57}Cu^a$	3.235
1099	$^{53}Fe(p,\gamma)^{54}Co^a$	4.353	1147	$^{54}Ni(\gamma,\alpha)^{50}Fe^a$	-7.160
1100	$^{53}Fe(\alpha,\gamma)^{57}Ni^a$	7.559	1148	$^{54}Ni(\gamma,p)^{53}Co^a$	-3.856
1101	$^{53}Fe(\alpha,p)^{56}Co^a$	0.230	1149	$^{54}Ni(\beta^+)^{54}Co^a$	8.799
1102	$^{53}Fe(\gamma,p)^{52}Mn^a$	-7.529	1150	$^{54}Zn(\gamma,\alpha)^{50}Ni$	-4.474
1103	$^{53}Fe(\beta^+)^{53}Mn^a$	3.745	1151	$^{55}Mn(p,\alpha)^{52}Cr^a$	2.571
1104	$^{53}Fe(\gamma,\alpha)^{49}Cr^a$	-8.041	1152	$^{55}Mn(p,\gamma)^{56}Fe^a$	10.184

Table C.2: – Continued.

Number	Reaction	Energy (Mev)	Number	Reaction	Energy (Mev)
1153	$^{55}Mn(\alpha,\gamma)^{59}Co^a$	6.942	1201	$^{56}Ni(\alpha,\gamma)^{60}Zn^a$	2.708
1154	$^{55}Mn(\alpha,p)^{58}Fe$	-0.422	1202	$^{56}Ni(\alpha,p)^{59}Cu^a$	-2.413
1155	$^{55}Mn(\gamma,\alpha)^{51}V^a$	-7.934	1203	$^{56}Ni(\beta^+)^{56}Co^a$	2.136
1156	$^{55}Mn(\gamma,p)^{54}Cr$	-8.067	1204	$^{56}Ni(\gamma,\alpha)^{52}Fe^a$	-7.995
1157	$^{55}Fe(p,\alpha)^{52}Mn^a$	-1.910	1205	$^{56}Ni(\gamma,p)^{55}Co^a$	-7.165
1158	$^{55}Fe(p,\gamma)^{56}Co^a$	5.849	1206	$^{56}Cu(p,\alpha)^{53}Ni^a$	-3.390
1159	$^{55}Fe(\alpha,\gamma)^{59}Ni^a$	6.101	1207	$^{56}Cu(p,\gamma)^{57}Zn^a$	1.520
1160	$^{55}Fe(\alpha,p)^{58}Co$	-2.498	1208	$^{56}Cu(\alpha,\gamma)^{60}Ga^a$	2.797
1161	$^{55}Fe(\gamma,p)^{54}Mn$	-9.213	1209	$^{56}Cu(\alpha,p)^{59}Zn^a$	3.284
1162	$^{55}Fe(\beta^+)^{55}Mn^a$	0.232	1210	$^{56}Cu(\gamma,\alpha)^{52}Co^a$	-6.001
1163	$^{55}Fe(\gamma,\alpha)^{51}Cr^a$	-8.455	1211	$^{56}Cu(\gamma,p)^{55}Ni^a$	-0.560
1164	$^{55}Co(p,\alpha)^{52}Fe^a$	-0.830	1212	$^{56}Cu(\beta^+)^{56}Ni^a$	15.402
1165	$^{55}Co(p,\gamma)^{56}Ni^a$	7.165	1213	$^{56}Zn(\alpha,p)^{59}Ga^a$	2.962
1166	$^{55}Co(\alpha,\gamma)^{59}Cu^a$	4.753	1214	$^{56}Zn(\alpha,\gamma)^{60}Ge^a$	3.852
1167	$^{55}Co(\alpha,p)^{58}Ni^a$	1.335	1215	$^{56}Zn(\beta^+)^{56}Cu^a$	10.489
1168	$^{55}Co(\beta^+)^{55}Fe^a$	3.451	1216	$^{56}Zn(\gamma,\alpha)^{52}Ni^a$	-4.808
1169	$^{55}Co(\gamma,\alpha)^{51}Mn^a$	-8.212	1217	$^{56}Zn(\gamma,p)^{55}Cu^a$	-1.038
1170	$^{55}Co(\gamma,p)^{54}Fe^a$	-5.064	1218	$^{57}Fe(p,\gamma)^{58}Co$	6.955
1171	$^{55}Ni(p,\alpha)^{52}Co^a$	-6.449	1219	$^{57}Fe(p,\alpha)^{54}Mn$	0.240
1172	$^{55}Ni(p,\gamma)^{56}Cu^a$	0.560	1220	$^{57}Fe(\alpha,\gamma)^{61}Ni^a$	6.466
1173	$^{55}Ni(\alpha,\gamma)^{59}Zn^a$	4.352	1221	$^{57}Fe(\gamma,\alpha)^{53}Cr^a$	-7.320
1174	$^{55}Ni(\alpha,p)^{58}Cu^a$	1.465	1222	$^{57}Co(p,\gamma)^{58}Ni^a$	8.172
1175	$^{55}Ni(\gamma,p)^{54}Co^a$	-4.614	1223	$^{57}Co(p,\alpha)^{54}Fe^a$	1.772
1176	$^{55}Ni(\beta^+)^{55}Co^a$	8.696	1224	$^{57}Co(\alpha,p)^{60}Ni^a$	0.264
1177	$^{55}Ni(\gamma,\alpha)^{51}Fe^a$	-7.538	1225	$^{57}Co(\alpha,\gamma)^{61}Cu^a$	5.065
1178	$^{55}Cu(p,\alpha)^{52}Ni^a$	-3.770	1226	$^{57}Co(\gamma,\alpha)^{53}Mn^a$	-7.081
1179	$^{55}Cu(p,\gamma)^{56}Zn^a$	1.038	1227	$^{57}Co(\gamma,p)^{56}Fe^a$	-6.028
1180	$^{55}Cu(\alpha,\gamma)^{59}Ga^a$	4.000	1228	$^{57}Co(\beta^+)^{57}Fe^a$	0.835
1181	$^{55}Cu(\alpha,p)^{58}Zn^a$	5.408	1229	$^{57}Ni(p,\gamma)^{58}Cu^a$	2.874
1182	$^{55}Cu(\gamma,\alpha)^{51}Co^a$	-5.942	1230	$^{57}Ni(p,\alpha)^{54}Co^a$	-3.205
1183	$^{55}Cu(\gamma,p)^{54}Ni^a$	0.300	1231	$^{57}Ni(\alpha,p)^{60}Cu^a$	-2.598
1184	$^{55}Zn(\alpha,\gamma)^{59}Ge$	4.400	1232	$^{57}Ni(\alpha,\gamma)^{61}Zn^a$	2.692
1185	$^{55}Zn(\gamma,\alpha)^{51}Ni$	-4.663	1233	$^{57}Ni(\gamma,p)^{56}Co^a$	-7.329
1186	$^{56}Fe(p,\alpha)^{53}Mn^a$	-1.053	1234	$^{57}Ni(\beta^+)^{57}Co^a$	3.265
1187	$^{56}Fe(p,\gamma)^{57}Co^a$	6.028	1235	$^{57}Ni(\gamma,\alpha)^{53}Fe^a$	-7.559
1188	$^{56}Fe(\alpha,\gamma)^{60}Ni^a$	6.292	1236	$^{57}Cu(p,\gamma)^{58}Zn^a$	2.277
1189	$^{56}Fe(\alpha,p)^{59}Co^a$	-3.242	1237	$^{57}Cu(p,\alpha)^{54}Ni^a$	-3.235
1190	$^{56}Fe(\gamma,\alpha)^{52}Cr^a$	-7.613	1238	$^{57}Cu(\alpha,p)^{60}Zn^a$	0.996
1191	$^{56}Fe(\gamma,p)^{55}Mn^a$	-10.184	1239	$^{57}Cu(\alpha,\gamma)^{61}Ga^a$	0.909
1192	$^{56}Co(p,\alpha)^{53}Fe^a$	-0.230	1240	$^{57}Cu(\gamma,\alpha)^{53}Co^a$	-7.091
1193	$^{56}Co(p,\gamma)^{57}Ni^a$	7.329	1241	$^{57}Cu(\gamma,p)^{56}Ni^a$	-0.695
1194	$^{56}Co(\alpha,\gamma)^{60}Cu^a$	4.731	1242	$^{57}Cu(\beta^+)^{57}Ni^a$	8.697
1195	$^{56}Co(\alpha,p)^{59}Ni^a$	0.252	1243	$^{57}Zn(\alpha,\gamma)^{61}Ge^a$	2.755
1196	$^{56}Co(\beta^+)^{56}Fe^a$	4.566	1244	$^{57}Zn(\alpha,p)^{60}Ga^a$	1.277
1197	$^{56}Co(\gamma,\alpha)^{52}Mn^a$	-7.759	1245	$^{57}Zn(\gamma,p)^{56}Ni^a$	13.924
1198	$^{56}Co(\gamma,p)^{55}Fe^a$	-5.849	1246	$^{57}Zn(\gamma,\alpha)^{53}Ni^a$	-4.910
1199	$^{56}Ni(p,\alpha)^{53}Co^a$	-6.396	1247	$^{57}Zn(\gamma,p)^{56}Cu^a$	-1.520
1200	$^{56}Ni(p,\gamma)^{57}Cu^a$	0.695	1248	$^{57}Zn(\beta^+)^{57}Cu^a$	14.770

Table C.2: – Continued.

Number	Reaction	Energy (Mev)	Number	Reaction	Energy (Mev)
1249	$^{58}Fe(p,\gamma)^{59}Co$	7.364	1297	$^{59}Cu(\gamma,\alpha)^{55}Co^{a}$	-4.753
1250	$^{58}Fe(p,\alpha)^{55}Mn$	0.422	1298	$^{59}Cu(\gamma,p)^{58}Ni^{a}$	-3.418
1251	$^{58}Fe(\alpha,\gamma)^{62}Ni$	7.019	1299	$^{59}Cu(\beta^{+})^{59}Ni^{a}$	4.799
1252	$^{58}Fe(\gamma,\alpha)^{54}Cr$	-7.645	1300	$^{59}Zn(p,\alpha)^{56}Cu^{a}$	-3.284
1253	$^{58}Co(p,\alpha)^{55}Fe$	2.498	1301	$^{59}Zn(p,\gamma)^{60}Ga^{a}$	0.030
1254	$^{58}Co(p,\gamma)^{59}Ni$	8.599	1302	$^{59}Zn(\alpha,\gamma)^{63}Ge$	1.480
1255	$^{58}Co(\alpha,\gamma)^{62}Cu$	5.378	1303	$^{59}Zn(\alpha,p)^{62}Ga$	-1.835
1256	$^{58}Co(\alpha,p)^{61}Ni$	-0.489	1304	$^{59}Zn(\gamma,p)^{58}Cu^{a}$	-2.887
1257	$^{58}Co(\beta^{+})^{58}Fe$	2.308	1305	$^{59}Zn(\beta^{+})^{59}Cu^{a}$	9.093
1258	$^{58}Co(\gamma,\alpha)^{54}Mn$	-6.715	1306	$^{59}Zn(\gamma,\alpha)^{55}Ni^{a}$	-4.352
1259	$^{58}Co(\gamma,p)^{57}Fe$	-6.955	1307	$^{59}Ga(p,\alpha)^{56}Zn^{a}$	-2.962
1260	$^{58}Ni(p,\alpha)^{55}Co^{a}$	-1.335	1308	$^{59}Ga(p,\gamma)^{60}Ge^{a}$	0.890
1261	$^{58}Ni(p,\gamma)^{59}Cu^{a}$	3.418	1309	$^{59}Ga(\alpha,p)^{62}Ge$	2.720
1262	$^{58}Ni(\alpha,\gamma)^{62}Zn$	3.369	1310	$^{59}Ga(\gamma,\alpha)^{55}Cu^{a}$	-4.000
1263	$^{58}Ni(\alpha,p)^{61}Cu^{a}$	-3.108	1311	$^{59}Ga(\gamma,p)^{58}Zn^{a}$	0.890
1264	$^{58}Ni(\gamma,p)^{57}Co^{a}$	-8.172	1312	$^{59}Ge(\gamma,\alpha)^{55}Zn$	-4.400
1265	$^{58}Ni(\gamma,\alpha)^{54}Fe^{a}$	-6.400	1313	$^{60}Ni(p,\alpha)^{57}Co^{a}$	-0.264
1266	$^{58}Cu(p,\alpha)^{55}Ni^{a}$	-1.465	1314	$^{60}Ni(p,\gamma)^{61}Cu^{a}$	4.801
1267	$^{58}Cu(p,\gamma)^{59}Zn^{a}$	2.887	1315	$^{60}Ni(\alpha,\gamma)^{64}Zn$	3.956
1268	$^{58}Cu(\alpha,\gamma)^{62}Ga$	2.761	1316	$^{60}Ni(\alpha,p)^{63}Cu$	-3.757
1269	$^{58}Cu(\alpha,p)^{61}Zn^{a}$	-0.182	1317	$^{60}Ni(\gamma,p)^{59}Co^{a}$	-9.534
1270	$^{58}Cu(\gamma,p)^{57}Ni^{a}$	-2.874	1318	$^{60}Ni(\gamma,\alpha)^{56}Fe^{a}$	-6.292
1271	$^{58}Cu(\beta^{+})^{58}Ni^{a}$	8.563	1319	$^{60}Cu(p,\alpha)^{57}Ni^{a}$	2.598
1272	$^{58}Cu(\gamma,\alpha)^{54}Co^{a}$	-6.079	1320	$^{60}Cu(p,\gamma)^{61}Zn^{a}$	5.290
1273	$^{58}Zn(p,\alpha)^{55}Cu^{a}$	-5.408	1321	$^{60}Cu(\alpha,\gamma)^{64}Ga$	2.919
1274	$^{58}Zn(p,\gamma)^{59}Ga^{a}$	-0.890	1322	$^{60}Cu(\alpha,p)^{63}Zn$	-0.996
1275	$^{58}Zn(\alpha,\gamma)^{62}Ge$	1.312	1323	$^{60}Cu(\gamma,p)^{59}Ni^{a}$	-4.479
1276	$^{58}Zn(\alpha,p)^{61}Ga^{a}$	-1.115	1324	$^{60}Cu(\beta^{+})^{60}Ni^{a}$	6.127
1277	$^{58}Zn(\gamma,p)^{57}Cu^{a}$	-2.277	1325	$^{60}Cu(\gamma,\alpha)^{56}Co^{a}$	-4.731
1278	$^{58}Zn(\beta^{+})^{58}Cu^{a}$	9.370	1326	$^{60}Zn(p,\alpha)^{57}Cu^{a}$	-0.996
1279	$^{58}Zn(\gamma,\alpha)^{54}Ni^{a}$	-5.512	1327	$^{60}Zn(p,\gamma)^{61}Ga^{a}$	0.190
1280	$^{59}Co(p,\alpha)^{56}Fe^{a}$	3.242	1328	$^{60}Zn(\alpha,\gamma)^{64}Ge$	2.667
1281	$^{59}Co(p,\gamma)^{60}Ni^{a}$	9.534	1329	$^{60}Zn(\alpha,p)^{63}Ga$	-2.358
1282	$^{59}Co(\alpha,\gamma)^{63}Cu$	5.777	1330	$^{60}Zn(\gamma,\alpha)^{56}Ni^{a}$	-2.708
1283	$^{59}Co(\alpha,p)^{62}Ni$	-0.346	1331	$^{60}Zn(\gamma,p)^{59}Cu^{a}$	-5.121
1284	$^{59}Co(\gamma,p)^{58}Fe$	-7.364	1332	$^{60}Zn(\beta^{+})^{60}Cu^{a}$	4.157
1285	$^{59}Co(\gamma,\alpha)^{55}Mn^{a}$	-6.942	1333	$^{60}Ga(p,\alpha)^{57}Zn^{a}$	-1.277
1286	$^{59}Ni(p,\alpha)^{56}Co^{a}$	-0.252	1334	$^{60}Ga(p,\gamma)^{61}Ge^{a}$	1.478
1287	$^{59}Ni(p,\gamma)^{60}Cu^{a}$	4.479	1335	$^{60}Ga(\alpha,\gamma)^{64}As$	1.746
1288	$^{59}Ni(\alpha,\gamma)^{63}Zn$	3.483	1336	$^{60}Ga(\alpha,p)^{63}Ge$	1.967
1289	$^{59}Ni(\alpha,p)^{62}Cu$	-3.221	1337	$^{60}Ga(\beta^{+})^{60}Zn^{a}$	12.950
1290	$^{59}Ni(\beta^{+})^{59}Co^{a}$	1.074	1338	$^{60}Ga(\gamma,\alpha)^{56}Cu^{a}$	-2.797
1291	$^{59}Ni(\gamma,\alpha)^{55}Fe^{a}$	-6.101	1339	$^{60}Ga(\gamma,p)^{59}Zn^{a}$	-0.030
1292	$^{59}Ni(\gamma,p)^{58}Co$	-8.599	1340	$^{60}Ge(\alpha,\gamma)^{64}Se$	1.696
1293	$^{59}Cu(p,\alpha)^{56}Ni^{a}$	2.413	1341	$^{60}Ge(\gamma,p)^{59}Ga^{a}$	-0.890
1294	$^{59}Cu(p,\gamma)^{60}Zn^{a}$	5.121	1342	$^{60}Ge(\beta^{+})^{60}Ga^{a}$	10.026
1295	$^{59}Cu(\alpha,\gamma)^{63}Ga$	2.763	1343	$^{60}Ge(\gamma,\alpha)^{56}Zn^{a}$	-3.852
1296	$^{59}Cu(\alpha,p)^{62}Zn$	-0.048	1344	$^{61}Ni(p,\alpha)^{58}Co$	0.489

Table C.2: – Continued.

Number	Reaction	Energy (Mev)	Number	Reaction	Energy (Mev)
1345	$^{61}Ni(p,\gamma)^{62}Cu^a$	5.867	1393	$^{62}Zn(\gamma,p)^{61}Cu^a$	-6.477
1346	$^{61}Ni(\alpha,\gamma)^{65}Zn$	4.116	1394	$^{62}Zn(\beta^+)^{62}Cu^a$	1.627
1347	$^{61}Ni(\alpha,p)^{64}Cu$	-3.660	1395	$^{62}Ga(p,\gamma)^{63}Ge^a$	3.315
1348	$^{61}Ni(\gamma,\alpha)^{57}Fe^a$	-6.466	1396	$^{62}Ga(p,\alpha)^{59}Zn$	1.835
1349	$^{61}Cu(p,\alpha)^{58}Ni^a$	3.108	1397	$^{62}Ga(\alpha,p)^{65}Ge$	-0.450
1350	$^{61}Cu(p,\gamma)^{62}Zn^a$	6.477	1398	$^{62}Ga(\alpha,\gamma)^{66}As$	2.500
1351	$^{61}Cu(\alpha,\gamma)^{65}Ga$	3.098	1399	$^{62}Ga(\gamma,p)^{61}Zn^a$	-2.943
1352	$^{61}Cu(\alpha,p)^{64}Zn$	-0.844	1400	$^{62}Ga(\beta^+)^{62}Zn^a$	9.171
1353	$^{61}Cu(\beta^+)^{61}Ni^a$	2.237	1401	$^{62}Ga(\gamma,\alpha)^{58}Cu$	-2.761
1354	$^{61}Cu(\gamma,\alpha)^{57}Co^a$	-5.065	1402	$^{62}Ge(p,\alpha)^{59}Ga$	-2.720
1355	$^{61}Cu(\gamma,p)^{60}Ni^a$	-4.801	1403	$^{62}Ge(\alpha,p)^{65}As$	-0.349
1356	$^{61}Zn(p,\alpha)^{58}Cu^a$	0.182	1404	$^{62}Ge(\alpha,\gamma)^{66}Se$	2.238
1357	$^{61}Zn(p,\gamma)^{62}Ga^a$	2.943	1405	$^{62}Ge(\gamma,p)^{61}Ga^a$	-2.427
1358	$^{61}Zn(\alpha,\gamma)^{65}Ge$	2.493	1406	$^{62}Ge(\beta^+)^{62}Ga^a$	7.898
1359	$^{61}Zn(\alpha,p)^{64}Ga$	-2.372	1407	$^{62}Ge(\gamma,\alpha)^{58}Zn$	-1.312
1360	$^{61}Zn(\beta^+)^{61}Cu^a$	5.638	1408	$^{63}Ni(p,\gamma)^{64}Cu$	7.201
1361	$^{61}Zn(\gamma,\alpha)^{57}Ni^a$	-2.692	1409	$^{63}Ni(\alpha,\gamma)^{67}Zn$	4.793
1362	$^{61}Zn(\gamma,p)^{60}Cu^a$	-5.290	1410	$^{63}Ni(\beta^+)^{63}Cu$	0.066
1363	$^{61}Ga(p,\alpha)^{58}Zn^a$	1.115	1411	$^{63}Cu(p,\gamma)^{64}Zn^a$	7.713
1364	$^{61}Ga(p,\gamma)^{62}Ge^a$	2.427	1412	$^{63}Cu(p,\alpha)^{60}Ni$	3.757
1365	$^{61}Ga(\alpha,\gamma)^{65}As$	2.078	1413	$^{63}Cu(\alpha,p)^{66}Zn$	-1.544
1366	$^{61}Ga(\alpha,p)^{64}Ge$	1.950	1414	$^{63}Cu(\alpha,\gamma)^{67}Ga$	3.725
1367	$^{61}Ga(\beta^+)^{61}Zn^a$	8.803	1415	$^{63}Cu(\gamma,\alpha)^{59}Co$	-5.777
1368	$^{61}Ga(\gamma,\alpha)^{57}Cu^a$	-0.909	1416	$^{63}Cu(\gamma,p)^{62}Ni^a$	-6.123
1369	$^{61}Ga(\gamma,p)^{60}Zn^a$	-0.190	1417	$^{63}Zn(p,\gamma)^{64}Ga^a$	3.915
1370	$^{61}Ge(\alpha,p)^{64}As$	0.268	1418	$^{63}Zn(p,\alpha)^{60}Cu$	0.996
1371	$^{61}Ge(\alpha,\gamma)^{65}Se$	1.769	1419	$^{63}Zn(\alpha,p)^{66}Ga$	-3.353
1372	$^{61}Ge(\beta^+)^{61}Ga^a$	13.620	1420	$^{63}Zn(\alpha,\gamma)^{67}Ge$	2.869
1373	$^{61}Ge(\gamma,p)^{60}Zn^a$	13.165	1421	$^{63}Zn(\beta^+)^{63}Cu^a$	3.367
1374	$^{61}Ge(\gamma,\alpha)^{57}Zn^a$	-2.755	1422	$^{63}Zn(\gamma,\alpha)^{59}Ni$	-3.483
1375	$^{61}Ge(\gamma,p)^{60}Ga^a$	-1.478	1423	$^{63}Zn(\gamma,p)^{62}Cu^a$	-6.704
1376	$^{62}Ni(p,\gamma)^{63}Cu^a$	6.123	1424	$^{63}Ga(p,\gamma)^{64}Ge^a$	5.025
1377	$^{62}Ni(p,\alpha)^{59}Co$	0.346	1425	$^{63}Ga(p,\alpha)^{60}Zn$	2.358
1378	$^{62}Ni(\alpha,p)^{65}Cu$	-4.348	1426	$^{63}Ga(\alpha,p)^{66}Ge$	0.067
1379	$^{62}Ni(\alpha,\gamma)^{66}Zn$	4.578	1427	$^{63}Ga(\alpha,\gamma)^{67}As$	2.379
1380	$^{62}Ni(\gamma,\alpha)^{58}Fe$	-7.019	1428	$^{63}Ga(\gamma,p)^{62}Zn^a$	-2.811
1381	$^{62}Cu(p,\gamma)^{63}Zn^a$	6.704	1429	$^{63}Ga(\beta^+)^{63}Zn^a$	5.520
1382	$^{62}Cu(p,\alpha)^{59}Ni$	3.221	1430	$^{63}Ga(\gamma,\alpha)^{59}Cu$	-2.763
1383	$^{62}Cu(\alpha,p)^{65}Zn$	-1.750	1431	$^{63}Ge(p,\gamma)^{64}As^a$	-0.100
1384	$^{62}Cu(\alpha,\gamma)^{66}Ga$	3.352	1432	$^{63}Ge(p,\alpha)^{60}Ga$	-1.967
1385	$^{62}Cu(\beta^+)^{62}Ni^a$	3.947	1433	$^{63}Ge(\alpha,p)^{66}As$	-0.749
1386	$^{62}Cu(\gamma,\alpha)^{58}Co$	-5.378	1434	$^{63}Ge(\alpha,\gamma)^{67}Se$	2.613
1387	$^{62}Cu(\gamma,p)^{61}Ni^a$	-5.867	1435	$^{63}Ge(\gamma,\alpha)^{59}Zn$	-1.480
1388	$^{62}Zn(p,\gamma)^{63}Ga^a$	2.811	1436	$^{63}Ge(\gamma,p)^{62}Ga^a$	-3.315
1389	$^{62}Zn(p,\alpha)^{59}Cu$	0.048	1437	$^{63}Ge(\beta^+)^{63}Ga^a$	9.300
1390	$^{62}Zn(\alpha,p)^{65}Ga$	-3.378	1438	$^{64}Ni(p,\gamma)^{65}Cu$	7.452
1391	$^{62}Zn(\alpha,\gamma)^{66}Ge$	2.879	1439	$^{64}Ni(\alpha,\gamma)^{68}Zn$	5.333
1392	$^{62}Zn(\gamma,\alpha)^{58}Ni$	-3.369	1440	$^{64}Cu(p,\gamma)^{65}Zn$	7.776

Table C.2: – Continued.

Number	Reaction	Energy (Mev)	Number	Reaction	Energy (Mev)
1441	$^{64}Cu(p,\alpha)^{61}Ni$	3.660	1489	$^{65}Ga(p,\alpha)^{62}Zn$	3.378
1442	$^{64}Cu(\alpha,p)^{67}Zn$	-2.408	1490	$^{65}Ga(\alpha,p)^{68}Ge$	-0.541
1443	$^{64}Cu(\alpha,\gamma)^{68}Ga$	4.087	1491	$^{65}Ga(\alpha,\gamma)^{69}As$	2.852
1444	$^{64}Cu(\beta^+)^{64}Zn$	0.577	1492	$^{65}Ga(\gamma,\alpha)^{61}Cu$	-3.098
1445	$^{64}Cu(\beta^+)^{64}Ni$	1.675	1493	$^{65}Ga(\gamma,p)^{64}Zn^a$	-3.942
1446	$^{64}Cu(\gamma,p)^{63}Ni$	-7.201	1494	$^{65}Ga(\beta^+)^{65}Zn^a$	3.256
1447	$^{64}Zn(p,\gamma)^{65}Ga^a$	3.942	1495	$^{65}Ge(p,\gamma)^{66}As^a$	2.950
1448	$^{64}Zn(p,\alpha)^{61}Cu$	0.844	1496	$^{65}Ge(p,\alpha)^{62}Ga$	0.450
1449	$^{64}Zn(\alpha,p)^{67}Ga$	-3.987	1497	$^{65}Ge(\alpha,p)^{68}As$	-2.398
1450	$^{64}Zn(\alpha,\gamma)^{68}Ge$	3.402	1498	$^{65}Ge(\alpha,\gamma)^{69}Se$	2.312
1451	$^{64}Zn(\gamma,\alpha)^{60}Ni$	-3.956	1499	$^{65}Ge(\gamma,p)^{64}Ga^a$	-4.865
1452	$^{64}Zn(\gamma,p)^{63}Cu^a$	-7.713	1500	$^{65}Ge(\beta^+)^{65}Ga^a$	6.244
1453	$^{64}Ga(p,\gamma)^{65}Ge^a$	4.865	1501	$^{65}Ge(\gamma,\alpha)^{61}Zn$	-2.493
1454	$^{64}Ga(p,\alpha)^{61}Zn$	2.372	1502	$^{65}As(p,\gamma)^{66}Se^a$	2.587
1455	$^{64}Ga(\alpha,p)^{67}Ge$	-1.045	1503	$^{65}As(p,\alpha)^{62}Ge$	0.349
1456	$^{64}Ga(\alpha,\gamma)^{68}As$	2.467	1504	$^{65}As(\alpha,p)^{68}Se$	2.814
1457	$^{64}Ga(\beta^+)^{64}Zn^a$	7.163	1505	$^{65}As(\alpha,\gamma)^{69}Br$	2.902
1458	$^{64}Ga(\gamma,\alpha)^{60}Cu$	-2.919	1506	$^{65}As(\beta^+)^{65}Ge^a$	9.100
1459	$^{64}Ga(\gamma,p)^{63}Zn^a$	-3.915	1507	$^{65}As(\gamma,\alpha)^{61}Ga$	-2.078
1460	$^{64}Ge(p,\gamma)^{65}As^a$	-0.080	1508	$^{65}As(\gamma,p)^{64}Ge^a$	0.080
1461	$^{64}Ge(p,\alpha)^{61}Ga$	-1.950	1509	$^{65}Se(\alpha,\gamma)^{69}Kr$	2.415
1462	$^{64}Ge(\alpha,p)^{67}As$	-1.940	1510	$^{65}Se(\alpha,p)^{68}Br$	1.006
1463	$^{64}Ge(\alpha,\gamma)^{68}Se$	2.942	1511	$^{65}Se(\gamma,\alpha)^{61}Ge$	-1.769
1464	$^{64}Ge(\beta^+)^{64}Ga^a$	4.407	1512	$^{65}Se(\gamma,p)^{64}As^a$	-1.501
1465	$^{64}Ge(\gamma,\alpha)^{60}Zn$	-2.667	1513	$^{65}Se(\beta^+)^{65}As^a$	14.140
1466	$^{64}Ge(\gamma,p)^{63}Ga^a$	-5.025	1514	$^{65}Se(\gamma,p)^{64}Ge^a$	14.216
1467	$^{64}As(p,\gamma)^{65}Se^a$	1.501	1515	$^{66}Zn(p,\alpha)^{63}Cu$	1.544
1468	$^{64}As(p,\alpha)^{61}Ge$	-0.268	1516	$^{66}Zn(p,\gamma)^{67}Ga^a$	5.269
1469	$^{64}As(\alpha,p)^{67}Se$	2.834	1517	$^{66}Zn(\alpha,\gamma)^{70}Ge$	4.089
1470	$^{64}As(\alpha,\gamma)^{68}Br$	2.507	1518	$^{66}Zn(\alpha,p)^{69}Ga$	-4.440
1471	$^{64}As(\beta^+)^{64}Ge^a$	12.896	1519	$^{66}Zn(\gamma,p)^{65}Cu^a$	-8.926
1472	$^{64}As(\gamma,\alpha)^{60}Ga$	-1.746	1520	$^{66}Zn(\gamma,\alpha)^{62}Ni$	-4.578
1473	$^{64}As(\gamma,p)^{63}Ge^a$	0.100	1521	$^{66}Ga(p,\alpha)^{63}Zn$	3.353
1474	$^{64}Se(\alpha,\gamma)^{68}Kr$	2.169	1522	$^{66}Ga(p,\gamma)^{67}Ge^a$	6.222
1475	$^{64}Se(\gamma,\alpha)^{60}Ge$	-1.696	1523	$^{66}Ga(\alpha,\gamma)^{70}As$	3.044
1476	$^{65}Cu(p,\gamma)^{66}Zn^a$	8.926	1524	$^{66}Ga(\alpha,p)^{69}Ge$	-1.492
1477	$^{65}Cu(p,\alpha)^{62}Ni$	4.348	1525	$^{66}Ga(\gamma,\alpha)^{62}Cu$	-3.352
1478	$^{65}Cu(\alpha,p)^{68}Zn$	-2.120	1526	$^{66}Ga(\gamma,p)^{65}Zn^a$	-5.102
1479	$^{65}Cu(\alpha,\gamma)^{69}Ga$	4.486	1527	$^{66}Ga(\beta^+)^{66}Zn^a$	5.173
1480	$^{65}Cu(\gamma,p)^{64}Ni$	-7.452	1528	$^{66}Ge(p,\alpha)^{63}Ga$	-0.067
1481	$^{65}Zn(p,\gamma)^{66}Ga^a$	5.102	1529	$^{66}Ge(p,\gamma)^{67}As^a$	2.312
1482	$^{65}Zn(p,\alpha)^{62}Cu$	1.750	1530	$^{66}Ge(\alpha,\gamma)^{70}Se$	3.515
1483	$^{65}Zn(\alpha,p)^{68}Ga$	-3.689	1531	$^{66}Ge(\alpha,p)^{69}As$	-2.620
1484	$^{65}Zn(\alpha,\gamma)^{69}Ge$	3.611	1532	$^{66}Ge(\beta^+)^{66}Ga^a$	2.102
1485	$^{65}Zn(\beta^+)^{65}Cu^a$	1.351	1533	$^{66}Ge(\gamma,\alpha)^{62}Zn$	-2.879
1486	$^{65}Zn(\gamma,\alpha)^{61}Ni$	-4.116	1534	$^{66}Ge(\gamma,p)^{65}Ga^a$	-6.257
1487	$^{65}Zn(\gamma,p)^{64}Cu$	-7.776	1535	$^{66}As(p,\alpha)^{63}Ge$	0.749
1488	$^{65}Ga(p,\gamma)^{66}Ge^a$	6.257	1536	$^{66}As(p,\gamma)^{67}Se^a$	3.362

Table C.2: – Continued.

Number	Reaction	Energy (Mev)	Number	Reaction	Energy (Mev)
1537	$^{66}As(\alpha,\gamma)^{70}Br$	3.034	1585	$^{68}Ga(p,\gamma)^{69}Ge$	7.300
1538	$^{66}As(\alpha,p)^{69}Se$	1.492	1586	$^{68}Ga(p,\alpha)^{65}Zn$	3.689
1539	$^{66}As(\gamma,p)^{65}Ge^{a}$	-2.950	1587	$^{68}Ga(\alpha,p)^{71}Ge$	-2.042
1540	$^{66}As(\beta^{+})^{66}Ge^{a}$	9.552	1588	$^{68}Ga(\alpha,\gamma)^{72}As$	3.571
1541	$^{66}As(\gamma,\alpha)^{62}Ga$	-2.500	1589	$^{68}Ga(\gamma,\alpha)^{64}Cu$	-4.087
1542	$^{66}Se(\alpha,p)^{69}Br$	0.315	1590	$^{68}Ga(\gamma,p)^{67}Zn$	-6.495
1543	$^{66}Se(\alpha,\gamma)^{70}Kr$	2.749	1591	$^{68}Ga(\beta^{+})^{68}Zn$	2.921
1544	$^{66}Se(\beta^{+})^{66}As^{a}$	7.720	1592	$^{68}Ge(p,\gamma)^{69}As^{a}$	3.393
1545	$^{66}Se(\gamma,\alpha)^{62}Ge$	-2.238	1593	$^{68}Ge(p,\alpha)^{65}Ga$	0.541
1546	$^{66}Se(\gamma,p)^{65}As^{a}$	-2.587	1594	$^{68}Ge(\alpha,p)^{71}As$	-3.949
1547	$^{67}Zn(p,\gamma)^{68}Ga$	6.495	1595	$^{68}Ge(\alpha,\gamma)^{72}Se$	3.342
1548	$^{67}Zn(p,\alpha)^{64}Cu$	2.408	1596	$^{68}Ge(\gamma,p)^{67}Ga^{a}$	-7.389
1549	$^{67}Zn(\alpha,p)^{70}Ga$	-3.836	1597	$^{68}Ge(\beta^{+})^{68}Ga$	0.107
1550	$^{67}Zn(\alpha,\gamma)^{71}Ge$	4.453	1598	$^{68}Ge(\gamma,\alpha)^{64}Zn$	-3.402
1551	$^{67}Zn(\gamma,\alpha)^{63}Ni$	-4.793	1599	$^{68}As(p,\gamma)^{69}Se^{a}$	4.710
1552	$^{67}Ga(p,\gamma)^{68}Ge^{a}$	7.389	1600	$^{68}As(p,\alpha)^{65}Ge$	2.398
1553	$^{67}Ga(p,\alpha)^{64}Zn$	3.987	1601	$^{68}As(\alpha,p)^{71}Se$	-0.277
1554	$^{67}Ga(\alpha,p)^{70}Ge$	-1.181	1602	$^{68}As(\alpha,\gamma)^{72}Br$	2.727
1555	$^{67}Ga(\alpha,\gamma)^{71}As$	3.440	1603	$^{68}As(\beta^{+})^{68}Ge^{a}$	8.098
1556	$^{67}Ga(\beta^{+})^{67}Zn$	1.001	1604	$^{68}As(\gamma,\alpha)^{64}Ga$	-2.467
1557	$^{67}Ga(\gamma,\alpha)^{63}Cu$	-3.725	1605	$^{68}As(\gamma,p)^{67}Ge^{a}$	-3.512
1558	$^{67}Ga(\gamma,p)^{66}Zn^{a}$	-5.269	1606	$^{68}Se(p,\gamma)^{69}Br^{a}$	-0.450
1559	$^{67}Ge(p,\gamma)^{68}As^{a}$	3.512	1607	$^{68}Se(p,\alpha)^{65}As$	-2.814
1560	$^{67}Ge(p,\alpha)^{64}Ga$	1.045	1608	$^{68}Se(\alpha,p)^{71}Br$	-1.623
1561	$^{67}Ge(\alpha,p)^{70}As$	-3.178	1609	$^{68}Se(\alpha,\gamma)^{72}Kr$	2.902
1562	$^{67}Ge(\alpha,\gamma)^{71}Se$	3.235	1610	$^{68}Se(\gamma,p)^{67}As^{a}$	-4.882
1563	$^{67}Ge(\beta^{+})^{67}Ga^{a}$	4.222	1611	$^{68}Se(\beta^{+})^{68}As^{a}$	4.800
1564	$^{67}Ge(\gamma,\alpha)^{63}Zn$	-2.869	1612	$^{68}Se(\gamma,\alpha)^{64}Ge$	-2.942
1565	$^{67}Ge(\gamma,p)^{66}Ga^{a}$	-6.222	1613	$^{68}Br(p,\gamma)^{69}Kr^{a}$	1.409
1566	$^{67}As(p,\gamma)^{68}Se^{a}$	4.882	1614	$^{68}Br(p,\alpha)^{65}Se$	-1.006
1567	$^{67}As(p,\alpha)^{64}Ge$	1.940	1615	$^{68}Br(\alpha,p)^{71}Kr$	3.097
1568	$^{67}As(\alpha,p)^{70}Se$	1.048	1616	$^{68}Br(\alpha,\gamma)^{72}Rb$	2.298
1569	$^{67}As(\alpha,\gamma)^{71}Br$	3.259	1617	$^{68}Br(\gamma,\alpha)^{64}As$	-2.507
1570	$^{67}As(\beta^{+})^{67}Ge^{a}$	6.006	1618	$^{68}Br(\gamma,p)^{67}Se^{a}$	0.560
1571	$^{67}As(\gamma,\alpha)^{63}Ga$	-2.379	1619	$^{68}Br(\beta^{+})^{68}Se^{a}$	12.223
1572	$^{67}As(\gamma,p)^{66}Ge^{a}$	-2.312	1620	$^{68}Kr(\alpha,\gamma)^{72}Sr$	2.100
1573	$^{67}Se(p,\gamma)^{68}Br^{a}$	-0.560	1621	$^{68}Kr(\beta^{+})^{68}Br$	10.204
1574	$^{67}Se(p,\alpha)^{64}As$	-2.834	1622	$^{68}Kr(\gamma,\alpha)^{64}Se$	-2.169
1575	$^{67}Se(\alpha,p)^{70}Br$	-0.328	1623	$^{69}Zn(p,\gamma)^{70}Ga$	7.779
1576	$^{67}Se(\alpha,\gamma)^{71}Kr$	2.770	1624	$^{69}Zn(\alpha,\gamma)^{73}Ge$	5.307
1577	$^{67}Se(\gamma,\alpha)^{63}Ge$	-2.613	1625	$^{69}Zn(\beta^{+})^{69}Ga$	0.905
1578	$^{67}Se(\gamma,p)^{66}As^{a}$	-3.362	1626	$^{69}Ga(p,\gamma)^{70}Ge$	8.529
1579	$^{67}Se(\beta^{+})^{67}As^{a}$	9.790	1627	$^{69}Ga(p,\alpha)^{66}Zn$	4.440
1580	$^{68}Zn(p,\gamma)^{69}Ga$	6.606	1628	$^{69}Ga(\alpha,p)^{72}Ge$	-1.600
1581	$^{68}Zn(p,\alpha)^{65}Cu$	2.120	1629	$^{69}Ga(\alpha,\gamma)^{73}As$	4.060
1582	$^{68}Zn(\alpha,p)^{71}Ga$	-4.734	1630	$^{69}Ga(\gamma,p)^{68}Zn$	-6.606
1583	$^{68}Zn(\alpha,\gamma)^{72}Ge$	5.006	1631	$^{69}Ga(\gamma,\alpha)^{65}Cu$	-4.486
1584	$^{68}Zn(\gamma,\alpha)^{64}Ni$	-5.333	1632	$^{69}Ge(p,\gamma)^{70}As$	4.536

Table C.2: – Continued.

Number	Reaction	Energy (Mev)	Number	Reaction	Energy (Mev)
1633	$^{69}Ge(p,\alpha)^{66}Ga$	1.492	1681	$^{70}As(p,\gamma)^{71}Se$	6.413
1634	$^{69}Ge(\alpha,p)^{72}As$	-3.729	1682	$^{70}As(\alpha,\gamma)^{74}Br$	3.390
1635	$^{69}Ge(\alpha,\gamma)^{73}Se$	3.547	1683	$^{70}As(\alpha,p)^{73}Se$	-0.989
1636	$^{69}Ge(\gamma,\alpha)^{65}Zn$	-3.611	1684	$^{70}As(\beta^+)^{70}Ge$	6.221
1637	$^{69}Ge(\gamma,p)^{68}Ga$	-7.300	1685	$^{70}As(\gamma,\alpha)^{66}Ga$	-3.044
1638	$^{69}Ge(\beta^+)^{69}Ga$	2.225	1686	$^{70}As(\gamma,p)^{69}Ge$	-4.536
1639	$^{69}As(p,\gamma)^{70}Se^a$	6.135	1687	$^{70}Se(p,\alpha)^{67}As$	-1.048
1640	$^{69}As(p,\alpha)^{66}Ge$	2.620	1688	$^{70}Se(p,\gamma)^{71}Br^a$	2.211
1641	$^{69}As(\alpha,p)^{72}Se$	-0.050	1689	$^{70}Se(\alpha,\gamma)^{74}Kr$	3.421
1642	$^{69}As(\alpha,\gamma)^{73}Br$	2.904	1690	$^{70}Se(\alpha,p)^{73}Br$	-2.476
1643	$^{69}As(\beta^+)^{69}Ge$	4.017	1691	$^{70}Se(\gamma,\alpha)^{66}Ge$	-3.515
1644	$^{69}As(\gamma,\alpha)^{65}Ga$	-2.852	1692	$^{70}Se(\gamma,p)^{69}As^a$	-6.135
1645	$^{69}As(\gamma,p)^{68}Ge^a$	-3.393	1693	$^{70}Se(\beta^+)^{70}As$	2.750
1646	$^{69}Se(p,\gamma)^{70}Br^a$	1.542	1694	$^{70}Br(p,\alpha)^{67}Se$	0.328
1647	$^{69}Se(p,\alpha)^{66}As$	-1.492	1695	$^{70}Br(p,\gamma)^{71}Kr^a$	3.098
1648	$^{69}Se(\alpha,p)^{72}Br$	-1.982	1696	$^{70}Br(\alpha,\gamma)^{74}Rb$	3.002
1649	$^{69}Se(\alpha,\gamma)^{73}Kr$	3.012	1697	$^{70}Br(\alpha,p)^{73}Kr$	0.874
1650	$^{69}Se(\beta^+)^{69}As^a$	6.790	1698	$^{70}Br(\gamma,p)^{69}Se^a$	-1.542
1651	$^{69}Se(\gamma,\alpha)^{65}Ge$	-2.312	1699	$^{70}Br(\beta^+)^{70}Se^a$	10.400
1652	$^{69}Se(\gamma,p)^{68}As^a$	-4.710	1700	$^{70}Br(\gamma,\alpha)^{66}As$	-3.034
1653	$^{69}Br(p,\gamma)^{70}Kr^a$	2.434	1701	$^{70}Kr(\alpha,p)^{73}Rb$	0.066
1654	$^{69}Br(p,\alpha)^{66}Se$	-0.315	1702	$^{70}Kr(\alpha,\gamma)^{74}Sr$	2.548
1655	$^{69}Br(\alpha,p)^{72}Kr$	2.814	1703	$^{70}Kr(\gamma,p)^{69}Br^a$	-2.434
1656	$^{69}Br(\alpha,\gamma)^{73}Rb$	2.500	1704	$^{70}Kr(\gamma,\alpha)^{66}Se$	-2.749
1657	$^{69}Br(\beta^+)^{69}Se^a$	9.500	1705	$^{70}Kr(\beta^+)^{70}Br^a$	6.608
1658	$^{69}Br(\gamma,\alpha)^{65}As$	-2.902	1706	$^{71}Ga(p,\gamma)^{72}Ge$	9.740
1659	$^{69}Br(\gamma,p)^{68}Se^a$	0.450	1707	$^{71}Ga(p,\alpha)^{68}Zn$	4.734
1660	$^{69}Kr(\alpha,\gamma)^{73}Sr$	2.252	1708	$^{71}Ga(\alpha,p)^{74}Ge$	-1.576
1661	$^{69}Kr(\alpha,p)^{72}Rb$	0.889	1709	$^{71}Ga(\alpha,\gamma)^{75}As$	5.323
1662	$^{69}Kr(\beta^+)^{69}Br^a$	14.105	1710	$^{71}Ga(\gamma,p)^{70}Zn$	-7.864
1663	$^{69}Kr(\gamma,p)^{68}Se^a$	14.555	1711	$^{71}Ge(p,\gamma)^{72}As$	5.613
1664	$^{69}Kr(\gamma,\alpha)^{65}Se$	-2.415	1712	$^{71}Ge(p,\alpha)^{68}Ga$	2.042
1665	$^{69}Kr(\gamma,p)^{68}Br^a$	-1.409	1713	$^{71}Ge(\alpha,p)^{74}As$	-3.910
1666	$^{70}Zn(p,\gamma)^{71}Ga$	7.864	1714	$^{71}Ge(\alpha,\gamma)^{75}Se$	4.688
1667	$^{70}Zn(\alpha,\gamma)^{74}Ge$	6.287	1715	$^{71}Ge(\gamma,p)^{70}Ga$	-8.289
1668	$^{70}Ga(p,\alpha)^{67}Zn$	3.836	1716	$^{71}Ge(\beta^+)^{71}Ga$	0.237
1669	$^{70}Ga(p,\gamma)^{71}Ge$	8.289	1717	$^{71}Ge(\gamma,\alpha)^{67}Zn$	-4.453
1670	$^{70}Ga(\alpha,\gamma)^{74}As$	4.379	1718	$^{71}As(p,\gamma)^{72}Se$	7.291
1671	$^{70}Ga(\alpha,p)^{73}Ge$	-2.473	1719	$^{71}As(p,\alpha)^{68}Ge$	3.949
1672	$^{70}Ga(\beta^+)^{70}Ge$	1.656	1720	$^{71}As(\alpha,p)^{74}Se$	-0.544
1673	$^{70}Ga(\gamma,p)^{69}Zn$	-7.779	1721	$^{71}As(\alpha,\gamma)^{75}Br$	3.671
1674	$^{70}Ge(p,\alpha)^{67}Ga$	1.181	1722	$^{71}As(\beta^+)^{71}Ge$	2.011
1675	$^{70}Ge(p,\gamma)^{71}As$	4.621	1723	$^{71}As(\gamma,\alpha)^{67}Ga$	-3.440
1676	$^{70}Ge(\alpha,\gamma)^{74}Se$	4.077	1724	$^{71}As(\gamma,p)^{70}Ge$	-4.621
1677	$^{70}Ge(\alpha,p)^{73}As$	-4.468	1725	$^{71}Se(p,\gamma)^{72}Br^a$	3.004
1678	$^{70}Ge(\gamma,\alpha)^{66}Zn$	-4.089	1726	$^{71}Se(p,\alpha)^{68}As$	0.277
1679	$^{70}Ge(\gamma,p)^{69}Ga$	-8.529	1727	$^{71}Se(\alpha,p)^{74}Br$	-3.023
1680	$^{70}As(p,\alpha)^{67}Ge$	3.178	1728	$^{71}Se(\alpha,\gamma)^{75}Kr$	3.200

Table C.2: – Continued.

Number	Reaction	Energy (Mev)	Number	Reaction	Energy (Mev)
1729	$^{71}Se(\gamma,p)^{70}As$	-6.413	1777	$^{72}Kr(\alpha,\gamma)^{76}Sr$	3.363
1730	$^{71}Se(\beta^+)^{71}As$	4.803	1778	$^{72}Kr(\gamma,\alpha)^{68}Se$	-2.902
1731	$^{71}Se(\gamma,\alpha)^{67}Ge$	-3.235	1779	$^{72}Kr(\gamma,p)^{71}Br^a$	-4.525
1732	$^{71}Br(p,\gamma)^{72}Kr^a$	4.525	1780	$^{72}Kr(\beta^+)^{72}Br^a$	5.060
1733	$^{71}Br(p,\alpha)^{68}Se$	1.623	1781	$^{72}Rb(p,\gamma)^{73}Sr$	1.363
1734	$^{71}Br(\alpha,p)^{74}Kr$	1.080	1782	$^{72}Rb(p,\alpha)^{69}Kr$	-0.889
1735	$^{71}Br(\alpha,\gamma)^{75}Rb$	3.421	1783	$^{72}Rb(\alpha,p)^{75}Sr$	3.874
1736	$^{71}Br(\gamma,\alpha)^{67}As$	-3.259	1784	$^{72}Rb(\alpha,\gamma)^{76}Y$	3.299
1737	$^{71}Br(\gamma,p)^{70}Se^a$	-2.211	1785	$^{72}Rb(\beta^+)^{72}Kr^a$	15.727
1738	$^{71}Br(\beta^+)^{71}Se^a$	6.500	1786	$^{72}Rb(\gamma,\alpha)^{68}Br$	-2.298
1739	$^{71}Kr(p,\gamma)^{72}Rb^a$	-1.520	1787	$^{72}Rb(\gamma,p)^{71}Kr^a$	1.520
1740	$^{71}Kr(p,\alpha)^{68}Br$	-3.097	1788	$^{72}Sr(\gamma,\alpha)^{68}Kr$	-2.100
1741	$^{71}Kr(\alpha,p)^{74}Rb$	-0.096	1789	$^{72}Sr(\beta^+)^{72}Rb$	12.236
1742	$^{71}Kr(\alpha,\gamma)^{75}Sr$	3.075	1790	$^{73}Ge(p,\gamma)^{74}As$	6.852
1743	$^{71}Kr(\gamma,\alpha)^{67}Se$	-2.770	1791	$^{73}Ge(p,\alpha)^{70}Ga$	2.473
1744	$^{71}Kr(\gamma,p)^{70}Br^a$	-3.098	1792	$^{73}Ge(\alpha,\gamma)^{77}Se$	5.727
1745	$^{71}Kr(\beta^+)^{71}Br^a$	10.490	1793	$^{73}Ge(\gamma,\alpha)^{69}Zn$	-5.307
1746	$^{71}Kr(\gamma,p)^{70}Se^a$	8.551	1794	$^{73}As(p,\gamma)^{74}Se$	8.545
1747	$^{72}Ge(p,\gamma)^{73}As$	5.660	1795	$^{73}As(p,\alpha)^{70}Ge$	4.468
1748	$^{72}Ge(p,\alpha)^{69}Ga$	1.600	1796	$^{73}As(\alpha,p)^{76}Se$	-0.569
1749	$^{72}Ge(\alpha,p)^{75}As$	-4.417	1797	$^{73}As(\alpha,\gamma)^{77}Br$	4.702
1750	$^{72}Ge(\alpha,\gamma)^{76}Se$	5.091	1798	$^{73}As(\beta^+)^{73}Ge$	0.338
1751	$^{72}Ge(\gamma,p)^{71}Ga$	-9.740	1799	$^{73}As(\gamma,\alpha)^{69}Ga$	-4.060
1752	$^{72}Ge(\gamma,\alpha)^{68}Zn$	-5.006	1800	$^{73}As(\gamma,p)^{72}Ge$	-5.660
1753	$^{72}As(p,\gamma)^{73}Se$	7.276	1801	$^{73}Se(p,\gamma)^{74}Br$	4.379
1754	$^{72}As(p,\alpha)^{69}Ge$	3.729	1802	$^{73}Se(p,\alpha)^{70}As$	0.989
1755	$^{72}As(\alpha,p)^{75}Se$	-0.925	1803	$^{73}Se(\alpha,p)^{76}Br$	-2.792
1756	$^{72}As(\alpha,\gamma)^{76}Br$	4.484	1804	$^{73}Se(\alpha,\gamma)^{77}Kr$	4.379
1757	$^{72}As(\gamma,p)^{71}Ge$	-5.613	1805	$^{73}Se(\gamma,\alpha)^{69}Ge$	-3.547
1758	$^{72}As(\beta^+)^{72}Ge$	4.354	1806	$^{73}Se(\gamma,p)^{72}As$	-7.276
1759	$^{72}As(\gamma,\alpha)^{68}Ga$	-3.571	1807	$^{73}Se(\beta^+)^{73}As$	2.740
1760	$^{72}Se(p,\gamma)^{73}Br^a$	2.954	1808	$^{73}Br(p,\gamma)^{74}Kr^a$	5.897
1761	$^{72}Se(p,\alpha)^{69}As$	0.050	1809	$^{73}Br(p,\alpha)^{70}Se$	2.476
1762	$^{72}Se(\alpha,p)^{75}Br$	-3.620	1810	$^{73}Br(\alpha,p)^{76}Kr$	0.554
1763	$^{72}Se(\alpha,\gamma)^{76}Kr$	3.508	1811	$^{73}Br(\alpha,\gamma)^{77}Rb$	3.691
1764	$^{72}Se(\gamma,p)^{71}As$	-7.291	1812	$^{73}Br(\gamma,p)^{72}Se^a$	-2.954
1765	$^{72}Se(\beta^+)^{72}As$	0.331	1813	$^{73}Br(\beta^+)^{73}Se$	4.575
1766	$^{72}Se(\gamma,\alpha)^{68}Ge$	-3.342	1814	$^{73}Br(\gamma,\alpha)^{69}As$	-2.904
1767	$^{72}Br(p,\gamma)^{73}Kr^a$	4.994	1815	$^{73}Kr(p,\gamma)^{74}Rb^a$	2.128
1768	$^{72}Br(p,\alpha)^{69}Se$	1.982	1816	$^{73}Kr(p,\alpha)^{70}Br$	-0.874
1769	$^{72}Br(\alpha,p)^{75}Kr$	0.196	1817	$^{73}Kr(\alpha,p)^{76}Rb$	-1.273
1770	$^{72}Br(\alpha,\gamma)^{76}Rb$	3.722	1818	$^{73}Kr(\alpha,\gamma)^{77}Sr$	3.513
1771	$^{72}Br(\gamma,p)^{71}Se^a$	-3.004	1819	$^{73}Kr(\gamma,\alpha)^{69}Se$	-3.012
1772	$^{72}Br(\beta^+)^{72}Se^a$	8.867	1820	$^{73}Kr(\beta^+)^{73}Br^a$	6.750
1773	$^{72}Br(\gamma,\alpha)^{68}As$	-2.727	1821	$^{73}Kr(\gamma,p)^{72}Br^a$	-4.994
1774	$^{72}Kr(p,\gamma)^{73}Rb^a$	-0.600	1822	$^{73}Rb(p,\gamma)^{74}Sr^a$	2.482
1775	$^{72}Kr(p,\alpha)^{69}Br$	-2.814	1823	$^{73}Rb(p,\alpha)^{70}Kr$	-0.066
1776	$^{72}Kr(\alpha,p)^{75}Rb$	-1.104	1824	$^{73}Rb(\alpha,p)^{76}Sr$	3.677

Table C.2: – Continued.

Number	Reaction	Energy (Mev)	Number	Reaction	Energy (Mev)
1825	$^{73}Rb(\alpha,\gamma)^{77}Y$	3.415	1873	$^{74}Rb(\gamma,\alpha)^{70}Br$	-3.002
1826	$^{73}Rb(\gamma,p)^{72}Kr^{a}$	0.600	1874	$^{74}Sr(\alpha,p)^{77}Y$	0.933
1827	$^{73}Rb(\beta^{+})^{73}Kr^{a}$	10.429	1875	$^{74}Sr(\alpha,\gamma)^{78}Zr$	2.627
1828	$^{73}Rb(\gamma,\alpha)^{69}Br$	-2.500	1876	$^{74}Sr(\beta^{+})^{74}Rb^{a}$	9.539
1829	$^{73}Sr(\alpha,\gamma)^{77}Zr$	2.738	1877	$^{74}Sr(\gamma,\alpha)^{70}Kr$	-2.548
1830	$^{73}Sr(\alpha,p)^{76}Y$	1.936	1878	$^{74}Sr(\gamma,p)^{73}Rb^{a}$	-2.482
1831	$^{73}Sr(\gamma,p)^{72}Rb$	-1.363	1879	$^{75}Ge(\alpha,\gamma)^{79}Se$	6.486
1832	$^{73}Sr(\beta^{+})^{73}Rb$	14.535	1880	$^{75}Ge(\beta^{+})^{75}As$	1.178
1833	$^{73}Sr(\gamma,p)^{72}Kr$	15.124	1881	$^{75}As(p,\gamma)^{76}Se$	9.508
1834	$^{73}Sr(\gamma,\alpha)^{69}Kr$	-2.252	1882	$^{75}As(p,\alpha)^{72}Ge$	4.417
1835	$^{74}Ge(p,\gamma)^{75}As$	6.899	1883	$^{75}As(\alpha,p)^{78}Se$	-0.871
1836	$^{74}Ge(p,\alpha)^{71}Ga$	1.576	1884	$^{75}As(\alpha,\gamma)^{79}Br$	5.460
1837	$^{74}Ge(\alpha,\gamma)^{78}Se$	6.028	1885	$^{75}As(\gamma,\alpha)^{71}Ga$	-5.323
1838	$^{74}Ge(\gamma,\alpha)^{70}Zn$	-6.287	1886	$^{75}As(\gamma,p)^{74}Ge$	-6.899
1839	$^{74}As(p,\alpha)^{71}Ge$	3.910	1887	$^{75}Se(p,\gamma)^{76}Br$	5.409
1840	$^{74}As(p,\gamma)^{75}Se$	8.598	1888	$^{75}Se(p,\alpha)^{72}As$	0.925
1841	$^{74}As(\alpha,\gamma)^{78}Br$	5.017	1889	$^{75}Se(\alpha,p)^{78}Br$	-3.581
1842	$^{74}As(\alpha,p)^{77}Se$	-1.125	1890	$^{75}Se(\alpha,\gamma)^{79}Kr$	4.698
1843	$^{74}As(\beta^{+})^{74}Se$	1.354	1891	$^{75}Se(\gamma,\alpha)^{71}Ge$	-4.688
1844	$^{74}As(\gamma,\alpha)^{70}Ga$	-4.379	1892	$^{75}Se(\gamma,p)^{74}As$	-8.598
1845	$^{74}As(\gamma,p)^{73}Ge$	-6.852	1893	$^{75}Se(\beta^{+})^{75}As$	0.864
1846	$^{74}As(\beta^{+})^{74}Ge$	2.562	1894	$^{75}Br(p,\gamma)^{76}Kr$	7.128
1847	$^{74}Se(p,\alpha)^{71}As$	0.544	1895	$^{75}Br(p,\alpha)^{72}Se$	3.620
1848	$^{74}Se(p,\gamma)^{75}Br$	4.215	1896	$^{75}Br(\alpha,p)^{78}Kr$	0.155
1849	$^{74}Se(\alpha,\gamma)^{78}Kr$	4.371	1897	$^{75}Br(\alpha,\gamma)^{79}Rb$	4.079
1850	$^{74}Se(\alpha,p)^{77}Br$	-3.842	1898	$^{75}Br(\gamma,\alpha)^{71}As$	-3.671
1851	$^{74}Se(\gamma,p)^{73}As$	-8.545	1899	$^{75}Br(\gamma,p)^{74}Se$	-4.215
1852	$^{74}Se(\gamma,\alpha)^{70}Ge$	-4.077	1900	$^{75}Br(\beta^{+})^{75}Se$	3.010
1853	$^{74}Br(p,\alpha)^{71}Se$	3.023	1901	$^{75}Kr(p,\gamma)^{76}Rb$	3.526
1854	$^{74}Br(p,\gamma)^{75}Kr$	6.223	1902	$^{75}Kr(p,\alpha)^{72}Br$	-0.196
1855	$^{74}Br(\alpha,\gamma)^{78}Rb$	4.053	1903	$^{75}Kr(\alpha,p)^{78}Rb$	-2.171
1856	$^{74}Br(\alpha,p)^{77}Kr$	0.000	1904	$^{75}Kr(\alpha,\gamma)^{79}Sr$	3.659
1857	$^{74}Br(\beta^{+})^{74}Se$	6.915	1905	$^{75}Kr(\gamma,p)^{74}Br$	-6.223
1858	$^{74}Br(\gamma,\alpha)^{70}As$	-3.390	1906	$^{75}Kr(\gamma,\alpha)^{71}Se$	-3.200
1859	$^{74}Br(\gamma,p)^{73}Se$	-4.379	1907	$^{75}Kr(\beta^{+})^{75}Br$	4.915
1860	$^{74}Kr(p,\alpha)^{71}Br$	-1.080	1908	$^{75}Rb(p,\gamma)^{76}Sr^{a}$	4.467
1861	$^{74}Kr(p,\gamma)^{75}Rb^{a}$	2.341	1909	$^{75}Rb(p,\alpha)^{72}Kr$	1.104
1862	$^{74}Kr(\alpha,\gamma)^{78}Sr$	3.428	1910	$^{75}Rb(\alpha,p)^{78}Sr$	1.087
1863	$^{74}Kr(\alpha,p)^{77}Rb$	-2.207	1911	$^{75}Rb(\alpha,\gamma)^{79}Y$	3.559
1864	$^{74}Kr(\gamma,p)^{73}Br^{a}$	-5.897	1912	$^{75}Rb(\gamma,p)^{74}Kr^{a}$	-2.341
1865	$^{74}Kr(\beta^{+})^{74}Br$	3.160	1913	$^{75}Rb(\beta^{+})^{75}Kr$	7.043
1866	$^{74}Kr(\gamma,\alpha)^{70}Se$	-3.421	1914	$^{75}Rb(\gamma,\alpha)^{71}Br$	-3.421
1867	$^{74}Rb(p,\alpha)^{71}Kr$	0.096	1915	$^{75}Sr(p,\gamma)^{76}Y^{a}$	-0.575
1868	$^{74}Rb(p,\gamma)^{75}Sr^{a}$	3.171	1916	$^{75}Sr(p,\alpha)^{72}Rb$	-3.874
1869	$^{74}Rb(\alpha,\gamma)^{78}Y$	3.380	1917	$^{75}Sr(\alpha,p)^{78}Y$	0.209
1870	$^{74}Rb(\alpha,p)^{77}Sr$	2.323	1918	$^{75}Sr(\alpha,\gamma)^{79}Zr$	2.567
1871	$^{74}Rb(\gamma,p)^{73}Kr^{a}$	-2.128	1919	$^{75}Sr(\gamma,\alpha)^{71}Kr$	-3.075
1872	$^{74}Rb(\beta^{+})^{74}Kr^{a}$	11.709	1920	$^{75}Sr(\gamma,p)^{74}Rb^{a}$	-3.171

Table C.2: – Continued.

Number	Reaction	Energy (Mev)	Number	Reaction	Energy (Mev)
1921	$^{75}Sr(\beta^+)^{75}Rb^a$	10.573	1969	$^{77}Br(p,\gamma)^{78}Kr$	8.213
1922	$^{75}Sr(\gamma,p)^{74}Kr^a$	8.231	1970	$^{77}Br(p,\alpha)^{74}Se$	3.842
1923	$^{76}Ge(\alpha,\gamma)^{80}Se$	6.971	1971	$^{77}Br(\alpha,p)^{80}Kr$	-0.205
1924	$^{76}Se(p,\gamma)^{77}Br$	5.271	1972	$^{77}Br(\alpha,\gamma)^{81}Rb$	4.646
1925	$^{76}Se(p,\alpha)^{73}As$	0.569	1973	$^{77}Br(\gamma,\alpha)^{73}As$	-4.702
1926	$^{76}Se(\alpha,p)^{79}Br$	-4.048	1974	$^{77}Br(\gamma,p)^{76}Se$	-5.271
1927	$^{76}Se(\alpha,\gamma)^{80}Kr$	5.066	1975	$^{77}Br(\beta^+)^{77}Se$	1.363
1928	$^{76}Se(\gamma,\alpha)^{72}Ge$	-5.091	1976	$^{77}Kr(p,\gamma)^{78}Rb$	4.053
1929	$^{76}Se(\gamma,p)^{75}As$	-9.508	1977	$^{77}Kr(p,\alpha)^{74}Br$	0.000
1930	$^{76}Br(p,\gamma)^{77}Kr$	7.171	1978	$^{77}Kr(\alpha,p)^{80}Rb$	-2.865
1931	$^{76}Br(p,\alpha)^{73}Se$	2.792	1979	$^{77}Kr(\alpha,\gamma)^{81}Sr$	3.778
1932	$^{76}Br(\alpha,p)^{79}Kr$	-0.711	1980	$^{77}Kr(\gamma,p)^{76}Br$	-7.171
1933	$^{76}Br(\alpha,\gamma)^{80}Rb$	4.306	1981	$^{77}Kr(\gamma,\alpha)^{73}Se$	-4.379
1934	$^{76}Br(\gamma,\alpha)^{72}As$	-4.484	1982	$^{77}Kr(\beta^+)^{77}Br$	3.010
1935	$^{76}Br(\gamma,p)^{75}Se$	-5.409	1983	$^{77}Rb(p,\gamma)^{78}Sr^a$	5.635
1936	$^{76}Br(\beta^+)^{76}Se$	4.952	1984	$^{77}Rb(p,\alpha)^{74}Kr$	2.207
1937	$^{76}Kr(p,\gamma)^{77}Rb$	3.137	1985	$^{77}Rb(\alpha,p)^{80}Sr$	0.612
1938	$^{76}Kr(p,\alpha)^{73}Br$	-0.554	1986	$^{77}Rb(\alpha,\gamma)^{81}Y$	3.612
1939	$^{76}Kr(\alpha,p)^{79}Rb$	-3.048	1987	$^{77}Rb(\beta^+)^{77}Kr$	5.277
1940	$^{76}Kr(\alpha,\gamma)^{80}Sr$	3.750	1988	$^{77}Rb(\gamma,\alpha)^{73}Br$	-3.691
1941	$^{76}Kr(\beta^+)^{76}Br$	1.333	1989	$^{77}Rb(\gamma,p)^{76}Kr$	-3.137
1942	$^{76}Kr(\gamma,\alpha)^{72}Se$	-3.508	1990	$^{77}Sr(p,\gamma)^{78}Y^a$	2.010
1943	$^{76}Kr(\gamma,p)^{75}Br$	-7.128	1991	$^{77}Sr(p,\alpha)^{74}Rb$	-2.323
1944	$^{76}Rb(p,\gamma)^{77}Sr^a$	4.786	1992	$^{77}Sr(\alpha,p)^{80}Y$	-1.450
1945	$^{76}Rb(p,\alpha)^{73}Kr$	1.273	1993	$^{77}Sr(\alpha,\gamma)^{81}Zr$	3.305
1946	$^{76}Rb(\alpha,p)^{79}Sr$	0.133	1994	$^{77}Sr(\beta^+)^{77}Rb^a$	7.335
1947	$^{76}Rb(\alpha,\gamma)^{80}Y$	5.303	1995	$^{77}Sr(\gamma,\alpha)^{73}Kr$	-3.513
1948	$^{76}Rb(\gamma,\alpha)^{72}Br$	-3.722	1996	$^{77}Sr(\gamma,p)^{76}Rb^a$	-4.786
1949	$^{76}Rb(\gamma,p)^{75}Kr$	-3.526	1997	$^{77}Y(p,\gamma)^{78}Zr^a$	2.090
1950	$^{76}Rb(\beta^+)^{76}Kr$	8.544	1998	$^{77}Y(p,\alpha)^{74}Sr$	-0.933
1951	$^{76}Sr(p,\gamma)^{77}Y^a$	-0.050	1999	$^{77}Y(\alpha,p)^{80}Zr$	2.559
1952	$^{76}Sr(p,\alpha)^{73}Rb$	-3.677	2000	$^{77}Y(\alpha,\gamma)^{81}Nb$	1.557
1953	$^{76}Sr(\alpha,p)^{79}Y$	-1.329	2001	$^{77}Y(\gamma,\alpha)^{73}Rb$	-3.415
1954	$^{76}Sr(\alpha,\gamma)^{80}Zr$	2.297	2002	$^{77}Y(\gamma,p)^{76}Sr^a$	0.050
1955	$^{76}Sr(\beta^+)^{76}Rb^a$	6.045	2003	$^{77}Y(\beta^+)^{77}Sr^a$	10.929
1956	$^{76}Sr(\gamma,\alpha)^{72}Kr$	-3.363	2004	$^{77}Zr(\beta^+)^{77}Y$	14.727
1957	$^{76}Sr(\gamma,p)^{75}Rb^a$	-4.467	2005	$^{77}Zr(\gamma,\alpha)^{73}Sr$	-2.738
1958	$^{76}Y(p,\gamma)^{77}Zr$	0.802	2006	$^{77}Zr(\gamma,p)^{76}Y$	-0.802
1959	$^{76}Y(p,\alpha)^{73}Sr$	-1.936	2007	$^{78}Se(p,\gamma)^{79}Br$	6.331
1960	$^{76}Y(\alpha,p)^{79}Zr$	3.142	2008	$^{78}Se(p,\alpha)^{75}As$	0.871
1961	$^{76}Y(\gamma,p)^{75}Sr^a$	0.575	2009	$^{78}Se(\alpha,p)^{81}Br$	-3.915
1962	$^{76}Y(\beta^+)^{76}Sr^a$	15.791	2010	$^{78}Se(\alpha,\gamma)^{82}Kr$	5.988
1963	$^{76}Y(\gamma,\alpha)^{72}Rb$	-3.299	2011	$^{78}Se(\gamma,\alpha)^{74}Ge$	-6.028
1964	$^{77}Se(p,\gamma)^{78}Br$	6.142	2012	$^{78}Br(p,\gamma)^{79}Kr$	8.279
1965	$^{77}Se(p,\alpha)^{74}As$	1.125	2013	$^{78}Br(p,\alpha)^{75}Se$	3.581
1966	$^{77}Se(\alpha,p)^{80}Br$	-3.575	2014	$^{78}Br(\alpha,p)^{81}Kr$	-0.623
1967	$^{77}Se(\alpha,\gamma)^{81}Kr$	5.519	2015	$^{78}Br(\alpha,\gamma)^{82}Rb$	5.160
1968	$^{77}Se(\gamma,\alpha)^{73}Ge$	-5.727	2016	$^{78}Br(\gamma,\alpha)^{74}As$	-5.017

Table C.2: – Continued.

Number	Reaction	Energy (Mev)	Number	Reaction	Energy (Mev)
2017	$^{78}Br(\gamma,p)^{77}Se$	-6.142	2065	$^{79}Kr(\gamma,p)^{78}Br$	-8.279
2018	$^{78}Br(\beta^+)^{78}Se$	3.574	2066	$^{79}Kr(\gamma,\alpha)^{75}Se$	-4.698
2019	$^{78}Kr(p,\gamma)^{79}Rb$	3.924	2067	$^{79}Kr(\beta^+)^{79}Br$	1.628
2020	$^{78}Kr(p,\alpha)^{75}Br$	-0.155	2068	$^{79}Rb(p,\alpha)^{76}Kr$	3.048
2021	$^{78}Kr(\alpha,p)^{81}Rb$	-3.567	2069	$^{79}Rb(p,\gamma)^{80}Sr$	6.798
2022	$^{78}Kr(\alpha,\gamma)^{82}Sr$	4.273	2070	$^{79}Rb(\alpha,\gamma)^{83}Y$	3.961
2023	$^{78}Kr(\gamma,p)^{77}Br$	-8.213	2071	$^{79}Rb(\alpha,p)^{82}Sr$	0.349
2024	$^{78}Kr(\gamma,\alpha)^{74}Se$	-4.371	2072	$^{79}Rb(\gamma,\alpha)^{75}Br$	-4.079
2025	$^{78}Rb(p,\gamma)^{79}Sr$	5.830	2073	$^{79}Rb(\gamma,p)^{78}Kr$	-3.924
2026	$^{78}Rb(p,\alpha)^{75}Kr$	2.171	2074	$^{79}Rb(\beta^+)^{79}Kr$	3.605
2027	$^{78}Rb(\alpha,p)^{81}Sr$	-0.274	2075	$^{79}Sr(p,\alpha)^{76}Rb$	-0.133
2028	$^{78}Rb(\alpha,\gamma)^{82}Y$	3.682	2076	$^{79}Sr(p,\gamma)^{80}Y$	5.170
2029	$^{78}Rb(\gamma,p)^{77}Kr$	-4.053	2077	$^{79}Sr(\alpha,\gamma)^{83}Zr$	3.412
2030	$^{78}Rb(\beta^+)^{78}Kr$	7.171	2078	$^{79}Sr(\alpha,p)^{82}Y$	-2.148
2031	$^{78}Rb(\gamma,\alpha)^{74}Br$	-4.053	2079	$^{79}Sr(\beta^+)^{79}Rb$	5.497
2032	$^{78}Sr(p,\gamma)^{79}Y^a$	2.472	2080	$^{79}Sr(\gamma,\alpha)^{75}Kr$	-3.659
2033	$^{78}Sr(p,\alpha)^{75}Rb$	-1.087	2081	$^{79}Sr(\gamma,p)^{78}Rb$	-5.830
2034	$^{78}Sr(\alpha,p)^{81}Y$	-2.022	2082	$^{79}Y(p,\alpha)^{76}Sr$	1.329
2035	$^{78}Sr(\alpha,\gamma)^{82}Zr$	3.444	2083	$^{79}Y(p,\gamma)^{80}Zr^a$	4.450
2036	$^{78}Sr(\beta^+)^{78}Rb$	3.591	2084	$^{79}Y(\alpha,\gamma)^{83}Nb$	3.031
2037	$^{78}Sr(\gamma,\alpha)^{74}Kr$	-3.428	2085	$^{79}Y(\alpha,p)^{82}Zr$	0.971
2038	$^{78}Sr(\gamma,p)^{77}Rb^a$	-5.635	2086	$^{79}Y(\beta^+)^{79}Sr$	7.649
2039	$^{78}Y(p,\gamma)^{79}Zr^a$	2.358	2087	$^{79}Y(\gamma,\alpha)^{75}Rb$	-3.559
2040	$^{78}Y(p,\alpha)^{75}Sr$	-0.209	2088	$^{79}Y(\gamma,p)^{78}Sr^a$	-2.472
2041	$^{78}Y(\alpha,p)^{81}Zr$	1.032	2089	$^{79}Zr(p,\alpha)^{76}Y$	-3.142
2042	$^{78}Y(\alpha,\gamma)^{82}Nb$	1.335	2090	$^{79}Zr(\alpha,\gamma)^{83}Mo$	0.234
2043	$^{78}Y(\gamma,p)^{77}Sr^a$	-2.010	2091	$^{79}Zr(\alpha,p)^{82}Nb$	0.750
2044	$^{78}Y(\beta^+)^{78}Sr^a$	11.950	2092	$^{79}Zr(\gamma,\alpha)^{75}Sr$	-2.567
2045	$^{78}Y(\gamma,\alpha)^{74}Rb$	-3.380	2093	$^{79}Zr(\gamma,p)^{78}Y^a$	-2.358
2046	$^{78}Zr(\alpha,\gamma)^{82}Mo$	0.193	2094	$^{79}Zr(\beta^+)^{79}Y^a$	11.320
2047	$^{78}Zr(\alpha,p)^{81}Nb$	0.910	2095	$^{80}Se(p,\gamma)^{81}Br$	7.504
2048	$^{78}Zr(\gamma,\alpha)^{74}Sr$	-2.627	2096	$^{80}Se(\alpha,\gamma)^{84}Kr$	7.095
2049	$^{78}Zr(\gamma,p)^{77}Y^a$	-2.090	2097	$^{80}Se(\gamma,\alpha)^{76}Ge$	-6.971
2050	$^{78}Zr(\beta^+)^{78}Y^a$	10.292	2098	$^{80}Br(p,\alpha)^{77}Se$	3.575
2051	$^{79}Se(p,\gamma)^{80}Br$	7.261	2099	$^{80}Br(p,\gamma)^{81}Kr$	9.094
2052	$^{79}Se(\alpha,\gamma)^{83}Kr$	6.488	2100	$^{80}Br(\alpha,\gamma)^{84}Rb$	6.285
2053	$^{79}Se(\gamma,\alpha)^{75}Ge$	-6.486	2101	$^{80}Br(\alpha,p)^{83}Kr$	-0.772
2054	$^{79}Se(\beta^+)^{79}Br$	0.151	2102	$^{80}Br(\gamma,p)^{79}Se$	-7.261
2055	$^{79}Br(p,\alpha)^{76}Se$	4.048	2103	$^{80}Br(\beta^+)^{80}Se$	1.871
2056	$^{79}Br(p,\gamma)^{80}Kr$	9.114	2104	$^{80}Br(\beta^+)^{80}Kr$	2.001
2057	$^{79}Br(\alpha,\gamma)^{83}Rb$	5.428	2105	$^{80}Kr(p,\alpha)^{77}Br$	0.205
2058	$^{79}Br(\alpha,p)^{82}Kr$	-0.344	2106	$^{80}Kr(p,\gamma)^{81}Rb$	4.851
2059	$^{79}Br(\gamma,p)^{78}Se$	-6.331	2107	$^{80}Kr(\alpha,\gamma)^{84}Sr$	5.175
2060	$^{79}Br(\gamma,\alpha)^{75}As$	-5.460	2108	$^{80}Kr(\alpha,p)^{83}Rb$	-3.686
2061	$^{79}Kr(p,\alpha)^{76}Br$	0.711	2109	$^{80}Kr(\gamma,\alpha)^{76}Se$	-5.066
2062	$^{79}Kr(p,\gamma)^{80}Rb$	5.017	2110	$^{80}Kr(\gamma,p)^{79}Br$	-9.114
2063	$^{79}Kr(\alpha,\gamma)^{83}Sr$	4.778	2111	$^{80}Rb(p,\alpha)^{77}Kr$	2.865
2064	$^{79}Kr(\alpha,p)^{82}Rb$	-3.120	2112	$^{80}Rb(p,\gamma)^{81}Sr$	6.643

Table C.2: – Continued.

Number	Reaction	Energy (Mev)	Number	Reaction	Energy (Mev)
2113	$^{80}Rb(\alpha,\gamma)^{84}Y$	4.487	2161	$^{81}Sr(p,\gamma)^{82}Y$	3.956
2114	$^{80}Rb(\alpha,p)^{83}Sr$	-0.239	2162	$^{81}Sr(\alpha,\gamma)^{85}Zr$	4.054
2115	$^{80}Rb(\gamma,\alpha)^{76}Br$	-4.306	2163	$^{81}Sr(\alpha,p)^{84}Y$	-2.155
2116	$^{80}Rb(\gamma,p)^{79}Kr$	-5.017	2164	$^{81}Sr(\gamma,p)^{80}Rb$	-6.643
2117	$^{80}Rb(\beta^+)^{80}Kr$	5.719	2165	$^{81}Sr(\beta^+)^{81}Rb$	3.991
2118	$^{80}Sr(p,\alpha)^{77}Rb$	-0.612	2166	$^{81}Sr(\gamma,\alpha)^{77}Kr$	-3.778
2119	$^{80}Sr(p,\gamma)^{81}Y$	3.000	2167	$^{81}Y(p,\alpha)^{78}Sr$	2.022
2120	$^{80}Sr(\alpha,\gamma)^{84}Zr$	4.115	2168	$^{81}Y(p,\gamma)^{82}Zr^a$	5.466
2121	$^{80}Sr(\alpha,p)^{83}Y$	-1.887	2169	$^{81}Y(\alpha,\gamma)^{85}Nb$	3.564
2122	$^{80}Sr(\gamma,\alpha)^{76}Kr$	-3.750	2170	$^{81}Y(\alpha,p)^{84}Zr$	1.455
2123	$^{80}Sr(\gamma,p)^{79}Rb$	-6.798	2171	$^{81}Y(\gamma,\alpha)^{77}Rb$	-3.612
2124	$^{80}Sr(\beta^+)^{80}Rb$	1.983	2172	$^{81}Y(\gamma,p)^{80}Sr$	-3.000
2125	$^{80}Y(p,\alpha)^{77}Sr$	1.450	2173	$^{81}Y(\beta^+)^{81}Sr$	5.520
2126	$^{80}Y(p,\gamma)^{81}Zr^a$	4.560	2174	$^{81}Zr(p,\alpha)^{78}Y$	-1.032
2127	$^{80}Y(\alpha,\gamma)^{84}Nb$	0.234	2175	$^{81}Zr(p,\gamma)^{82}Nb^a$	1.780
2128	$^{80}Y(\alpha,p)^{83}Zr$	0.380	2176	$^{81}Zr(\alpha,\gamma)^{85}Mo$	0.164
2129	$^{80}Y(\gamma,p)^{79}Sr$	-5.170	2177	$^{81}Zr(\alpha,p)^{84}Nb$	-1.470
2130	$^{80}Y(\beta^+)^{80}Sr$	7.397	2178	$^{81}Zr(\gamma,p)^{80}Y^a$	-4.560
2131	$^{80}Y(\gamma,\alpha)^{76}Rb$	-5.303	2179	$^{81}Zr(\beta^+)^{81}Y^a$	8.121
2132	$^{80}Zr(p,\alpha)^{77}Y$	-2.559	2180	$^{81}Zr(\gamma,\alpha)^{77}Sr$	-3.305
2133	$^{80}Zr(p,\gamma)^{81}Nb^a$	-0.750	2181	$^{81}Nb(p,\alpha)^{78}Zr$	-0.910
2134	$^{80}Zr(\alpha,\gamma)^{84}Mo$	-0.574	2182	$^{81}Nb(p,\gamma)^{82}Mo^a$	0.330
2135	$^{80}Zr(\alpha,p)^{83}Nb$	-1.420	2183	$^{81}Nb(\alpha,\gamma)^{85}Tc$	-0.230
2136	$^{80}Zr(\gamma,p)^{79}Y^a$	-4.450	2184	$^{81}Nb(\alpha,p)^{84}Mo$	0.428
2137	$^{80}Zr(\beta^+)^{80}Y^a$	6.604	2185	$^{81}Nb(\gamma,\alpha)^{77}Y$	-1.557
2138	$^{80}Zr(\gamma,\alpha)^{76}Sr$	-2.297	2186	$^{81}Nb(\gamma,p)^{80}Zr^a$	0.750
2139	$^{81}Se(\alpha,\gamma)^{85}Kr$	7.514	2187	$^{81}Nb(\beta^+)^{81}Zr^a$	11.461
2140	$^{81}Se(\beta^+)^{81}Br$	1.587	2188	$^{82}Se(\alpha,\gamma)^{86}Kr$	8.093
2141	$^{81}Br(p,\alpha)^{78}Se$	3.915	2189	$^{82}Kr(p,\alpha)^{79}Br$	0.344
2142	$^{81}Br(p,\gamma)^{82}Kr$	9.903	2190	$^{82}Kr(p,\gamma)^{83}Rb$	5.772
2143	$^{81}Br(\alpha,\gamma)^{85}Rb$	6.616	2191	$^{82}Kr(\alpha,\gamma)^{86}Sr$	6.356
2144	$^{81}Br(\alpha,p)^{84}Kr$	-0.408	2192	$^{82}Kr(\alpha,p)^{85}Rb$	-3.288
2145	$^{81}Br(\gamma,p)^{80}Se$	-7.504	2193	$^{82}Kr(\gamma,\alpha)^{78}Se$	-5.988
2146	$^{81}Kr(p,\alpha)^{78}Br$	0.623	2194	$^{82}Kr(\gamma,p)^{81}Br$	-9.903
2147	$^{81}Kr(p,\gamma)^{82}Rb$	5.783	2195	$^{82}Rb(p,\alpha)^{79}Kr$	3.120
2148	$^{81}Kr(\alpha,\gamma)^{85}Sr$	5.832	2196	$^{82}Rb(p,\gamma)^{83}Sr$	7.898
2149	$^{81}Kr(\alpha,p)^{84}Rb$	-2.809	2197	$^{82}Rb(\alpha,\gamma)^{86}Y$	5.517
2150	$^{81}Kr(\beta^+)^{81}Br$	0.280	2198	$^{82}Rb(\alpha,p)^{85}Sr$	0.049
2151	$^{81}Kr(\gamma,p)^{80}Br$	-9.094	2199	$^{82}Rb(\beta^+)^{82}Kr$	4.389
2152	$^{81}Kr(\gamma,\alpha)^{77}Se$	-5.519	2200	$^{82}Rb(\gamma,\alpha)^{78}Br$	-5.160
2153	$^{81}Rb(p,\alpha)^{78}Kr$	3.567	2201	$^{82}Rb(\gamma,p)^{81}Kr$	-5.783
2154	$^{81}Rb(p,\gamma)^{82}Sr$	7.840	2202	$^{82}Sr(p,\alpha)^{79}Rb$	-0.349
2155	$^{81}Rb(\alpha,\gamma)^{85}Y$	4.815	2203	$^{82}Sr(p,\gamma)^{83}Y$	3.612
2156	$^{81}Rb(\alpha,p)^{84}Sr$	0.323	2204	$^{82}Sr(\alpha,\gamma)^{86}Zr$	4.225
2157	$^{81}Rb(\gamma,\alpha)^{77}Br$	-4.646	2205	$^{82}Sr(\alpha,p)^{85}Y$	-3.025
2158	$^{81}Rb(\gamma,p)^{80}Kr$	-4.851	2206	$^{82}Sr(\gamma,p)^{81}Rb$	-7.840
2159	$^{81}Rb(\beta^+)^{81}Kr$	2.236	2207	$^{82}Sr(\beta^+)^{82}Rb$	0.205
2160	$^{81}Sr(p,\alpha)^{78}Rb$	0.274	2208	$^{82}Sr(\gamma,\alpha)^{78}Kr$	-4.273

Table C.2: – Continued.

Number	Reaction	Energy (Mev)	Number	Reaction	Energy (Mev)
2209	$^{82}Y(p,\alpha)^{79}Sr$	2.148	2257	$^{83}Y(\alpha,\gamma)^{87}Nb$	4.276
2210	$^{82}Y(p,\gamma)^{83}Zr^{a}$	5.560	2258	$^{83}Y(\beta^{+})^{83}Sr$	4.408
2211	$^{82}Y(\alpha,\gamma)^{86}Nb$	4.063	2259	$^{83}Y(\gamma,\alpha)^{79}Rb$	-3.961
2212	$^{82}Y(\alpha,p)^{85}Zr$	0.098	2260	$^{83}Y(\gamma,p)^{82}Sr$	-3.612
2213	$^{82}Y(\gamma,p)^{81}Sr$	-3.956	2261	$^{83}Zr(p,\gamma)^{84}Nb^{a}$	1.931
2214	$^{82}Y(\beta^{+})^{82}Sr$	7.817	2262	$^{83}Zr(p,\alpha)^{80}Y$	-0.380
2215	$^{82}Y(\gamma,\alpha)^{78}Rb$	-3.682	2263	$^{83}Zr(\alpha,p)^{86}Nb$	-1.498
2216	$^{82}Zr(p,\alpha)^{79}Y$	-0.971	2264	$^{83}Zr(\alpha,\gamma)^{87}Mo$	3.657
2217	$^{82}Zr(p,\gamma)^{83}Nb^{a}$	2.060	2265	$^{83}Zr(\beta^{+})^{83}Y$	7.207
2218	$^{82}Zr(\alpha,\gamma)^{86}Mo$	3.405	2266	$^{83}Zr(\gamma,\alpha)^{79}Sr$	-3.412
2219	$^{82}Zr(\alpha,p)^{85}Nb$	-1.258	2267	$^{83}Zr(\gamma,p)^{82}Y^{a}$	-5.560
2220	$^{82}Zr(\gamma,\alpha)^{78}Sr$	-3.444	2268	$^{83}Nb(p,\gamma)^{84}Mo^{a}$	4.140
2221	$^{82}Zr(\gamma,p)^{81}Y^{a}$	-5.466	2269	$^{83}Nb(p,\alpha)^{80}Zr$	1.420
2222	$^{82}Zr(\beta^{+})^{82}Y^{a}$	5.043	2270	$^{83}Nb(\alpha,p)^{86}Mo$	0.972
2223	$^{82}Nb(p,\alpha)^{79}Zr$	-0.750	2271	$^{83}Nb(\alpha,\gamma)^{87}Tc$	2.073
2224	$^{82}Nb(p,\gamma)^{83}Mo^{a}$	2.060	2272	$^{83}Nb(\gamma,\alpha)^{79}Y$	-3.031
2225	$^{82}Nb(\alpha,\gamma)^{86}Tc$	0.425	2273	$^{83}Nb(\gamma,p)^{82}Zr^{a}$	-2.060
2226	$^{82}Nb(\alpha,p)^{85}Mo$	1.270	2274	$^{83}Nb(\beta^{+})^{83}Zr^{a}$	7.722
2227	$^{82}Nb(\gamma,\alpha)^{78}Y$	-1.335	2275	$^{83}Mo(\alpha,\gamma)^{87}Ru$	1.531
2228	$^{82}Nb(\gamma,p)^{81}Zr^{a}$	-1.780	2276	$^{83}Mo(\alpha,p)^{86}Tc$	0.600
2229	$^{82}Nb(\beta^{+})^{82}Zr^{a}$	10.721	2277	$^{83}Mo(\gamma,p)^{82}Nb^{a}$	-2.060
2230	$^{82}Mo(\alpha,p)^{85}Tc$	-0.560	2278	$^{83}Mo(\beta^{+})^{83}Nb^{a}$	11.897
2231	$^{82}Mo(\alpha,\gamma)^{86}Ru$	1.280	2279	$^{83}Mo(\gamma,\alpha)^{79}Zr$	-0.234
2232	$^{82}Mo(\gamma,\alpha)^{78}Zr$	-0.193	2280	$^{84}Kr(p,\alpha)^{81}Br$	0.408
2233	$^{82}Mo(\gamma,p)^{81}Nb^{a}$	-0.330	2281	$^{84}Kr(p,\gamma)^{85}Rb$	7.024
2234	$^{82}Mo(\beta^{+})^{82}Nb^{a}$	11.434	2282	$^{84}Kr(\alpha,\gamma)^{88}Sr$	7.913
2235	$^{83}Kr(p,\gamma)^{84}Rb$	7.057	2283	$^{84}Kr(\alpha,p)^{87}Rb$	-2.701
2236	$^{83}Kr(p,\alpha)^{80}Br$	0.772	2284	$^{84}Kr(\gamma,\alpha)^{80}Se$	-7.095
2237	$^{83}Kr(\alpha,p)^{86}Rb$	-2.101	2285	$^{84}Rb(p,\alpha)^{81}Kr$	2.809
2238	$^{83}Kr(\alpha,\gamma)^{87}Sr$	7.320	2286	$^{84}Rb(p,\gamma)^{85}Sr$	8.641
2239	$^{83}Kr(\gamma,\alpha)^{79}Se$	-6.488	2287	$^{84}Rb(\alpha,\gamma)^{88}Y$	6.971
2240	$^{83}Rb(p,\gamma)^{84}Sr$	8.861	2288	$^{84}Rb(\alpha,p)^{87}Sr$	0.263
2241	$^{83}Rb(p,\alpha)^{80}Kr$	3.686	2289	$^{84}Rb(\gamma,\alpha)^{80}Br$	-6.285
2242	$^{83}Rb(\alpha,p)^{86}Sr$	0.584	2290	$^{84}Rb(\gamma,p)^{83}Kr$	-7.057
2243	$^{83}Rb(\alpha,\gamma)^{87}Y$	6.368	2291	$^{84}Rb(\beta^{+})^{84}Sr$	0.383
2244	$^{83}Rb(\gamma,p)^{82}Kr$	-5.772	2292	$^{84}Rb(\beta^{+})^{84}Kr$	2.685
2245	$^{83}Rb(\beta^{+})^{83}Kr$	0.939	2293	$^{84}Sr(p,\alpha)^{81}Rb$	-0.323
2246	$^{83}Rb(\gamma,\alpha)^{79}Br$	-5.428	2294	$^{84}Sr(p,\gamma)^{85}Y$	4.492
2247	$^{83}Sr(p,\gamma)^{84}Y$	4.726	2295	$^{84}Sr(\alpha,\gamma)^{88}Zr$	5.407
2248	$^{83}Sr(p,\alpha)^{80}Rb$	0.239	2296	$^{84}Sr(\alpha,p)^{87}Y$	-2.493
2249	$^{83}Sr(\alpha,p)^{86}Y$	-2.380	2297	$^{84}Sr(\gamma,\alpha)^{80}Kr$	-5.175
2250	$^{83}Sr(\alpha,\gamma)^{87}Zr$	4.979	2298	$^{84}Sr(\gamma,p)^{83}Rb$	-8.861
2251	$^{83}Sr(\gamma,p)^{82}Rb$	-7.898	2299	$^{84}Y(p,\alpha)^{81}Sr$	2.155
2252	$^{83}Sr(\beta^{+})^{83}Rb$	2.256	2300	$^{84}Y(p,\gamma)^{85}Zr$	6.209
2253	$^{83}Sr(\gamma,\alpha)^{79}Kr$	-4.778	2301	$^{84}Y(\alpha,\gamma)^{88}Nb$	4.267
2254	$^{83}Y(p,\gamma)^{84}Zr$	6.002	2302	$^{84}Y(\alpha,p)^{87}Zr$	0.252
2255	$^{83}Y(p,\alpha)^{80}Sr$	1.887	2303	$^{84}Y(\gamma,\alpha)^{80}Rb$	-4.487
2256	$^{83}Y(\alpha,p)^{86}Zr$	0.613	2304	$^{84}Y(\gamma,p)^{83}Sr$	-4.726

Table C.2: – Continued.

Number	Reaction	Energy (Mev)	Number	Reaction	Energy (Mev)
2305	$^{84}Y(\beta^+)^{84}Sr$	6.410	2353	$^{85}Zr(\alpha,p)^{88}Nb$	-1.941
2306	$^{84}Zr(p,\alpha)^{81}Y$	-1.455	2354	$^{85}Zr(\beta^+)^{85}Y$	4.689
2307	$^{84}Zr(p,\gamma)^{85}Nb$	2.109	2355	$^{85}Zr(\gamma,\alpha)^{81}Sr$	-4.054
2308	$^{84}Zr(\alpha,\gamma)^{88}Mo$	4.096	2356	$^{85}Zr(\gamma,p)^{84}Y$	-6.209
2309	$^{84}Zr(\alpha,p)^{87}Nb$	-1.714	2357	$^{85}Nb(p,\alpha)^{82}Zr$	1.258
2310	$^{84}Zr(\gamma,p)^{83}Y$	-6.002	2358	$^{85}Nb(p,\gamma)^{86}Mo^a$	4.663
2311	$^{84}Zr(\beta^+)^{84}Y$	3.404	2359	$^{85}Nb(\alpha,\gamma)^{89}Tc$	2.767
2312	$^{84}Zr(\gamma,\alpha)^{80}Sr$	-4.115	2360	$^{85}Nb(\alpha,p)^{88}Mo$	0.685
2313	$^{84}Nb(p,\alpha)^{81}Zr$	1.470	2361	$^{85}Nb(\beta^+)^{85}Zr$	7.465
2314	$^{84}Nb(p,\gamma)^{85}Mo^a$	4.510	2362	$^{85}Nb(\gamma,\alpha)^{81}Y$	-3.564
2315	$^{84}Nb(\alpha,\gamma)^{88}Tc$	3.822	2363	$^{85}Nb(\gamma,p)^{84}Zr$	-2.109
2316	$^{84}Nb(\alpha,p)^{87}Mo$	1.911	2364	$^{85}Mo(p,\alpha)^{82}Nb$	-1.270
2317	$^{84}Nb(\gamma,\alpha)^{80}Y$	-0.234	2365	$^{85}Mo(p,\gamma)^{86}Tc^a$	1.390
2318	$^{84}Nb(\gamma,p)^{83}Zr^a$	-1.931	2366	$^{85}Mo(\alpha,\gamma)^{89}Ru$	3.774
2319	$^{84}Nb(\beta^+)^{84}Zr$	11.278	2367	$^{85}Mo(\alpha,p)^{88}Tc$	-1.260
2320	$^{84}Mo(p,\alpha)^{81}Nb$	-0.428	2368	$^{85}Mo(\gamma,\alpha)^{81}Zr$	-0.164
2321	$^{84}Mo(p,\gamma)^{85}Tc^a$	-0.850	2369	$^{85}Mo(\gamma,p)^{84}Nb^a$	-4.510
2322	$^{84}Mo(\alpha,\gamma)^{88}Ru$	3.370	2370	$^{85}Mo(\beta^+)^{85}Nb^a$	9.602
2323	$^{84}Mo(\alpha,p)^{87}Tc$	-1.550	2371	$^{85}Tc(p,\gamma)^{86}Ru^a$	1.840
2324	$^{84}Mo(\gamma,p)^{83}Nb^a$	-4.140	2372	$^{85}Tc(p,\alpha)^{82}Mo$	0.560
2325	$^{84}Mo(\gamma,\alpha)^{80}Zr$	0.574	2373	$^{85}Tc(\alpha,p)^{88}Ru$	4.028
2326	$^{84}Mo(\beta^+)^{84}Nb^a$	7.412	2374	$^{85}Tc(\alpha,\gamma)^{89}Rh$	3.526
2327	$^{85}Kr(p,\gamma)^{86}Rb$	8.556	2375	$^{85}Tc(\gamma,\alpha)^{81}Nb$	0.230
2328	$^{85}Kr(\gamma,\alpha)^{81}Se$	-7.514	2376	$^{85}Tc(\gamma,p)^{84}Mo^a$	0.850
2329	$^{85}Kr(\beta^+)^{85}Rb$	0.176	2377	$^{85}Tc(\beta^+)^{85}Mo^a$	11.855
2330	$^{85}Rb(p,\alpha)^{82}Kr$	3.288	2378	$^{86}Kr(p,\gamma)^{87}Rb$	8.620
2331	$^{85}Rb(p,\gamma)^{86}Sr$	9.644	2379	$^{86}Kr(\gamma,\alpha)^{82}Se$	-8.093
2332	$^{85}Rb(\alpha,\gamma)^{89}Y$	7.961	2380	$^{86}Rb(p,\alpha)^{83}Kr$	2.101
2333	$^{85}Rb(\alpha,p)^{88}Sr$	0.888	2381	$^{86}Rb(p,\gamma)^{87}Sr$	9.421
2334	$^{85}Rb(\gamma,p)^{84}Kr$	-7.024	2382	$^{86}Rb(\beta^+)^{86}Sr$	1.262
2335	$^{85}Rb(\gamma,\alpha)^{81}Br$	-6.616	2383	$^{86}Rb(\gamma,p)^{85}Kr$	-8.556
2336	$^{85}Sr(p,\alpha)^{82}Rb$	-0.049	2384	$^{86}Sr(p,\alpha)^{83}Rb$	-0.584
2337	$^{85}Sr(p,\gamma)^{86}Y$	5.468	2385	$^{86}Sr(p,\gamma)^{87}Y$	5.784
2338	$^{85}Sr(\alpha,\gamma)^{89}Zr$	6.194	2386	$^{86}Sr(\alpha,\gamma)^{90}Zr$	6.675
2339	$^{85}Sr(\alpha,p)^{88}Y$	-1.669	2387	$^{86}Sr(\alpha,p)^{89}Y$	-1.682
2340	$^{85}Sr(\gamma,\alpha)^{81}Kr$	-5.832	2388	$^{86}Sr(\gamma,\alpha)^{82}Kr$	-6.356
2341	$^{85}Sr(\gamma,p)^{84}Rb$	-8.641	2389	$^{86}Sr(\gamma,p)^{85}Rb$	-9.644
2342	$^{85}Sr(\beta^+)^{85}Rb$	1.065	2390	$^{86}Y(p,\alpha)^{83}Sr$	2.380
2343	$^{85}Y(p,\alpha)^{82}Sr$	3.025	2391	$^{86}Y(p,\gamma)^{87}Zr$	7.359
2344	$^{85}Y(p,\gamma)^{86}Zr$	7.250	2392	$^{86}Y(\alpha,\gamma)^{90}Nb$	5.804
2345	$^{85}Y(\alpha,\gamma)^{89}Nb$	5.159	2393	$^{86}Y(\alpha,p)^{89}Zr$	0.726
2346	$^{85}Y(\alpha,p)^{88}Zr$	0.916	2394	$^{86}Y(\gamma,p)^{85}Sr$	-5.468
2347	$^{85}Y(\gamma,\alpha)^{81}Rb$	-4.815	2395	$^{86}Y(\beta^+)^{86}Sr$	5.238
2348	$^{85}Y(\gamma,p)^{84}Sr$	-4.492	2396	$^{86}Y(\gamma,\alpha)^{82}Rb$	-5.517
2349	$^{85}Y(\beta^+)^{85}Sr$	3.260	2397	$^{86}Zr(p,\alpha)^{83}Y$	-0.613
2350	$^{85}Zr(p,\alpha)^{82}Y$	-0.098	2398	$^{86}Zr(p,\gamma)^{87}Nb$	3.663
2351	$^{85}Zr(p,\gamma)^{86}Nb$	3.965	2399	$^{86}Zr(\alpha,\gamma)^{90}Mo$	4.788
2352	$^{85}Zr(\alpha,\gamma)^{89}Mo$	4.277	2400	$^{86}Zr(\alpha,p)^{89}Nb$	-2.091

Table C.2: – Continued.

Number	Reaction	Energy (Mev)	Number	Reaction	Energy (Mev)
2401	$^{86}Zr(\gamma,p)^{85}Y$	-7.250	2449	$^{87}Zr(\alpha,\gamma)^{91}Mo$	5.281
2402	$^{86}Zr(\beta^+)^{86}Y$	1.298	2450	$^{87}Zr(\beta^+)^{87}Y$	3.664
2403	$^{86}Zr(\gamma,\alpha)^{82}Sr$	-4.225	2451	$^{87}Zr(\gamma,\alpha)^{83}Sr$	-4.979
2404	$^{86}Nb(p,\alpha)^{83}Zr$	1.498	2452	$^{87}Zr(\gamma,p)^{86}Y$	-7.359
2405	$^{86}Nb(p,\gamma)^{87}Mo$	5.155	2453	$^{87}Nb(p,\gamma)^{88}Mo$	5.810
2406	$^{86}Nb(\alpha,\gamma)^{90}Tc$	3.885	2454	$^{87}Nb(p,\alpha)^{84}Zr$	1.714
2407	$^{86}Nb(\alpha,p)^{89}Mo$	0.312	2455	$^{87}Nb(\alpha,p)^{90}Mo$	1.125
2408	$^{86}Nb(\beta^+)^{86}Zr$	9.456	2456	$^{87}Nb(\alpha,\gamma)^{91}Tc$	4.230
2409	$^{86}Nb(\gamma,\alpha)^{82}Y$	-4.063	2457	$^{87}Nb(\gamma,p)^{86}Zr$	-3.663
2410	$^{86}Nb(\gamma,p)^{85}Zr$	-3.965	2458	$^{87}Nb(\beta^+)^{87}Zr$	5.168
2411	$^{86}Mo(p,\alpha)^{83}Nb$	-0.972	2459	$^{87}Nb(\gamma,\alpha)^{83}Y$	-4.276
2412	$^{86}Mo(p,\gamma)^{87}Tc^a$	1.860	2460	$^{87}Mo(p,\gamma)^{88}Tc$	2.300
2413	$^{86}Mo(\alpha,\gamma)^{90}Ru$	3.985	2461	$^{87}Mo(p,\alpha)^{84}Nb$	-1.911
2414	$^{86}Mo(\alpha,p)^{89}Tc$	-0.569	2462	$^{87}Mo(\alpha,p)^{90}Tc$	-1.270
2415	$^{86}Mo(\gamma,p)^{85}Nb^a$	-4.663	2463	$^{87}Mo(\alpha,\gamma)^{91}Ru$	3.311
2416	$^{86}Mo(\beta^+)^{86}Nb$	5.782	2464	$^{87}Mo(\gamma,p)^{86}Nb$	-5.155
2417	$^{86}Mo(\gamma,\alpha)^{82}Zr$	-3.405	2465	$^{87}Mo(\beta^+)^{87}Nb$	7.772
2418	$^{86}Tc(p,\gamma)^{87}Ru^a$	1.420	2466	$^{87}Mo(\gamma,\alpha)^{83}Zr$	-3.657
2419	$^{86}Tc(p,\alpha)^{83}Mo$	-0.600	2467	$^{87}Tc(p,\alpha)^{84}Mo$	1.550
2420	$^{86}Tc(\alpha,p)^{89}Ru$	3.210	2468	$^{87}Tc(p,\gamma)^{88}Ru^a$	3.538
2421	$^{86}Tc(\alpha,\gamma)^{90}Rh$	3.832	2469	$^{87}Tc(\alpha,\gamma)^{91}Rh$	4.021
2422	$^{86}Tc(\beta^+)^{86}Mo^a$	13.701	2470	$^{87}Tc(\alpha,p)^{90}Ru$	2.884
2423	$^{86}Tc(\gamma,\alpha)^{82}Nb$	-0.425	2471	$^{87}Tc(\gamma,\alpha)^{83}Nb$	-2.073
2424	$^{86}Tc(\gamma,p)^{85}Mo^a$	-1.390	2472	$^{87}Tc(\gamma,p)^{86}Mo^a$	-1.860
2425	$^{86}Ru(\alpha,\gamma)^{90}Pd$	3.212	2473	$^{87}Tc(\beta^+)^{87}Mo$	9.491
2426	$^{86}Ru(\alpha,p)^{89}Rh$	1.686	2474	$^{87}Ru(\alpha,p)^{90}Rh$	1.469
2427	$^{86}Ru(\gamma,p)^{85}Tc^a$	-1.840	2475	$^{87}Ru(\alpha,\gamma)^{91}Pd$	3.491
2428	$^{86}Ru(\beta^+)^{86}Tc^a$	10.579	2476	$^{87}Ru(\gamma,\alpha)^{83}Mo$	-1.531
2429	$^{86}Ru(\gamma,\alpha)^{82}Mo$	-1.280	2477	$^{87}Ru(\gamma,p)^{86}Tc^a$	-1.420
2430	$^{87}Rb(p,\alpha)^{84}Kr$	2.701	2478	$^{87}Ru(\beta^+)^{87}Tc^a$	12.439
2431	$^{87}Rb(p,\gamma)^{88}Sr$	10.614	2479	$^{88}Sr(p,\gamma)^{89}Y$	7.073
2432	$^{87}Rb(\gamma,p)^{86}Kr$	-8.620	2480	$^{88}Sr(p,\alpha)^{85}Rb$	-0.888
2433	$^{87}Rb(\beta^+)^{87}Sr$	-0.230	2481	$^{88}Sr(\alpha,\gamma)^{92}Zr$	2.963
2434	$^{87}Sr(p,\gamma)^{88}Y$	6.708	2482	$^{88}Sr(\gamma,\alpha)^{84}Kr$	-7.913
2435	$^{87}Sr(p,\alpha)^{84}Rb$	-0.263	2483	$^{88}Sr(\gamma,p)^{87}Rb$	-10.614
2436	$^{87}Sr(\alpha,\gamma)^{91}Zr$	5.441	2484	$^{88}Y(p,\alpha)^{85}Sr$	1.669
2437	$^{87}Sr(\gamma,p)^{86}Rb$	-9.421	2485	$^{88}Y(p,\gamma)^{89}Zr$	7.863
2438	$^{87}Sr(\gamma,\alpha)^{83}Kr$	-7.320	2486	$^{88}Y(\alpha,\gamma)^{92}Nb$	4.580
2439	$^{87}Y(p,\gamma)^{88}Zr$	7.900	2487	$^{88}Y(\alpha,p)^{91}Zr$	-1.267
2440	$^{87}Y(p,\alpha)^{84}Sr$	2.493	2488	$^{88}Y(\beta^+)^{88}Sr$	3.622
2441	$^{87}Y(\alpha,p)^{90}Zr$	0.890	2489	$^{88}Y(\gamma,\alpha)^{84}Rb$	-6.971
2442	$^{87}Y(\alpha,\gamma)^{91}Nb$	6.049	2490	$^{88}Y(\gamma,p)^{87}Sr$	-6.708
2443	$^{87}Y(\gamma,p)^{86}Sr$	-5.784	2491	$^{88}Zr(p,\alpha)^{85}Y$	-0.916
2444	$^{87}Y(\beta^+)^{87}Sr$	1.861	2492	$^{88}Zr(p,\gamma)^{89}Nb$	4.243
2445	$^{87}Y(\gamma,\alpha)^{83}Rb$	-6.368	2493	$^{88}Zr(\alpha,\gamma)^{92}Mo$	5.606
2446	$^{87}Zr(p,\gamma)^{88}Nb$	4.015	2494	$^{88}Zr(\alpha,p)^{91}Nb$	-1.850
2447	$^{87}Zr(p,\alpha)^{84}Y$	-0.252	2495	$^{88}Zr(\gamma,p)^{87}Y$	-7.900
2448	$^{87}Zr(\alpha,p)^{90}Nb$	-1.555	2496	$^{88}Zr(\beta^+)^{88}Y$	0.668

Table C.2: – Continued.

Number	Reaction	Energy (Mev)	Number	Reaction	Energy (Mev)
2497	$^{88}Zr(\gamma,\alpha)^{84}Sr$	-5.407	2545	$^{89}Nb(\beta^+)^{89}Zr$	4.247
2498	$^{88}Nb(p,\alpha)^{85}Zr$	1.941	2546	$^{89}Mo(p,\alpha)^{86}Nb$	-0.312
2499	$^{88}Nb(p,\gamma)^{89}Mo$	6.218	2547	$^{89}Mo(p,\gamma)^{90}Tc$	3.573
2500	$^{88}Nb(\alpha,\gamma)^{92}Tc$	5.286	2548	$^{89}Mo(\alpha,\gamma)^{93}Ru$	4.688
2501	$^{88}Nb(\alpha,p)^{91}Mo$	1.266	2549	$^{89}Mo(\alpha,p)^{92}Tc$	-0.932
2502	$^{88}Nb(\gamma,p)^{87}Zr$	-4.015	2550	$^{89}Mo(\beta^+)^{89}Nb$	5.618
2503	$^{88}Nb(\beta^+)^{88}Zr$	7.196	2551	$^{89}Mo(\gamma,\alpha)^{85}Zr$	-4.277
2504	$^{88}Nb(\gamma,\alpha)^{84}Y$	-4.267	2552	$^{89}Mo(\gamma,p)^{88}Nb$	-6.218
2505	$^{88}Mo(p,\alpha)^{85}Nb$	-0.685	2553	$^{89}Tc(p,\gamma)^{90}Ru$	4.554
2506	$^{88}Mo(p,\gamma)^{89}Tc$	2.082	2554	$^{89}Tc(p,\alpha)^{86}Mo$	0.569
2507	$^{88}Mo(\alpha,\gamma)^{92}Ru$	4.706	2555	$^{89}Tc(\alpha,p)^{92}Ru$	2.599
2508	$^{88}Mo(\alpha,p)^{91}Tc$	-0.848	2556	$^{89}Tc(\alpha,\gamma)^{93}Rh$	4.601
2509	$^{88}Mo(\beta^+)^{88}Nb$	4.206	2557	$^{89}Tc(\gamma,\alpha)^{85}Nb$	-2.767
2510	$^{88}Mo(\gamma,\alpha)^{84}Zr$	-4.096	2558	$^{89}Tc(\gamma,p)^{88}Mo$	-2.082
2511	$^{88}Mo(\gamma,p)^{87}Nb$	-5.810	2559	$^{89}Tc(\beta^+)^{89}Mo$	7.940
2512	$^{88}Tc(p,\gamma)^{89}Ru^a$	3.737	2560	$^{89}Ru(p,\gamma)^{90}Rh^a$	0.990
2513	$^{88}Tc(p,\alpha)^{85}Mo$	1.260	2561	$^{89}Ru(p,\alpha)^{86}Tc$	-3.210
2514	$^{88}Tc(\alpha,p)^{91}Ru$	2.495	2562	$^{89}Ru(\alpha,p)^{92}Rh$	-1.020
2515	$^{88}Tc(\alpha,\gamma)^{92}Rh$	4.352	2563	$^{89}Ru(\alpha,\gamma)^{93}Pd$	4.009
2516	$^{88}Tc(\beta^+)^{88}Mo$	11.552	2564	$^{89}Ru(\gamma,p)^{88}Tc^a$	-3.737
2517	$^{88}Tc(\gamma,\alpha)^{84}Nb$	-3.822	2565	$^{89}Ru(\beta^+)^{89}Tc$	9.922
2518	$^{88}Tc(\gamma,p)^{87}Mo$	-2.300	2566	$^{89}Ru(\gamma,\alpha)^{85}Mo$	-3.774
2519	$^{88}Ru(p,\gamma)^{89}Rh^a$	-0.700	2567	$^{89}Rh(p,\alpha)^{86}Ru$	-1.686
2520	$^{88}Ru(p,\alpha)^{85}Tc$	-4.028	2568	$^{89}Rh(p,\gamma)^{90}Pd^a$	1.526
2521	$^{88}Ru(\alpha,p)^{91}Rh$	-1.410	2569	$^{89}Rh(\alpha,p)^{92}Pd$	4.172
2522	$^{88}Ru(\alpha,\gamma)^{92}Pd$	3.670	2570	$^{89}Rh(\alpha,\gamma)^{93}Ag$	3.680
2523	$^{88}Ru(\beta^+)^{88}Tc^a$	7.864	2571	$^{89}Rh(\gamma,p)^{88}Ru^a$	0.700
2524	$^{88}Ru(\gamma,\alpha)^{84}Mo$	-3.370	2572	$^{89}Rh(\beta^+)^{89}Ru^a$	12.103
2525	$^{88}Ru(\gamma,p)^{87}Tc^a$	-3.538	2573	$^{89}Rh(\gamma,\alpha)^{85}Tc$	-3.526
2526	$^{89}Y(p,\alpha)^{86}Sr$	1.682	2574	$^{90}Zr(p,\gamma)^{91}Nb$	5.159
2527	$^{89}Y(p,\gamma)^{90}Zr$	8.357	2575	$^{90}Zr(p,\alpha)^{87}Y$	-0.890
2528	$^{89}Y(\alpha,\gamma)^{93}Nb$	1.933	2576	$^{90}Zr(\alpha,p)^{93}Nb$	-6.423
2529	$^{89}Y(\alpha,p)^{92}Zr$	-4.110	2577	$^{90}Zr(\alpha,\gamma)^{94}Mo$	2.067
2530	$^{89}Y(\gamma,\alpha)^{85}Rb$	-7.961	2578	$^{90}Zr(\gamma,\alpha)^{86}Sr$	-6.675
2531	$^{89}Y(\gamma,p)^{88}Sr$	-7.073	2579	$^{90}Zr(\gamma,p)^{89}Y$	-8.357
2532	$^{89}Zr(p,\alpha)^{86}Y$	-0.726	2580	$^{90}Nb(p,\gamma)^{91}Mo$	6.836
2533	$^{89}Zr(p,\gamma)^{90}Nb$	5.078	2581	$^{90}Nb(p,\alpha)^{87}Zr$	1.555
2534	$^{89}Zr(\alpha,\gamma)^{93}Mo$	4.360	2582	$^{90}Nb(\alpha,p)^{93}Mo$	-0.718
2535	$^{89}Zr(\alpha,p)^{92}Nb$	-3.283	2583	$^{90}Nb(\alpha,\gamma)^{94}Tc$	3.922
2536	$^{89}Zr(\beta^+)^{89}Y$	2.833	2584	$^{90}Nb(\gamma,p)^{89}Zr$	-5.078
2537	$^{89}Zr(\gamma,\alpha)^{85}Sr$	-6.194	2585	$^{90}Nb(\beta^+)^{90}Zr$	6.109
2538	$^{89}Zr(\gamma,p)^{88}Y$	-7.863	2586	$^{90}Nb(\gamma,\alpha)^{86}Y$	-5.804
2539	$^{89}Nb(p,\alpha)^{86}Zr$	2.091	2587	$^{90}Mo(p,\gamma)^{91}Tc$	3.105
2540	$^{89}Nb(p,\gamma)^{90}Mo$	6.879	2588	$^{90}Mo(p,\alpha)^{87}Nb$	-1.125
2541	$^{89}Nb(\alpha,\gamma)^{93}Tc$	5.449	2589	$^{90}Mo(\alpha,p)^{93}Tc$	-1.430
2542	$^{89}Nb(\alpha,p)^{92}Mo$	1.362	2590	$^{90}Mo(\alpha,\gamma)^{94}Ru$	4.818
2543	$^{89}Nb(\gamma,\alpha)^{85}Y$	-5.159	2591	$^{90}Mo(\gamma,p)^{89}Nb$	-6.879
2544	$^{89}Nb(\gamma,p)^{88}Zr$	-4.243	2592	$^{90}Mo(\beta^+)^{90}Nb$	2.487

Table C.2: – Continued.

Number	Reaction	Energy (Mev)	Number	Reaction	Energy (Mev)
2593	$^{90}Mo(\gamma,\alpha)^{86}Zr$	-4.788	2641	$^{91}Tc(\alpha,\gamma)^{95}Rh$	4.775
2594	$^{90}Tc(p,\alpha)^{87}Mo$	1.270	2642	$^{91}Tc(\gamma,\alpha)^{87}Nb$	-4.230
2595	$^{90}Tc(p,\gamma)^{91}Ru$	4.581	2643	$^{91}Tc(\gamma,p)^{90}Mo$	-3.105
2596	$^{90}Tc(\alpha,\gamma)^{94}Rh$	4.700	2644	$^{91}Tc(\beta^+)^{91}Mo$	6.220
2597	$^{90}Tc(\alpha,p)^{93}Ru$	1.935	2645	$^{91}Ru(p,\gamma)^{92}Rh^a$	1.857
2598	$^{90}Tc(\gamma,\alpha)^{86}Nb$	-3.885	2646	$^{91}Ru(p,\alpha)^{88}Tc$	-2.495
2599	$^{90}Tc(\gamma,p)^{89}Mo$	-3.573	2647	$^{91}Ru(\alpha,p)^{94}Rh$	-0.002
2600	$^{90}Tc(\beta^+)^{90}Mo$	9.846	2648	$^{91}Ru(\alpha,\gamma)^{95}Pd$	4.395
2601	$^{90}Ru(p,\alpha)^{87}Tc$	-2.884	2649	$^{91}Ru(\gamma,\alpha)^{87}Mo$	-3.311
2602	$^{90}Ru(p,\gamma)^{91}Rh^a$	1.137	2650	$^{91}Ru(\gamma,p)^{90}Tc$	-4.581
2603	$^{90}Ru(\alpha,\gamma)^{94}Pd$	4.412	2651	$^{91}Ru(\beta^+)^{91}Tc$	8.209
2604	$^{90}Ru(\alpha,p)^{93}Rh$	0.047	2652	$^{91}Rh(p,\alpha)^{88}Ru$	1.410
2605	$^{90}Ru(\beta^+)^{90}Tc$	6.311	2653	$^{91}Rh(p,\gamma)^{92}Pd^a$	3.187
2606	$^{90}Ru(\gamma,\alpha)^{86}Mo$	-3.985	2654	$^{91}Rh(\alpha,\gamma)^{95}Ag$	4.235
2607	$^{90}Ru(\gamma,p)^{89}Tc$	-4.554	2655	$^{91}Rh(\alpha,p)^{94}Pd$	3.275
2608	$^{90}Rh(p,\gamma)^{91}Pd^a$	1.480	2656	$^{91}Rh(\beta^+)^{91}Ru^a$	9.876
2609	$^{90}Rh(p,\alpha)^{87}Ru$	-1.469	2657	$^{91}Rh(\gamma,\alpha)^{87}Tc$	-4.021
2610	$^{90}Rh(\alpha,\gamma)^{94}Ag$	4.011	2658	$^{91}Rh(\gamma,p)^{90}Ru^a$	-1.137
2611	$^{90}Rh(\alpha,p)^{93}Pd$	3.387	2659	$^{91}Pd(p,\gamma)^{92}Ag$	-0.674
2612	$^{90}Rh(\gamma,\alpha)^{86}Tc$	-3.832	2660	$^{91}Pd(\alpha,p)^{94}Ag$	1.989
2613	$^{90}Rh(\gamma,p)^{89}Ru^a$	-0.990	2661	$^{91}Pd(\alpha,\gamma)^{95}Cd$	3.940
2614	$^{90}Rh(\beta^+)^{90}Ru^a$	13.854	2662	$^{91}Pd(\gamma,p)^{90}Rh^a$	-1.480
2615	$^{90}Pd(\alpha,\gamma)^{94}Cd$	3.634	2663	$^{91}Pd(\beta^+)^{91}Rh^a$	12.969
2616	$^{90}Pd(\alpha,p)^{93}Ag$	2.154	2664	$^{91}Pd(\gamma,\alpha)^{87}Ru$	-3.491
2617	$^{90}Pd(\gamma,\alpha)^{86}Ru$	-3.212	2665	$^{92}Zr(p,\gamma)^{93}Nb$	6.043
2618	$^{90}Pd(\gamma,p)^{89}Rh^a$	-1.526	2666	$^{92}Zr(p,\alpha)^{89}Y$	4.110
2619	$^{90}Pd(\beta^+)^{90}Rh^a$	11.199	2667	$^{92}Zr(\alpha,\gamma)^{96}Mo$	2.761
2620	$^{91}Zr(p,\alpha)^{88}Y$	1.267	2668	$^{92}Zr(\gamma,\alpha)^{88}Sr$	-2.963
2621	$^{91}Zr(p,\gamma)^{92}Nb$	5.847	2669	$^{92}Nb(p,\alpha)^{89}Zr$	3.283
2622	$^{91}Zr(\alpha,\gamma)^{95}Mo$	2.241	2670	$^{92}Nb(p,\gamma)^{93}Mo$	7.643
2623	$^{91}Zr(\gamma,\alpha)^{87}Sr$	-5.441	2671	$^{92}Nb(\alpha,\gamma)^{96}Tc$	1.793
2624	$^{91}Nb(p,\alpha)^{88}Zr$	1.850	2672	$^{92}Nb(\alpha,p)^{95}Mo$	-3.606
2625	$^{91}Nb(p,\gamma)^{92}Mo$	7.456	2673	$^{92}Nb(\beta^+)^{92}Mo$	-0.152
2626	$^{91}Nb(\alpha,\gamma)^{95}Tc$	1.803	2674	$^{92}Nb(\gamma,\alpha)^{88}Y$	-4.580
2627	$^{91}Nb(\alpha,p)^{94}Mo$	-3.092	2675	$^{92}Nb(\gamma,p)^{91}Zr$	-5.847
2628	$^{91}Nb(\beta^+)^{91}Zr$	1.253	2676	$^{92}Nb(\beta^+)^{92}Zr$	2.006
2629	$^{91}Nb(\gamma,\alpha)^{87}Y$	-6.049	2677	$^{92}Mo(p,\alpha)^{89}Nb$	-1.362
2630	$^{91}Nb(\gamma,p)^{90}Zr$	-5.159	2678	$^{92}Mo(p,\gamma)^{93}Tc$	4.087
2631	$^{91}Mo(p,\alpha)^{88}Nb$	-1.266	2679	$^{92}Mo(\alpha,\gamma)^{96}Ru$	1.685
2632	$^{91}Mo(p,\gamma)^{92}Tc$	4.020	2680	$^{92}Mo(\alpha,p)^{95}Tc$	-5.653
2633	$^{91}Mo(\alpha,\gamma)^{95}Ru$	3.665	2681	$^{92}Mo(\gamma,p)^{91}Nb$	-7.456
2634	$^{91}Mo(\alpha,p)^{94}Tc$	-2.914	2682	$^{92}Mo(\gamma,\alpha)^{88}Zr$	-5.606
2635	$^{91}Mo(\gamma,\alpha)^{87}Zr$	-5.281	2683	$^{92}Tc(p,\gamma)^{93}Ru$	5.620
2636	$^{91}Mo(\gamma,p)^{90}Nb$	-6.836	2684	$^{92}Tc(p,\alpha)^{89}Mo$	0.932
2637	$^{91}Mo(\beta^+)^{91}Nb$	4.438	2685	$^{92}Tc(\alpha,p)^{95}Ru$	-0.355
2638	$^{91}Tc(p,\gamma)^{92}Ru$	5.554	2686	$^{92}Tc(\alpha,\gamma)^{96}Rh$	3.109
2639	$^{91}Tc(p,\alpha)^{88}Mo$	0.848	2687	$^{92}Tc(\gamma,p)^{91}Mo$	-4.020
2640	$^{91}Tc(\alpha,p)^{94}Ru$	1.713	2688	$^{92}Tc(\beta^+)^{92}Mo$	7.870

Table C.2: – Continued.

Number	Reaction	Energy (Mev)	Number	Reaction	Energy (Mev)
2689	$^{92}Tc(\gamma,\alpha)^{88}Nb$	-5.286	2737	$^{93}Tc(\beta^+)^{93}Mo$	3.198
2690	$^{92}Ru(p,\gamma)^{93}Rh$	2.002	2738	$^{93}Ru(p,\gamma)^{94}Rh$	2.765
2691	$^{92}Ru(p,\alpha)^{89}Tc$	-2.599	2739	$^{93}Ru(p,\alpha)^{90}Tc$	-1.935
2692	$^{92}Ru(\alpha,p)^{95}Rh$	-0.488	2740	$^{93}Ru(\alpha,p)^{96}Rh$	-2.511
2693	$^{92}Ru(\alpha,\gamma)^{96}Pd$	4.636	2741	$^{93}Ru(\alpha,\gamma)^{97}Pd$	2.952
2694	$^{92}Ru(\beta^+)^{92}Tc$	4.512	2742	$^{93}Ru(\beta^+)^{93}Tc$	6.336
2695	$^{92}Ru(\gamma,\alpha)^{88}Mo$	-4.706	2743	$^{93}Ru(\gamma,\alpha)^{89}Mo$	-4.688
2696	$^{92}Ru(\gamma,p)^{91}Tc$	-5.554	2744	$^{93}Ru(\gamma,p)^{92}Tc$	-5.620
2697	$^{92}Rh(p,\alpha)^{89}Ru$	1.020	2745	$^{93}Rh(p,\alpha)^{90}Ru$	-0.047
2698	$^{92}Rh(p,\gamma)^{93}Pd^a$	3.394	2746	$^{93}Rh(p,\gamma)^{94}Pd^a$	4.365
2699	$^{92}Rh(\alpha,\gamma)^{96}Ag$	4.404	2747	$^{93}Rh(\alpha,\gamma)^{97}Ag$	4.369
2700	$^{92}Rh(\alpha,p)^{95}Pd$	2.538	2748	$^{93}Rh(\alpha,p)^{96}Pd$	2.634
2701	$^{92}Rh(\beta^+)^{92}Ru$	11.906	2749	$^{93}Rh(\gamma,\alpha)^{89}Tc$	-4.601
2702	$^{92}Rh(\gamma,\alpha)^{88}Tc$	-4.352	2750	$^{93}Rh(\gamma,p)^{92}Ru$	-2.002
2703	$^{92}Rh(\gamma,p)^{91}Ru^a$	-1.857	2751	$^{93}Rh(\beta^+)^{93}Ru$	8.199
2704	$^{92}Pd(p,\alpha)^{89}Rh$	-4.172	2752	$^{93}Pd(p,\alpha)^{90}Rh$	-3.387
2705	$^{92}Pd(p,\gamma)^{93}Ag^a$	-0.492	2753	$^{93}Pd(p,\gamma)^{94}Ag^a$	0.624
2706	$^{92}Pd(\alpha,\gamma)^{96}Cd$	4.249	2754	$^{93}Pd(\alpha,p)^{96}Ag$	1.010
2707	$^{92}Pd(\alpha,p)^{95}Ag$	1.048	2755	$^{93}Pd(\alpha,\gamma)^{97}Cd$	4.268
2708	$^{92}Pd(\gamma,\alpha)^{88}Ru$	-3.670	2756	$^{93}Pd(\beta^+)^{93}Rh^a$	10.514
2709	$^{92}Pd(\gamma,p)^{91}Rh^a$	-3.187	2757	$^{93}Pd(\gamma,\alpha)^{89}Ru$	-4.009
2710	$^{92}Pd(\beta^+)^{92}Rh^a$	8.546	2758	$^{93}Pd(\gamma,p)^{92}Rh^a$	-3.394
2711	$^{92}Ag(p,\gamma)^{93}Cd$	0.693	2759	$^{93}Ag(p,\gamma)^{94}Cd$	1.480
2712	$^{92}Ag(\alpha,\gamma)^{96}In$	4.236	2760	$^{93}Ag(p,\alpha)^{90}Pd$	-2.154
2713	$^{92}Ag(\alpha,p)^{95}Cd$	4.614	2761	$^{93}Ag(\alpha,\gamma)^{97}In$	4.397
2714	$^{92}Ag(\gamma,p)^{91}Pd$	0.674	2762	$^{93}Ag(\alpha,p)^{96}Cd$	4.741
2715	$^{92}Ag(\beta^+)^{92}Pd$	16.830	2763	$^{93}Ag(\beta^+)^{93}Pd^a$	12.430
2716	$^{93}Zr(\alpha,\gamma)^{97}Mo$	2.848	2764	$^{93}Ag(\gamma,\alpha)^{89}Rh$	-3.680
2717	$^{93}Zr(\beta^+)^{93}Nb$	-0.422	2765	$^{93}Ag(\gamma,p)^{92}Pd^a$	0.492
2718	$^{93}Nb(p,\alpha)^{90}Zr$	6.423	2766	$^{93}Cd(\alpha,p)^{96}In$	3.543
2719	$^{93}Nb(p,\gamma)^{94}Mo$	8.490	2767	$^{93}Cd(\alpha,\gamma)^{97}Sn$	4.338
2720	$^{93}Nb(\alpha,\gamma)^{97}Tc$	2.436	2768	$^{93}Cd(\beta^+)^{93}Ag$	15.650
2721	$^{93}Nb(\alpha,p)^{96}Mo$	-3.283	2769	$^{93}Cd(\gamma,p)^{92}Ag$	-0.693
2722	$^{93}Nb(\gamma,p)^{92}Zr$	-6.043	2770	$^{94}Zr(\alpha,\gamma)^{98}Mo$	3.270
2723	$^{93}Nb(\gamma,\alpha)^{89}Y$	-1.933	2771	$^{94}Mo(p,\alpha)^{91}Nb$	3.092
2724	$^{93}Mo(p,\alpha)^{90}Nb$	0.718	2772	$^{94}Mo(p,\gamma)^{95}Tc$	4.895
2725	$^{93}Mo(p,\gamma)^{94}Tc$	4.640	2773	$^{94}Mo(\alpha,\gamma)^{98}Ru$	2.238
2726	$^{93}Mo(\alpha,\gamma)^{97}Ru$	1.727	2774	$^{94}Mo(\alpha,p)^{97}Tc$	-6.054
2727	$^{93}Mo(\alpha,p)^{96}Tc$	-5.850	2775	$^{94}Mo(\gamma,p)^{93}Nb$	-8.490
2728	$^{93}Mo(\gamma,p)^{92}Nb$	-7.643	2776	$^{94}Mo(\gamma,\alpha)^{90}Zr$	-2.067
2729	$^{93}Mo(\beta^+)^{93}Nb$	0.404	2777	$^{94}Tc(p,\gamma)^{95}Ru$	6.579
2730	$^{93}Mo(\gamma,\alpha)^{89}Zr$	-4.360	2778	$^{94}Tc(p,\alpha)^{91}Mo$	2.914
2731	$^{93}Tc(p,\gamma)^{94}Ru$	6.248	2779	$^{94}Tc(\alpha,p)^{97}Ru$	-2.912
2732	$^{93}Tc(p,\alpha)^{90}Mo$	1.430	2780	$^{94}Tc(\alpha,\gamma)^{98}Rh$	1.437
2733	$^{93}Tc(\alpha,p)^{96}Ru$	-2.401	2781	$^{94}Tc(\gamma,p)^{93}Mo$	-4.640
2734	$^{93}Tc(\alpha,\gamma)^{97}Rh$	1.405	2782	$^{94}Tc(\beta^+)^{94}Mo$	4.256
2735	$^{93}Tc(\gamma,\alpha)^{89}Nb$	-5.449	2783	$^{94}Tc(\gamma,\alpha)^{90}Nb$	-3.922
2736	$^{93}Tc(\gamma,p)^{92}Mo$	-4.087	2784	$^{94}Ru(p,\gamma)^{95}Rh$	3.062

Table C.2: – Continued.

Number	Reaction	Energy (Mev)	Number	Reaction	Energy (Mev)
2785	$^{94}Ru(p,\alpha)^{91}Tc$	-1.713	2833	$^{95}Ru(\alpha,p)^{98}Rh$	-5.142
2786	$^{94}Ru(\alpha,p)^{97}Rh$	-4.843	2834	$^{95}Ru(\gamma,p)^{94}Tc$	-6.579
2787	$^{94}Ru(\alpha,\gamma)^{98}Pd$	1.157	2835	$^{95}Ru(\beta^+)^{95}Tc$	2.569
2788	$^{94}Ru(\gamma,p)^{93}Tc$	-6.248	2836	$^{95}Ru(\gamma,\alpha)^{91}Mo$	-3.665
2789	$^{94}Ru(\beta^+)^{94}Tc$	1.590	2837	$^{95}Rh(p,\gamma)^{96}Pd$	5.124
2790	$^{94}Ru(\gamma,\alpha)^{90}Mo$	-4.818	2838	$^{95}Rh(p,\alpha)^{92}Ru$	0.488
2791	$^{94}Rh(p,\alpha)^{91}Ru$	0.002	2839	$^{95}Rh(\alpha,\gamma)^{99}Ag$	0.809
2792	$^{94}Rh(p,\gamma)^{95}Pd$	4.397	2840	$^{95}Rh(\alpha,p)^{98}Pd$	-1.905
2793	$^{94}Rh(\alpha,\gamma)^{98}Ag$	2.924	2841	$^{95}Rh(\gamma,p)^{94}Ru$	-3.062
2794	$^{94}Rh(\alpha,p)^{97}Pd$	0.554	2842	$^{95}Rh(\beta^+)^{95}Ru$	5.109
2795	$^{94}Rh(\gamma,\alpha)^{90}Tc$	-4.700	2843	$^{95}Rh(\gamma,\alpha)^{91}Tc$	-4.775
2796	$^{94}Rh(\gamma,p)^{93}Ru$	-2.765	2844	$^{95}Pd(p,\alpha)^{92}Rh$	-2.538
2797	$^{94}Rh(\beta^+)^{94}Ru$	10.207	2845	$^{95}Pd(p,\gamma)^{96}Ag$	1.866
2798	$^{94}Pd(p,\alpha)^{91}Rh$	-3.275	2846	$^{95}Pd(\alpha,p)^{98}Ag$	-1.473
2799	$^{94}Pd(p,\gamma)^{95}Ag^a$	0.960	2847	$^{95}Pd(\alpha,\gamma)^{99}Cd$	2.635
2800	$^{94}Pd(\alpha,\gamma)^{98}Cd$	4.323	2848	$^{95}Pd(\beta^+)^{95}Rh$	8.698
2801	$^{94}Pd(\alpha,p)^{97}Ag$	0.004	2849	$^{95}Pd(\gamma,\alpha)^{91}Ru$	-4.395
2802	$^{94}Pd(\gamma,\alpha)^{90}Ru$	-4.412	2850	$^{95}Pd(\gamma,p)^{94}Rh$	-4.397
2803	$^{94}Pd(\gamma,p)^{93}Rh^a$	-4.365	2851	$^{95}Ag(p,\alpha)^{92}Pd$	-1.048
2804	$^{94}Pd(\beta^+)^{94}Rh$	6.599	2852	$^{95}Ag(p,\gamma)^{96}Cd^a$	3.201
2805	$^{94}Ag(p,\alpha)^{91}Pd$	-1.989	2853	$^{95}Ag(\alpha,p)^{98}Cd$	3.363
2806	$^{94}Ag(p,\gamma)^{95}Cd^a$	1.951	2854	$^{95}Ag(\alpha,\gamma)^{99}In$	4.655
2807	$^{94}Ag(\alpha,p)^{97}Cd$	3.644	2855	$^{95}Ag(\gamma,\alpha)^{91}Rh$	-4.235
2808	$^{94}Ag(\alpha,\gamma)^{98}In$	4.536	2856	$^{95}Ag(\gamma,p)^{94}Pd^a$	-0.960
2809	$^{94}Ag(\beta^+)^{94}Pd^a$	14.250	2857	$^{95}Ag(\beta^+)^{95}Pd$	10.040
2810	$^{94}Ag(\gamma,\alpha)^{90}Rh$	-4.011	2858	$^{95}Cd(p,\gamma)^{96}In^a$	-0.378
2811	$^{94}Ag(\gamma,p)^{93}Pd^a$	-0.624	2859	$^{95}Cd(p,\alpha)^{92}Ag$	-4.614
2812	$^{94}Cd(\alpha,p)^{97}In$	2.917	2860	$^{95}Cd(\alpha,\gamma)^{99}Sn$	4.472
2813	$^{94}Cd(\alpha,\gamma)^{98}Sn$	4.568	2861	$^{95}Cd(\alpha,p)^{98}In$	2.585
2814	$^{94}Cd(\gamma,p)^{93}Ag$	-1.480	2862	$^{95}Cd(\gamma,\alpha)^{91}Pd$	-3.940
2815	$^{94}Cd(\beta^+)^{94}Ag$	11.580	2863	$^{95}Cd(\gamma,p)^{94}Ag^a$	-1.951
2816	$^{94}Cd(\gamma,\alpha)^{90}Pd$	-3.634	2864	$^{95}Cd(\beta^+)^{95}Ag^a$	13.260
2817	$^{95}Zr(\alpha,\gamma)^{99}Mo$	2.733	2865	$^{96}Zr(\alpha,\gamma)^{100}Mo$	3.168
2818	$^{95}Mo(p,\gamma)^{96}Tc$	5.399	2866	$^{96}Mo(p,\alpha)^{93}Nb$	3.283
2819	$^{95}Mo(p,\alpha)^{92}Nb$	3.606	2867	$^{96}Mo(p,\gamma)^{97}Tc$	5.719
2820	$^{95}Mo(\alpha,p)^{98}Tc$	-6.144	2868	$^{96}Mo(\alpha,\gamma)^{100}Ru$	2.852
2821	$^{95}Mo(\alpha,\gamma)^{99}Ru$	2.334	2869	$^{96}Mo(\alpha,p)^{99}Tc$	-6.332
2822	$^{95}Mo(\gamma,\alpha)^{91}Zr$	-2.241	2870	$^{96}Mo(\gamma,\alpha)^{92}Zr$	-2.761
2823	$^{95}Tc(p,\alpha)^{92}Mo$	5.653	2871	$^{96}Tc(p,\gamma)^{97}Ru$	7.577
2824	$^{95}Tc(p,\gamma)^{96}Ru$	7.338	2872	$^{96}Tc(p,\alpha)^{93}Mo$	5.850
2825	$^{95}Tc(\alpha,\gamma)^{99}Rh$	1.922	2873	$^{96}Tc(\alpha,p)^{99}Ru$	-3.065
2826	$^{95}Tc(\alpha,p)^{98}Ru$	-2.657	2874	$^{96}Tc(\alpha,\gamma)^{100}Rh$	2.196
2827	$^{95}Tc(\gamma,\alpha)^{91}Nb$	-1.803	2875	$^{96}Tc(\gamma,p)^{95}Mo$	-5.399
2828	$^{95}Tc(\gamma,p)^{94}Mo$	-4.895	2876	$^{96}Tc(\beta^+)^{96}Mo$	2.973
2829	$^{95}Tc(\beta^+)^{95}Mo$	1.691	2877	$^{96}Tc(\beta^+)^{96}Ru$	-0.259
2830	$^{95}Ru(p,\alpha)^{92}Tc$	0.355	2878	$^{96}Tc(\gamma,\alpha)^{92}Nb$	-1.793
2831	$^{95}Ru(p,\gamma)^{96}Rh$	3.464	2879	$^{96}Ru(p,\gamma)^{97}Rh$	3.806
2832	$^{95}Ru(\alpha,\gamma)^{99}Pd$	1.129	2880	$^{96}Ru(p,\alpha)^{93}Tc$	2.401

Table C.2: – Continued.

Number	Reaction	Energy (Mev)	Number	Reaction	Energy (Mev)
2881	$^{96}Ru(\alpha,p)^{99}Rh$	-5.416	2929	$^{97}Tc(\beta^+)^{97}Mo$	0.320
2882	$^{96}Ru(\alpha,\gamma)^{100}Pd$	1.585	2930	$^{97}Ru(p,\alpha)^{94}Tc$	2.912
2883	$^{96}Ru(\gamma,\alpha)^{92}Mo$	-1.685	2931	$^{97}Ru(p,\gamma)^{98}Rh$	4.349
2884	$^{96}Ru(\gamma,p)^{95}Tc$	-7.338	2932	$^{97}Ru(\alpha,\gamma)^{101}Pd$	1.747
2885	$^{96}Rh(p,\alpha)^{93}Ru$	2.511	2933	$^{97}Ru(\alpha,p)^{100}Rh$	-5.381
2886	$^{96}Rh(p,\gamma)^{97}Pd$	5.463	2934	$^{97}Ru(\gamma,\alpha)^{93}Mo$	-1.727
2887	$^{96}Rh(\alpha,\gamma)^{100}Ag$	0.958	2935	$^{97}Ru(\gamma,p)^{96}Tc$	-7.577
2888	$^{96}Rh(\alpha,p)^{99}Pd$	-2.335	2936	$^{97}Ru(\beta^+)^{97}Tc$	1.111
2889	$^{96}Rh(\gamma,p)^{95}Ru$	-3.464	2937	$^{97}Rh(p,\gamma)^{98}Pd$	6.000
2890	$^{96}Rh(\beta^+)^{96}Ru$	6.441	2938	$^{97}Rh(p,\alpha)^{94}Ru$	4.843
2891	$^{96}Rh(\gamma,\alpha)^{92}Tc$	-3.109	2939	$^{97}Rh(\alpha,\gamma)^{101}Ag$	1.066
2892	$^{96}Pd(p,\alpha)^{93}Rh$	-2.634	2940	$^{97}Rh(\alpha,p)^{100}Pd$	-2.221
2893	$^{96}Pd(p,\gamma)^{97}Ag$	1.735	2941	$^{97}Rh(\beta^+)^{97}Ru$	3.511
2894	$^{96}Pd(\alpha,\gamma)^{100}Cd$	0.518	2942	$^{97}Rh(\gamma,\alpha)^{93}Tc$	-1.405
2895	$^{96}Pd(\alpha,p)^{99}Ag$	-4.315	2943	$^{97}Rh(\gamma,p)^{96}Ru$	-3.806
2896	$^{96}Pd(\gamma,\alpha)^{92}Ru$	-4.636	2944	$^{97}Pd(p,\alpha)^{94}Rh$	-0.554
2897	$^{96}Pd(\gamma,p)^{95}Rh$	-5.124	2945	$^{97}Pd(p,\gamma)^{98}Ag$	2.370
2898	$^{96}Pd(\beta^+)^{96}Rh$	3.130	2946	$^{97}Pd(\alpha,p)^{100}Ag$	-4.505
2899	$^{96}Ag(p,\alpha)^{93}Pd$	-1.010	2947	$^{97}Pd(\alpha,\gamma)^{101}Cd$	0.379
2900	$^{96}Ag(p,\gamma)^{97}Cd^a$	3.258	2948	$^{97}Pd(\beta^+)^{97}Rh$	4.862
2901	$^{96}Ag(\alpha,p)^{99}Cd$	0.769	2949	$^{97}Pd(\gamma,\alpha)^{93}Ru$	-2.952
2902	$^{96}Ag(\alpha,\gamma)^{100}In$	2.831	2950	$^{97}Pd(\gamma,p)^{96}Rh$	-5.463
2903	$^{96}Ag(\gamma,\alpha)^{92}Rh$	-4.404	2951	$^{97}Ag(p,\alpha)^{94}Pd$	-0.004
2904	$^{96}Ag(\gamma,p)^{95}Pd$	-1.866	2952	$^{97}Ag(p,\gamma)^{98}Cd^a$	4.319
2905	$^{96}Ag(\beta^+)^{96}Pd$	12.130	2953	$^{97}Ag(\alpha,p)^{100}Cd$	-1.110
2906	$^{96}Cd(p,\alpha)^{93}Ag$	-4.741	2954	$^{97}Ag(\alpha,\gamma)^{101}In$	0.825
2907	$^{96}Cd(p,\gamma)^{97}In^a$	-0.344	2955	$^{97}Ag(\gamma,\alpha)^{93}Rh$	-4.369
2908	$^{96}Cd(\alpha,p)^{99}In$	1.454	2956	$^{97}Ag(\gamma,p)^{96}Pd$	-1.735
2909	$^{96}Cd(\alpha,\gamma)^{100}Sn$	4.441	2957	$^{97}Ag(\beta^+)^{97}Pd$	6.700
2910	$^{96}Cd(\beta^+)^{96}Ag^a$	8.710	2958	$^{97}Cd(p,\gamma)^{98}In^a$	0.892
2911	$^{96}Cd(\gamma,\alpha)^{92}Pd$	-4.249	2959	$^{97}Cd(p,\alpha)^{94}Ag$	-3.644
2912	$^{96}Cd(\gamma,p)^{95}Ag^a$	-3.201	2960	$^{97}Cd(\alpha,\gamma)^{101}Sn$	2.895
2913	$^{96}In(p,\alpha)^{93}Cd$	-3.543	2961	$^{97}Cd(\alpha,p)^{100}In$	-0.427
2914	$^{96}In(p,\gamma)^{97}Sn$	0.795	2962	$^{97}Cd(\gamma,p)^{96}Ag^a$	-3.258
2915	$^{96}In(\alpha,p)^{99}Sn$	4.850	2963	$^{97}Cd(\beta^+)^{97}Ag^a$	10.610
2916	$^{96}In(\beta^+)^{96}Cd^a$	16.840	2964	$^{97}Cd(\gamma,\alpha)^{93}Pd$	-4.268
2917	$^{96}In(\gamma,\alpha)^{92}Ag$	-4.236	2965	$^{97}In(p,\alpha)^{94}Cd$	-2.917
2918	$^{96}In(\gamma,p)^{95}Cd^a$	0.378	2966	$^{97}In(p,\gamma)^{98}Sn$	1.651
2919	$^{97}Mo(p,\gamma)^{98}Tc$	6.176	2967	$^{97}In(\alpha,p)^{100}Sn$	4.785
2920	$^{97}Mo(\alpha,\gamma)^{101}Ru$	2.833	2968	$^{97}In(\gamma,\alpha)^{93}Ag$	-4.397
2921	$^{97}Mo(\alpha,p)^{100}Tc$	-6.389	2969	$^{97}In(\gamma,p)^{96}Cd^a$	0.344
2922	$^{97}Mo(\gamma,\alpha)^{93}Zr$	-2.848	2970	$^{97}In(\beta^+)^{97}Cd^a$	12.310
2923	$^{97}Tc(p,\alpha)^{94}Mo$	6.054	2971	$^{97}Sn(\beta^+)^{97}In$	15.700
2924	$^{97}Tc(p,\gamma)^{98}Ru$	8.292	2972	$^{97}Sn(\gamma,\alpha)^{93}Cd$	-4.338
2925	$^{97}Tc(\alpha,\gamma)^{101}Rh$	2.612	2973	$^{97}Sn(\gamma,p)^{96}In$	-0.795
2926	$^{97}Tc(\alpha,p)^{100}Ru$	-2.866	2974	$^{98}Mo(p,\gamma)^{99}Tc$	6.500
2927	$^{97}Tc(\gamma,\alpha)^{93}Nb$	-2.436	2975	$^{98}Mo(\alpha,\gamma)^{102}Ru$	3.410
2928	$^{97}Tc(\gamma,p)^{96}Mo$	-5.719	2976	$^{98}Mo(\gamma,\alpha)^{94}Zr$	-3.270

Table C.2: – Continued.

Number	Reaction	Energy (Mev)	Number	Reaction	Energy (Mev)
2977	$^{98}Tc(p,\alpha)^{95}Mo$	6.144	3025	$^{98}Sn(\beta^+)^{98}In$	11.550
2978	$^{98}Tc(p,\gamma)^{99}Ru$	8.478	3026	$^{99}Mo(p,\gamma)^{100}Tc$	7.339
2979	$^{98}Tc(\alpha,\gamma)^{102}Rh$	2.772	3027	$^{99}Mo(\alpha,\gamma)^{103}Ru$	3.718
2980	$^{98}Tc(\alpha,p)^{101}Ru$	-3.343	3028	$^{99}Mo(\gamma,\alpha)^{95}Zr$	-2.733
2981	$^{98}Tc(\gamma,p)^{97}Mo$	-6.176	3029	$^{99}Mo(\beta^+)^{99}Tc$	0.846
2982	$^{98}Tc(\beta^+)^{98}Ru$	1.285	3030	$^{99}Tc(p,\alpha)^{96}Mo$	6.332
2983	$^{98}Ru(p,\alpha)^{95}Tc$	2.657	3031	$^{99}Tc(p,\gamma)^{100}Ru$	9.184
2984	$^{98}Ru(p,\gamma)^{99}Rh$	4.579	3032	$^{99}Tc(\alpha,\gamma)^{103}Rh$	3.124
2985	$^{98}Ru(\alpha,\gamma)^{102}Pd$	2.127	3033	$^{99}Tc(\alpha,p)^{102}Ru$	-3.089
2986	$^{98}Ru(\alpha,p)^{101}Rh$	-5.680	3034	$^{99}Tc(\gamma,p)^{98}Mo$	-6.500
2987	$^{98}Ru(\gamma,\alpha)^{94}Mo$	-2.238	3035	$^{99}Tc(\beta^+)^{99}Ru$	-0.217
2988	$^{98}Ru(\gamma,p)^{97}Tc$	-8.292	3036	$^{99}Ru(p,\alpha)^{96}Tc$	3.065
2989	$^{98}Rh(p,\gamma)^{99}Pd$	6.271	3037	$^{99}Ru(p,\gamma)^{100}Rh$	5.261
2990	$^{98}Rh(p,\alpha)^{95}Ru$	5.142	3038	$^{99}Ru(\alpha,\gamma)^{103}Pd$	2.287
2991	$^{98}Rh(\alpha,\gamma)^{102}Ag$	1.261	3039	$^{99}Ru(\alpha,p)^{102}Rh$	-5.706
2992	$^{98}Rh(\alpha,p)^{101}Pd$	-2.603	3040	$^{99}Ru(\gamma,p)^{98}Tc$	-8.478
2993	$^{98}Rh(\beta^+)^{98}Ru$	5.057	3041	$^{99}Ru(\gamma,\alpha)^{95}Mo$	-2.334
2994	$^{98}Rh(\gamma,\alpha)^{94}Tc$	-1.437	3042	$^{99}Rh(p,\gamma)^{100}Pd$	7.001
2995	$^{98}Rh(\gamma,p)^{97}Ru$	-4.349	3043	$^{99}Rh(p,\alpha)^{96}Ru$	5.416
2996	$^{98}Pd(p,\alpha)^{95}Rh$	1.905	3044	$^{99}Rh(\alpha,\gamma)^{103}Ag$	1.702
2997	$^{98}Pd(p,\gamma)^{99}Ag$	2.714	3045	$^{99}Rh(\alpha,p)^{102}Pd$	-2.452
2998	$^{98}Pd(\alpha,\gamma)^{102}Cd$	0.546	3046	$^{99}Rh(\beta^+)^{99}Ru$	2.099
2999	$^{98}Pd(\alpha,p)^{101}Ag$	-4.934	3047	$^{99}Rh(\gamma,\alpha)^{95}Tc$	-1.922
3000	$^{98}Pd(\gamma,\alpha)^{94}Ru$	-1.157	3048	$^{99}Rh(\gamma,p)^{98}Ru$	-4.579
3001	$^{98}Pd(\gamma,p)^{97}Rh$	-6.000	3049	$^{99}Pd(p,\alpha)^{96}Rh$	2.335
3002	$^{98}Pd(\beta^+)^{98}Rh$	1.676	3050	$^{99}Pd(p,\gamma)^{100}Ag$	3.293
3003	$^{98}Ag(p,\gamma)^{99}Cd^a$	4.108	3051	$^{99}Pd(\alpha,p)^{102}Ag$	-5.011
3004	$^{98}Ag(p,\alpha)^{95}Pd$	1.473	3052	$^{99}Pd(\alpha,\gamma)^{103}Cd$	0.925
3005	$^{98}Ag(\alpha,\gamma)^{102}In$	0.066	3053	$^{99}Pd(\gamma,p)^{98}Rh$	-6.271
3006	$^{98}Ag(\alpha,p)^{101}Cd$	-1.991	3054	$^{99}Pd(\beta^+)^{99}Rh$	3.498
3007	$^{98}Ag(\gamma,\alpha)^{94}Rh$	-2.924	3055	$^{99}Pd(\gamma,\alpha)^{95}Ru$	-1.129
3008	$^{98}Ag(\gamma,p)^{97}Pd$	-2.370	3056	$^{99}Ag(p,\alpha)^{96}Pd$	4.315
3009	$^{98}Ag(\beta^+)^{98}Pd$	8.420	3057	$^{99}Ag(p,\gamma)^{100}Cd$	4.833
3010	$^{98}Cd(p,\gamma)^{99}In^a$	1.292	3058	$^{99}Ag(\alpha,p)^{102}Cd$	-2.168
3011	$^{98}Cd(p,\alpha)^{95}Ag$	-3.363	3059	$^{99}Ag(\alpha,\gamma)^{103}In$	0.305
3012	$^{98}Cd(\alpha,\gamma)^{102}Sn$	0.639	3060	$^{99}Ag(\gamma,\alpha)^{95}Rh$	-0.809
3013	$^{98}Cd(\alpha,p)^{101}In$	-3.494	3061	$^{99}Ag(\gamma,p)^{98}Pd$	-2.714
3014	$^{98}Cd(\gamma,\alpha)^{94}Pd$	-4.323	3062	$^{99}Ag(\beta^+)^{99}Pd$	5.430
3015	$^{98}Cd(\gamma,p)^{97}Ag^a$	-4.319	3063	$^{99}Cd(p,\gamma)^{100}In^a$	2.062
3016	$^{98}Cd(\beta^+)^{98}Ag^a$	5.200	3064	$^{99}Cd(p,\alpha)^{96}Ag$	-0.769
3017	$^{98}In(p,\gamma)^{99}Sn$	1.887	3065	$^{99}Cd(\alpha,\gamma)^{103}Sn$	0.573
3018	$^{98}In(p,\alpha)^{95}Cd$	-2.585	3066	$^{99}Cd(\alpha,p)^{102}In$	-3.522
3019	$^{98}In(\alpha,p)^{101}Sn$	2.003	3067	$^{99}Cd(\beta^+)^{99}Ag$	6.890
3020	$^{98}In(\gamma,p)^{97}Cd^a$	-0.892	3068	$^{99}Cd(\gamma,\alpha)^{95}Pd$	-2.635
3021	$^{98}In(\beta^+)^{98}Cd^a$	14.040	3069	$^{99}Cd(\gamma,p)^{98}Ag^a$	-4.108
3022	$^{98}In(\gamma,\alpha)^{94}Ag$	-4.536	3070	$^{99}In(p,\alpha)^{96}Cd$	-1.454
3023	$^{98}Sn(\gamma,\alpha)^{94}Cd$	-4.568	3071	$^{99}In(p,\gamma)^{100}Sn^a$	2.987
3024	$^{98}Sn(\gamma,p)^{97}In$	-1.651	3072	$^{99}In(\alpha,p)^{102}Sn$	-0.653

Table C.2: – Continued.

Number	Reaction	Energy (Mev)	Number	Reaction	Energy (Mev)
3073	$^{99}In(\beta^+)^{99}Cd^a$	8.020	3121	$^{100}In(p,\alpha)^{97}Cd$	0.427
3074	$^{99}In(\gamma,\alpha)^{95}Ag$	-4.655	3122	$^{100}In(p,\gamma)^{101}Sn^a$	3.322
3075	$^{99}In(\gamma,p)^{98}Cd^a$	-1.292	3123	$^{100}In(\alpha,p)^{103}Sn$	-1.489
3076	$^{99}Sn(p,\alpha)^{96}In$	-4.850	3124	$^{100}In(\alpha,\gamma)^{104}Sb$	-3.189
3077	$^{99}Sn(\beta^+)^{99}In$	13.440	3125	$^{100}In(\beta^+)^{100}Cd$	9.655
3078	$^{99}Sn(\gamma,\alpha)^{95}Cd$	-4.472	3126	$^{100}In(\gamma,\alpha)^{96}Ag$	-2.831
3079	$^{99}Sn(\gamma,p)^{98}In$	-1.887	3127	$^{100}In(\gamma,p)^{99}Cd^a$	-2.062
3080	$^{100}Mo(\alpha,\gamma)^{104}Ru$	4.332	3128	$^{100}Sn(p,\alpha)^{97}In$	-4.785
3081	$^{100}Mo(\gamma,\alpha)^{96}Zr$	-3.168	3129	$^{100}Sn(\gamma,p)^{99}In^a$	-2.987
3082	$^{100}Tc(p,\gamma)^{101}Ru$	9.222	3130	$^{100}Sn(\beta^+)^{100}In^a$	6.880
3083	$^{100}Tc(p,\alpha)^{97}Mo$	6.389	3131	$^{100}Sn(\gamma,\alpha)^{96}Cd$	-4.441
3084	$^{100}Tc(\alpha,p)^{103}Ru$	-3.622	3132	$^{101}Ru(p,\gamma)^{102}Rh$	6.115
3085	$^{100}Tc(\beta^+)^{100}Ru$	2.690	3133	$^{101}Ru(p,\alpha)^{98}Tc$	3.343
3086	$^{100}Tc(\gamma,p)^{99}Mo$	-7.339	3134	$^{101}Ru(\alpha,\gamma)^{105}Pd$	2.889
3087	$^{100}Ru(p,\gamma)^{101}Rh$	5.478	3135	$^{101}Ru(\gamma,p)^{100}Tc$	-9.222
3088	$^{100}Ru(p,\alpha)^{97}Tc$	2.866	3136	$^{101}Ru(\gamma,\alpha)^{97}Mo$	-2.833
3089	$^{100}Ru(\alpha,p)^{103}Rh$	-6.061	3137	$^{101}Rh(p,\alpha)^{98}Ru$	5.680
3090	$^{100}Ru(\alpha,\gamma)^{104}Pd$	2.597	3138	$^{101}Rh(p,\gamma)^{102}Pd$	7.807
3091	$^{100}Ru(\gamma,p)^{99}Tc$	-9.184	3139	$^{101}Rh(\alpha,\gamma)^{105}Ag$	2.085
3092	$^{100}Ru(\gamma,\alpha)^{96}Mo$	-2.852	3140	$^{101}Rh(\alpha,p)^{104}Pd$	-2.881
3093	$^{100}Rh(p,\alpha)^{97}Ru$	5.381	3141	$^{101}Rh(\beta^+)^{101}Ru$	0.536
3094	$^{100}Rh(p,\gamma)^{101}Pd$	7.128	3142	$^{101}Rh(\gamma,\alpha)^{97}Tc$	-2.612
3095	$^{100}Rh(\alpha,\gamma)^{104}Ag$	1.948	3143	$^{101}Rh(\gamma,p)^{100}Ru$	-5.478
3096	$^{100}Rh(\alpha,p)^{103}Pd$	-2.974	3144	$^{101}Pd(p,\alpha)^{98}Rh$	2.603
3097	$^{100}Rh(\gamma,p)^{99}Ru$	-5.261	3145	$^{101}Pd(p,\gamma)^{102}Ag$	3.864
3098	$^{100}Rh(\beta^+)^{100}Ru$	3.628	3146	$^{101}Pd(\alpha,p)^{104}Ag$	-5.180
3099	$^{100}Rh(\gamma,\alpha)^{96}Tc$	-2.196	3147	$^{101}Pd(\alpha,\gamma)^{105}Cd$	1.326
3100	$^{100}Pd(p,\alpha)^{97}Rh$	2.221	3148	$^{101}Pd(\gamma,\alpha)^{97}Ru$	-1.747
3101	$^{100}Pd(p,\gamma)^{101}Ag$	3.287	3149	$^{101}Pd(\gamma,p)^{100}Rh$	-7.128
3102	$^{100}Pd(\alpha,\gamma)^{104}Cd$	1.174	3150	$^{101}Pd(\beta^+)^{101}Rh$	1.957
3103	$^{100}Pd(\alpha,p)^{103}Ag$	-5.299	3151	$^{101}Ag(p,\gamma)^{102}Cd$	5.480
3104	$^{100}Pd(\gamma,p)^{99}Rh$	-7.001	3152	$^{101}Ag(p,\alpha)^{98}Pd$	4.934
3105	$^{100}Pd(\beta^+)^{100}Rh$	0.454	3153	$^{101}Ag(\alpha,\gamma)^{105}In$	0.681
3106	$^{100}Pd(\gamma,\alpha)^{96}Ru$	-1.585	3154	$^{101}Ag(\alpha,p)^{104}Cd$	-2.113
3107	$^{100}Ag(p,\alpha)^{97}Pd$	4.505	3155	$^{101}Ag(\gamma,\alpha)^{97}Rh$	-1.066
3108	$^{100}Ag(p,\gamma)^{101}Cd$	4.884	3156	$^{101}Ag(\gamma,p)^{100}Pd$	-3.287
3109	$^{100}Ag(\alpha,p)^{103}Cd$	-2.367	3157	$^{101}Ag(\beta^+)^{101}Pd$	4.204
3110	$^{100}Ag(\alpha,\gamma)^{104}In$	0.339	3158	$^{101}Cd(p,\alpha)^{98}Ag$	1.991
3111	$^{100}Ag(\gamma,p)^{99}Pd$	-3.293	3159	$^{101}Cd(p,\gamma)^{102}In$	2.057
3112	$^{100}Ag(\beta^+)^{100}Pd$	7.046	3160	$^{101}Cd(\alpha,p)^{104}In$	-4.546
3113	$^{100}Ag(\gamma,\alpha)^{96}Rh$	-0.958	3161	$^{101}Cd(\alpha,\gamma)^{105}Sn$	-0.091
3114	$^{100}Cd(p,\alpha)^{97}Ag$	1.110	3162	$^{101}Cd(\gamma,\alpha)^{97}Pd$	-0.379
3115	$^{100}Cd(p,\gamma)^{101}In$	1.935	3163	$^{101}Cd(\gamma,p)^{100}Ag$	-4.884
3116	$^{100}Cd(\alpha,p)^{103}In$	-4.527	3164	$^{101}Cd(\beta^+)^{101}Ag$	5.476
3117	$^{100}Cd(\alpha,\gamma)^{104}Sn$	-0.286	3165	$^{101}In(p,\gamma)^{102}Sn^a$	4.133
3118	$^{100}Cd(\beta^+)^{100}Ag$	3.876	3166	$^{101}In(p,\alpha)^{98}Cd$	3.494
3119	$^{100}Cd(\gamma,\alpha)^{96}Pd$	-0.518	3167	$^{101}In(\alpha,\gamma)^{105}Sb$	-3.199
3120	$^{100}Cd(\gamma,p)^{99}Ag$	-4.833	3168	$^{101}In(\alpha,p)^{104}Sn$	-1.706

Table C.2: – Continued.

Number	Reaction	Energy (Mev)	Number	Reaction	Energy (Mev)
3169	$^{101}In(\beta^+)^{101}Cd$	6.410	3217	$^{102}Sn(p,\alpha)^{99}In$	0.653
3170	$^{101}In(\gamma,\alpha)^{97}Ag$	-0.825	3218	$^{102}Sn(\alpha,\gamma)^{106}Te$	-6.015
3171	$^{101}In(\gamma,p)^{100}Cd$	-1.935	3219	$^{102}Sn(\alpha,p)^{105}Sb$	-7.332
3172	$^{101}Sn(p,\alpha)^{98}In$	-2.003	3220	$^{102}Sn(\gamma,\alpha)^{98}Cd$	-0.639
3173	$^{101}Sn(\alpha,\gamma)^{105}Te$	-6.314	3221	$^{102}Sn(\gamma,p)^{101}In^a$	-4.133
3174	$^{101}Sn(\alpha,p)^{104}Sb$	-6.511	3222	$^{102}Sn(\beta^+)^{102}In^a$	5.150
3175	$^{101}Sn(\beta^+)^{101}In^a$	8.550	3223	$^{103}Ru(p,\alpha)^{100}Tc$	3.622
3176	$^{101}Sn(\gamma,\alpha)^{97}Cd$	-2.895	3224	$^{103}Ru(\alpha,\gamma)^{107}Pd$	3.537
3177	$^{101}Sn(\gamma,p)^{100}In^a$	-3.322	3225	$^{103}Ru(\gamma,\alpha)^{99}Mo$	-3.718
3178	$^{102}Ru(p,\alpha)^{99}Tc$	3.089	3226	$^{103}Ru(\beta^+)^{103}Rh$	0.257
3179	$^{102}Ru(p,\gamma)^{103}Rh$	6.213	3227	$^{103}Rh(p,\alpha)^{100}Ru$	6.061
3180	$^{102}Ru(\alpha,\gamma)^{106}Pd$	3.231	3228	$^{103}Rh(p,\gamma)^{104}Pd$	8.658
3181	$^{102}Ru(\gamma,\alpha)^{98}Mo$	-3.410	3229	$^{103}Rh(\alpha,\gamma)^{107}Ag$	2.807
3182	$^{102}Rh(p,\alpha)^{99}Ru$	5.706	3230	$^{103}Rh(\alpha,p)^{106}Pd$	-2.983
3183	$^{102}Rh(p,\gamma)^{103}Pd$	7.993	3231	$^{103}Rh(\gamma,p)^{102}Ru$	-6.213
3184	$^{102}Rh(\alpha,\gamma)^{106}Ag$	2.588	3232	$^{103}Rh(\gamma,\alpha)^{99}Tc$	-3.124
3185	$^{102}Rh(\alpha,p)^{105}Pd$	-3.226	3233	$^{103}Pd(p,\alpha)^{100}Rh$	2.974
3186	$^{102}Rh(\beta^+)^{102}Ru$	2.296	3234	$^{103}Pd(p,\gamma)^{104}Ag$	4.922
3187	$^{102}Rh(\beta^+)^{102}Pd$	0.588	3235	$^{103}Pd(\alpha,p)^{106}Ag$	-5.405
3188	$^{102}Rh(\gamma,\alpha)^{98}Tc$	-2.772	3236	$^{103}Pd(\alpha,\gamma)^{107}Cd$	1.933
3189	$^{102}Rh(\gamma,p)^{101}Ru$	-6.115	3237	$^{103}Pd(\gamma,p)^{102}Rh$	-7.993
3190	$^{102}Pd(p,\alpha)^{99}Rh$	2.452	3238	$^{103}Pd(\beta^+)^{103}Rh$	0.722
3191	$^{102}Pd(p,\gamma)^{103}Ag$	4.154	3239	$^{103}Pd(\gamma,\alpha)^{99}Ru$	-2.287
3192	$^{102}Pd(\alpha,\gamma)^{106}Cd$	1.632	3240	$^{103}Ag(p,\gamma)^{104}Cd$	6.473
3193	$^{102}Pd(\alpha,p)^{105}Ag$	-5.722	3241	$^{103}Ag(p,\alpha)^{100}Pd$	5.299
3194	$^{102}Pd(\gamma,\alpha)^{98}Ru$	-2.127	3242	$^{103}Ag(\alpha,\gamma)^{107}In$	1.195
3195	$^{102}Pd(\gamma,p)^{101}Rh$	-7.807	3243	$^{103}Ag(\alpha,p)^{106}Cd$	-2.522
3196	$^{102}Ag(p,\alpha)^{99}Pd$	5.011	3244	$^{103}Ag(\beta^+)^{103}Pd$	2.687
3197	$^{102}Ag(p,\gamma)^{103}Cd$	5.936	3245	$^{103}Ag(\gamma,\alpha)^{99}Rh$	-1.702
3198	$^{102}Ag(\alpha,p)^{105}Cd$	-2.538	3246	$^{103}Ag(\gamma,p)^{102}Pd$	-4.154
3199	$^{102}Ag(\alpha,\gamma)^{106}In$	1.034	3247	$^{103}Cd(p,\alpha)^{100}Ag$	2.367
3200	$^{102}Ag(\gamma,p)^{101}Pd$	-3.864	3248	$^{103}Cd(p,\gamma)^{104}In$	2.706
3201	$^{102}Ag(\beta^+)^{102}Pd$	5.955	3249	$^{103}Cd(\alpha,p)^{106}In$	-4.902
3202	$^{102}Ag(\gamma,\alpha)^{98}Rh$	-1.261	3250	$^{103}Cd(\alpha,\gamma)^{107}Sn$	0.337
3203	$^{102}Cd(p,\alpha)^{99}Ag$	2.168	3251	$^{103}Cd(\gamma,\alpha)^{99}Pd$	-0.925
3204	$^{102}Cd(p,\gamma)^{103}In$	2.473	3252	$^{103}Cd(\gamma,p)^{102}Ag$	-5.936
3205	$^{102}Cd(\alpha,p)^{105}In$	-4.799	3253	$^{103}Cd(\beta^+)^{103}Ag$	4.142
3206	$^{102}Cd(\alpha,\gamma)^{106}Sn$	0.437	3254	$^{103}In(p,\gamma)^{104}Sn^a$	4.241
3207	$^{102}Cd(\gamma,\alpha)^{98}Pd$	-0.546	3255	$^{103}In(p,\alpha)^{100}Cd$	4.527
3208	$^{102}Cd(\gamma,p)^{101}Ag$	-5.480	3256	$^{103}In(\alpha,\gamma)^{107}Sb$	-2.466
3209	$^{102}Cd(\beta^+)^{102}Ag$	2.587	3257	$^{103}In(\alpha,p)^{106}Sn$	-2.081
3210	$^{102}In(p,\alpha)^{99}Cd$	3.522	3258	$^{103}In(\gamma,\alpha)^{99}Ag$	-0.305
3211	$^{102}In(p,\gamma)^{103}Sn^a$	4.095	3259	$^{103}In(\gamma,p)^{102}Cd$	-2.473
3212	$^{102}In(\alpha,p)^{105}Sn$	-2.147	3260	$^{103}In(\beta^+)^{103}Cd$	6.050
3213	$^{102}In(\alpha,\gamma)^{106}Sb$	-1.198	3261	$^{103}Sn(p,\alpha)^{100}In$	1.489
3214	$^{102}In(\gamma,p)^{101}Cd$	-2.057	3262	$^{103}Sn(p,\gamma)^{104}Sb^a$	-1.700
3215	$^{102}In(\beta^+)^{102}Cd$	9.250	3263	$^{103}Sn(\alpha,p)^{106}Sb$	-6.875
3216	$^{102}In(\gamma,\alpha)^{98}Ag$	-0.066	3264	$^{103}Sn(\alpha,\gamma)^{107}Te$	-5.548

Table C.2: – Continued.

Number	Reaction	Energy (Mev)	Number	Reaction	Energy (Mev)
3265	$^{103}Sn(\beta^+)^{103}In^a$	6.870	3313	$^{105}Pd(\alpha,\gamma)^{109}Cd$	2.516
3266	$^{103}Sn(\gamma,\alpha)^{99}Cd$	-0.573	3314	$^{105}Pd(\alpha,p)^{108}Ag$	-5.675
3267	$^{103}Sn(\gamma,p)^{102}In^a$	-4.095	3315	$^{105}Pd(\gamma,\alpha)^{101}Ru$	-2.889
3268	$^{104}Ru(\alpha,\gamma)^{108}Pd$	3.854	3316	$^{105}Ag(p,\alpha)^{102}Pd$	5.722
3269	$^{104}Ru(\gamma,\alpha)^{100}Mo$	-4.332	3317	$^{105}Ag(p,\gamma)^{106}Cd$	7.354
3270	$^{104}Pd(p,\gamma)^{105}Ag$	4.966	3318	$^{105}Ag(\alpha,p)^{108}Cd$	-2.680
3271	$^{104}Pd(p,\alpha)^{101}Rh$	2.881	3319	$^{105}Ag(\alpha,\gamma)^{109}In$	1.841
3272	$^{104}Pd(\alpha,\gamma)^{108}Cd$	2.286	3320	$^{105}Ag(\beta^+)^{105}Pd$	1.346
3273	$^{104}Pd(\alpha,p)^{107}Ag$	-5.851	3321	$^{105}Ag(\gamma,\alpha)^{101}Rh$	-2.085
3274	$^{104}Pd(\gamma,\alpha)^{100}Ru$	-2.597	3322	$^{105}Ag(\gamma,p)^{104}Pd$	-4.966
3275	$^{104}Pd(\gamma,p)^{103}Rh$	-8.658	3323	$^{105}Cd(p,\gamma)^{106}In$	3.572
3276	$^{104}Ag(p,\alpha)^{101}Pd$	5.180	3324	$^{105}Cd(p,\alpha)^{102}Ag$	2.538
3277	$^{104}Ag(p,\gamma)^{105}Cd$	6.506	3325	$^{105}Cd(\alpha,\gamma)^{109}Sn$	0.730
3278	$^{104}Ag(\alpha,p)^{107}Cd$	-2.989	3326	$^{105}Cd(\alpha,p)^{108}In$	-5.089
3279	$^{104}Ag(\alpha,\gamma)^{108}In$	1.417	3327	$^{105}Cd(\gamma,p)^{104}Ag$	-6.506
3280	$^{104}Ag(\gamma,\alpha)^{100}Rh$	-1.948	3328	$^{105}Cd(\beta^+)^{105}Ag$	2.738
3281	$^{104}Ag(\gamma,p)^{103}Pd$	-4.922	3329	$^{105}Cd(\gamma,\alpha)^{101}Pd$	-1.326
3282	$^{104}Ag(\beta^+)^{104}Pd$	4.279	3330	$^{105}In(p,\alpha)^{102}Cd$	4.799
3283	$^{104}Cd(p,\alpha)^{101}Ag$	2.113	3331	$^{105}In(p,\gamma)^{106}Sn$	5.236
3284	$^{104}Cd(p,\gamma)^{105}In$	2.794	3332	$^{105}In(\alpha,p)^{108}Sn$	-2.332
3285	$^{104}Cd(\alpha,p)^{107}In$	-5.278	3333	$^{105}In(\alpha,\gamma)^{109}Sb$	-0.801
3286	$^{104}Cd(\alpha,\gamma)^{108}Sn$	0.462	3334	$^{105}In(\beta^+)^{105}Cd$	4.849
3287	$^{104}Cd(\gamma,\alpha)^{100}Pd$	-1.174	3335	$^{105}In(\gamma,\alpha)^{101}Ag$	-0.681
3288	$^{104}Cd(\gamma,p)^{103}Ag$	-6.473	3336	$^{105}In(\gamma,p)^{104}Cd$	-2.794
3289	$^{104}Cd(\beta^+)^{104}Ag$	1.136	3337	$^{105}Sn(p,\gamma)^{106}Sb^a$	0.949
3290	$^{104}In(p,\alpha)^{101}Cd$	4.546	3338	$^{105}Sn(p,\alpha)^{102}In$	2.147
3291	$^{104}In(p,\gamma)^{105}Sn^a$	4.455	3339	$^{105}Sn(\alpha,\gamma)^{109}Te$	-3.226
3292	$^{104}In(\alpha,p)^{107}Sn$	-2.761	3340	$^{105}Sn(\alpha,p)^{108}Sb$	-5.631
3293	$^{104}In(\alpha,\gamma)^{108}Sb$	-2.177	3341	$^{105}Sn(\beta^+)^{105}In$	6.257
3294	$^{104}In(\beta^+)^{104}Cd$	7.909	3342	$^{105}Sn(\gamma,\alpha)^{101}Cd$	0.091
3295	$^{104}In(\gamma,\alpha)^{100}Ag$	-0.339	3343	$^{105}Sn(\gamma,p)^{104}In^a$	-4.455
3296	$^{104}In(\gamma,p)^{103}Cd$	-2.706	3344	$^{105}Sb(p,\alpha)^{102}Sn$	7.332
3297	$^{104}Sn(p,\alpha)^{101}In$	1.706	3345	$^{105}Sb(p,\gamma)^{106}Te^a$	1.317
3298	$^{104}Sn(p,\gamma)^{105}Sb^a$	-1.493	3346	$^{105}Sb(\alpha,\gamma)^{109}I$	-4.481
3299	$^{104}Sn(\alpha,p)^{107}Sb$	-5.662	3347	$^{105}Sb(\alpha,p)^{108}Te$	-3.661
3300	$^{104}Sn(\alpha,\gamma)^{108}Te$	-3.442	3348	$^{105}Sb(\beta^+)^{105}Sn^a$	9.443
3301	$^{104}Sn(\gamma,\alpha)^{100}Cd$	0.286	3349	$^{105}Sb(\gamma,\alpha)^{101}In$	3.199
3302	$^{104}Sn(\gamma,p)^{103}In^a$	-4.241	3350	$^{105}Sb(\gamma,p)^{104}Sn^a$	1.493
3303	$^{104}Sn(\beta^+)^{104}In^a$	4.515	3351	$^{105}Te(\alpha,\gamma)^{109}Xe$	-4.807
3304	$^{104}Sb(p,\alpha)^{101}Sn$	6.511	3352	$^{105}Te(\alpha,p)^{108}I$	-5.170
3305	$^{104}Sb(p,\gamma)^{105}Te$	0.197	3353	$^{105}Te(\gamma,\alpha)^{101}Sn$	6.305
3306	$^{104}Sb(\alpha,p)^{107}Te$	-3.848	3354	$^{105}Te(\gamma,p)^{104}Sb$	-0.197
3307	$^{104}Sb(\alpha,\gamma)^{108}I$	-4.973	3355	$^{105}Te(\beta^+)^{105}Sb$	11.660
3308	$^{104}Sb(\gamma,p)^{103}Sn^a$	1.700	3356	$^{106}Pd(p,\gamma)^{107}Ag$	5.790
3309	$^{104}Sb(\beta^+)^{104}Sn^a$	13.350	3357	$^{106}Pd(p,\alpha)^{103}Rh$	2.983
3310	$^{104}Sb(\gamma,\alpha)^{100}In$	3.189	3358	$^{106}Pd(\alpha,p)^{109}Ag$	-6.049
3311	$^{105}Pd(p,\gamma)^{106}Ag$	5.814	3359	$^{106}Pd(\gamma,\alpha)^{102}Ru$	-3.231
3312	$^{105}Pd(p,\alpha)^{102}Rh$	3.226	3360	$^{106}Ag(p,\alpha)^{103}Pd$	5.405

Table C.2: – Continued.

Number	Reaction	Energy (Mev)	Number	Reaction	Energy (Mev)
3361	$^{106}Ag(p,\gamma)^{107}Cd$	7.338	3409	$^{107}In(p,\alpha)^{104}Cd$	5.278
3362	$^{106}Ag(\alpha,p)^{109}Cd$	-3.298	3410	$^{107}In(\gamma,p)^{106}Cd$	-3.717
3363	$^{106}Ag(\gamma,p)^{105}Pd$	-5.814	3411	$^{107}In(\beta^+)^{107}Cd$	3.426
3364	$^{106}Ag(\beta^+)^{106}Pd$	2.965	3412	$^{107}In(\gamma,\alpha)^{103}Ag$	-1.195
3365	$^{106}Ag(\gamma,\alpha)^{102}Rh$	-2.588	3413	$^{107}Sn(p,\gamma)^{108}Sb$	0.584
3366	$^{106}Cd(p,\alpha)^{103}Ag$	2.522	3414	$^{107}Sn(p,\alpha)^{104}In$	2.761
3367	$^{106}Cd(p,\gamma)^{107}In$	3.717	3415	$^{107}Sn(\alpha,\gamma)^{111}Te$	-2.663
3368	$^{106}Cd(\alpha,p)^{109}In$	-5.513	3416	$^{107}Sn(\alpha,p)^{110}Sb$	-6.611
3369	$^{106}Cd(\gamma,p)^{105}Ag$	-7.354	3417	$^{107}Sn(\beta^+)^{107}In$	5.006
3370	$^{106}Cd(\gamma,\alpha)^{102}Pd$	-1.632	3418	$^{107}Sn(\gamma,\alpha)^{103}Cd$	-0.337
3371	$^{106}In(p,\alpha)^{103}Cd$	4.902	3419	$^{107}Sn(\gamma,p)^{106}In$	-5.239
3372	$^{106}In(p,\gamma)^{107}Sn$	5.239	3420	$^{107}Sb(p,\gamma)^{108}Te$	2.220
3373	$^{106}In(\alpha,p)^{109}Sn$	-2.842	3421	$^{107}Sb(p,\alpha)^{104}Sn$	5.662
3374	$^{106}In(\alpha,\gamma)^{110}Sb$	-1.372	3422	$^{107}Sb(\alpha,\gamma)^{111}I$	-3.582
3375	$^{106}In(\gamma,\alpha)^{102}Ag$	-1.034	3423	$^{107}Sb(\alpha,p)^{110}Te$	-3.648
3376	$^{106}In(\gamma,p)^{105}Cd$	-3.572	3424	$^{107}Sb(\gamma,\alpha)^{103}In$	2.466
3377	$^{106}In(\beta^+)^{106}Cd$	6.524	3425	$^{107}Sb(\gamma,p)^{106}Sn$	0.385
3378	$^{106}Sn(p,\gamma)^{107}Sb$	-0.385	3426	$^{107}Sb(\beta^+)^{107}Sn$	8.530
3379	$^{106}Sn(p,\alpha)^{103}In$	2.081	3427	$^{107}Te(p,\alpha)^{104}Sb$	3.848
3380	$^{106}Sn(\alpha,\gamma)^{110}Te$	-2.723	3428	$^{107}Te(p,\gamma)^{108}I$	-1.125
3381	$^{106}Sn(\alpha,p)^{109}Sb$	-6.037	3429	$^{107}Te(\alpha,\gamma)^{111}Xe$	-4.078
3382	$^{106}Sn(\gamma,\alpha)^{102}Cd$	-0.437	3430	$^{107}Te(\alpha,p)^{110}I$	-5.360
3383	$^{106}Sn(\gamma,p)^{105}In$	-5.236	3431	$^{107}Te(\gamma,p)^{106}Sb^a$	-1.327
3384	$^{106}Sn(\beta^+)^{106}In$	3.185	3432	$^{107}Te(\beta^+)^{107}Sb$	9.960
3385	$^{106}Sb(p,\alpha)^{103}Sn$	6.875	3433	$^{107}Te(\gamma,\alpha)^{103}Sn$	5.555
3386	$^{106}Sb(p,\gamma)^{107}Te^a$	1.327	3434	$^{108}Pd(p,\gamma)^{109}Ag$	6.487
3387	$^{106}Sb(\alpha,\gamma)^{110}I$	-3.581	3435	$^{108}Pd(\gamma,\alpha)^{104}Ru$	-3.854
3388	$^{106}Sb(\alpha,p)^{109}Te$	-4.175	3436	$^{108}Ag(p,\alpha)^{105}Pd$	5.675
3389	$^{106}Sb(\gamma,\alpha)^{102}In$	1.198	3437	$^{108}Ag(p,\gamma)^{109}Cd$	8.191
3390	$^{106}Sb(\gamma,p)^{105}Sn^a$	-0.949	3438	$^{108}Ag(\beta^+)^{108}Cd$	1.918
3391	$^{106}Sb(\beta^+)^{106}Sn$	10.528	3439	$^{108}Ag(\gamma,p)^{107}Pd$	-6.520
3392	$^{106}Te(\alpha,p)^{109}I$	-5.798	3440	$^{108}Cd(p,\alpha)^{105}Ag$	2.680
3393	$^{106}Te(\alpha,\gamma)^{110}Xe$	-4.607	3441	$^{108}Cd(p,\gamma)^{109}In$	4.521
3394	$^{106}Te(\gamma,p)^{105}Sb^a$	-1.317	3442	$^{108}Cd(\gamma,\alpha)^{104}Pd$	-2.286
3395	$^{106}Te(\beta^+)^{106}Sb^a$	8.390	3443	$^{108}Cd(\gamma,p)^{107}Ag$	-8.137
3396	$^{106}Te(\gamma,\alpha)^{102}Sn$	6.015	3444	$^{108}In(p,\alpha)^{105}Cd$	5.089
3397	$^{107}Pd(p,\gamma)^{108}Ag$	6.520	3445	$^{108}In(p,\gamma)^{109}Sn$	5.819
3398	$^{107}Pd(\gamma,\alpha)^{103}Ru$	-3.537	3446	$^{108}In(\gamma,p)^{107}Cd$	-4.406
3399	$^{107}Ag(p,\alpha)^{104}Pd$	5.851	3447	$^{108}In(\beta^+)^{108}Cd$	5.157
3400	$^{107}Ag(p,\gamma)^{108}Cd$	8.137	3448	$^{108}In(\gamma,\alpha)^{104}Ag$	-1.417
3401	$^{107}Ag(\gamma,\alpha)^{103}Rh$	-2.807	3449	$^{108}Sn(p,\gamma)^{109}Sb$	1.531
3402	$^{107}Ag(\gamma,p)^{106}Pd$	-5.790	3450	$^{108}Sn(p,\alpha)^{105}In$	2.332
3403	$^{107}Cd(p,\alpha)^{104}Ag$	2.989	3451	$^{108}Sn(\gamma,p)^{107}In$	-5.740
3404	$^{107}Cd(p,\gamma)^{108}In$	4.406	3452	$^{108}Sn(\beta^+)^{108}In$	2.092
3405	$^{107}Cd(\gamma,\alpha)^{103}Pd$	-1.933	3453	$^{108}Sn(\gamma,\alpha)^{104}Cd$	-0.462
3406	$^{107}Cd(\gamma,p)^{106}Ag$	-7.338	3454	$^{108}Sb(p,\alpha)^{105}Sn$	5.631
3407	$^{107}Cd(\beta^+)^{107}Ag$	1.417	3455	$^{108}Sb(p,\gamma)^{109}Te$	2.405
3408	$^{107}In(p,\gamma)^{108}Sn$	5.740	3456	$^{108}Sb(\alpha,p)^{111}Te$	-3.966

Table C.2: – Continued.

Number	Reaction	Energy (Mev)	Number	Reaction	Energy (Mev)
3457	$^{108}Sb(\alpha,\gamma)^{112}I$	-3.028	3504	$^{109}I(\gamma,p)^{108}Te$	0.820
3458	$^{108}Sb(\gamma,\alpha)^{104}In$	2.177	3505	$^{109}I(\gamma,\alpha)^{105}Sb$	4.481
3459	$^{108}Sb(\gamma,p)^{107}Sn$	-0.584	3506	$^{109}I(\beta^+)^{109}Te$	10.000
3460	$^{108}Sb(\beta^+)^{108}Sn$	10.070	3507	$^{109}Xe(\gamma,p)^{108}I$	-0.363
3461	$^{108}Te(p,\alpha)^{105}Sb$	3.661	3508	$^{109}Xe(\gamma,\alpha)^{105}Te$	4.807
3462	$^{108}Te(p,\gamma)^{109}I$	-0.820	3509	$^{109}Xe(\beta^+)^{109}I$	11.990
3463	$^{108}Te(\alpha,p)^{111}I$	-5.493	3510	$^{110}Sb(p,\alpha)^{107}Sn$	6.611
3464	$^{108}Te(\alpha,\gamma)^{112}Xe$	-3.317	3511	$^{110}Sb(p,\gamma)^{111}Te$	3.948
3465	$^{108}Te(\beta^+)^{108}Sb$	6.890	3512	$^{110}Sb(\gamma,p)^{109}Sn$	-1.470
3466	$^{108}Te(\gamma,\alpha)^{104}Sn$	3.444	3513	$^{110}Sb(\gamma,\alpha)^{106}In$	1.372
3467	$^{108}Te(\gamma,p)^{107}Sb$	-2.220	3514	$^{110}Te(p,\alpha)^{107}Sb$	3.648
3468	$^{108}I(p,\gamma)^{109}Xe$	0.363	3515	$^{110}Te(p,\gamma)^{111}I$	0.066
3469	$^{108}I(p,\alpha)^{105}Te$	5.170	3516	$^{110}Te(\beta^+)^{110}Sb$	4.540
3470	$^{108}I(\alpha,p)^{111}Xe$	-2.953	3517	$^{110}Te(\gamma,p)^{109}Sb$	-3.314
3471	$^{108}I(\gamma,\alpha)^{104}Sb$	4.975	3518	$^{110}Te(\gamma,\alpha)^{106}Sn$	2.723
3472	$^{108}I(\beta^+)^{108}Te$	13.300	3519	$^{110}I(p,\gamma)^{111}Xe$	1.282
3473	$^{108}I(\gamma,p)^{107}Te$	1.125	3520	$^{110}I(p,\alpha)^{107}Te$	5.360
3474	$^{109}Ag(p,\alpha)^{106}Pd$	6.049	3521	$^{110}I(\alpha,p)^{113}Xe$	-3.690
3475	$^{109}Ag(\gamma,p)^{108}Pd$	-6.487	3522	$^{110}I(\gamma,p)^{109}Te$	-0.594
3476	$^{109}Cd(p,\alpha)^{106}Ag$	3.298	3523	$^{110}I(\gamma,\alpha)^{106}Sb$	3.581
3477	$^{109}Cd(\beta^+)^{109}Ag$	0.215	3524	$^{110}I(\beta^+)^{110}Te$	11.389
3478	$^{109}Cd(\gamma,\alpha)^{105}Pd$	-2.516	3525	$^{110}Xe(\gamma,p)^{109}I$	-1.191
3479	$^{109}Cd(\gamma,p)^{108}Ag$	-8.191	3526	$^{110}Xe(\gamma,\alpha)^{106}Te$	4.607
3480	$^{109}In(p,\alpha)^{106}Cd$	5.513	3527	$^{110}Xe(\beta^+)^{110}I$	8.960
3481	$^{109}In(\gamma,\alpha)^{105}Ag$	-1.841	3528	$^{111}Te(p,\alpha)^{108}Sb$	3.966
3482	$^{109}In(\gamma,p)^{108}Cd$	-4.521	3529	$^{111}Te(p,\gamma)^{112}I$	0.938
3483	$^{109}In(\beta^+)^{109}Cd$	2.020	3530	$^{111}Te(\gamma,p)^{110}Sb$	-3.948
3484	$^{109}Sn(p,\gamma)^{110}Sb$	1.470	3531	$^{111}Te(\gamma,\alpha)^{107}Sn$	2.663
3485	$^{109}Sn(p,\alpha)^{106}In$	2.842	3532	$^{111}I(p,\alpha)^{108}Te$	5.493
3486	$^{109}Sn(\beta^+)^{109}In$	3.849	3533	$^{111}I(p,\gamma)^{112}Xe$	2.176
3487	$^{109}Sn(\gamma,\alpha)^{105}Cd$	-0.730	3534	$^{111}I(\beta^+)^{111}Te$	8.730
3488	$^{109}Sn(\gamma,p)^{108}In$	-5.819	3535	$^{111}I(\gamma,p)^{110}Te$	-0.066
3489	$^{109}Sb(p,\alpha)^{106}Sn$	6.037	3536	$^{111}I(\gamma,\alpha)^{107}Sb$	3.582
3490	$^{109}Sb(p,\gamma)^{110}Te$	3.314	3537	$^{111}Xe(p,\alpha)^{108}I$	2.953
3491	$^{109}Sb(\gamma,p)^{108}Sn$	-1.531	3538	$^{111}Xe(\gamma,\alpha)^{107}Te$	4.078
3492	$^{109}Sb(\beta^+)^{109}Sn$	6.380	3539	$^{111}Xe(\beta^+)^{111}I$	10.450
3493	$^{109}Sb(\gamma,\alpha)^{105}In$	0.801	3540	$^{111}Xe(\gamma,p)^{110}I$	-1.282
3494	$^{109}Te(p,\gamma)^{110}I$	0.594	3541	$^{112}I(p,\gamma)^{113}Xe$	2.355
3495	$^{109}Te(p,\alpha)^{106}Sb$	4.175	3542	$^{112}I(p,\alpha)^{109}Te$	5.451
3496	$^{109}Te(\alpha,\gamma)^{113}Xe$	-3.096	3543	$^{112}I(\gamma,\alpha)^{108}Sb$	3.028
3497	$^{109}Te(\alpha,p)^{112}I$	-5.451	3544	$^{112}I(\gamma,p)^{111}Te$	-0.938
3498	$^{109}Te(\beta^+)^{109}Sb$	8.682	3545	$^{112}Xe(p,\alpha)^{109}I$	2.497
3499	$^{109}Te(\gamma,\alpha)^{105}Sn$	3.225	3546	$^{112}Xe(\beta^+)^{112}I$	7.490
3500	$^{109}Te(\gamma,p)^{108}Sb$	-2.405	3547	$^{112}Xe(\gamma,p)^{111}I$	-2.176
3501	$^{109}I(p,\alpha)^{106}Te$	5.798	3548	$^{112}Xe(\gamma,\alpha)^{108}Te$	3.317
3502	$^{109}I(p,\gamma)^{110}Xe$	1.191	3549	$^{113}Xe(p,\alpha)^{110}I$	3.690
3503	$^{109}I(\alpha,p)^{112}Xe$	-2.497	3550	$^{113}Xe(\gamma,p)^{112}I$	-2.355

Table C.2: – Continued.

Number	Reaction	Energy (Mev)	Number	Reaction	Energy (Mev)
3551	$^{113}Xe(\gamma,\alpha)^{109}Te$	3.096			

Bibliography

Amthor, A. M., Galaviz, D., Heger, A., Sakharuk, A., Schatz, H., & Smith, K., 2006, *Proceedings of Science, PoS(NIC-IX) 068*

Angulo, C., Arnould, M., Rayet, M., Descouvemont, P., Baye, D., Leclercq-Willain, C., Coc, A., Barhoumi, S., Aguer, P., Rolfs, C., Kunz, R., Hammer, J. W., Mayer, A., Paradellis, T., Kossionides, S., Chronidou, C., Spyrou, K., Degi-Innocenti, S., Fiorentini, G., Ricci, B., Zavatarelli, S., Providencia, C., Wolters, H., Soares, J., Grama, C., Rahighi, J., Shotter, A., & Rachti, M. L., 1999, *Nuclear Physics A* **656**, 3

Arnould, M. & Goriely, S., 2006, *Nuclear Physics A* **777**, 157

Audi, G., Bersillon, O., Blachot, J., & Wapstra, A. H., 2003a, *Nuclear Physics A* **729**, 3

Audi, G., Wapstra, A. H., & Thibault, C., 2003b, *Nuclear Physics A* **729**, 337

Ayasli, S. & Joss, P. C., 1982, *ApJ* **256**, 637

Bahcall, J. N., Huebner, W. F., Lubow, S. H., Parker, P. D., & Ulrich, R. K., 1982, *Rev. Mod. Phys.* **54**, 767

Baym, G. & Pethick, C., 1979, *Ann. Rev. Astron. Atrophys.* **17**, 415

Belian, R. D., Conner, J. P., & Evans, W. D., 1976, *ApJ* **206**, L135

Bildsten, L., 1997, *arXiv:astro-ph/9709094*

Bildsten, L., 2000, *arXiv:astro-ph/0001135v1*

Bildsten, L., Chang, P., & Paerels, F., 2003, *ApJ* **591**, L29

Bildsten, L. & Cumming, A., 1998b, *ApJ* **506**, 842

Bildsten, L. & Cutler, C., 1995, *ApJ* **440**, 800

Bildsten, L., Salperter, E. E., & Wasserman, I., 1992, *ApJ* **384**, 143

Blackmon, J. C., Bardayan, D. W., Bradfield-Smith, W., Brummitt, R., Champagne, A. E., Chen, A. A., Davinson, T., Dessieux, L., Guidry, M. W., Hahn, K. I., Hale, G. M., Hix, W. R., Kozub, R. L., Ma, Z., Parker, P. D., Rajbaidya, G., Runkle, R. C., Rowland, C. M., Shotter, A. C., Smith, M. S., Wormer, L. A., Visser, D. W., & Woods, P. J., 2003, *Nuclear Physics A* **718**, 127

Blinnikov, S. I., Dunina-Barkovskaya, N. V., & Nadyozhin, D. K., 1996, *ApJS* **106**, 171

Boffin, H. M. J., Paulus, G., Arnould, M., & Mowlavi, N., 1993, *A&A* **279**, 173

Brown, E. F., 2004, *ApJ* **614**, L57

Brown, E. F. & Bildsten, L., 1998, *ApJ* **496**, 915

Brush, S. G., Sahlin, H. L., & Teller, E., 1996, *The Journal of Chemical Physics* **45**, 2102

Buchmann, L., 1996, *ApJ* **468**, L127

Carobbi, C. F. M., Cati, M., & Millanta, L. M., 2003

Chang, P., Bildsten, L., & Wasserman, I., 2005, *ApJ* **629**, 998

Chang, P., Morsink, S., Bildsten, L., & Wasserman, I., 2006, *ApJ* **636**, L117

Chartier, M., Gomez-Hornillos, M. B., Mittig, W., Lepine-Szily, A., Ontanaya, L. C., Demonchy, C. E., Georgiev, G., Orr, N. A., Politi, G., Rousseau, M., Roussel-Chomaz, P., & Villari, A. C. C., 2005, *Journal of Physics* **G31**, S1771

Chen, A. A., Swartz, R., Visser, K. B., Parker, D. W., & Parker, P. D., 2001, *Physical Review C* **63**, 065807

Christy, R. F., 1964, *Rev. Mod. Phys.* **36**, 555

Clark, J. A., Savard, G., Sharma, K. S., Vaz, J., Wang, J. C., Zhou, Z., Heinz, A., Blank, B., Buchinger, F., Crawford, J. E., Gulick, S., Lee, J. K. P., Levand, A. F., Seweryniak, D., Sprouse, G. D., & Trimble, W., 2004, *Physical Review Letters* **92(19)**, 192501

Clark, J. A., Savard, G., Sharma, K. S., Wang, J. C., Zhou, Z., Blank, B., Buchinger, F., Crawford, J. E., Gulick, S., Lee, J. K. P., Levand, A. F., Seweryniak, D., & Trimble, W., 2007, *Physical Review C* **75**, 032801

Coc, A., Vangioni-Flam, E., Cassé, M., & Rabiet, M., 2002, *Physical Review D* **65(4)**, 043510

Coc, A., Vangioni-Flam, E., Descouvemont, P., Adahchour, A., & Angulo, C., 2004, *ApJ* **600**, 544

Cooper, R. L., Mukhopadhyay, B., Steeghs, D., & Narayan, R., 2006, *ApJ* **642**, 443

Cooper, R. L. & Narayan, R., 2004, *American Astronomical Society* **36**, 941

Cooper, R. L. & Narayan, R., 2005, *ApJ* **629**, 422

Cornelisse, R., Heise, J., Kuulkers, E., Verbunt, F., & in't Zand, J. J. M., 2000, *A&A* **357**, L21

Cornelisse, R., in't Zand, J. J. M., Verbunt, F., Kuulkers, E., Heise, J., den Hartog, P. R., Cocchi, M., Natalucci, L., & Bazzano, A., 2003, *A&A* **405**, 105

Cottam, J., Paerels, F., & Mendez, M., 2002, *Nature* **420**, 51

Cottam, J., Paerels, F., Mendez, M., Boirin, L., Lewin, W. H. G., Kuulkers, E., & Miller, J. M., 2008, *ApJ* **672**, 504

Cumming, A., 2005, *Nuclear Physics A* **758**, 439c

Cumming, A., 2009, in *Defining the Neutron Star Crust: X-ray Bursts, Superbursts and Giant Flares*, Santa Fe

Cumming, A. & Bildsten, L., 2001, *ApJ* **559**, L127

Cumming, A., Morsink, S., Bildsten, L., Friedman, J. L., & Holz, D. E., 2002, *ApJ* **564**, 343

Damen, E., Magnier, E., Lewin, W. H. G., Tan, J., Penninx, W., & van Paradijs, J., 1990, *A&A* **237**, 103

Davids, B., van den Berg, A. M., Dendooven, P., Fleurot, F., Hunyadi, M., de Huu, M. A., Siemssen, R. H., Wilschut, H. W., Wörtche, H. J., Hernanz, M., José, J., Rehm, K. E., Wuosmaa, A. H., & Segel, R. E., 2003, *Physical Review C* **67(6)**, 065808

DeWitt, H. E., 1976, *Physical Review A* **14**, 1290

DeWitt, H. E., Graboske, H. C., & Cooper, M. S., 1973, *ApJ* **181**, 439

Elomaa, V. V., Vorobjev, G. K., Kankainen, A., Batist, L., Eliseev, S., Eronen, T., Hakala, J., Jokinen, A., Moore, I. D., Novikov, Y. N., Penttilä, H., Popov, A., Rahaman, S., Rissanen, J., Saastamoinen, A., Schatz, H., Seliverstov, D. M., Weber, C., & Äystö, J., 2009, *Physical Review Letters* **102(25)**, 252501

Falanga, M., Chenevez, J., Cumming, A., Kuulkers, E., Trap, G., & Goldwurm, A., 2008, *A&A* **484**, 43

Fisker, J. L., Görres, J., Wiescher, M. C., & Davids, B., 2006, *ApJ* **650**, 332

Fisker, J. L., Schatz, H., & Thielemann, F. K., 2008, *ApJ* **174**, 261

Fisker, J. L., Tan, W. P., Görres, J., Wiescher, M. C., & Cooper, R. L., 2007, *ApJ* **665**, 637

Fisker, J. L., Thielemann, F. K., & Wiescher, M. C., 2004, *ApJ* **608**, L61

Forstner, O., Herndl, H., Oberhummer, H., Schatz, H., & Brown, B. A., 2001, *Physical Review C* **64**, 045801

Fu, C., Goldberg, V. Z., Mukhamedzhanov, A. M., Chubarian, G. G., Rogachev, G. V., Skorodumov, B., McCleskey, M., Zhai, Y., Al-Abdullah, T., Tabacaru, G., Trache, L., & Tribble, R. E., 2007, *Physical Review C* **76**, 021603(R)

Fujimoto, M. Y., Sztajno, M., Lewin, W. H. G., & van Paradijs, J., 1988, *A&A* **199**, L9

Fuller, G. M., Fowler, W. A., & Newman, M. J., 1982a, *ApJ* **252**, 715

Fuller, G. M., Fowler, W. A., & Newman, M. J., 1982b, *ApJ* **48**, 279

Galloway, D. K., Muno, M. P., Hartman, J. M., Psaltis, D., & Chakrabarty, D., 2008, *ApJS* **179**, 360

Goriely, S., 1998, N. Prantzos and S. Harissopulos (eds.), Editions Frontieres

Görres, J., Wiescher, M., & Thielemann, F. K., 1995, *Physical Review C* **51**, 392

Graboske, H. C., DeWitt, H. E., Grossman, A. S., & Cooper, M. S., 1973, *ApJ* **181**, 457

Grindlay, J., Gursky, H., Schnopper, H., Parsignault, D. R., Heise, J., Brinkman, A. C., & Schrijver, J., 1976, *ApJ* **205**, L127

Groombridge, D., Shotter, A. C., Bradfield-Smith, W., Cherubini, S., Davinson, T., Di Pietro, A., Görres, J., Graulich, J. S., Laird, A. M., Leleux, P., Musumarra, A., Ninane, A., Ostrowski, A. N., Rahighi, J., Schatz, H., Wiescher, M., & Woods, P. J., 2002, *Physical Review C* **66**, 055802

Guardiola, R., Higón, E., & Ros, J., 1995, Universitat de València, València

Hahn, K. I., García, A., Adelberger, E. G., Magnus, P. V., Bacher, A. D., Bateman, N., Berg, G. P. A., Blackmon, J. C., Champagne, A. E., Davids, B., Howard, A. J., Liu, J., Lund, B., Mao, Z. Q., Markoff, D. M., Parker, P. D., Smith, M. S., Stephenson, E. J., Swartz, K. B., Utku, S., Vogelaar, R. B., & Yildiz, K., 1996, *Physical Review C* **54**, 1999

Hanawa, T., Sugimoto, D., & Hashimoto, M. A., 1983, *PASJ* **35**, 491

Hansen, C. J. & Van Horn, H. M., 1975, *ApJ* **195**, 735

Hansen, J. P., Torrie, G. M., & Vieillefosse, P., 1977, *Physical Review A* **16**, 2153

He, J. J., Kubono, S., Teranishi, T., Hu, J., Notani, M., Baba, H., Nishimura, S., Moon, J. Y., Nishimura, M., Iwasaki, H., Yanagisawa, Y., Hokoiwa, N., Kibe, M., Lee, J. H., Kato, S., Gono, Y., & Lee, C. S., 2009, *Physical Review C* **80**, 015801

He, J. J., Kubono, S., Teranishi, T., Notani, M., Baba, H., Nishimura, S., Moon, J. Y., Nishimura, M., Michimasa, S., Iwasaki, H., Yanagisawa, Y., Hokoiwa, N., Kibe, M., Lee, J. H., Kato, S., Gono, Y., & Lee, C. S., 2008, *European Physical Journal A* **36**, 1

Heger, A., Cumming, A., Galloway, D. K., & Woosley, S. E., 2007, *ApJ* **671**, L141

Henyey, L. G., Forbes, E., & Gould, N. L., 1964, *ApJ* **139**, 306

Herndl, H., Görres, J., Wiescher, M., Brown, B. A., & van Wormer, L., 1995, *Physical Review C* **52**, 1078

Hix, W. R., Smith, M. S., Mezzacappa, A., Starrfield, S., & Smith, D. L., 2000, *arXiv:astro-ph/0001487v1*

Hix, W. R., Smith, M. S., Mezzacappa, A., Starrfield, S., & Smith, D. L., 2002, E. Brown, J. Niemeyer, R. Rosner and J. Truran (eds.), University Chicago Press

Hix, W. R., Smith, M. S., Mezzacappa, A., Starrfield, S., & Smith, D. L., 2003, *Nuclear Physics A* **718**, 620

Hoffman, J. A., Marshall, H. L., & Lewin, W. H. G., 1978, *Nature* **271**, 630

Iliadis, C., 2007, Wiley-VCH (eds.)

Iliadis, C., Champagne, A., José, J., Starrfield, S., & Tupper, P., 2002, *ApJS* **142**, 105

Iliadis, C., D'Auria, J. M., Starrfield, S., Thompson, W. J., & Wiescher, M., 2001, *ApJ* **134**, 151

Iliadis, C., Endt, P. M., Prantzos, N., & Thompson, W. J., 1999, *ApJ* **524**, 434

in 't Zand, J. J. M., Cornelisse, R., & Cumming, A., 2004, *A&A* **426**, 257

in 't Zand, J. J. M., Keek, A., Heger, A., Cumming, A., & Weinberg, N., 2009, in *Defining the Neutron Star Crust: X-ray Bursts, Superbursts and Giant Flares*, Santa Fe

Izzard, R. G., Lugaro, M., Karakas, A. I., & van Raai, M., 2007, *A&A* **466**, 641

Jonker, P. G., Galloway, D. K., McClintock, J. E., Buxton, M., Garcia, M., & Murray, S., 2004, *MNRAS* **354**, 666

Jordan, G., Gupta, S., & Meyer, B., 2003, *Physical Review C* **68**, 065801

José, J., 1996, *Ph.D. thesis*, University of Barcelona

José, J. & Hernanz, M., 1998, *ApJ* **494**, 680

José, J. & Moreno, F., 2006, *Proceedings of Science, PoS(NIC-IX) 123*

Joss, P. C., 1977, *Nature* **270**, 310

Joss, P. C., 1978, *ApJ* **225**, L123

Kippenhahn, R., Weiger, A., & Hofmeister, E., 1967, *Methods in Computional Physics* **7**, 129

Koike, O., Hashimoto, M., Arai, K., & Wanajo, S., 1999, *A&A* **342**, 464

Koike, O., Hashimoto, M., Kuromizu, R., & Fujimoto, S., 2004, *ApJ* **603**, 242

Kong, A. K. H., Miller, J. M., Mendez, M., Cottam, J., NewAuthor4, Paerels, F., Kuulkers, E., Wijnands, R., & van der Klis, M., 2007, *ApJ* **670**, L17

Krauss, L. M. & Romanelli, P., 1990, *ApJ* **358**, 47

Kunz, R., Fey, M., Jaeger, M., Mayer, A., & Hammer, J. W., 2002, *ApJ* **567**, 643

Kutter, G. S. & Sparks, W. M., 1972, *ApJ* **175**, 407

Kutter, G. S. & Sparks, W. M., 1980, *ApJ* **239**, 988

Kuulkers, E., 2004, *Nuclear Physics B* **132**, 466

Kuulkers, E., den Hartog, P. R., in't Zand, J. J. M., Verbunt, F. W. M., Harris, W. E., & Cocchi, M., 2003, *A&A* **399**, 663

Kuulkers, E., in't Zand, J. J. M., van Kerkwijk, M. H., Cornelisse, R., Smith, D. A., Heise, J., Bazzano, A., Cocchi, M., Natalucci, L., & Ubertini, P., 2002, *A&A* **382**, 503

Langanke, K. & Martínez-Pinedo, G., 2000, *Nuclear Physics A* **673**, 481

Lattimer, J. M., 2009, *private communication*

Lattimer, J. M. & Prakash, M., 2004, *Science* **304**, 536

Lattimer, J. M. & Prakash, M., 2006, *Nuclear Physics A* **777**, 479

Lattimer, J. M. & Prakash, M., 2007, *Physics Reports* **442**, 109

Lewin, W. H. G., 1977, *Ann. New York Acad. Sci.* **302**, 210

Lewin, W. H. G., Clark, G., & Doty, J., 1976a, *IAUC* **2922**, 1

Lewin, W. H. G., Doty, J., Clark, G. W., Rappaport, S. A., Bradt, H. V. D., Doxsey, R., Hearn, D. R., Hoffman, J. A., Jernigan, J. G., Li, F. K., Mayer, W., McClintock, J., Primini, F., & Richardson, J., 1976b, *ApJ* **207**, L95

Lewin, W. H. G., van Paradijs, J., & Taam, R. E., 1993, *Space Science Review* **62**, 223

Limpert, E., Stahel, W., & Abbt, M., 2001, *BioScience* **51(5)**, 341

Liu, Q. Z., van Paradijs, J., & van den Heuvel, E. P. J., 2007, *A&A* **469**, 807

Lotay, G., Woods, P. J., Seweryniak, D., Carpenter, M. P., Janssens, R. V. F., & Zhu, S., 2009, *Physical Review Letters* **102(16)**, 162502

MacAlpine, G. M., Ecklund, T. C., Lester, W. R., & Vanderveer, S. J., 2007, *AJ* **133**, 81

Manchester, R. N. & Taylor, J. H., 1977, *Pulsars*, San Francisco: Freeman

Maraschi, L. & Cavaliere, A., 1977, Vol. 4, p. 127, E. A., Müller

May, M. M. & White, R. H., 1967, *Hydrodynamic Calculations of General Relativistic Collapse*, pp 96–+

Miralda-Escudé, J., Paczynski, B., & Haensel, P., 1990, *ApJ* **362**, 572

Narayan, R. & Heyl, J. S., 2003, *ApJ* **599**, 419

Notani, M., Kubono, S., Teranishi, T., Yanagisawa, Y., Michimasa, S., Ue, K., He, J. J., Iwasaki, H., Baba, H., Tamaki, M., Minemura, T., Shimoura, S., Hokoiwa, N., Wakabayashi, Y., Sasaki, T., Fukuchi, T., Odahara, A., Gono, Y., Fülöp, Z., Lee, E. K., Hahn, K. I., Moon, J. Y., Yun, C. C., Lee, J. H., Lee, C. S., & Kato, S., 2004a, *Nuclear Physics A* **738**, 411

Notani, M., Kubono, S., Teranishi, T., Yanagisawa, Y., Michimasa, S., Ue, K., He, J. J., Iwasaki, H., Baba, H., Tamaki, M., Minemura, T., Shimoura, S., Hokoiwa, N., Wakabayashi, Y., Sasaki, T., Fukuchi, T., Odahara, A., Gono, Y., Fülöp, Z., Lee, E. K., Hahn, K. I., Moon, J. Y., Yun, C. C., Lee, J. H., Lee, C. S., & Kato, S., 2004b, *Nuclear Physics A* **746**, 113c

Ogata, S. & Ichimaru, S., 1987, *Physical Review A* **36**, 5451

Paczyński, B., 1983, *ApJ* **264**, 282

Page, D. & Cumming, A., 2005, *ApJ* **635**, L157

Parikh, A., José, J., Iliadis, C., Moreno, F., & Rauscher, T., 2009, *Nuclear Physics C* **79(4)**, 045802

Penninx, W., Damen, E., van Paradijs, J., Tan, J., & Lewin, W. H. G., 1989, *A&A* **208**, 146

Pietsch, W. & Haberl, F., 2005, *A&A* **430**, L45

Pollock, E. L. & Hansen, J. P., 1973, *Physical Review A* **8**, 3110

Potter, D., 1973, John Wiley and Sons (eds.)

Prantzos, N., Arnould, M., & Arcoragi, J. P., 1987, *ApJ* **315**, 209

Prialnik, D., Shara, M. M., & Shaviv, G., 1979, *A&A* **72**, 192

Rauch, T., Suleimanov, V., & Werner, K., 2008, *A&A* **490**, 1127

Rauscher, T. & Thielemann, F. K., 2000, *Atomic Data and Nuclear Data Tables* **75**, 1

Rhoades, C. E. & Ruffini, R., 1974, *Physical Review Letters* **32**, 324

Richtmyer, R. D. & Morton, K. W., 1994, Krieger Pub Co, 2 edition edition

Roberts, L. F., Hix, W. R., Smith, M. S., & Fisker, J. L., 2006, *Proceedings of Science, PoS(NIC-IX) 202*

Rodríguez, D., Kolhinen, V. S., Audi, G., Äystö, J., Beck, D., Blaum, K., Bollen, G., Herfurth, F., Jokinen, A., Kellerbauer, A., Kluge, H. J., Oinonen, M., Schatz, H., Sauvan, E., & Schwarz, S., 2004, *Physical Review Letters* **93**, 161104

Ruiz, C., Parikh, A., José, J., Buchmann, L., Caggiano, J. A., Chen, A. A., Clark, J. A., Crawford, H., Davids, B., D'Auria, J. M., Davis, C., Deibel, C., Erikson, L., Fogarty, L., Frekers, D., Greife, U., Hussein, A., Hutcheon, D. A., Huyse, M., Jewett, C., Laird, A. M., Lewis, R., Mumby-Croft, P., Olin, A., Ottewell, D. F.,

Ouellet, C. V., Parker, P., Pearson, J., Ruprecht, G., Trinezek, M., Vockenhuber, C., & Wrede, C., 2006, *Physical Review Letters* **96**, 252501

Salperter, E. E., 1954, *Australian Journal of Physics* **7**, 373

Schatz, H., 2006, *Proceedings of Science, PoS(NIC-IX) 002*

Schatz, H., Aprahamian, A., Barnard, V., Bildsten, L., Cumming, A., Ouellette, M., Rauscher, T., Thielemann, F. K., & Wiescher, M., 2001, *Physical Review Letters* **86(16)**, 3471

Schatz, H., Aprahamian, A., Görres, J., Wiescher, M., Rauscher, T., Rembges, J. F., Thielemann, F. K., Pfeiffer, B., Möller, P., Kratz, K. L., Herndl, H., Brown, B. A., & Rebel, H., 1998, *Physics Reports* **294**, 167

Schatz, H., Bildsten, L., & Cumming, A., 2003, *ApJ* **583**, L87

Schatz, H., Bildsten, L., Cumming, A., & Wiescher, M., 1999, *ApJ* **524**, 1014

Schatz, H., Görres, J., Herndl, H., Kaloskamis, N. I., Stech, E., Tischhauser, P., Wiescher, M., Bacher, A., Berg, G. P. A., Black, T. C., Choi, S., Foster, C. C., Jiang, K., & Stephenson, E. J., 1997, *Physical Review Letters* **79(20)**, 3845

Schatz, H. & Rehm, K. E., 2006, *Nuclear Physics A* **777**, 601

Schury, P., Bachelet, C., Block, M., Bollen, G., Davies, D. A., Facina, M., Folden III, C. M., Guénaut, C., Huikari, J., Kwan, E., Kwiatkowski, A., Morrissey, D. J., Ringle, R., Pang, G. K., Prinke, A., Savory, J., Schatz, H., Schwarz, S., Sumithrarachchi, C. S., & Sun, T., 2007, *Physical Review C* **75**, 055801

Shapiro, S. L. & Teukolsky, S. A., 1983, Wiley-Interscience, 1 edition edition

Slattery, W. L., Doolen, G. D., & DeWitt, H. E., 1980, *Physical Review A* **21**, 2087

Slattery, W. L., Doolen, G. D., & DeWitt, H. E., 1982, *Physical Review A* **26**, 2255

Smale, A. P., 2001, *ApJ* **562**, 957

Smith, M. S., Hix, W. R., Parete-Koon, S., Dessieux, L., Guidry, M. W., Bardayan, D. W., Starrfield, S., Smith, D. L., & Mezzacappa, A., 2002, M. Hernanz and J. José (eds.), New York: AIP

Smith, M. S., Kawano, L. H., & Malaney, R. A., 1993, *ApJS* **85**, 219

Strohmayer, T. & Bildsten, L., 2003, *arXiv:astro-ph/0301544v2*

Strohmayer, T. & Brown, E. F., 2002, *ApJ* **566**, 1045

Taam, R. E., 1980, *ApJ* **241**, 358

Taam, R. E., 1985, *Ann. Rev. Nucl. Part. Sci.* **35**, 1

Taam, R. E. & Picklum, R. E., 1978, *ApJ* **224**, 210

Taam, R. E., Woosley, S. E., & Lamb, D. Q., 1996, *ApJ* **459**, 271

Taam, R. E., Woosley, S. E., Weaver, T. A., & Lamb, D. Q., 1993, *ApJ* **413**, 324

Tan, W. P., Fisker, J. L., Görres, J., Couder, M., & Wiescher, M. C., 2007, *Physical Review Letters* **98**, 242503

The, L. S., Clayton, D. D., Jin, L., & Meyer, B. S., 1998, *ApJ* **504**, 500

Thielemann, F. K., Brachwitz, F., Freiburghaus, C., Kolbe, E., Martínez-Pinedo, G., Rauscher, T., Rembges, F., Hix, W. R., Liebendoerfer, M., Mezzacappa, A., Kratz, K. L., Pfeiffer, B., Langanke, K., Nomoto, K., Rosswog, S., Schatz, H., & Wiescher, M., 2001, *Prog. Part. Nucl. Phys.* **46**, 5

Thorsett, S. E., Arzoumanian, Z., McKinnon, M. M., & Taylor, J. H., 1993, *ApJ* **405**, L29

Thorsett, S. E. & Chakrabarty, D., 1999, *ApJ* **512**, 288

Tur, C., Austin, S. M., Wuosmaa, A., Lighthall, J., Marley, S., Goodman, N., & Bos, J. J., 2006, *Proceedings of Science, PoS(NIC-IX) 050*

van Paradijs, J., Penninx, W., & Lewin, W. H. G., 1998, *MNRAS* **223**, 437

Villarreal, A. R. & Strohmayer, T., 2004, *ApJ* **614**, L121

Vogelaar, R. B., 1989, *Ph.D. thesis*, California Institute of Technology

von Newmann, J. & Richtmyer, R. D., 1950, *J. Appl. Phys.* **21**, 232

Wagoner, R. W., 1969, *ApJS* **18**, 247

Waki, I., Inoue, H., Koyama, K., Matsuoka, M., Murakami, T., Ogawara, Y., Ohashi, T., Tanaka, Y., Hayakawa, S., Tawara, Y., Miyamoto, S., Tsunemi, H., & Kondo, I., 1984, *Publ. Astron. Soc. Japan* **36**, 819

Wallace, R. K. & Woosley, S. E., 1981, *ApJS* **45**, 389

Wallace, R. K. & Woosley, S. E., 1984, S. E. Woosley (ed.), New York: AIP

Watts, A. L. & Maurer, I., 2007, *A&A* **467**, L33

Weinberg, N. & Bildsten, L., 2007, *ApJ* **670**, 1291

Weinberg, N., Bildsten, L., & Brown, E. F., 2006a, *ApJ* **650**, L199

Weinberg, N., Bildsten, L., & Schatz, H., 2006b, *ApJ* **639**, 1018

White, N. E., Nagase, F., & Parmar, A. N., 1995, in *X-ray binaries*, pp 1–57

Wijnands, R., 2001, *ApJ* **554**, L59

Wöhr, A., Aprahamian, A., Boutachkov, P., Galache, J. L., Görres, J., Shawcross, M., Teymurazyan, A., Wiescher, M., Brenner, D. S., Davids, C. N., Fischer, S. M., Heinz, A., Janssens, R. V. F., & Seweryniak, D., 2004, *Nuclear Physics A* **742**, 349

Woosley, S. E., Heger, A., Cumming, A., Hoffman, R. D., Pruet, J., Rauscher, T., Fisker, J. L., Schatz, H., Brown, B. A., & Wiescher, M., 2004, *ApJS* **151**, 75

Woosley, S. E. & Taam, R. E., 1976, *Nature* **263**, 101

Woosley, S. E. & Weaver, T. A., 1984, S. E. Woosley (ed.), New York: AIP

Yakovlev, D. G. & Shalybkov, D. A., 1989, *Soviet Scientific Reviews E: Astrophysics and Space Physics Reviews* **7**, 311